Development, implementation and application of kinematic hardening models for overconsolidated clays



by

Angeliki Grammatikopoulou

Dipl.(Eng.), MSc, DIC

June 2004

A thesis submitted to the University of London (Imperial College)
in partial fulfilment of the requirements for the degree of
Doctor of Philosophy in the Faculty of Engineering

Abstract

The pre-failure behaviour of overconsolidated clays is now well known to be highly non-linear and inelastic. Conventional constitutive soil models fail to predict this observed behaviour and recently a family of elasto-plastic soil models, the kinematic hardening models, has been developed to overcome these limitations. The kinematic hardening models allow for plasticity and non-linearity to be invoked within the conventionally defined yield surface, through the introduction of kinematic surfaces. The aim of this thesis is to improve the predictions of the behaviour of overconsolidated clays, particularly the pre-failure behaviour, through the study of elasto-plastic constitutive models based on this concept.

Two existing kinematic hardening models, formulated within the framework of critical state soil mechanics, were chosen to be implemented into the Imperial College Finite Element Program (ICFEP), the two-surface model developed by Al-Tabbaa (1987), and the three-surface model developed by Stallebrass (1990). Both models were generalised in order to make their implementation into a finite element code possible.

Although these models form a substantial improvement in modelling the behaviour of overconsolidated clays they cannot predict a smooth transition from elastic to elasto-plastic behaviour. This feature of behaviour, which proves to be an important drawback when simulating pre-failure non-linearity, was improved by changing the hardening modulus of each model and in this way two new generalised models were formulated.

The implementation of the four models into ICFEP was validated through a number of single finite element analyses. The performance of the models was then evaluated through simulation of a series of laboratory tests on overconsolidated clays and comparison of the predictions with experimental data, where possible. The models were further used in the finite element analyses of two boundary value problems. The first of these modelled an embankment founded on a soft clay deposit. The second boundary value problem involved the analyses of tunnels excavated within the heavily overconsolidated London Clay. An analysis of the twin tunnels beneath St. James's Park, London, constructed as part of the Jubilee Line Extension of the London Underground network, is also presented. The predictions of the models were compared with field data, where available.

Acknowledgements

First, I would like to thank my supervisors Dr. L. Zdravkovic and Prof. D.M. Potts for initially giving me the chance to do research and then guiding me and assisting me throughout the period of this work.

The research presented in this thesis was funded in the first stages by the Soil Mechanics section at Imperial College and the last stages by the Engineering and Physical Science Research Council (EPSRC). Their support is gratefully acknowledged.

Many thanks are due to the academic staff in the Soil Mechanics section, who have contributed in this thesis, and especially Prof. R.J. Jardine and Prof. D.W. Hight for providing test data on London Clay and Dr. M. Coop for useful soil mechanics discussions.

Being part of the research group in the Soil Mechanics section at Imperial College has been a great experience. I would like to thank all the people that made the environment friendly and lively. Special thanks are due to Felix, Reinaldo, Niki and particularly Kostis, for not only being friends from the very beginning but also helping me in my work in numerous ways. I would also like to thank the friends that I have made during the last stages of my time at Imperial College, Liana, Alessandra and especially my flatmate Stavroula for making my last years so fun.

It would not be possible to express here my gratitude to my Stuart for his help, love and support throughout my work, and most importantly for being who he is. Thank you for always being there for me.

Finally, my last thanks go to my family, for loving me, supporting me and encouraging me in everything I have done in life, and especially my sister without whom I would never have completed this thesis.

Table of contents

Abstract 2

Acknowledgments 3

Table of contents 4

List of figures 13

List of tables 30

Chapter 1

Introduction 34

1.1 General 34

1.2 Aims of research 35

1.3 Outline of thesis 36

1.4 Definitions of stress and strain variables 38

Chapter 2

Literature review 45

2.1 Introduction 45

2.2 Pre-failure deformation of overconsolidated clays 45

2.2.1 Introduction 45

2.2.2 Critical state framework 46

2.2.2.1 Limitations of the critical state framework 50

2.2.3 Realisation of non-linearity 51

2.2.4 Simplified schemes of pre-failure behaviour 53

2.2.4.1 Existence of linear elastic region 56

2.2.5 Factors that affect soil stiffness 59

2.2.5.1 Current stress state-volume state 59

2.2.5.2 Soil structure 63

2.2.5.3 Ageing 66

2.2.5.4 Recent stress history 68

2.2.5.5 Stress path direction 72

2.3 Constitutive models for overconsolidated clays 77
2.3.1 Introduction 77
2.3.2 Classical theory of elasto-plasticity 77
2.3.2.1 Basic concepts 77
2.3.2.2 Formulation of the elasto-plastic constitutive matrix 80
2.3.3 Elasto-plastic constitutive models 81
2.3.3.1 Models based on the classical theory of elasto-plasticity 82
2.3.3.2 Models based on extensions of the classical theory of elasto-plasticity 85
2.3.3.3 Other models 94
2.4 Summary 96

Chapter 3

The finite element method 98

3.1 Introduction 98
3.2 Finite element theory for linear materials 99
3.2.1 Element discretisation 99
3.2.2 Primary variable approximation 99
3.2.3 Element equations 101
3.2.3.1 Numerical integration 103
3.2.4 Global equations 105
3.2.5 Boundary conditions 105
3.2.6 Solution of global equations 105
3.3 Geotechnical considerations 106
3.3.1 Pore water pressure considerations 106
3.3.1.1 Undrained analysis 106
3.3.1.2 Drained analysis 108
3.4 Finite element theory for non-linear materials 108
3.4.1 The modified Newton-Raphson method 109
3.4.1.1 Stress point alogorithm 111
3.5 Summary 113

Chapter 4

Two-surface model 114

4.1 Introduction 114

4.2 Modified Cam Clay model 115

4.3 Original formulation in triaxial stress space 118

4.3.1 Introduction 118

4.3.2 Equations of the surfaces 118

4.3.3 Flow rule 119

4.3.4 Hardening rules 119

4.3.4.1 Isotropic hardening of the bounding surface 119

4.3.4.2 Translation rule of the kinematic yield surface 120

4.3.5 Hardening modulus 121

4.3.6 Elastic part of the model 124

4.3.7 Model parameters 125

4.3.8 Discussion 126

4.4 Formulation in general stress space 127

4.4.1 Introduction 127

4.4.1.1 Stress and strain variables 128

4.4.1.2 Yield and plastic potential surfaces in the deviatoric plane 128

4.4.1.3 Translation rule for the case that the two surfaces are in contact 129

4.4.2 Notation 130

4.4.3 Equations of the surfaces 130

4.4.4 Flow rule 133

4.4.5 Hardening rules 134

4.4.5.1 Isotropic hardening of the bounding surface 134

4.4.5.2 Translation rules of the kinematic yield surface 134

4.4.6 Hardening modulus 136

4.4.7 Elastic part of the model 138

4.4.8 Overview of the model 139

4.4.9 Model parameters 140

4.5 Implementation 141

4.5.1 Introduction 141

4.5.2 Calculation of the partial derivatives of the yield function 142

4.5.3 Calculation of the partial derivatives of the plastic potential

function 145
4.5.4 Calculation of the hardening modulus, A 146
4.5.5 Calculation of the elastic constitutive matrix, $[D']$ 146
4.5.6 Calculation of the changes in hardening parameters 147
4.6 Validation 148
4.6.1 Introduction 148
4.6.2 Comparison with stress paths from Al-Tabbaa (1987) 148
4.6.3 Different yield and plastic potential surfaces in the deviatoric plane 161
4.6.4 Stress paths involving rotation of the principal stresses 168
4.6.5 Elasto-plastic transition 173
4.7 Summary 175

Chapter 5

Three-surface model **177**

5.1 Introduction 177
5.2 Original formulation in triaxial stress space 178
5.2.1 Introduction 178
5.2.2 Equations of the surfaces 178
5.2.3 Flow rule 179
5.2.4 Hardening rules 179
5.2.4.1 Isotropic hardening of the bounding surface 180
5.2.4.2 Translation rules for the history surface 180
5.2.4.3 Translation rules for the yield surface 182
5.2.5 Hardening modulus 183
5.2.6 Elastic part of the model 187
5.2.7 Model parameters 187
5.2.8 Discussion 189
5.3 Formulation in general stress space 190
5.3.1 Introduction 190
5.3.1.1 Stress and strain variables 190
5.3.1.2 Yield and plastic potential surfaces in the deviatoric plane 191
5.3.1.3 Concept of changing the active yield surface 191
5.3.2 Equations of the surfaces 192

5.3.3 Flow rule 194
5.3.4 Hardening rules 195
5.3.4.1 Isotropic hardening of the bounding surface 195
5.3.4.2 Translation rules for the history surface 195
5.3.4.3 Translation rules for the yield surface 197
5.3.5 Hardening modulus 198
5.3.6 Elastic part of the model 202
5.3.7 Overview of the model 203
5.3.8 Model parameters 204
5.4 Implementation 205
5.4.1 Introduction 205
5.4.2 Calculation of the partial derivatives of the yield function 205
5.4.3 Calculation of the partial derivatives of the plastic potential function 208
5.4.4 Calculation of the hardening modulus, A 209
5.4.5 Calculation of the elastic constitutive matrix, $[D']$ 211
5.4.6 Calculation of the changes in hardening parameters 211
5.5 Validation 212
5.5.1 Introduction 212
5.5.2 Comparison with stress paths from Stallebrass (1990) 212
5.5.3 Different yield and plastic potential surfaces in the deviatoric plane 220
5.5.4 Elasto-plastic transition 222
5.6 Summary 227

Chapter 6

Modified two- and three-surface models **229**

6.1 Introduction 229
6.2 Modified two-surface model 229
6.2.1 Introduction 229
6.2.2 Original hardening modulus of the two-surface model 230
6.2.3 Investigating a new hardening function 232
6.2.4 Proposed hardening modulus for the modified two-surface model 237
6.2.5 Model parameters 240

6.2.6 Implementation 241
6.2.7 General characteristics 242
6.2.7.1 Elasto-plastic transition and non-linearity 242
6.3 Modified three-surface model 244
6.3.1 Introduction 244
6.3.2 Proposed hardening modulus 245
6.3.3 Model parameters 251
6.3.4 Implementation 252
6.3.5 General characteristics of the model 254
6.3.5.1 Elasto-plastic transition and non-linearity 255
6.4 Summary 255

Chapter 7

Evaluation **257**

7.1 Introduction 257
7.2 Modelling triaxial tests on reconstituted London Clay 257
7.2.1 Introduction 257
7.2.2 Model parameters 258
7.2.3 Evaluation of the models' predictions 277
7.2.3.1 Two-surface model 278
7.2.3.2 Modified two-surface model 283
7.2.3.3 Three-surface model 283
7.2.3.4 Modified three-surface model 286
7.2.4 Summary 289
7.3 Modelling the effect of recent stress history 290
7.3.1 Introduction 290
7.3.2 Model parameters 290
7.3.3 Evaluation of the models' predictions 292
7.3.3.1 Two-surface model 292
7.3.3.2 Modified two-surface model 296
7.3.3.3 Three-surface model 298
7.3.3.4 Modified three-surface model 300
7.3.4 Summary 303
7.4 Modelling the effect of stress path direction 304

7.4.1 Introduction 304
7.4.2 Model parameters 306
7.4.3 Evaluation of the models' predictions 306
7.4.4 Summary 311
7.5 Summary 312

Chapter 8

Analysis of an embankment on soft clay using the kinematic hardening models 313

8.1 Introduction 313
8.2 Boundary value problem analysed 313
8.2.1 Ground conditions at Saint-Alban 314
8.2.2 Geometry and construction of test embankment A 315
8.3 Previous finite element analyses of test embankment A 316
8.4 Constitutive models used in the analyses 318
8.4.1 Clay deposit 318
8.4.2 Fill material 319
8.5 Pre-failure behaviour of the embankment 319
8.5.1 Introduction 319
8.5.2 Analyses with kinematic hardening models and modified Cam Clay model 320
8.5.2.1 Introduction 320
8.5.2.2 Analyses details 320
8.5.2.3 Model parameters 321
8.5.2.4 Analyses results 329
8.5.3 Analyses with kinematic hardening models and K_o = 1.0 340
8.5.3.1 Introduction 340
8.5.3.2 Analyses details 340
8.5.3.3 Model parameters 341
8.5.3.4 Analyses results 344
8.6 The effect of the deviatoric shapes on the failure height of the embankment 347
8.6.1 Introduction 347

8.6.2 Analyses details 347
8.6.3 Model parameters 348
8.6.4 Analyses results 350
8.7 Summary and conclusions 352

Chapter 9

The behaviour of kinematic hardening models in tunnelling problems 356

9.1 Introduction 356
9.2 Constitutive models in tunnelling problems 356
9.3 Geometry of the problem 360
9.4 Constitutive models used in the analyses 360
9.4.1 London Clay 360
9.4.2 Terrace Gravel 363
9.4.3 Made Ground/Alluvium 363
9.5 Analyses of a tunnel in London Clay 364
9.5.1 Introduction 364
9.5.2 Model parameters 365
9.5.3 Analyses details 367
9.5.4 Analyses results 372
9.5.4.1 Sets 1 and 2 - Effect of the configuration of the kinematic surfaces 372
9.5.4.2 Sets 1, 2 and 5 – Comparison with the non-linear model J4 383
9.5.4.3 Sets 3 and 5 - Effect of K_o profile 386
9.5.4.4 Set 4 – Effect of rate of decay of stiffness 392
9.6 Analyses of the twin tunnels at St. James's Park 394
9.6.1 Introduction 394
9.6.2 Model parameters 394
9.6.3 Analyses details 398
9.6.4 Analyses results 400
9.6.4.1 Westbound tunnel 400
9.6.4.2 Eastbound tunnel 404
9.7 Summary and conclusions 406

Chapter 10

Summary and conclusions **411**

10.1 Introduction 411

10.2 Typical characteristics of overconsolidated clays 412

10.3 Kinematic hardening models 412

10.4 Evaluation of the kinematic hardening models 415

10.5 The use of kinematic hardening models in the analyses of an embankment 417

10.6 The use of kinematic hardening models in tunnelling problems 419

10.7 Recommendations for further research 423

10.7.1 Experimental studies 423

10.7.2 Evaluation of kinematic hardening models 423

10.7.3 Numerical studies 424

10.7.4 Constitutive modelling 424

References **426**

Appendix I

Calculation of the derivatives $\{\partial Q/\partial s\}$ and $\{\partial \det(s\text{-}s_a)/\partial s\}$ **439**

Appendix II

Flowchart for the two-surface model **442**

Appendix III

Undrained strength for the two- and three- surface models **447**

Appendix IV

Flowchart for the three-surface model **451**

Appendix V

Flowchart for the modified two-surface model **458**

Appendix VI

Flowchart for the modified three-surface model **463**

List of figures

Figure 1.1: a) Principal stress space and b) deviatoric plane (figure after Potts and Zdravkovic (1999)) 40

Figure 2.1: Isotropic compression line, swelling line and critical state line 47

Figure 2.2: State boundary surface of the critical state framework in normalised stress space (after Atkinson and Bransby (1978)) 48

Figure 2.3: State boundary surface of the critical state framework in v-p'-q space (after Atkinson and Bransby (1978)) 48

Figure 2.4: Elastic wall (after Atkinson and Bransby (1978)) 49

Figure 2.5: Variation of the undrained Young's modulus, E_u, with mean effective stress for a number of sites on London Clay (after St. John (1975)) 51

Figure 2.6: Typical London Clay unconsolidated undrained test data from Canons Park a) initial stress-strain behaviour; b) stiffness-strain characteristics (after Jardine et al. (1985)) 52

Figure 2.7: An idealisation for the variation of stiffness with strain for soil (after Atkinson and Sallfors (1991)) 54

Figure 2.8: Scheme of kinematic strain regions (after Jardine (1992)) 54

Figure 2.9: Movement and evolution of kinematic strain regions due to K_o swelling: Magnus till (after Jardine (1992)) 55

Figure 2.10: Comparison between shear stiffness obtained in resonant column and undrained triaxial compression tests: Vallericca clay (after Georgiannou et al. (1991)) 57

Figure 2.11: Initial portion of stiffness-strain curves for three geomaterials (after Clayton and Heymann (2001)) 57

Figure 2.12: Undrained stress-strain response of undisturbed Tokyo Bay Clay and reconstituted kaolin a) stress paths b) stress-strain curve of isotropically consolidated kaolin (c) stress-strain curve of anisotropically consolidated kaolin d) stress-strain curve of anisotropically consolidated Tokyo Bay Clay (after Tatsuoka and Shibuya (1992)) 58

Figure 2.13: Definition of isotropic overconsolidation ratio 61

Figure 2.14: Variation of stiffness parameters A, n and m with plasticity index (after Viggiani and Atkinson (1995)) 62

Figure 2.15: Effects of strain on stress level exponent n (after Jardine (1995)) 62

Figure 2.16: Variation of the parameters A and n with strain (after Viggiani and Atkinson (1995)) 63

Figure 2.17: Vallericca clay: initial shear modulus versus a) mean effective stress and b) specific volume (after Rampello and Silvestri (1993)) 64

Figure 2.18: Vallericca clay: initial shear modulus normalised by a) the intrinsic and b) the appropriate equivalent pressure (after Rampello and Silvestri (1993)) 64

Figure 2.19: Normalised shear stiffness of both natural and reconstituted Pappadai clay (after Cotecchia and Chandler (1997)) 65

Figure 2.20: The effect of creep on the yield stress of normally consolidated clay (after Bjerrum (1967)) 66

Figure 2.21: The effect of cementation on the yield stress of normally consolidated clay (after Bjerrum (1967)) 67

Figure 2.22: The effect of ageing on the yield stress of normally consolidated clay (redrawn by Burland (1990) after Leonards and Ramiah (1959)) 68

Figure 2.23: Stress paths followed in constant p' tests (after Atkinson et al. (1990)) 69

Figure 2.24: Stiffness of reconstituted London Clay versus strain measured in constant p' tests (after Atkinson et al. (1990)) 69

Figure 2.25: Undrained compression stiffness of natural Bothkennar Clay for two different reconsolidation paths (after Smith (1992)) 70

Figure 2.26: Stress paths followed in a single sample of natural Bothkennar Clay (after Clayton and Heymann (2001)) 71

Figure 2.27: Stiffness versus strain for a single Bothkennar Clay specimen subjected to three identical repeated loading paths (after Clayton and Heymann (2001)) 72

Figure 2.28: Stress paths applied to a) Bothkennar Clay and b) London Clay (after Clayton and Heymann (2001)) 73

Figure 2.29: Bothkennar clay: normalised stiffness versus strain from

undrained triaxial compression and extension tests (after Clayton and Heymann (2001)) 74

Figure 2.30: London Clay: normalised stiffness versus strain from undrained triaxial compression and extension tests (after Clayton and Heymann (2001)) 75

Figure 2.31: Reconstituted London Clay: results from undrained triaxial compression and extension tests (redrawn by Hight et al. (2003) after Jardine (1985)) 76

Figure 2.32: Bothkennar Clay: typical normalised stiffness versus strain characteristics from undrained triaxial compression and extension tests (after Smith (1992)) 76

Figure 2.33: Diagram showing the kinematic yield surface in strain space adopted in model LC (after Simpson et al. (1979)) 83

Figure 2.34: Kinematic regions of high stiffness (after Puzrin and Burland (1998)) 84

Figure 2.35: Schematic illustration of the bounding surface and definition of image points in general stress space (after Dafalias and Herrmann (1982)) 86

Figure 2.36: Open hysteresis loop during unloading and reloading due to the elastic behaviour predicted on unloading 87

Figure 2.37: Conceptual model of unload-reload used by MIT-E3 for hydrostatic compression: a) perfect hysteresis b) hysteresis and bounding surface plasticity (after Whittle (1993)) 87

Figure 2.38: Multi-surface model a) nesting surfaces; b) variation of hardening moduli at conjugate points on nesting surfaces (redrawn by Mroz and Norris (1982) after Mroz et al. (1978)) 89

Figure 2.39: Two-surface model: kinematic yield surface and bounding surface (redrawn by Mroz and Norris (1982) after Mroz et al. (1979)) 90

Figure 2.40: Model with an infinite number of surfaces: a) first reverse loading b) second reverse loading (after Mroz and Norris (1982)) 90

Figure 2.41: Typical configuration of surfaces in the three-surface model (after Hashiguchi (1985)) 91

Figure 2.42: Two-surface model (after Al-Tabbaa (1987)) 92

Figure 2.43: Three-surface model (after Stallebrass (1990)) 93

Figure 2.44: The S-shaped curve (after Simpson (1992)) 94

Figure 2.45: A man pulling bricks attached to him by strings (after Simpson (1992)) 95

Figure 2.46: The S-shaped curve represented in stepwise fashion (after Simpson (1992)) 95

Figure 3.1: 8-noded isoparametric element (after Potts and Zdravkovic (1999)) 100

Figure 3.2: Location of Gauss points for an 8-noded isoparametric element (after Potts and Zdravkovic (1999)) 104

Figure 3.3: Graphical representation of the modified Newton-Raphson scheme (after Potts and Zdravkovic (1999)) 110

Figure 4.1: The modified Cam Clay model in a) q-p' space b) ln$v$-lnp' space 116

Figure 4.2: Diagram showing the yield and bounding surfaces and the symbols chosen for their centres (after Al-Tabbaa (1987)) 118

Figure 4.3: Assumed relative translation of the kinematic yield surface along the vector β joining the current stress point C to its conjugate point D (after Al-Tabbaa (1987)) 120

Figure 4.4: Diagram showing singularity points and unstable regions on the yield surface due to the function h_o (after Al-Tabbaa (1987)) 122

Figure 4.5: Diagram showing the vector β and the vector n (after Al-Tabbaa (1987)) 123

Figure 4.6: Diagram showing the position of the stress point A for the maximum value of b, b_{max} (after Al-Tabbaa (1987)) 124

Figure 4.7: Example of one triaxial multi-stage test from which all the model parameters can be obtained (after Al-Tabbaa (1987)) 126

Figure 4.8: Failure surfaces in the deviatoric plane 129

Figure 4.9: Two-surface model a) Representation of the yield and bounding surfaces in triaxial stress space b) Deviatoric section through the yield and bounding surfaces (with the Van Eekelen equation taking the Lade shape) 132

Figure 4.10: Slow cyclic constant q triaxial test: $\eta = q / p'$ against ε_v a) experimental observations (after Al-Tabbaa (1987)) b) model predictions (after Al-Tabbaa (1987)) c) predictions of two-surface model as implemented into ICFEP 149

Figure 4.11: Slow cyclic constant q triaxial test: $\eta = q / p'$ against ε_s a) experimental observations (after Al-Tabbaa (1987)) b) model

predictions (after Al-Tabbaa (1987)) c) predictions of two-surface model as implemented into ICFEP 150

Figure 4.12: Predicted undrained stress paths after an isotropic stress history a) model predictions (after Al-Tabbaa (1987)) b) predictions of two-surface model as implemented into ICFEP 153

Figure 4.13: Predicted undrained stress paths after a one-dimensional stress history a) model predictions (after Al-Tabbaa (1987)) b) predictions of two-surface model as implemented into ICFEP 154

Figure 4.14: Experimental undrained stress paths using spestone kaolin a) after an isotropic stress history b) after a one-dimensional stress history (Figure 10.33 of Al-Tabbaa (1987) after Parry and Nadarajah (1973)) 155

Figure 4.15: Predicted undrained stress paths a) after an isotropic stress history b) after a one-dimensional stress history 156

Figure 4.16: Predicted relative motion of kinematic yield and bounding surfaces during undrained triaxial compression after an isotropic stress history a) original translation rule b) current version of the two-surface model 157

Figure 4.17: Predicted relative motion of kinematic yield and bounding surfaces during drained triaxial compression after an isotropic stress history a) original translation rule b) current version of the two-surface model 158

Figure 4.18: Failure surfaces in the deviatoric plane and the values of $g(\theta_f)$ obtained for each case 163

Figure 4.19: Predicted undrained stress paths after an isotropic stress history for case A - circular shape for the yield surface and the plastic potential in the deviatoric plane a) triaxial compression b) triaxial extension c) plane strain compression 164

Figure 4.20: Predicted undrained stress paths after an isotropic stress history for case B – Mohr-Coulomb shape for the yield surface and circular shape for the plastic potential in the deviatoric plane a) triaxial compression b) triaxial extension c) plane strain compression 165

Figure 4.21: Predicted undrained stress paths after an isotropic stress history for case C – Lade shape for the yield surface and the plastic potential in the deviatoric plane a) triaxial compression b) triaxial extension c) plane strain compression 166

Figure 4.22: Predicted undrained stress paths after an isotropic stress history for case D – Lade shape for the yield surface and circular shape for the plastic potential in the deviatoric plane a) triaxial compression b) triaxial extension c) plane strain compression 167

Figure 4.23: Stress and strains within the hollow cylinder apparatus (figure after Potts and Zdravkovic (1999)) 169

Figure 4.24: Predictions of hollow cylinder stress paths involving: undrained unloading, undrained rotation of the principal stresses ($\alpha = 30^{\circ}$) and undrained shearing to failure at constant $b = 0.5$ 170

Figure 4.25: Predictions of undrained shearing stage at constant α and $b = 0.5$ a) stress paths b) stiffness-strain curves 171

Figure 4.26: Predictions of undrained shearing stage at constant α and $b = 0.5$ and the kinematic yield surface centred around the current stress state at the beginning of shearing a) stress paths b) stiffness-strain curves 172

Figure 4.27: Normalised stiffness-strain curve (p'_i is the mean effective stress at the start of shearing) for an undrained triaxial compression test on overconsolidated reconstituted London Clay (experimental results after Jardine (1985)) 174

Figure 5.1: Diagram showing the yield, history and bounding surfaces (after Stallebrass (1990)) 178

Figure 5.2: Diagram illustrating the definition of a conjugate point and the translation of the history surface along the vector β (after Stallebrass (1990)) 181

Figure 5.3: Diagram illustrating the definition of a conjugate point and the translation of the yield surface along the vector γ (after Stallebrass (1990)) 182

Figure 5.4: Diagram defining the main components of the parameters b_1 and b_2 (after Stallebrass (1990)) 185

Figure 5.5: Diagram showing the position of the surfaces when b_1 and b_2 are at a maximum (after Stallebrass (1990)) 186

Figure 5.6: Sketch showing a) isotropic stress paths required to determine values for the parameters T and S b) typical stiffness plots from which T and S can be estimated (after Stallebrass (1990)) 188

Figure 5.7: Three surface model a) Representation of the yield, history and bounding surfaces in triaxial stress space b) Deviatoric section through the yield, history and bounding surfaces (with the Van

Eekelen equation taking the Lade shape) 193

Figure 5.8: Drained constant p' triaxial tests a) model predictions after Stallebrass (1990) b) predictions of three-surface model as implemented into ICFEP 214

Figure 5.9: Definition of the angle θ_r 215

Figure 5.10: Constant p' loading after four stress path rotations: G against q a) experimental data (after Stallebrass (1990)) b) model predictions (after Stallebrass (1990)) c) predictions of three-surface model as implemented into ICFEP 216

Figure 5.11: Configuration of the three surfaces at the start and end of each cycle a) after Stallebrass (1990)) b) current version of the three-surface model 217

Figure 5.12: Cycles of constant p′ loading (θ_r = -90° and θ_r = 180°): q versus ε_s a) experimental data and model predictions (after Stallebrass (1990)) b) predictions of three-surface model as implemented into ICFEP c) sketch showing the location of the surfaces at the start and finish of each cycle 218

Figure 5.13: Constant p' loading after four stress path rotations: ε_v against ε_s a) experimental data (after Stallebrass (1990)) b) model predictions (after Stallebrass (1990)) c) predictions of three-surface model as implemented into ICFEP 219

Figure 5.14: Failure surfaces in the deviatoric plane and the values of $g(\theta_f)$ obtained for each case 222

Figure 5.15: Predicted undrained stress paths after an isotropic stress history for case A - circular shape for the yield surface and the plastic potential in the deviatoric plane a) triaxial compression b) triaxial extension c) plane strain compression 223

Figure 5.16: Predicted undrained stress paths after an isotropic stress history for case B – Mohr-Coulomb shape for the yield surface and circular shape for the plastic potential in the deviatoric plane a) triaxial compression b) triaxial extension c) plane strain compression 224

Figure 5.17: Predicted undrained stress paths after an isotropic stress history for case C – Lade shape for the yield surface and the plastic potential in the deviatoric plane a) triaxial compression b) triaxial extension c) plane strain compression 225

Figure 5.18: Predicted undrained stress paths after an isotropic stress history for case D – Lade shape for the yield surface and circular shape for the plastic potential in the deviatoric plane a) triaxial compression b) triaxial extension c) plane strain compression 226

Figure 5.19: Normalised stiffness-strain curve (p'_i is the mean effective stress at the start of shearing) for an undrained triaxial compression test on overconsolidated reconstituted London Clay (experimental results after Jardine (1985)) 227

Figure 6.1: Representation in triaxial stress space: diagram showing the main components of the parameter b and the position of the kinematic surface for the maximum value of b, b_{max} 231

Figure 6.2: Schematic representation of typical results of the first formulation for an undrained triaxial compression test a) stress path b) stiffness-strain curve c) ratio b/b_{max} versus strain 233

Figure 6.3: Representation in triaxial stress space: calculation of b_{max} for the second formulation (ignoring changes in p'_o) 234

Figure 6.4: Schematic representation of typical results of the second formulation for a constant p' test following isotropic swelling a) stress path b) stiffness-strain curve c) ratio b/b_{max} versus strain 235

Figure 6.5: Representation in triaxial stress space: calculation of b_o for the third formulation (ignoring changes in p'_o) 236

Figure 6.6: Representation in triaxial stress space of a) previous loading stage i-1 b) current loading stage i c) configuration of the surfaces for the calculation of the value of b^*_o 239

Figure 6.7: Predictions of the modified two-surface model for an undrained triaxial compression test on overconsolidated reconstituted London Clay (test data after Jardine (1985)): Normalised stiffness-strain curve (p'_i is the value of p' at the start of shearing) 243

Figure 6.8: Predictions of the modified two-surface model for an undrained triaxial compression test and for different increment sizes a) ratio b^*/b^*_{max} versus strain b) stress-strain curve 244

Figure 6.9: Representation in triaxial stress space: diagram defining the main components of the parameters b^*_1 and b^*_2 246

Figure 6.10: Representation in triaxial stress space of a) Previous loading stage i-1 b) Current loading stage i c) Configuration of surfaces for the calculation of the values of $b^*_{1,o}$ and $b^*_{2,o}$ 248

Figure 6.11: Predictions of the modified three-surface model for an undrained triaxial compression test on overconsolidated reconstituted London Clay (test data after Jardine (1985)): Normalised stiffness-strain curve (p'_i is the value of p' at the start of shearing) 255

Figure 7.1: Determination of compression parameters (N and λ^*) for reconstituted London Clay (test data from Jardine (1985)) 259

Figure 7.2: Normalised bulk modulus decay curves selected for analysis at T5 (after Hight et al. (2003)) 259

Figure 7.3: Effect of varying R for the two-surface model – Test LR7 a) normalised stiffness-strain curve b) stress-strain curve c) stress-strain curve – larger strains (test data from Jardine (1985)) 262

Figure 7.4: Effect of varying ψ for the two-surface model – Test LR7 a) normalised stiffness-strain curve b) stress-strain curve c) stress-strain curve – larger strains (test data from Jardine (1985)) 263

Figure 7.5: Effect of varying R for the modified two-surface model – Test LR7 a) normalised stiffness-strain curve b) stress-strain curve c) stress-strain curve – larger strains (test data from Jardine (1985)) 264

Figure 7.6: Effect of varying α for the modified two-surface model – Test LR7 a) normalised stiffness-strain curve b) stress-strain curve c) stress-strain curve – larger strains (test data from Jardine (1985)) 265

Figure 7.7: Effect of varying S for the three-surface model – Test LR7 a) normalised stiffness-strain curve b) stress-strain curve c) stress-strain curve – larger strains (test data from Jardine (1985)) 267

Figure 7.8: Effect of varying T for the three-surface model – Test LR7 a) normalised stiffness-strain curve b) stress-strain curve c) stress-strain curve – larger strains (test data from Jardine (1985)) 268

Figure 7.9: Effect of varying ψ for the three-surface model – Test LR7 a) normalised stiffness-strain curve b) stress-strain curve c) stress-strain curve – larger strains (test data from Jardine (1985)) 269

Figure 7.10: Effect of varying S for the modified three-surface model – Test LR7 a) normalised stiffness-strain curve b) stress-strain curve c) stress-strain curve – larger strains (test data from Jardine (1985)) 271

Figure 7.11: Effect of varying T for the modified three-surface model – Test LR7 a) normalised stiffness-strain curve b) stress-strain curve c) stress-strain curve – larger strains (test data from Jardine (1985)) 272

Figure 7.12: Effect of varying α_1 for the modified three-surface model – Test LR7 a) normalised stiffness-strain curve b) stress-strain curve c)

stress-strain curve – larger strains (test data from Jardine (1985)) 273

Figure 7.13: Effect of varying α_2 for the modified three-surface model – Test LR7 a) normalised stiffness-strain curve b) stress-strain curve c) stress-strain curve – larger strains (test data from Jardine (1985)) 274

Figure 7.14: Example of curve fitting of the initial part of the stress-strain curve for test LR1.5 278

Figure 7.15: Predictions of the two-surface model for the triaxial compression paths a) normalised stiffness-strain curve b) stress-strain curve c) stress-strain curve – larger strains (test data from Jardine (1985)) 279

Figure 7.16: Predictions of the two-surface model for the triaxial extension paths a) normalised stiffness-strain curve b) stress-strain curve c) stress-strain curve – larger strains (test data from Jardine (1985)) 280

Figure 7.17: Predictions of the modified two-surface model for the triaxial compression paths a) normalised stiffness-strain curve b) stress-strain curve c) stress-strain curve – larger strains (test data from Jardine (1985)) 281

Figure 7.18: Predictions of the modified two-surface model for the triaxial extension paths a) normalised stiffness-strain curve b) stress-strain curve c) stress-strain curve – larger strains (test data from Jardine (1985)) 282

Figure 7.19: Predictions of the three-surface model for the triaxial compression paths a) normalised stiffness-strain curve b) stress-strain curve c) stress-strain curve – larger strains (test data from Jardine (1985)) 284

Figure 7.20: Predictions of the three-surface model for the triaxial extension paths a) normalised stiffness-strain curve b) stress-strain curve c) stress-strain curve – larger strains (test data from Jardine (1985)) 285

Figure 7.21: Predictions of the modified three-surface model for the triaxial compression paths a) normalised stiffness-strain curve b) stress-strain curve c) stress-strain curve – larger strains (test data from Jardine (1985)) 287

Figure 7.22: Predictions of the modified three-surface model for the triaxial extension paths a) normalised stiffness-strain curve b) stress-strain curve c) stress-strain curve – larger strains (test data from Jardine (1985)) 288

Figure 7.23: Constant p' loading after four stress path rotations: G against q a) experimental data (after Stallebrass (1990)) b) predictions of two-surface model 292

Figure 7.24: Configuration of the surfaces at the start and end of each cycle for the two-surface model 293

Figure 7.25: Constant p' loading after four stress path rotations: ε_v against ε_s a) experimental data (after Stallebrass (1990)) b) predictions of two-surface model c) predictions of two-surface model – bigger scale 294

Figure 7.26: Constant p' loading after four stress path rotations: G against q a) experimental data (after Stallebrass (1990)) b) predictions of modified two-surface model 295

Figure 7.27: Configuration of the surfaces at the start and end of each cycle for the modified two-surface model 296

Figure 7.28: Constant p' loading after four stress path rotations: ε_v against ε_s a) experimental data (after Stallebrass (1990)) b) predictions of modified two-surface model c) predictions of modified two-surface model – bigger scale 297

Figure 7.29: Constant p' loading after four stress path rotations: G against q a) experimental data (after Stallebrass (1990)) b) predictions of modified three-surface model 299

Figure 7.30: Configuration of the surfaces at the start and end of each cycle for the modified three-surface model 300

Figure 7.31: Configuration of the surfaces and plastic strain increment vector at q = 30 kPa for the modified three-surface model 301

Figure 7.32: Configuration of the surfaces and plastic strain increment vector at q = 20 kPa for θ_r = 90° a) modified two-surface model b) modified three-surface model 301

Figure 7.33: Constant p' loading after four stress path rotations: ε_v against ε_s a) experimental data (after Stallebrass (1990)) b) predictions of modified three-surface model 302

Figure 7.34: Schematic diagram showing a) current stress state C b), c) configuration of kinematic surfaces at the end of two possible previous stress histories d) centring of the kinematic surfaces around the current stress state 305

Figure 7.35: Predictions of the two-surface model for analyses 'sh-c': normalised stiffness-strain curves 307

Figure 7.36: Predictions of the modified two-surface model for analyses 'sh-c': normalised stiffness-strain curves 307

Figure 7.37: Predictions of the three-surface model for analyses 'sh-c': normalised stiffness-strain curves 308

Figure 7.38: Predictions of the modified three-surface model for analyses 'sh-c': normalised stiffness-strain curves 308

Figure 7.39: Comparison of the predictions of the two-surface model for analyses 'sh-c' and 'sh': normalised stiffness-strain curves 309

Figure 7.40: Comparison of the predictions of the modified two-surface model for analyses 'sh-c' and 'sh': normalised stiffness-strain curves 309

Figure 7.41: Comparison of the predictions of the three-surface model for analyses 'sh-c' and 'sh': normalised stiffness-strain curves 310

Figure 7.42: Comparison of the predictions of the modified three-surface model for analyses 'sh-c' and 'sh': normalised stiffness-strain curves 310

Figure 8.1: Soil profile at the site of Saint-Alban 314

Figure 8.2: Undrained strength profiles for the clay at Saint-Alban (data after La Rochelle et al. (1974)) 315

Figure 8.3: Test embankment A a) plan view b) cross section A-A 316

Figure 8.4: Undrained strength profiles for the clay at Saint-Alban – comparison of MIT-E3 predictions with field and experimental data (after Zdravkovic et al. (2002)) 317

Figure 8.5: Relevance of laboratory tests to the stress paths followed by soil elements along the failure surface beneath an embankment (after Bjerrum (1973)) 319

Figure 8.6: Finite element mesh 321

Figure 8.7: Determination of compression parameters (N and λ^*) for the clay at Saint-Alban (test data from Leroueil (1977)) 322

Figure 8.8: Determination of parameter κ^* for the clay at Saint-Alban (test data from Leroueil (1977)) 322

Figure 8.9: G_e profile for the kinematic hardening models 323

Figure 8.10: Predictions of the 2-SKH and M2-SKH models for an undrained triaxial compression test at a depth of 2.0 m a) stiffness-strain curve b) stress-strain curve 324

Figure 8.11: G_e profile for the modified Cam Clay model 326

Figure 8.12: Predictions of the 2-SKH, M2-SKH and MCC models for an undrained triaxial compression test at a depth of 2.0 m a) stiffness-strain curve b) stress-strain curve 327

Figure 8.13: *OCR* profile assumed in the analyses 328

Figure 8.14: Undrained strength profiles predicted by the 2-SKH, M2-SKH and MCC models 328

Figure 8.15: Vectors of incremental displacement at failure for analysis MCC-B 330

Figure 8.16: Vertical settlement at the centreline of the embankment versus embankment height predicted by the 2-SKH and M2-SKH models 330

Figure 8.17: Comparison between observed and predicted vertical settlement at the centreline of the embankment 331

Figure 8.18: Horizontal displacement at the toe of the embankment versus embankment height predicted by the 2-SKH and M2-SKH models 331

Figure 8.19: Predictions of the 2-SKH and M2-SKH models for a plane strain compression and extension test at a depth of 2.0 m a) stiffness-strain curve b) stress-strain curve 332

Figure 8.20: Movements predicted by the 2-SKH and M2-SKH models for embankment heights of 0.9 m and 3.3 m a) vertical displacement at the centreline of the embankment b) horizontal displacement under the toe of the embankment 333

Figure 8.21: Vertical settlement at the centreline of the embankment versus embankment height predicted by a) the 2-SKH and MCC models (analysis MCC-A) b) the M2-SKH and MCC models (analysis MCC-B) 334

Figure 8.22: Horizontal displacement at the toe of the embankment versus embankment height predicted by a) the 2-SKH and MCC models (analysis MCC-A) b) the M2-SKH and MCC models (analysis MCC-B) 335

Figure 8.23: Predictions of the 2-SKH and MCC models (analysis MCC-A) for a plane strain compression and extension test at a depth of 2.0 m a) stiffness-strain curve b) stress-strain curve 336

Figure 8.24: Predictions of the M2-SKH and MCC models (analysis MCC-B) for a plane strain compression and extension test at a depth of 2.0 m a) stiffness-strain curve b) stress-strain curve 337

Figure 8.25: Movements predicted by the 2-SKH and MCC models (analysis MCC-A) for embankment heights of 0.9 m and 3.3 m a) vertical displacement at the centreline of the embankment b) horizontal displacement under the toe of the embankment 338

Figure 8.26: Movements predicted by the M2-SKH and MCC models (analysis MCC-B) for embankment heights of 0.9 m and 3.3 m a) vertical displacement at the centreline of the embankment b) horizontal displacement under the toe of the embankment 339

Figure 8.27: Finite element mesh 341

Figure 8.28: Predictions of the 2-SKH and M2-SKH models for an undrained triaxial compression test at a depth of 2.0 m for K_o = 1.0 a) stiffness-strain curve b) stress-strain curve 342

Figure 8.29: Predictions of the 2-SKH and M2-SKH models for an undrained triaxial compression test at a depth of 0.9 m for K_o = 1.0 a) stiffness-strain curve b) stress-strain curve 343

Figure 8.30: Vectors of incremental displacement at failure for the 2-SKH model and K_o = 1.0 344

Figure 8.31: Vertical settlement at the centreline of the embankment versus embankment height predicted by the 2-SKH and M2-SKH models for K_o = 1.0 344

Figure 8.32: Horizontal displacement at the toe of the embankment versus embankment height predicted by the 2-SKH and M2-SKH models for K_o = 1.0 345

Figure 8.33: Movements predicted by the 2-SKH and M2-SKH models for K_o = 1.0 and embankment heights of 0.9 m and 1.8 m a) vertical displacement at the centreline of the embankment b) horizontal displacement under the toe of the embankment 346

Figure 8.34: Undrained strength profiles predicted by cases A, B, C and D 349

Figure 8.35: Failure surfaces in the deviatoric plane and the values of $g(\theta)$ obtained at plane strain conditions 349

Figure 8.36: Vertical settlement at the centreline of the embankment versus embankment height predicted by cases A, B, C and D 350

Figure 8.37: Horizontal displacement at the toe of the embankment versus embankment height predicted by cases A, B, C and D 351

Figure 9.1: The effect of non-linearity on the predicted surface settlement trough: St. James's Park (after Addenbrooke et al. (1997)) 357

Figure 9.2: The effect of anisotropy on the predicted surface settlement trough: St. James's Park (after Addenbrooke et al. (1997)) 357

Figure 9.3: The effect of recent stress history on the predicted surface settlement trough a) shallow tunnel b) deep tunnel (after Stallebrass et al. (1994)) 359

Figure 9.4: Soil profile and tunnel geometry at St. James's Park 360

Figure 9.5: Finite element mesh 361

Figure 9.6: Mohr-Coulomb yield surface a) J-p' space b) Deviatoric plane 362

Figure 9.7: Mohr-Coulomb yield surface and plastic potential surface 363

Figure 9.8: a) Configuration of the kinematic surfaces at the end of the assumed geological history for an element of London Clay in the vicinity of the tunnels b) centring of the kinematic surfaces at the end of the geological history 364

Figure 9.9: Choice of parameters for the non-linear elastic part of model J4 366

Figure 9.10: K_o profiles predicted at the end of the geological history 368

Figure 9.11: p'_o / p' profiles predicted at the end of the geological history 369

Figure 9.12: Assumed K_o profiles for the analyses of set 3 370

Figure 9.13: Assumed K_o profiles for the analyses of model J4 – set 5 371

Figure 9.14: K_o profiles predicted at the end of the geological history and the K_o profile calculated from the equation of Mayne and Kulhawy (1982) 372

Figure 9.15: Surface settlement profiles predicted by set 1: 30.5 m deep tunnel 373

Figure 9.16: Surface settlement profiles predicted by set 2: 30.5 m deep tunnel 374

Figure 9.17: Comparison of surface settlement profiles predicted by sets 1 and 2: 30.5 m deep tunnel a) two-surface model b) modified two-surface model c) three-surface model d) modified three-surface model 375

Figure 9.18: Forces imposed on the tunnel boundary due to excavation 376

Figure 9.19: Comparison of stiffness-strain curves at the springline and crown of the tunnel for sets 1 and 2: 30.5 m deep tunnel a) two-surface model b) modified two-surface model c) three-surface model d) modified three-surface model 377

Figure 9.20: Comparison of normalised surface settlement profiles with the Gaussian distribution: 30.5 m deep tunnel 378

Figure 9.21: Surface settlement profiles predicted by set 1: 20 m deep tunnel 379

Figure 9.22: Surface settlement profiles predicted by set 2: 20 m deep tunnel 379

Figure 9.23: Comparison of surface settlement profiles predicted by sets 1 and 2: 20 m deep tunnel a) two-surface model b) modified two-surface model c) three-surface model d) modified three-surface model 380

Figure 9.24: Comparison of stiffness-strain curves at the springline and crown of the tunnel for sets 1 and 2: 20 m deep tunnel a) two-surface model b) modified two-surface model c) three-surface model d) modified three-surface model 381

Figure 9.25: Comparison of normalised surface settlement profiles with the Gaussian distribution: 20 m deep tunnel 382

Figure 9.26: Surface settlement profiles predicted by model J4 (K_o profiles B and D): 30.5 m deep tunnel 383

Figure 9.27: Comparison of stiffness-strain curves at the springline and crown of the tunnel for analysis J4-5B: 30.5 m deep tunnel 383

Figure 9.28: Comparison of normalised surface settlement profiles predicted by model J4 (K_o profiles B and D) with the Gaussian distribution: 30.5 m deep tunnel 384

Figure 9.29: Surface settlement profiles predicted by model J4 (K_o profiles B and D): 20 m deep tunnel 384

Figure 9.30: Comparison of stiffness-strain curves at the springline and crown of the tunnel for analysis J4-5B: 20 m deep tunnel 385

Figure 9.31: Comparison of normalised surface settlement profiles predicted by model J4 (K_o profiles B and D) with the Gaussian distribution: 20 m deep tunnel 385

Figure 9.32: Surface settlement profiles predicted by linear elastic model with constant stiffness (K_o profiles A and C): 30.5 m deep tunnel 386

Figure 9.33: Comparison of stiffness-strain curves at the springline and crown of the tunnel for linear elastic model with constant stiffness (K_o profiles A and C): 30.5 m deep tunnel 387

Figure 9.34: Surface settlement profiles predicted by set 3 (K_o profiles A, B and C): 30.5 m deep tunnel a) two-surface model b) modified two-surface model c) three-surface model d) modified three-

surface model 387

Figure 9.35: Comparison of stiffness-strain curves at the springline and crown of the tunnel for set 3 (K_o profiles A and C): 30.5 m deep tunnel a) two-surface model b) modified two-surface model c) three-surface model d) modified three-surface model 388

Figure 9.36: Surface settlement profiles predicted by model J4 (K_o profiles A, B and C): 30.5 m deep tunnel 389

Figure 9.37: Comparison of stiffness-strain curves at the springline and crown of the tunnel for model J4 (K_o profiles A and C): 30.5 m deep tunnel 390

Figure 9.38: Surface settlement profiles predicted by set 3 (K_o profiles A, B and C): 20 m deep tunnel a) two-surface model b) modified two-surface model c) three-surface model d) modified three-surface model 390

Figure 9.39: Comparison of stiffness-strain curves at the springline and crown of the tunnel for set 3 (K_o profiles A and C): 20 m deep tunnel a) two-surface model b) modified two-surface model c) three-surface model d) modified three-surface model 391

Figure 9.40: Surface settlement profiles predicted by model J4 (K_o profiles A, B and C): 20 m deep tunnel 392

Figure 9.41: Surface settlement profiles predicted by the two-surface model – set 4: 30.5 m deep tunnel 393

Figure 9.42: Predictions of the models' parameters for an undrained triaxial compression test at the westbound tunnel axis a) normalised stiffness-strain curve b) stress-strain curve 396

Figure 9.43: Predictions of the models' parameters for an undrained triaxial extension test at the westbound tunnel axis a) normalised stiffness-strain curve b) stress-strain curve 397

Figure 9.44: Surface settlement profiles: westbound tunnel 400

Figure 9.45: Distribution of vertical movements with depth: westbound tunnel 402

Figure 9.46: Distribution of horizontal movements with depth: westbound tunnel 403

Figure 9.47: Surface settlement profiles: eastbound tunnel 404

Figure 9.48: Stress path experienced by an element close to the eastbound tunnel axis due to construction of the westbound tunnel 405

List of tables

Table 4.1: Material parameters used by Al-Tabbaa (1987) in the two-surface model for the simulation of tests on speswhite kaolin 151

Table 4.2: Material parameters used in the current version of the two-surface model implemented into ICFEP for the simulation of tests on speswhite kaolin 151

Table 4.3: Values of p'_{cs} and q_{cs} calculated from the equations of Appendix III for the undrained stress paths of Figure 4.12 and values of p'_o at the start of shearing (p'_i is the mean effective stress at the start of shearing) 160

Table 4.4: Values of p'_{cs} and q_{cs} calculated from the equations of Appendix III for the undrained stress paths of Figure 4.13 and values of p'_o at the start of shearing (p'_i is the mean effective stress at the start of shearing) 160

Table 4.5: Model parameters defining the shape of the yield and plastic potential surfaces in the deviatoric plane 162

Table 4.6: Values of θ_f, $g(\theta_f)$ and equivalent values of φ'_f for the four cases analysed 163

Table 4.7: Material parameters used in the current version of the two-surface model for the simulation of the triaxial test in Figure 4.27 174

Table 5.1: Material parameters used in the three-surface model for the simulation of tests on speswhite kaolin (after Stallebrass (1990)) 213

Table 5.2: Material parameters used in the current version of the three-surface model implemented into ICFEP for the simulation of tests on speswhite kaolin 213

Table 5.3: Model parameters defining the shape of the yield and plastic potential surfaces in the deviatoric plane 221

Table 5.4: Values of θ_f, $g(\theta_f)$ and equivalent values of φ'_f for the four cases analysed 221

Table 5.5: Material parameters used in the current version of the three-surface model for the simulation of the triaxial test in Figure 5.19 227

Table 6.1: Material parameters used in the modified two-surface model for the simulation of the triaxial test in Figure 6.7 243

Table 6.2: Material parameters used in the modified three-surface model for

the simulation of the triaxial test in Figure 6.11 255

Table 7.1: Material parameters for the two-surface model for the simulation of tests on reconstituted London Clay 276

Table 7.2: Material parameters for the modified two-surface model for the simulation of tests on reconstituted London Clay 276

Table 7.3: Material parameters for the three-surface model for the simulation of tests on reconstituted London Clay 277

Table 7.4: Material parameters for the modified three-surface model for the simulation of tests on reconstituted London Clay 277

Table 7.5: Material parameters used in the two-surface model for the simulation of the multi-stage test on speswhite kaolin 291

Table 7.6: Material parameters used in the modified two-surface model for the simulation of the multi-stage test on speswhite kaolin 291

Table 7.7: Material parameters used in the modified three-surface model for the simulation of the multi-stage test on speswhite kaolin 291

Table 8.1: Material parameters for the two-surface model for the clay at Saint-Alban 325

Table 8.2: Material parameters for the modified two-surface model for the clay at Saint-Alban 325

Table 8.3: Material parameters for the modified Cam Clay model for the clay at Saint-Alban 329

Table 8.4: Percentage difference between the maximum movements predicted by the 2-SKH and M2-SKH models 334

Table 8.5: Percentage difference between the maximum movements predicted by the 2-SKH and MCC models (analysis MCC-A) 339

Table 8.6: Percentage difference between the maximum movements predicted by the M2-SKH and MCC models (analysis MCC-B) 339

Table 8.7: Material parameters for the two-surface model for the analyses with $K_o = 1.0$ 341

Table 8.8: Material parameters for the modified two-surface model for the analyses with $K_o = 1.0$ – soil within the crust 341

Table 8.9: Material parameters for the modified two-surface model for the analyses with $K_o = 1.0$ – soil below the crust 341

Table 8.10: Percentage difference between the maximum movements

predicted by the 2-SKH and M2-SKH models: K_o = 1.0 346

Table 8.11: Model parameters defining the shape of the yield and plastic potential surfaces in the deviatoric plane 348

Table 8.12: Values of θ, $g(\theta)$ and equivalent values of φ' for the four cases analysed 348

Table 8.13: Predicted embankment failure heights 351

Table 9.1: Material parameters for the non-linear elastic part of model J4 for London Clay 366

Table 9.2: Material parameters for the non-linear elastic part of model J4 for Terrace Gravel 367

Table 9.3: Mohr-Coulomb yield and plastic potential parameters for model J4 367

Table 9.4: Volume loss and percentage of unloading for set 1: 30.5 m deep tunnel 375

Table 9.5: Volume loss and percentage of unloading for set 2: 30.5 m deep tunnel 375

Table 9.6: Volume loss and percentage of unloading for set 1: 20 m deep tunnel 380

Table 9.7: Volume loss and percentage of unloading for set 2: 20 m deep tunnel 380

Table 9.8: Volume loss and percentage of unloading for analyses J4-5B and J4-5D 386

Table 9.9: Volume loss and percentage of unloading for set 4 (2-SKH model): 30.5 m deep tunnel 393

Table 9.10: Material parameters for the non-linear elastic part of model J4 for London Clay used in the analysis of the twin tunnels at St. James's Park 397

Table 9.11: Material parameters for the modified two-surface model for London Clay used in the analysis of the twin tunnels at St. James's Park 398

Table 9.12: Material parameters for the three-surface model for London Clay used in the analysis of the twin tunnels at St. James's Park 398

Table 9.13: Material parameters for the modified three-surface for London Clay used in the analysis of the twin tunnels at St. James's Park 398

Table 9.14: Tunnel lining parameters 398

Table 9.15: Volume loss and percentage of unloading before the lining was constructed to achieve the volume loss of 3.3% for the westbound tunnel excavation 400

Table 9.16: Volume loss and percentage of unloading before the lining was constructed to achieve the volume loss of 2.9% for the eastbound tunnel excavation 405

Chapter 1

Introduction

1.1 General

Construction in an urban environment requires the accurate calculation of the stresses and ground movements around geotechnical structures. In most cases the engineer is not only interested in the stresses and movements at failure, but also in the stresses and movements under working loads and the effect that these may impose on existing structures.

A method of analysis which is capable of analysing complex soil-structure interaction problems is numerical analysis. However, although numerical analysis is a powerful tool, the predictions obtained are dependent on the constitutive soil models adopted. Clearly, the use of appropriate soil models that can describe satisfactorily the observed soil behaviour is necessary in order to obtain realistic predictions.

In the past, the calculation of ground movements under working loads was commonly based on the assumption that the pre-failure behaviour of overconsolidated clays is linear elastic. Nowadays, it is well known that the behaviour of such soils is highly non-linear and inelastic from the early stages of loading (Jardine et al. (1984)). Moreover, examination of the straining induced in the ground under engineering construction shows that it is within this non-linear range that geotechnical structures operate under working loads (Burland (1989)). Hence, in order to obtain accurate predictions of the deformational response it is necessary to investigate and model the soil behaviour within this range of strains.

Constitutive models which incorporate non-linear behaviour have been used in the numerical analysis of geotechnical structures and have been shown to improve considerably the predictions of ground movements for overconsolidated clays (e.g. Simpson et al. (1979), Jardine et al. (1986)). Although these models are a substantial improvement over linear elastic models, they are usually derived by fitting empirical expressions to the observed stress-strain curves. In addition, the pre-failure behaviour of overconsolidated soils is still modelled as being mainly elastic.

During the past two decades a number of elasto-plastic constitutive soils models have been developed which allow for plastic strains to develop from the early stages of loading, simulating in this way both non-linearity and irrecoverable strains. A family of models that falls within this category are the kinematic hardening models. These allow for plasticity and non-linearity to be invoked within the conventionally defined yield surface (termed bounding surface) by the introduction of a number of kinematic surfaces. Models that are based on this concept and which simulate the behaviour of overconsolidated clays are usually extensions of existing constitutive models for normally consolidated clays and have a more sound theoretical basis than non-linear elastic pre-failure models.

1.2 Aims of research

The aim of this research was to improve the predictions of the behaviour of overconsolidated clays, and especially the pre-failure behaviour, through the study of constitutive models based on the kinematic hardening concept. In particular to:

i) Choose existing constitutive models that are based on this concept and can describe important features of the behaviour of overconsolidated clays and improve them, where possible.

ii) Implement the constitutive models into a finite element program, which is capable of analysing geotechnical problems, evaluate them, and then use them to analyse a number of boundary value problems.

1.3 Outline of thesis

Two existing kinematic hardening models were chosen to be implemented in ICFEP, the two-surface model, developed by Al-Tabbaa (1987), and the three-surface, developed by Stallebrass (1990). The two-surface model is an extension of the modified Cam Clay model and introduces a single kinematic yield surface within the modified Cam Clay bounding surface. The three-surface model is an extension of the two-surface model and employs an additional kinematic surface within the bounding surface. As a part of this work these two models were further improved (for example by introducing different shapes for the yield and plastic potential surfaces in the deviatoric plane) and were generalised so as to make their implementation into a finite element code possible. Both models were then implemented into the Imperial College Finite Element Program (ICFEP). Although these two models constitute a significant improvement in modelling the behaviour of overconsolidated clays, early use of the models revealed that they predict a non-smooth transition from elastic to elasto-plastic behaviour. This feature of behaviour, which proves to be a significant deficiency when simulating pre-failure non-linearity, was improved by changing the hardening modulus in both models. In this way two new models were formulated, the modified two-surface and modified three-surface models. The two new models were implemented into ICFEP and were evaluated together with the two previously implemented models. The two-surface and modified two-surface models were then used in the finite element analyses of an embankment on soft clay. All four models were used in the finite element analyses of tunnels excavated in overconsolidated London Clay.

The outline of the work presented in this thesis is the following:

The remaining part of this chapter introduces the definitions of the stress and strain variables used in this thesis.

Chapter 2 is subdivided into two main parts. The first part reviews the current knowledge of the pre-failure deformational behaviour of overconsolidated clays. A discussion on the behaviour of overconsolidated clays within the critical state framework and the limitations of the framework is included. Existing schemes of pre-failure soil behaviour are reviewed and the main factors that influence pre-failure soil stiffness are summarised and discussed. Particular emphasis is given on the effects of recent stress history and stress path direction and the influence that ageing periods have on them. The second part presents a review of the existing elasto-plastic constitutive models for

overconsolidated soils. In particular the capability of the models to simulate the pre-failure behaviour is examined.

Chapter 3 gives a brief description of the finite element method and discusses some basic modifications necessary to enable the theory to be used in geotechnical engineering.

Chapter 4 presents the two-surface kinematic hardening model. A brief description of the modified Cam Clay model, which is the basis of the two-surface model, is also included. The original formulation of the model in triaxial stress space, as proposed by Al-Tabbaa (1987), is presented first. This is followed by the formulation of the model in general stress space and the improvements made as a part of this work. The implementation of the general formulation of the model into ICFEP and the validation of the model through a series of single finite element analyses is also given in this chapter.

Chapter 5 presents the three-surface kinematic hardening model. This includes the original description of the model in triaxial stress space, after Stallebrass (1990), the formulation of the model in general stress space and the improvements made during this work, the implementation of the general formulation of the model into ICFEP and the validation of the implementation through single finite element analyses.

Chapter 6 introduces the new hardening modulus adopted in the modified two-surface and modified three-surface kinematic hardening models and demonstrates that this results in a smooth elasto-plastic transition for both models.

Chapter 7 presents an evaluation of all four kinematic hardening models presented in Chapters 4-6 and is divided into three parts. In the first part a set of triaxial tests on reconstituted London Clay is simulated. Particular emphasis is given on the ability of the models to predict pre-failure non-linearity. The second part examines the capability of the models to simulate the effect of recent stress history, while the third part investigates the way the models can reproduce the effect of stress path direction.

Chapter 8 presents the finite element analyses of an embankment founded on soft clay. Two studies are presented in this chapter. The first study involves a comparison of the pre-failure deformational behaviour predicted by the two-surface, modified two-surface and modified Cam Clay models, when the same undrained strength profile is assigned to all three models. The second study examines the effect of the shape of the yield and plastic potential surfaces in the deviatoric plane on the predicted failure height of the

embankment.

Chapter 9 investigates the behaviour of kinematic hardening models in tunnelling problems. Two studies are presented. The first study examines the effect of the initial configuration of the kinematic surfaces and the K_o profile on the behaviour of a tunnel excavated in overconsolidated London Clay, for each of the four kinematic hardening models described in Chapters 4-6. The effect of the rate of decay of stiffness assumed in the models is also explored. The second study models the twin tunnels, which were constructed as part of the Jubilee Line Extension beneath St. James's Park. In this study the predictions of the models are compared with field data. In both studies the predictions of the kinematic hardening models are compared with the predictions of a non-linear elastic pre-yield model.

Finally, Chapter 10 gives a summary of the work carried out in this thesis and the conclusions reached, and gives recommendations for further research.

1.4 Definitions of stress and strain variables

Stress is a second order tensor which is defined by six components. Equation 1.1 gives the effective stress tensor:

$$\boldsymbol{\sigma}' = \begin{bmatrix} \sigma'_x & \tau_{xy} & \tau_{xz} \\ \tau_{yx} & \sigma'_y & \tau_{yz} \\ \tau_{zx} & \tau_{zy} & \sigma'_z \end{bmatrix} \tag{1.1}$$

where $\tau_{xy} = \tau_{yx}$, $\tau_{xz} = \tau_{zx}$ and $\tau_{zy} = \tau_{yz}$.

The stress tensor can be divided into two components, the volumetric component and the deviatoric component:

$$\boldsymbol{\sigma}' = \begin{bmatrix} \sigma'_x & \tau_{xy} & \tau_{xz} \\ \tau_{yx} & \sigma'_y & \tau_{yz} \\ \tau_{zx} & \tau_{zy} & \sigma'_z \end{bmatrix} = \underbrace{\begin{bmatrix} p' & 0 & 0 \\ 0 & p' & 0 \\ 0 & 0 & p' \end{bmatrix}}_{\textit{Volumetric component}} + \underbrace{\begin{bmatrix} \sigma'_x - p' & \tau_{xy} & \tau_{xz} \\ \tau_{yx} & \sigma'_y - p' & \tau_{yz} \\ \tau_{zx} & \tau_{zy} & \sigma'_z - p' \end{bmatrix}}_{\textit{Deviatoric component}} \tag{1.2}$$

In the above equation p' is the mean effective stress:

$$p' = \frac{1}{3}\left(\sigma'_x + \sigma'_y + \sigma'_z\right) \tag{1.3}$$

Equation 1.2 can be rewritten as follows:

$$\boldsymbol{\sigma}' = p'\boldsymbol{I} + \boldsymbol{s} \tag{1.4}$$

where $\boldsymbol{\sigma}'$ is the effective stress tensor, p' is the mean effective stress, $\boldsymbol{s}$ is the deviatoric stress tensor and $\boldsymbol{I}$ is the second-rank identity tensor (the tensor quantities are represented by bold-faced characters).

It is common to represent the state of stress with three stress invariants, the mean effective stress, p', the deviatoric stress, J or q and the Lode's angle, θ. The mean effective stress, p', can be calculated from Equation 1.3. The deviatoric stress, J or q, and the Lode's angle, θ, are defined as follows:

$$\begin{aligned} J &= \left[\frac{1}{2}\left(\boldsymbol{s}:\boldsymbol{s}\right)\right]^{1/2} \\ &= \left[\frac{1}{2}\left[\left(\sigma'_x - p'\right)^2 + \left(\sigma'_y - p'\right)^2 + \left(\sigma'_z - p'\right)^2 + 2\tau_{xy}{}^2 + 2\tau_{yz}{}^2 + 2\tau_{zx}{}^2\right]\right]^{1/2} \end{aligned} \tag{1.5}$$

$$q = \sqrt{3}J \tag{1.6}$$

$$\theta = -\frac{1}{3}\sin^{-1}\left[\frac{3\sqrt{3}}{2}\frac{\det\left(\boldsymbol{s}\right)}{\left[\left[\frac{1}{2}\left(\boldsymbol{s}:\boldsymbol{s}\right)\right]^{\frac{1}{2}}\right]^3}\right] \tag{1.7}$$

where det($\boldsymbol{s}$) is the determinant of the deviatoric stress tensor $\boldsymbol{s}$.

These three invariants can be expressed in terms of the principal effective stresses σ'_1, σ'_2 and σ'_3 as follows:

$$p' = \frac{1}{3}\left(\sigma'_1 + \sigma'_2 + \sigma'_3\right) \tag{1.8}$$

$$J = \frac{1}{\sqrt{6}}\left[\left(\sigma_1' - \sigma_3'\right)^2 + \left(\sigma_2' - \sigma_3'\right)^2 + \left(\sigma_1' - \sigma_2'\right)^2\right]^{1/2} \tag{1.9}$$

or $$q = \frac{1}{\sqrt{2}}\left[\left(\sigma_1' - \sigma_3'\right)^2 + \left(\sigma_2' - \sigma_3'\right)^2 + \left(\sigma_1' - \sigma_2'\right)^2\right]^{1/2} \tag{1.10}$$

$$\theta = \tan^{-1}\left[\frac{1}{\sqrt{3}}\left(2\frac{\left(\sigma_2' - \sigma_3'\right)}{\left(\sigma_1' - \sigma_3'\right)} - 1\right)\right] \tag{1.11}$$

Alternatively:

$$\theta = \tan^{-1}\left[\frac{1}{\sqrt{3}}(2b - 1)\right] \tag{1.12}$$

where:

$$b = \frac{\left(\sigma_2' - \sigma_3'\right)}{\left(\sigma_1' - \sigma_3'\right)} \tag{1.13}$$

The above three quantities, p', J or q, and θ, have a geometrical significance in principal effective stress space. Figure 1.1a shows the principal effective stress space with the space diagonal ($\sigma'_1 = \sigma'_2 = \sigma'_3$) and a deviatoric plane (defined as any plane perpendicular to the space diagonal). Figure 1.1b shows the projection of the principal stress space

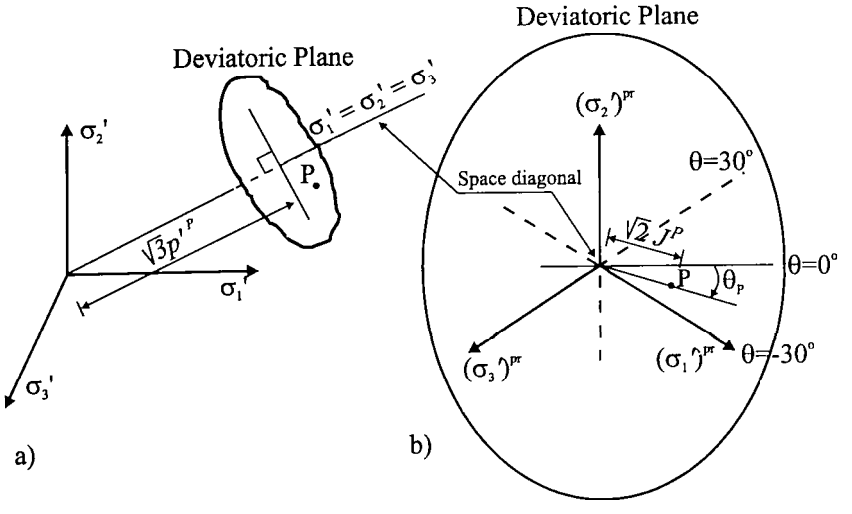


Figure 1.1: a) Principal stress space and b) deviatoric plane (figure after Potts and Zdravkovic (1999))

onto the deviatoric plane. It can be seen that the mean effective stress, p', is a measure of the distance of the current deviatoric plane from the origin along the space diagonal. The deviatoric stress, q or J, is a measure of the distance of the current stress state from the space diagonal in the deviatoric plane. Finally the Lode's angle, θ, defines the orientation of the stress state within the deviatoric plane, and varies between +30° (which corresponds to triaxial extension, $\sigma'_1 = \sigma'_2 \geq \sigma'_3$ and $b = 1$) and -30° (which corresponds to triaxial compression, $\sigma'_1 \geq \sigma'_2 = \sigma'_3$ and $b = 0$).

The three stress invariants, p', J or q and θ are commonly used in order to define the stress state of a loaded body. However, although they define the overall magnitude of the stress state, they do not provide any information on the direction of the planes on which the principal effective stresses act. This is not necessary if the material considered is isotropic, in which case the material properties are the same in all directions. However, if the material considered is anisotropic (i.e. its properties are directional dependent), then the direction of the principal effective stress planes becomes significant and the use of just the three stress invariants, p', J or q and θ is not sufficient. This is the reason why these stress invariants have been used extensively in the formulation of isotropic constitutive models, whereas in the case of anisotropic constitutive models the formulation usually involves the calculation of the whole stress tensor.

Strain, like stress, is a second order tensor, defined by six components.

$$\varepsilon = \begin{bmatrix} \varepsilon_x & \frac{1}{2}\gamma_{xy} & \frac{1}{2}\gamma_{xz} \\ \frac{1}{2}\gamma_{yx} & \varepsilon_y & \frac{1}{2}\gamma_{yz} \\ \frac{1}{2}\gamma_{zx} & \frac{1}{2}\gamma_{zy} & \varepsilon_z \end{bmatrix} \tag{1.14}$$

where $\gamma_{xy} = \gamma_{yx}$, $\gamma_{xz} = \gamma_{zx}$ and $\gamma_{zy} = \gamma_{yz}$.

The strain tensor can be divided into two components, the volumetric and deviatoric components:

$$\begin{bmatrix} \varepsilon_x & \frac{1}{2}\gamma_{xy} & \frac{1}{2}\gamma_{xz} \\ \frac{1}{2}\gamma_{yx} & \varepsilon_y & \frac{1}{2}\gamma_{yz} \\ \frac{1}{2}\gamma_{zx} & \frac{1}{2}\gamma_{zy} & \varepsilon_z \end{bmatrix} = \underbrace{\begin{bmatrix} e_v & 0 & 0 \\ 0 & e_v & 0 \\ 0 & 0 & e_v \end{bmatrix}}_{\textit{Volumetric component}} + \underbrace{\begin{bmatrix} \varepsilon_x - e_v & \frac{1}{2}\gamma_{xy} & \frac{1}{2}\gamma_{xz} \\ \frac{1}{2}\gamma_{yx} & \varepsilon_y - e_v & \frac{1}{2}\gamma_{yz} \\ \frac{1}{2}\gamma_{zx} & \frac{1}{2}\gamma_{zy} & \varepsilon_z - e_v \end{bmatrix}}_{\textit{Deviatoric component}} \tag{1.15}$$

In the above equation e_v is equal to:

$$e_v = \frac{1}{3}\left(\varepsilon_x + \varepsilon_y + \varepsilon_z\right) = \frac{1}{3}\varepsilon_v \tag{1.16}$$

where ε_v is the volumetric strain.

Equation 1.15 can be rewritten as:

$$\boldsymbol{\varepsilon} = \frac{1}{3}\varepsilon_v \boldsymbol{I} + \boldsymbol{e}_s \tag{1.17}$$

where $\boldsymbol{\varepsilon}$ is the strain tensor, ε_v is the volumetric strain and $\boldsymbol{e}_s$ is the deviatoric strain tensor.

The strain invariants corresponding to the previously described stress invariants are the volumetric strain, ε_v, given by Equation 1.16 and the deviatoric strain E_d, if the stress invariant J is chosen, or ε_s, if the stress invariant q is used. These are defined from the following equations:

$$\begin{aligned} E_d &= \left[2\left(\boldsymbol{e}_s : \boldsymbol{e}_s\right)\right]^{1/2} \\ &= \left[2\left[\left(\varepsilon_x - e_v\right)^2 + \left(\varepsilon_y - e_v\right)^2 + \left(\varepsilon_z - e_v\right)^2 + \frac{1}{2}\gamma_{xy}{}^2 + \frac{1}{2}\gamma_{yz}{}^2 + \frac{1}{2}\gamma_{zx}{}^2\right]\right]^{1/2} \end{aligned} \tag{1.18}$$

$$\varepsilon_s = \frac{1}{\sqrt{3}} E_d \tag{1.19}$$

The above equations are expressed in terms of the principal strains, ε_1, ε_2 and ε_3 as follows:

$$\varepsilon_v = \varepsilon_1 + \varepsilon_2 + \varepsilon_3 \tag{1.20}$$

$$E_d = \frac{2}{\sqrt{6}}\left[\left(\varepsilon_1 - \varepsilon_3\right)^2 + \left(\varepsilon_2 - \varepsilon_3\right)^2 + \left(\varepsilon_1 - \varepsilon_2\right)^2\right]^{1/2} \tag{1.21}$$

or $$\varepsilon_s = \frac{\sqrt{2}}{3}\left[\left(\varepsilon_1 - \varepsilon_3\right)^2 + \left(\varepsilon_2 - \varepsilon_3\right)^2 + \left(\varepsilon_1 - \varepsilon_2\right)^2\right]^{1/2} \tag{1.22}$$

Triaxial stress space

In triaxial stress space the most commonly adopted stress and strain invariants are the mean effective stress, p', the shear stress, q, the volumetric strain, ε_v, and the shear strain, ε_s. In this case of axially symmetric conditions Equations 1.8, 1.10, 1.20 and 1.22 reduce to:

$$p' = \frac{1}{3}\left(\sigma'_a + 2\sigma'_r\right) \tag{1.23}$$

$$q = \sigma'_\alpha - \sigma'_r \tag{1.24}$$

$$\varepsilon_v = \varepsilon_a + 2\varepsilon_r \tag{1.25}$$

$$\varepsilon_s = \frac{2}{3}\left(\varepsilon_a - \varepsilon_r\right) \tag{1.26}$$

where σ'_a and σ'_r are the axial and radial effective stresses and ε_a and ε_r are the axial and radial strains respectively.

For triaxial conditions the increments of stresses are related to the increments of strains as follows:

$$\begin{Bmatrix} d\varepsilon_v \\ d\varepsilon_s \end{Bmatrix} = \begin{bmatrix} \frac{1}{K} & \frac{1}{J_{qp}} \\ \frac{1}{J_{pq}} & \frac{1}{3G} \end{bmatrix} \begin{Bmatrix} dp' \\ dq \end{Bmatrix} \tag{1.27}$$

where K is the bulk modulus, G is the shear modulus and the parameters J_{qp} and J_{pq} are coupling moduli that express the cross dependence of the volumetric strain on the shear stress, q, and of the shear strain on the mean effective stress, p'. Hence, the shear modulus G can be calculated from a test where $dp' = 0$ and the bulk modulus K can be calculated from a test where $dq = 0$:

$$3G = \frac{dq}{d\varepsilon_s} \tag{1.28}$$

$$K = \frac{dp'}{d\varepsilon_v} \tag{1.29}$$

For any other stress path the cross coupling of the shear and volumetric components does not allow direct calculation of the bulk and shear moduli. For a material that is elastic and isotropic $J_{qp} = J_{pq} = \infty$, and the shearing and volumetric components are essentially decoupled. In this case the bulk and shear moduli, K and G, can be calculated from any stress path directly from Equations 1.28 and 1.29. Moreover for such a material K and G are related through the Poisson's ratio, μ:

$$G = \frac{3(1-2\mu)}{2(1+\mu)} K \tag{1.30}$$

For undrained conditions, where there is no volume change, the undrained Young's modulus, E_u, can be calculated as follows (for an elastic isotropic material):

$$E_u = 3G \tag{1.31}$$

It should be noted that, unless otherwise stated, all plots of stiffness data presented in this thesis are in terms of tangent stiffness (rather than secant).

Chapter 2

Literature review

2.1 Introduction

This chapter is divided into two parts. The first part presents a review of the current knowledge of the pre-failure deformational behaviour of soils, with particular reference to the behaviour of overconsolidated clays. The main factors that affect soil stiffness are summarised and discussed. In the second part a review of the constitutive models that have been developed to simulate overconsolidated soil behaviour is presented. The basic concepts of the elasto-plastic framework, within which many of these models have been developed, are also described.

2.2 Pre-failure deformation of overconsolidated clays

2.2.1 Introduction

Prior to the 1980's common practice for the prediction of soil deformations under working loads was to assume that the behaviour of overconsolidated clays was linear elastic. Moreover, in the critical state theory (which has been used with great success for the prediction of the behaviour of normally consolidated clays) the pre-failure behaviour of overconsolidated clays is assumed to be elastic and slightly non-linear; the stiffness is linked to the values of the mean effective stress, p', and the specific volume, v. However, later developments in laboratory instrumentation revealed that the pre-failure behaviour of overconsolidated clays is in reality highly-non-linear and inelastic. Over the last two decades the knowledge concerning the pre-failure characteristics of overconsolidated

clays has developed considerably and now it is well known that there is a wide variety of factors that influence the pre-failure soil stiffness.

The first part of this section gives a brief description of the critical state theory and shows how overconsolidated clays behave within this framework. A discussion on the limitations of the framework follows, since the models used in this thesis are extensions of the critical state models and the critical state theory will be used as a general frame of reference. The second part of this section reports the developments in the laboratory techniques that helped realise the highly non-linear pre-failure soil behaviour and points out the relevance of this non-linearity to practice. The third part reviews existing schemes of pre-failure soil behaviour. Finally, the last part discusses the main factors that influence pre-failure soil stiffness.

2.2.2 Critical state framework

The critical state framework was formulated in the 1960's at the University of Cambridge. It essentially combined the work of Rendulic (1937) for normally consolidated clays and that of Hvorslev (1937) for overconsolidated clays. The framework was developed from the results of tests on reconstituted clays. Its main hypotheses are the following:

i) If a sample of normally consolidated clay is compressed isotropically then this will follow the isotropic compression line. This is assumed to be a straight line in the v-lnp' space, see Figure 2.1, and is given by the following equation:

$$v = N - \lambda \ln p' \tag{2.1}$$

where N is the specific volume of the isotropic compression line for $p' = 1$ kPa and λ is the slope of the line in the v-lnp' space.

If the sample is isotropically swelled then this will move up a swelling line, see Figure 2.1. The swelling line is also assumed to be a straight line in the v-lnp' space and is described by an equation of the form:

$$v = v_\kappa - \kappa \ln p' \tag{2.2}$$

where v_κ is the specific volume of the swelling line for $p' = 1$ kPa and κ is the slope of the line in the v-lnp' space.

ii) When sheared, all soils ultimately reach a critical state at which large shear distortions occur with no change in stress or specific volume. The critical state line is defined in the v-lnp'-q space. Its projection onto the q-p' space and the v-lnp' space is described by Equations 2.3 and 2.4 respectively:

$$q = Mp' \tag{2.3}$$

and

$$v = \Gamma - \lambda \ln p' \tag{2.4}$$

where M is the gradient of the critical state line in the q-p' space and Γ is the specific volume of the critical state line for $p' = 1$ kPa. The projection of the critical state line onto the v-lnp' space can be seen in Figure 2.1.

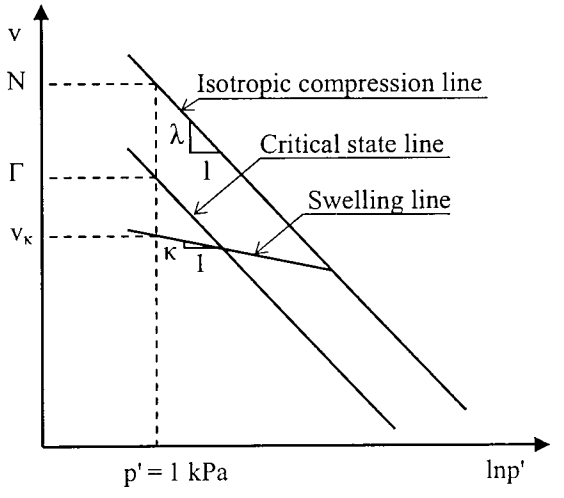


Figure 2.1: Isotropic compression line, swelling line and critical state line

iii) A unique state boundary surface exists, which separates possible from impossible states. The state of the soil described by the stress parameters p', q and v always lies within or on the state boundary surface. When a sample of clay is sheared then its stress path will rise up to the state boundary surface and then it will traverse the surface until it reaches the critical state line. The state boundary surface in normalised stress space can be seen in Figure 2.2, after Atkinson and Bransby (1978) (p'_e is the equivalent pressure on the isotropic compression line at the current specific volume). It consists of the Hvorslev surface for heavily overconsolidated clays and the Roscoe surface, for normally consolidated and lightly overconsolidated clays. The Roscoe surface was based on the results of Rendulic (1937). As shown in Figure 2.2 the two surfaces meet at the

critical state line. The state boundary surface in *v-p'-q* space can be seen in Figure 2.3.

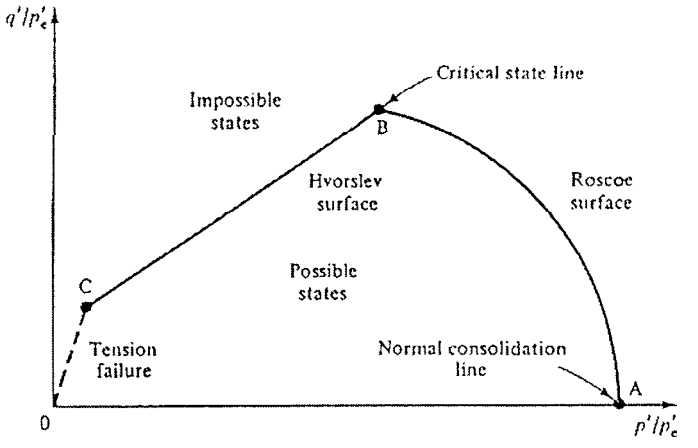


Figure 2.2: State boundary surface of the critical state framework in normalised stress space (after Atkinson and Bransby (1978))

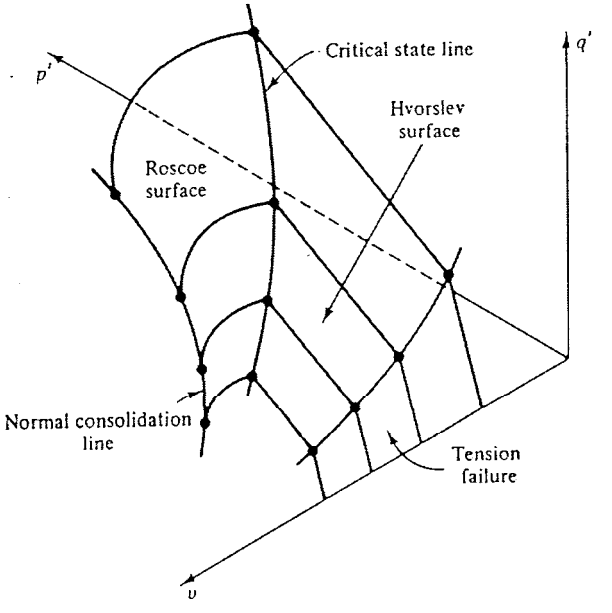


Figure 2.3: State boundary surface of the critical state framework in *v-p'-q* space (after Atkinson and Bransby (1978))

iv) The behaviour of a sample within the state boundary surface is assumed to be elastic; this means that only recoverable strains occur. The behaviour of a sample on the state boundary surface is assumed to be elasto-plastic; in this case both recoverable (elastic) and irrecoverable (plastic) strains develop. Above each swelling line an "elastic wall" exists within which behaviour is purely elastic, see Figure 2.4. This elastic wall intersects the state boundary surface along a line which is called yield locus. The critical state models, Cam Clay (Roscoe and Schofield (1963)) and modified Cam Clay (Roscoe

and Burland (1968)), give an equation to this line.

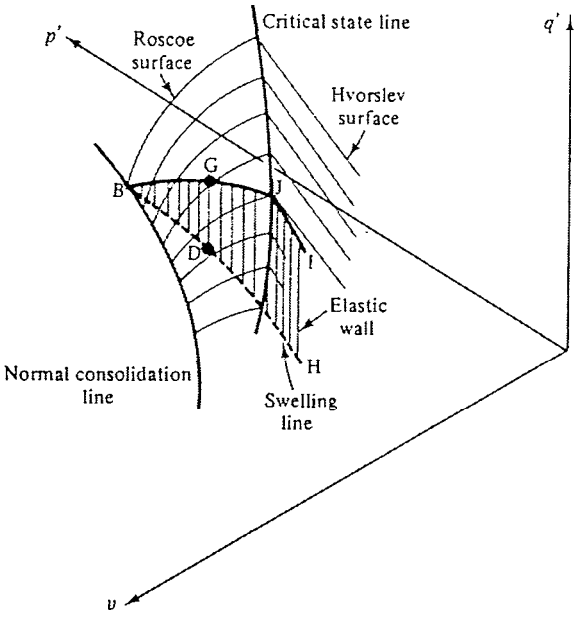


Figure 2.4: Elastic wall (after Atkinson and Bransby (1978))

Overconsolidated soils result from unloading of the soil and are represented by stress states within the state boundary surface. (In natural soils 'apparent' overconsolidation can also result from other processes, such as for example ageing). The critical state framework predicts that when an overconsolidated soil is sheared, elastic behaviour occurs until the stress state reaches the state boundary surface. Thereafter elasto-plastic behaviour is predicted. The elastic bulk modulus, K, is linked to the values of the mean effective stress, p', and the specific volume, v:

$$K = \frac{vp'}{\kappa} \tag{2.5}$$

The elastic shear stiffness, G, is related to the elastic bulk modulus, K, through the Poisson's ratio, μ.

$$\frac{G}{K} = \frac{3(1-2\mu)}{2(1+\mu)} \tag{2.6}$$

An infinite shear modulus was assumed in the initial formulations of the critical state models. In subsequent applications of the models either a constant shear modulus, G, or a constant Poisson's ratio, μ, was usually assumed. For a constant Poisson's ratio, μ, the shear stiffness is also linked to p' and v (Zytynski et al. (1978) have demonstrated that

this formulation is not conservative and can lead to the development of permanent shear strains for a loading-unloading cycle that remains within the yield surface). The dependence of stiffness on p' and v results in a slightly non-linear elastic behaviour, since no significant changes in both p' and v are expected until the stress path reaches the state boundary surface.

2.2.2.1 Limitations of the critical state framework

This thesis is concerned with the stress-strain behaviour of overconsolidated clays for stress states that remain mainly within the state boundary surface. For such soils the critical state framework assumes an approximately linear elastic behaviour. This is a limitation of the initial critical state models, since, as it will be discussed later, it is well known now that the pre-failure behaviour of overconsolidated clays is highly non-linear and inelastic from the very early stages of loading. This limitation seems to have been overcome with the development of models, which are extensions of the critical state models, and allow for plasticity and high non-linearity to be invoked for stress paths that remain within the state boundary surface. Examples of such models will be discussed in the second part of this chapter.

A second limitation of the critical state framework has to do with the assumption that all clays ultimately reach a critical state. This is not always true for overconsolidated clays. While lightly overconsolidated soils reach an ultimate critical state, heavily overconsolidated clays often tend to form shear bands, where clay particle alignment takes place in preferred directions, giving rise to strengths much lower than the critical state strength (Atkinson and Bransby (1978)). This is particularly the case for high plasticity clays. Since this thesis is concerned with constitutive models that are extensions of the critical state models, this drawback will still exist. However, since the investigation is concentrated in the pre-failure behaviour of overconsolidated clays this drawback will not be considered significant for the problems considered in this study.

Finally, it is important to remember that the critical state framework was based on the results of tests on reconstituted clays. Natural clays differ from reconstituted clays in a number of ways, due to the different structure that they posses compared with that of the reconstituted clays. Structure is defined as the combination of fabric (arrangement of particles) and interparticle bonding (Lambe and Whitman (1969)). The difference in the structure between the natural and reconstituted clays causes the natural clays to exist at stress states that plot outside the state boundary surface of the reconstituted clays. In this

way a natural state boundary surface is defined. When sheared, natural clays tend to destructure moving towards the reconstituted state boundary surface. Several frameworks have been developed trying to bring coherence to many aspects of the behaviour of natural clays (Leroueil and Vaughan (1990), Burland (1990), Cotecchia and Chandler (2000)), and a number of constitutive models have been developed to model the effects of destructuration in natural clays. However, as this thesis is concerned with modelling the pre-failure deformational behaviour of overconsolidated clays it is outside its scope to investigate further such destructuration effects in natural clays.

2.2.3 Realisation of non-linearity

In the 1970's conventional laboratory measurements of stiffness of overconsolidated clays showed values much lower than those estimated from the back analysis of the field performance of structures. Figure 2.5 shows the variation of the undrained Young's modulus, E_u, back analysed from a number of different field studies, with the mean effective stress, p' (after St. John (1975)). Also shown in this figure are the laboratory triaxial tests on samples from Ashford Common (Bishop et al. (1965)). It can be seen that there is a big difference between the laboratory stiffness data and the back analysed

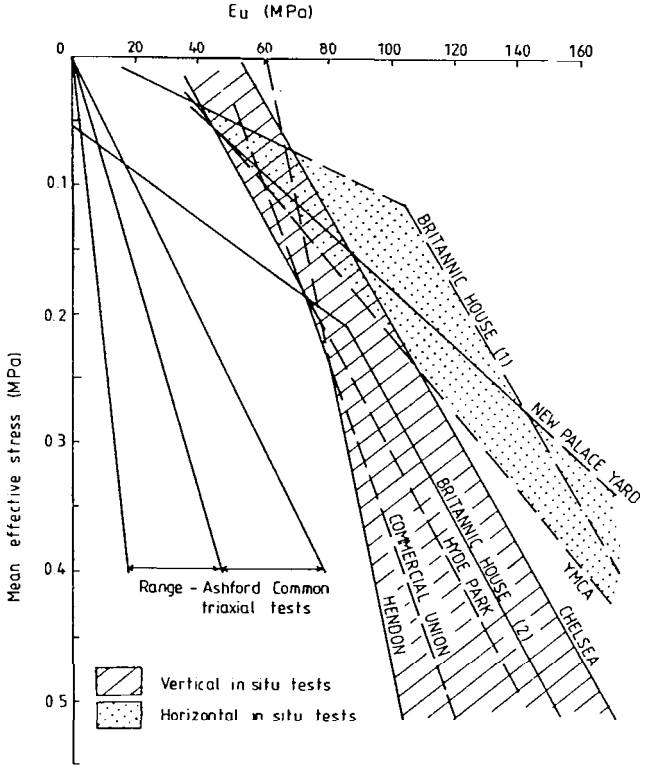


Figure 2.5: Variation of the undrained Young's modulus, E_u, with mean effective stress for a number of sites on London Clay (after St. John (1975))

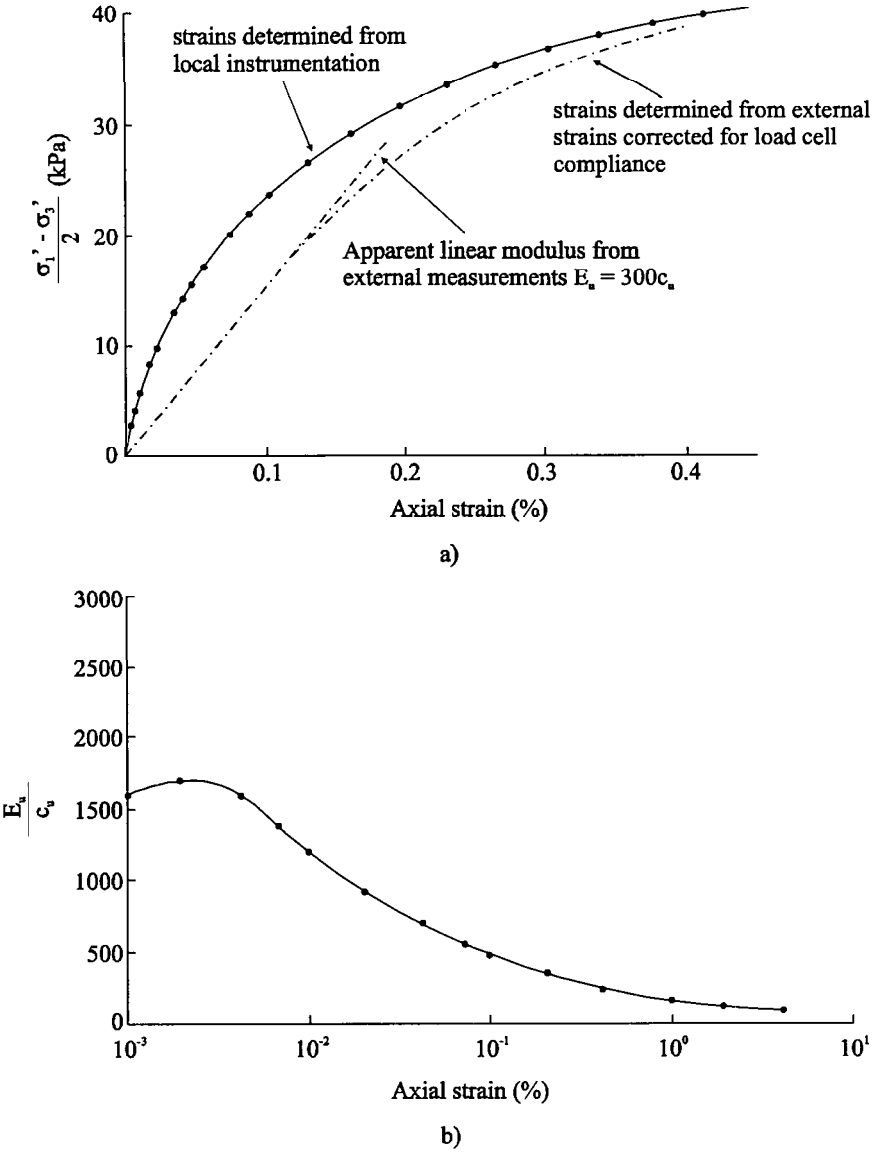


Figure 2.6: Typical London Clay unconsolidated undrained test data from Canons Park a) initial stress-strain behaviour; b) stiffness-strain characteristics (after Jardine et al. (1985))

values of stiffness.

Similar differences were also found when the laboratory stiffness data was compared with values of stiffness derived from in situ field tests. Marsland (1971) reported that values of stiffness derived from plate loading tests were between 1.8 and 4.8 times those determined from undrained triaxial tests. At the time the low stiffness values determined in laboratory tests were attributed to sample disturbance and the applicability of laboratory measurements as a reliable method of determining in situ stiffness was questioned.

However, developments in the measurements of soil stiffness in the laboratory have since shown that the reported discrepancies were due to inaccurate measurements of stiffness at small strains. Local measurements of strains on the samples revealed that the stress-strain behaviour of overconsolidated clays is strongly non-linear, with high values of stiffness at small strains, which were not measured correctly with the earlier conventional overall measurements of strain (Costa-Filho and Vaughan (1980), Burland and Symes (1982) Jardine et al. (1984)). Figure 2.6a shows the initial stress-strain behaviour of a sample of undisturbed London Clay from Canons Park subjected to unconsolidated undrained triaxial compression (after Jardine et al. (1985)). Both the conventional external and the local measurements are shown in the figure. It can be seen that the external measurements show an apparently linear initial stress-strain behaviour. However, the local measurements show a much stiffer non-linear behaviour. Figure 2.6b plots the stiffness determined from the local measurements in terms of E_u/c_u versus log strain where E_u is the secant undrained Young's modulus. The strongly non-linear behaviour of the sample, with stiffness reducing rapidly with strain, is evident. Jardine et al. (1985) demonstrated that when the local instrumentation on the samples was used for the measurements of strains then close agreement was found between laboratory and field tests.

Burland (1989) demonstrated the importance of the non-linear behaviour of the soil at small strains by examining the amount of straining that the ground is subjected to under engineering construction. He showed that for a range of construction projects the direct straining in the ground under working loads is generally less than 0.1%. As indicated by Figure 2.6b, it is within this range of strains, that the behaviour of the soil is expected to be highly non-linear. Therefore the small strain non-linearity plays an important role on the overall deformation response of the ground to engineering structures.

2.2.4 Simplified schemes of pre-failure behaviour

The stiffness-strain curve of overconsolidated clays is often idealised as an S-shaped curve, shown in Figure 2.7 (Atkinson and Sallfors (1991)). The stress-strain behaviour is highly non-linear as demonstrated by the stiffness variation with strain. Moreover at very small strains a region exists where the stiffness is almost a constant and behaviour is approximately linear. It is often assumed that in this region the soil behaviour is linear elastic. Once this region is crossed irrecoverable strains start to develop and the behaviour becomes highly non-linear. The stiffness-strain curve is often divided in three regions as shown in Figure 2.7. The very small strains region where stiffness is almost

constant with strain, this usually corresponds to strains generally less than 0.001%, the small strains region where the stress-strain behaviour is highly non-linear, this corresponds to strains generally between 0.001% and 1%, and the large strains where the stiffness is low and the soil is approaching failure, this correspond to strains generally larger than 1% (Atkinson and Sallfors (1991)).

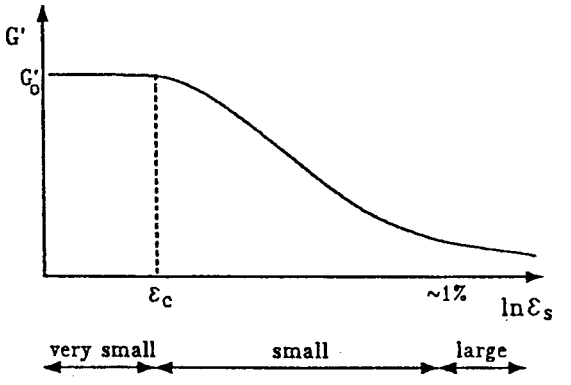


Figure 2.7: An idealisation for the variation of stiffness with strain for soil (after Atkinson and Sallfors (1991))

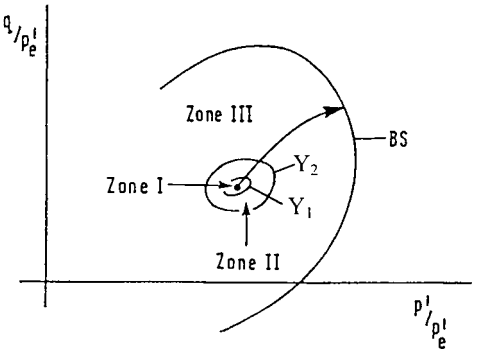


Figure 2.8: Scheme of kinematic strain regions (after Jardine (1992))

Jardine (1985), (1992), based on the results of an extensive series of tests on a reconstituted low plasticity clay (Magnus till), proposed the following scheme of pre-failure behaviour, shown in Figure 2.8. It was suggested that three distinct zones of behaviour exist. The boundaries of these zones are considered as sub-yield surfaces, which are kinematic (i.e. move with the current effective stress point) and are termed Y_1 and Y_2. The behaviour within Zone I is assumed to be linear elastic. As soon as the Y_1 surface is engaged, the soil enters Zone II. Within this zone the stress-strain behaviour is non-linear and hysteretic but load-unload cycles show recoverable behaviour. The mechanical behaviour within this region is thought to be the result of micro-yielding and

fretting at particle contacts, with stiffness being highly dependent on recent stress history. When the Y_2 surface is engaged, (Zone III), irrecoverable strains start to develop, which increase significantly as the bounding surface is approached. It is thought that in this zone, particles start to slide relative to one another and load columns break and reform continuously.

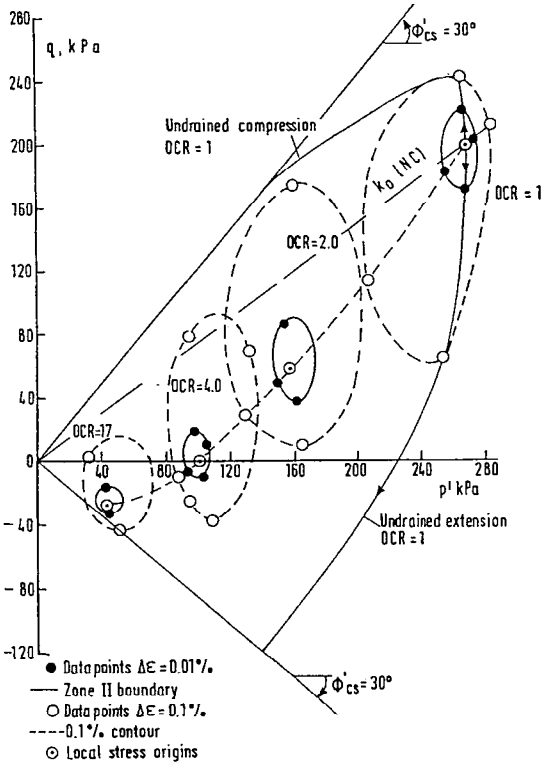


Figure 2.9: Movement and evolution of kinematic strain regions due to K_o swelling: Magnus till (after Jardine (1992))

Figure 2.9 shows the movement and evolution of the kinematic strain regions due to K_o swelling of Magnus till. Zone I could not be found with the resolution of the local instrumentation ($\varepsilon_a \sim 0.001\%$). The Zone II boundary was approximated with a contour representing axial strains of 0.01%. The contour that represents axial strains of 0.1% is also drawn on the same figure; this falls within Zone III and does not represent any particular boundary. The distance of the current stress point from a given strain contour in a certain direction represents a measure of the stiffness response of the soil for loading along that direction. The fact that the strain contours are not symmetrical around each current stress point and their shape and size is different at the various overconsolidation ratios, implies different stiffness response for different loading paths at each overconsolidation ratio and indicates the effect of stress history. For example, at $OCR = 1$ the loading response is softer than that for unloading, whereas the opposite is

true for heavily overconsolidated states. Other tests suggested that the material's stress-strain behaviour is time dependent and that ageing periods cause the surfaces to expand and/or change position.

Jardine (1985), (1992) defined the kinematic regions in terms of the magnitude of the major principal strain. Burland (1989) pointed out that the definition of the regions needs more study and suggested the use of the incremental strain energy. (For a definition of strain energy see section 2.3.3.1.)

In any case the idealisation of pre-failure behaviour involves the assumption that at very small strains the behaviour of the soil is linear elastic. Such an assumption is particularly attractive because of its conceptual simplicity; however the question arises whether such a region exists at all in reality. This is discussed further in the next section.

2.2.4.1 Existence of linear elastic region

The assumption of linear elasticity at very small strains stems from the observation that the initial values of stiffness measured in triaxial tests with local instrumentation were comparable with the values obtained in dynamic tests, in which by definition the behaviour is assumed to be linear elastic. Figure 2.10 compares stiffness curves obtained from undrained triaxial compression tests and resonant column tests on Vallericca clay (Georgiannou et al. (1991)). It can be seen that the initial values of stiffness obtained from the triaxial tests are in close agreement with the maximum level recorded in the resonant column tests. This could be considered as an indication of the existence of a linear elastic region. However, the results of the resonant column tests have to be examined with caution since the interpretation of the test assumes a linear elastic soil response and therefore the test is not applicable outside that region. Moreover, rate dependency effects could make the linear elastic plateau, seen in resonant column tests, extend further than in static constant strain rate tests (Isenhower and Stokoe (1981)). Also the local instrumentation used in the triaxial tests had relatively poor accuracy and the stiffness data was limited to a strain of 0.01% showing no plateau of constant stiffness with strain. (Recent studies (Lings et al. (2000)) have demonstrated that an agreement between the stiffness measured in undrained triaxial tests and dynamic tests can only be expected for an isotropic soil.)

Nowadays developments in the local instrumentation allow the stiffness of the soil to be determined at much smaller strain levels. Figure 2.11 shows the initial part of stiffness-strain curves obtained in undrained triaxial compression tests for three geomaterials,

Chalk, London Clay and Bothkennar Clay (Clayton and Heymann (2001)). The stiffness of all three geomaterials appears to be constant for strains up to approximately 0.001%

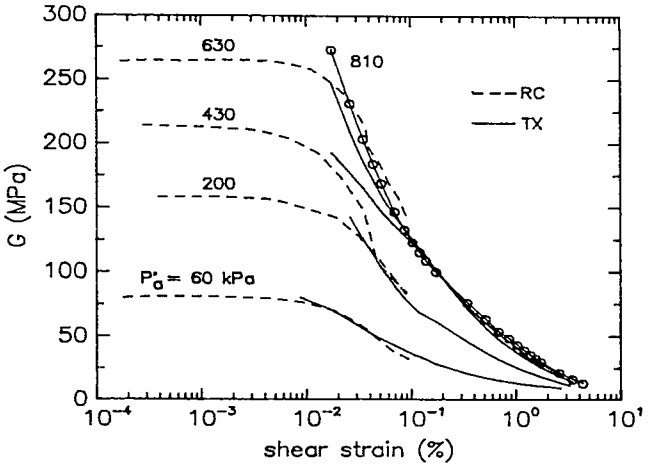


Figure 2.10: Comparison between shear stiffness obtained in resonant column and undrained triaxial compression tests: Vallericca clay (after Georgiannou et al. (1991))

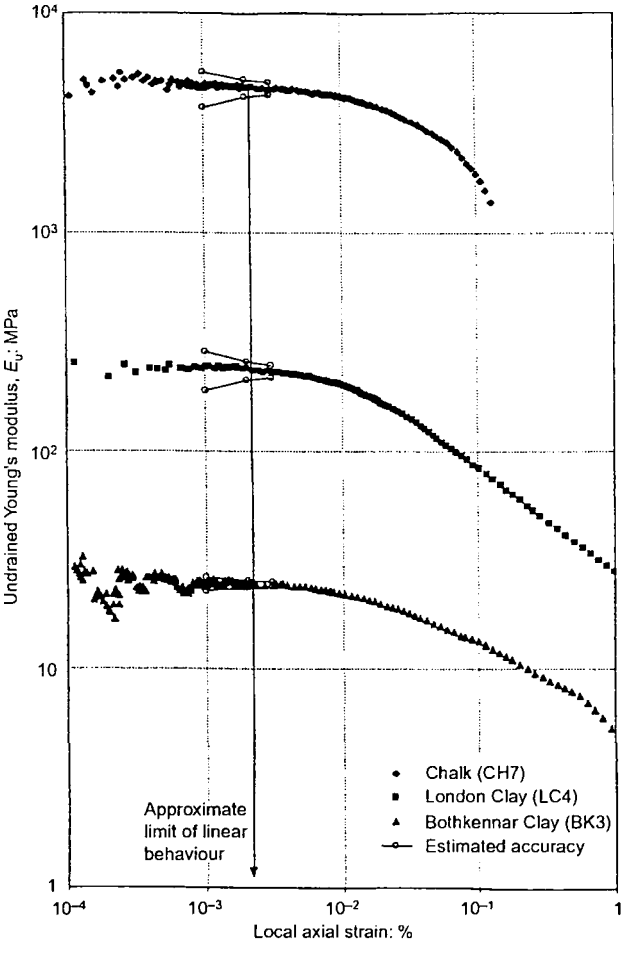


Figure 2.11: Initial portion of stiffness-strain curves for three geomaterials (after Clayton and Heymann (2001))

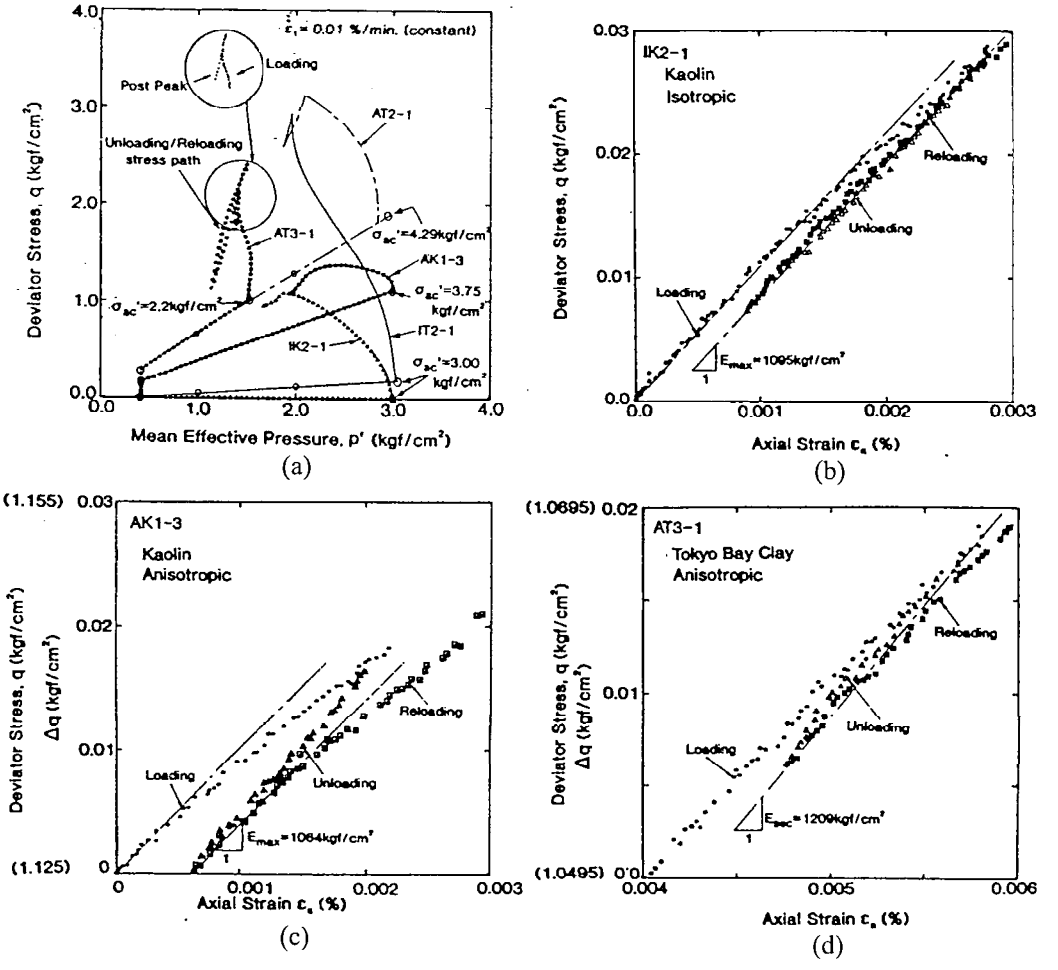


Figure 2.12: Undrained stress-strain response of undisturbed Tokyo Bay Clay and reconstituted kaolin a) stress paths b) stress-strain curve of isotropically consolidated kaolin (c) stress-strain curve of anisotropically consolidated kaolin d) stress-strain curve of anisotropically consolidated Tokyo Bay Clay (after Tatsuoka and Shibuya (1992))

to 0.002%. This plateau is indicative of linear stress-strain behaviour; however the error bands shown in the figure have to be taken into account when examining the validity of linear behaviour.

In order to prove that the behaviour at small strains is not only linear but also elastic then the behaviour has to be shown to be totally recoverable, so that load-unload loops show no hysteresis. Figure 2.12 shows the results of consolidated undrained triaxial tests carried out on natural samples of Tokyo Bay Clay and reconstituted kaolin (Tatsuoka and Shibuya (1992)). The Tokyo Bay Clay sample (AT3-1) was anisotropically consolidated to the estimated in situ stresses and the kaolin samples were either consolidated isotropically (sample IK2-1) or anisotropically (sample AK1-3), see Figure 2.12a. All three specimens were sheared undrained and were subjected to a number of unloading-reloading cycles. Figures 2.12b, 2.12c and 2.12d show the initial portion of

the stress-strain curves at very small strains for the samples IK2-1, AK1-3 and AT3-1 respectively. Although not shown in the figures, the limit of linear behaviour extended to approximately 0.002% axial strain for the Tokyo Bay Clay (AT3-1) and to 0.001% for the kaolin. The first unloading-reloading cycle at very small strains did not show fully recoverable behaviour in any case. This could be attributed to the fact that the cycles were carried out outside the limit of linear behaviour. However, an indication of elastic behaviour in these tests is the fact that the initial stiffness during the first loading is the same with the initial stiffness during reloading.

From the evidence presented above it can be concluded that although the existence of a small linear elastic region has not be proven fully up to date, there are strong indications that the behaviour at very small strains can be considered as linear elastic. This together with its conceptual simplicity makes the linear elastic idealisation an assumption commonly adopted in numerical analysis.

2.2.5 Factors that affect soil stiffness

There is a great number of factors that affect soil stiffness. Here only the most important ones will be reviewed. These can be summarised as: current stress state-volume state, soil structure, ageing, recent stress history and stress path direction. Each of these factors is discussed in the next sections. Particular emphasis is given on the effects of recent stress history and stress path direction, and the influence that ageing has on them, since these are the effects that have been explored in the numerical analyses carried out in this thesis. In many cases the soil response is going to be considered in terms of very small strains, small strains and large strains as defined in section 2.2.4. A more extensive review of factors that affect soil stiffness can be found in Atkinson and Sallfors (1991), Jardine (1995) and Heymann (1998).

2.2.5.1 Current stress state-volume state

The dependence of the soil stiffness on the current stress state has been approached by either idealising the soil as an assembly of elastic spheres or considering its mechanical behaviour to be essentially frictional. If the mechanical behaviour of the soil is assumed to be purely frictional then its strength and stiffness is directly proportional to the mean effective stress, p'. If the soil is idealised as an assembly of elastic spheres then the theoretical work by Hertz and Mindlin (as reported by Richart et al. (1970)) suggests that the soil stiffness varies with the mean effective stress, p', raised to the power of n

equal to 1/3. Viggiani and Atkinson (1995) suggested that at very small strains the soil is expected to follow the theory of the elastic spheres while at large strains the purely frictional case is expected to apply.

Very small strains

Experimental evidence suggests that at very small strains the power coefficient, n, is higher than 1/3. Apart from small slippage and rearrangement, which would indicate inelastic behaviour, this could also be attributed to the soil particles having different sizes, shapes and angularity within a real soil (Jovicic (1997)). A number of equations have been proposed in the literature for the calculation of stiffness at very small strains. Although relying on a theoretical background, these relationships are generally derived from dynamic tests and are therefore semi-empirical.

Hardin and Black (1968), based on the results of resonant column tests on normally consolidated kaolin and Boston Blue clay, proposed the following relationship for the shear stiffness at very small strains:

$$G_o = A(T)\,F(e)\,p'^{n} \tag{2.7}$$

Equation 2.7 shows the dependence of the stiffness on the mean effective stress and the void ratio. In this equation $F(e)$ is a function of the void ratio, n is the power coefficient which for the material tested was found equal to 0.5, and $A(T)$ is a constant which groups together the influence of all other factors.

Hardin and Black (1969), based on the results of resonant column tests on a range of clays, extended the above equation to account for overconsolidated stress states:

$$G_o = A(T)\,F(e)\,p'^{n}OCR^{k} \tag{2.8}$$

In the above equation OCR is the overconsolidation ratio, defined as the ratio of the maximum past vertical stress to the current vertical stress, and k is the corresponding power coefficient which depends on the plasticity index.

Hardin (1978) combined Equation 2.8 with the work of Janbu (1963) and the elastic stress-strain relationships by Rowe (1971) and proposed a more general equation of the following form:

$$G_o = A\,F(e)\,p'^{n} OCR^{k} p_a^{1-n} \tag{2.9}$$

The introduction of the atmospheric pressure, p_a, in the above equation makes the parameter A dimensionless.

It can be seen that the above equations make use of the three variables; mean effective stress, void ratio and overconsolidation ratio. Within the framework of critical state soil mechanics these three variables can be interrelated, if the overconsolidation ratio is redefined as the isotropic overconsolidation ratio, R_o. This is equal to the ratio of the maximum past mean effective stress, to the current mean effective stress, $R_o = p'_p / p'$, as shown in Figure 2.13 (Viggiani and Atkinson (1995)). In this case only two of the three variables are necessary in the above equations.

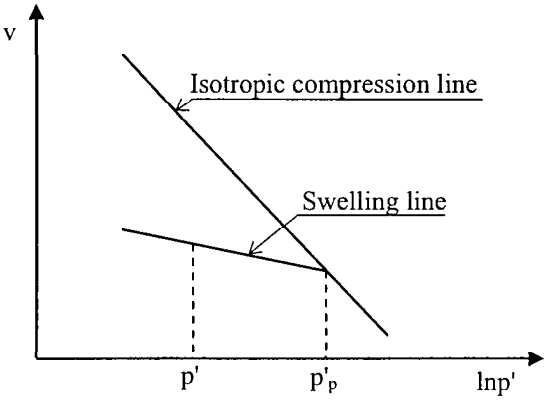


Figure 2.13: Definition of isotropic overconsolidation ratio

Viggiani (1992), based on the results of bender element tests on reconstituted samples of a number of clays, proposed the following equation for the small strain shear modulus, making use of only two variables, the mean effective stress, p', and the isotropic overconsolidation ratio R_o:

$$\frac{G_o}{p_r} = A\left(\frac{p'}{p_r}\right)^{n} R_o^{\,m} \tag{2.10}$$

In the above equation p_r is a reference pressure which is usually taken equal to 1 kPa and A, n and m are dimensionless parameters which depend on the plasticity index, see Figure 2.14. For normally consolidated clays R_o becomes equal to unity and the equation reduces to the one proposed by Wroth and Houlsby (1985) for the shear modulus of sands.

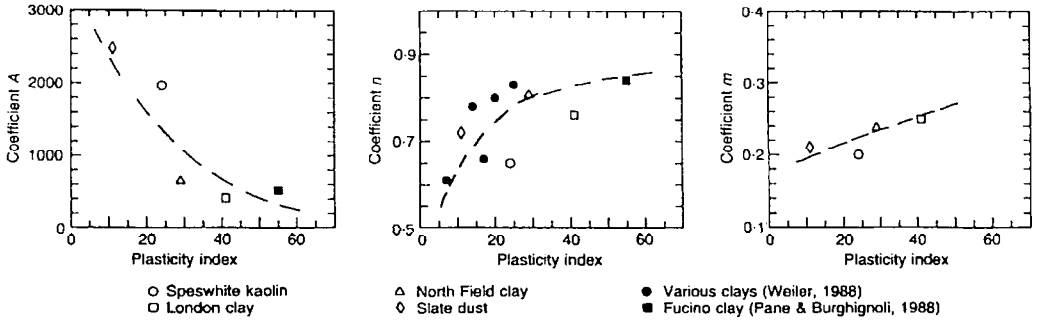


Figure 2.14: Variation of stiffness parameters A, n and m with plasticity index (after Viggiani and Atkinson (1995))

Small to large strains

As it was mentioned before, at large strains the soil is expected to resemble an assembly of rigid frictional particles, in which case the stiffness varies linearly with the mean effective stress, and n is equal to 1. This is confirmed by the work of Gens (1982) on Lower Cromer Till, who showed, from undrained triaxial tests on normally consolidated and overconsolidated samples, that the behaviour at large strains is linearly normalisable by the mean effective stress.

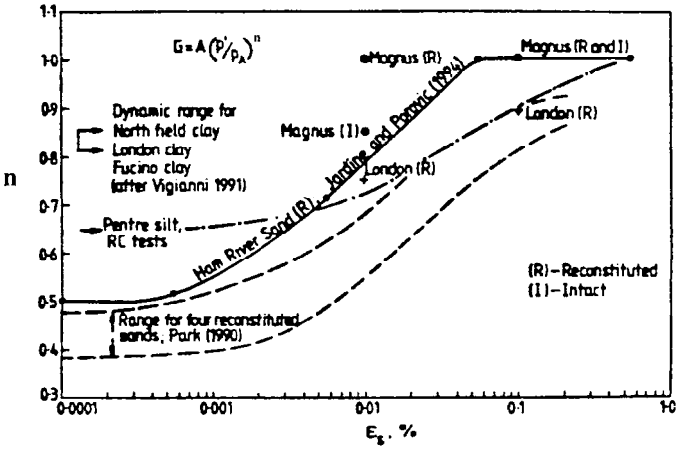


Figure 2.15: Effects of strain on stress level exponent n (after Jardine (1995))

In the intermediate range of small strains it is expected that the stress level dependency of the stiffness varies with strain level, from the value of n at very small strains to the value of $n = 1$ at large strains. Jardine (1995) presents a summary of the way the exponent n varies with strain level, for a range of soils, see Figure 2.15. It can be seen that n increases with strain level tending to unity at large strains. Viggiani and Atkinson (1995) suggested that Equation 2.10, which was originally derived for the very small

strain range, is also applicable at higher levels of strain, but with values of A, n and m that vary with the strain level. Figure 2.16 shows the variation of the parameters A and n with strain level, derived from a set of constant p' drained triaxial compression tests carried out on normally consolidated samples of kaolin clay. Again it is shown that the exponent n increases from the value determined from the bender element test towards unity at large strains, while the exponent A is shown to decrease with strain level.

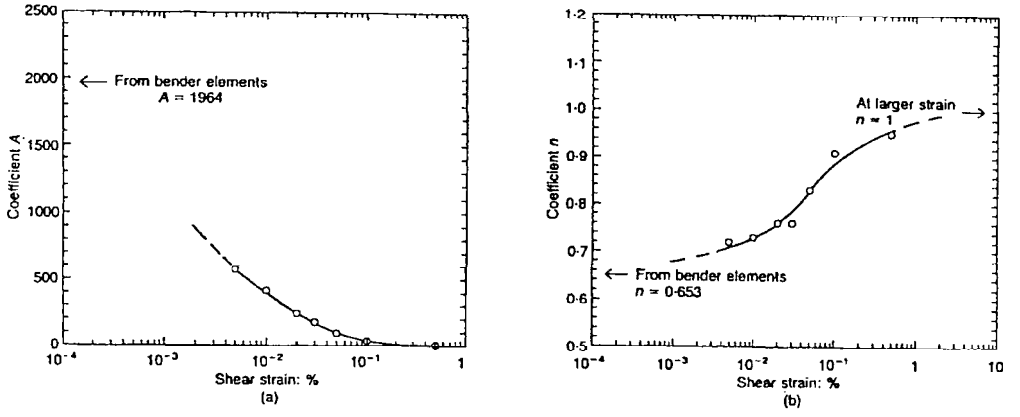


Figure 2.16: Variation of the parameters A and n with strain (after Viggiani and Atkinson (1995))

2.2.5.2 Soil structure

As it has already been mentioned, structure is the combination of fabric and bonding. In this section two issues of the influence of soil structure on soil stiffness are discussed. The first one is the effect of the different structure that the natural clays possess compared to the reconstituted clays and the second one is the effect of the anisotropic fabric that both natural and reconstituted clays can exhibit.

i) Effect of different structure between natural and reconstituted clays

Rampello and Silvestri (1993) examined the very small strain stiffness of natural and reconstituted Vallericca clay, a stiff overconsolidated clay, using resonant column tests. The stiffness of the natural samples was shown to be generally higher than the stiffness of the reconstituted samples, see Figure 2.17. This difference was attributed to the different location of the isotropic compression lines. The natural isotropic compression line plotted well to the right of the reconstituted one (termed intrinsic, after Burland (1990)), showing the effect of the difference in structure between the natural and the reconstituted material. Rampello and Silvestri (1993) went on to show that when the stiffness data was normalised with respect to the equivalent pressure on the appropriate

isotropic compression line then the stiffness of the natural and reconstituted samples plot very closely, see Figure 2.18.

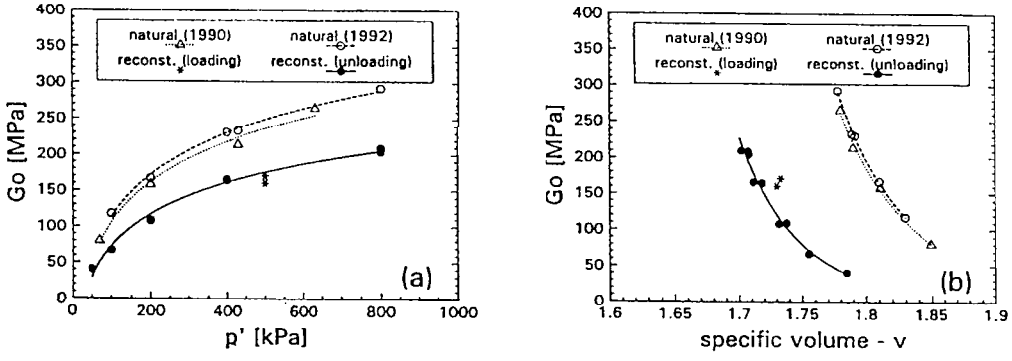


Figure 2.17: Vallericca clay: initial shear modulus versus a) mean effective stress and b) specific volume (after Rampello and Silvestri (1993))

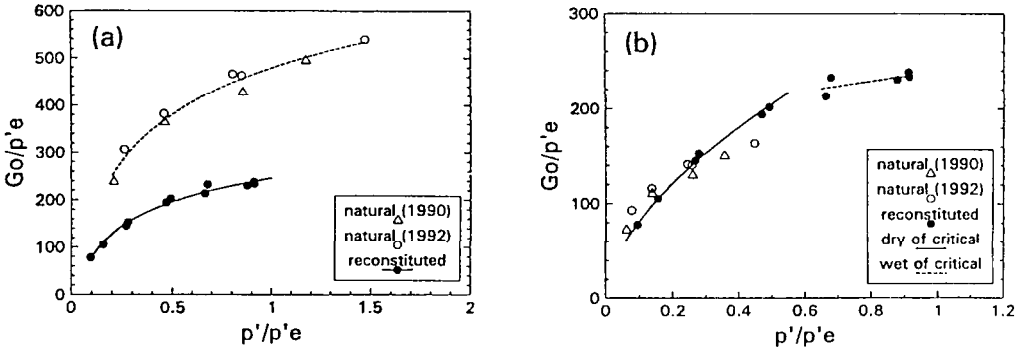


Figure 2.18: Vallericca clay: initial shear modulus normalised by a) the intrinsic and b) the appropriate equivalent pressure (after Rampello and Silvestri (1993))

Cotecchia and Chandler (1997) compared the pre-failure behaviour of natural and reconstituted Pappadai clay, a stiff overconsolidated clay, in undrained triaxial compression tests. They showed that there is little difference between the normalised stiffness $G/(p')^n$ of the natural and reconstituted samples in the small to intermediate strain range, if this is plotted against either the isotropic overconsolidation ratio, R_o, in the case of the reconstituted samples or the yield stress ratio in isotropic compression, YSR_{is}, in the case of the natural samples, Figure 2.19. Similar findings were reported by Coop et al. (1995), who showed that there was no clear distinction between the stiffness of natural and reconstituted Boom clay (a stiff overconsolidated clay), in the small to intermediate strain range, if the state relative to the appropriate natural or intrinsic isotropic compression line was taken account of.

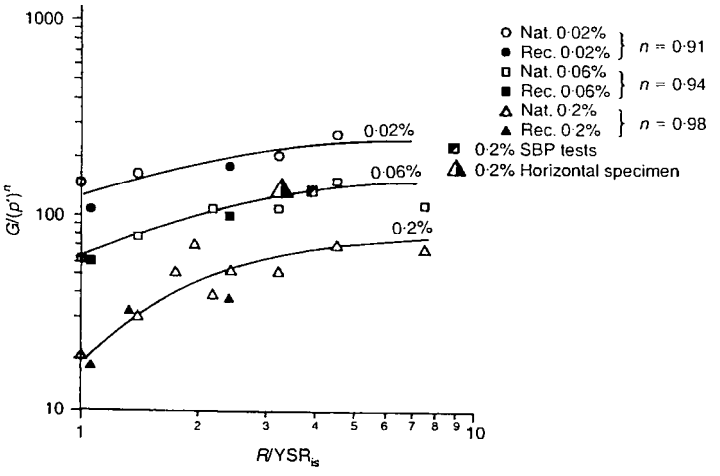


Figure 2.19: Normalised shear stiffness of both natural and reconstituted Pappadai clay (after Cotecchia and Chandler (1997))

ii) Effect of anisotropic fabric

Soils generally posses an anisotropic fabric. This can be the result of a number of factors, like deposition, anisotropic consolidation and subsequent stress history. This anisotropic fabric on a macro scale gives rise to mechanical anisotropy of the soil, which means that its properties become directional dependent (Mitchell (1976)).

Anisotropy of the soil results in anisotropic state boundary surfaces that are no more centred around the isotropic axis, as is the case for the state boundary surfaces of isotropically consolidated soils (eg. Parry and Nadarajah (1973), Graham et al. (1983)). The initial anisotropy of a soil at a current stress state can change with straining due to subsequent loading, causing the shape, size and orientation of the initial anisotropic state boundary surface to change as well.

In terms of small strain deformations, soils are often assumed to behave as cross-anisotropic materials, due to the way they were deposited. This means that they are assumed to have symmetry around the vertical axis so that they behave the same way in any of the two horizontal directions and differently in the vertical direction. Jamiolkowski et al. (1995) investigated the anisotropy of the very small strain stiffness of six natural clays. The tests were performed using an oedometer equipped with bender elements so that the shear wave velocities propagating at three different directions could be measured. They found that the ratio of the shear modulus in the horizontal plane to the shear modulus in the vertical plane, G_{hh}/G_{hv}, which is an expression of the degree of anisotropy, varied between 1.2 and 2. Jovicic and Coop (1998) examined the very small strain stiffness anisotropy of London Clay by conducting bender element tests on

natural and reconstituted samples. The reconstituted samples followed the geological history of the natural deposit. The ratio G_{hh}/G_{hv} was found to be equal to 1.5 for both natural and reconstituted samples. Furthermore the values of G_{vh} and G_{hv} (shear moduli in either vertical planes) were found to be equal for the natural samples, indicating that London Clay behaves as a cross-anisotropic material at very small strains.

2.2.5.3 Ageing

Ageing generally increases the soil stiffness with two mechanisms; increased interparticle bonding and volume reduction under constant stress due to creep. Since there is not much data available for overconsolidated clays, this section will include work undertaken on normally consolidated clays.

Som (1968) was one of the first to note the effects of ageing in the laboratory. In some of his oedometer tests, he observed that after keeping the loading constant for an extended period of time, an exceptionally high stiffness was recorded for the next small increment of applied strain.

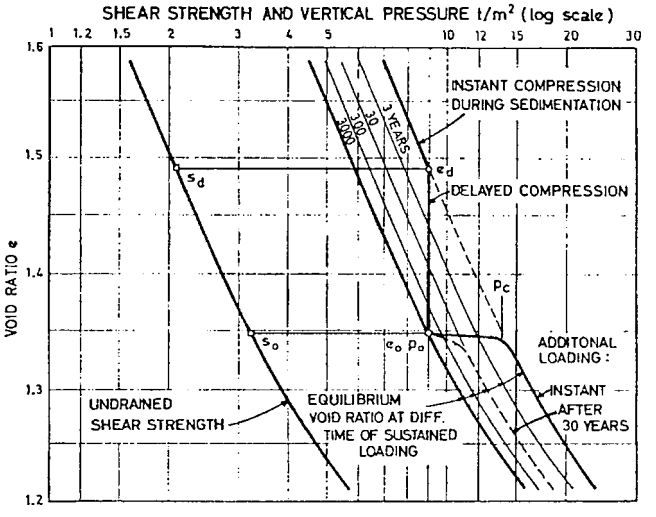


Figure 2.20: The effect of creep on the yield stress of normally consolidated clay (after Bjerrum (1967))

Bjerrum (1967) discussed the effect of ageing on the compressibility of soft Norwegian clays. It was shown that when a normally consolidated clay was kept under constant effective stress, volume reduction occurred due to secondary consolidation and the yield stress recorded on subsequent loading was much higher than the current stress. Figure 2.20 shows the system of lines that Bjerrum used to illustrate the effect of creep. It can be seen that when a soil element is loaded after a certain rest period then this yields on

the compression line that the same soil element would have followed if no creep had occurred. This demonstrates only the effect of ageing due to volumetric creep. Bjerrum (1967) recognised that apart from the effect of creep, increased interparticle bonding can develop during the rest period which leads to further increase of the yield stress, Figure 2.21. It has to be noted that from Figure 2.21 it seems that the effect of increased interparticle bonding acts in addition to the effect of creep. Both effects result in an increased resistance to compression.

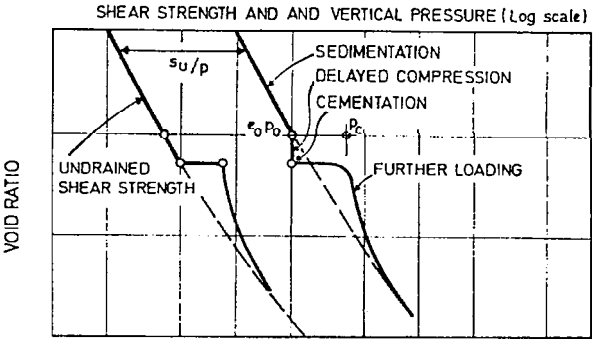


Figure 2.21: The effect of cementation on the yield stress of normally consolidated clay (after Bjerrum (1967))

Leonards and Ramiah (1959) investigated the effect of ageing on the one dimensional compression of normally consolidated reconstituted clays. Figure 2.22 shows some of their results (after Burland (1990)). The first curve, in this figure, represents a standard oedometer test, the second curve represents a standard oedometer test with a rest period of 12 weeks at σ'_v = 40 kPa and the third curve shows the results of a test with a rest period of 12 weeks at σ'_v = 40 kPa but in which creep was prevented during the rest period. The fourth curve represents a test with a 12 week rest period at 40 kPa, conducted with a lucite oedometer (the side friction of which was known to be very small (Burland (1990)). It can be seen that after the rest period there is an increase in the yield stress irrespective of whether or not creep was allowed. This is evidence that the increased resistance due to ageing is not just because of the effect of creep but also because of the bonding developing during the rest period.

Schmertmann (1991) reviewed many results in which the effect of ageing was to increase the stiffness of the soil. However, his examples showed no evidence of increase of bonding during the rest period and it was argued that it was the mechanical features of ageing that resulted in increased stiffness. This is in contrast to the examples discussed in this section. Heymann (1998) argued that Schmertmann's conclusion should be regarded with caution. This is because his technique can generally be considered

reliable only at strains in excess of 0.5%. According to Heymann, at these strains destructuring could have reduced the effects of bonding, which is important at lower levels of strain but can break down under loading, as also shown in Figure 2.21.

Jardine (1992) demonstrated that ageing influences the kinematic strain regions shown in Figures 2.8 and 2.9 and discussed in section 2.2.4. The effect of ageing on normally consolidated Magnus till resulted in the Y_2 surface and the bounding surface growing away from the maintained stress point with time.

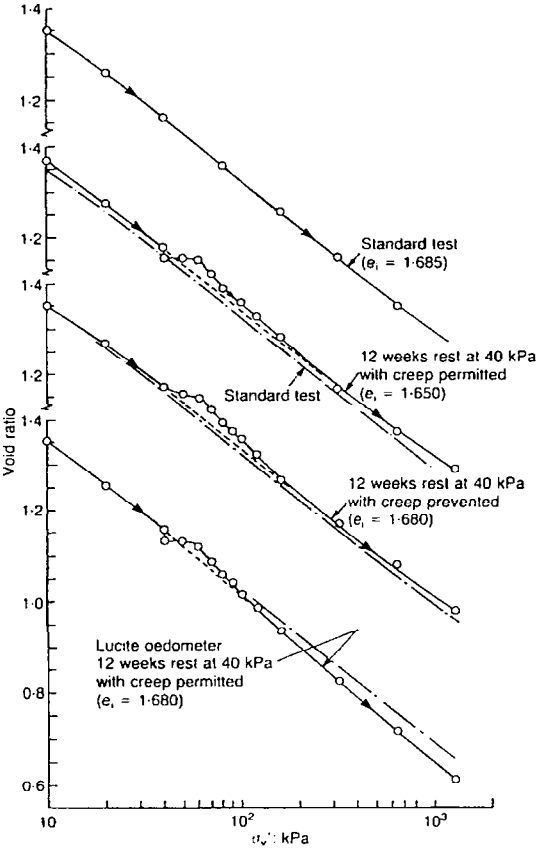


Figure 2.22: The effect of ageing on the yield stress of normally consolidated clay (redrawn by Burland (1990) after Leonards and Ramiah (1959))

2.2.5.4 Recent stress history

Atkinson et al. (1990) studied the effect of recent stress history on the stiffness of overconsolidated soil by performing drained triaxial constant p' and constant q tests on reconstituted overconsolidated samples of London Clay. The tests involved bringing the samples to a common stress state by following different approaching paths and then shearing along a common loading path, path OA in the constant p' tests, see Figure 2.23.

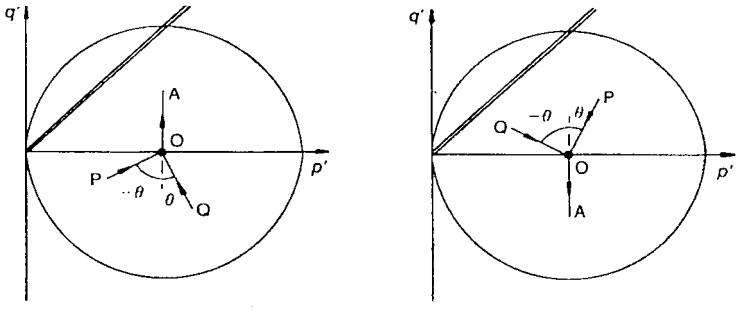


Figure 2.23: Stress paths followed in constant p' tests (after Atkinson et al. (1990))

This resulted in an angle, θ, between the approaching path and the loading path equal to 0°, +90°, -90° and 180°. Plots of tangent stiffness against strain are presented in Figure 2.24. The accuracy of the equipment allowed strain measurements in the small to large strain range. It can be seen that at small strains the highest stiffness is observed for the case of $\theta = 180°$, where there is a complete reversal in the stress path direction, whereas the lowest stiffness is observed for $\theta = 0°$ where there is no change in the stress path direction. This effect of the direction of the approaching path relative to the direction of the loading path is termed the effect of recent stress history.

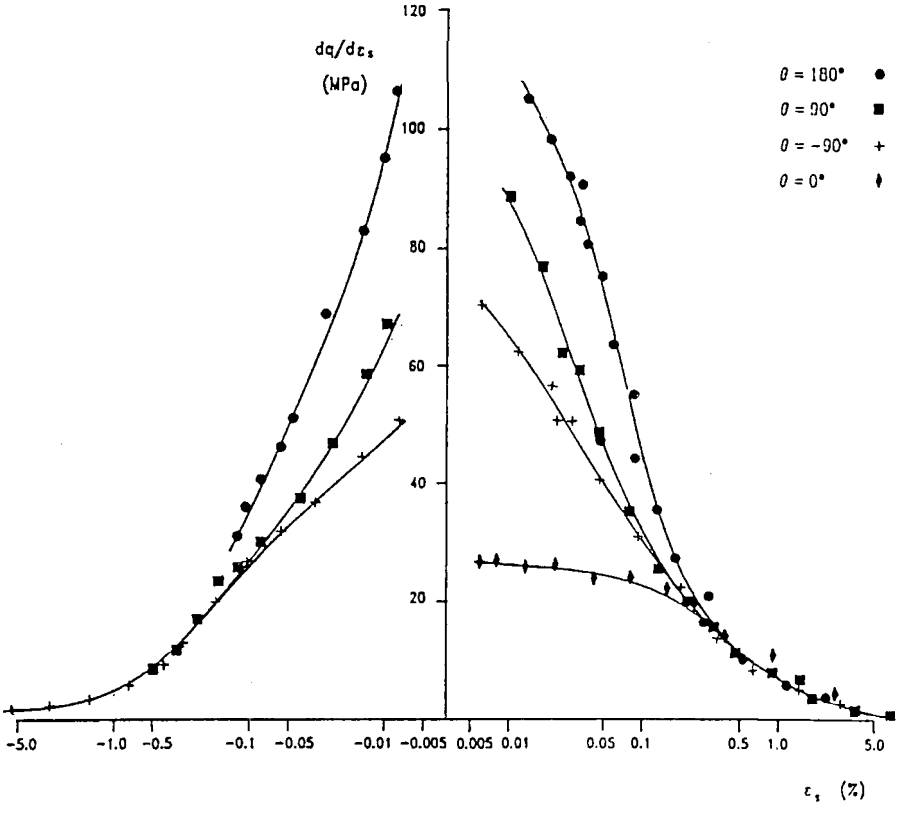


Figure 2.24: Stiffness of reconstituted London Clay versus strain measured in constant p' tests (after Atkinson et al. (1990))

Figure 2.24 shows that this effect seems to decrease as the soil is loaded and becomes negligible after strains of about 0.5%. Before loading along the path OA the samples were held at a constant stress for a period of three hours. This was twice the time required for primary consolidation but was probably not sufficient in order to minimise the effect of creep, as suggested by Heymann (1988). Therefore it is possible that the results presented by Atkinson et al. (1990) are influenced by the effect of creep and in this case it is reasonable to measure an increased stiffness after a stress path reversal and a reduced stiffness in the case of no stress path reversal.

The effect of recent stress history is also shown in the data of Smith (1992), on natural Bothkennar Clay. Figure 2.25 shows plots of shear stiffness with strain for two 'identical' block quality samples subjected to undrained triaxial compression. A different reconsolidation path was used for each sample; one followed the most direct route ED, whereas the other followed the indirect route ABCD. Local instrumentation allowed the measurement of stiffness in the small strain range. It can be seen that the stiffness of the sample that followed route ABCD, in which case there was a reversal in the stress path direction is much higher than the stiffness of the sample that followed route ED, where there was no change in the stress path direction. Before the start of shearing along the common path, ageing periods were maintained at stress state D. A limiting axial creep rate of 0.05% per day was adopted. Although this ageing period was much longer than the three hours adopted by Atkinson et al. (1990), the effect of recent stress history is still evident in the results presented in Figure 2.25.

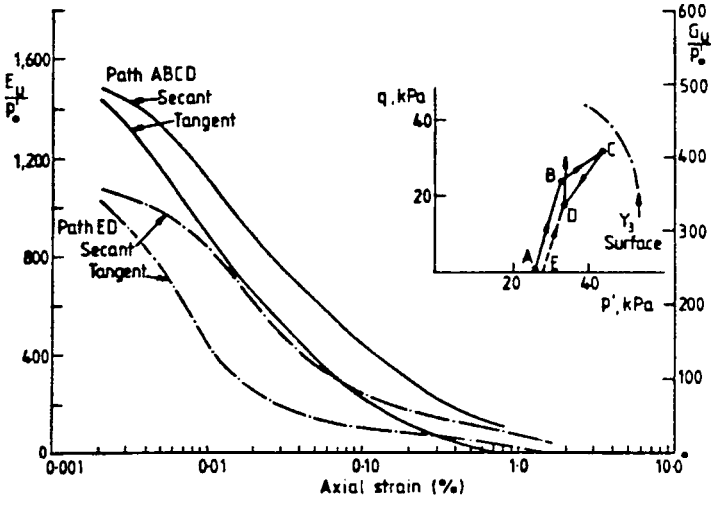


Figure 2.25: Undrained compression stiffness of natural Bothkennar Clay for two different reconsolidation paths (after Smith (1992))

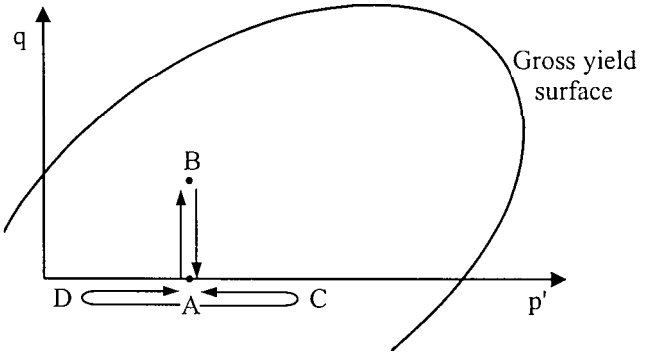


Figure 2.26: Stress paths followed in a single sample of natural Bothkennar Clay (after Clayton and Heymann (2001))

Clayton and Heymann (2001) investigated the effect of recent stress history on natural Bothkennar Clay by conducting tests similar to Atkinson et al. (1990). Figure 2.26 shows the stress paths followed in a single sample. The incoming stress paths BA, CA and DA had relative angles to the outgoing stress path starting from A equal to 180°, +90° and -90° respectively. A rest period was applied at point A before the beginning of the common loading stage. This rest period varied from 1 to 3 days and ensured that the locally measured creep rates were less than 0.01% per day at the start of each shearing stage. Local instrumentation allowed the measurement of strains at the very small to small strain range. Figure 2.27 presents plots of undrained stiffness with strain for the three repeated loading paths. As it can be seen, no perceptible difference in the three stiffness-strain curves was observed, in either the very small strain region or in the small strain region. Based on these results, Clayton and Heymann (2001) suggested that if enough time is allowed for the effect of creep then there is no effect of recent stress history.

When comparing the results of Smith (1992) and Clayton and Heymann (2001), it seems that the stricter limiting creep rate in the latter case results in erasing the effect of recent stress history. However there is also an important difference between the two investigations. The stress paths conducted by Smith were closer to the gross yield surface and involved more straining before the start of the common loading path than the stress paths conducted by Clayton and Heymann, and this could also explain part of the discrepancy between their results.

From the evidence presented above, one could postulate that the recent stress history is an effect which itself depends on time. It seems to be very important if little time is allowed between the incoming and outgoing stress paths and seems to diminish and even vanish as long rest (ageing) periods are allowed between the stress paths. In terms of

kinematic regions surrounding the current stress point, Jardine (1992) has already showed that these change with ageing time, which could explain the effect of recent stress history diminishing with time. Moreover the effect of recent stress history seems also to depend on the amount of straining that takes place before the outgoing stress path, the more the straining the more evident the effect seems to be.

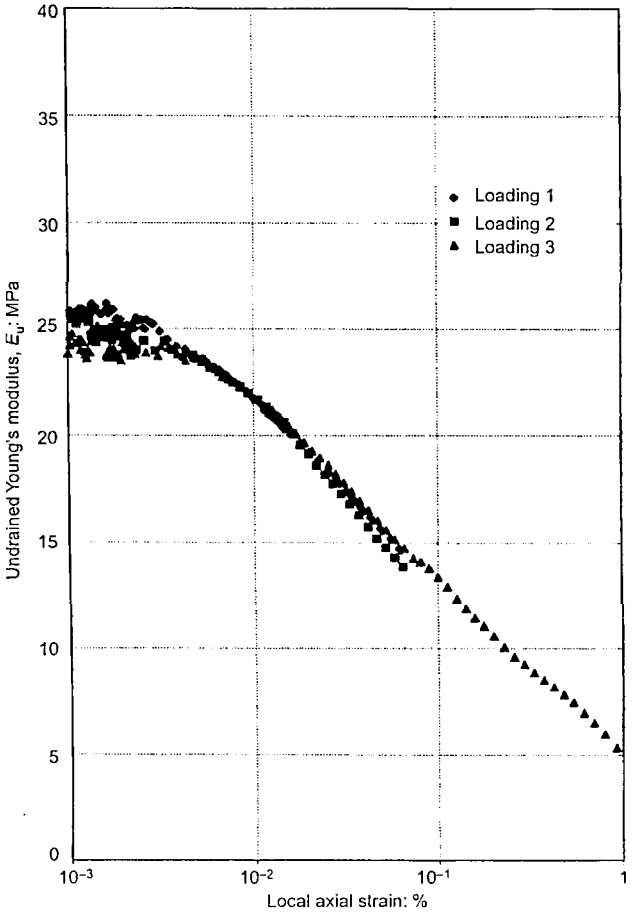


Figure 2.27: Stiffness versus strain for a single Bothkennar Clay specimen subjected to three identical repeated loading paths (after Clayton and Heymann (2001))

2.2.5.5 Stress path direction

Clayton and Heymann (2001) suggested that what really influences stiffness is the direction of the current loading path, rather than recent stress history. This observation was based on the results of undrained triaxial compression and extension tests on natural samples of Bothkennar and London Clay. Figure 2.28 shows the stress paths applied to the samples. Each sample was initially reconsolidated to its estimated in situ stresses, point B, and was used for both the compression and extension tests. Before the start of each shearing stage, pause periods were again maintained so that the locally measured creep rates were less than 0.01%. Figures 2.29 and 2.30 show the normalised

stiffness-strain curves for the Bothkennar Clay sample and the London Clay sample respectively.

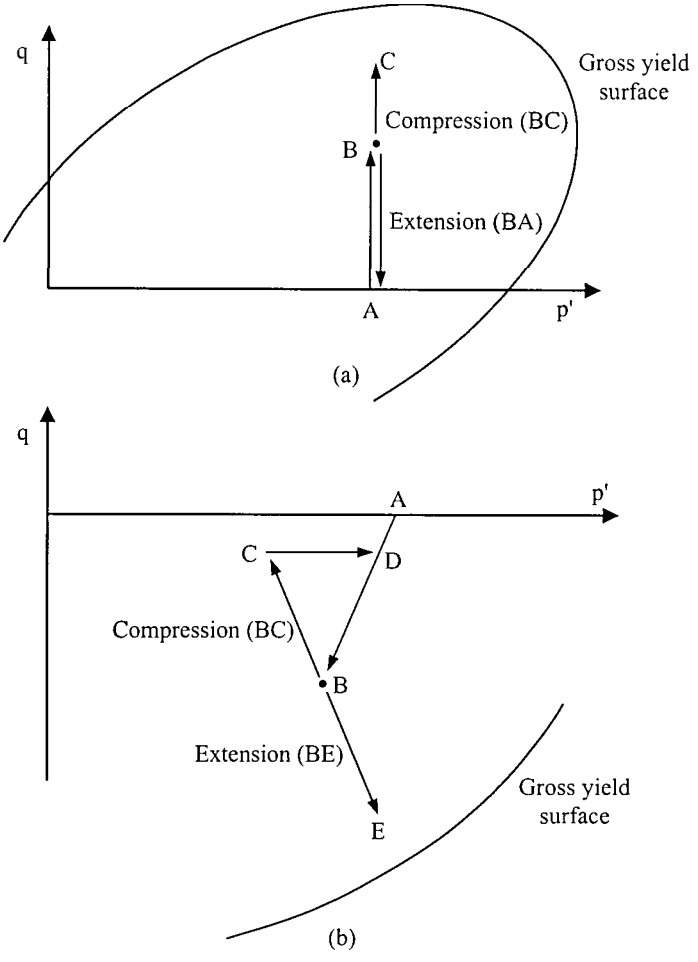


Figure 2.28: Stress paths applied to a) Bothkennar Clay and b) London Clay (after Clayton and Heymann (2001))

It can be seen that the very small strain stiffness of each sample is the same for compression and extension but the rate of stiffness degradation with strain, in the small strain range, is affected by the shearing mode. In the case of the Bothkennar Clay sample the stiffness in compression is softer than the stiffness in extension whereas for the London Clay sample the opposite is true. Clayton and Heymann (2001) suggested that these results are reminiscent of those reported by Atkinson et al. (1990), in the sense that the stress path that shows the higher stiffness in the small strain range is also the one involving a stress path reversal (Figure 2.28). However, the fact that the very small strain stiffness does not seem to be influenced by the direction of the previous stress path combined with their results on recent stress history shown in Figure 2.27 led them to suggest that what is shown in Figures 2.29 and 2.30 is the result of the effect of the

outgoing stress path direction relative to the gross yield surface. It seems that in both cases the stress path that takes the loading close to the gross yield surface shows softer behaviour than the stress path that takes it away from the gross yield surface. Therefore it was concluded that it is the effect of the current stress path direction that is important.

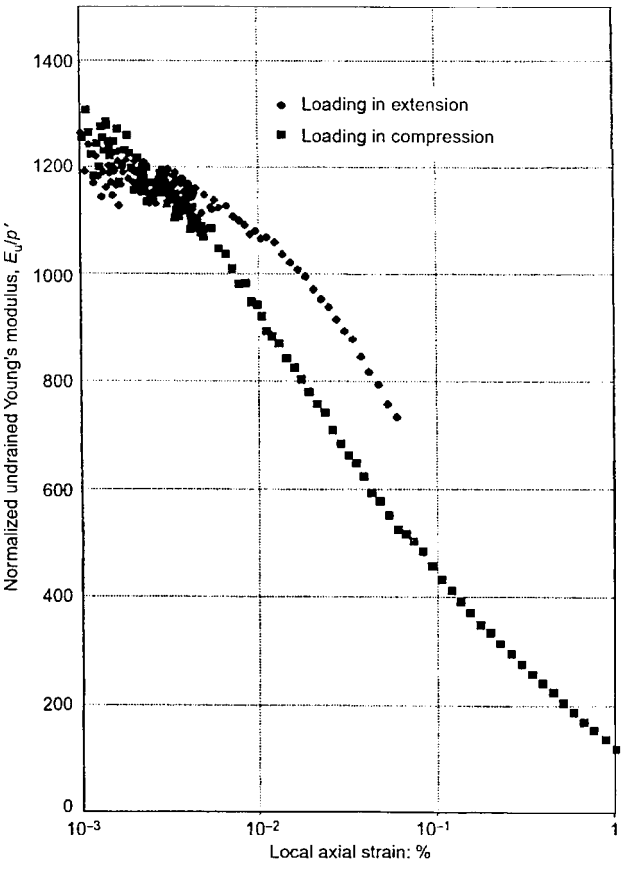


Figure 2.29: Bothkennar clay: normalised stiffness versus strain from undrained triaxial compression and extension tests (after Clayton and Heymann (2001))

This effect can also be seen in the work of others, but in some cases it is difficult to isolate it from the effect of recent stress history. Jardine (1985) and Fourie (1984) presented a series of tests on reconstituted London Clay. The samples were one-dimensionally compressed and swelled to various overconsolidation ratios and then subjected to undrained triaxial compression and extension. The results can be seen in Figure 2.31; LR denotes the compression tests, LRE denotes the extension tests and the following number denotes the overconsolidation ratio. A limiting creep rate of 0.05% per day, greater than the limiting creep rate of Clayton and Heymann, was adopted before the start of each shearing stage. For overconsolidation ratios of 3 and 7 the stiffness in compression was higher than the stiffness in extension as can be seen in Figure 2.31. One could postulate that this is an effect of the direction of the current

stress path. However this could also be interpreted as an effect of recent stress history, since the path that involves a stress reversal (i.e. compression loading), and gives the highest stiffness, coincides with the path that takes the stress state away from the gross yield surface. In this case it is difficult to assess whether it is solely an effect of stress path direction or recent stress history, or a combination of both. However, for an overconsolidation ratio of 1.5 the stiffness in compression is still higher than the stiffness in extension, although the compression path takes the stress path closer to the gross yield surface. This clearly indicates an effect of stress history rather than stress path direction.

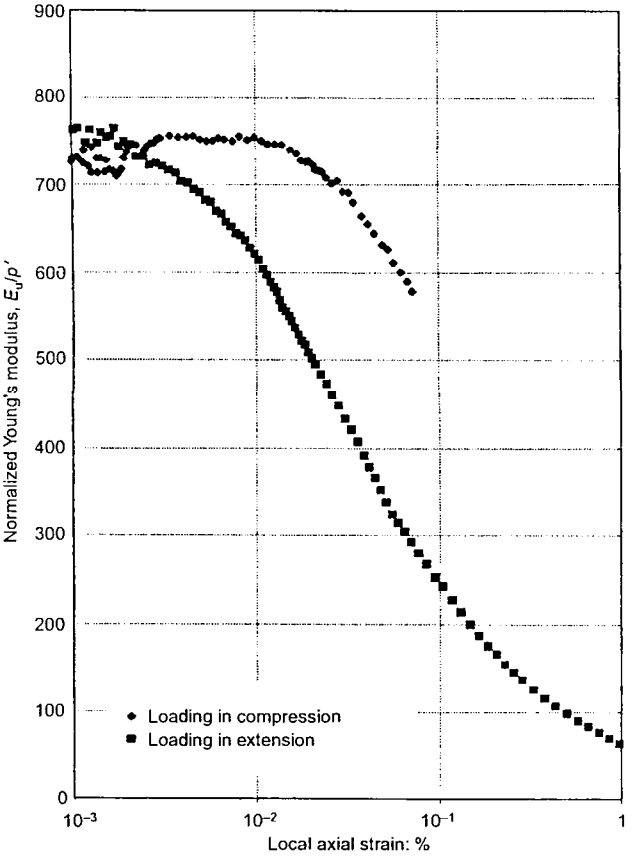


Figure 2.30: London Clay: normalised stiffness versus strain from undrained triaxial compression and extension tests (after Clayton and Heymann (2001))

Smith (1992) reported typical stiffness-strain curves from undrained compression and extension tests carried out on natural samples of Bothkennar Clay, Figure 2.32. The samples were reconsolidated back to their in situ stresses along the stress path ABCD, shown in Figure 2.25, retracing in this way their lightly overconsolidated stress history. Again pause creep periods with limiting axial creep rate of 0.05%, greater than the limiting creep rate of Clayton and Heymann, were imposed at point D, before the start of

shearing. Figure 2.32 shows that the stiffness in compression is initially higher than the stiffness in extension. This indicates an effect of recent stress history since the compression loading involves a stress reversal, however, it does not indicate an effect of current stress path direction since this is also the path that brings the loading closer to the gross yield surface.

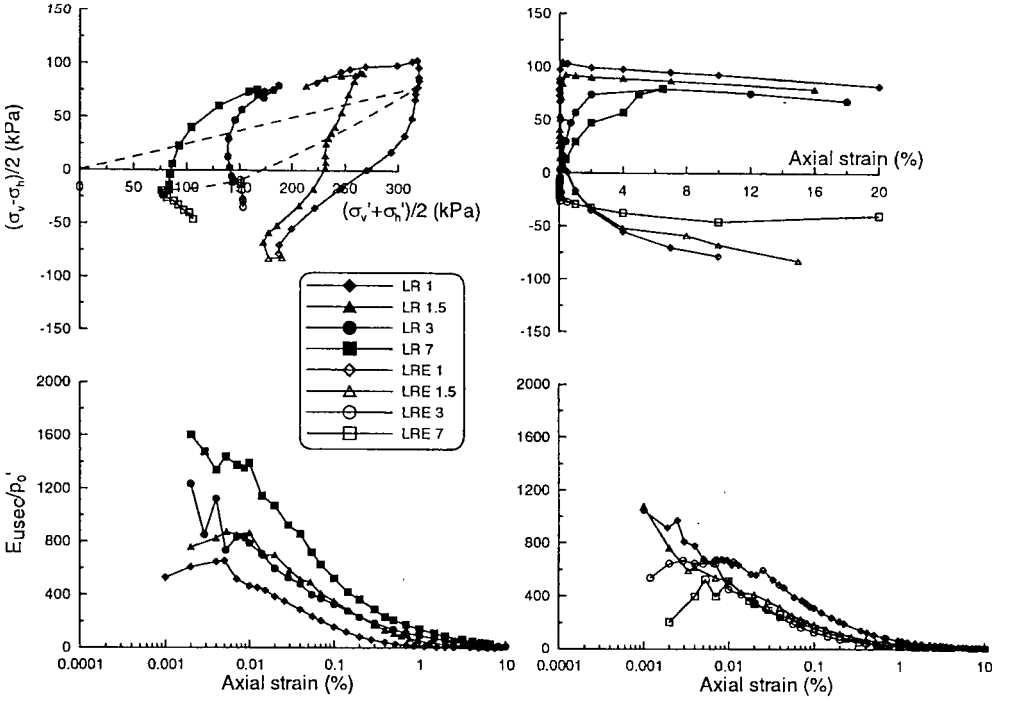


Figure 2.31: Reconstituted London Clay: results from undrained triaxial compression and extension tests (redrawn by Hight et al. (2003) after Jardine (1985))

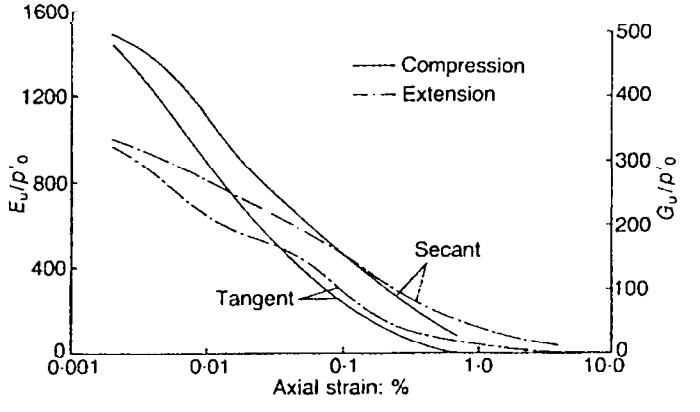


Figure 2.32: Bothkennar Clay: typical normalised stiffness versus strain characteristics from undrained triaxial compression and extension tests (after Smith (1992))

It has to be noted that the instrumentation used in the work of Jardine (1985) and Smith (1992) had lower resolution than the one used by Clayton and Heymann (2001) and there is no information on the stiffness at very small strains, so as to see whether the same initial stiffness is observed for both loading paths.

Intuitively, one would tend to think that a stress path that takes the loading closer to the gross yield surface would generally show softer response, or at least a faster decay in stiffness with strain, than a stress path that takes it away from the gross yield surface. From the results of Jardine (1985) and Smith (1992) it seems that this effect could be influenced from the effect of recent stress history. However, as recent stress history seems to diminish with ageing time, one could postulate that the effect of stress path direction becomes more pronounced.

From the evidence presented above, it is obvious that more research is required in order to clarify the effect of recent stress history and stress path direction and the influence that ageing periods have one them.

2.3 Constitutive models for overconsolidated clays

2.3.1 Introduction

Most constitutive models for soils have been developed within the framework of elasto-plasticity. For this reason, before reviewing existing models for overconsolidated soils, a description of the classical theory of elasto-placity will first be given.

2.3.2 Classical theory of elasto-plasticity

This section presents a description of the basic concepts of the theory, followed by the formulation of the elasto-plastic constitutive matrix. A more detailed description can be found in Potts and Zdravkovic (1999) and Zienkiewicz et al. (1999).

2.3.2.1 Basic concepts

In order to formulate an elasto-plastic constitutive model four main ingredients need to be defined: an equation for the yield surface, a flow rule, a hardening rule and finally the elastic part of the model. These will be explained briefly in the next sections.

i) Yield surface

A yield surface separates purely elastic behaviour from elasto-plastic behaviour. The yield function, F, is a function of the stress state, $\{\sigma\}$, and the hardening (or otherwise termed state) parameters, $\{k\}$:

$$F\left(\{\sigma\},\{k\}\right)=0 \tag{2.11}$$

For stress states that remain within the yield surface, that is $F < 0$, purely elastic behaviour occurs, whereas for stress states on the yield surface, $F = 0$, the behaviour is elasto-plastic.

ii) Flow rule

The flow rule determines the plastic strain increments. This is usually constructed with the assumption of a plastic potential surface, whose outward normal vector at the current stress state represents the plastic strain increment vector. The flow rule can be expressed as following:

$$\left\{d\varepsilon^{p}\right\}=\Lambda\left\{\frac{\partial P\left(\{\sigma\},\{m\}\right)}{\partial\sigma}\right\} \tag{2.12}$$

where $\{d\varepsilon^{p}\}$ is the plastic strain increment vector, $P(\{\sigma\},\{m\}) = 0$, is the plastic potential function and Λ is an unknown scalar multiplier. The values of the vector $\{m\}$ are immaterial since only the differentials of the plastic potential function with respect to the stress components are required in the flow rule.

It has to be noted that in Equation 2.12 the plastic potential function defines just the relative magnitudes of the plastic strain increments and it is the scalar multiplier, Λ, which determines their actual magnitude. The way the scalar multiplier, Λ, is determined will be discussed later.

If the plastic potential function is assumed to be the same as the yield function, $P(\{\sigma\},\{m\})= F(\{\sigma\},\{k\})$, the flow rule is said to be associated and a normality condition applies. In the general case, where the plastic potential function is different from the yield function, $P(\{\sigma\},\{m\})\neq F(\{\sigma\},\{k\})$, the flow rule is said to be non-associated.

iii) Hardening rule

The hardening rule describes the evolution of the yield surface in the course of plastic deformation. It defines how the hardening parameters $\{k\}$ change with plastic straining. If the elasto-plastic model is assumed to be perfectly plastic then the hardening parameters $\{k\}$ are constant and no hardening rule is needed. Otherwise the hardening parameters are usually assumed to be a function of either the plastic work or the plastic strains.

iv) Elastic part

The elastic part of the model defines the purely elastic behaviour, when the stress state remains within the yield surface, as well as the elastic deformations which occur as part of the elasto-plastic behaviour, when the stress state is on the yield surface.

Determination of the scalar multiplier, Λ

The scalar multiplier, Λ, is determined by employing the consistency condition. When the soil is yielding the consistency condition requires the stress state to remain always on the yield surface, so that $dF = 0$. As mentioned previously the yield function depends on the stress state, $\{\sigma\}$, and the hardening parameters, $\{k\}$, so the chain rule of differentiation gives:

$$dF = \left\{\frac{\partial F}{\partial \sigma}\right\}^T \{d\sigma\} + \left\{\frac{\partial F}{\partial k}\right\}^T \{dk\} = 0 \tag{2.13}$$

If the hardening parameters are a function of the plastic strains then:

$$\{dk\} = \left[\frac{\partial k}{\partial \varepsilon^p}\right]\{\partial \varepsilon^p\} \tag{2.14}$$

So Equation 2.13 becomes:

$$dF = \left\{\frac{\partial F}{\partial \sigma}\right\}^T \{d\sigma\} + \left\{\frac{\partial F}{\partial k}\right\}^T \left[\frac{\partial k}{\partial \varepsilon^p}\right]\{\partial \varepsilon^p\} = 0 \tag{2.15}$$

By substitution of the flow rule in the above equation this becomes:

$$dF = \left\{\frac{\partial F}{\partial \sigma}\right\}^T \{d\sigma\} + \left\{\frac{\partial F}{\partial k}\right\}^T \left[\frac{\partial k}{\partial \varepsilon^p}\right] \Lambda \left\{\frac{\partial P}{\partial \sigma}\right\} = 0 \tag{2.16}$$

After a simple manipulation, the scalar quantity, Λ, is obtained as:

$$\Lambda = \frac{1}{A}\left\{\frac{\partial F}{\partial \sigma}\right\}^T \{d\sigma\} \tag{2.17}$$

where A denotes the hardening modulus (or otherwise termed plastic modulus) given by the following equation:

$$A = -\left\{\frac{\partial F}{\partial k}\right\}^T \left[\frac{\partial k}{\partial \varepsilon^p}\right] \left\{\frac{\partial P}{\partial \sigma}\right\} \tag{2.18}$$

The plastic strains can then be calculated from the flow rule given by Equation 2.12.

2.3.2.2 Formulation of the elasto-plastic constitutive matrix

In this section it will be shown how the elasto-plastic constitutive matrix can be formulated in terms of the basic ingredients described in the previous section.

In an elasto-plastic constitutive model, the elasto-plastic constitutive matrix, $[D^{ep}]$, provides the relationship between the changes in stresses and strains.

$$\{d\sigma\} = \left[D^{ep}\right] \{d\varepsilon\} \tag{2.19}$$

The changes in total strains can be divided into two components, the elastic strains and the plastic strains:

$$\{d\varepsilon\} = \{d\varepsilon^e\} + \{d\varepsilon^p\} \tag{2.20}$$

where $\{d\varepsilon^e\}$ and $\{d\varepsilon^p\}$ are the changes in elastic and plastic strains respectively.

The changes in stresses are related to the changes in elastic strains through the elastic constitutive matrix $[D]$ as follows:

$$\{d\sigma\} = [D]\{d\varepsilon^e\} \tag{2.21}$$

Substituting Equation 2.20 into Equation 2.21 gives:

$$\{d\sigma\} = [D]\{d\varepsilon - d\varepsilon^p\} \tag{2.22}$$

Substitution of the flow rule in the above Equation gives:

$$\{d\sigma\} = [D]\{d\varepsilon\} - [D]\Lambda\left\{\frac{\partial P}{\partial \sigma}\right\} \tag{2.23}$$

If Equation 2.23 is substituted in Equation 2.17 then the scalar multiplier, Λ, becomes:

$$\Lambda = \frac{\left\{\frac{\partial F}{\partial \sigma}\right\}^T [D]\{d\varepsilon\}}{\left\{\frac{\partial F}{\partial \sigma}\right\}^T [D]\left\{\frac{\partial P}{\partial \sigma}\right\} + A} \tag{2.24}$$

Substitution of the above equation in Equation (2.23) gives:

$$\{d\sigma\} = [D]\{d\varepsilon\} - \frac{[D]\left\{\frac{\partial P}{\partial \sigma}\right\}\left\{\frac{\partial F}{\partial \sigma}\right\}^T [D]\{d\varepsilon\}}{\left\{\frac{\partial F}{\partial \sigma}\right\}^T [D]\left\{\frac{\partial P}{\partial \sigma}\right\} + A} \tag{2.25}$$

Equation 2.25 provides a relationship between changes in stresses and strains. Therefore from Equation 2.19 the elasto-plastic constitutive matrix is:

$$\left[D^{ep}\right] = [D] - \frac{[D]\left\{\frac{\partial P}{\partial \sigma}\right\}\left\{\frac{\partial F}{\partial \sigma}\right\}^T [D]}{\left\{\frac{\partial F}{\partial \sigma}\right\}^T [D]\left\{\frac{\partial P}{\partial \sigma}\right\} + A} \tag{2.26}$$

2.3.3 Elasto-plastic constitutive models

The classical theory of elasto-plasticity has been used extensively for the development of constitutive models that simulate the behaviour of clays. The original critical state models, the Cam Clay model and the modified Cam Clay model, are classical examples of models formulated within the elasto-plastic framework. In these models an equation is ascribed to the yield surface that lies above each swelling line, as discussed in section 2.2.2. The critical state models have been shown to be very successful in simulating the behaviour of normally consolidated clays. However, the behaviour within the yield surface is assumed to be elastic. The consequence of this is that these models cannot

reproduce satisfactorily the behaviour of overconsolidated clays, which has been shown to be inelastic from very early stages of loading. This is a limitation of the classical theory of elasto-plasticity, rather than the critical state models themselves, since the framework cannot allow for plastic deformations to develop within the yield surface.

Models that try to simulate the behaviour of overconsolidated clays fall within three categories. The first category includes models that are based on the classical theory of elasto-plasticity and therefore assume elastic strains within the yield surface. The second category includes models that are based on extensions of the classical theory of elasto-plasticity, which allow for plastic strains to develop within the conventionally defined yield surface in the classical theory. Finally, the third category includes models that are elasto-plastic but are not based on either the classical theory of elasto-plasticity or extensions of the classical elasto-plastic framework discussed in the second category.

2.3.3.1 Models based on the classical theory of elasto-plasticity

Although these models cannot simulate plasticity from early stages of loading, they generally adopt non-linear stress-strain behaviour pre-yield, in order to reproduce the highly non-linear behaviour of the overconsolidated clays from the early stages of loading.

The model LC (Simpson et al. (1979)) was developed to specifically predict the behaviour of London Clay. The model adopted a kinematic yield surface defined as a sphere in strain space, Figure 2.33. When enough straining occurred so that the soil reached the kinematic yield surface, then further straining caused it to move (hence "kinematic"). Although this sphere was named kinematic yield surface, in reality it was not a yield surface since the strains that occurred once it was engaged continued to be elastic. The behaviour within this small region was assumed to be cross anisotropic and the stiffness was ten times higher than that beyond this region. Plastic strains were delayed until a state boundary surface was engaged. The state boundary surface was based on curve-fitting of laboratory test results. If the direction of straining reversed then the high stiffness within the kinematic yield surface applied, until this started moving again. In this way the model predicted a bi-linear response with high stiffness at very small strains, until the stress state engaged the state boundary surface, and high initial stiffness at stress reversals. The model was shown to predict improved surface settlement troughs behind diaphragm walls, as compared to those predicted by analyses assuming linear elastic behaviour.

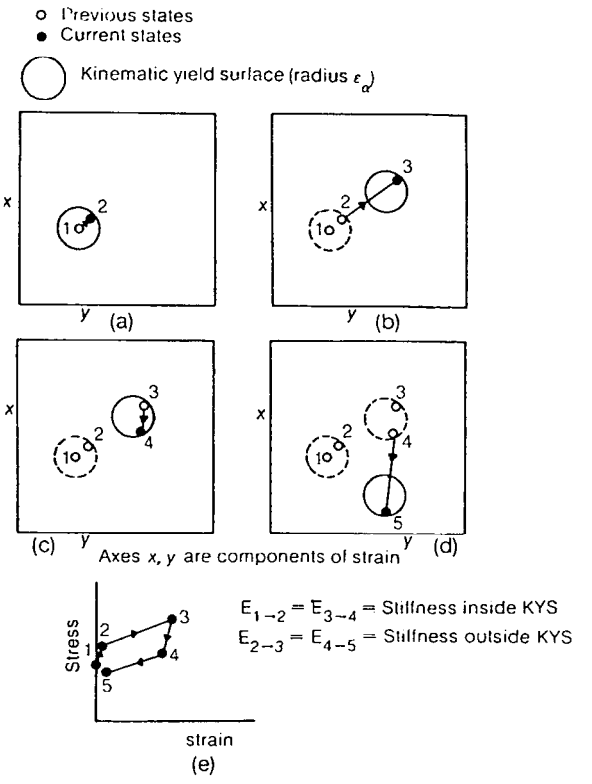


Figure 2.33: Diagram showing the kinematic yield surface in strain space adopted in model LC (after Simpson et al. (1979))

Jardine et al. (1986) and Jardine et al. (1991) developed an empirical soil pre-yield model, based on the results of high quality test data obtained with local measurements of strain. The high pre-yield non-linearity was modelled by adopting periodic logarithmic functions which related the shear and bulk modulus, G and K, to the shear and volumetric strains, ε_s and ε_v respectively. The secant shear, G_{sec}, and bulk moduli, K_{sec}, were given as:

$$\frac{3G_{sec}}{p'} = A + B\cos\left[\alpha\left(\log_{10}\left(\frac{\varepsilon_s}{C}\right)\right)^{\gamma}\right] \tag{2.27}$$

$$\frac{K_{sec}}{p'} = R + S\cos\left[\delta\left(\log_{10}\left(\frac{\varepsilon_v}{T}\right)\right)^{\eta}\right] \tag{2.28}$$

where the deviatoric and volumetric strains are given by Equations 1.22 and 1.20 respectively.

The tangent shear and bulk moduli were obtained by differentiation of Equations 2.27 and 2.28. The constants A, B, C, R, S, T, α, γ, δ and η were obtained from a fit to the

laboratory data. This pre-yield model is independent of the way plastic behaviour is modelled at large strains. Jardine et al. (1991) used it in conjunction with a Mohr Coulomb yield surface. The model has been used in a wide range of geotechnical problems, including deep excavations, tunnels and offshore structures and the results have compared satisfactorily with field observations, highlighting the importance of modelling the highly non-linear behaviour of overconsolidated soils.

Hird and Pierpoint (1997) used a cross-anisotropic non-linear elastic model to reproduce the stress-strain behaviour of the heavily overconsolidated Oxford Clay. In this model the material non-linearity was dependent on the incremental strain energy. As mentioned before, the incremental strain energy criterion was suggested by Burland (1989) for the definition of the kinematic regions proposed by Jardine (1985), (1992). This is expressed as:

$$\Delta U = \sum_{0}^{\varepsilon_1} \Delta\sigma'_1 \delta\varepsilon_1 + \sum_{0}^{\varepsilon_2} \Delta\sigma'_2 \delta\varepsilon_2 + \sum_{0}^{\varepsilon_3} \Delta\sigma'_3 \delta\varepsilon_3 \qquad (2.29)$$

where $\Delta\sigma'_1$, $\Delta\sigma'_2$, $\Delta\sigma'_3$ are the changes in the principal stresses σ'_1, σ'_2, σ'_3 during the strain increments $\delta\varepsilon_1$, $\delta\varepsilon_2$, $\delta\varepsilon_3$.

The stiffness in the model was also dependent on the stress path direction, with different stiffness assigned for compression and extension paths. The model was used in the numerical analysis of a trial excavation in Oxford Clay. It was shown to predict the horizontal displacements more satisfactorily than the vertical displacements.

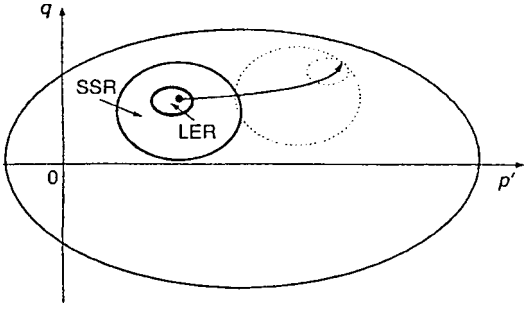


Figure 2.34: Kinematic regions of high stiffness (after Puzrin and Burland (1998))

Puzrin and Burland (1998) developed a small strain pre-yield model based on the concept of kinematic regions proposed by Jardine (1985), (1992). The linear elastic region, (LER), in Figure 2.34, was associated with Zone I, in Figure 2.8 and the small strain region, (SSR), was associated with Zone II. The boundaries of these two regions

were elliptical surfaces. Behaviour within the LER was assumed to be anisotropic linear elastic, whereas within the SSR a non-linear deviatoric and volumetric stress-strain behaviour was modelled, by means of a logarithmic function. The work of Puzrin and Burland (1998) was concentrated on the behaviour within the SSR boundary. However, they noted that it is possible to use an elasto-plastic model for the SSR boundary and therefore associate it with the Y_2 surface and initial yielding. Alternatively, this non-linear pre-yield model can be used in conjunction with any plastic model that can model the bounding surface. A stress path reversal in the model results in the relocation of the local stress origin at the reversal point and in this way a high stiffness is reinvoked. The model was validated against the results of triaxial tests on undisturbed Bothkennar Clay.

2.3.3.2 Models based on extensions of the classical theory of elasto-plasticity

As it has already been mentioned, the classical theory of elasto-plasicity assumes that the interior of the yield surface is an elastic domain. Although this is sufficient in order to simulate the gross yield of soils, it is not possible to predict realistically either the inelastic behaviour of overconsolidated soils from the very early stages of loading, or cyclic loading behaviour. This led to extensions of the elasto-plastic framework so that plastic deformations are allowed for stress states within the conventionally defined yield surface in the classical theory. These extensions were originally developed in order to simulate the behaviour of metals under cyclic loading and were later applied to soils. Many terms have been used in order to describe the conventionally defined yield surface, with the most common being the bounding surface. Other terms are the consolidation surface, or the normal-yield surface. Here the term bounding surface is going to be used for this reason, although in the original publications a different name might have been used.

In these models the hardening modulus, A, varies within the bounding surface, usually from a high value far from the bounding surface to a smaller value on the bounding surface. This results in plastic deformations occurring, within the bounding surface, in a progressive rate and gives rise to a non-linear stress-strain behaviour. The variation of the hardening modulus, A, within the bounding surface is an extra ingredient that has to be defined in this type of models, in addition to the four main ingredients required in the conventional theory of elasto-plasticity. Models based on these extensions of the elasto-plastic framework can be divided into two groups, due to their different structures. The first group includes the bounding surface models and the subloading surface models

whereas the second one includes the kinematic hardening models.

i) Bounding surface models and subloading surface models

The bounding surface models and the subloading surface models have similar structures. The bounding surface models were initially developed by Dafalias and Herrmann (1980), (1982). The calculation of the plastic deformations for stress states within the bounding surface was based on the following idea. Each stress point within the bounding surface was associated to a unique image point on the bounding surface according to a specific rule (Dafalias and Herrmann applied a simple radial rule). The hardening modulus for each stress point within the bounding surface depended on the distance between this stress point and the image point and reduced to the bounding surface hardening modulus when the stress point reached the bounding surface, see Figure 2.35. The loading-unloading direction was defined by the gradient of the bounding surface at the image point. During unloading only elastic behaviour was predicted. This resulted in a stress-strain curve with an open hysteresis loop for an unloading-reloading cycle, see Figure 2.36.

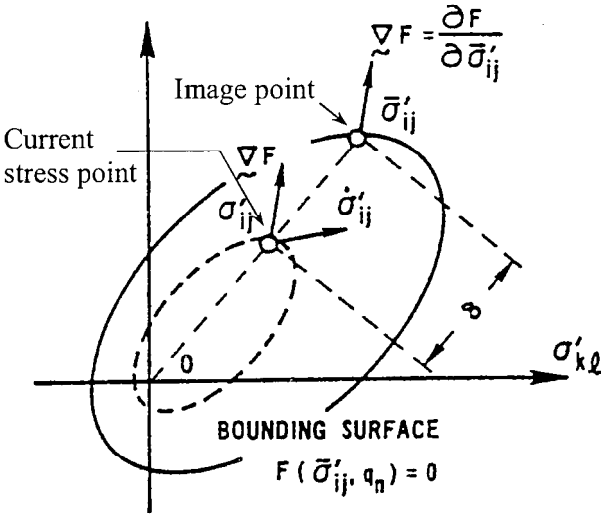


Figure 2.35: Schematic illustration of the bounding surface and definition of image points in general stress space (after Dafalias and Herrmann (1982))

Whittle (1993) incorporated the bounding surface plasticity concept in an anisotropic model for normally to moderately overconsolidated clays, referred to as MIT-E3. The bounding surface adopted was an anisotropic form of the elliptical modified Cam Clay yield surface. The model used a closed, symmetric, hysteresis loop during unloading, combined with bounding surface plasticity to develop plastic strains during reloading,

see Figure 2.37. In this way, although the strains were elastic during unloading, the open hysteresis loop of the original formulation was avoided. The model requires 15 material parameters. Whittle (1993) demonstrated the capability of the model to predict satisfactorily the anisotropic behaviour of three clays over a wide variety of laboratory tests. It has also been shown to adequately predict the behaviour of a deep excavation in Boston Blue Clay (Whittle et al. (1993)). The model has since been used in a parametric study of the pull-out capacity of bucket foundations in soft clay (Zdravkovic et al. (2001)) and was shown to predict successfully the failure height of an embankment founded on soft clay at Saint-Alban, Quebec (Zdravkovic et al. (2002)).

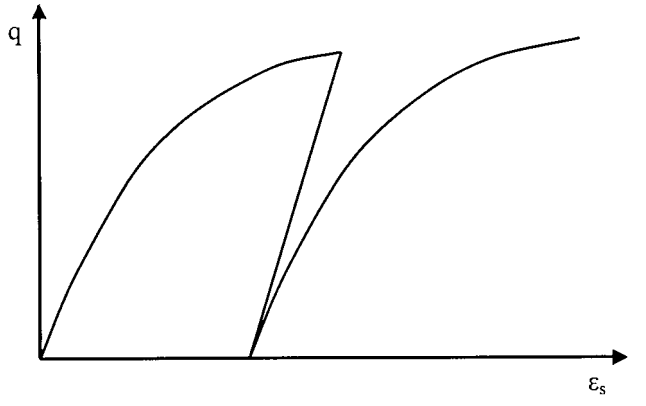


Figure 2.36: Open hysteresis loop during unloading and reloading due to the elastic behaviour predicted on unloading

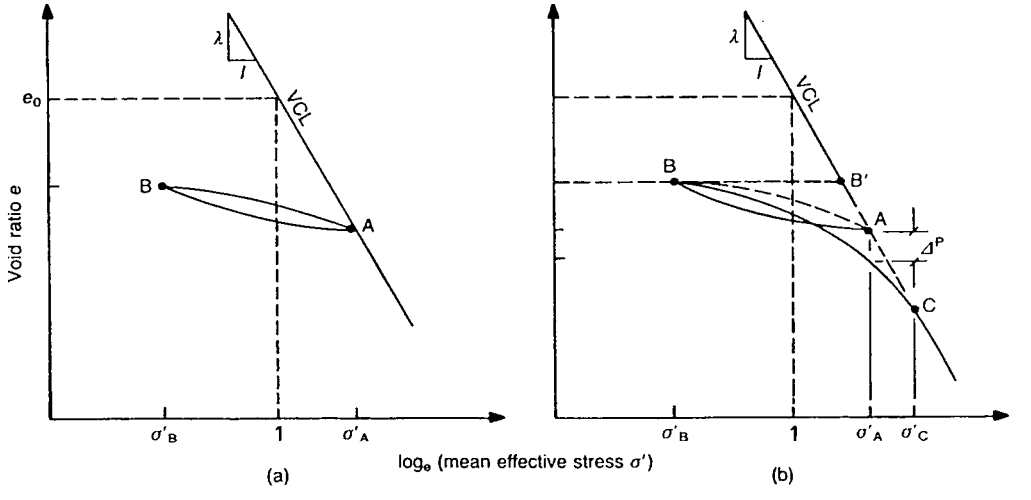


Figure 2.37: Conceptual model of unload-reload used by MIT-E3 for hydrostatic compression: a) perfect hysteresis b) hysteresis and bounding surface plasticity (after Whittle (1993))

The subloading surface models were initially proposed by Hashiguchi and Ueno (1977) and Hashiguchi (1980) and they use a similar idea to the bounding surface models. The basic idea of the model was the assumption of a subloading surface which always passes through the current stress point and retains a gometrical similarity to the outer bounding surface (here termed normal-yield surface). In this model the hardening modulus depended on the ratio of the size of the subloading surface to that of the normal yield surface. On unloading elastic behaviour was predicted resulting again in an open hysteresis loop during a cycle of unloading-reloading. This was overcome with later modifications of the model (Hashiguchi (1989)), where the centre of similarity of the subloading and normal yield surfaces was allowed to translate with plastic deformation.

ii) Kinematic hardening models

These models introduce a number of kinematic yield surfaces within the bounding surface. Mroz (1967) was one of the first to develop such a model for metals. In order to describe the variation of the hardening modulus, Mroz (1967), introduced a set of kinematic nesting surfaces of constant hardening moduli. The behaviour within the first kinematic nesting surface was assumed to be elastic. As soon as the stress state reached the first kinematic nesting surface the behaviour became elasto-plastic, the hardening modulus associated with this surface applied and the nesting surface was dragged along the stress path. Subsequent loading led to the next nesting surface, the hardening modulus associated with the new surface applied and both surfaces were dragged along the stress path. Therefore the "field of hardening moduli", as termed by Mroz was defined by the configuration of these surfaces in stress space and consequently a piecewise linear stress-strain behaviour was predicted. Iwan (1967) developed independently a model similar to the one proposed by Mroz (1967) by introducing a collection of yield surfaces.

The first ones to apply the concept of multi-surface models to soils were Prevost (1977), (1978a) who applied the concept of a field of hardening moduli to a model formulated for the undrained deformation of clays, and Prevost (1978b) and Mroz et al. (1978) who applied the same concept to models that dealt with both drained and undrained soil conditions. Figure 2.38 shows an example of the multi-surface model developed by Mroz et al. (1978). In this figure the surfaces $f_o = 0$ and $f_l = 0$ are in contact at the point P_l and they translate towards the surface $f_{l+1} = 0$. The surfaces are not allowed to intersect but are assumed to come in contact at points with the same outward normal vector (termed conjugate points). An interpolation rule is postulated, in order to specify

the variation of the hardening moduli at the conjugate points, see Figure 2.38b (in the horizontal axis n is the total number of the nesting surfaces and k is the number of the current nesting surface, k = 0, 1, 2,...n). In these models, the configuration of the surfaces in stress space provides a memory of the previous loading history.

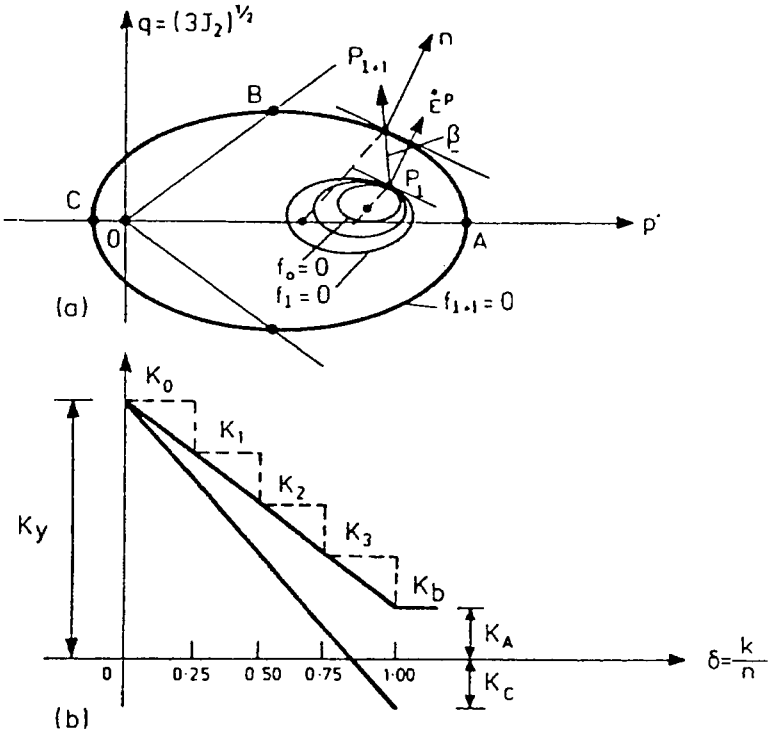


Figure 2.38: Multi-surface model a) nesting surfaces; b) variation of hardening moduli at conjugate points on nesting surfaces (redrawn by Mroz and Norris (1982) after Mroz et al. (1978))

Mroz et al. (1978), (1979) simplified the above multi-surface models to a two-surface model by considering only one kinematic yield surface within the bounding surface, Figure 2.39. The behaviour within this kinematic yield surface was assumed to be elastic; it became elasto-plastic when the stress state reached the surface. For further loading the kinematic yield surface followed the stress path. The variation of the hardening modulus was described by using an interpolation rule between the values of the hardening modulus on the yield and the bounding surfaces and depended on the distance between the stress point and a conjugate point (with the same outward normal) on the bounding surface. Similar modifications of the field of hardening moduli had already been developed independently by Krieg (1975) and Dafalias and Popov (1975), (1976) for metals.

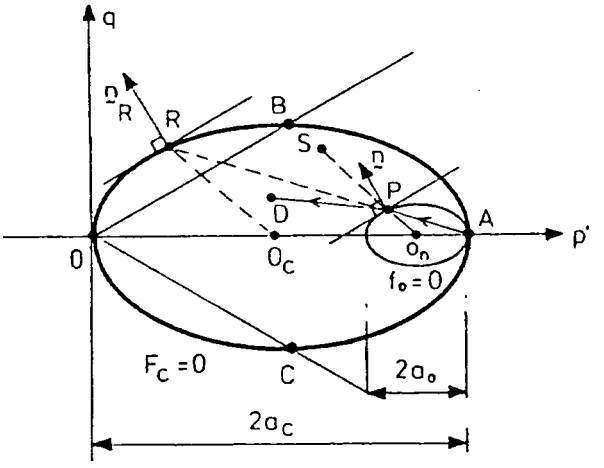


Figure 2.39: Two-surface model: kinematic yield surface and bounding surface (redrawn by Mroz and Norris (1982) after Mroz et al. (1979))

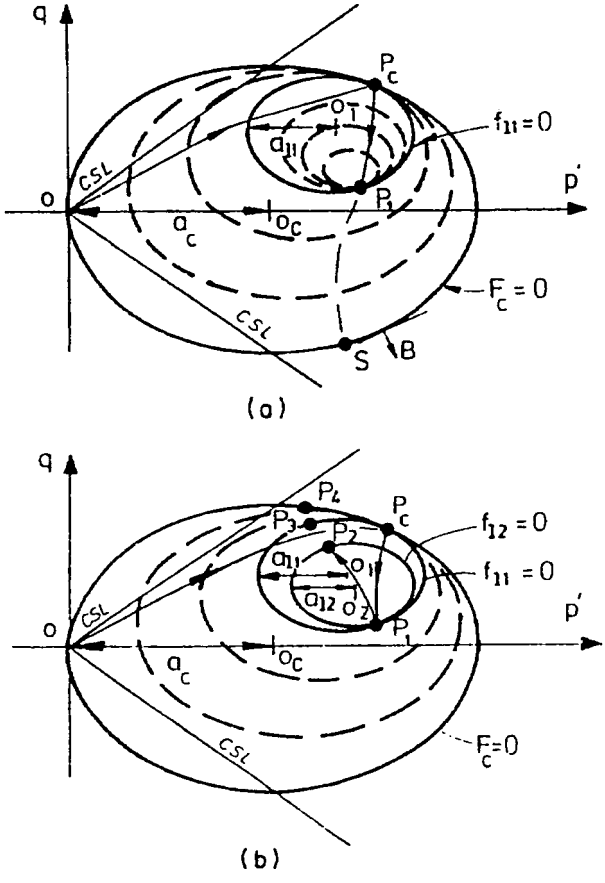


Figure 2.40: Model with an infinite number of surfaces: a) first reverse loading b) second reverse loading (after Mroz and Norris (1982))

Mroz and Norris (1982) discussed an alternative modification of the field of hardening moduli in which an infinite number of nesting surfaces was assumed within the bounding surface, see Figure 2.40. The elastic domain was reduced to a point and the hardening modulus depended on the ratio of the diameters of the current nesting surface and the bounding surface. When a stress reversal occurred the nesting surface associated with the stress reversal point became a stress-reversal surface. For example in Figure 2.40a a stress reversal takes place at the stress point P_c and the surface $F_c = 0$ becomes the stress-reversal surface for the reverse loading path P_c-S. If a second stress reversal takes place at the stress point P_1, as shown in Figure 2.40b, then the surface f_{11} becomes the second stress-reversal surface. However if the reverse stress path from stress point P_1 continues to the stress point P_3 then the second stress-reversal surface and the second reverse loading P_1-P_3 is erased from the material memory. In this way the memory of past loading events was incorporated into a stack of stress reversal surfaces and the memory of any reverse loading event was erased by any subsequent loading event of larger amplitude.

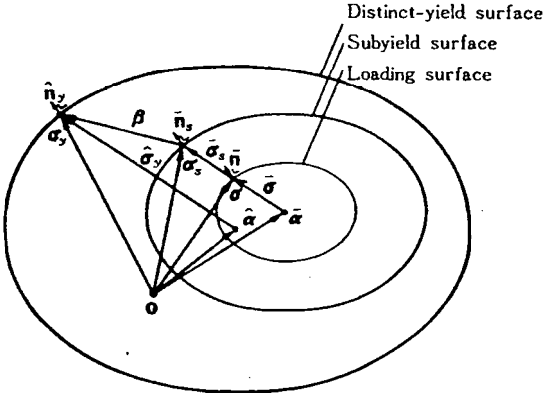


Figure 2.41: Typical configuration of surfaces in the three-surface model (after Hashiguchi (1985))

Hashiguchi (1985) proposed a two-surface model similar to the model described by Mroz et al. (1979). In order to obtain a smooth elasto-plastic transition he introduced a third surface (loading surface) within the kinematic yield surface (termed here subyield surface). This loading surface was co centric with the subyield surface (which in reality was not a yield surface anymore) and passed always through the current stress state, Figure 2.41. It behaved as a subloading surface with respect to the subyield surface in the sense that the hardening modulus within the subyield surface depended on the ratio of the size of the loading surface to that of the subyield surface.

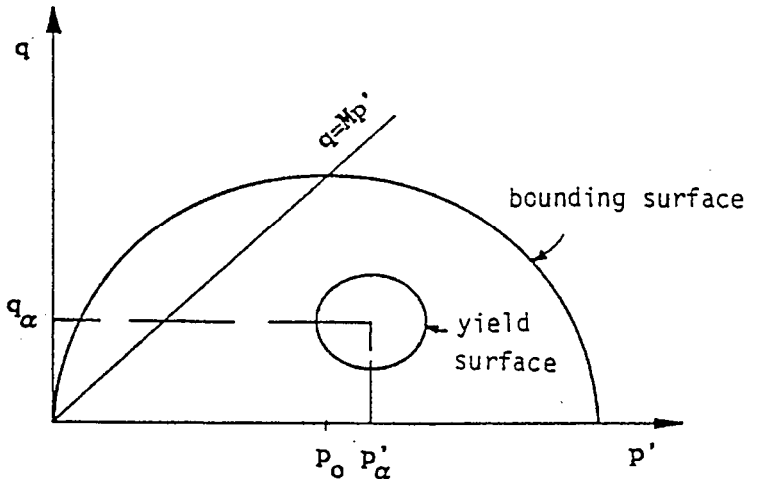


Figure 2.42: Two-surface model (after Al-Tabbaa (1987))

Al-Tabbaa (1987) and Al-Tabbaa and Wood (1989), based on the previous models of Mroz et al. (1979) and Hashiguchi (1985), formulated a two-surface model within the framework of critical state soil mechanics, Figure 2.42. A single kinematic yield surface was introduced within the modified Cam Clay yield surface, which in this model acted as the bounding surface. The behaviour within the kinematic yield surface was assumed to be isotropic elastic. The hardening modulus depended again on the degree of approach of the two surfaces. The model degenerates to the modified Cam Clay model for monotonic loading and for continuous yielding. It requires seven parameters, five of which have their origin in the modified Cam Clay model. Al-Tabbaa (1987) showed that the model is capable of predicting satisfactorily the cyclic behaviour of speswhite kaolin.

Stallebrass (1990) and Stallebrass and Taylor (1997) extended the two-surface model proposed by Al-Tabbaa (1987) by incorporating a third surface within the modified Cam Clay bounding surface, Figure 2.43. This surface was introduced in order to provide a better memory of the previous loading path and in this way simulate more realistically the effect of recent stress history on overconsolidated soils, as reported by Atkinson et al. (1990) and Stallebrass (1990). The model requires one additional parameter to the seven of the two surface-model and has been applied to a number of boundary value problems.

Puzrin and Burland (2000) incorporated the small strain pre-yield model described earlier (Puzrin and Burland (1998)), into the framework of kinematic hardening plasticity. In this new model the boundaries of the LER and SSR were assumed to be kinematic yield surfaces (Y_1 and Y_2 respectively) and were represented by rotated ellipses of the same shape. The modified Cam Clay surface was adopted as the

bounding surface. The behaviour within the Y_1 surface was assumed to be elastic with cross-coupling between the shear and volumetric stress-strain components. As soon as the Y_1 surface was engaged the behaviour became elasto-plastic. The hardening modulus between the Y_1 and Y_2 surfaces was governed by an infinite number of loading surfaces, after Mroz and Norris (1982), so as to have a realistic simulation of soil behaviour at small strains. The hardening modulus between the Y_2 surface and the modified Cam Clay bounding surface depended on the distance between these two surfaces. The model requires 12 parameters.

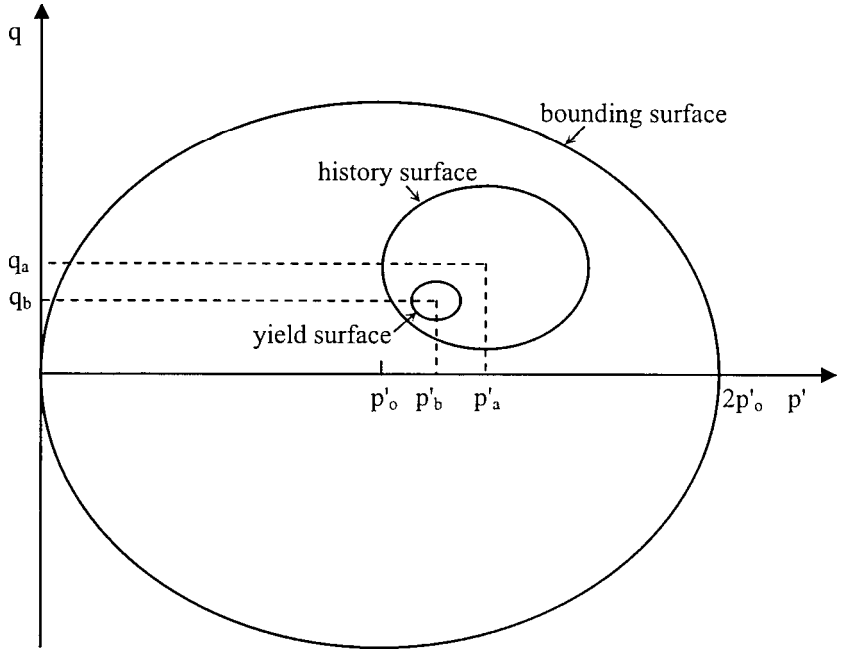


Figure 2.43: Three-surface model (after Stallebrass (1990))

During the last few years, the kinematic hardening models have been extended to account for the effects of structure in natural soils. Recent developments include the models proposed by Kavvadas and Amorosi (2000), Rouainia and Muir Wood (2000), which is an extension of the two-surface model developed by Al-Tabbaa (1987), and Baudet (2001), which is an extension of the three-surface model developed by Stallebrass (1990). Moreover the models presented by Gajo and Muir Wood (2001) and Callisto et al. (2002) incorporate additional effects of anisotropy. However it is outside the scope of this thesis to review these models here in greater detail.

2.3.3.3 Other models

The Brick model (Simpson (1992)) is an example of an elasto-plastic model, which is based on neither the classical framework of elasto-plasticity nor any extensions of the classical theory of elasto-plasticity, presented in the previous section 2.3.3.2. The model is based around an analogue of a man dragging a series of bricks inside a room and simulates the S-shaped curve of stiffness degradation with strain and the recent stress history effect, as reported by Atkinson et al. (1990) and Stallebrass (1990). The S-shaped curve is treated as a graph showing what proportion of the soil behaves plastically as straining proceeds, see Figure 2.44. Initially, at very small strains the material behaves elastically, however, as strains develop the proportion of the material that behaves plastically increases.

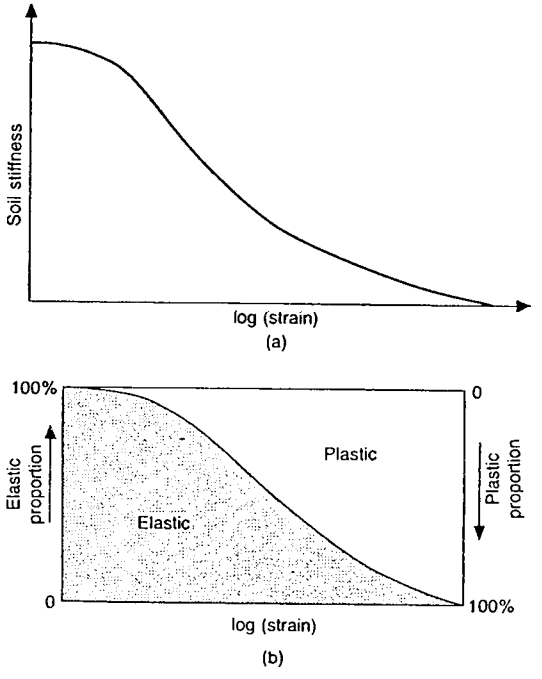


Figure 2.44: The S-shaped curve (after Simpson (1992))

Simpson (1992) postulated that there is a striking resemblance between the behaviour reported by Atkinson et al. (1990), see Figure 2.24, and a physical analogue of a man walking around a room and pulling a series of bricks behind him, each on a separate string. Figure 2.45 shows some possible paths for the man and the bricks. Figure 2.45a shows the man pulling the bricks in a continuous direction and the bricks lined up behind him. If the man reverses, the bricks initially do not move (Figure 2.45b), then the bricks on the shorter strings start to move followed by the bricks with the longer strings (Figure 2.45c). If the man turns through 90° then the bricks initially continue moving in

their previous direction and then gradually align behind him (Figure 2.45d).

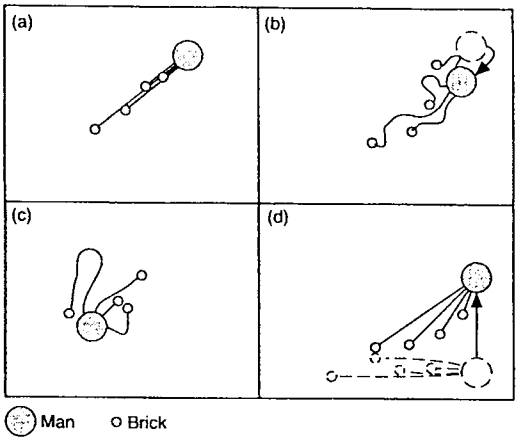


Figure 2.45: A man pulling bricks attached to him by strings (after Simpson (1992))

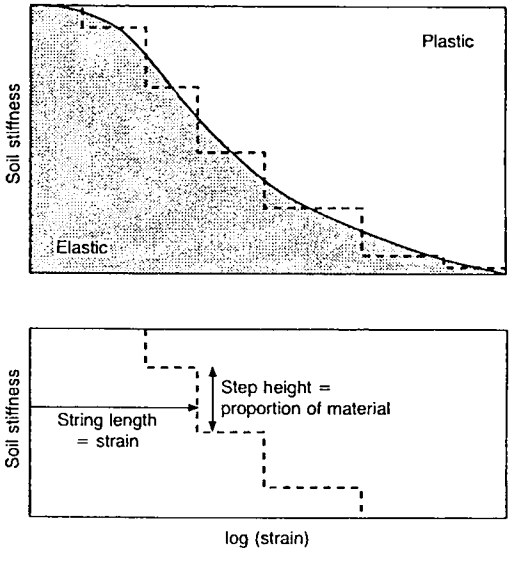


Figure 2.46: The S-shaped curve represented in stepwise fashion (after Simpson (1992))

Simpson regarded the room in this physical analogue as strain space, with the man representing the point within that strain space of a soil element. Each brick represented a proportion of the soil element. Movement of a brick was considered to represent plastic strain. The elastic strain was given by the difference between the movement of the man and the sum of the movements of the bricks, each weighted by the proportion of the soil it represented. Therefore Figure 2.45b represented an initially elastic behaviour, when none of the bricks were moving, which became elasto-plastic when the first bricks started to move, followed by predominantly plastic behaviour when all the bricks aligned behind the man, as in Figure 2.45a. It was also assumed that only elastic strains

can cause changes in stresses.

The brick analogue was used to represent the S-shaped curve in a stepwise fashion as shown in Figure 2.46. The height of each step was considered to be the proportion of the material represented by each brick, whereas the length to each step was considered to be the strain at which the brick starts to move and is represented by the string length in the analogue.

The model was formulated in plane strain conditions. A number of additional assumptions taken from critical state soil mechanics were used in conjunction with the brick concept in order to complete the model. The model requires five parameters and a series of data (the string lengths together with the proportion of the material that each represents) in order to simulate the S-shaped curve. The model was used by Simpson (1992) in the analyses of two deep excavations (British Library in London Clay and United Overseas Bank in soft Singapore clay) and compared well with measurements of ground movements. It has since been used in the analysis of another deep excavation in Gault Clay at Lion Yard, Cambridge, and showed generally good agreement with field observations (Ng and Lings (1995)).

2.4 Summary

The literature review presented in the first part of this chapter has emphasized the fact that, unlike what used to be the common belief in the past, nowadays it is well known that the pre-failure deformation of overconsolidated clays is highly non-linear and inelastic. This non-linear and inelastic nature of deformation is exhibited from the early stages of loading, except at very small strains where a region of almost constant stiffness with strain is usually identified. Behaviour within this region is often idealised as linear elastic.

The pre-failure deformation of overconsolidated clays is influenced by a great number of factors. The most important ones were identified as: stress state-volume state, soil structure, ageing, recent stress history and stress path direction. Each of these factors seems to affect the stress-strain behaviour of clays in a different way and this was also discussed in the first part of this chapter.

The review of existing constitutive models for overconsolidated clays showed that three classes of models exist. The first class includes the models that are based on the classical

framework of elasto-plasticity. These models assume elastic pre-failure behaviour and usually simulate high pre-yield non-linearity by fitting empirical expressions to the observed stress-strain curves (with exception the model developed by Puzrin and Burland (1998)).

The second class of models is based on extensions of the classical theory of elasto-plasticity. These extensions allow for plastic strains to develop within the conventionally defined yield surface, which is now termed the bounding surface. Plastic deformations occur in a progressive rate within the bounding surface, which results in a non-linear stress-strain behaviour. From this class of models, the kinematic hardening models have also the additional advantage that they permit the retention of some information concerning the recent stress history of the material.

The third class includes the Brick model, which is an elasto-plastic model based on the physical analogue of a man walking around a room and pulling a series of bricks behind him. The model is capable of simulating non-linearity and plasticity from early stages of loading as well as the effect of recent stress history.

Chapter 3

The finite element method

3.1 Introduction

The finite element method is a complex form of numerical analysis that has been relatively recently introduced in geotechnical engineering. Unlike classical methods of analysis (e.g. limit equilibrium, limit analysis, etc.) it is capable of satisfying all four basic requirements for a complete theoretical solution: equilibrium of forces, compatibility of displacements, material constitutive behaviour and boundary conditions.

The analyses presented in this thesis have been carried out with a program which makes use of the displacement based finite element method and has been developed specifically for the analysis of geotechnical structures, the Imperial College Finite Element Program (ICFEP). ICFEP is capable of performing both two-dimensional and three-dimensional analysis, however, only plane strain and axisymmetric analyses were performed in this study.

This chapter gives a brief description of the finite element method, with particular reference to the approach followed in ICFEP. The first part presents the basic theory for linear materials and the second part some basic modifications necessary to enable this theory to be used in geotechnical engineering. Since soil can rarely be considered as a linear material, the finite element theory for linear materials has to be extended, in order to make use of non-linear elastic or elasto-plastic constitutive models. This is discussed in the last part of this chapter. A more detailed description of the finite element theory formulation can be found in e.g. Potts and Zdravkovic (1999).

3.2 Finite element theory for linear materials

The finite element method consists of the following steps: element discretisation, primary variable approximation, formulation of the element equations, assembly of the global equations, formulation of the boundary conditions and solution of the global equations. Each of these steps is discussed briefly in the following sections.

3.2.1 Element discretisation

The first step in the finite element method is to divide the domain under consideration into discrete regions, called finite elements. These are usually triangular or quadrilateral in shape, for two-dimensional analysis, and are connected at their nodes. The assembly of the finite elements is called a finite element mesh. The nodes are usually located at the corners of the elements, although additional nodes, usually at the midpoints of the sides, can also be used, resulting in 6-noded triangular and 8-noded quadrilateral elements. The smaller the finite elements are, the higher the accuracy of the solution is, at the cost though of longer computational time.

3.2.2 Primary variable approximation

In the finite element method a primary unknown quantity has to be chosen. All other quantities are then treated as secondary quantities which can be determined once this primary unknown quantity has been calculated. In the displacement based finite element method, the primary unknown quantity is the displacement field, as suggested by the name. The stresses and strains are considered as secondary quantities.

The displacement field varies over the problem domain and it is assumed that the displacements within each element can be expressed as a function of its nodal displacements through a set of functions called the shape functions. In two-dimensional analyses the displacement field is characterised by the two displacements u and v, in the x and y directions respectively. In this case the displacement field within an element is given by:

$$\begin{Bmatrix} u \\ v \end{Bmatrix} = [N] \begin{Bmatrix} u \\ v \end{Bmatrix}_{nodes} \tag{3.1}$$

where $[N]$ is the matrix of the shape functions. The nodal displacements are often

referred to as unknown degrees of freedom.

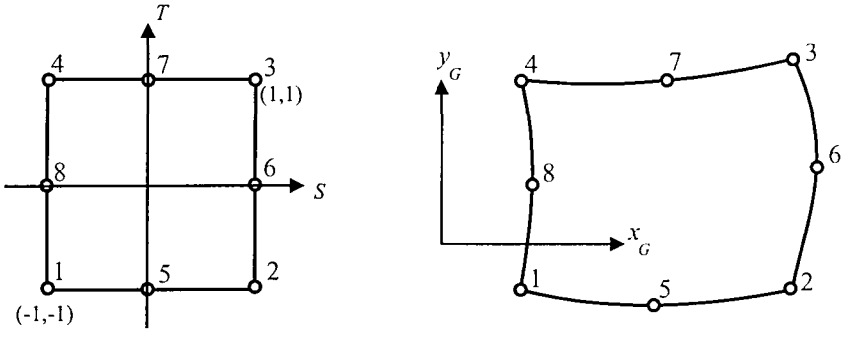
Equation 3.1 reduces the problem of determining the displacement field over the entire problem domain to determining the displacement components at a finite number of nodes.

The elements used in ICFEP are isoparametric. An example of an 8-noded quadrilateral isoparametric element is shown in Figure 3.1. For an isoparemetric element the global element, as it appears in the finite element mesh, is derived from a parent element, which has the same number of nodes but is defined with respect to a natural coordinate system ($-1 \leq S \leq 1$ and $-1 \leq T \leq 1$). Such an element is called isoparameteric because the same shape functions $[N]$ that are used to define the displacement field within the element, as a function of its nodal displacements, are also used in order to map the geometry of the element from the global to the natural coordinate system.

The global coordinates of a point in the element are expressed as:

$$x = \sum_{i=1}^{8} N_i x_i \quad , \quad y = \sum_{i=1}^{8} N_i y_i \tag{3.2}$$

where x_i and y_i are the global coordinates of the eight nodes of the element and N_i are interpolation functions. For isoparametric elements the interpolation functions are used as the shape functions in Equation 3.1. The interpolation functions are expressed in terms of the natural coordinates S and T and for an 8-noded quadrilateral isoparametric element can be found in e.g. Potts and Zdravkovic (1999).



a) Parent Element b) Global Element

Figure 3.1: 8-noded isoparametric element (after Potts and Zdravkovic (1999))

3.2.3 Element equations

The element equations govern the deformational behaviour of each element by combining the compatibility, equilibrium and constitutive behaviour. These will be described here for an element subjected to plane strain conditions.

The compatibility expressions for such an element, considering a compression positive sign convention, are given as:

$$\Delta\varepsilon_x = -\frac{\partial \Delta u}{\partial x},\ \Delta\varepsilon_y = -\frac{\partial \Delta v}{\partial y},\ \Delta\gamma_{xy} = -\frac{\partial \Delta u}{\partial y} - \frac{\partial \Delta v}{\partial x},\ \Delta\varepsilon_z = \Delta\gamma_{xz} = \Delta\gamma_{zy} = 0 \quad (3.3)$$

By replacing the displacements in Equation 3.3 with the approximations given in Equation 3.1, the strains can be expressed as a function of the nodal displacements.

$$\{\Delta\varepsilon\} = [B]\begin{Bmatrix}\Delta u \\ \Delta v\end{Bmatrix}_n = [B]\{\Delta d\}_n \quad (3.4)$$

where the matrix $[B]$ contains the global derivatives of the shape functions N_i and $\{\Delta d\}_n$ contains the nodal displacements of the element.

The constitutive behaviour of the material provides a relationship between stresses and strains and therefore provides a link between equilibrium and compatibility. This can be expressed as:

$$\{\Delta\sigma\} = [D]\{\Delta\varepsilon\} \quad (3.5)$$

where $[D]$ is the constitutive matrix. The constitutive matrix for isotropic linear elastic materials and for plane strain conditions takes the following form:

$$\begin{Bmatrix}\Delta\sigma_x \\ \Delta\sigma_y \\ \Delta\sigma_z \\ \Delta\tau_{xy}\end{Bmatrix} = \frac{E}{(1+\mu)(1-2\mu)}\begin{bmatrix}(1-\mu) & \mu & \mu & 0 \\ \mu & (1-\mu) & \mu & 0 \\ \mu & \mu & (1-\mu) & 0 \\ 0 & 0 & 0 & (1/2-\mu)\end{bmatrix}\begin{Bmatrix}\Delta\varepsilon_x \\ \Delta\varepsilon_y \\ \Delta\varepsilon_z \\ \Delta\gamma_{xy}\end{Bmatrix} \quad (3.6)$$

where μ is the Poisson's ratio and E is the Young's modulus.

The element equations are obtained by applying the principle of minimum potential energy. The incremental potential energy of a single element is defined as:

$$\begin{aligned} &Incremental\ potential\ energy\left(\Delta E\right) = Incremental\ strain\ energy\left(\Delta W\right) \\ &\quad - Incremental\ work\ done\ by\ the\ applied\ loads\left(\Delta L\right) \end{aligned} \tag{3.7}$$

In the above equation the incremental strain energy and incremental work done by the applied loads are given by Equations 3.8 and 3.9 respectively:

$$\Delta W = \frac{1}{2}\int_{Vol}\left\{\Delta\varepsilon\right\}^{T}\left\{\Delta\sigma\right\}dVol \tag{3.8}$$

$$\Delta L = \int_{Vol}\left\{\Delta d\right\}^{T}\left\{\Delta F\right\}dVol + \int_{Surface}\left\{\Delta d\right\}^{T}\left\{\Delta T\right\}dSurface \tag{3.9}$$

where $\{\Delta d\}^{T} = \{\Delta u, \Delta v\}$ = displacement vector, $\{\Delta F\}^{T} = \{\Delta F_x, \Delta F_y\}$ = body force vector and $\{\Delta T\}^{T} = \{\Delta T_x, \Delta T_y\}$ = surface tractions vector.

According to the principle of minimum potential energy, a loaded body exists in a static equilibrium condition when the potential energy is at a minimum. This can be expressed as:

$$\delta\Delta E = \delta\Delta W - \delta\Delta L = 0 \tag{3.10}$$

By substituting Equations 3.8 and 3.9 into Equation 3.10 and using Equations 3.1, 3.4 and 3.5 it can be shown that the equilibrium equations for each element take the following form (Potts and Zdravkovic (1999)):

$$\left[K_E\right]\left\{\Delta d\right\}_n = \left\{\Delta R_E\right\} \tag{3.11}$$

where $\left[K_E\right] = \int_{Vol}\left[B\right]^{T}\left[D\right]\left[B\right]dVol$ is the element stiffness matrix and

$\left\{\Delta R_E\right\} = \int_{Vol}\left[N\right]^{T}\left\{\Delta F\right\}dVol + \int_{Surface}\left[N\right]^{T}\left\{\Delta T\right\}dSurface$ is the right hand side load vector.

As mentioned earlier the shape functions depend only on the natural coordinates S and T. Therefore the global derivatives of the shape functions with respect to the global coordinates x and y in the matrix $[B]$ cannot be determined directly. The global derivatives of the shape functions can be calculated from the natural derivatives using the chain rule of differentiation:

$$\left\{\frac{\partial N_i}{\partial S} \quad \frac{\partial N_i}{\partial T}\right\}^T = [J]\left\{\frac{\partial N_i}{\partial x} \quad \frac{\partial N_i}{\partial y}\right\}^T \tag{3.12}$$

where $[J]$ is the Jacobian matrix:

$$[J] = \begin{bmatrix} \frac{\partial x}{\partial S} & \frac{\partial y}{\partial S} \\ \frac{\partial x}{\partial T} & \frac{\partial y}{\partial T} \end{bmatrix} \tag{3.13}$$

Equation 3.13 can be inverted to give the global derivatives of the shape functions as:

$$\begin{Bmatrix} \frac{\partial N_i}{\partial x} \\ \frac{\partial N_i}{\partial y} \end{Bmatrix} = \frac{1}{|J|}\begin{bmatrix} \frac{\partial y}{\partial T} & -\frac{\partial y}{\partial S} \\ -\frac{\partial x}{\partial T} & \frac{\partial x}{\partial S} \end{bmatrix}\begin{Bmatrix} \frac{\partial N_i}{\partial S} \\ \frac{\partial N_i}{\partial T} \end{Bmatrix} \tag{3.14}$$

where $|J|$ is the determinant of the Jacobian matrix.

The volume and surface integrals in Equation 3.11 are expressed in terms of the global coordinates x and y. However, for an isoparametric element these can be evaluated using the natural coordinate system of the parent element T and S. For example the isoparametric coordinate transformation of the volume integral for an element of thickness t is given by the following equation:

$$dVol = t\,dx\,dy = t|J|\,dS\,dT \tag{3.15}$$

For plane strain conditions the thickness t is taken equal to unity.

The main advantage of the isoparametric formulation is that the element equations need only be evaluated in the parent element coordinate system. The integrations can be performed over a square, with S and T varying between -1 and 1. Therefore, for each element in the mesh a standard procedure can be used to evaluate the integrals that constitute the stiffness matrix and the right hand side vector.

3.2.3.1 Numerical integration

In most cases the explicit evaluation of the integrals in Equation 3.11 is not possible and therefore numerical integration is usually employed. ICFEP uses a Gaussian integration scheme. In this scheme the integral of a function is replaced by a weighted sum of

the function evaluated at a number of integration points. For example, the one dimensional integral of a function $f(x)$ (i.e. $-1 < x < 1$) is given as:

$$\int_{-1}^{1} f(x)\,dx \approx \sum_{i=1}^{n} W_i\, f(x_i) \tag{3.16}$$

where $f(x_i)$ are the values of the function at the n integration points and W_i are the corresponding values of the weighting coefficients. The number of integration points determines the integration order. The accuracy of the integration increases with the integration order, but this results in longer computational time since the number of function evaluations increases too.

In the Gaussian integration scheme the integration points are often referred to as Gauss points. Figure 3.2 shows the location of the Gauss points for a 2x2 and 3x3 integration order for an 8-noded quadrilateral element. The 2x2 and 3x3 integration orders are usually referred to as reduced and full integration respectively. In the analyses performed in this thesis a 2x2 order (reduced integration) was adopted.

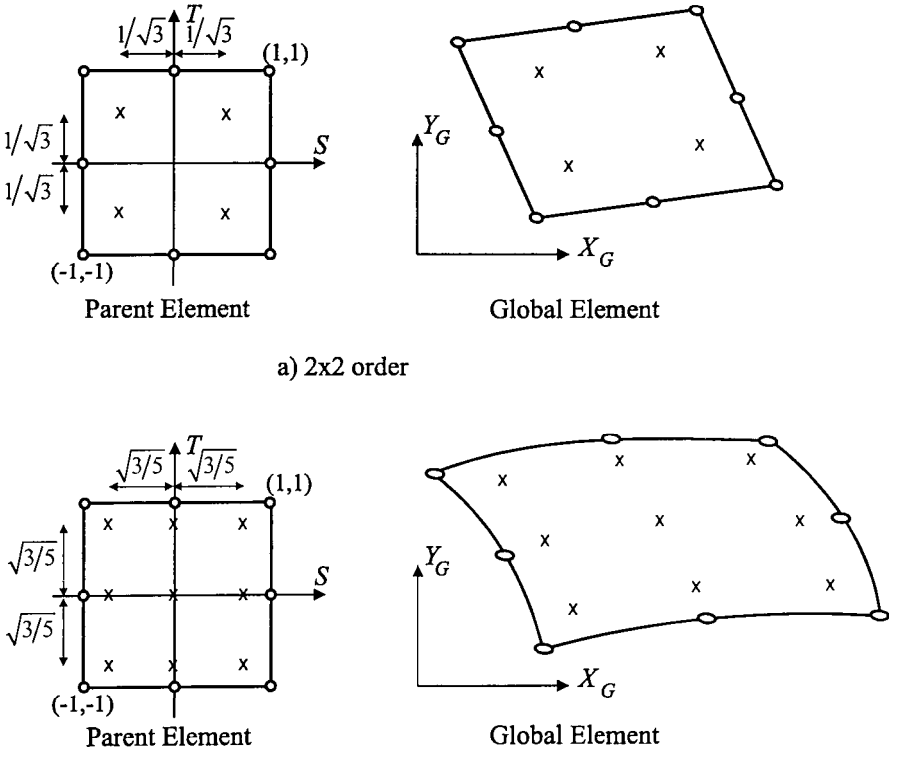


Figure 3.2: Location of Gauss points for an 8-noded isoparametric element (after Potts and Zdravkovic (1999))

3.2.4 Global equations

Once the element equations have been formulated the global equations can be obtained by assembling the separate element equations. The resulting global equations have a form similar to Equation 3.11:

$$[K_G]\{\Delta d\}_{nG} = \{\Delta R_G\} \tag{3.17}$$

where $[K_G]$ is the global stiffness matrix, $\{\Delta d\}_{nG}$ is the vector of the unknown nodal displacements (degrees of freedom) for all the nodes of the finite element mesh and $\{\Delta R_G\}$ is the global right hand side load vector.

3.2.5 Boundary conditions

The next step in the finite element formulation is the incorporation of the appropriate boundary conditions. Boundary conditions fall into two categories, the loading conditions and the displacement conditions.

The loading conditions affect the right hand side vector $\{\Delta R_G\}$ of the global system of equations. Examples of such conditions are line loads, surcharge loads, body forces, excavation, construction etc.

The displacement conditions affect the list of nodal displacements $\{\Delta d\}_{nG}$. Sufficient displacement conditions must be prescribed to make sure that rigid body motion of the whole finite element mesh is not possible.

3.2.6 Solution of global equations

The last stage in the finite element formulation is the solution of the global equations to give the list of unknown nodal displacements $\{\Delta d\}_{nG}$. These mathematically form a large system of simultaneous equations. One mathematical technique for solving large systems of equations, adopted by most finite element programs, is the Gaussian elimination method (Potts and Zdravkovic (1999)). Once the nodal displacements have been found, which are the primary unknown quantity, the secondary quantities such as stresses and strains can be calculated by Equations 3.4 and 3.5 respectively.

3.3 Geotechnical considerations

The finite element theory presented in the previous section is applicable to any linear continuum. However in order to apply this theory to geotechnical engineering a number of modifications have to be made.

3.3.1 Pore water pressure considerations

Soil is generally considered as a two phase material composed of the soil skeleton and the water which fills the pores of the soil skeleton. In some cases the voids between the soil particles can be filled with a mixture of air and water and then the soil is treated as a three phase material, but this will not be considered in this thesis.

The finite element theory described previously can be applied to any single phase linear material. If this theory is to be applied to geotechnical analysis then the two phase nature of the soil has to be taken into account. In this case the equations governing the flow of the water through the soil skeleton have to be combined with the equations governing the deformation of the soil and the pore water pressure is introduced as an extra degree of freedom. Such a theory is called coupled because it couples together the pore water flow and the soil deformation. Details on coupled analysis can be found in Potts and Zdravkovic (1999).

The analyses considered in this thesis adopt two extreme conditions of the above coupled process, the fully drained and undrained conditions. Fully drained conditions occur when loading is applied slowly on a soil with very high permeability. In this case a steady state drainage pattern is assumed to exist and the pore water pressures are independent of the soil deformation. Undrained conditions occur when loading is applied rapidly on a soil with very low permeability. In this case pore water flow is assumed to be prevented and the pore water pressures developed are linked in a unique way to the deformation of the soil. In both cases the problem reduces to that of a single phase material and with minor modifications the finite element theory already presented is still valid.

3.3.1.1 Undrained analysis

The constitutive behaviour in Equation 3.5 is expressed in terms of total stresses. The principle of effective stress relates the changes of the total stress to the changes of the

effective stress and the pore water pressure:

$$\{\Delta\sigma\} = \{\Delta\sigma'\} + \{\Delta\sigma_f\} \tag{3.18}$$

where $\Delta\sigma$ is the change in total stress, $\Delta\sigma'$ is the change in effective stress and $\Delta\sigma_f$ is the change in pore water pressure. The vector $\Delta\sigma_f$ is given as:

$$\{\Delta\sigma_f\}^T = \{\Delta u \quad \Delta u \quad \Delta u \quad 0 \quad 0 \quad 0\} \tag{3.19}$$

In undrained conditions no flow of water is assumed to occur and the solid and water phases are assumed to deform together. This results in the total constitutive matrix, [D], being expressed as a function of the effective constitutive matrix, [D'], and the pore water stiffness matrix, [D_f], as follows:

$$[D] = [D'] + [D_f] \tag{3.20}$$

The pore water stiffness matrix, [D_f], is related to the bulk modulus of the pore water, K_f, and it has the following form in the general three dimensional case:

$$[D_f] = K_e \{m\}\{m\}^T \tag{3.21}$$

where $K_e = \Delta u / \Delta\varepsilon_v$ (3.22)

and $\{m\}^T = \{1 \quad 1 \quad 1 \quad 0 \quad 0 \quad 0\}$ (3.23)

It can be shown (Potts and Zdravkovic (1999)) that K_e can be approximated by K_f so that the total constitutive matrix is given by:

$$[D] = [D'] + K_f \{m\}\{m\}^T \tag{3.24}$$

Equation 3.24 can be incorporated in the finite element theory presented in the previous section in the following way. The components of the effective constitutive matrix, [D'], are calculated and the bulk modulus of the pore water, K_f, is specified. These are then combined through Equation 3.24 to give the total constitutive matrix [D], which is then used in the procedure outlined in section 3.2 to determine the unknown nodal displacements. Once these have been found the effective stresses are calculated by using the effective constitutive matrix, [D'], and the pore water pressures by using the pore

water bulk modulus, K_f. The total stresses are either calculated using the total constitutive matrix, [D], or through Equation 3.18.

Alternatively if the constitutive model is formulated in terms of total stresses, as it is usually the case for simple constitutive models, the total constitutive matrix [D] can be used directly in Equation 3.5. However, in this case it is not possible to obtain any information on the changes in pore water pressure. Moreover most advanced models including all the models described in the previous chapter are formulated in terms of effective stresses. For these models the approach described earlier is adopted.

3.3.1.2 Drained analysis

In drained conditions no change in the pore water pressure, u, is assumed to occur and the change in the total stress is assumed to be equal to the change in the effective stress. In this case the total constitutive matrix, [D], is equal to the effective constitutive matrix, [D']. The decomposition of the total constitutive matrix, [D], into the effective constitutive matrix, [D'], and the pore water stiffness matrix, [D_f], as described in the previous section, can still be used but in this case the pore water bulk modulus, K_f, is set equal to zero.

3.4 Finite element theory for non-linear materials

The finite element theory presented so far is applicable only to linear elastic materials. If non-linear elastic or elasto-plastic constitutive models are to be used to simulate more realistically the observed soil behaviour, then the finite element theory has to be extended. In the case of non-linear elastic constitutive models the elastic constitutive matrix [D] is no longer constant but varies with stress and/or strain. In elasto-plastic models this is replaced by the elasto-plastic constitutive matrix [D^{ep}], given by Equation 2.26, which varies with stress and the hardening parameters. In any case the resulting global stiffness matrix [K_G] is not constant but changes during a finite element analysis. In order to deal with the changing global stiffness matrix the boundary conditions are applied in a series of increments and Equation 3.17 is expressed in an incremental form:

$$\left[K_G\right]^i \left\{\Delta d\right\}^i_{nG} = \left\{\Delta R_G\right\}^i \tag{3.25}$$

where $[K_G]^i$ is the incremental global stiffness matrix, $\{\Delta d\}^i_{nG}$ is the vector of the incremental nodal displacements and $\{\Delta R_G\}^i$ is the incremental right hand side load

vector. For each increment Equation 3.25 is solved and the final solution is obtained by adding together the results of each increment. However, the global stiffness matrix still varies over the increment and this should be taken into account when solving Equation 3.25. A number of different solution strategies exist, e.g. the tangent stiffness method, the visco-plastic method, the Newton-Raphson method, etc. For a solution strategy to be sufficiently accurate, this should not be sensitive to increment size. The analyses presented in this thesis were carried out using the modified Newton-Raphson scheme and this is explained briefly in the next section.

3.4.1 The modified Newton-Raphson method

In the modified Newton-Raphson method each increment is solved in a number of iterations. The first iteration essentially consists of the solution of Equation 3.25 using a global stiffness matrix $[K_G]^o$, which is calculated using the current stresses at the beginning of the increment. The technique recognises that due to the variation of the global stiffness matrix over the increment, the solution obtained from the first iteration is in error. The predicted displacements from the first iteration, Δd^1, are used in order to calculate a measure of the error in the prediction, the residual load vector, ψ^1. This process is illustrated in Figure 3.3. The way the residual load vector is calculated will be explained later. The residual load vector, ψ^1, is then used as the right hand side vector in Equation 3.25 which is solved again, to obtain the predicted displacements Δd^2. The residual load vector, ψ^2, at the end of the second iteration is then calculated and this is used as the new right hand side vector in Equation 3.25 which can be rewritten as:

$$[K_G]^i \left(\{\Delta d\}^i_{nG} \right)^j = \{\psi\}^{j-1} \tag{3.26}$$

where j is the iteration number and for the first iteration $\{\psi\}^o = \{\Delta R_G\}^i$.

The procedure continues until some convergence criteria are satisfied. The incremental displacements are then equal to the sum of the iterative displacements. In ICFEP convergence limits are set on the norms of both the iterative displacements $(\{\Delta d\}^i_{nG})^j$ and the residual loads $\{\psi\}^j$, given by equations 3.27 and 3.28 respectively.

$$\left\| \left(\{\Delta d\}^i_{nG} \right)^j \right\| = \sqrt{\left(\left(\{\Delta d\}^i_{nG} \right)^j \right)^T \left(\{\Delta d\}^i_{nG} \right)^j} \tag{3.27}$$

$$\left\|\{\psi\}^j\right\| = \sqrt{\left(\{\psi\}^j\right)^T \{\psi\}^j} \tag{3.28}$$

The value of Equation 3.27 is checked against the norms of the incremental and accumulated displacements and the value of Equation 3.28 is checked against the norms of the incremental and accumulated global right hand side vectors. The default convergence limits set in ICFEP are such that the values of Equations 3.27 and 3.28 are less than 2% of the equivalent incremental and accumulated norms and these are also the limits used in this thesis.

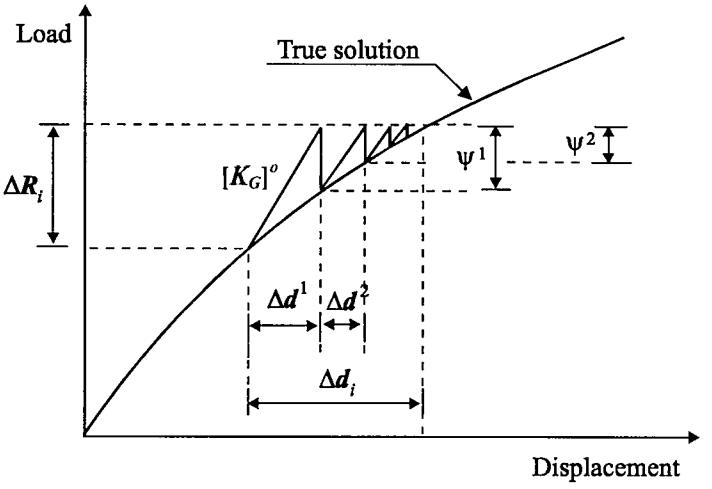


Figure 3.3: Graphical representation of the modified Newton-Raphson scheme (after Potts and Zdravkovic (1999))

The residual load vector at the end of each iteration is obtained from the following process. The current estimate of the incremental displacements is calculated and these are used to find the corresponding strains. The constitutive model is then integrated along the incremental strain path and an estimate of the stress changes is calculated. These stress changes are added to the stresses at the beginning of the increment and used to evaluate the equivalent nodal forces. The residual load vector is the difference between these nodal forces and the externally applied loads. The integration of the constitutive model along the incremental strain path is carried out with methods which are called stress point algorithms.

In the modified Newton-Raphson method the global stiffness matrix, $[K_G]^o$, which is calculated and inverted at the beginning of the increment, is then used for all the iterations within this increment. This reduces the computational time compared with the original Newton-Raphson method in which the stiffness matrix is calculated and inverted at the beginning of each iteration. In the modified Newton-Raphson method

used in ICFEP the option exists for the stiffness matrix to be updated every certain number of iterations. Another option that exists is to calculate the incremental global stiffness matrix by using the elastic constitutive matrix, $[D]$, rather than the elasto-plastic constitutive matrix, $[D^{ep}]$. This is because, as mentioned before, the direct solution of Equation 3.25 is anyway in error (due to the incremental global stiffness matrix varying over the increment) and it is within the iterative technique employed that the constitutive equations are satisfied in order to obtain the correct solution.

3.4.1.1 Stress point alogorithm

The algorithm used in the analyses presented in this thesis is a substepping algorithm with a modified Euler integration scheme. The procedure starts with the determination of the elastic proportion of the increment. Once this has been calculated the remaining elasto-plastic strain increment is split into a series of substeps. A modified Euler approximation is used for the integration of the constitutive equations over each substep. The size of the substep can be determined by estimating the error in the numerical integration. The overall stress changes at the end of the iteration are obtained by summing the stress changes from each substep.

This can be explained in more detail as follows: If the elastic part of the increment is equal to α, then the remaining strain increment is equal to $(1-\alpha)\{\Delta\varepsilon\}$ and is associated with elasto-plastic behaviour. At the beginning of the remaining elasto-plastic increment the stresses and strains are equal to:

$$\{\sigma\} = \{\sigma_o\} + \{\Delta\sigma^e\} \tag{3.29}$$

$$\{\Delta\varepsilon_s\} = (1-\alpha)\{\Delta\varepsilon\} \tag{3.30}$$

where $\{\sigma_o\}$ are the stresses at the beginning of the increment, $\{\Delta\sigma^e\}$ is the elastic portion of the stress increment and $\{\Delta\varepsilon_s\}$is the elasto-plastic part of the strain increment, $\{\Delta\varepsilon\}$, which is then split into a number of substeps. The first substep strain is equal to:

$$\{\Delta\varepsilon_{ss}\} = \Delta T\{\Delta\varepsilon_s\} \tag{3.31}$$

where ΔT expresses the proportion of the elasto-plastic part of the strain increment that the current substep represents. Initially it is assumed that only one substep is necessary. In this case ΔT is equal to unity. A first estimate of the associated changes in stresses, plastic strains and hardening parameters are calculated using a first order Euler

approximation:

$$\{\Delta\sigma_1\} = \left[D^{ep}\left(\{\sigma\},\{k\}\right)\right]\{\Delta\varepsilon_{ss}\} \tag{3.32}$$

$$\left\{\Delta\varepsilon_1^p\right\} = \Lambda\left(\{\sigma\},\{k\},\{\Delta\varepsilon_{ss}\}\right)\frac{\partial P\left(\{\sigma\},\{m_1\}\right)}{\partial\sigma} \tag{3.33}$$

$$\{\Delta k_1\} = \left\{\Delta k\left(\left\{\Delta\varepsilon_1^p\right\}\right)\right\} \tag{3.34}$$

Using Equations 3.33 and 3.34 the stresses and hardening parameters at the end of the substep are obtained as $\{\sigma\}+\{\Delta\sigma_1\}$ and $\{k\}+\{\Delta k_1\}$. These are then used to obtain a second estimate of the stress, plastic strain and hardening parameters changes over the substep as follows:

$$\{\Delta\sigma_2\} = \left[D^{ep}\left(\{\sigma+\Delta\sigma_1\},\{k+\Delta k_1\}\right)\right]\{\Delta\varepsilon_{ss}\} \tag{3.35}$$

$$\left\{\Delta\varepsilon_2^p\right\} = \Lambda\left(\{\sigma+\Delta\sigma_1\},\{k+\Delta k_1\},\{\Delta\varepsilon_{ss}\}\right)\frac{\partial P\left(\{\sigma+\Delta\sigma_1\},\{m_2\}\right)}{\partial\sigma} \tag{3.36}$$

$$\{\Delta k_2\} = \left\{\Delta k\left(\left\{\Delta\varepsilon_2^p\right\}\right)\right\} \tag{3.37}$$

In this way a more accurate modified Euler estimate of the changes in stress, plastic strain and hardening parameters can be obtained as:

$$\{\Delta\sigma\} = \frac{1}{2}\left(\{\Delta\sigma_1\}+\{\Delta\sigma_2\}\right) \tag{3.38}$$

$$\left\{\Delta\varepsilon^p\right\} = \frac{1}{2}\left(\left\{\Delta\varepsilon_1^p\right\}+\left\{\Delta\varepsilon_2^p\right\}\right) \tag{3.39}$$

$$\{\Delta k\} = \frac{1}{2}\left(\{\Delta k_1\}+\{\Delta k_2\}\right) \tag{3.40}$$

The error in the prediction is expressed as a function of the difference between the two stress changes $\Delta\sigma_1$ and $\Delta\sigma_2$, given by Equations 3.32 and 3.35 respectively. This is checked against a user defined tolerance and if the error is unacceptable then the substep size is reduced. The same procedure is repeated with a new value of ΔT in Equation 3.31 until the error becomes less than the tolerance and the substep size is accepted. The

accumulated stresses, plastic strains and hardening parameters are then updated and the next substep can be applied. This procedure is based on a scheme proposed by Sloan (1987) and further information on the calculation of the error in the prediction, the user defined tolerance and the estimate of the size of the substep can be found in Potts and Zdravkovic (1999). If the elastic part of the increment is also non-linear then a similar substepping procedure has to be carried out within the elastic region $\alpha\{\Delta\varepsilon\}$.

3.5 Summary

The first part of this chapter detailed the basic steps that are required in the formulation of the finite element method for linear materials. These are: element discretisation, primary variable approximation, formulation of the element equations, assemblage of the global equations, formulation of the boundary conditions and solution of the global equations.

The second part of the chapter concentrated on the two phase nature of the soil and the pore water pressure considerations that need to be taken into account in order to make possible the application of the finite element theory in geotechnical engineering. Only two extreme conditions were considered, the fully drained conditions in which there is no change in the pore water pressure and the fully undrained conditions in which there is no flow of water. In both of these extreme conditions the problem reduces to that of a single phase material, so only minor modifications are required in the original finite element theory. However for any other conditions the flow of water has to be coupled to the deformation of the soil, although this was not considered in this thesis.

The theory presented up to this point is applicable to any linear elastic continuum. The last part of the chapter presented the modifications in the finite element theory for linear materials necessary to accommodate non-linear elastic or elasto-plastic constitutive models. In these cases the global stiffness matrix is not a constant any more, the boundary conditions have to be applied in a number of increments and the global equations have to be solved for each increment. The modified Newton-Raphson method, which was used as a solution strategy for all the analyses carried out for this thesis, and the stress point algorithm adopted in the modified Newton-Raphson scheme were also discussed in this last part of the chapter.

Chapter 4

Two-surface model

4.1 Introduction

Chapter 2 emphasized the fact that the pre-failure behaviour of overconsolidated clays is highly non-linear and inelastic, except at very small strains where stiffness is almost constant with strain. The review of constitutive models available in the literature showed that models which are capable of predicting both non-linearity and plasticity from the early stages of loading are those which are based on extensions of the conventional elasto-plastic framework, in which plastic strains are allowed for stress states within the conventionally defined yield surface (termed the bounding surface). The kinematic hardening models, particularly, introduce kinematic yield surfaces within the bounding surface and in this way are capable of retaining some memory of the previous stress history.

From the kinematic hardening models reviewed in Chapter 2, the simplest and most theoretically attractive is the two-surface model developed by Al-Tabbaa (1987). As already mentioned, this is an extension of the modified Cam Clay model, which has been used successfully in the prediction of the behaviour of normally consolidated clays. The model introduces a single kinematic yield surface within the modified Cam Clay bounding surface. The development of the model was based on the slow cyclic response of speswhite kaolin and the model was shown to successfully match many of the important aspects of the observed response, like hysteresis and accumulation of permanent strains for loading-unloading cycles that remained within the bounding surface. The model has not been developed and used specifically for modelling the pre-failure behaviour of overconsolidated clays; however, it seems to be able to reproduce

important features of the behaviour of such soils, like non-linearity and inelasticity from early stages of loading. It has the additional advantage that it requires only a small number of parameters - seven, five of which have their origin in the modified Cam Clay model. For the above reasons the two-surface model proposed by Al-Tabbaa (1987) was the first model implemented into ICFEP.

The next model chosen to be implemented into ICFEP was the three-surface model developed by Stallebrass (1990), which is an extension of the two-surface model. This model introduces a second surface within the modified Cam Clay bounding surface and was shown to predict better the effect of recent stress history. This model is discussed in further detail in the next chapter.

This chapter starts with a brief description of the modified Cam Clay model, which was used by Al-Tabbaa (1987) as the basis for the formulation of the two-surface model, in section 4.2. The original formulation of the two-surface model, which was developed in triaxial stress space, follows in section 4.3. In order to implement a constitutive model into a finite element program this has to be formulated in general stress space. The general formulation of the two-surface model and the improvements that have been made as part of the author's research are presented in section 4.4. Section 4.5 describes the implementation of the general formulation of the two-surface model into ICFEP and section 4.6 presents the validation of the model through a series of single finite element analyses. Further evaluation of the model is given in Chapter 7.

4.2 Modified Cam Clay model

The modified Cam Clay model is based on the critical state framework, discussed in section 2.2.2. The original formulation of the model is described in detail by Roscoe and Burland (1968). This section gives a brief description of the version of the modified Cam Clay model used by Al-Tabbaa (1987) in order to facilitate the derivation of the two-surface model.

The development of the model is based on laboratory results from triaxial tests. Hence, the stress and strain invariants used in the model are the mean effective stress, p', the deviatoric stress, q, the volumetric strain, ε_v, and the deviatoric strain, ε_s, given by Equations 1.23-1.26.

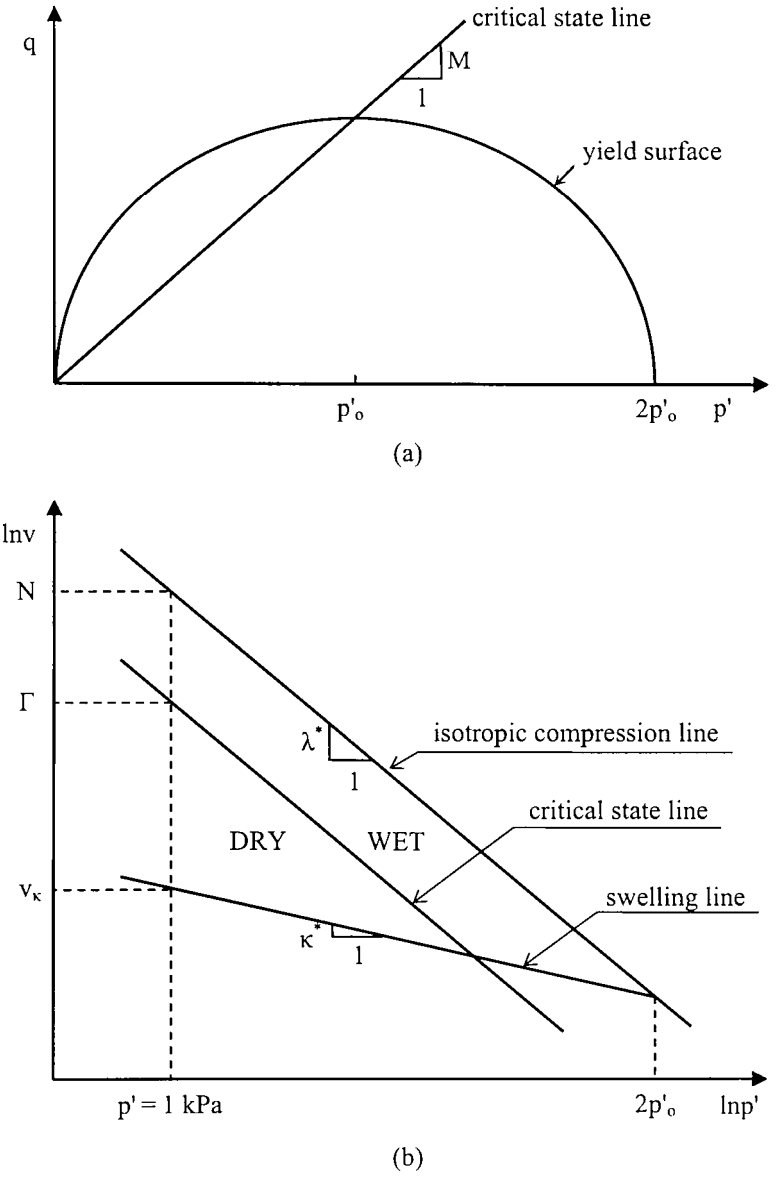


Figure 4.1: The modified Cam Clay model in a) q-p' space b) ln$v$-lnp' space

In the modified Cam Clay model the projection of the yield surface, that lies above each swelling line, onto the q-p' plane is elliptical (see Figure 4.1a) and can be expressed as:

$$\left(p' - p'_o\right)^2 + \frac{q^2}{M^2} = p'^2_o \tag{4.1}$$

where M is the slope of the critical state line in q-p' space and p'_o is half the value of the mean effective stress at the intersection of the current swelling line with the isotropic compression line. (In the original formulation of the model p'_o was used in order to denote the whole value of the mean effective stress at the intersection of the current swelling line with the isotropic compression line, rather than half the value used in this

version of the model.)

The normality rule is assumed to apply and hence the plastic strain increment vector is normal to the yield surface at the current stress state.

In this version of the model the natural compression law proposed by Butterfield (1979) is adopted such that the isotropic normal compression and swelling lines are assumed to be straight in ln$v$-lnp' space, rather than v-lnp' space assumed in the original formulation. The slopes of the isotropic normal compression and swelling lines in ln$v$-lnp' space are denoted by λ^* and κ^* respectively, as shown in Figure 4.1b. Soils that exist at stress states to the right and left of the critical state line in Figure 4.1b are known as 'wet of critical' and 'dry of critical' respectively.

An isotropic hardening rule is used in order to define the change in size of the yield surface, linking the parameter p'_o to the plastic volumetric strain, ε_v:

$$\frac{dp'_o}{p'_o} = \frac{d\varepsilon_v^p}{\lambda^* - \kappa^*} \tag{4.2}$$

Consideration of the consistency condition of the yield surface results in the following expression for the calculation of the plastic strains:

$$\begin{Bmatrix} d\varepsilon_v^p \\ d\varepsilon_s^p \end{Bmatrix} = \frac{\lambda^* - \kappa^*}{(p' - p'_o)p'p'_o} \begin{bmatrix} (p' - p'_o)^2 & (p' - p'_o)\frac{q}{M^2} \\ (p' - p'_o)\frac{q}{M^2} & \left(\frac{q}{M^2}\right)^2 \end{bmatrix} \begin{Bmatrix} dp' \\ dq \end{Bmatrix} \tag{4.3}$$

Equation 4.3 can be obtained by calculating the scalar multiplier, Λ, from the consistency condition of the yield surface (Equation 2.17) and substituting this into the flow rule (Equation 2.12) (see section 2.3.2.1).

If the stress path remains within the yield surface the deformation of the soil is purely elastic and isotropic. The elastic volumetric strains can be calculated from the equation of the elastic swelling line:

$$d\varepsilon_v^e = \kappa^* \frac{dp'}{p'} \tag{4.4}$$

This gives the elastic bulk modulus, K, as:

$$K = \frac{p'}{\kappa^*} \tag{4.5}$$

In the original formulation of the model no elastic shear strains were considered. In later applications of the model the elastic shear strains were usually computed by assuming either an elastic shear modulus, G, or an elastic Poisson's ratio, μ.

4.3 Original formulation in triaxial stress space

4.3.1 Introduction

The development of the two-surface model was based on axially symmetric test results (triaxial and oedometer tests) and hence the stress and strain invariants described by Equations 1.23-1.26 were used for the original formulation of the model in triaxial stress space.

4.3.2 Equations of the surfaces

The bounding surface in this model is represented by the modified Cam Clay yield surface:

$$\left(p' - p'_o\right)^2 + \frac{q^2}{M^2} = p'^2_o \tag{4.6}$$

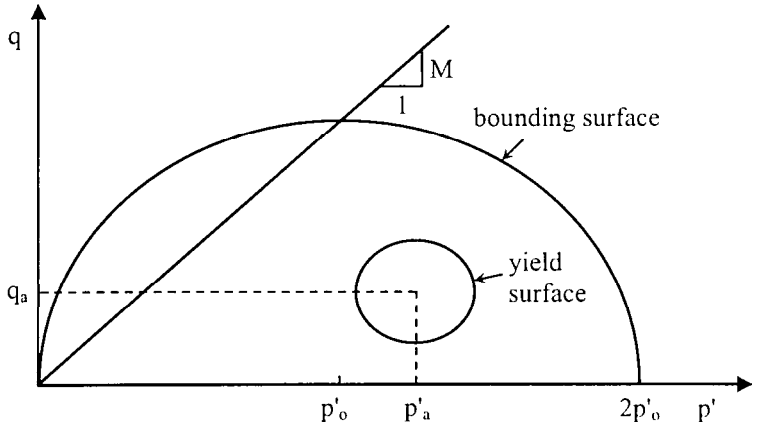


Figure 4.2: Diagram showing the yield and bounding surfaces and the symbols chosen for their centres (after Al-Tabbaa (1987))

The kinematic yield surface, enclosing the truly elastic region, has the same shape as the bounding surface, but is smaller in size. The equation for this surface is:

$$\left(p' - p'_a\right)^2 + \frac{\left(q - q_a\right)^2}{M^2} = R^2 p'^2_o \tag{4.7}$$

where R is the ratio of the size of the kinematic yield surface to that of the bounding surface and (p'_a, q_a) is the centre of the kinematic yield surface, Figure 4.2.

4.3.3 Flow rule

The plastic strain increment vector is assumed to be normal to the kinematic yield surface at the current stress state. Consequently, the flow rule of the model is associated and the plastic potential is given by Equation 4.7.

4.3.4 Hardening rules

The evolution of the bounding surface is described by isotropic hardening; this means that the surface either expands or contracts during plastic flow. The evolution of the kinematic yield surface is described by a combination of kinematic and isotropic hardening, in which the surface translates in the stress space following the current stress point and changes size simultaneously. This combination of kinematic and isotropic hardening forms the translation rule of the kinematic yield surface.

4.3.4.1 Isotropic hardening of the bounding surface

The model adopts the volumetric hardening rule of the modified Cam Clay model. The change in size of the bounding surface is controlled by the change in plastic volumetric strain.

$$\frac{dp'_o}{p'_o} = \frac{d\varepsilon_v^p}{\lambda^* - \kappa^*} \tag{4.8}$$

In the above equation λ^* and κ^* represent the slope of the isotropic normal compression line and the slope of the swelling line, for an unloading path lying entirely within the kinematic yield surface, in ln$v$-lnp'space.

4.3.4.2 Translation rule of the kinematic yield surface

The translation rule of the kinematic yield surface is formulated in a manner that guarantees that the two surfaces can come in contact at a common normal but never intersect. This is achieved by making sure that the centre of the kinematic yield surface moves always along a vector, β, which joins the current stress state, C, to its conjugate point, D, on the bounding surface, see Figure 4.3. The conjugate point D is defined as the point on the bounding surface with the same outward normal as point C. The vector β is given as:

$$\beta = \begin{Bmatrix} \dfrac{p' - p'_a}{R} - (p' - p'_o) \\ \dfrac{q - q_a}{R} - q \end{Bmatrix} \tag{4.9}$$

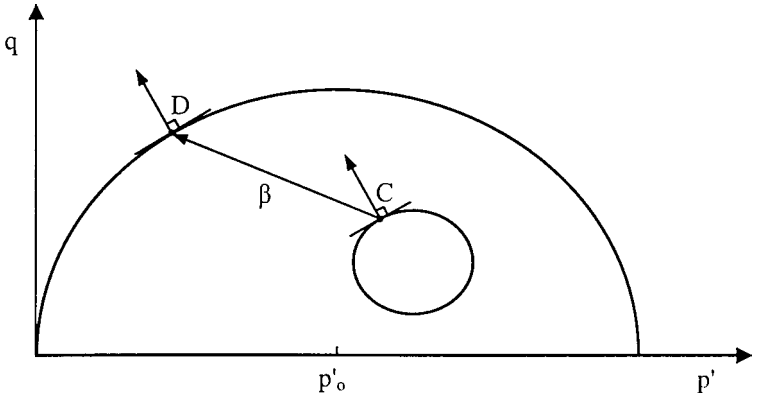


Figure 4.3: Assumed relative translation of the kinematic yield surface along the vector β joining the current stress point C to its conjugate point D (after Al-Tabbaa (1987))

The translation rule is divided into two components. One is associated with the change in size of the kinematic yield surface due to isotropic expansion or contraction of the bounding surface, the other is associated with the movement of the kinematic yield surface along the vector β. The resulting translation rule is the following:

$$\begin{Bmatrix} dp'_a \\ dq_a \end{Bmatrix} = \frac{dp'_o}{p'_o} \begin{Bmatrix} p'_a \\ q_a \end{Bmatrix} + S \begin{Bmatrix} \dfrac{p' - p'_a}{R} - (p' - p'_o) \\ \dfrac{q - q_a}{R} - q \end{Bmatrix} \tag{4.10}$$

In the above equation the first part is the change in (p'_a, q_a) due to change in p'_o and the second part is the assumed translation along the vector β. The scalar quantity S can be

obtained by substituting dp'_a and dq_a from Equation 4.10 into the consistency condition for the kinematic yield surface (Equation 2.13) and using Equation 4.7.

$$S=\frac{\left(p'-p'_a\right)\left(dp'-\frac{dp'_o}{p'_o}p'\right)+\frac{q-q_a}{M^2}\left(dq-\frac{dp'_o}{p'_o}q\right)}{\left(p'-p'_a\right)\left[\frac{p'-p'_a}{R}-\left(p'-p'_o\right)\right]+\frac{q-q_a}{M^2}\left(\frac{q-q_a}{R}-q\right)} \tag{4.11}$$

When the two surfaces are in contact at the current stress state, the vector β is equal to zero and the translation rule reduces to:

$$\begin{Bmatrix} dp'_a \\ dq_a \end{Bmatrix}=\frac{dp'_o}{p'_a}\begin{Bmatrix} p'_a \\ q_a \end{Bmatrix} \tag{4.12}$$

4.3.5 Hardening modulus

The hardening modulus is defined in such a way that, when the two surfaces are in contact and for continuous yielding, the model predicts the same behaviour as the modified Cam Clay model. It is initially formulated for the special case that the two surfaces are in contact and then modified for the other cases when the two surfaces are not in contact and the stress state is within the bounding surface. The hardening modulus in these last cases depends on the degree of approach of the kinematic yield surface to the bounding surface and reduces to the value of the hardening modulus on the bounding surface when the two surfaces come in contact.

For the special case when the two surfaces are in contact the plastic strain increments on the kinematic yield surface are the following:

$$\begin{Bmatrix} d\varepsilon_v^p \\ d\varepsilon_s^p \end{Bmatrix}=\frac{1}{h_o}\begin{bmatrix} \left(p'-p'_a\right)^2 & \left(p'-p'_a\right)\frac{q-q_a}{M^2} \\ \left(p'-p'_a\right)\frac{q-q_a}{M^2} & \left(\frac{q-q_a}{M^2}\right)^2 \end{bmatrix}\begin{Bmatrix} dp' \\ dq \end{Bmatrix} \tag{4.13}$$

where the hardening function h_o is given by the following equation:

$$h_o=\frac{p'-p'_a}{\lambda^*-\kappa^*}\left[p'\left(p'-p'_a\right)+\frac{q\left(q-q_a\right)}{M^2}\right] \tag{4.14}$$

Equation 4.13 can be obtained as follows. The scalar multiplier, Λ, is calculated from the

consistency condition of the kinematic yield surface when the two surfaces are in contact, through the use of Equations 4.8 and 4.12, and then this is substituted into the flow rule (see section 2.3.2.1). The hardening function, h_o, is equal to $h_o = ¼(A)$, where A is the hardening modulus as defined in Equation 2.18. A comparison between Equations 4.13 and 4.3 shows that, when the two surfaces are in contact, the plastic strain increments calculated from Equation 4.13 become equal to those calculated using the modified Cam Clay model (Equation 4.3) since in this case the vector β is equal to zero and $(p' - p'_a)/R = (p' - p'_o)$ and $(q - q_a)/R = q$.

In order to calculate the plastic strains whenever they occur, whether or not the kinematic yield surface and the bounding surface are in contact, Al-Tabbaa (1987) replaced h_o in Equation 4.13 with a more general expression:

$$h = h_o + H \tag{4.15}$$

where h_o is given by Equation 4.14 and H is a scalar quantity which is a function of the stress state.

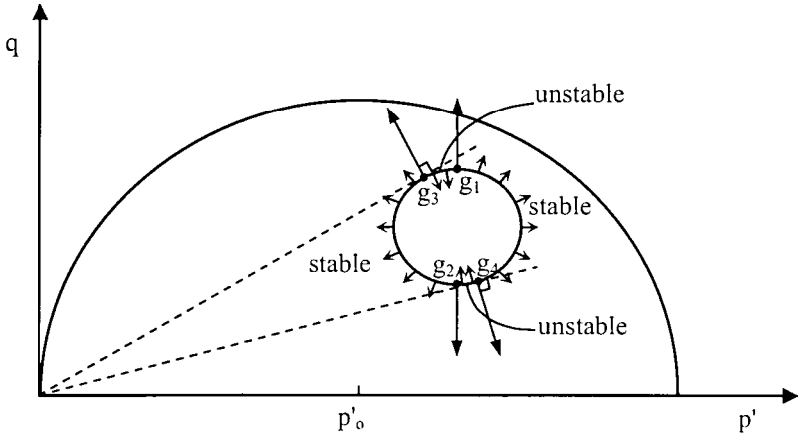


Figure 4.4: Diagram showing singularity points and unstable regions on the yield surface due to the function h_o (after Al-Tabbaa (1987))

Al-Tabbaa (1987) observed that in Equation 4.15 a value of H equal to zero would not be appropriate because the hardening function h_o falls to zero at four "singularity points", which implies unlimited plastic strains. Two singularity points exist for $p' = p'_a$, this is when the stress state is at the top or bottom of the kinematic yield surface (see points g_1 and g_2 in Figure 4.4). The other two singularity points exist at the points where the vector that joins the origin with the current stress state becomes perpendicular to the vector normal to the kinematic yield surface at that stress state. In this case the term

$[p'(p' - p'_a) + q(q - q_a) / M^2]$ in the hardening function h_o becomes equal to zero. The position of these points depends on the location of the kinematic yield surface relative to the origin. Figure 4.4 shows one example of these two points (points g_3 and g_4). These four singularity points define two unstable regions as can be seen in Figure 4.4. An unstable region is defined by Al-Tabbaa (1987) as the region in which the plastic shear strain increment is in the opposite direction to the shear stress increment i.e. where the hardening function becomes negative and softening behaviour is predicted.

A number of constraints were introduced on the values that H could take. First of all since unstable behaviour had not been observed for stress states where $\eta = q / p' < M$, it was required that $h_o + H > 0$ in that region. Then for the plastic strain increments on the kinematic yield surface to be less or equal than those on the bounding surface, H is required to be greater or equal to zero. Finally H should reduce to zero only when the two surfaces come in contact at the current stress state.

Al-Tabbaa (1987) assumed, after Hashiguchi (1985), that H is a function of a measure, b, of the proximity of the kinematic yield surface to the bounding surface. The measure, b, used in this model is the scalar product of the vector β and a vector normal to the yield surface at the current stress state, n, see Figure 4.5, divided by a measure of the size of the yield surface.

$$b = \frac{1}{Rp'_o}\left[(p' - p'_a)\left[\frac{p' - p'_a}{R} - (p' - p'_o)\right] + \frac{q - q_a}{M^2}\left(\frac{q - q_a}{R} - q\right)\right] \qquad (4.16)$$

For $M < 1$ the function b has its maximum value for the configuration of the surfaces shown in Figure 4.6.

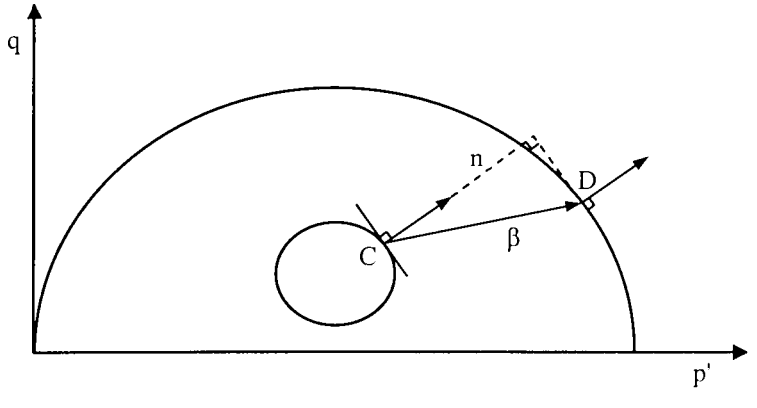


Figure 4.5: Diagram showing the vector β and the vector n (after Al-Tabbaa (1987))

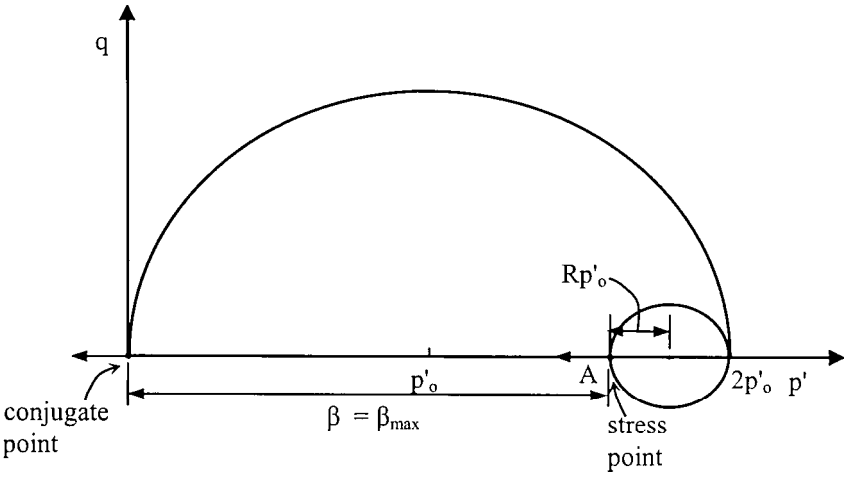


Figure 4.6: Diagram showing the position of the stress point A for the maximum value of b, b_{max} (after Al-Tabbaa (1987))

$$b_{\max} = 2p_o'(1-R) \tag{4.17}$$

The hardening function H was assumed to be of the form:

$$H = \frac{1}{\lambda^* - \kappa^*}\left(\frac{b}{b_{\max}}\right)^{\psi}(p_o')^3 \tag{4.18}$$

where ψ is an experimentally determined positive real exponent. Al-Tabbaa (1987) noted that the choice of the function H is not unique and different interpolation rules could be used.

The resulting hardening function is:

$$h = \frac{1}{\lambda^* - \kappa^*}\left[(p'-p_a')\left[p'(p'-p_a') + \frac{q(q-q_a)}{M^2}\right] + \left(\frac{b}{b_{\max}}\right)^{\psi}(p_o')^3\right] \tag{4.19}$$

4.3.6 Elastic part of the model

If the stress path remains within the kinematic yield surface, the predicted behaviour is isotropic elastic. The elastic bulk modulus, K_e, is the same as in the case of the modified Cam Clay model:

$$K_e = \frac{p'}{\kappa^*} \tag{4.20}$$

For the calculation of the elastic shear strains a constant Poisson's ratio, μ, was assumed. This results in the following elastic shear modulus G_e:

$$G_e = \frac{3p'}{2\kappa^*}\frac{(1-2\mu)}{(1+\mu)} \tag{4.21}$$

Therefore the elastic strain increments are given as follows:

$$\begin{Bmatrix} d\varepsilon_v^e \\ d\varepsilon_s^e \end{Bmatrix} = \begin{bmatrix} \frac{1}{K_e} & 0 \\ 0 & \frac{1}{3G_e} \end{bmatrix} \begin{Bmatrix} dp' \\ dq \end{Bmatrix} \tag{4.22}$$

where the elastic bulk and shear moduli, K_e and G_e, are given by Equations 4.20 and 4.21 respectively.

4.3.7 Model parameters

The seven material parameters required to define the model are:

λ^*: the slope of the isotropic normal compression line in ln$v$-lnp' space

κ^*: the slope of the swelling line in ln$v$-lnp' space for a stress path that lies entirely within the kinematic yield surface

μ: the Poisson's ratio

M: the slope of the critical state line in q- p' space

R: the ratio of the size of the kinematic yield surface to that of the bounding surface

ψ: the exponent in the hardening function H

N: one additional parameter is required to fix the model in ln$v$-lnp' space and this is usually taken as the specific volume of the isotropic compression line at $p' = 1$ kPa

Al-Tabbaa (1987) noted that the model parameters can be obtained from simple standard tests or alternatively from a multi-stage test using the triaxial apparatus. Figure 4.7 shows an example of such a test. The test starts with an isotropic compression stage from which the value of λ^* can be determined. An isotropic swelling stage follows. The

initial part of the swelling curve can be used to derive the values of κ^* and R, while the later part of this curve can be used to determine the value of the parameter ψ. The parameter ψ cannot be measured directly from test data and has to be determined by varying the value in a series of simulations of the test. The sample can then be isotropically compressed to a lightly overconsolidated state and from then on either an undrained test with pore pressure measurement or a drained test to failure can be performed, from which the values of M and μ can be derived. A volume measurement at a known stress state on the isotropic compression line fixes the model in ln$v$-lnp'space.

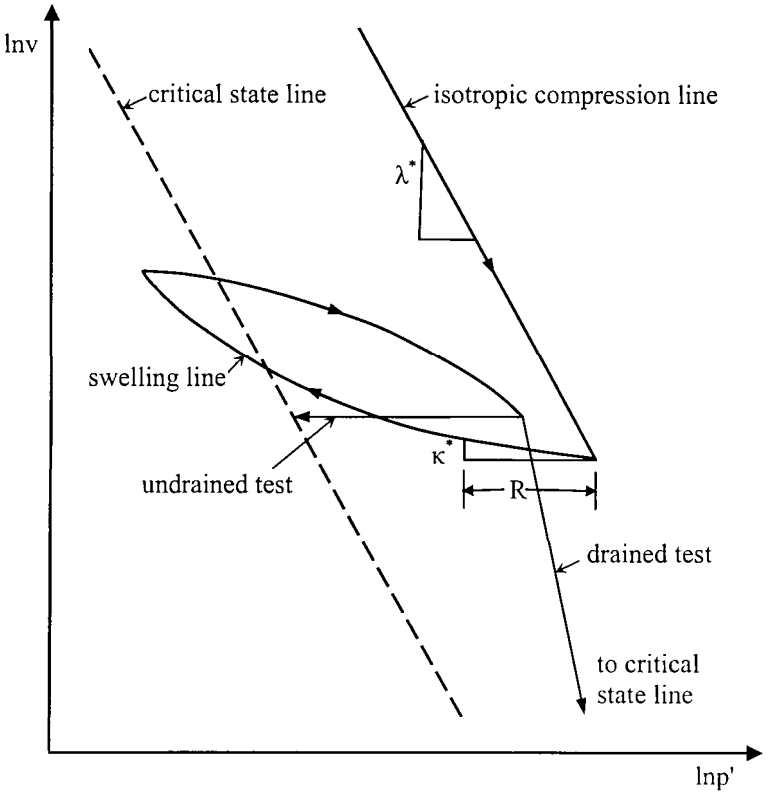


Figure 4.7: Example of one triaxial multi-stage test from which all the model parameters can be obtained (after Al-Tabbaa (1987))

4.3.8 Discussion

This discussion will be concentrated on the translation rule of the kinematic yield surface assumed in the model and the derivation of the hardening function, for the special case that the two surfaces are in contact.

As mentioned in section 4.3.4, when the two surfaces are in contact at the current stress state, the vector β becomes equal to zero and the translation rule is given by Equation 4.12. However, as Stallebrass (1990) noted, Equation 4.12 is only sufficient in the special case that the loading is always in the direction of the outward normal to the two

surfaces at the current stress state. For all other cases the rule does not make sure that the two surfaces remain in contact. Therefore, for the case that the two surfaces are in contact a new translation rule has to be assumed so that contact between the two surfaces is maintained for any further loading.

However, the assumption of a different translation rule for the case that the two surfaces are in contact is not consistent with the derivation of the hardening function, h_o (Equation 4.14), for the same special case that the surfaces are in contact. This is because, as mentioned in section 4.3.5, the hardening function, h_o, is calculated by substituting Equation 4.12 into the consistency condition of the kinematic yield surface. Therefore the use of a translation rule different than that described by Equation 4.12 together with a hardening function, h_o, given by Equation 4.14 would result in the non-satisfaction of the consistency condition of the kinematic yield surface for the special case that the two surfaces are in contact.

Gajo and Muir Wood (2001) noted that the interpolation rule chosen in the model is such that the incremental response tends asymptotically to the response on the bounding surface and for this reason the yield and bounding surfaces can never actually make contact. If this is true then there is no need for a different translation rule for all the stress states that start within the bounding surface, since the surfaces never actually come in contact. However, for normally consolidated states, which start on the bounding surface and for which the two surfaces are assumed to be in contact, a different translation rule is still required, in order to maintain the surfaces in contact for further loading.

In the formulation of the model in general stress space a different translation rule is adopted for the special case that the surfaces are in contact and the way in which the resulting inconsistency is dealt with is discussed.

4.4 Formulation in general stress space

4.4.1 Introduction

This section describes the extension of the two-surface model from triaxial to general stress space, which is necessary in order to implement the model into a finite element program like ICFEP. Before the formulation of the model in general stress space is

presented, three issues will be discussed; the stress and strain variables adopted in this general formulation, the shape of the yield and plastic potential surfaces assumed in the deviatoric plane and the translation rule adopted for the special case that the two surfaces are in contact.

4.4.1.1 Stress and strain variables

As mentioned in Chapter 1, if a constitutive model is isotropic then it can be formulated in general stress space in terms of the stress invariants, p', J or q, and θ and the strain invariants, ε_v and E_d or ε_s. However, if a model is anisotropic then it cannot be formulated in terms of the above stress and strain invariants, since this would inevitably lead to an isotropic formulation. In the case of the two-surface model the bounding surface is centred around the isotropic axis and therefore behaviour on the bounding surface is isotropic. However, yielding is controlled by the kinematic yield surface which is not centred around the isotropic axis. This means that depending on the position of the kinematic yield surface the predicted behaviour can be anisotropic. More specifically the model could predict anisotropic yielding and stiffness for stress paths that initiate within the bounding surface, but isotropic failure conditions since this is controlled by the bounding surface which is isotropic. Therefore the model requires an anisotropic formulation and the use of stress and strain invariants has to be abandoned. The model is formulated instead in terms of the volumetric and the deviatoric components of the stress and strain tensors, described by Equations 1.2-1.4 and 1.14-1.17 respectively.

4.4.1.2 Yield and plastic potential surfaces in the deviatoric plane

The extension of the model in general stress space requires some assumption of the shape of the yield and plastic potential surfaces in the deviatoric plane. Early generalisations of the modified Cam Clay and other models assumed a circular shape of the yield and plastic potential surfaces (and hence the failure surface) in the deviatoric plane. However, a circle implies that the model is independent of the Lode's angle, θ, and consequently of the magnitude of the intermediate principal stress. Experimental evidence shows that if the circular shape is chosen to match the strength in triaxial compression then it overestimates the strength in triaxial extension and does not generally represent well the failure conditions for soils. A better approximation is the use of a Mohr Coulomb hexagon, see Figure 4.8. This is superior to a circle and is consistent with conventional practice. However, a Mohr Coulomb hexagon assumes an

angle of shearing resistance which is independent of the intermediate principal stress. Experimental results show that the angle of shearing resistance varies with the magnitude of the intermediate principal stress, although there is not always a very strong dependence. For this reason, alternative continuous shapes have been proposed in the literature for the failure conditions of soils, with the better known being the ones suggested by Matsuoka and Nakai (1974) and Lade (Lade and Duncan (1975)), see Figure 4.8. In the present formulation the yield surface can take either the shape of a Mohr Coulomb hexagon, or the general shape proposed by van Eekelen (1980). The latter, depending on the choice of the input parameters can simulate different shapes in the deviatoric plane, including the one proposed by Lade and a circular shape. The plastic potential surface can take the general shape suggested by van Eekelen (1980).

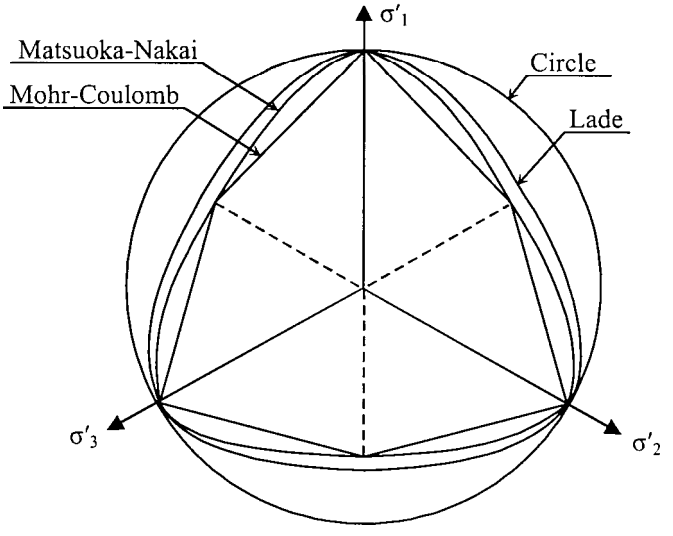


Figure 4.8: Failure surfaces in the deviatoric plane

4.4.1.3 Translation rule for the case that the two surfaces are in contact

In this general formulation of the two-surface model a different translation rule is adopted for the special case that the kinematic yield surface and the bounding surface are in contact, so that the two surfaces remain tangential for any further loading. As discussed in section 4.3.8, this new translation rule is inconsistent with the hardening modulus in the case that the two surfaces are in contact and results in the non-satisfaction of the consistency condition of the kinematic yield surface for this special case. To overcome this problem when the two surfaces are in contact the active yield surface is changed from the kinematic yield surface to the bounding surface. For example, when the kinematic yield surface moves within the bounding surface the active yield surface is the kinematic yield surface and the plastic potential and hardening

modulus associated with this surface apply. In the special case that the two surfaces are in contact the bounding surface is the one that becomes the active yield surface and the model reduces to the modified Cam Clay model. In this case the plastic potential surface and the hardening modulus associated with the bounding surface apply, and the now inactive kinematic yield surface is just dragged by the current stress state. In this way the consistency condition of the bounding surface, which is now the active yield surface is satisfied. If the stress path reverses so that the stress state re-enters the kinematic yield surface and for further loading touches it then this becomes again the active yield surface. This concept will be explained in greater detail in the course of the chapter.

4.4.2 Notation

As already mentioned, the extension of the two-surface model in general stress space requires the model to be described in terms of the volumetric and deviatoric components of the stress and strain tensors. The notation used to represent tensorial magnitudes in chapters 2 and 3 was a vector-matrix notation. Second order tensors, like stress and strain, were represented by vectors, e.g. $\{\sigma\}$, and fourth order tensors, like the constitutive matrix, were represented by matrices, e.g. $[D]$. This notation is very useful in numerical computations and for this reason it was followed in the previous chapters. However for the description of the two-surface model in general stress space a tensor notation is going to be adopted, in which the tensor quantities will be represented by bold-faced characters.

4.4.3 Equations of the surfaces

The equation of the bounding surface in general stress space is formulated as follows:

$$F_b = \left(p' - \frac{p'_o}{2} \right)^2 + \frac{1}{2} \frac{\boldsymbol{s} : \boldsymbol{s}}{g^2(\theta_b)} - \frac{p'^2_o}{4} = 0 \tag{4.23}$$

The symbol : indicates the tensorial contraction. In the above equation p'_o represents the value of the mean effective stress at the intersection of the current swelling line with the isotropic compression line, in accordance with the original formulation of the modified Cam Clay model, rather than half the value used in the triaxial formulation of the two-surface model. The function $g(\theta_b)$, where θ_b is the value of the Lode's angle for the bounding surface, defines the shape of the bounding surface in the deviatoric plane. The

choice of the function $g(\theta_b)$ will be discussed later. The Lode's angle, θ_b, is given as:

$$\theta_b = -\frac{1}{3}\sin^{-1}\left[\frac{3\sqrt{3}}{2}\frac{\det(\boldsymbol{s})}{\left[\left[\frac{1}{2}(\boldsymbol{s}:\boldsymbol{s})\right]^{\frac{1}{2}}\right]^3}\right] \tag{4.24}$$

The equation of the kinematic yield surface in general stress space is:

$$F_y = (p' - p'_a)^2 + \frac{1}{2}\frac{(\boldsymbol{s}-\boldsymbol{s}_a):(\boldsymbol{s}-\boldsymbol{s}_a)}{g^2(\theta_y)} - R^2\frac{p'^2_o}{4} = 0 \tag{4.25}$$

In Equation 4.25 p'_a and $\boldsymbol{s}_a$ are the mean effective stress and the deviatoric stress tensor at the centre of the kinematic yield surface respectively, and the function $g(\theta_y)$, defines again the shape of the kinematic yield surface in the deviatoric plane. The Lode's angle, θ_y, for the kinematic yield surface is calculated by using as origin the centre of the kinematic yield surface:

$$\theta_y = -\frac{1}{3}\sin^{-1}\left[\frac{3\sqrt{3}}{2}\frac{\det(\boldsymbol{s}-\boldsymbol{s}_a)}{\left[\left[\frac{1}{2}\left[(\boldsymbol{s}-\boldsymbol{s}_a):(\boldsymbol{s}-\boldsymbol{s}_a)\right]\right]^{\frac{1}{2}}\right]^3}\right] \tag{4.26}$$

The representation of Equations 4.23 and 4.25 in the triaxial stress space can be seen in Figure 4.9a.

As mentioned earlier two options are adopted for the function $g(\theta)$. The first one gives the shape of a Mohr-Coulomb hexagon in the deviatoric plane, see Figure 4.9b. In this case the function $g(\theta)$ is given as:

$$g(\theta) = \frac{\sin\varphi'}{\cos\theta + \frac{\sin\theta\sin\varphi'}{\sqrt{3}}} \tag{4.27}$$

where φ' is the angle of shearing resistance.

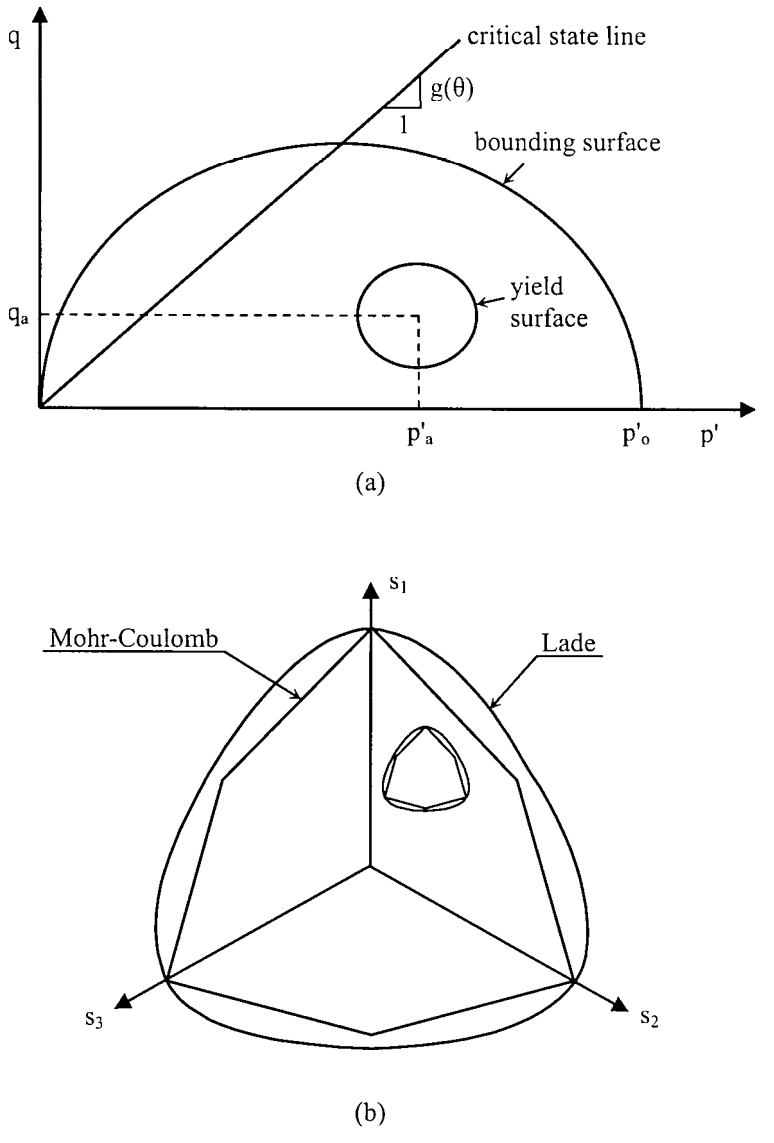


Figure 4.9: Two-surface model a) Representation of the yield and bounding surfaces in triaxial stress space b) Deviatoric section through the yield and bounding surfaces (with the van Eekelen equation taking the Lade shape)

The second option gives the family of continuous surfaces in the deviatoric plane proposed by van Eekelen (1980):

$$g(\theta) = \frac{X}{(1 + Y \sin 3\theta)^Z} \tag{4.28}$$

where X, Y and Z are material constants. In particular $X = \sin(\varphi'_{\theta=0^\circ})$ where $\varphi'_{\theta=0^\circ}$ is the angle of shearing resistance associated with a Lode's angle $\theta = 0^\circ$. In order to obtain convex surfaces, certain restrictions apply on the values of Y and Z and these are discussed in detail by van Eekelen (1980). As mentioned before, depending on the

values of these constants, different shapes can be obtained in the deviatoric plane, including a Lade shape, see Figure 4.9b. A circular shape can be obtained by setting $Y = 0$ and $Z = 1.0$. In the latter case the function $g(\theta)$ is a constant and equal to $X = M/\sqrt{3}$, where M is the gradient of the critical state line in the triaxial q- p' plane.

It should be noted that the kinematic yield surface and the bounding surface always have the same shape in the deviatoric plane, given either by Equation 4.27 or 4.28, with θ equal to θ_y for the kinematic yield surface and θ_b for the bounding surface.

4.4.4 Flow rule

The plastic potential surface associated with the bounding surface is given by the following equation:

$$P_b = \left(p' - \frac{p'_o}{2}\right)^2 + \frac{1}{2}\frac{\boldsymbol{s}:\boldsymbol{s}}{g_p^{\,2}(\theta_b)} - \frac{p_o'^2}{4} = 0 \tag{4.29}$$

Equation 4.29 is the same as Equation 4.23, but with the function $g(\theta_b)$ replaced by the function $g_p(\theta_b)$. The function $g_p(\theta_b)$ defines the variation of the plastic potential surface in the deviatoric plane.

The plastic potential surface associated with the kinematic yield surface is:

$$P_y = \left(p' - p'_a\right)^2 + \frac{1}{2}\frac{\left(\boldsymbol{s}-\boldsymbol{s}_a\right):\left(\boldsymbol{s}-\boldsymbol{s}_a\right)}{g_p^{\,2}\left(\theta_y\right)} - R^2\frac{p_o'^2}{4} = 0 \tag{4.30}$$

Again Equation 4.30 is the same as Equation 4.25 but with $g(\theta_y)$ replaced by $g_p(\theta_y)$.

The function $g_p(\theta)$ is assumed to be given by the family of surfaces proposed by van Eekelen (1980), which in the case of the plastic potential surfaces takes the following form:

$$g_p(\theta) = \frac{X_p}{\left(1 + Y_p \sin 3\theta\right)^{Z_p}} \tag{4.31}$$

where Y_p and Z_p are material constants and X_p varies such that when the soil is yielding the current plastic potential surface always passes through the current stress state.

Depending on the choice of parameters it is possible that the shapes of the active yield and plastic potential surfaces are different in the deviatoric plane. In this case the flow rule of the model becomes non-associated.

4.4.5 Hardening rules

The formulation of the hardening rules in general stress space is the following:

4.4.5.1 Isotropic hardening of the bounding surface

The isotropic hardening of the bounding surface is given by Equation 4.8.

4.4.5.2 Translation rules of the kinematic yield surface

Two different translation rules are adopted, one for the case when the kinematic yield surface moves within the bounding surface and one for the special case when the two surfaces are in contact.

i) Translation rule when the kinematic yield surface moves within the bounding surface

In this case the translation rule proposed by Al-Tabbaa (1987) is formulated in general stress space:

$$d\boldsymbol{\sigma}'_a = \frac{dp'_o}{p'_o}\boldsymbol{\sigma}'_a + S\left[\frac{\boldsymbol{\sigma}' - \boldsymbol{\sigma}'_a}{R} - \left(\boldsymbol{\sigma}' - \frac{\boldsymbol{\sigma}'_o}{2}\right)\right] \tag{4.32}$$

The above equation can be written in terms of the isotropic and deviatoric components of the stress tensor as follows:

$$dp'_a = \frac{dp'_o}{p'_o}p'_a + S\left[\frac{p' - p'_a}{R} - \left(p' - \frac{p'_o}{2}\right)\right] \tag{4.33}$$

$$d\boldsymbol{s}_a = \frac{dp'_o}{p'_o}\boldsymbol{s}_a + S\left(\frac{\boldsymbol{s} - \boldsymbol{s}_a}{R} - \boldsymbol{s}\right) \tag{4.34}$$

The scalar quantity S can be obtained as before by substituting Equations 4.33 and 4.34 into the consistency condition for the kinematic yield surface and using Equation 4.25. The consistency condition of the kinematic yield surface can be written as:

$$dF_y = \frac{\partial F_y}{\partial p'} dp' + \frac{\partial F_y}{\partial \boldsymbol{s}} : d\boldsymbol{s} + \frac{\partial F_y}{\partial p'_a} dp'_a + \frac{\partial F_y}{\partial \boldsymbol{s}_a} : d\boldsymbol{s}_a + \frac{\partial F_y}{\partial p'_o} dp'_o = 0 \tag{4.35}$$

The scalar quantity S is calculated as:

$$S = \frac{\left(p' - p'_a\right)\left(dp' - \frac{dp'_o}{p'_o} p'_a\right) + \frac{1}{2}\left[\frac{\partial F_y}{\partial \boldsymbol{s}} : \left(d\boldsymbol{s} - \frac{dp'_o}{p'_o}\boldsymbol{s}_a\right)\right] - \frac{R^2 p'_o dp'_o}{4}}{\left(p' - p'_a\right)\left[\frac{p' - p'_a}{R} - \left(p' - \frac{p'_o}{2}\right)\right] + \frac{1}{2}\left[\frac{\partial F_y}{\partial \boldsymbol{s}} : \left(\frac{\boldsymbol{s} - \boldsymbol{s}_a}{R} - \boldsymbol{s}\right)\right]} \tag{4.36}$$

Equation 4.36 requires the partial differentials of the kinematic yield surface with respect to the deviatoric stress tensor, $\partial F_y/\partial \boldsymbol{s}$. In the case that the shape of the kinematic yield surface is circular in the deviatoric plane, the function $g(\theta_y)$ is a constant and equal to X, and the differentials can be calculated from the following equation:

$$\frac{\partial F_y}{\partial \boldsymbol{s}} = \frac{\boldsymbol{s} - \boldsymbol{s}_a}{X^2} \tag{4.37}$$

In this case, substitution of Equation 4.37 into Equation 4.36 gives:

$$S = \frac{\left(p' - p'_a\right)\left(dp' - \frac{dp'_o}{p'_o} p'\right) + \frac{1}{2X^2}\left[\left(\boldsymbol{s} - \boldsymbol{s}_a\right) : \left(d\boldsymbol{s} - \frac{dp'_o}{p'_o}\boldsymbol{s}\right)\right]}{\left(p' - p'_a\right)\left[\frac{p' - p'_a}{R} - \left(p' - \frac{p'_o}{2}\right)\right] + \frac{1}{2X^2}\left[\left(\boldsymbol{s} - \boldsymbol{s}_a\right) : \left(\frac{\boldsymbol{s} - \boldsymbol{s}_a}{R} - \boldsymbol{s}\right)\right]} \tag{4.38}$$

However, if the shape of the kinematic yield surface is other than circular in the deviatoric plane, then the calculation of the partial differentials of the kinematic yield surface with respect to the deviatoric stress tensor, $\partial F_y/\partial \boldsymbol{s}$, becomes more complicated. In order not to interrupt the flow of this section the calculation of these derivatives will be presented in the next section which describes the implementation of the model into ICFEP.

ii) Translation rule when the two surfaces are in contact

The translation rule adopted in the special case that the two surfaces are in contact is in accordance with Stallebrass (1990) and ensures that the two surfaces remain tangential to each other for further loading:

$$d\boldsymbol{\sigma}'_a = (1-R)\,d\boldsymbol{\sigma}' + R\frac{d\boldsymbol{\sigma}'_o}{2} \tag{4.39}$$

In terms of the isotropic and deviatoric components of the stress tensor Equation 4.39 can be rewritten as:

$$dp'_a = (1-R)\,dp' + R\frac{dp'_o}{2} \tag{4.40}$$

$$d\boldsymbol{s}_a = (1-R)\,d\boldsymbol{s} \tag{4.41}$$

4.4.6 Hardening modulus

The hardening modulus is formulated for the two different cases; the first one when the kinematic yield surface moves within the bounding surface and the second one when the two surfaces are in contact. In the first case the kinematic yield surface is the active yield surface and the formulation of the hardening modulus follows the one proposed by Al-Tabbaa (1987) and described in section 4.3.5. In the second case the active yield surface is the bounding surface and the hardening modulus reduces to the modified Cam Clay hardening modulus.

i) Hardening modulus when the kinematic yield surface moves within the bounding surface

The hardening modulus, A, is formulated in general stress space as follows:

$$A = \frac{4}{\lambda^* - \kappa^*}\left[(p'-p'_a)\left[p'_a(p'-p'_a) + \frac{1}{2}\left(\frac{\partial F_y}{\partial \boldsymbol{s}} : \boldsymbol{s}_a\right) + \frac{R^2 p_o'^2}{4}\right] + \left(\frac{b}{b_{\max}}\right)^{\psi}\left(\frac{p'_o}{2}\right)^3\right] \tag{4.42}$$

Equation 4.42 is divided into two parts. The first part is the hardening modulus, A_o, which is equivalent to the hardening function h_o in the original triaxial formulation:

$$A_o = \frac{4}{\lambda^* - \kappa^*}\left[(p'-p'_a)\left[p'_a(p'-p'_a) + \frac{1}{2}\left(\frac{\partial F_y}{\partial \boldsymbol{s}} : \boldsymbol{s}_a\right) + \frac{R^2 p_o'^2}{4}\right]\right] \tag{4.43}$$

The second part of Equation 4.42 is the additional component of the hardening modulus,

A_1, which is a function of the degree of proximity of the kinematic yield surface to the bounding surface. This is equivalent to the hardening function H in the original formulation and reduces to zero when the two surfaces are in contact:

$$A_1 = \frac{4}{\lambda^* - \kappa^*}\left(\frac{b}{b_{\max}}\right)^{\psi}\left(\frac{p'_o}{2}\right)^3 \tag{4.44}$$

In the original triaxial formulation the hardening function h_o was derived from the consistency condition of the kinematic yield surface for the special case that the two surfaces are in contact. In this general formulation of the model a new translation rule has been assumed for the case that the two surfaces are in contact (Equation 4.39), and in this way the above expression of the hardening modulus, A_o, cannot be derived anymore. However, the use of Equation 4.42 as the hardening modulus, A, does not represent a problem for the case that the kinematic yield surface moves within the bounding surface. This is because in this case, the consistency condition of the kinematic yield surface is satisfied anyway through the calculation of the scalar multiplier S (in Equation 4.32), which is derived exactly though the use of the same consistency condition. In fact any hardening modulus could be assumed for the case that the kinematic yield surface moves within the bounding surface and the consistency condition of the kinematic yield surface would still be satisfied. The problem arises for the case that the two surfaces are in contact. In this case the consistency condition of the kinematic yield surface is not satisfied anymore. However, since in this case both surfaces predict the same plastic strains, the active yield surface can be changed to the bounding surface and the model then reduces to the modified Cam Clay model. In this way the consistency condition of the bounding surface, which is the active yield surface, is satisfied and the inactive kinematic yield surface is just dragged along the current stress path, following the new translation rule (Equation 4.39).

The measure, b, of the proximity of the kinematic yield surface to the bounding surface takes the following form in general stress space:

$$b = \frac{1}{R\frac{p'_o}{2}}\left[\left(p' - p'_a\right)\left[\frac{p' - p'_a}{R} - \left(p' - \frac{p'_o}{2}\right)\right] + \frac{1}{2}\left[\frac{\partial F_y}{\partial \boldsymbol{s}} : \left(\frac{\boldsymbol{s} - \boldsymbol{s}_a}{R} - \boldsymbol{s}\right)\right]\right] \tag{4.45}$$

The maximum value of the function, b, is:

$$b_{\max} = p'_o(1-R) \tag{4.46}$$

Equations 4.42 and 4.45 require the partial differentials of the kinematic yield surface with respect to the deviatoric stress tensor, $\partial F_y/\partial \boldsymbol{s}$. As mentioned before, for the cases that the shape of the kinematic yield surface is other than circular in the deviatoric plane, these become complicated and will be given in the next section. For a circular shape of the yield surface in the deviatoric plane, substitution of Equation 4.37 into Equations 4.42 and 4.45 results in:

$$A = \frac{4}{\lambda^* - \kappa^*}\left[(p'-p'_a)\left[p'(p'-p'_a)+\frac{1}{2X^2}\left[(\boldsymbol{s}-\boldsymbol{s}_a):\boldsymbol{s}\right]\right]+\left(\frac{b}{b_{\max}}\right)^{\psi}\left(\frac{p'_o}{2}\right)^3\right] \tag{4.47}$$

$$b = \frac{1}{R\frac{p'_o}{2}}\left[(p'-p'_a)\left[\frac{p'-p'_a}{R}-\left(p'-\frac{p'_o}{2}\right)\right]+\frac{1}{2X^2}\left[\boldsymbol{s}-\boldsymbol{s}_a:\left(\frac{\boldsymbol{s}-\boldsymbol{s}_a}{R}-\boldsymbol{s}\right)\right]\right] \tag{4.48}$$

ii) Hardening modulus when the two surfaces are in contact

When the two surfaces are in contact the bounding surface is the active yield surface and the hardening modulus, A, reduces to the hardening modulus of the modified Cam Clay model:

$$A = \frac{4}{\lambda^* - \kappa^*}\left[\left(p'-\frac{p'_o}{2}\right)p'\frac{p'_o}{2}\right] \tag{4.49}$$

4.4.7 Elastic part of the model

The elastic stress tensor is related to the elastic strain tensor through the elastic constitutive tensor:

$$d\boldsymbol{\sigma} = \boldsymbol{D}' : d\boldsymbol{\varepsilon}^e \tag{4.50}$$

The elastic constitutive tensor, $\boldsymbol{D}'$, is expressed in terms of the isotropic elastic bulk and shear moduli, K_e and G_e.

The elastic bulk modulus, K_e, is given by Equation 4.20. In the present formulation four

options exist for the elastic shear modulus, G_e. The first one assumes a constant Poisson's ratio, μ, as in the original formulation. In this case the resulting shear modulus, G_e, is given by Equation 4.21. The second option assumes a constant shear modulus, G_e. The third option assumes that the shear modulus G_e is dependent on the mean effective stress p'. Finally, the last option assumes that the elastic shear modulus is described by the equation proposed by Viggiani (Equation 2.10) which in this case takes the form:

$$\frac{G_e}{p_r} = A\left(\frac{p'}{p_r}\right)^n R_o^{\ m} \tag{4.51}$$

where A, n and m are material parameters, $R_o = p'_o / p'$ and p_r is taken equal to 1 kPa.

4.4.8 Overview of the model

An overview of the way the model is formulated in general stress space is important in order to understand how the model works and will also be used later in the implementation of the model.

Elastic behaviour:

When the stress state is within the kinematic yield surface the behaviour is elastic and is described by Equation 4.50.

Elasto-plastic behaviour:

i) When the stress state is on the kinematic yield surface and this moves within the bounding surface

In this case the kinematic yield surface is the active yield surface. The yield and plastic potential functions associated with this surface are given by Equations 4.25 and 4.30 respectively. The hardening modulus in this case is calculated from Equation 4.42. The isotropic hardening of the bounding surface is given by Equation 4.8 and the translation of the kinematic yield surface is described by Equation 4.32. The consistency condition of the kinematic yield surface which is the active yield surface is satisfied, since the scalar multiplier S in Equation 4.32 is derived from the same consistency condition.

ii) When the two surfaces are in contact at the current stress state

In this case the bounding surface is the active yield surface and the model reduces to the

modified Cam Clay model. The yield and plastic potential functions associated with the bounding surface are described by Equations 4.23 and 4.29 respectively. The hardening modulus is given by Equation 4.49. This is consistent with the isotropic hardening of the bounding surface described by Equation 4.8 and in this way the consistency condition of the bounding surface is satisfied. The kinematic yield surface is inactive in this case but still follows the stress state, obeying the translation rule described by Equation 4.39, which ensures that the two surfaces remain tangential to each other for any further loading.

4.4.9 Model parameters

The above formulation of the model in general stress space requires either nine parameters, when a Mohr-Coulomb hexagon is chosen for the shape of the yield surface in the deviatoric plane, or eleven parameters, when a general shape is adopted. Additionally the use of Equation 4.51 for the calculation of the elastic shear modulus, G_e, introduces two more extra parameters. The parameters required are the following:

λ^*: the slope of the isotropic normal compression line in $\ln v$-$\ln p'$ space

κ^*: the slope of the swelling line in $\ln v$-$\ln p'$ space for a stress path that lies entirely within the kinematic yield surface

μ or G_e, or G_e/p': the Poisson's ratio or the elastic shear stiffness. If Equation 4.51 is used then the material parameters A, n and m must be provided

φ' or X, Y and Z: the angle of shearing resistance or the constants $X = \sin(\varphi'_{\theta=0^\circ})$, Y and Z in Equation 4.28 at the critical state

Y_p and Z_p: the constants Y_p and Z_p in Equation 4.31

R: the ratio of the size of the kinematic yield surface to that of the bounding surface

ψ: the exponent in the hardening function A

N: one additional parameter is required to fix the model in $\ln v$-$\ln p'$ space and this is usually taken as the specific volume of the isotropic compression line at $p' = 1$ kPa

4.5 Implementation

4.5.1 Introduction

The implementation of a constitutive model into a finite element program, like ICFEP, involves:

i) The calculation of the elasto-plastic constitutive matrix, $[D^{ep}]$. As described in Chapter 3, this is used in the formulation of the incremental element stiffness matrix, $[K_E]$, from which the incremental global stiffness matrix, $[K_G]$, is obtained. The incremental global stiffness matrix, $[K_G]$, is then used in order to form the global set of equations. The elasto-plastic constitutive matrix, $[D^{ep}]$, can be calculated from Equation 2.26. Alternatively the elastic constitutive matrix [D] can be used in the formulation of the global set of equations, instead of the elasto-plastic matrix $[D^{ep}]$. In this case the calculation of the elastic constitutive matrix $[D]$ is sufficient.

ii) The calculation of the residual load vector, $\{\psi\}^j$, at the end of each iteration, in the case that a modified Newton-Raphson scheme is used as a non-linear solver. As described in Chapter 3 the residual load vector, $\{\psi\}^j$, is calculated by integrating the constitutive equations along the estimated incremental strain path (through the use of the stress point algorithm) and obtaining an estimate of the stress changes. In order to obtain this estimate of the stress changes the stress point algorithm requires the calculation of the changes in stresses, plastic strains and hardening parameters during each substep (section 3.4.1.1). The changes in stresses and plastic strains can be obtained from Equations 2.22 and 2.12 respectively.

If the constitutive model is formulated in terms of effective stresses then Equations 2.11 to 2.26 are also expressed in terms of effective stresses. In this case, inspection of Equations 2.12, 2.22 and 2.26 shows that in order to solve them the calculation of the following terms is required: the partial derivatives of the yield function with respect to stress, $\{\partial F/\partial \sigma'\}$, the partial derivatives of the plastic potential function with respect to stress, $\{\partial P/\partial \sigma'\}$, the elastic constitutive matrix, $[D']$, and the hardening modulus, A.

This section describes the calculations which were required in order to implement the two-surface model into ICFEP. These involved the calculation of the terms $\{\partial F/\partial \sigma'\}$, $\{\partial P/\partial \sigma'\}$, $[D']$ and A in Equations 2.12, 2.22 and 2.26, and the changes in the hardening parameters required in the stress point algorithm. A flowchart of the ICFEP subroutine which is used by the stress point algorithm to calculate the changes in stresses,

plastic strains and hardening parameters during a substep, is presented in Appendix II. Additionally, the calculation of the partial derivatives of the kinematic yield surface with respect to the deviatoric stress tensor, $\partial F_y/\partial \boldsymbol{s}$, which is required in Equations 4.36, 4.42 and 4.45 of the previous section, is also presented here.

4.5.2 Calculation of the partial derivatives of the yield function

The derivatives of the yield function are calculated by the program for the surface that is the active yield surface at the time.

i) When the kinematic yield surface is the active yield surface

In this case the yield function is given by Equation 4.25. The calculation of the partial derivatives of the kinematic yield surface with respect to the deviatoric stress tensor, $\partial F_y/\partial \boldsymbol{s}$, will first be given, followed by the calculation of the derivatives of the yield function with respect to stress, $\{\partial F_y/\partial \sigma'\}$. For the numerical computations it is convenient to represent the partial derivatives of the kinematic yield surface with respect to the deviatoric stress tensor by the vector $\{\partial F_y/\partial s\}$ where $\{s\}$ is given by:

$$\{s\}^T = \{\sigma'_x - p' \quad \sigma'_y - p' \quad \sigma'_z - p' \quad \tau_{xy} \quad \tau_{yz} \quad \tau_{zx}\} \tag{4.52}$$

Calculation of terms $\{\partial F_y/\partial s\}$

If we set:

$$Q = (\boldsymbol{s} - \boldsymbol{s}_a) : (\boldsymbol{s} - \boldsymbol{s}_a) \tag{4.53}$$

then Equation 4.25 can be rewritten as:

$$F_y = (p' - p'_a)^2 + \frac{1}{2}\frac{Q}{g^2(\theta_y)} - R^2\frac{p_o'^2}{4} = 0 \tag{4.54}$$

The partial differentials of Equation 4.54 with respect to $\{s\}$ can then be calculated by:

$$\left\{\frac{\partial F_y}{\partial s}\right\} = \frac{\partial F_y}{\partial Q}\left\{\frac{\partial Q}{\partial s}\right\} + \frac{\partial F_y}{\partial \theta_y}\left\{\frac{\partial \theta_y}{\partial s}\right\} \tag{4.55}$$

where the term $\{\partial \theta_y/\partial s\}$ is given as:

$$\left\{\frac{\partial \theta_y}{\partial s}\right\}=\frac{\sqrt{3}}{2\cos\left(3\theta_y\right)\left(\frac{1}{2}Q\right)^{3/2}}\left[\frac{3\det\left(\boldsymbol{s}-\boldsymbol{s}_a\right)}{2Q}\left\{\frac{\partial Q}{\partial s}\right\}-\left\{\frac{\partial \det\left(\boldsymbol{s}-\boldsymbol{s}_a\right)}{\partial s}\right\}\right] \tag{4.56}$$

Substitution of Equation 4.56 into Equation 4.55 gives:

$$\left\{\frac{\partial F_y}{\partial s}\right\}=\left[\frac{\partial F_y}{\partial Q}+\frac{\partial F_y}{\partial \theta_y}\frac{3\sqrt{3}\det\left(\boldsymbol{s}-\boldsymbol{s}_a\right)}{8\cos\left(3\theta_y\right)\left(\frac{1}{2}Q\right)^{5/2}}\right]\left\{\frac{\partial Q}{\partial s}\right\}- \frac{\sqrt{3}}{2\cos\left(3\theta_y\right)\left(\frac{1}{2}Q\right)^{3/2}}\frac{\partial F_y}{\partial \theta_y}\left\{\frac{\partial \det\left(\boldsymbol{s}-\boldsymbol{s}_a\right)}{\partial s}\right\} \tag{4.57}$$

Equation 4.57 can be written in a more compact way as:

$$\left\{\frac{\partial F_y}{\partial s}\right\}=\alpha_1\left\{\frac{\partial Q}{\partial s}\right\}+\alpha_2\left\{\frac{\partial \det\left(\boldsymbol{s}-\boldsymbol{s}_a\right)}{\partial s}\right\} \tag{4.58}$$

where the constants α_1 and α_2 depend on $\partial F_y/\partial Q$ and $\partial F_y/\partial \theta_y$ as can be seen by comparison of Equations 4.57 and 4.58.

The calculation of the derivatives $\{\partial Q/\partial s\}$ and $\{\partial \det(\boldsymbol{s}-\boldsymbol{s}_a)/\partial s\}$ is given in Appendix I.

The derivative $\partial F_y/\partial Q$ is calculated as:

$$\frac{\partial F_y}{\partial Q}=\frac{1}{2}\frac{1}{g^2\left(\theta_y\right)} \tag{4.59}$$

The derivative $\partial F_y/\partial \theta_y$ depends on the choice of the function $g(\theta_y)$. If a Mohr Coulomb hexagon is adopted for the shape of the kinematic yield surface in the deviatoric plane, then the function $g(\theta_y)$ is given by Equation 4.27 and the derivative $\partial F_y/\partial \theta_y$ is calculated as:

$$\frac{\partial F_y}{\partial \theta_y}=\frac{Q}{g\left(\theta_y\right)}\left(\frac{\cos\theta_y}{\sqrt{3}}-\frac{\sin\theta_y}{\sin\varphi'}\right) \tag{4.60}$$

If a general shape is adopted then the function $g(\theta_y)$ is given by Equation 4.28 and the

derivative $\partial F_y/\partial\theta_y$ is equal to:

$$\frac{\partial F_y}{\partial \theta_y} = \frac{3Q\,Z\,Y\cos\left(3\theta_y\right)}{g^2\left(\theta_y\right)\left[1+Y\sin\left(3\theta_y\right)\right]} \tag{4.61}$$

Calculation of terms $\{\partial F_y/\partial\sigma'\}$

The derivatives $\partial F_y/\partial\tau_{xy}$, $\partial F_y/\partial\tau_{yz}$, $\partial F_y/\partial\tau_{zx}$ have already been calculated from Equation 4.55. The remaining derivatives, in order to form the vector $\{\partial F_y/\partial\sigma'\}$, are the following: $\partial F_y/\partial\sigma'_x$, $\partial F_y/\partial\sigma'_y$ and $\partial F_y/\partial\sigma'_z$. These are calculated from the derivatives $\partial F_y/\partial(\sigma'_x\text{-}p')$, $\partial F_y/\partial(\sigma'_y\text{-}p')$ and $\partial F_y/\partial(\sigma'_z\text{-}p')$ as follows:

$$\frac{\partial F_y}{\partial \sigma'_x} = \frac{\partial F_y}{\partial p'}\frac{\partial p'}{\partial \sigma'_x} + \frac{\partial F_y}{\partial s}\frac{\partial s}{\partial \sigma'_x} = \\ = \frac{2}{3}\left(p'-p'_a\right) + \frac{1}{3}\left[2\frac{\partial F_y}{\partial\left(\sigma'_x-p'\right)} - \frac{\partial F_y}{\partial\left(\sigma'_y-p'\right)} - \frac{\partial F_y}{\partial\left(\sigma'_z-p'\right)}\right] \tag{4.62}$$

$$\frac{\partial F_y}{\partial \sigma'_y} = \frac{2}{3}\left(p'-p'_a\right) + \frac{1}{3}\left[-\frac{\partial F_y}{\partial\left(\sigma'_x-p'\right)} + 2\frac{\partial F_y}{\partial\left(\sigma'_y-p'\right)} - \frac{\partial F_y}{\partial\left(\sigma'_z-p'\right)}\right] \tag{4.63}$$

$$\frac{\partial F_y}{\partial \sigma'_z} = \frac{2}{3}\left(p'-p'_a\right) + \frac{1}{3}\left[-\frac{\partial F_y}{\partial\left(\sigma'_x-p'\right)} - \frac{\partial F_y}{\partial\left(\sigma'_y-p'\right)} + 2\frac{\partial F_y}{\partial\left(\sigma'_z-p'\right)}\right] \tag{4.64}$$

ii) When the bounding surface is the active yield surface

In this case the yield function is given by Equation 4.23. Inspection of Equations 4.23 and 4.25 shows that the former can be obtained from the latter if in Equation 4.25 p'_a is set equal to half the value of p'_o, s_a is set equal to zero and R equal to 1.0. This means that the derivatives $\{\partial F_b/\partial\sigma'\}$ can be obtained from the same equations that were described earlier for the calculation of the derivatives $\{\partial F_y/\partial\sigma'\}$, by setting p'_a, s_a and R equal to the values just mentioned. For the calculation of the yield function derivatives the program uses Equations 4.53-4.64 with temporary values $p'^{\,t}_a$, $\{s_a\}^t$ and R^t, depending on which is the active yield surface. If the kinematic yield surface is the active yield surface the temporary values are set equal to the real values, $p'^{\,t}_a = p'_a$, $\{s_a\}^t = s_a$ and $R^t = R$. If the bounding surface is the active yield surface the temporary values are set equal to $p'^{\,t}_a = 0.5\,p'_o$, $\{s_a\}^t = 0$ and $R^t = 1.0$.

4.5.3 Calculation of the partial derivatives of the plastic potential function

The derivatives of the plastic potential function are calculated for the surface that is the active yield surface at the time.

i) When the kinematic yield surface is the active yield surface

The plastic potential function is given by Equation 4.30. Substitution of Equation 4.53 into Equation 4.30 gives:

$$P_y = \left(p' - p'_a\right)^2 + \frac{1}{2}\frac{Q}{g_p^{\,2}\left(\theta_y\right)} - R^2\frac{p_o'^{\,2}}{4} = 0 \tag{4.65}$$

Equation 4.65 is of the same form as Equation 4.54 but with $g(\theta_y)$ replaced by the function $g_p(\theta_y)$. For the calculation of the derivatives of the plastic potential function a similar process to section 4.5.2 can be followed, the derivatives $\{\partial P_y/\partial s\}$ can be calculated first, followed by the calculation of the derivatives $\{\partial P_y/\partial \sigma'\}$.

Calculation of terms $\{\partial P_y/\partial s\}$

The derivatives $\{\partial P_y/\partial s\}$ can be calculated by the following expression:

$$\left\{\frac{\partial P_y}{\partial s}\right\} = \frac{\partial P_y}{\partial Q}\left\{\frac{\partial Q}{\partial s}\right\} + \frac{\partial P_y}{\partial \theta_y}\left\{\frac{\partial \theta_y}{\partial s}\right\} \tag{4.66}$$

The terms in the above equation can be obtained from similar equations to those used to calculate the yield function derivatives (Equations 4.57-4.59) but with $g(\theta_y)$ replaced by the function $g_p(\theta_y)$. The only difference arises in the calculation of the derivative $\partial P_y/\partial \theta_y$. The plastic potential function can only take the general shape in the deviatoric plane and the function $g_p(\theta_y)$ is given by Equation 4.31. The derivative $\partial P_y/\partial \theta_y$ is calculated as:

$$\frac{\partial P_y}{\partial \theta_y} = \frac{3Q\,Z_p\,Y_p\cos\left(3\theta_y\right)}{g^2\left(\theta_y\right)\left[1 + Y_p\sin\left(3\theta_y\right)\right]} \tag{4.67}$$

Calculation of terms $\{\partial P_y/\partial \sigma'\}$

The derivatives $\{\partial P_y/\partial \sigma'\}$ can be calculated by equations similar to Equations 4.62-4.64.

ii) When the bounding surface is the active yield surface

The plastic potential function is given by Equation 4.29. Similar to the process followed in section 4.5.2, the plastic potential derivatives are calculated by using temporary values p'^{t}_{a}, $\{s_a\}^t$ and R^t, depending on which is the active yield surface. Again, if the kinematic yield surface is the active yield surface the temporary values are $p'^{t}_{a} = p'_a$, $\{s_a\}^t = \{s_a\}$and $R^t = R$ whereas if the bounding surface is the active yield surface these become equal to $p'^{t}_{a} = 0.5p'_o$, $\{s_a\}^t = 0$ and $R^t = 1.0$.

4.5.4 Calculation of the hardening modulus, A

The hardening modulus, A, is calculated for the surface that is the active yield surface at the time.

i) When the kinematic yield surface is the active yield surface

The hardening modulus, A, is given by Equation 4.42. If the derivatives of the kinematic yield surface are represented by the vector $\{\partial F_y/\partial s\}$ then Equation 4.42 can be rewritten as:

$$A = \frac{4}{\lambda^* - \kappa^*}\left[\left(p' - p'_a\right)\left[p'_a\left(p' - p'_a\right) + \frac{1}{2}\left\{\frac{\partial F_y}{\partial s}\right\}^T \{s_a\} + \frac{R^2 p'^2_o}{4}\right] + \left(\frac{b}{b_{\max}}\right)^{\psi}\left(\frac{p'_o}{2}\right)^3\right] \tag{4.68}$$

where

$$b = \frac{1}{R\dfrac{p'_o}{2}}\left[\left(p' - p'_a\right)\left[\frac{p' - p'_a}{R} - \left(p' - \frac{p'_o}{2}\right)\right] + \frac{1}{2}\left\{\frac{\partial F_y}{\partial s}\right\}^T \left\{\frac{s - s_a}{R} - s\right\}\right] \tag{4.69}$$

i) When the bounding surface is the active yield surface

The hardening modulus is calculated by Equation 4.49.

4.5.5 Calculation of the elastic constitutive matrix, $[D']$

The elastic matrix $[D']$ can be expressed in terms of the elastic shear modulus, G_e, and

the elastic bulk modulus, K_e, as follows:

$$[D'] = \begin{bmatrix} K_e + \frac{4}{3}G_e & K_e - \frac{2}{3}G_e & K_e - \frac{2}{3}G_e & 0 & 0 & 0 \\ & K_e + \frac{4}{3}G_e & K_e - \frac{2}{3}G_e & 0 & 0 & 0 \\ & & K_e + \frac{4}{3}G_e & 0 & 0 & 0 \\ & & & G_e & 0 & 0 \\ & sym & & & G_e & 0 \\ & & & & & G_e \end{bmatrix} \tag{4.70}$$

The elastic shear modulus, G_e, and the elastic bulk modulus, K_e, have already been discussed in section 4.4.7.

4.5.6 Calculation of the changes in hardening parameters

The hardening parameters in this model are the parameter p'_o, which defines the size of the bounding surface and the centre of the kinematic yield surface, which in vector notation is described by p'_a and $\{s_a\}$.

i) When the kinematic yield surface is the active yield surface

The change in p'_o is described by Equation 4.8 and the changes in p'_a and $\{s_a\}$ can be obtained from Equation 4.32. The change in p'_a is given by Equation 4.33, while Equation 4.34 can be written in vector notation in order to obtain the change in $\{s_a\}$:

$$\{ds_a\} = \frac{dp'_o}{p'_o}\{s_a\} + S\left\{\frac{s - s_a}{R} - s\right\} \tag{4.71}$$

If the derivatives of the kinematic yield surface are represented by $\{\partial F_y/\partial s\}$, then the scalar multiplier S in Equation 4.32 can be rewritten as:

$$S = \frac{(p' - p'_a)\left(dp' - \frac{dp'_o}{p'_o}p'_a\right) + \frac{1}{2}\left\{\frac{\partial F_y}{\partial s}\right\}^T \left\{ds - \frac{dp'_o}{p'_o}s_a\right\} - \frac{R^2 p'_o dp'_o}{4}}{(p' - p'_a)\left[\frac{p' - p'_a}{R} - \left(p' - \frac{p'_o}{2}\right)\right] + \frac{1}{2}\left\{\frac{\partial F_y}{\partial s}\right\}^T \left\{\frac{s - s_a}{R} - s\right\}} \tag{4.72}$$

ii) When the bounding surface is the active yield surface

The change in p'_o is described by Equation 4.8 and the changes in p'_a and $\{s_a\}$ can be

obtained from Equation 4.39. The change in p'_a is given by Equation 4.40 and the change in $\{s_a\}$ can be obtained by writing Equation 4.41 in vector notation:

$$\{ds_a\} = (1-R)\{ds\} \tag{4.73}$$

4.6 Validation

4.6.1 Introduction

This section presents a series of single finite element analyses performed in order to validate the implementation of the two-surface model and the improvements that have been made in this version of the model and demonstrate some of its capabilities and limitations (further evaluation of the model is presented in Chapter 7). The first part of this section involves the simulation of a number of stress paths quoted by Al-Tabbaa (1987) and the comparison of the results with the already published data. The second part explores different shapes of the yield and plastic potential surfaces in the deviatoric plane and the third part demonstrates the performance of the model at stress paths involving rotation of the principal stresses. Finally, the last part discusses the hardening function assumed in the model and the resulting elasto-plastic transition.

4.6.2 Comparison with stress paths from Al-Tabbaa (1987)

Al-Tabbaa (1987) used the two-surface model in order to reproduce a number of slow cyclic oedometer and triaxial tests on speswhite kaolin and compared the model predictions with the experimental results. A number of monotonic stress paths were also simulated and the failure conditions obtained were investigated.

The stress paths repeated in this thesis are a slow cyclic stress path at constant shear stress and a number of monotonic undrained stress paths.

i) Slow cyclic constant q triaxial test

This slow cyclic triaxial test at constant shear stress, q, with p' varying was initiated from a one-dimensionally normally consolidated state. Figures 4.10a and 4.11a show the experimental results and Figures 4.10b and 4.11b show the model calculations presented by Al-Tabbaa (1987). The model parameters were derived from the slow cyclic

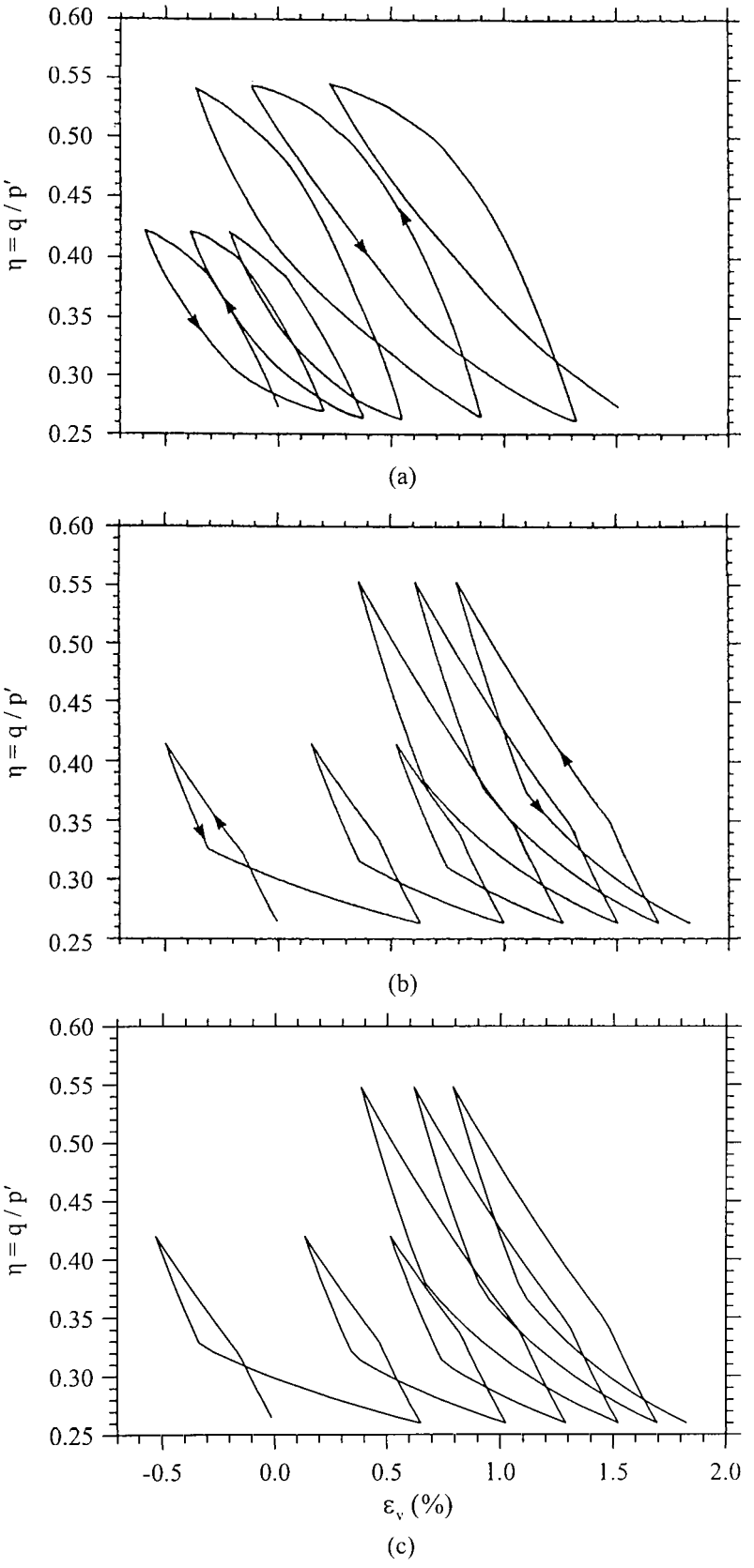


Figure 4.10: Slow cyclic constant q triaxial test: $\eta = q / p'$ against ε_v a) experimental observations (after Al-Tabbaa (1987)) b) model predictions (after Al-Tabbaa (1987)) c) predictions of two-surface model as implemented into ICFEP

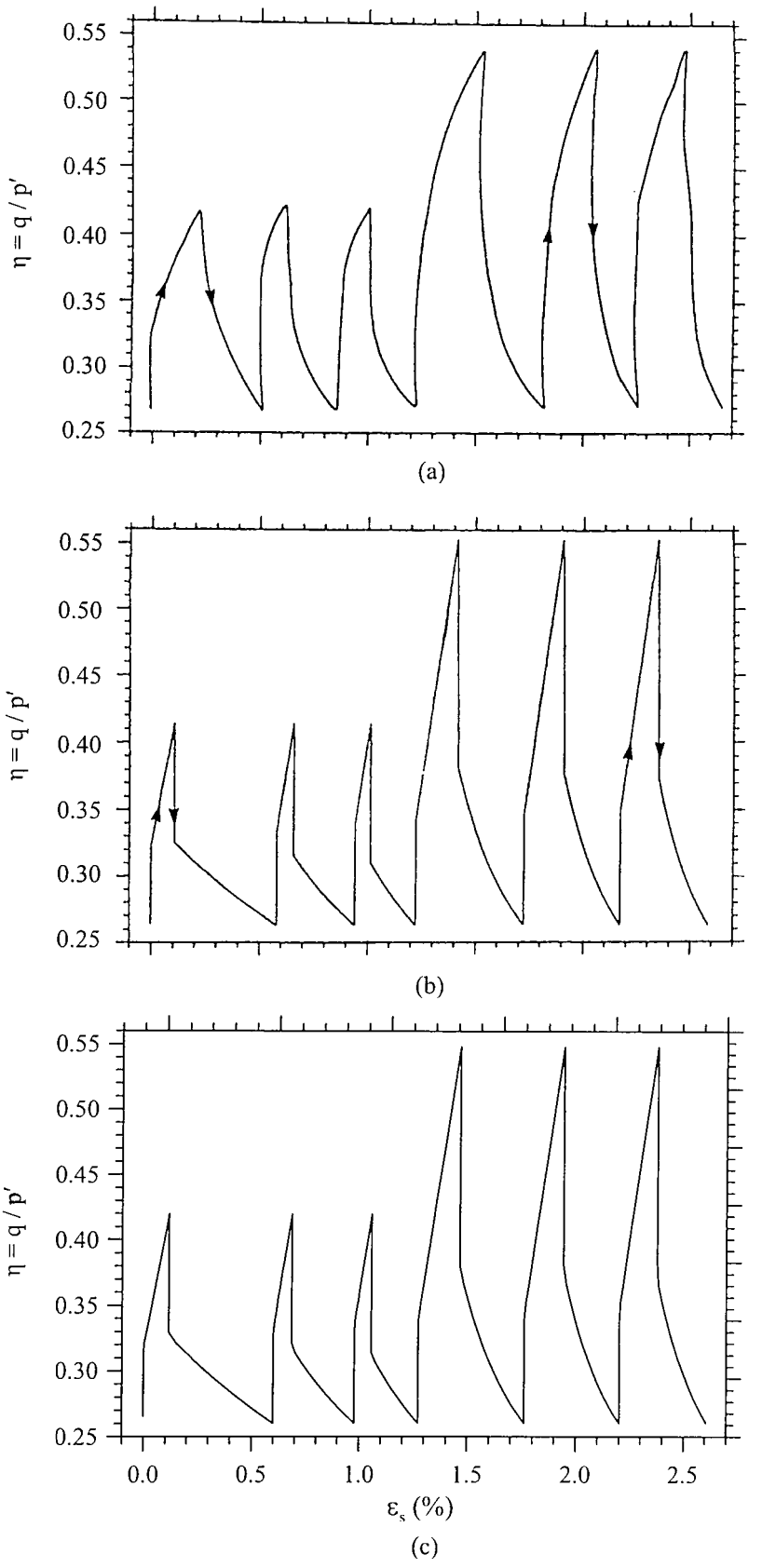


Figure 4.11: Slow cyclic constant q triaxial test: $\eta = q / p'$ against ε_s a) experimental observations (after Al-Tabbaa (1987)) b) model predictions (after Al-Tabbaa (1987)) c) predictions of two-surface model as implemented into ICFEP

λ^*	κ^*	μ	M	R	ψ
0.085	0.0078	0.3	0.9	0.2	1.5

Table 4.1: Material parameters used by Al-Tabbaa (1987) in the two-surface model for the simulation of tests on speswhite kaolin

λ^*	κ^*	μ	$X = M/\sqrt{3}$	Y	Z	Y_p	Z_p	R	ψ
0.085	0.007	0.3	0.52	0.0	1.0	0.0	1.0	0.2	1.5

Table 4.2: Material parameters used in the current version of the two-surface model implemented into ICFEP for the simulation of tests on speswhite kaolin

oedometer and triaxial tests and are given in Table 4.1. In order to repeat this stress path with the current version of the two-surface model a circle has to be assumed for the yield and plastic potential surfaces in the deviatoric plane and the equivalent parameters are quoted in Table 4.2. Figures 4.10c and 4.11c present the model predictions obtained from the two-surface model as implemented into ICFEP. Comparison of Figures 4.10b and 4.11b with Figures 4.10c and 4.11c shows that the predictions of the current version of the two-surface model are the same as those presented by Al-Tabbaa (1987).

Comparison of the model predictions with the experimental results shows that the overall response predicted by the model is similar to that observed experimentally. Important aspects of the observed behaviour, like hysteresis loops on unloading-reloading cycles and the continuous accumulation of shear strains in a test where the shear stress is kept constant and the stress path remains within the state boundary surface are well represented (such features of behaviour would not be predicted by the modified Cam Clay model which assumes elastic strains within the state boundary surface).

It can be seen in Figures 4.10b-c and 4.11b-c that a number of kinks are observed in the model predictions. These are the points at which the stress state reaches the kinematic yield surface and the state changes from elastic to elasto-plastic. These points can be seen as kinks because the model does not predict a smooth elasto-plastic transition and hence there is an abrupt change in stiffness on reaching the kinematic yield surface. Al-Tabbaa (1987) noted that this feature is related to the form of the hardening function assumed in the model and could be improved by modifying it.

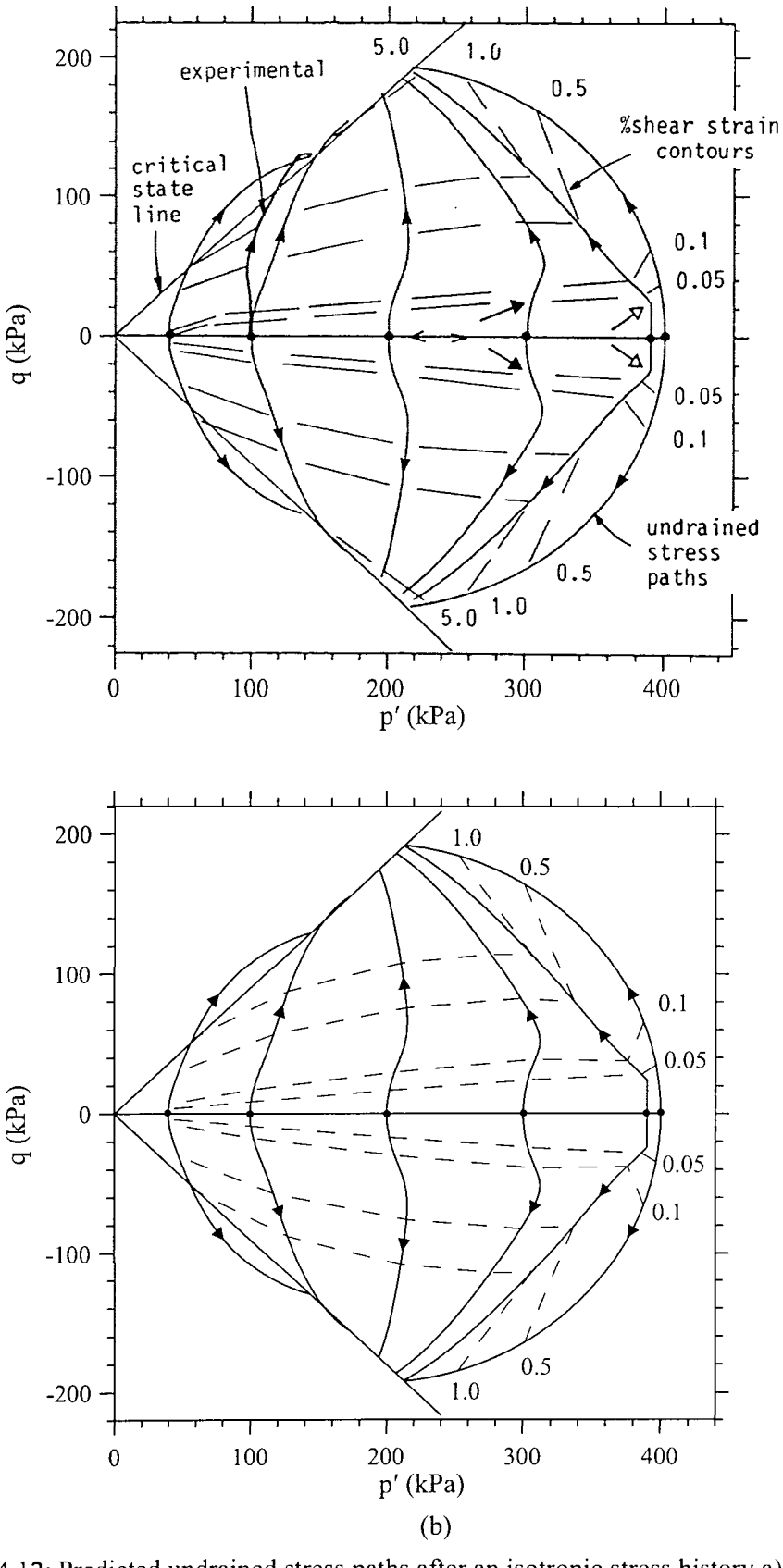
ii) Monotonic triaxial stress paths

Figures 4.12a and 4.13a show a number of predicted undrained stress paths initiated from isotropically and one-dimensionally normally and overconsolidated states, quoted by Al-Tabbaa (1987). The parameters used in the model calculations are those given in Table 4.1. Superimposed on these two figures are also two experimental undrained tests; however, these were performed in reality after a number of stress cycles and hence are not directly comparable to the model predictions. Al-Tabbaa (1987) noted that Figures 4.12a and 4.13a compared well with experimental results on lightly overconsolidated spestone kaolin (Parry and Nadarajah (1973)), which are shown here in Figures 4.14a and 4.14b. The predictions of the version of the two-surface model implemented into ICFEP can be seen in Figures 4.12b and 4.13b and the parameters used in the analyses are those quoted in Table 4.2. Comparison of Figures 4.12a and 4.13a with Figures 4.12b and 4.13b respectively, shows that the implemented version of the two-surface model reproduces the same stress paths to the ones presented by Al-Tabbaa (1987).

Translation rule for the case that the two surfaces are in contact

It should be noted, that for the stress paths initiating from normally consolidated states, the two surfaces are in contact at the start of shearing. Therefore, in the current version of the two-surface model, and in accordance with the formulation described in section 4.4 and the implementation in section 4.5, if in these cases the shearing stress path is one of continuous yielding, then this is calculated with the bounding surface being the active yield surface and the new translation rule is employed for the kinematic yield surface (Equation 4.39), different to the one assumed in the original formulation (Equation 4.12). In Figure 4.12 both compression and extension paths starting from normally consolidated states are stress paths of continuous yielding, whereas in Figure 4.13 only the compression path is one of continuous yielding, the extension path enters the kinematic yield surface, hence the kink in the stress path.

An attempt to calculate the above stress paths with the equations of the kinematic yield surface together with the translation rule described in the original formulation (Equation 4.12) results in the stress paths shown in Figure 4.15. It can be seen that the stress paths of continuous yielding predicted in this case are different from the ones obtained with the current version of the two-surface model (which actually coincide with the modified Cam Clay predictions). This is because, as discussed in section 4.3.8, Equation 4.12 does not ensure that the two surfaces remain in contact for further loading. Figure 4.16 shows



(b)

Figure 4.12: Predicted undrained stress paths after an isotropic stress history a) model predictions (after Al-Tabbaa (1987)) b) predictions of two-surface model as implemented into ICFEP

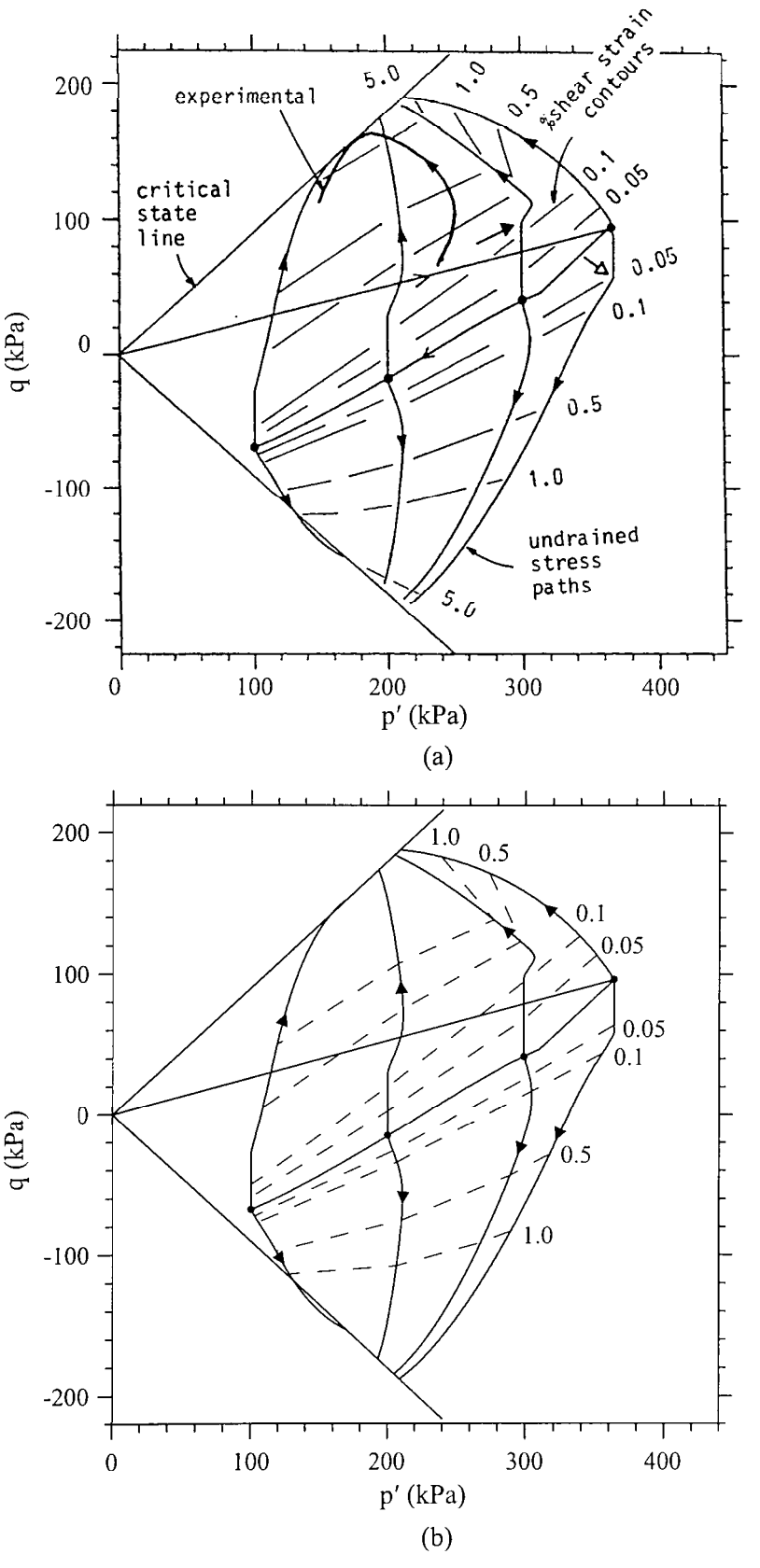
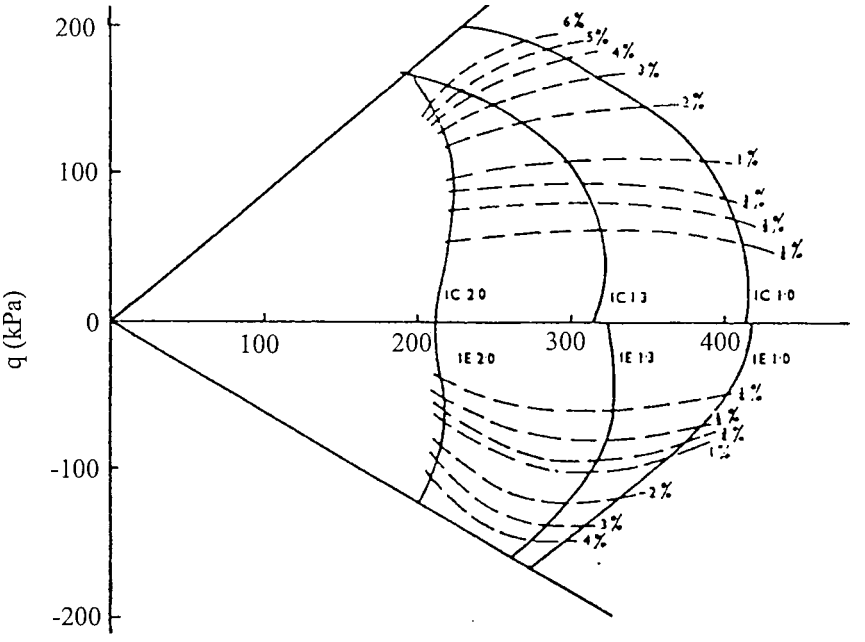
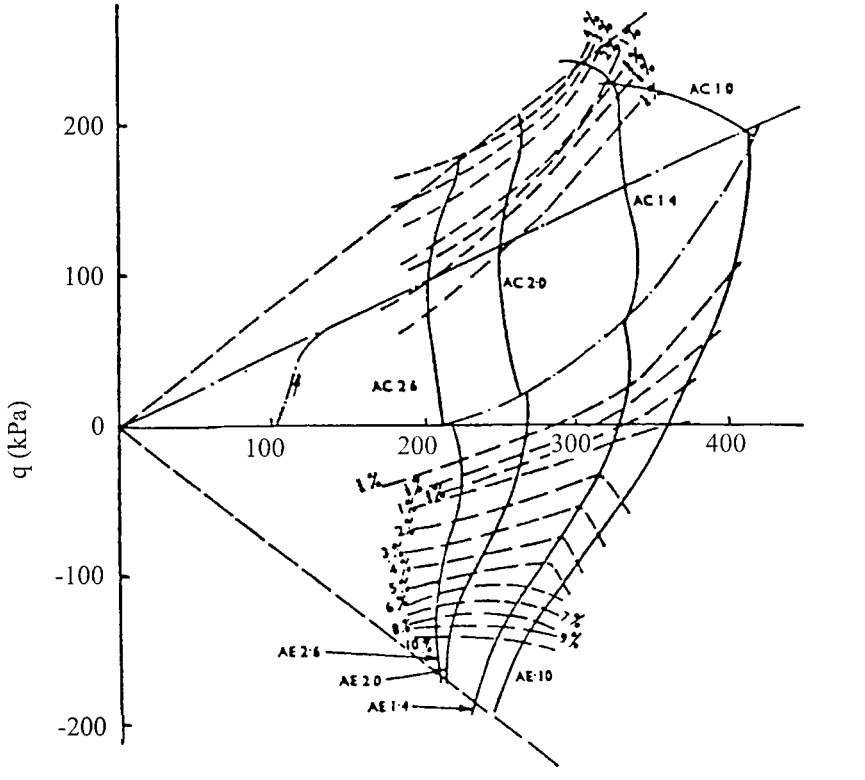


Figure 4.13: Predicted undrained stress paths after a one-dimensional stress history a) model predictions (after Al-Tabbaa (1987)) b) predictions of two-surface model as implemented into ICFEP

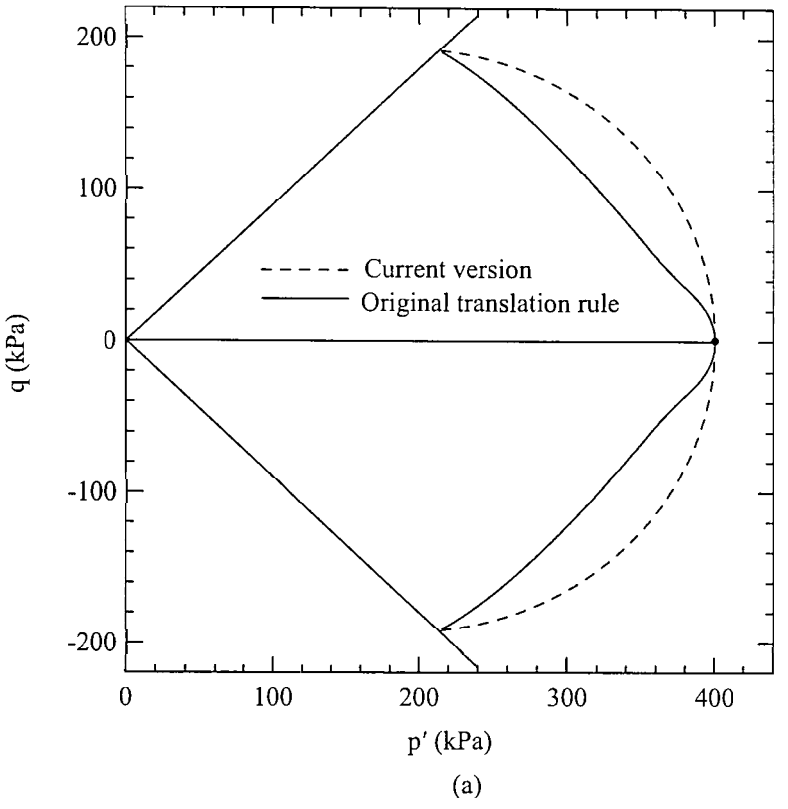


(a)



(b)

Figure 4.14: Experimental undrained stress paths using spestone kaolin a) after an isotropic stress history b) after a one-dimensional stress history (Figure 10.33 of Al-Tabbaa (1987) after Parry and Nadarajah (1973))



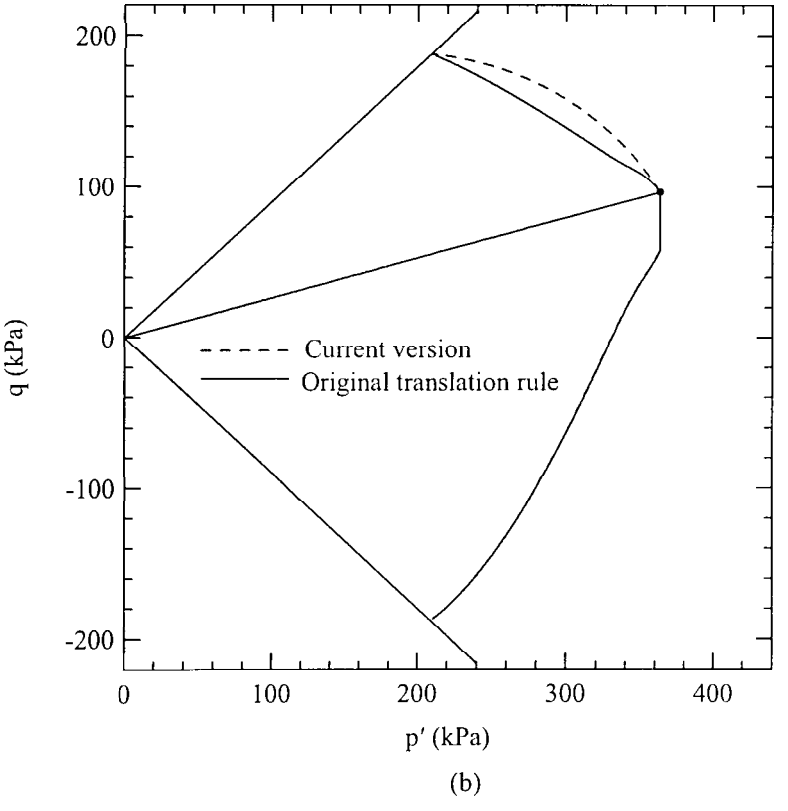
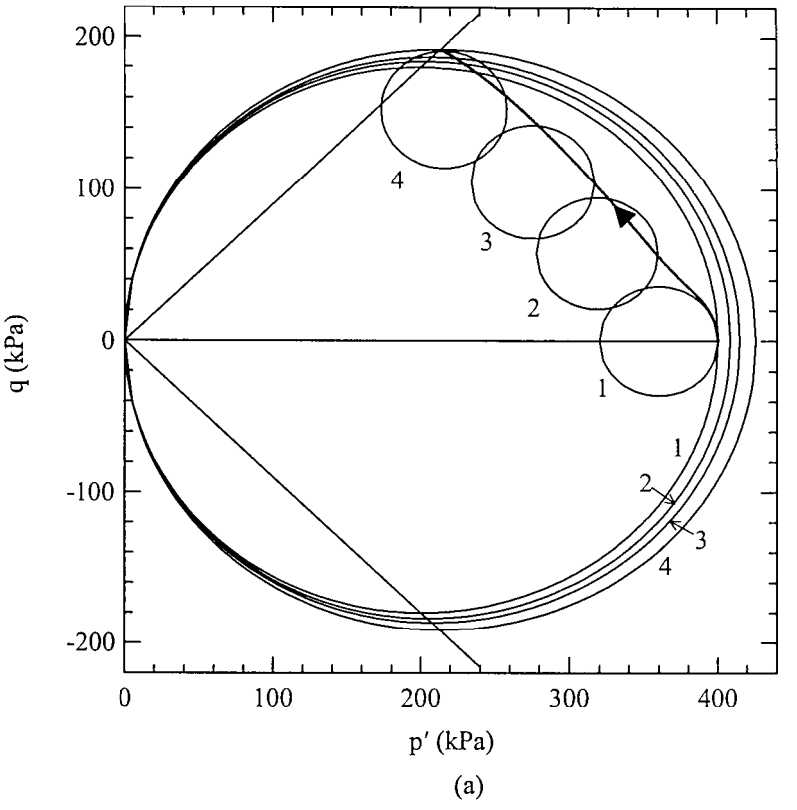
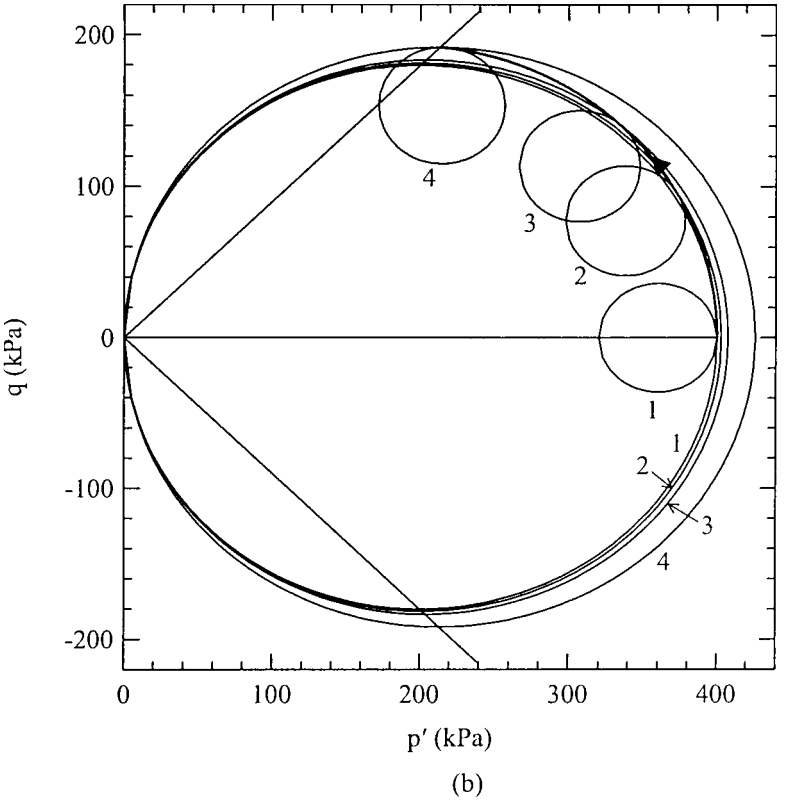


Figure 4.15: Predicted undrained stress paths a) after an isotropic stress history b) after a one-dimensional stress history

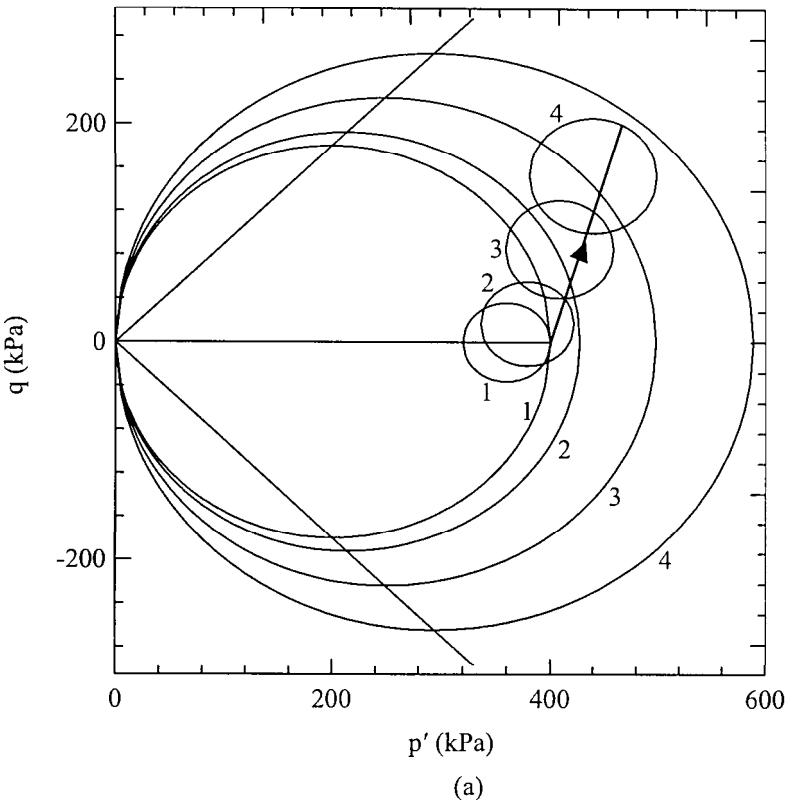


(a)

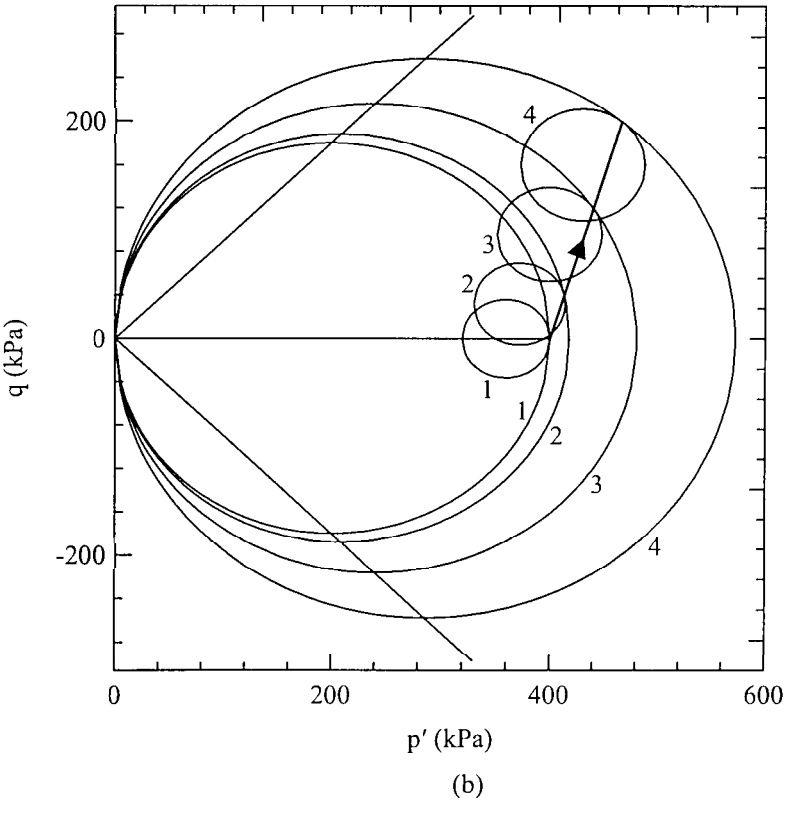


(b)

Figure 4.16: Predicted relative motion of kinematic yield and bounding surfaces during undrained triaxial compression after an isotropic stress history a) original translation rule b) current version of the two-surface model



(a)



(b)

Figure 4.17: Predicted relative motion of kinematic yield and bounding surfaces during drained triaxial compression after an isotropic stress history a) original translation rule b) current version of the two-surface model

the position of the kinematic yield and bounding surfaces for the compression path starting from isotropic conditions and shown in Figure 4.15. In Figure 4.16a the stress state ends up within the bounding surface and the stress path predicted is different from the one predicted by the current version of the two-surface model and the modified Cam Clay model. It is not clear how Al-Tabbaa (1987) obtained the stress paths initiating from normally consolidated states in Figures 4.12a and 4.13a.

The inability of the original translation rule to maintain the two surfaces in contact for further loading can also be seen, probably more clearly, in a drained triaxial compression path starting from normally consolidated isotropic conditions. Figure 4.17 shows the positions of the two surfaces for such a path. In Figure 4.17a, although the two surfaces are in contact at the start of the shearing stage, they do not remain in contact during further shearing. On the contrary, Figure 4.17b shows that in the current version of the model the two surfaces remain tangential to each other. Therefore Figures 4.16a and 4.17a confirm that the original translation rule assumed in the model does not ensure that the two-surfaces remain in contact for further loading. If this original translation rule is used together with the equations of the kinematic yield surface then the model cannot predict the modified Cam Clay behaviour for normally consolidated stress paths of continuous yielding. This confirms the need to use a translation rule which guarantees that the two surfaces remain tangential for further loading. In this case the bounding surface has to be the active yield surface, as already discussed, since otherwise the consistency condition of the kinematic yield surface is not satisfied.

Undrained strength

The undrained strength predicted by the two-surface model can be calculated analytically if the size of the bounding surface (i.e. the hardening parameter p'_o) is known at the beginning of the undrained shearing. The derivation of the expression is given in Appendix III. Tables 4.3 and 4.4 give the values of p'_{cs} and q_{cs} (p' and q at the critical state) calculated from the Equations of Appendix III, for the previous undrained stress paths of Figures 4.12 and 4.13 (the values of p'_o at the start of the shearing are also quoted in the table). There is no difference between the values calculated for compression or extension since a circular shape was adopted in the deviatoric plane. These values of p'_{cs} and q_{cs} can be seen to agree with the values of p' and q at the ultimate states shown in Figures 4.12 and 4.13.

However, it should be noted that the size of the bounding surface changes depending on

p'_i (kPa)	400	390	300	200	100	40
p'_o (kPa)	400	400	398.4	387.6	365.3	327.6
p'_{cs} (kPa)	231.1	212.6	206.8	194.4	172.8	143.9
q_{cs} (kPa)	192.0	191.6	186.3	175.1	155.7	130

Table 4.3: Values of p'_{cs} and q_{cs} calculated from the equations of Appendix III for the undrained stress paths of Figure 4.12 and values of p'_o at the start of shearing (p'_i is the mean effective stress at the start of shearing)

p'_i (kPa)	363.3	298.7	200	100.5
p'_o (kPa)	394.7	394.2	384.6	358.3
p'_{cs} (kPa)	208.7	204.8	193	170
q_{cs} (kPa)	188	184.4	173.8	153

Table 4.4: Values of p'_{cs} and q_{cs} calculated from the equations of Appendix III for the undrained stress paths of Figure 4.13 and values of p'_o at the start of shearing (p'_i is the mean effective stress at the start of shearing)

the stress path followed to reach the stress state at the start of shearing and consequently it is not always easy to estimate p'_o. This implies that the undrained strength predicted by the model depends on recent stress history rather than distant history. The same was concluded by Al-Tabbaa (1987) for the failure conditions predicted in both undrained and drained tests.

Peak drained strength for overconsolidated states

As discussed in Chapter 2, the peak drained strength of heavily overconsolidated clays is typically found to lie on the so-called Hvorslev surface. In the modified Cam Clay model the peak failure stresses of such clays are overestimated, since the stress state has to reach the elliptical yield surface before softening of the material starts.

In the two-surface model, the function H was introduced in the hardening function $h = H + h_o$ so as to discourage strain softening for stress states on the unstable regions of the kinematic yield surface when this is not in contact with the modified Cam Clay bounding surface, as discussed in section 4.3.5. However, as Al-Tabbaa and Wood

(1989) note, the influence of H reduces as the kinematic yield surface approaches the bounding surface and strain softening can eventually develop within the bounding surface when $H = -h_o$. This results in lower peak stresses than those predicted by the modified Cam Clay model.

4.6.3 Different yield and plastic potential surfaces in the deviatoric plane

As it has already been mentioned in the formulation of the model in general stress space, an improvement that has been made in this current version of the model is that the yield and plastic potential surfaces do not necessarily have a circular shape in the deviatoric plane, but can take different shapes. The shapes implemented in this work are a Mohr-Coulomb hexagon and a general shape proposed by van Eekelen (1980), for the case of the yield surface, and a general shape (van Eekelen (1980)), for the case of the plastic potential. Depending on the selection of the model parameters, the general shape can take a variety of forms, including the one suggested by Lade (Lade and Duncan (1975)) and a circular shape.

The objective of this section is to show that the different deviatoric plane shapes have been implemented correctly into this version of the two-surface model. In order to prove this, three of the monotonic undrained triaxial compression and extension tests starting from isotropic conditions ($p' = 400$ kPa, $p' = 300$ kPa and $p' = 100$ kPa), and shown in Figure 4.12, were repeated for different shapes of the yield and plastic potential surfaces. Moreover, an undrained plane strain compression test was performed for each case. The obtained failure conditions of the triaxial and plane strain tests can demonstrate whether the different shapes have been implemented correctly.

Four different cases were considered for the deviatoric shapes of the yield and plastic potential surfaces. In the first case (case A) the yield and plastic potential surfaces were assumed to have a circular shape in the deviatoric plane. This is the same case as that shown in Figure 4.12. In the second case (case B) the yield surface had the shape of a Mohr-Coulomb hexagon and the plastic potential had a circular shape. In the third case (case C) both the yield and plastic potential surfaces had the shape proposed by Lade. Finally in the last case (case D) the yield surface took the Lade shape and the plastic potential took a circular shape. In cases A and C the flow rule was associated whereas in cases B and D the flow rule was non-associated.

The reasoning behind these different combinations of yield and plastic potential shapes

is as follows. The yield surface defines the shape of the failure surface in the deviatoric plane and is therefore important. However, for problems involving plane strain deformation, Potts and Gens (1984) have demonstrated that the shape assumed for the plastic potential is also important because it actually determines the value of the Lode's angle, θ_f, at which failure takes place. Moreover, Potts and Gens (1984) showed that in some cases it is necessary to assume a different shape for the yield and plastic potential surfaces in the deviatoric plane. For example, if a Mohr-Coulomb hexagon is adopted for the shape of the yield surface (and hence the failure surface) in a critical state model, then a different shape must be adopted for the plastic potential surface, otherwise plane strain failure occurs at either $\theta_f = 30°$ or $\theta_f = -30°$ which is clearly unrealistic. This is the reason why in case B where the yield surface takes the shape of the Mohr-Coulomb hexagon, a circular shape was adopted for the plastic potential. If the general shape is adopted for the plastic potential, then the Lode's angle, θ_f, at failure can be determined from the following equation:

$$\tan\theta = -\frac{3Z_p Y_p \cos 3\theta}{\left(1 + Y_p \sin 3\theta\right)} \tag{4.74}$$

The parameters adopted for the shape of the yield and plastic potential surfaces in the deviatoric plane for each case can be seen in Table 4.5, the rest of the parameters are given in Table 4.2. The parameters of Table 4.5 have been chosen such that all four cases predict the same strength in triaxial compression. Table 4.6 gives the values of θ_f and $g(\theta_f)$ calculated for each case, as well as the equivalent values of φ' at failure. The values of $g(\theta_f)$ have been obtained from Equations 4.27 and 4.28 and the values of θ_f for plane strain failure have been calculated from Equation 4.74. Figure 4.18 shows the shape of the failure surfaces for each case and the $g(\theta_f)$ values tabulated in Table 4.6.

Case	X	Y	Z	Y_p	Z_p
A	0.52	0.0	1.0	0.0	1.0
C	0.47	0.36	0.25	0.36	0.25
D	0.47	0.36	0.25	0.0	1.0
	φ'	-	-	Y_p	Z_p
B	23°	-	-	0.0	1.0

Table 4.5: Model parameters defining the shape of the yield and plastic potential surfaces in the deviatoric plane

Case	Triaxial Compression			Triaxial Extension			Plane strain Compression		
	θ_f	$g(\theta_f)$	φ'_f	θ_f	$g(\theta_f)$	φ'_f	θ_f	$g(\theta_f)$	φ'_f
A	-30°	0.52	23°	30°	0.52	32°	0°	0.52	31.3°
B	-30°	0.52	23°	30°	0.4	23°	0°	0.39	23°
C	-30°	0.52	23°	30°	0.43	25.2°	-14.5°	0.5	26.8°
D	-30°	0.52	23°	30°	0.43	25.2°	0°	0.47	27.7°

Table 4.6: Values of θ_f, $g(\theta_f)$ and equivalent values of φ'_f for the four cases analysed

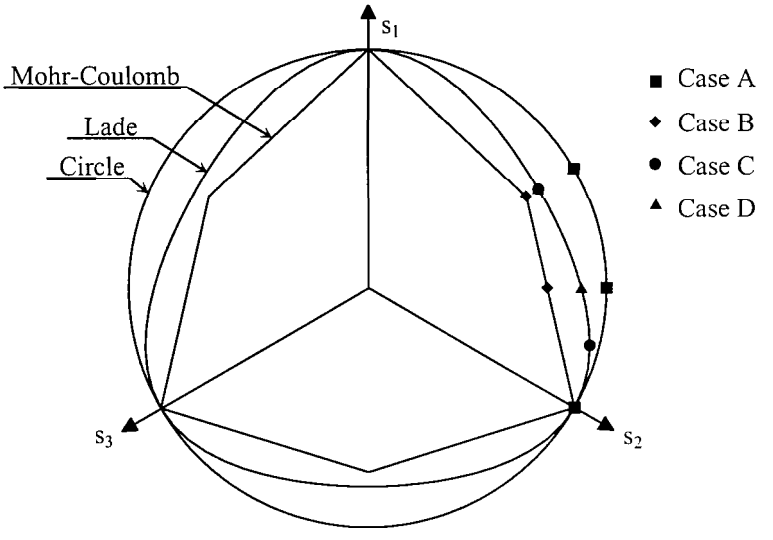


Figure 4.18: Failure surfaces in the deviatoric plane and the values of $g(\theta_f)$ obtained for each case

Figures 4.19, 4.20, 4.21 and 4.22 show the undrained stress paths in J-p' space for the first, second, third and fourth cases, respectively. On each plot the failure lines corresponding to the values of $g(\theta_f)$, tabulated in Table 4.6, for each case are shown. It can be seen that in all four cases the undrained stress paths predict satisfactorily the expected failure conditions, indicating that the implementation of the different shapes of the yield and plastic surfaces in the deviatoric plane is correct.

Moreover, comparison of Figures 4.19-4.22 shows that although all four cases predict the same strength in triaxial compression, the assumption of different yield (and

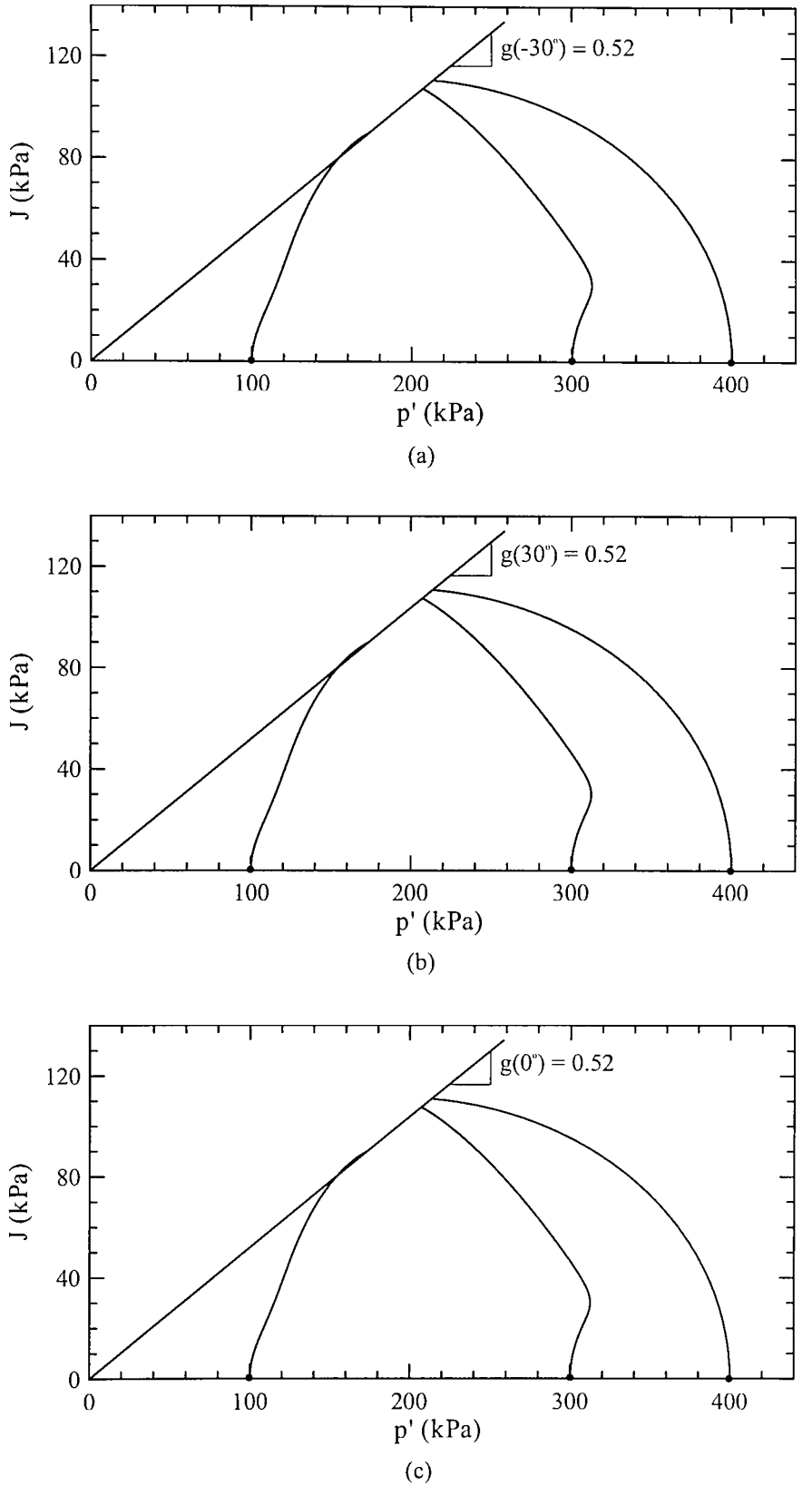


Figure 4.19: Predicted undrained stress paths after an isotropic stress history for case A - circular shape for the yield surface and the plastic potential in the deviatoric plane a) triaxial compression b) triaxial extension c) plane strain compression

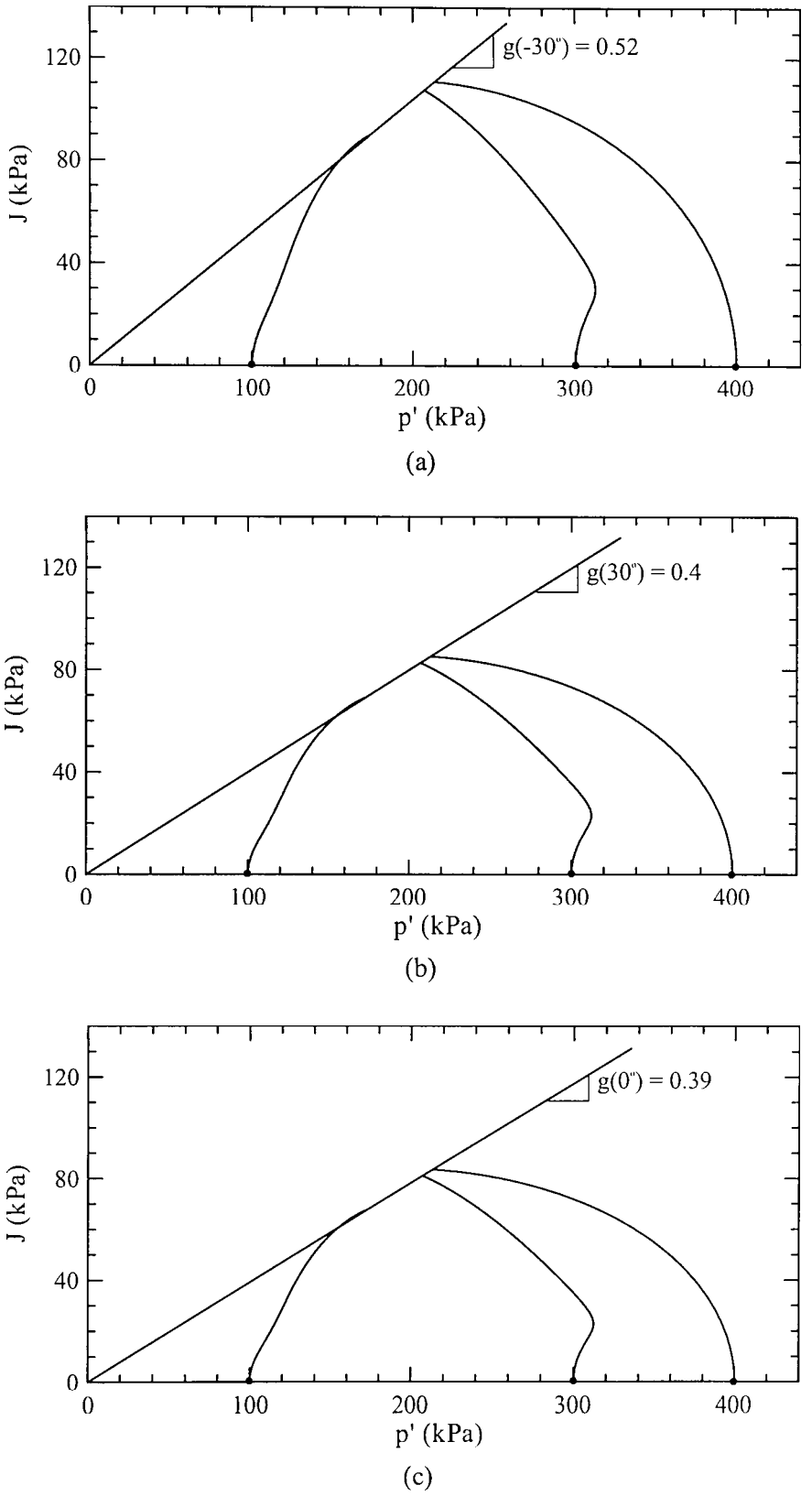


Figure 4.20: Predicted undrained stress paths after an isotropic stress history for case B – Mohr-Coulomb shape for the yield surface and circular shape for the plastic potential in the deviatoric plane a) triaxial compression b) triaxial extension c) plane strain compression

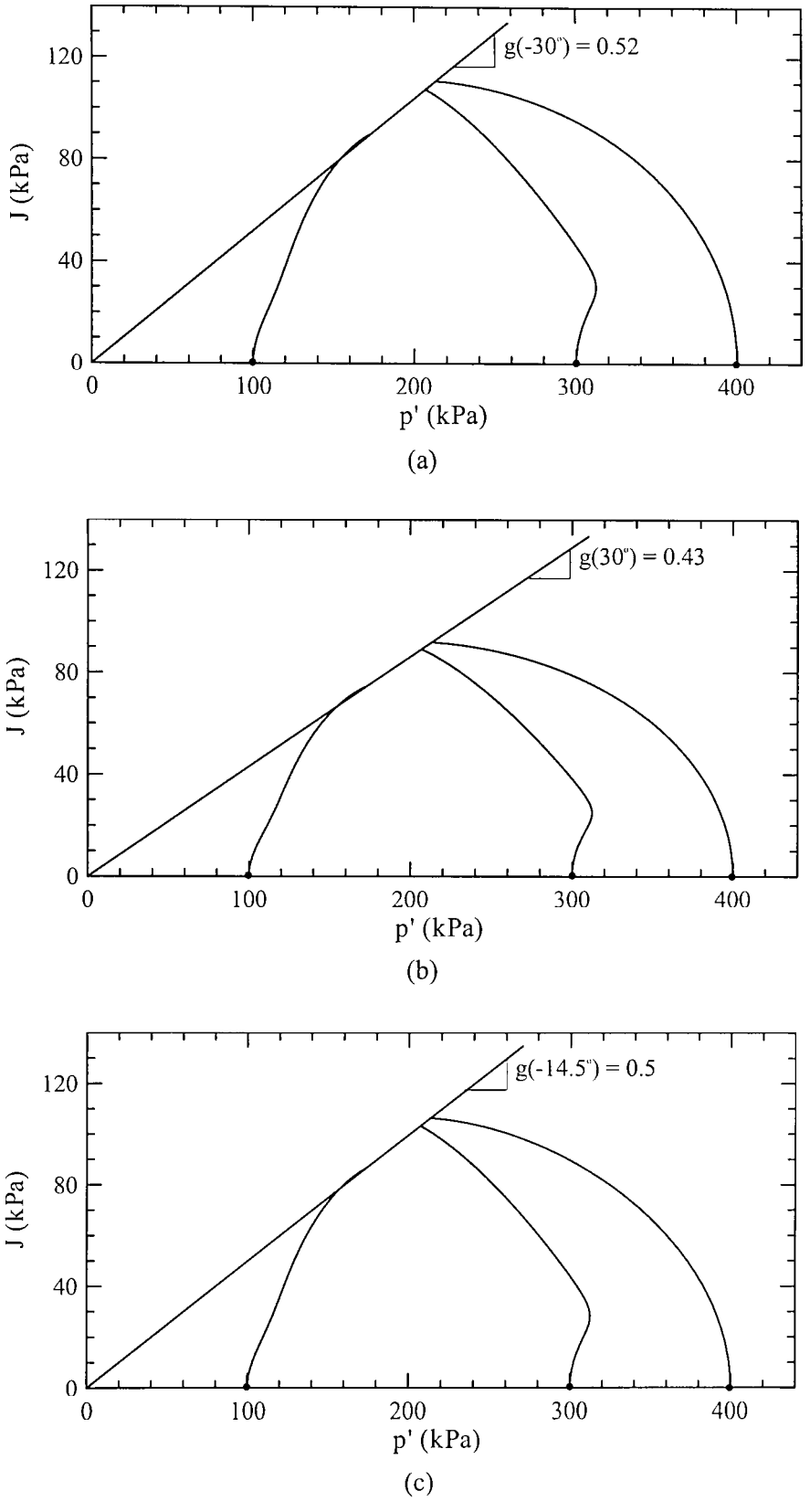


Figure 4.21: Predicted undrained stress paths after an isotropic stress history for case C – Lade shape for the yield surface and the plastic potential in the deviatoric plane a) triaxial compression b) triaxial extension c) plane strain compression

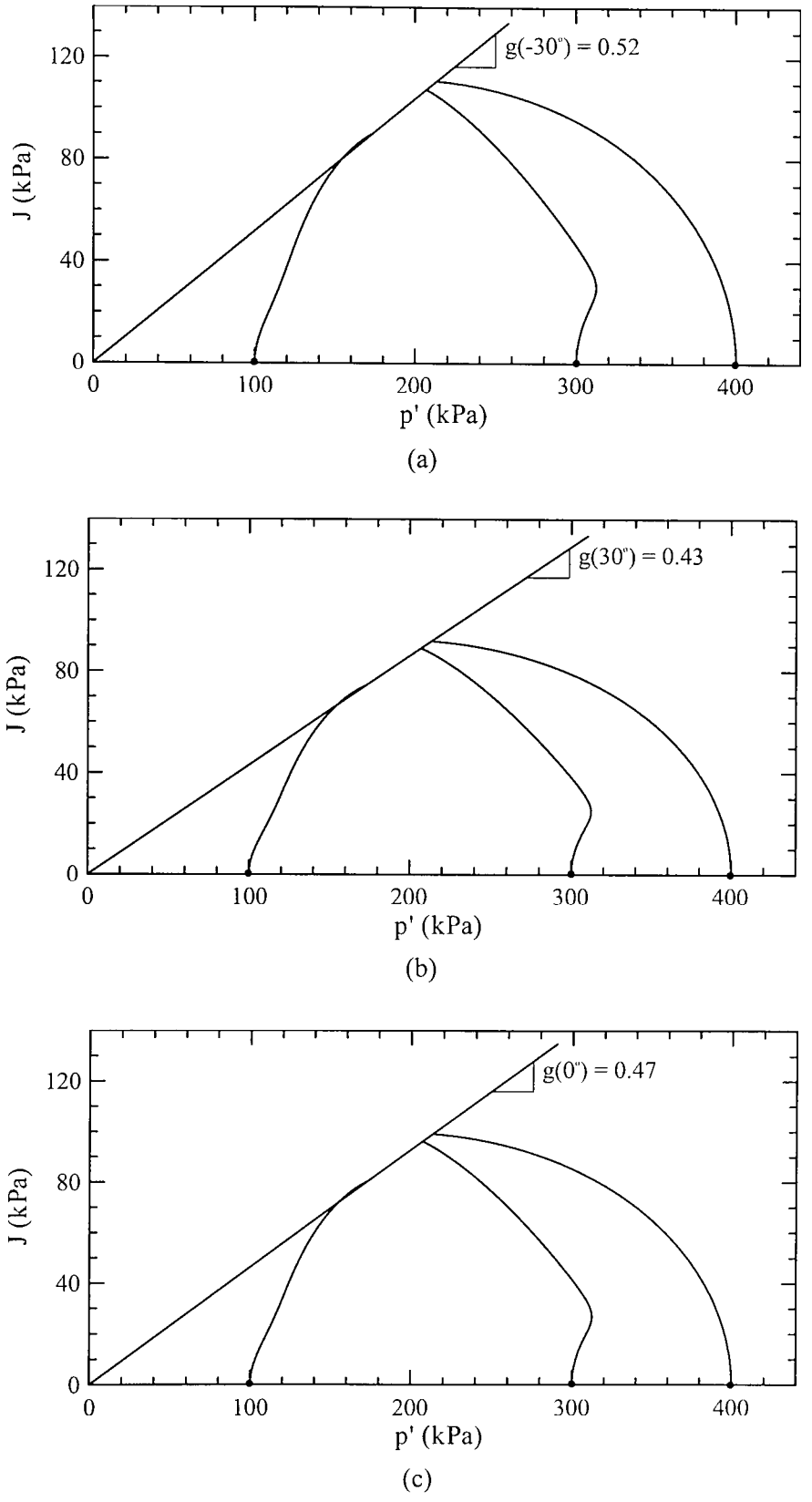


Figure 4.22: Predicted undrained stress paths after an isotropic stress history for case D – Lade shape for the yield surface and circular shape for the plastic potential in the deviatoric plane a) triaxial compression b) triaxial extension c) plane strain compression

therefore failure) surfaces in the deviatoric plane results in significantly different strengths predicted under triaxial extension and plane strain conditions. As discussed earlier, in the latter case the strength is not only dependent on the shape of the yield surface, but also on the shape of the plastic potential. In case A, Figure 4.19, the values of J at failure, J_f, predicted by all three stress paths are the same, which is expected since a circular failure surface is independent of the Lode's angle, θ. In case B, which assumes a Mohr Coulomb failure surface in the deviatoric plane, Figure 4.20, the values of J_f predicted in plane strain compression and triaxial extension conditions are much smaller than the value of J_f predicted in triaxial compression; with the value of J_f in plane strain compression being slightly lower than the value of J_f in triaxial extension. In case C, which assumes a Lade shape for both the yield and plastic potential surfaces, Figure 4.21, the values of J_f predicted by the plane strain and triaxial extension stress paths are again smaller than the value of J_f in triaxial compression. However, in this case the J_f in plane strain compression is higher than the J_f in triaxial extension and both of these values are higher than the equivalent ones obtained from a Mohr Coulomb failure surface. As mentioned before, the strength under plane strain conditions is also dependent on the shape of the plastic potential surface. This is emphasised by comparison of the cases C and D which both assume a Lade shape for the yield surface but adopt different plastic potential shapes. Figures 4.21 and 4.22 show that the strengths under triaxial compression and extension are the same in both cases, since these are governed by the adopted failure surface. However under plane strain conditions different values of the Lode's angle, θ_f, at failure are predicted for each case and hence different strengths are obtained. It is interesting to note that although the value of $g(\theta_f)$ for case C is higher than the value of $g(\theta_f)$ for case D under plane strain conditions, the equivalent value of φ'_f for case C is lower than the value of φ'_f for case D (see Table 4.6).

4.6.4 Stress paths involving rotation of the principal stresses

In order to demonstrate the anisotropic formulation of the two-surface model, a number of single element analyses were performed, modelling stress paths in the hollow cylinder apparatus (HCA). In the HCA, hollow cylindrical soil samples can be subjected to axial load, torque about the central vertical axis and external and internal radial pressures (Hight et al. (1983)), see Figure 4.23. This allows control over four of the component stresses σ_z, σ_r, σ_θ and $\tau_{z\theta}$, while $\tau_{r\theta}$ and τ_{rz} are zero. In this way the magnitude and direction of the major and minor principal stresses, as well as the magnitude of the intermediate principal stress, can be controlled. In the HCA the component stresses σ_z,

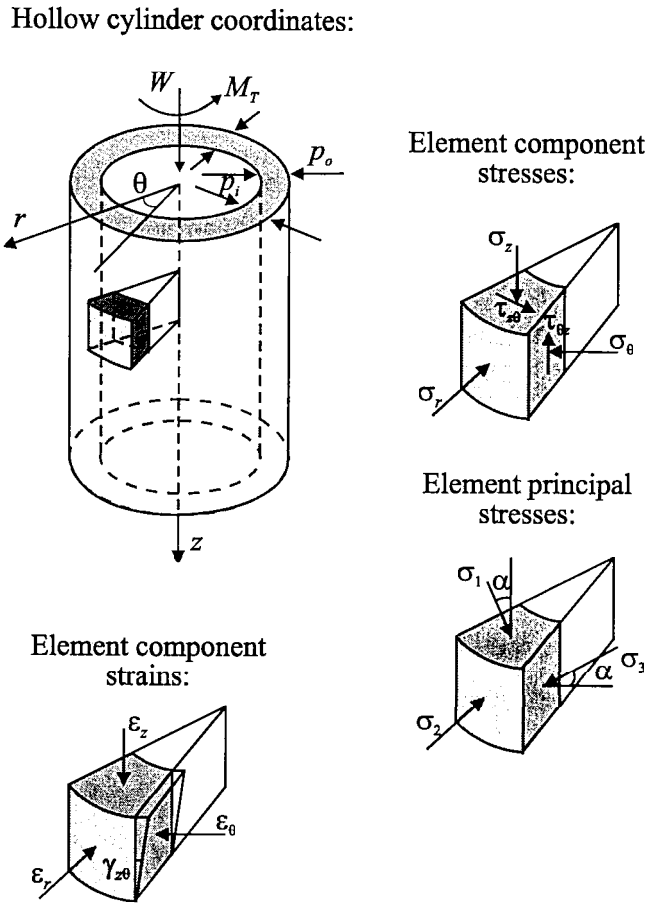


Figure 4.23: Stress and strains within the hollow cylinder apparatus (figure after Potts and Zdravkovic (2001))

σ_r, σ_θ and $\tau_{z\theta}$ can be expressed as a function of the control parameters t, p, b and α:

$$\sigma_z = p - t\left[\frac{2b-1}{3} - \cos 2\alpha\right] \tag{4.75}$$

$$\sigma_r = p - t\left[\frac{2(1-2b)}{3}\right] \tag{4.76}$$

$$\sigma_\theta = p - t\left[\frac{2b-1}{3} + \cos 2\alpha\right] \tag{4.77}$$

$$\tau_{z\theta} = t \sin 2\alpha \tag{4.78}$$

where:

$p = (\sigma_1 + \sigma_2 + \sigma_3)/3$ is the mean total stress, $t = (\sigma_1 - \sigma_3)/2$ is half of the deviator stress, $b = (\sigma_2 - \sigma_3)/(\sigma_1 - \sigma_3)$ is the parameter controlling the intermediate principal stress and

α is the angle of the major principal stress direction with respect to the vertical.

An eight nodded isoparametric brick element (with a node at each corner) was used to simulate the behaviour in the HCA. The first stress path simulated is an undrained stress path that started from normally consolidated conditions with $p = p' = 200$ kPa, $t = 75$ kPa ($J = 75$ kPa), $b = 0.5$ and $\alpha = 0^\circ$ (point A in Figure 4.24). The first stage of the test involved undrained unloading to $t = 45$ kPa ($J = 45$ kPa) (i.e. point B), keeping b and α constant. The second stage involved undrained rotation of the major principal stress direction from 0° to 30° at constant t and b. Finally an undrained shearing stage followed in which t was increased monotonically to failure while keeping α and b constant at 30° and 0.5 respectively. The mean total stress, p, was kept throughout the whole test constant and equal to 200 kPa.

This first stress path was simulated using both the two-surface model and the modified Cam Clay model. The parameters used in the two-surface model are those quoted in Table 4.2. The modified Cam Clay analysis was obtained by using the two-surface model but with the size of the kinematic yield surface equal to the size of the bounding surface, $R = 1.0$, and the rest of the parameters equal to the values given in Table 4.2.

Figure 4.24 shows the predicted stress paths in J-p' space. It can be seen that the modified Cam Clay model does not predict any plastic strains for the principal stress

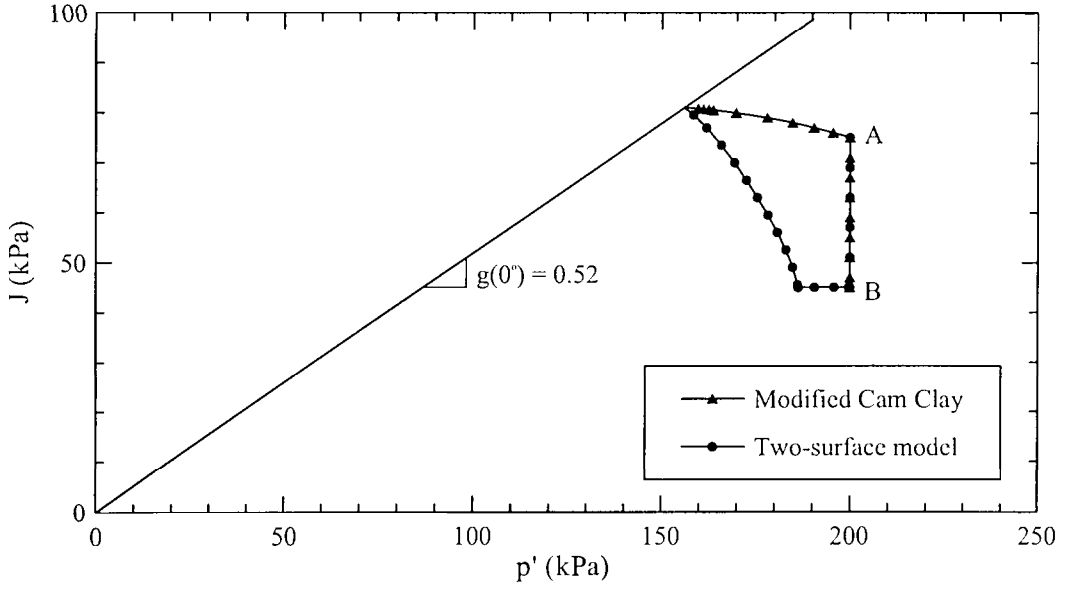


Figure 4.24: Predictions of hollow cylinder stress paths involving: undrained unloading, undrained rotation of the principal stresses ($\alpha = 30^\circ$) and undrained shearing to failure at constant $b = 0.5$

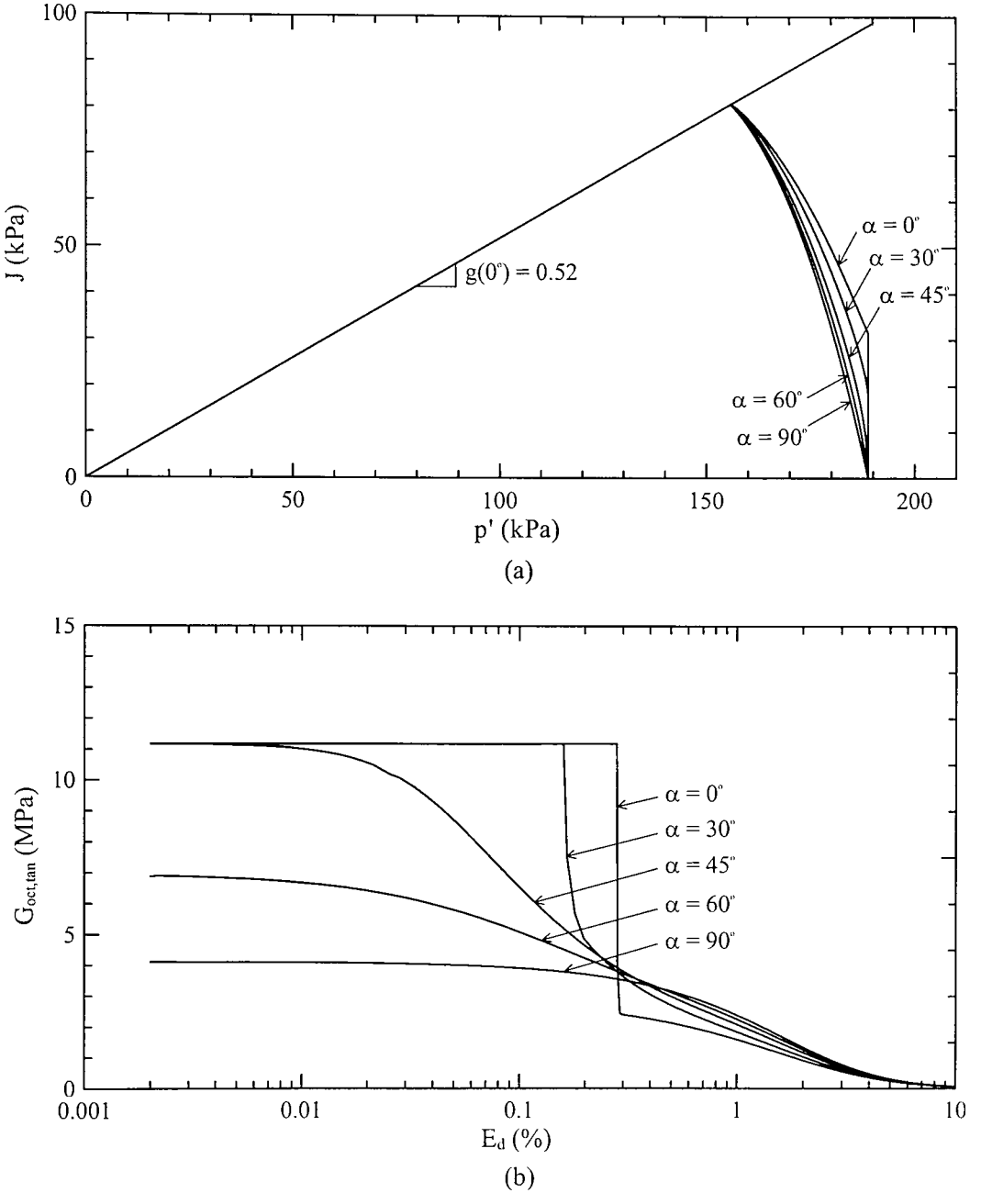


Figure 4.25: Predictions of undrained shearing stage at constant α and $b = 0.5$ a) stress paths b) stiffness-strain curves

rotation stage, which is not surprising since it is an isotropic model. On the contrary, the two-surface model does predict plastic strains during this stage and demonstrates in this way anisotropic behaviour. However, the undrained shearing stage that follows shows that the same ultimate conditions are obtained from both models. This confirms the fact that the two-surface model has anisotropic yielding but isotropic strength governed by the isotropic bounding surface.

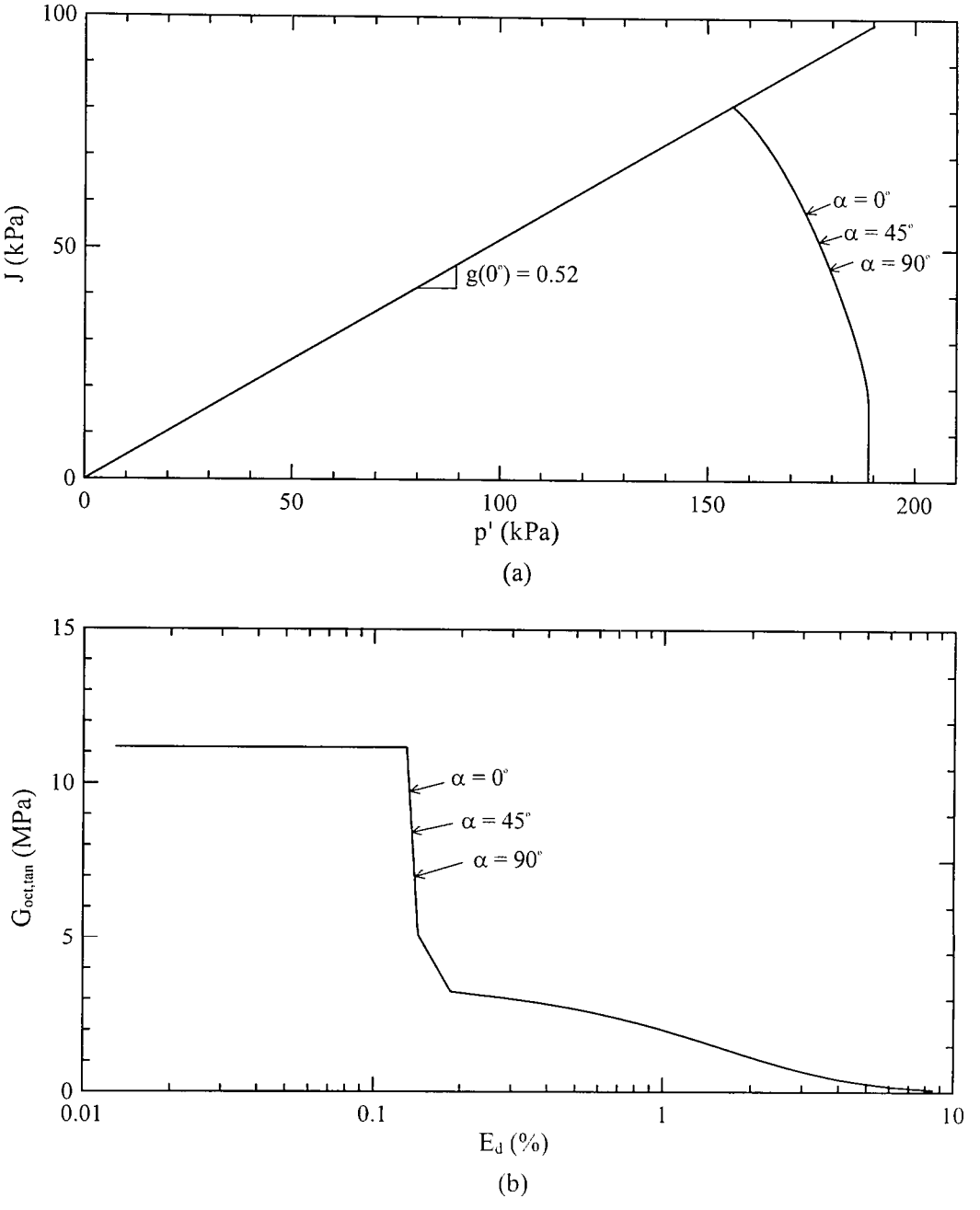


Figure 4.26: Predictions of undrained shearing stage at constant α and $b = 0.5$ and the kinematic yield surface centred around the current stress state at the beginning of shearing a) stress paths b) stiffness-strain curves

In order to investigate the stiffness anisotropy of the two-surface model a similar stress path to the one described above was undertaken. In this case the first undrained stage involved complete unloading of the sample. At $t = 0$ ($J = 0$) undrained rotation of the principal stresses does not apply any loading on the sample. The following undrained shearing stage was repeated for a number of different values of α. The resulting stress paths in J-p' space can be seen in Figure 4.25a and the corresponding plots of tangent stiffness in general stress space $G_{oct} = \mathrm{d}J/\mathrm{d}E_d$ versus shear strain E_d can be seen in Figure

4.25b. Figure 4.25a shows that the model predicts different stress paths depending on the rotation angle α. The lower the angle α is the stiffest the stress path seems to be. Inspection of Figure 4.25b reveals that the highest initial stiffness is observed for $\alpha = 0^\circ$ whereas the lowest stiffness is observed for $\alpha = 90^\circ$. More specifically the stiffness degradation curves corresponding to $\alpha = 0^\circ$, 30° and 45° show an elastic plateau, which is smaller the higher the value of α is, whereas the curves corresponding to $\alpha = 60^\circ$ and 90° initiate from gradually lower stiffness values. This is due to the fact that as the angle α increases, the corresponding stress path changes from a complete stress reversal to the previous stress path direction (for $\alpha = 0^\circ$) to a complete continuation of the previous stress path direction (for $\alpha = 90^\circ$). (It should be noted that $\alpha = 0^\circ$ corresponds to a compression path, whereas $\alpha = 90^\circ$ corresponds to an extension path). Hence, this anisotropy in stiffness is attributed to the position of the kinematic yield surface relative to the stress state at the start of shearing.

The last undrained shearing stage of this stress path was then repeated, with the only difference that the kinematic yield surface was centred around the current stress state (and hence around the isotropic axis) before the beginning of shearing. The resulting stress paths and stiffness degradation curves can be seen in Figure 4.26. It can be seen that the model predicts the same response irrespective of the angle α. This isotropic behaviour is attributed to the fact that the kinematic yield surface is centred around the isotropic axis. (As it will be shown in Chapter 7, for a stress path initiating from $K_o \neq 1.0$, the stiffness predicted by the model, once yielding is initiated, is anisotropic even if the kinematic surface is centred around the current stress state).

4.6.5 Elasto-plastic transition

As it has already been discussed in section 4.6.2 the form of the hardening function chosen is such that the model does not predict a smooth elasto-plastic transition when the stress state reaches the kinematic yield surface and the behaviour changes from elastic to elasto-plastic. This can be seen as kinks in the stress paths shown in Figures 4.10b-c and 4.11b-c. It can also be seen as kinks in Figure 4.25a, in the stress paths corresponding to $\alpha = 0^\circ$ and 30°, and as a drop in stiffness in Figure 4.25b, for the same values of α.

This feature of behaviour may not be very important for the reason that the two-surface model was originally developed, which is the prediction of slow cyclic behaviour. In this case one is interested in reproducing the overall patterns of behaviour, rather than, for

N	λ^*	κ^*	A	n	m	φ'	Y_p	Z_p	R
3.43	0.097	0.003	590.0	0.87	0.28	22.5°	0.0	1.0	0.016

Table 4.7: Material parameters used in the current version of the two-surface model for the simulation of the triaxial test in Figure 4.27

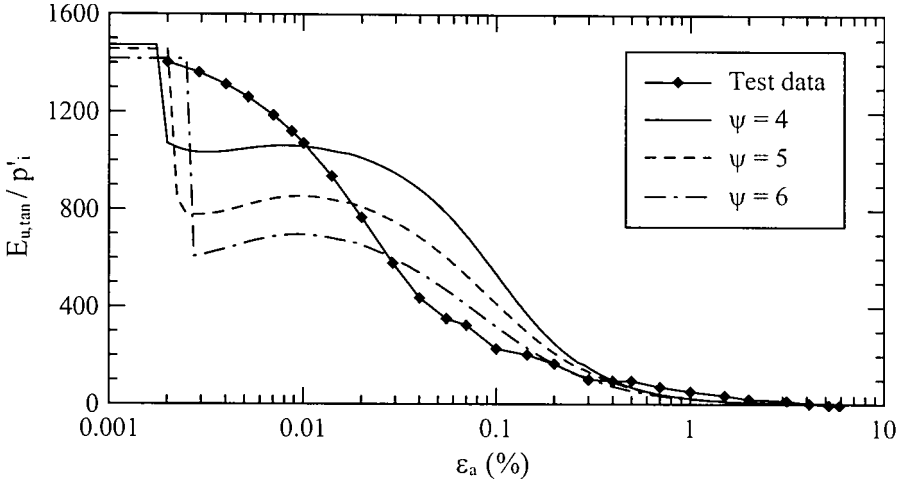


Figure 4.27: Normalised stiffness-strain curve (p'_i is the mean effective stress at the start of shearing) for an undrained triaxial compression test on overconsolidated reconstituted London Clay (experimental results after Jardine (1985))

example, just accurately predicting the first cycle. However, if the model is to be used in modelling the pre-failure behaviour of overconsolidated clays, then this abrupt elasto-plastic transition is an important drawback in simulating accurately the highly non-linear stiffness degradation with strain. Figure 4.27 shows the predictions of the two-surface model for an undrained triaxial compression test on reconstituted London Clay. Before shearing, the sample was one-dimensionally compressed and then swelled to an overconsolidation ratio, *OCR*, of 7. This is one of the tests repeated in Chapter 7 and will not be discussed here in great detail (the experimental data is taken from Jardine (1985)). The model parameters used are given in Table 4.7. It should be noted that Al-Tabbaa (1987) used a much bigger size of the kinematic yield surface in order to reproduce the cyclic behaviour of the speswhite kaolin than was used here in order to simulate the extend of the assumed elastic plateau of the pre-failure behaviour of reconstituted London Clay. Figure 4.27 shows that the drop in stiffness predicted by the two-surface model makes it difficult to reproduce the observed non-linear stiffness degradation with strain in the small strain range. Therefore, it seems that, while the hardening function chosen in the model may predict satisfactorily cyclic behaviour, it cannot simulate

realistically the highly non-linear behaviour of overconsolidated clays. Moreover, as discussed in Chapter 2, since the amount of straining that the ground is subjected to falls within the small strain range, it is important that within this strain range the pre-failure behaviour is modelled accurately. Al-Tabbaa (1987) noted that the hardening function chosen in the model is not unique and could be modified. This is attempted in Chapter 6 where a new hardening function is adopted for the two-surface model, so that more realistic predictions of the stiffness curves in the small strain range can be obtained.

4.7 Summary

This chapter was divided into five parts. The first part described briefly the modified Cam Clay model, which forms the basis of the two-surface model, developed by Al-Tabbaa (1987). The description of the original formulation of the two-surface model followed in the second part of the chapter. The two-surface model introduces a single kinematic yield surface within the modified Cam Clay bounding surface. This allows the simulation of non-linearity and early yielding for stress paths within the bounding surface, which are important aspects of the pre-failure behaviour of overconsolidated clays. The model requires seven parameters, five of which are based on the modified Cam Clay model. A discussion at the end of this second part, concerning the formulation of the model, showed that for the special case that the two surfaces are in contact, the translation rule assumed in the model cannot ensure that the two surfaces remain in contact for any further loading. However, the assumption of a different translation rule would not be consistent with the derivation of the hardening function for that special case.

The original formulation of the two-surface model applied only to triaxial stress conditions. In order to implement a constitutive model into a finite element program, this has to be formulated in general stress space. The generalisation of the two-surface model and the improvements that have been made to the model as part of this work were described in the third part of the chapter. The model has an anisotropic general formulation; it is formulated in terms of the volumetric and deviatoric components of the stress and strain tensors. This is because yielding in the model can be anisotropic, although the strength predicted is isotropic. An improvement made in this general formulation of the model is that the yield and plastic potential surfaces (and hence the failure surface) are not necessarily circular in the deviatoric plane but can take a number of different shapes, simulating in this way more realistic failure conditions. Moreover,

an additional improvement is that a different translation rule has been assumed for the case that the two surfaces are in contact so that they remain in contact for any further loading. The way the resulting inconsistency was dealt with was to change the active yield surface from the kinematic yield surface to the bounding surface when the two surfaces are in contact and this was discussed in detail in this third part of the chapter.

The implementation of the above general formulation of the two-surface model into ICFEP was subsequently described in the fourth part. In the finite element method the constitutive model influences both the formulation and solution of the global equations. This was discussed in this part of the chapter and the calculation of the terms required in the implementation of the model was presented.

Finally, the last part of the chapter presented the validation of the version of the two-surface model implemented into ICFEP through a series of single finite element analyses. This involved the following: Firstly, a number of stress paths simulated by Al-Tabbaa (1987) were repeated and the results were compared with the already published data. Secondly, different shapes of the yield and plastic potential surfaces in the deviatoric plane were explored and the failure conditions obtained were validated through comparison with analytical calculations. Thirdly, the anisotropic performance of the model was demonstrated in a number of stress paths involving rotation of the principal stresses. Finally, the elasto-plastic transition predicted by the two-surface model was discussed. It was shown that the hardening modulus assumed in the model results in a non-smooth elasto-plastic transition when the stress state reaches the kinematic yield surface. Although this may not be very important in the simulation of cyclic behaviour (for which the model was originally developed), it proves a significant drawback in the simulation of pre-failure behaviour. However, since the hardening modulus is not unique and could be altered, a new hardening modulus is assumed for the two-surface model in Chapter 6. Further evaluation of the current version of the two-surface model is presented in Chapter 7.

Chapter 5

Three-surface model

5.1 Introduction

As mentioned in Chapter 4, the second model chosen to be implemented into ICFEP is the three-surface model proposed by Stallebrass (1990). In order to simulate both non-linearity and the effect of recent stress history on the behaviour of reconstituted overconsolidated clays, Stallebrass (1990) extended the two-surface model developed by Al-Tabbaa (1987) by incorporating an additional kinematic surface. The first kinematic surface in the three-surface model is a yield surface, which defines the onset of plastic deformations (similarly to the two-surface model). The second kinematic surface defines the end of the influence of recent stress history and hence is named the history surface. The model requires one additional parameter to the seven required by the two-surface model.

This chapter starts with the description of the original formulation of the three-surface model, as developed by Stallebrass (1990), in section 5.2. Similarly to the two-surface model, the three-surface model was originally developed in triaxial stress space. The formulation of the model in general stress space and the improvements made during this thesis are presented in section 5.3. Section 5.4 presents the implementation of the general formulation of the model into ICFEP. The validation of the implementation of the model, through a number of single finite element analyses, is described in section 5.5. Further evaluation of the three-surface model follows in Chapter 7.

5.2 Original formulation in triaxial stress space

5.2.1 Introduction

This section describes the formulation of the three-surface model in triaxial stress space as originally presented by Stallebrass (1990). The model is formulated in terms of the triaxial stress and strain invariants described by Equations 1.23-1.26.

5.2.2 Equations of the surfaces

The modified Cam Clay yield surface is used in order to represent the bounding surface in this model. The equation of the bounding surface is:

$$\left(p' - p'_o\right)^2 + \frac{q^2}{M^2} = p'^2_o \tag{5.1}$$

where p'_o represents half the value of the mean effective stress at the intersection of the current swelling line with the isotropic compression line and M is the slope of the critical state line in q-p' space, see Figure 5.1.

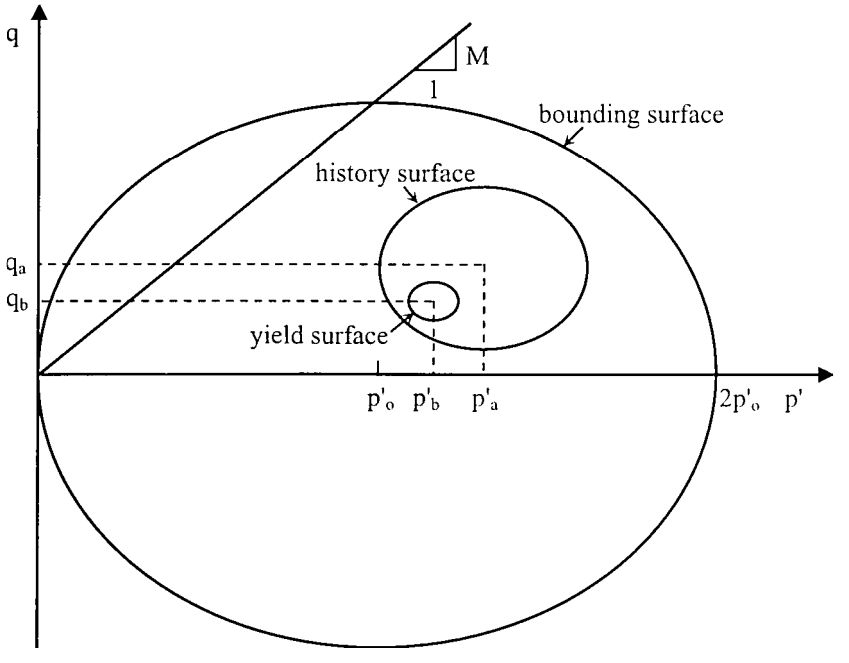


Figure 5.1: Diagram showing the yield, history and bounding surfaces (after Stallebrass (1990))

The two inner kinematic surfaces are similar in shape to the bounding surface but smaller in size by constant ratios. The equation of the history surface, which represents the limit of the influence of recent stress history, is:

$$(p' - p'_a)^2 + \frac{(q - q_a)^2}{M^2} = T^2 p'^2_o \tag{5.2}$$

where T is the ratio of the size of the history surface to that of the bounding surface and (p'_a, q_a) represents the centre of the history surface, see Figure 5.1.

The yield surface, which defines the region in stress space within which only elastic behaviour occurs, is represented by the following equation:

$$(p' - p'_b)^2 + \frac{(q - q_b)^2}{M^2} = T^2 S^2 p'^2_o \tag{5.3}$$

where S is the ratio of the size of the yield surface to that of the history surface and (p'_b, q_b) is the centre of the yield surface in stress space.

5.2.3 Flow rule

The flow rule of the model is assumed to be associated and therefore the plastic potential surface is described by Equation 5.3.

5.2.4 Hardening rules

The bounding surface follows an isotropic hardening rule, as in the two-surface model. The inner kinematic surfaces follow translation rules which control their movement as these are dragged by the current stress state. For a monotonic stress path starting within the yield surface, the behaviour is initially elastic and remains elastic as long as the stress path stays within the yield surface. As soon as the stress state touches the yield surface the behaviour becomes elasto-plastic and the yield surface is dragged along the stress path, approaching the history surface. As long as the stress state remains on the yield surface and within the history surface, the history surface expands or contracts isotropically. When the yield surface touches the history surface then both surfaces are dragged along the stress path moving towards the bounding surface.

Stallebrass (1990) realised that the single translation rule employed by Al-Tabbaa (1987)

guaranteed that the surfaces came in contact tangentially and never intersected, but did not make sure that when the surfaces did come in contact they also remained in contact for any further loading, as already discussed in section 4.3.8. Consequently, the translation rules of each surface, in the three-surface model, are divided into two expressions: the first one is similar to that adopted by Al-Tabbaa (1987) and controls the movement of a surface when it is translating within another surface, the second one controls the movement of a surface which is in contact with one or more surfaces.

5.2.4.1 Isotropic hardening of the bounding surface

The model adopts the volumetric hardening rule of the modified Cam Clay model, in which the change in size of the bounding surface is controlled by the change in plastic volumetric strain:

$$\frac{dp'_o}{p'_o} = \frac{d\varepsilon_v^p}{\lambda^* - \kappa^*} \tag{5.4}$$

As in the two-surface model, the parameters λ^* and κ^* represent the slope of the isotropic normal compression line and the slope of the swelling line, for an unloading path lying entirely within the kinematic yield surface, in ln$v$-lnp' space.

5.2.4.2 Translation rules for the history surface

The two translation rules that govern the movement of the history surface are the following:

i) Translation rule for the history surface when it is moving within the bounding surface

When the current stress state is on the history surface the translation rule for this surface when it is moving within the bounding surface is given by an equation similar to the one adopted by Al-Tabbaa (1987):

$$\begin{Bmatrix} dp'_a \\ dq_a \end{Bmatrix} = \frac{dp'_o}{p'_o} \begin{Bmatrix} p'_a \\ q_a \end{Bmatrix} + W \begin{Bmatrix} \frac{p' - p'_a}{T} - (p' - p'_o) \\ \frac{q - q_a}{T} - q \end{Bmatrix} \tag{5.5}$$

This translation rule is a combination of isotropic and kinematic hardening and therefore can be divided into two components. The first one represents the expansion or

contraction of the history surface due to isotropic expansion or contraction of the bounding surface. The second represents the translation along a vector, β, which joins the current stress state A with the equivalent conjugate point on the bounding surface A_c, see Figure 5.2. The scalar quantity W can be obtained by substituting dp'_a and dq_a from Equation 5.5 into the consistency condition for the history surface and using Equation 5.2:

$$W = \frac{(p'-p'_a)\left(dp' - \frac{dp'_o}{p'_o}p'\right) + \frac{q-q_a}{M^2}\left(dq - \frac{dp'_o}{p'_o}q\right)}{(p'-p'_a)\left[\frac{p'-p'_a}{T} - (p'-p'_a)\right] + \frac{q-q_a}{M^2}\left(\frac{q-q_a}{T} - q\right)} \tag{5.6}$$

When the current stress state is inside the history surface the surface will still move to allow for the expansion or contraction of the bounding surface. In this case the movement of the history surface is just given by the first part of Equation 5.5:

$$\begin{Bmatrix} dp'_a \\ dq_a \end{Bmatrix} = \frac{dp'_o}{p'_a}\begin{Bmatrix} p'_a \\ q_a \end{Bmatrix} \tag{5.7}$$

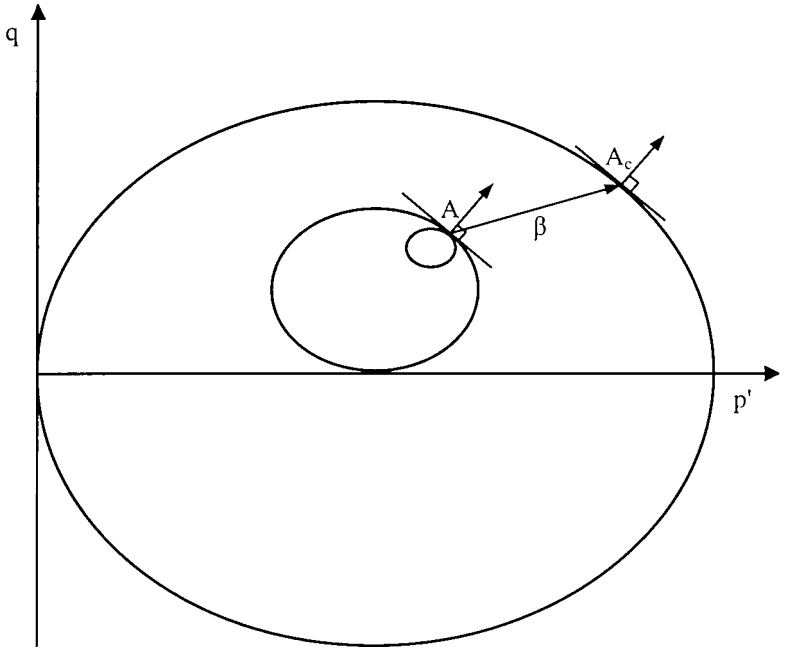


Figure 5.2: Diagram illustrating the definition of a conjugate point and the translation of the history surface along the vector β (after Stallebrass (1990))

ii) Translation rule for the history surface when it is in contact with the bounding surface

When the history surface is in contact with the bounding surface the translation rule that is employed ensures that the surfaces remain tangential for any subsequent loading:

$$\begin{Bmatrix} dp'_a \\ dq_a \end{Bmatrix} = (1-T)\begin{Bmatrix} dp' \\ dq \end{Bmatrix} + T\begin{Bmatrix} dp'_o \\ 0 \end{Bmatrix} \tag{5.8}$$

5.2.4.3 Translation rules for the yield surface

The following two translation rules govern the movement of the yield surface:

i) Translation rule for the yield surface when it is moving within the history surface

The translation rule adopted is of a similar form to Equation 5.5:

$$\begin{Bmatrix} dp'_b \\ dq_b \end{Bmatrix} = \frac{dp'_o}{p'_o}\begin{Bmatrix} p'_b \\ q_b \end{Bmatrix} + Z\begin{Bmatrix} \frac{p'-p'_b}{S} - (p'-p'_a) \\ \frac{q-q_b}{S} - (q-q_a) \end{Bmatrix} \tag{5.9}$$

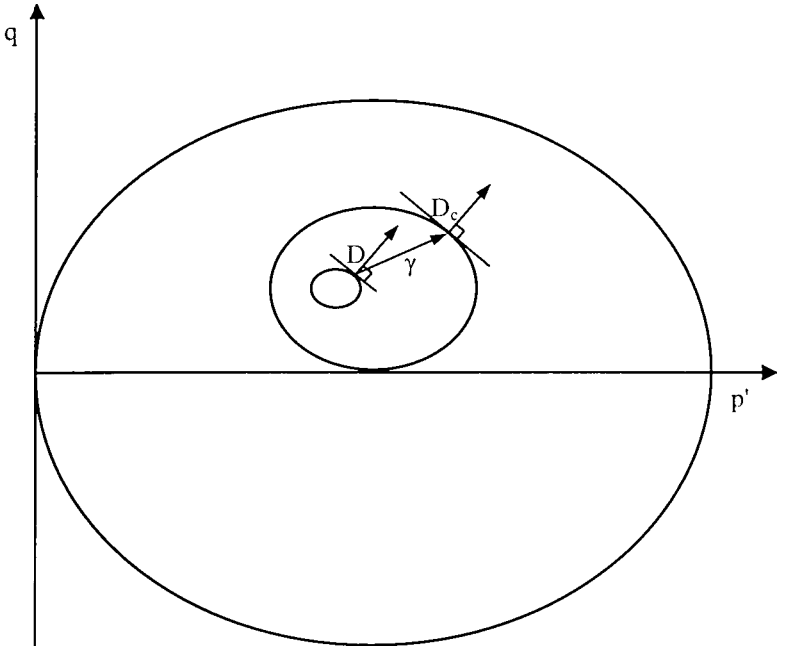


Figure 5.3: Diagram illustrating the definition of a conjugate point and the translation of the yield surface along the vector γ (after Stallebrass (1990))

Similar to Equation 5.5, Equation 5.9 can be divided in two parts. The first part governs the expansion/contraction of the yield surface due to isotropic expansion/contraction of the bounding surface and the second governs the translation of the yield surface along a vector, γ, joining the current stress state, D, to its conjugate point D_c, on the history surface (Figure 5.3). The scalar quantity Z can be derived by employing the consistency condition for the yield surface.

$$Z = \frac{(p'-p'_b)\left(dp' - \frac{dp'_o}{p'_o}p'\right) + \frac{q-q_b}{M^2}\left(dq - \frac{dp'_o}{p'_o}q\right)}{(p'-p'_b)\left[\frac{p'-p'_b}{S} - (p'-p'_a)\right] + \frac{q-q_b}{M^2}\left[\frac{q-q_b}{S} - (q-q_a)\right]} \tag{5.10}$$

ii) Translation rule for the yield surface when it is in contact with the history surface

When the yield surface is in contact with the history surface the translation rule becomes:

$$\begin{Bmatrix} dp'_b \\ dq_b \end{Bmatrix} = (1-S)\begin{Bmatrix} dp' \\ dq \end{Bmatrix} + S\begin{Bmatrix} dp'_a \\ dq_a \end{Bmatrix} \tag{5.11}$$

5.2.5 Hardening modulus

The hardening modulus is formulated in the same way as for the two-surface model. It is initially formulated for the special case that all three surfaces are in contact and then modified for all the other cases that the surfaces are not in contact and the stress state is within the bounding surface. For these cases the hardening modulus depends on the degree of approach of the yield surface to the history surface and the degree of approach of the history surface to the bounding surface and reduces to the value of the hardening modulus on the bounding surface when all three surfaces are in contact.

The expression for the calculation of the plastic strain increments on the yield surface, when all three surfaces are in contact, is the following:

$$\begin{Bmatrix} d\varepsilon_v^p \\ d\varepsilon_s^p \end{Bmatrix} = \frac{1}{h_o}\begin{bmatrix} (p'-p'_b)^2 & (p'-p'_b)\frac{q-q_b}{M^2} \\ (p'-p'_b)\frac{q-q_b}{M^2} & \left(\frac{q-q_b}{M^2}\right)^2 \end{bmatrix}\begin{Bmatrix} dp' \\ dq \end{Bmatrix} \tag{5.12}$$

where the hardening function h_o is given by an expression similar to the one employed in

the two-surface model:

$$h_o = \frac{p' - p'_b}{\lambda^* - \kappa^*}\left[p'\left(p' - p'_b\right) + \frac{q\left(q - q_b\right)}{M^2} \right] \tag{5.13}$$

When all three surfaces are in contact Equation 5.12 predicts the same plastic strain increments as those calculated by the modified Cam Clay model (Equation 4.3), since in this case $(p' - p'_b)/TS = (p' - p'_o)$ and $(q - q_b)/TS = q$. Stallebrass (1990) noted that the above expression of the hardening function, h_o, cannot be derived from the consistency condition of the yield surface when all surfaces are in contact and hence is not consistent with the translation rules for this special case. This inconsistency of the model will be discussed in further detail later.

Following Al-Tabbaa (1987) the function h_o in Equation 5.12 is replaced with a more general expression of the form:

$$h = h_o + H_1 + H_2 \tag{5.14}$$

where h_o is given by Equation 5.13, H_1 is a function of the degree of approach of the history surface to the bounding surface and H_2 is a function of the degree of approach of the yield surface to the history surface.

Similar to Al-Tabbaa (1987) a number of restrictions were introduced on the values that H_1 and H_2 could take. First of all for $\eta < M$, where instability had not been observed, $h_o + H_1 + H_2$ had to be greater than zero. Then when all three surfaces are in contact $H_1 + H_2 = 0$ so that they all predict the same strains. Moreover when the stress point lies on the history and yield surfaces and within the bounding surface $H_2 = 0$, so that the two surfaces in contact predict the same strains. Finally the plastic strains had to be lowest on the yield surface, therefore H_2 was required to be greater or equal to zero; and greatest on the bounding surface, hence H_1 was required to be greater or equal to zero.

The above criteria were fulfilled by linking H_1 and H_2 to the position of the yield and history surfaces respectively. The measure of the degree of approach of the history surface to the bounding surface used in the model, b_1, is the scalar product of the vector β and a vector normal to the history surface, n_h, at the conjugate stress point (p'_s, q_s), see Figure 5.4, divided by a measure of the size of the history surface:

$$b_1 = \frac{1}{Tp'_o}\left[\frac{p'-p'_b}{S}\left[\frac{p'-p'_b}{TS}-\left(\frac{p'-p'_b}{S}+p'_a-p'_o\right)\right]+\frac{q-q_b}{SM^2}\left[\frac{q-q_b}{ST}-\left(\frac{q-q_b}{S}+q_a\right)\right]\right] \tag{5.15}$$

Similarly the measure of the proximity of the yield surface to the history surface, b_2, is the scalar product of the vector, γ, and a vector normal to the yield surface at the current stress state, n_γ, see Figure 5.4, divided by a measure for the size of the yield surface:

$$b_2 = \frac{1}{STp'_o}\left[\left(p'-p'_b\right)\left[\frac{p'-p'_b}{S}-\left(p'-p'_a\right)\right]+\frac{q-q_b}{M^2}\left[\frac{q-q_b}{S}-\left(q-q_a\right)\right]\right] \tag{5.16}$$

The functions b_1 and b_2 take their maximum values when the surfaces are in the configuration shown in Figure 5.5. These maximum values are:

$$b_{1\max} = 2p'_o\left(1-T\right) \tag{5.17}$$

$$b_{2\max} = 2Tp'_o\left(1-S\right) \tag{5.18}$$

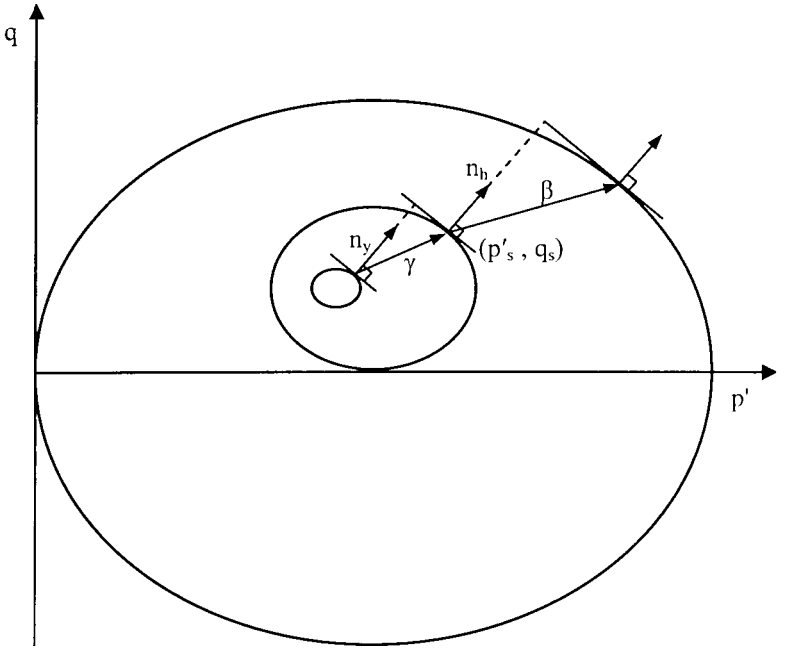


Figure 5.4: Diagram defining the main components of the parameters b_1 and b_2 (after Stallebrass (1990))

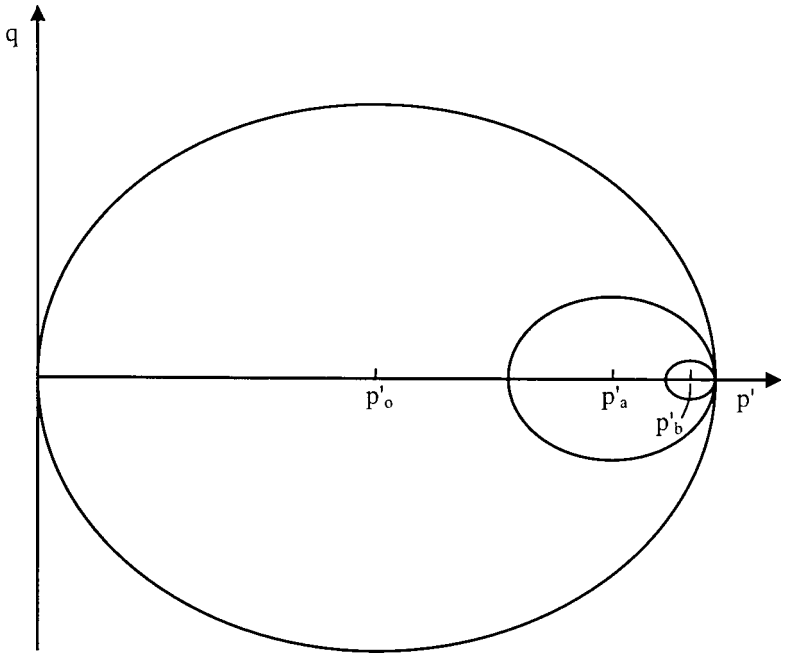


Figure 5.5: Diagram showing the position of the surfaces when b_1 and b_2 are at a maximum (after Stallebrass (1990))

Stallebrass (1990) adopted the following functions for H_1 and H_2:

$$H_1 = \frac{1}{\lambda^* - \kappa^*}\left(\frac{b_1}{b_{1\max}}\right)^{\psi}\left(p'_o\right)^3 S^2 \tag{5.19}$$

$$H_2 = \frac{1}{\lambda^* - \kappa^*}\left(\frac{Tb_2}{b_{2\max}}\right)^{\psi}\left(p'_o\right)^3 \tag{5.20}$$

where ψ is an exponent which controls the rate of decay of stiffness.

Therefore the resulting hardening function is:

$$h = \frac{1}{\lambda^* - \kappa^*}\left[\left(p' - p'_b\right)\left[p'\left(p' - p'_b\right) + \frac{q\left(q - q_b\right)}{M^2}\right] + \left(\frac{b_1}{b_{1\max}}\right)^{\psi}\left(p'_o\right)^3 S^2 + \left(\frac{Tb_2}{b_{2\max}}\right)^{\psi}\left(p'_o\right)^3\right] \tag{5.21}$$

It can be shown that when the yield and history surfaces are in contact, $b_2 = 0$ and $H_2 = 0$ and the model predicts the same plastic strain increments as the two-surface model for the case that the kinematic surface moves within the bounding surface.

5.2.6 Elastic part of the model

As in the two-surface model, the elastic bulk modulus, K_e, is equal to:

$$K_e = \frac{p'}{\kappa^*} \tag{5.22}$$

For the calculation of the elastic shear strains an elastic shear modulus G_e is assumed. Therefore the elastic strain increments are the following:

$$\begin{Bmatrix} d\varepsilon_v^e \\ d\varepsilon_s^e \end{Bmatrix} = \begin{bmatrix} \frac{1}{K_e} & 0 \\ 0 & \frac{1}{3G_e} \end{bmatrix} \begin{Bmatrix} dp' \\ dq \end{Bmatrix} \tag{5.23}$$

where the elastic bulk modulus, K_e, is given by Equation 5.22 and the elastic shear modulus, G_e, is an input parameter.

5.2.7 Model parameters

The three surface model is defined by eight parameters:

λ^*: the slope of the isotropic normal compression line in ln$v$-lnp' space

κ^*: the slope of the swelling line in ln$v$-lnp' space for a stress path that lies entirely within the kinematic yield surface

G_e: the elastic shear modulus

M: the slope of the critical state line in q- p' space

T: the ratio of the size of the history surface to that of the bounding surface

S: the ratio of the size of the yield surface to that of the history surface

ψ: the exponent in the hardening function H

N: one additional parameter is required to fix the model in ln$v$-lnp' space and this is usually taken as the specific volume of the isotropic compression line at p' = 1KPa

The parameters, λ^*, κ^*, M and N have the same definition as in the two-surface model

and can therefore be derived in the same way. The elastic shear stiffness, G_e, can be estimated from the start of a constant p' shearing test following a complete stress reversal, if strain measurements can be made with sufficient accuracy. Alternatively, this can be determined from dynamic measurements. The parameters S and T can be estimated from two isotropic stress paths in which the same loading stage is repeated for two different stress histories, one with $\theta_r = 0°$ and the other with $\theta_r = 180°$, where θ_r is

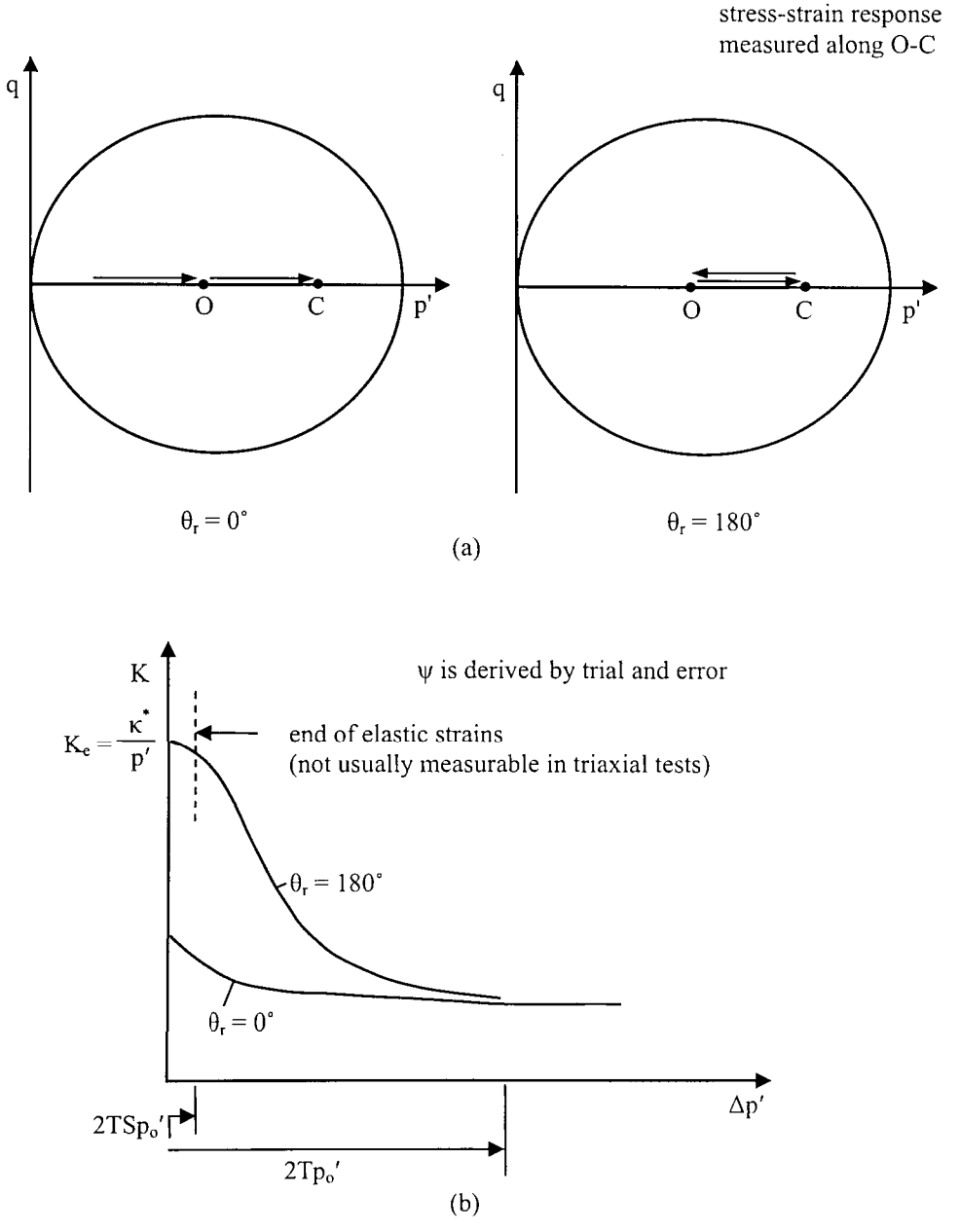


Figure 5.6: Sketch showing a) isotropic stress paths required to determine values for the parameters T and S b) typical stiffness plots from which T and S can be estimated (after Stallebrass (1990))

used to denote here the angle between the approaching and loading paths, see Figure 5.6a. In Figure 5.6b the bulk modulus, K, is plotted against $\Delta p'$, for two such tests. (The initial values of K for $\theta_r = 180^\circ$ give an estimate of the parameter κ^*). The parameter S can be calculated from the stress change for which strains are elastic. Stallebrass (1990) noted that since the elastic region is generally difficult to measure, it is advisable to check this against shear stiffness curves. The stress change at which the two stiffness curves seem to converge can be assumed to define the end of the extent of the effect of recent stress history and can be used to estimate the parameter T. Again it is suggested that this is checked against shear stiffness curves. Finally the parameter ψ cannot be measured directly and its value has to be derived from parametric studies.

5.2.8 Discussion

As mentioned before, the expression for the hardening function, h_o, given by Equation 5.13 is not consistent with the rule that describes the translation of the surfaces when they are in contact, given by Equations 5.8 and 5.11. This ultimately leads to the non-satisfaction of the consistency condition of the yield surface when all three surfaces are in contact. Moreover when the yield and history surfaces are in contact the resulting hardening function, $h = h_o + H_1$ ($H_2 = 0$ in this case), is not consistent with the translation rule of the yield surface when this is in contact with the history surface, given by Equation 5.8. This would lead to the non-satisfaction of the consistency condition of the yield surface in the case that the yield and history surfaces are in contact. Stallebrass (1990) noted that further work is required in order to derive a more consistent version of either the translation rule or the hardening function. In the next section, which describes the formulation of the model in general stress space, it will be shown that in order to make the model consistent it is not necessary to derive a new expression of either the translation rule or the hardening function, but it is sufficient to adopt the same concept of changing the current active yield surface as in the general formulation of the two-surface model.

It is interesting to note that, as already discussed in section 5.2.5, the interpolation rule of the model reduces to the interpolation rule of the two-surface model, when the yield and history surfaces are in contact. This implies that the same argument of Gajo and Muir Wood (2001) for the two-surface model is also valid for the three-surface model. According to their argument, since the incremental response tends asymptotically to the response on the bounding surface, then the yield and history surfaces can never actually come in contact with the bounding surface. If this is true then there is no need to have

different translation rules for the yield and history surfaces for the case that all three surfaces are in contact. However, similar to the two-surface model, for normally consolidated states which start on the bounding surface, and for which the three-surfaces are in contact, it is still necessary to have different translations rules, which ensure that the three surfaces remain in contact for further loading.

Moreover, one could argue that the same situation applies in the case that the yield surface moves within the history surface, since when $b_2 = 0$ the hardening modulus reduces to the hardening modulus of the two-surface model. This would then imply that the yield and history surfaces cannot actually come in contact. However, this is not true since the behaviour of the three-surface model reduces to the behaviour of the two-surface model for the case that the history surface translates within the bounding surface according to Equation 5.5 and not for the case that the history surface expands or contracts isotropically according to Equation 5.7.

5.3 Formulation in general stress space

5.3.1 Introduction

In order to implement the three-surface model into a finite element program, like ICFEP, it has to be formulated in general stress space. This section describes the extension of the three-surface model from triaxial to general stress space.

5.3.1.1 Stress and strain variables

Similarly to the two-surface model the three-surface model can predict anisotropic yielding depending on the position of the yield and history surfaces, although the strength predicted by the model is isotropic, since this is governed by the isotropic bounding surface. Stallebrass and Taylor (1997) carried out the first generalisation of the model in which q in the triaxial formulation was replaced by the deviatoric stress tensor $\boldsymbol{s}$. This is equivalent to formulating the model in terms of the volumetric and deviatoric components of the stress and strain tensors, described by Equations 1.2-1.4 and 1.14-1.17 and already used in the general formulation of the two-surface model.

5.3.1.2 Yield and plastic potential surfaces in the deviatoric plane

In the first generalisation of the three-surface model, Stallebrass and Taylor (1997), assumed a circular shape of the yield and plastic potential surfaces in the deviatoric plane. However, as mentioned before, the circular shape in the deviatoric plane overestimates the strength in triaxial extension and does not represent satisfactorily the failure conditions of the soil. In the current formulation of the model in general stress space, this feature of the model has been improved. The yield surface can take either the shape of a Mohr Coulomb hexagon or the general shape proposed by van Eekelen (1980), which, depending on the chosen values of the input parameters, can take different shapes in the deviatoric plane, including the shape proposed by Lade (Lade and Duncan (1975)) and a circular shape. The plastic potential surface can take the general shape suggested by van Eekelen (1980).

5.3.1.3 Concept of changing the active yield surface

In this general formulation of the three-surface model the same concept of changing the current active yield surface every time the surfaces come in contact, as in the two-surface model, was adopted. This can be explained as follows; when the stress state is on the yield surface and this moves within the history surface, then the yield surface is the active yield surface and the plastic potential and hardening modulus associated with this surface apply. When the yield surface comes in contact with the history surface and both of them move within the bounding surface, then the history surface becomes the active yield surface, the plastic potential and hardening modulus associated with this surface apply and the model reduces to the general formulation of the two-surface model. In this case the yield surface is inactive and is just dragged by the current stress state. Finally, when all three surfaces are in contact, the bounding surface becomes the current active yield surface, the plastic potential and hardening modulus associated with this surface apply and the model reduces to the modified Cam Clay model. In this case the yield and history surfaces are inactive and are just dragged by the current stress state. When the stress path direction changes so that the stress state re-enters the yield and history surfaces, then the yield surface becomes the active yield surface, until this comes in contact with the history surface, in which case the latter becomes the active yield surface and the inactive yield surface is again just dragged by the current stress state. This concept of changing the current active yield surface was found to be the solution to the problem of the inconsistent hardening modulus and translation rules discussed in section

5.2.8 and will become clearer in the course of this section.

5.3.2 Equations of the surfaces

The equation of the bounding surface is formulated in general stress space as follows:

$$F_b = \left(p' - \frac{p'_o}{2} \right)^2 + \frac{1}{2} \frac{\boldsymbol{s} : \boldsymbol{s}}{g^2(\theta_b)} - \frac{p'^2_o}{4} = 0 \tag{5.24}$$

where p'_o represents the value of the mean effective stress at the intersection of the current swelling line with the isotropic compression line, rather than half the value used in the original formulation of the three-surface model, the function $g(\theta_b)$ defines the shape of the bounding surface in the deviatoric plane and will be discussed later and θ_b is the Lode's angle for the bounding surface, which is given by the following equation:

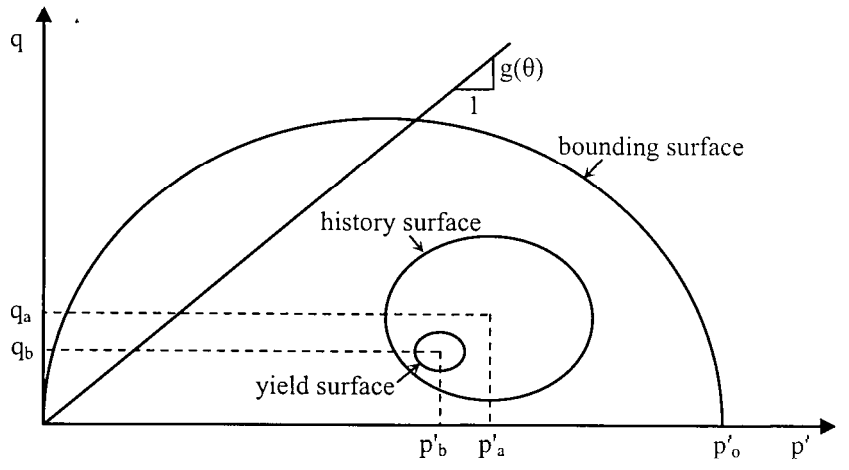
$$\theta_b = -\frac{1}{3} \sin^{-1} \left[\frac{3\sqrt{3}}{2} \frac{\det(\boldsymbol{s})}{\left[\left[\frac{1}{2} (\boldsymbol{s} : \boldsymbol{s}) \right]^{\frac{1}{2}} \right]^3} \right] \tag{5.25}$$

The equation of the history surface in general stress space is:

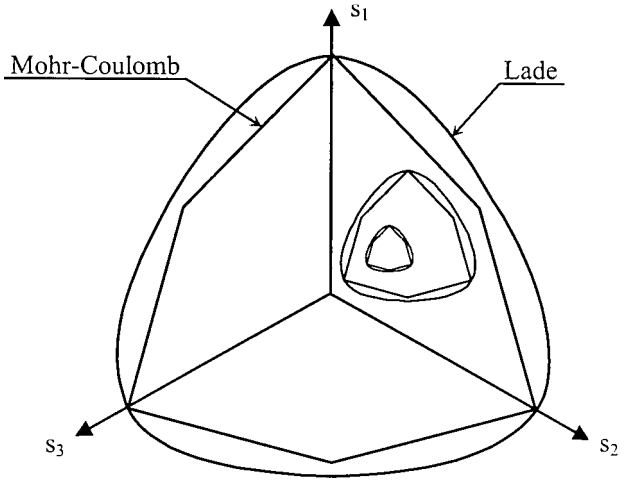
$$F_h = (p' - p'_a)^2 + \frac{1}{2} \frac{(\boldsymbol{s} - \boldsymbol{s}_a) : (\boldsymbol{s} - \boldsymbol{s}_a)}{g^2(\theta_h)} - T^2 \frac{p'^2_o}{4} = 0 \tag{5.26}$$

where p'_a and $\boldsymbol{s}_a$ are the mean effective stress and the deviatoric stress tensor at the centre of the history surface respectively, the function $g(\theta_h)$ defines the shape of the history surface in the deviatoric plane and θ_h is the Lode's angle for the history surface, which is calculated by using the centre of the history surface as origin:

$$\theta_h = -\frac{1}{3} \sin^{-1} \left[\frac{3\sqrt{3}}{2} \frac{\det(\boldsymbol{s} - \boldsymbol{s}_a)}{\left[\left[\frac{1}{2} \left[(\boldsymbol{s} - \boldsymbol{s}_a) : (\boldsymbol{s} - \boldsymbol{s}_a) \right] \right]^{\frac{1}{2}} \right]^3} \right] \tag{5.27}$$



(a)



(b)

Figure 5.7: Three surface model a) Representation of the yield, history and bounding surfaces in triaxial stress space b) Deviatoric section through the yield, history and bounding surfaces (with the van Eekelen equation taking the Lade shape)

The yield surface is represented in general stress space by an equation of the form:

$$F_y = \left(p' - p'_b\right)^2 + \frac{1}{2}\frac{\left(\boldsymbol{s}-\boldsymbol{s}_b\right):\left(\boldsymbol{s}-\boldsymbol{s}_b\right)}{g^2\left(\theta_y\right)} - T^2 S^2 \frac{p'^2_o}{4} = 0 \tag{5.28}$$

where p'_b and $\boldsymbol{s}_b$ are the mean effective stress and the deviatoric stress tensor at the centre of the yield surface respectively, the function $g(\theta_y)$ defines the shape of the yield surface in the deviatoric plane and θ_y is the Lode's angle for the yield surface, which is calculated by using the centre of the yield surface as origin:

$$\theta_y = -\frac{1}{3}\sin^{-1}\left[\frac{3\sqrt{3}}{2}\frac{\det(\boldsymbol{s}-\boldsymbol{s}_b)}{\left[\left[\frac{1}{2}\left[(\boldsymbol{s}-\boldsymbol{s}_b):(\boldsymbol{s}-\boldsymbol{s}_b)\right]\right]^{\frac{1}{2}}\right]^3}\right] \tag{5.29}$$

The representation of the bounding, history and yield surfaces in the triaxial stress space can be seen in Figure 5.7a.

Two options are adopted for the function $g(\theta)$. The first option gives the shape of a Mohr-Coulomb hexagon in the deviatoric plane and the second option gives the family of continuous curves suggested by van Eekelen (1980), see Figure 5.7b (in this figure the van Eekelen curve takes the Lade shape). These two options are the same as those adopted in the general formulation of the two-surface model and have already been discussed in section 4.4.3. The Mohr-Coulomb hexagon is described by Equation 4.27 and the general shape proposed by van Eekelen (1980) is given by Equation 4.28.

The bounding, history and yield surfaces always have the same shape in the deviatoric plane, given either by Equation 4.27 or 4.28, with θ replaced by θ_y for the yield surface, θ_h for the history surface and θ_b for the bounding surface.

5.3.3 Flow rule

The plastic potential surface associated with the bounding surface is represented by the following equation:

$$P_b = \left(p' - \frac{p'_o}{2}\right)^2 + \frac{1}{2}\frac{\boldsymbol{s}:\boldsymbol{s}}{g_p^{\,2}(\theta_b)} - \frac{p'^2_o}{4} = 0 \tag{5.30}$$

where the function $g_p(\theta_b)$ defines the variation of the plastic potential surface in the deviatoric plane.

The plastic potential surface associated with the history surface is:

$$P_h = \left(p' - p'_a\right)^2 + \frac{1}{2}\frac{(\boldsymbol{s}-\boldsymbol{s}_a):(\boldsymbol{s}-\boldsymbol{s}_a)}{g_p^{\,2}(\theta_h)} - T^2\frac{p'^2_o}{4} = 0 \tag{5.31}$$

where the function $g_p(\theta_h)$ defines again the variation of the plastic potential surface in

the deviatoric plane.

Finally, the plastic potential surface associated with the yield surface is formulated as follows:

$$P_y = \left(p' - p'_b\right)^2 + \frac{1}{2}\frac{\left(\boldsymbol{s}-\boldsymbol{s}_b\right):\left(\boldsymbol{s}-\boldsymbol{s}_b\right)}{g_p{}^2\left(\theta_y\right)} - T^2 S^2 \frac{p_o'^2}{4} = 0 \tag{5.32}$$

As in the general formulation of the two-surface model, the function $g_p(\theta)$ is given by the general shape proposed by van Eekelen (1980). This is described by Equation 4.31 and has already been discussed in section 4.4.4.

5.3.4 Hardening rules

The formulation of the hardening rules in general stress space is the following:

5.3.4.1 Isotropic hardening of the bounding surface

This is described by Equation 5.4.

5.3.4.2 Translation rules for the history surface

The two translation rules that govern the movement of the history surface are formulated in general stress space as follows:

i) Translation rule for the history surface when it is moving within the bounding surface

When the current stress state is on the history surface and this moves within the bounding surface, the history surface is the active yield surface. The translation rule of the history surface is given in general stress space as follows:

$$d\boldsymbol{\sigma}'_a = \frac{dp'_o}{p'_o}\boldsymbol{\sigma}'_a + W\left[\frac{\boldsymbol{\sigma}' - \boldsymbol{\sigma}'_a}{T} - \left(\boldsymbol{\sigma}' - \frac{\boldsymbol{\sigma}'_o}{2}\right)\right] \tag{5.33}$$

Equation 5.33 can be rewritten in terms of the isotropic and deviatoric components of the stress tensor:

$$dp'_a = \frac{dp'_o}{p'_o} p'_a + W\left[\frac{p' - p'_a}{R} - \left(p' - \frac{p'_o}{2}\right)\right] \tag{5.34}$$

$$d\boldsymbol{s}_a = \frac{dp'_o}{p'_o}\boldsymbol{s}_a + W\left(\frac{\boldsymbol{s} - \boldsymbol{s}_a}{T} - \boldsymbol{s}\right) \tag{5.35}$$

As in the original triaxial formulation, the scalar quantity W can be obtained by substituting Equations 5.34 and 5.35 into the consistency condition of the history surface and using Equation 5.26. The consistency condition of the history surface is:

$$dF_h = \frac{\partial F_h}{\partial p'}dp' + \frac{\partial F_h}{\partial \boldsymbol{s}} : d\boldsymbol{s} + \frac{\partial F_h}{\partial p'_a}dp'_a + \frac{\partial F_h}{\partial \boldsymbol{s}_a} : d\boldsymbol{s}_a + \frac{\partial F_h}{\partial p'_o}dp'_o = 0 \tag{5.36}$$

The scalar quantity W is calculated as:

$$W = \frac{\left(p' - p'_a\right)\left(dp' - \frac{dp'_o}{p'_o}p'_a\right) + \frac{1}{2}\left[\frac{\partial F_h}{\partial \boldsymbol{s}} : \left(d\boldsymbol{s} - \frac{dp'_o}{p'_o}\boldsymbol{s}_a\right)\right] - \frac{T^2 p'_o dp'_o}{4}}{\left(p' - p'_a\right)\left[\frac{p' - p'_a}{T} - \left(p' - \frac{p'_o}{2}\right)\right] + \frac{1}{2}\left[\frac{\partial F_h}{\partial \boldsymbol{s}} : \left(\frac{\boldsymbol{s} - \boldsymbol{s}_a}{T} - \boldsymbol{s}\right)\right]} \tag{5.37}$$

Equation 5.37 requires the partial differentials of the history surface with respect to the deviatoric stress tensor, $\partial F_h/\partial \boldsymbol{s}$. Similarly to the two-surface model, in the case that the shape of the history surface in the deviatoric plane is a circle, the function $g(\theta_h)$ is a constant and equal to X, and the differentials are:

$$\frac{\partial F_h}{\partial \boldsymbol{s}} = \frac{\boldsymbol{s} - \boldsymbol{s}_a}{X^2} \tag{5.38}$$

However, for any other shape of the history surface in the deviatoric plane the calculation of the differentials $\partial F_h/\partial \boldsymbol{s}$ becomes much more complicated. The calculation of these derivatives will be presented in the next section which describes the implementation of the three-surface model into ICFEP.

When the stress state is within the history surface then the yield surface is the current active yield surface and the translation of the history surface is given by the first part of Equation 5.33:

$$d\boldsymbol{\sigma}'_a = \frac{dp'_o}{p'_o}\boldsymbol{\sigma}'_a \tag{5.39}$$

ii) Translation rule for the history surface when it is in contact with the bounding surface

When the history surface is in contact with the bounding surface, the latter is the active yield surface, and the history surface is just dragged by the current stress point. The translation rule of the history surface ensures that the history and bounding surfaces remain tangential for further loading and is formulated in general stress space as follows:

$$d\boldsymbol{\sigma}'_a = (1-T)\,d\boldsymbol{\sigma}' + T\frac{d\boldsymbol{\sigma}'_o}{2} \tag{5.40}$$

5.3.4.3 Translation rules for the yield surface

The two translations rules that govern the movement of the yield surface are formulated in general stress space as follows:

i) Translation rule for the yield surface when it is moving within the history surface

In this case the yield surface is the active yield surface and its translation rule is given as:

$$d\boldsymbol{\sigma}'_b = \frac{dp'_o}{p'_o}\boldsymbol{\sigma}'_b + Z\left[\frac{\boldsymbol{\sigma}'-\boldsymbol{\sigma}'_b}{S} - (\boldsymbol{\sigma}'-\boldsymbol{\sigma}'_a)\right] \tag{5.41}$$

The above equation can be rewritten in terms of the isotropic and deviatoric components of the stress tensor:

$$dp'_b = \frac{dp'_o}{p'_o}p'_b + Z\left[\frac{p'-p'_b}{S} - (p'-p'_a)\right] \tag{5.42}$$

$$d\boldsymbol{s}_b = \frac{dp'_o}{p'_o}\boldsymbol{s}_b + Z\left[\frac{\boldsymbol{s}-\boldsymbol{s}_b}{S} - (\boldsymbol{s}-\boldsymbol{s}_a)\right] \tag{5.43}$$

The scalar quantity Z is derived by using the consistency condition for the yield surface:

$$dF_y = \frac{\partial F_y}{\partial p'}dp' + \frac{\partial F_y}{\partial \boldsymbol{s}} : d\boldsymbol{s} + \frac{\partial F_y}{\partial p'_b}dp'_b + \frac{\partial F_y}{\partial \boldsymbol{s}_b} : d\boldsymbol{s}_b + \frac{\partial F_y}{\partial p'_o}dp'_o = 0 \tag{5.44}$$

Substitution of Equations 5.42 and 5.43 into Equation 5.44 and use of Equation 5.28

gives the expression for Z:

$$Z=\frac{\left(p'-p'_b\right)\left(dp'-\frac{dp'_o}{p'_o}p'_b\right)+\frac{1}{2}\left[\frac{\partial F_y}{\partial \boldsymbol{s}}:\left(d\boldsymbol{s}-\frac{dp'_o}{p'_o}\boldsymbol{s}_b\right)\right]-\frac{T^2S^2p'_o dp'_o}{4}}{\left(p'-p'_b\right)\left[\frac{p'-p'_b}{S}-\left(p'-p'_a\right)\right]+\frac{1}{2}\left[\frac{\partial F_y}{\partial \boldsymbol{s}}:\left[\frac{\boldsymbol{s}-\boldsymbol{s}_b}{S}-\left(\boldsymbol{s}-\boldsymbol{s}_a\right)\right]\right]} \tag{5.45}$$

The calculation of Equation 5.45 requires the partial differentials of the yield surface with respect to the deviatoric stress tensor, $\partial F_y/\partial \boldsymbol{s}$. As before, if the shape of the yield surface in the deviatoric plane is circular then the differentials are calculated as:

$$\frac{\partial F_y}{\partial \boldsymbol{s}}=\frac{\boldsymbol{s}-\boldsymbol{s}_b}{X^2} \tag{5.46}$$

For any other shape of the yield surface in the deviatoric plane the calculation of the above differentials is complicated and will be given in the next section.

ii) Translation rule for the yield surface when it is in contact with the history surface

In this case the history surface is the active yield surface. The translation rule of the inactive yield surface is formulated in general stress space as:

$$d\boldsymbol{\sigma}'_b=\left(1-S\right)d\boldsymbol{\sigma}'+Sd\boldsymbol{\sigma}'_a \tag{5.47}$$

5.3.5 Hardening modulus

The hardening modulus is formulated for three different cases. The first one is the case that the kinematic yield surface moves within the history and bounding surfaces, the second one is the case that the kinematic yield surface is in touch with the history surface and they both move within the bounding surface and the third case is the one that all three surfaces are in contact. In the first case the yield surface is the active yield surface and the formulation of the hardening modulus follows the one proposed by Stallebrass (1990) and described in section 5.2.5. In the second case the history surface is the active yield surface. The hardening modulus in this case reduces to the hardening modulus of the two-surface model for the case that the kinematic surface moves within the bounding surface. Finally in the third case the bounding surface is the active yield surface and the hardening modulus reduces to the modified Cam Clay hardening

modulus.

i) Hardening modulus for the yield surface when it is moving within the history and bounding surfaces

The hardening modulus, A, is formulated in general stress space as follows:

$$A=\frac{4}{\lambda^*-\kappa^*}\left[\left(p'-p'_b\right)\left[p'_b\left(p'-p'_b\right)+\frac{1}{2}\left(\frac{\partial F_y}{\partial \boldsymbol{s}}:\boldsymbol{s}_b\right)+\frac{T^2S^2p_o'^2}{4}\right]+\left(\frac{b_1}{b_{1\max}}\right)^{\psi}\left(\frac{p'_o}{2}\right)^3S^2+\left(\frac{Tb_2}{b_{2\max}}\right)^{\psi}\left(\frac{p'_o}{2}\right)^3\right] \tag{5.48}$$

Equation 5.48 is divided into three parts. The first part is the hardening modulus A_o, which is equivalent to the hardening function h_o in the triaxial formulation:

$$A_o=\frac{4}{\lambda^*-\kappa^*}\left[\left(p'-p'_b\right)\left[p'_b\left(p'-p'_b\right)+\frac{1}{2}\left(\frac{\partial F_y}{\partial \boldsymbol{s}}:\boldsymbol{s}_b\right)+\frac{T^2S^2p_o'^2}{4}\right]\right] \tag{5.49}$$

The second part of Equation 5.49 is the additional component of the hardening modulus, A_1, associated with the degree of approach of the history surface to the bounding surface:

$$A_1=\frac{4}{\lambda^*-\kappa^*}\left(\frac{b_1}{b_{1\max}}\right)^{\psi}\left(\frac{p'_o}{2}\right)^3S^2 \tag{5.50}$$

This is equivalent to the hardening function H_1 in the original triaxial formulation.

The third part of Equation 5.49 is the additional component of the hardening modulus A_2, associated with the degree of proximity of the yield surface to the history surface:

$$A_2=\frac{4}{\lambda^*-\kappa^*}\left(\frac{Tb_2}{b_{2\max}}\right)^{\psi}\left(\frac{p'_o}{2}\right)^3 \tag{5.51}$$

This is equivalent to the hardening function H_2 in the original triaxial formulation.

Similarly to the hardening function h_o in the triaxial formulation, the above expression of A_o in general stress space cannot be derived from the consistency condition of the yield surface when all three surfaces are in contact, because of the translation rule adopted for the yield surface when the surfaces are in contact (Equation 5.47). However,

Equation 5.48 can still be used as the hardening modulus, A, in the case that the yield surface moves within the history and bounding surfaces. This is because the derivation of the scalar multiplier Z (in Equation 5.41) from the consistency condition of the yield surface ensures that the consistency condition of the active yield surface is satisfied. As in the two-surface model, any hardening modulus could be assumed in this case and the consistency condition of the yield surface would still be satisfied anyway. The problem arises when the yield surface is in contact with either the history surface or both the history and bounding surfaces. In any of these cases the consistency condition of the yield surface is not satisfied. However, since in the first case the plastic strain increments calculated by the yield and history surfaces are the same, the active yield surface can be changed to the history surface and the model then reduces to the general formulation of the two-surface model. In this way the consistency condition of the history surface is satisfied while the yield surface is inactive and just follows the current stress point according to Equation 5.47. Moreover, in the second case all three surfaces predict the same strains and hence the active yield surface can be changed to the bounding surface and the model then reduces to the modified Cam Clay model. Both the yield and history surfaces are then inactive and are dragged along the current stress path following Equations 5.47 and 5.40 respectively.

The formulation in general stress space of the degree of approach of the history surface to the bounding surface, b_1, is:

$$b_1 = \frac{1}{T\frac{p'_o}{2}}\left[\frac{p'-p'_b}{S}\left[\frac{p'-p'_b}{TS}-\left(\frac{p'-p'_b}{S}+p'_a-\frac{p'_o}{2}\right)\right]+\frac{1}{2S}\left[\frac{\partial F_y}{\partial \boldsymbol{s}}:\left[\frac{\boldsymbol{s}-\boldsymbol{s}_b}{ST}-\left(\frac{\boldsymbol{s}-\boldsymbol{s}_b}{S}+\boldsymbol{s}_a\right)\right]\right]\right] \tag{5.52}$$

The maximum value of the function b_1 is:

$$b_{1\max} = p'_o(1-T) \tag{5.53}$$

The degree of proximity of the yield surface to the history surface, b_2, becomes:

$$b_2 = \frac{1}{ST\frac{p'_o}{2}}\left[\left(p'-p'_b\right)\left[\frac{p'-p'_b}{S}-\left(p'-p'_a\right)\right]+\frac{1}{2}\left[\frac{\partial F_y}{\partial \boldsymbol{s}}:\left[\frac{\boldsymbol{s}-\boldsymbol{s}_b}{S}-\left(\boldsymbol{s}-\boldsymbol{s}_a\right)\right]\right]\right] \tag{5.54}$$

The maximum value of the function b_2 is:

$$b_{2\max} = Tp'_o(1-S) \tag{5.55}$$

Equations 5.48, 5.52 and 5.54 require the partial differentials of the yield surface with respect to the deviatoric stress tensor, $\partial F_y/\partial \boldsymbol{s}$. As previously mentioned, if a circle is adopted as the shape of the yield surface in the deviatoric plane then the differentials are calculated by Equation 5.46. For any other shape the calculation of the differentials is given in section 5.4.

ii) Hardening modulus for the history surface when it is in contact with the yield surface and they are both moving within the bounding surface

In this case b_2 is equal to zero, A_2 is equal to zero, the history surface becomes the active yield surface and the hardening modulus, A, reduces to the hardening modulus of the two-surface model:

$$A = \frac{4}{\lambda^* - \kappa^*}\left[(p'-p'_a)\left[p'_a(p'-p'_a)+\frac{1}{2}\left(\frac{\partial F_h}{\partial \boldsymbol{s}}:\boldsymbol{s}_a\right)+\frac{T^2 p_o'^2}{4}\right]+\left(\frac{b_1}{b_{1\max}}\right)^{\psi}\left(\frac{p'_o}{2}\right)^3\right] \tag{5.56}$$

Equation 5.56 is divided into two parts. The first part is the hardening modulus A_o which is of the same form as the hardening modulus A_o of the two-surface model but with R replaced by T and F_y replaced by F_h:

$$A_o = \frac{4}{\lambda^* - \kappa^*}\left[(p'-p'_a)\left[p'_a(p'-p'_a)+\frac{1}{2}\left(\frac{\partial F_h}{\partial \boldsymbol{s}}:\boldsymbol{s}_a\right)+\frac{T^2 p_o'^2}{4}\right]\right] \tag{5.57}$$

The second part is the component of the hardening modulus A_1 which is of the same form as the hardening modulus A_1 of the two-surface model, but with b replaced by b_1:

$$A_1 = \frac{4}{\lambda^* - \kappa^*}\left(\frac{b_1}{b_{1\max}}\right)^{\psi}\left(\frac{p'_o}{2}\right)^3 \tag{5.58}$$

Similar to the general formulation of the two-surface model, the above expression of the hardening modulus, A_o, cannot be derived from the consistency condition of the history surface when all three surfaces are in contact because of the translation rule adopted

for the history surface when the surfaces are in contact (Equation 5.40). However, Equation 5.56 can be used as the hardening modulus for the case that the history and yield surfaces are in contact and they both move within the bounding surface. This is due to the fact that the scalar parameter W (in Equation 5.33) is derived from the consistency condition of the history surface, which is the active yield surface in this case and in this way the consistency condition of the active yield surface is always satisfied. However, the consistency condition of the history surface is not satisfied when all three surfaces are in contact. In this case, as previously mentioned, the bounding surface can become the active yield surface and the model then reduces to the modified Cam Clay model.

The degree of proximity, b_1, of the history surface to the bounding surface is formulated in general stress space as follows:

$$b_1 = \frac{1}{T\dfrac{p'_o}{2}}\left[\left(p'-p'_a\right)\left[\frac{p'-p'_a}{T}-\left(p'-\frac{p'_o}{2}\right)\right]+\frac{1}{2}\left[\frac{\partial F_h}{\partial \boldsymbol{s}}:\left[\frac{\boldsymbol{s}-\boldsymbol{s}_a}{T}-\boldsymbol{s}\right]\right]\right] \tag{5.59}$$

The degree of proximity, b_1, is again of the same form as the degree of proximity, b, in the two-surface model but with R replaced by T and F_y replaced by F_h.

Equations 5.56 and 5.59 require the calculation of the partial differentials of the history surface with respect to the deviatoric stress tensor, $\partial F_h/\partial \boldsymbol{s}$. As mentioned before, for a circular shape of the history surface in the deviatoric plane these are given by Equation 5.38, whereas for any other shape they are calculated in section 5.4.

iii) Hardening modulus for the bounding surface when all three surfaces are in contact

In this case the bounding surface is the active yield surface and the hardening modulus reduces to the modified Cam Clay hardening modulus:

$$A = \frac{4}{\lambda^* - \kappa^*}\left[\left(p'-\frac{p'_o}{2}\right)p'\frac{p'_o}{2}\right] \tag{5.60}$$

5.3.6 Elastic part of the model

The elastic stress tensor is calculated from the elastic strain tensor through the elastic constitutive tensor:

$$d\boldsymbol{\sigma} = \boldsymbol{D}' : d\boldsymbol{\varepsilon}^e \tag{5.61}$$

where the elastic constitutive tensor, D', is a function of the isotropic elastic bulk modulus, K_e, and the shear modulus, G_e.

The elastic bulk modulus, K_e, is given by Equation 5.22. For the calculation of the elastic shear stiffness, G_e, four options exist. These are the same as in the general formulation of the two-surface model and have already been discussed in section 4.4.7.

5.3.7 Overview of the model

An overview of the model serves to clarify the way the model operates in this general formulation and is the basis of the implementation of the model into ICFEP.

Elastic behaviour:

When the stress state is within the yield surface the behaviour is purely elastic and is described by Equation 5.61.

Elasto-plastic behaviour:

i) When the stress state is on the yield surface and this moves within the history and bounding surfaces

The yield surface is the active yield surface. The yield and plastic potential functions associated with this surface are described by Equations 5.28 and 5.32 respectively. The hardening modulus is provided by Equation 5.48. The isotropic hardening of the bounding surface is given by Equation 5.4 and the translations of the yield and history surfaces are described by Equations 5.41 and 5.39 respectively. The scalar multiplier Z in Equation 5.41 is derived from the consistency condition of the yield surface and therefore the consistency condition of the active yield surface is satisfied.

ii) When the stress state is on the yield and history surfaces and these move within the bounding surface

In this case the history surface is the active yield surface, and the model reduces to the two-surface model. The yield and plastic potential functions of the history surface are given by Equations 5.26 and 5.31 respectively. The hardening modulus is described by Equation 5.56 and the isotropic hardening of the bounding surface is again given by

Equation 5.4. The translation of the history surface is described by Equation 5.33 and the consistency condition of this surface, which is now the active yield surface, is satisfied, since the scalar multiplier W in Equation 5.33 is derived directly from the same consistency condition. The yield surface is inactive but follows the current stress state according to Equation 5.47.

iii) When the stress state is on all three surfaces

The bounding surface is the active yield surface and the model reduces to the modified Cam Clay model. The yield function and plastic potential, in this case, are provided by Equations 5.24 and 5.30 respectively. The hardening modulus is given by Equation 5.60, which is consistent with the isotropic hardening of the bounding surface described by Equation 5.4. In this way the consistency condition of the bounding surface, which is the active yield surface, is satisfied. The translation of the inactive yield and history surfaces is described by Equations 5.47 and 5.40 respectively.

5.3.8 Model parameters

The formulation of the three-surface model in general stress space described in this section requires either ten parameters, when a Mohr-Coulomb hexagon is adopted for the shape of the yield surface in the deviatoric plane, or twelve parameters, when a general shape is chosen. If the elastic shear modulus, G_e, is calculated by Equation 4.51, then two additional parameters are required. The model parameters are:

λ^*: the slope of the isotropic normal compression line in $\ln v$-$\ln p'$ space

κ^*: the slope of the swelling line in $\ln v$-$\ln p'$ space for a stress path that lies entirely within the kinematic yield surface

μ or G_e, or G_e/p': the Poisson's ratio or the elastic shear stiffness. If Equation 4.51 is used then the material parameters A, n and m must be provided

φ' or X, Y and Z: the angle of shearing resistance or the constants $X = \sin(\varphi'_{0-0^+})$, Y and Z in Equation 4.28 at the critical state

Y_p and Z_p: the constants Y_p and Z_p in Equation 4.31

T: the ratio of the size of the history surface to that of the bounding

surface

S: the ratio of the size of the yield surface to that of the history surface

ψ: the exponent in the hardening function A

N: one additional parameter is required to fix the model in Inv-lnp'space and this is usually taken as the specific volume of the isotropic compression line at $p' = 1$KPa

5.4 Implementation

5.4.1 Introduction

The implementation of a constitutive model into a finite element program has already been discussed in the implementation of the two-surface model into ICFEP, section 4.5.1. Similarly to the two-surface model, the implementation of the three-surface model into ICFEP involved the calculation of the following terms: the partial derivatives of the yield function with respect to stress, $\{\partial F/\partial\sigma'\}$, the partial derivatives of the plastic potential function with respect to stress, $\{\partial P/\partial\sigma'\}$, the elastic constitutive matrix, $[D']$, the hardening modulus, A, and the change in the hardening parameters. A flowchart of the ICFEP subroutine which is used by the stress point algorithm in order to calculate the changes in stresses, plastic strains and hardening parameters during a substep, for the three-surface model is presented in Appendix IV. This section also presents the calculation of the partial derivatives of the yield surface with respect to the deviatoric stress tensor, $\partial F_y/\partial \boldsymbol{s}$, which are required in Equations 5.45, 5.48, 5.52 and 5.54, and the partial derivatives of the history surface with respect to the deviatoric stress tensor, $\partial F_h/\partial \boldsymbol{s}$, which are required in Equations 5.37, 5.56 and 5.59 of the previous section.

5.4.2 Calculation of the partial derivatives of the yield function

The derivatives of the yield function are calculated by the program for the surface that is the active yield surface at the time.

i) When the yield surface is the active yield surface

In this case the yield function is given by Equation 5.28. For convenience in the

numerical computations, the partial derivatives of the yield surface with respect to the deviatoric stress tensor, $\partial F_y/\partial \boldsymbol{s}$, will be represented by the vector $\{\partial F_y/\partial s\}$, where $\{s\}$ is given by Equation 4.52 (Chapter 4). The derivatives $\{\partial F_y/\partial s\}$ will be calculated first, followed by the calculation of the derivatives $\{\partial F_y/\partial \sigma'\}$. A similar process to the one adopted in the two-surface model will be followed.

Calculation of terms $\{\partial F_y/\partial s\}$

The terms $\{\partial F_y/\partial s\}$ can be calculated in the same way that they were calculated for the two-surface model by rewriting Equation 4.53 as:

$$Q = (\boldsymbol{s} - \boldsymbol{s}_b) : (\boldsymbol{s} - \boldsymbol{s}_b) \tag{5.62}$$

Equation 5.28 is then rewritten as follows:

$$F_y = (p' - p'_b)^2 + \frac{1}{2}\frac{Q}{g^2(\theta_y)} - T^2 S^2 \frac{p_o'^2}{4} = 0 \tag{5.63}$$

The partial derivatives $\{\partial F_y/\partial s\}$ can be obtained by differentiating Equation 5.63:

$$\left\{\frac{\partial F_y}{\partial s}\right\} = \frac{\partial F_y}{\partial Q}\left\{\frac{\partial Q}{\partial s}\right\} + \frac{\partial F_y}{\partial \theta_y}\left\{\frac{\partial \theta_y}{\partial s}\right\} \tag{5.64}$$

In the above Equation the term $\{\partial \theta_y/\partial s\}$ is:

$$\left\{\frac{\partial \theta_y}{\partial s}\right\} = \frac{\sqrt{3}}{2\cos(3\theta_y)\left(\frac{1}{2}Q\right)^{3/2}}\left[\frac{3\det(\boldsymbol{s}-\boldsymbol{s}_b)}{2Q}\left\{\frac{\partial Q}{\partial s}\right\} - \left\{\frac{\partial \det(\boldsymbol{s}-\boldsymbol{s}_b)}{\partial s}\right\}\right] \tag{5.65}$$

Substitution of Equation 5.65 into Equation 5.64 gives:

$$\left\{\frac{\partial F_y}{\partial s}\right\} = \left[\frac{\partial F_y}{\partial Q} + \frac{\partial F_y}{\partial \theta_y}\frac{3\sqrt{3}\det(\boldsymbol{s}-\boldsymbol{s}_b)}{8\cos(3\theta_y)\left(\frac{1}{2}Q\right)^{5/2}}\right]\left\{\frac{\partial Q}{\partial s}\right\} - \frac{\sqrt{3}}{2\cos(3\theta_y)\left(\frac{1}{2}Q\right)^{3/2}}\frac{\partial F_y}{\partial \theta_y}\left\{\frac{\partial \det(\boldsymbol{s}-\boldsymbol{s}_b)}{\partial s}\right\} \tag{5.66}$$

Equation 5.66 is of the same form as Equation 4.57 (Chapter 4) but with $\boldsymbol{s}_a$ replaced by $\boldsymbol{s}_b$. Equation 5.66 can be rewritten as:

$$\left\{\frac{\partial F_y}{\partial s}\right\} = \alpha_1 \left\{\frac{\partial Q}{\partial s}\right\} + \alpha_2 \left\{\frac{\partial \det(\boldsymbol{s} - \boldsymbol{s}_b)}{\partial s}\right\} \tag{5.67}$$

where the constants α_1 and α_2 depend on $\partial F_y/\partial Q$ and $\partial F_y/\partial \theta_y$. These can be calculated by Equations 4.59-4.61 with Q from Equation 5.62 and θ_y from Equation 5.29. The derivatives $\{\partial Q/\partial s\}$ and $\{\partial \det(\boldsymbol{s}-\boldsymbol{s}_b)/\partial s\}$ in Equation 5.67 can be calculated from Appendix I by replacing $\boldsymbol{s}_a$ with $\boldsymbol{s}_b$.

Calculation of terms $\{\partial F_y/\partial \sigma'\}$

The derivatives $\partial F_y/\partial \tau_{xy}$, $\partial F_y/\partial \tau_{yz}$, $\partial F_y/\partial \tau_{zx}$ have already been calculated from Equation 5.67. The remaining derivatives, $\partial F_y/\partial \sigma'_x$, $\partial F_y/\partial \sigma'_y$ and $\partial F_y/\partial \sigma'_z$, can be calculated from the derivatives $\partial F_y/\partial(\sigma'_x - p')$, $\partial F_y/\partial(\sigma'_y - p')$ and $\partial F_y/\partial(\sigma'_z - p')$:

$$\frac{\partial F_y}{\partial \sigma'_x} = \frac{2}{3}(p' - p'_b) + \frac{1}{3}\left[2\frac{\partial F_y}{\partial(\sigma'_x - p')} - \frac{\partial F_y}{\partial(\sigma'_y - p')} - \frac{\partial F_y}{\partial(\sigma'_z - p')}\right] \tag{5.68}$$

$$\frac{\partial F_y}{\partial \sigma'_y} = \frac{2}{3}(p' - p'_b) + \frac{1}{3}\left[-\frac{\partial F_y}{\partial(\sigma'_x - p')} + 2\frac{\partial F_y}{\partial(\sigma'_y - p')} - \frac{\partial F_y}{\partial(\sigma'_z - p')}\right] \tag{5.69}$$

$$\frac{\partial F_y}{\partial \sigma'_z} = \frac{2}{3}(p' - p'_b) + \frac{1}{3}\left[-\frac{\partial F_y}{\partial(\sigma'_x - p')} - \frac{\partial F_y}{\partial(\sigma'_y - p')} + 2\frac{\partial F_y}{\partial(\sigma'_z - p')}\right] \tag{5.70}$$

ii) When the history surface is the active yield surface

The yield function is given by Equation 5.26. Inspection of Equations 5.26 and 5.28 shows that the former can be obtained from the latter by setting p'_h equal to p'_a, $\boldsymbol{s}_h$ equal to $\boldsymbol{s}_a$ and S equal to 1.0. Therefore the derivatives $\{\partial F_h/\partial s\}$ and $\{\partial F_h/\partial \sigma'\}$ can be calculated from the same equations used to calculate the derivatives $\{\partial F_y/\partial s\}$ and $\{\partial F_y/\partial \sigma'\}$, by setting p'_b, $\boldsymbol{s}_b$ and S equal to the above values.

iii) When the bounding surface is the active yield surface

The yield function is given by Equation 5.24, which can be obtained from Equation 5.28

by setting p'_b equal to half the value of p'_o, s_b equal to zero and S and T equal to 1.0. The same equations used for the calculation of the derivatives $\{\partial F_y/\partial\sigma'\}$ can also be used for the calculation of the derivatives $\{\partial F_b/\partial\sigma'\}$ by setting p'_b, s_b, S and T equal to the values just mentioned.

For the calculation of the yield function derivatives a similar process to the one used in the two-surface model is followed. The program calculates the yield function derivatives from Equations 5.62-5.70 with temporary values $p'_b{}^t$, $\{s_b\}^t$, S^t and T^t, depending on which is the active yield surface. If the yield surface is the active yield surface, the temporary values are set equal to the real values $p'_b{}^t = p'_b$, $\{s_b\}^t = \{s_b\}$, $S^t = S$ and $T^t = T$. If the history surface is the active yield surface then the temporary values are equal to $p'_b{}^t = p'_a$, $\{s_b\}^t = \{s_a\}$, $S^t = 1.0$ and $T^t = T$. Finally if the bounding surface is the active yield surface the temporary values are set equal to $p'_b{}^t = 0.5p'_o$, $\{s_b\}^t = 0.0$, $S^t = 1.0$ and $T^t = 1.0$.

5.4.3 Calculation of the partial derivatives of the plastic potential function

The program calculates the plastic potential derivatives associated with the current active yield surface at the time.

i) When the yield surface is the active yield surface

Substitution of Equation 5.62 into Equation 5.32, which describes the plastic potential function associated with the yield surface gives:

$$P_y = \left(p' - p'_b\right)^2 + \frac{1}{2}\frac{Q}{g_p{}^2\left(\theta_y\right)} - T^2S^2\frac{p'^2_o}{4} = 0 \qquad (5.71)$$

A similar process to the calculation of the yield function derivatives is followed. The partial derivatives $\{\partial P_y/\partial s\}$ are calculated first, followed by the calculation of the partial derivatives $\{\partial P_y/\partial\sigma'\}$.

Calculation of terms $\{\partial P_y/\partial s\}$

The partial derivatives $\{\partial P_y/\partial s\}$ can be calculated as follows:

$$\left\{\frac{\partial P_y}{\partial s}\right\} = \frac{\partial P_y}{\partial Q}\left\{\frac{\partial Q}{\partial s}\right\} + \frac{\partial P_y}{\partial \theta_y}\left\{\frac{\partial \theta_y}{\partial s}\right\} \tag{5.72}$$

The terms in Equation 5.72 are obtained from similar equations to those used to calculate the yield function derivatives $\{\partial F_y/\partial s\}$ but with $g(\theta_y)$ replaced by the function $g_p(\theta_y)$. The only difference is in the calculation of the derivative $\partial P_y/\partial \theta_y$. This can be calculated by Equation 4.67 with the appropriate values of Q and θ_y.

Calculation of terms $\{\partial P_y/\partial \sigma'\}$

The derivatives $\{\partial P_y/\partial \sigma'\}$ can be calculated from the derivatives $\{\partial P_y/\partial s\}$ by using equations similar to Equations 5.68-5.70.

ii) When the history surface is the active yield surface

The plastic potential function is given by Equation 5.31 and the derivatives can be calculated from the equations used to calculate the derivatives of the plastic potential function when the yield surface is the active yield surface by setting p'_b equal to p'_a, $\boldsymbol{s}_b$ equal to $\boldsymbol{s}_a$ and S equal to 1.0.

iii) When the bounding surface is the active yield surface

The plastic potential is described by Equation 5.30 and the derivatives can be calculated as in the case that the yield surface is the active yield surface by setting p'_b equal to half the value of p'_o, $\boldsymbol{s}_b$ equal to zero and S and T equal to 1.0.

A similar process to section 5.4.2 is followed and the derivatives of the plastic potential function are calculated from Equations 5.71-5.72 by using temporary values $p'_b{}'$, $\{s_b\}'$, S' and T', depending on which is the active yield surface.

5.4.4 Calculation of the hardening modulus, A

i) When the yield surface is the active yield surface

If the derivatives of the yield surface are represented by the vector $\{\partial F_y/\partial s\}$, Equation 5.48 can be rewritten as:

$$A=\frac{4}{\lambda^{*}-\kappa^{*}}\left[\left(p'-p'_b\right)\left[p'_b\left(p'-p'_b\right)+\frac{1}{2}\left\{\frac{\partial F_y}{\partial s}\right\}^{T}\{s_b\}+\frac{T^2S^2p_o'^2}{4}\right]+\left(\frac{b_1}{b_{1\max}}\right)^{\psi}\left(\frac{p'_o}{2}\right)^{3}S^2+\left(\frac{Tb_2}{b_{2\max}}\right)^{\psi}\left(\frac{p'_o}{2}\right)^{3}\right] \tag{5.73}$$

where

$$b_1=\frac{1}{T\frac{p'_o}{2}}\left[\frac{p'-p'_b}{S}\left[\frac{p'-p'_b}{TS}-\left(\frac{p'-p'_b}{S}+p'_a-\frac{p'_o}{2}\right)\right]+\frac{1}{2S}\left\{\frac{\partial F_y}{\partial s}\right\}^{T}\left\{\frac{s-s_b}{ST}-\left(\frac{s-s_b}{S}+s_a\right)\right\}\right] \tag{5.74}$$

$$b_2=\frac{1}{ST\frac{p'_o}{2}}\left[\left(p'-p'_b\right)\left[\frac{p'-p'_b}{S}-\left(p'-p'_a\right)\right]+\frac{1}{2}\left\{\frac{\partial F_y}{\partial s}\right\}^{T}\left\{\frac{s-s_b}{S}-\left(s-s_a\right)\right\}\right] \tag{5.75}$$

ii) When the history surface is the active yield surface

Equation 5.56 can be rewritten as:

$$A=\frac{4}{\lambda^{*}-\kappa^{*}}\left[\left(p'-p'_a\right)\left[p'_a\left(p'-p'_a\right)+\frac{1}{2}\left\{\frac{\partial F_h}{\partial s}\right\}^{T}\{s_a\}+\frac{T^2p_o'^2}{4}\right]+\left(\frac{b_1}{b_{1\max}}\right)^{\psi}\left(\frac{p'_o}{2}\right)^{3}\right] \tag{5.76}$$

where

$$b_1=\frac{1}{T\frac{p'_o}{2}}\left[\left(p'-p'_a\right)\left[\frac{p'-p'_a}{T}-\left(p'-\frac{p'_o}{2}\right)\right]+\frac{1}{2}\left\{\frac{\partial F_h}{\partial s}\right\}^{T}\left\{\frac{s-s_a}{T}-s\right\}\right] \tag{5.77}$$

iii) When the bounding surface is the active yield surface

The hardening modulus is calculated by Equation 5.60.

5.4.5 Calculation of the elastic constitutive matrix, [D']

The elastic constitutive matrix is the same as for the two-surface model and this has already been discussed in section 4.5.5.

5.4.6 Calculation of the changes in hardening parameters

The hardening parameters are the parameter p'_o and the centres of the yield and history surfaces which in vector notation are represented by p'_b, $\{s_b\}$ and p'_a, $\{s_a\}$ respectively.

i) When the yield surface is the active yield surface

The change in p'_o is given by Equation 5.4. The changes in p'_b and $\{s_b\}$ can be obtained from Equation 5.41 if this is written in a vector notation form (an example of this process is given in section 4.5.6). The changes in p'_a and $\{s_a\}$ can be similarly obtained from Equation 5.39. If the derivatives of the kinematic yield surface are represented by $\{\partial F_y/\partial s\}$, then the scalar multiplier Z in Equation 5.41 can be calculated as:

$$Z=\frac{\left(p'-p'_b\right)\left(dp'-\frac{dp'_o}{p'_o}p'_b\right)+\frac{1}{2}\left\{\frac{\partial F_y}{\partial s}\right\}^T\left\{ds-\frac{dp'_o}{p'_o}s_b\right\}-\frac{T^2S^2p'_o dp'_o}{4}}{\left(p'-p'_b\right)\left[\frac{p'-p'_b}{S}-\left(p'-p'_a\right)\right]+\frac{1}{2}\left\{\frac{\partial F_y}{\partial s}\right\}^T\left\{\frac{s-s_b}{S}-\left(s-s_a\right)\right\}} \tag{5.78}$$

ii) When the history surface is the active yield surface

The change in p'_o is given by Equation 5.4, the changes in p'_b and $\{s_b\}$ can be obtained from Equation 5.47 and the changes in p'_a and $\{s_a\}$ from Equation 5.33. If the derivatives of the kinematic yield surface are represented by $\{\partial F_y/\partial s\}$, then the scalar multiplier W in Equation 5.33 is rewritten as:

$$W=\frac{\left(p'-p'_a\right)\left(dp'-\frac{dp'_o}{p'_o}p'_a\right)+\frac{1}{2}\left\{\frac{\partial F_h}{\partial s}\right\}^T\left\{ds-\frac{dp'_o}{p'_o}s_a\right\}-\frac{T^2p'_o dp'_o}{4}}{\left(p'-p'_a\right)\left[\frac{p'-p'_a}{T}-\left(p'-\frac{p'_o}{2}\right)\right]+\frac{1}{2}\left\{\frac{\partial F_h}{\partial s}\right\}^T\left\{\frac{s-s_a}{T}-s\right\}} \tag{5.79}$$

iii) When the bounding surface is the active yield surface

The change in p'_o is described by Equation 5.4, the changes in p'_b and $\{s_b\}$ can be

obtained from Equation 5.47 and the changes in p'_a and $\{s_a\}$ from Equation 5.40.

5.5 Validation

5.5.1 Introduction

This section presents a number of single finite element analyses performed in order to validate the implementation of the version of the three-surface model described in section 5.3. In the first part of the section the simulation of a number of triaxial tests quoted by Stallebrass (1990) is repeated and the results obtained are compared with the already published data. In the second part the implementation of different yield and plastic potential surfaces in the deviatoric plane is examined. When subjected to stress paths involving rotation of the principal stresses, the model can be shown to predict anisotropic stiffness characteristics (depending on the position of the kinematic surfaces) and isotropic strength, similar to the two-surface model, however, this set of tests will not be repeated here. Finally, in the last part of the section the hardening function assumed in the model and the resulting elasto-plastic transition are discussed. The above single finite element analyses do not only validate the implementation of the current version of the three-surface model but also serve to demonstrate some of its capabilities and limitations. Further evaluation of the three-surface model is presented in Chapter 7.

5.5.2 Comparison with stress paths from Stallebrass (1990)

Stallebrass (1990) used the three-surface model in order to reproduce a number of triaxial tests which investigated the effect of recent stress history on the behaviour of reconstituted speswhite kaolin.

The stress paths repeated in this thesis are three constant p' tests taken to failure, in order to show typical failure characteristics of the three-surface model, and a multi-stage test, in which the stress-strain behaviour along a common constant p' loading path was investigated after four different approaching paths.

i) Constant p' tests to failure

Stallebrass (1990) simulated three constant p' tests to failure, initiating from highly overconsolidated stress states, and compared the predictions of the three-surface model

with corresponding predictions of the modified Cam Clay model, see Figure 5.8a. The model parameters used in the three-surface model can be seen in Table 5.1 and have been derived by Stallebrass (1990) for speswhite kaolin. Each initial stress state represents a different overconsolidation ratio as all three tests were subjected to a maximum mean effective stress of 400 kPa. Figure 5.8a shows that the three-surface model predicts lower peak stress ratios than the modified Cam Clay model. As Stallebrass (1990) noted, this happens for two reasons. The first one is that within the bounding surface, plastic dilatant deformations are occurring for these stress paths and therefore the surfaces contract and in this way it is difficult to reach the high peak state predicted by the modified Cam Clay model. The second reason is that as Al-Tabbaa (1987) and Al-Tabbaa and Wood (1989) observed for the two-surface model, the hardening function can become equal to zero and softening behaviour can be observed for stress states within the bounding surface (see section 4.6.2). In the case of the three-surface model this condition may arise when the term $h_o + H_1 + H_2$ becomes equal to zero.

In order to reproduce the stress paths of Figure 5.8a with the current version of the three-surface model implemented into ICFEP, a circular deviatoric shape has to be assumed for the yield and plastic potential surfaces. The equivalent parameters are quoted in Table 5.2. Figure 5.8b shows the corresponding predictions for the three constant p' tests of Figure 5.8a. Comparison of Figures 5.8a and b indicates that the implemented version of the three-surface model gives the same predictions as the ones presented by Stallebrass (1990).

N	λ^*	κ^*	G_e (kPa)	M	T	S	ψ
3.139	0.073	0.005	60000.0	0.89	0.25	0.08	2.5

Table 5.1: Material parameters used in the three-surface model for the simulation of tests on speswhite kaolin (after Stallebrass (1990))

N	λ^*	κ^*	G_e (kPa)	X	Y	Z	Y_p	Z_p	T	S	ψ
3.139	0.073	0.005	60000.0	0.51	0.0	1.0	0.0	1.0	0.25	0.08	2.5

Table 5.2: Material parameters used in the current version of the three-surface model implemented into ICFEP for the simulation of tests on speswhite kaolin

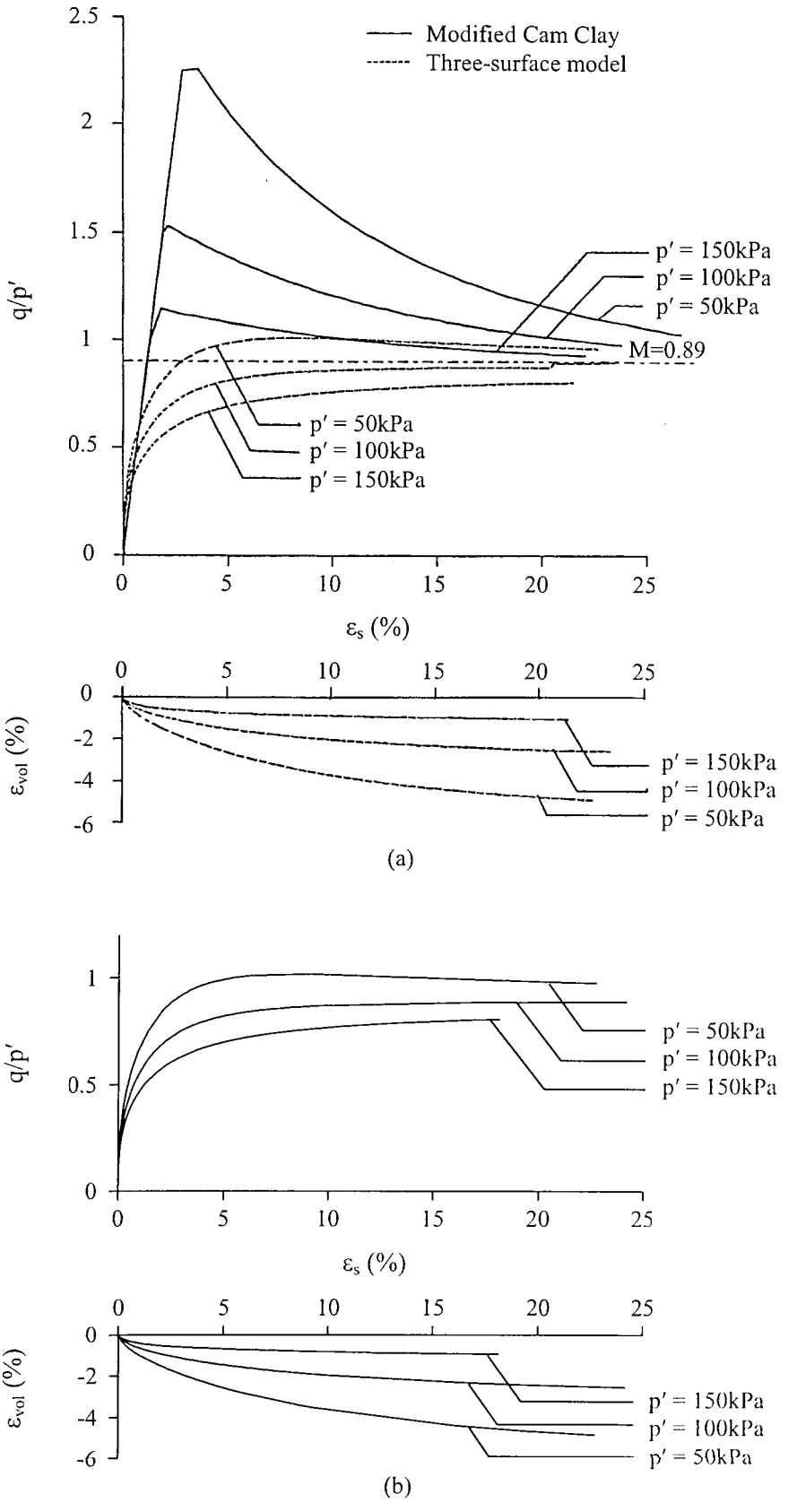


Figure 5.8: Drained constant p' triaxial tests a) model predictions after Stallebrass (1990) b) predictions of three-surface model as implemented into ICFEP

ii) Multi-stage test investigating the effect of recent stress history

This multi-stage test on speswhite kaolin investigated the behaviour along a common constant p' loading path after four different stress path rotations, θ_r = 90°, 0°, -90° and 180° (θ_r is the angle by which the incoming path has to rotate to follow the outgoing path and is taken as positive when the rotation is in a clockwise direction, see Figure 5.9. It is denoted here as θ_r, as opposed to θ used in Chapter 2 to avoid any confusion with the Lode's angle θ). This rotation of the stress path should not be confused with the rotation of the principal stress directions which are fixed in a triaxial test. Stallebrass (1990) followed similar procedures to the work of Atkinson et al. (1990) (reviewed in Chapter 2) and her results showed similar effects of the recent stress history. Figure 5.10a shows the experimental stiffness against stress change curves obtained for the constant p' loading path. It can be seen that the stiffness along the common path is strongly influenced by the direction of the approaching path.

Figure 5.10b shows the model predictions presented by Stallebrass (1990). The test was reproduced by following the same stress paths, in the same order and the parameters used are given in Table 5.1. The configuration of the surfaces at the start and end of each shearing stage can be seen in Figure 5.11a. Comparison of Figures 5.10a and b shows that the patterns of behaviour are reasonably well reproduced. However, for θ_r = -90° and θ_r = 180° a drop in the stiffness curves can be observed. This is the point at which the current stress state reaches the first kinematic surface and the behaviour becomes elasto-plastic. Similarly to the two-surface model, this observed drop in stiffness can be attributed to the fact that the model does not predict a smooth elasto-plastic transition and is related to the form of the hardening function assumed in the model.

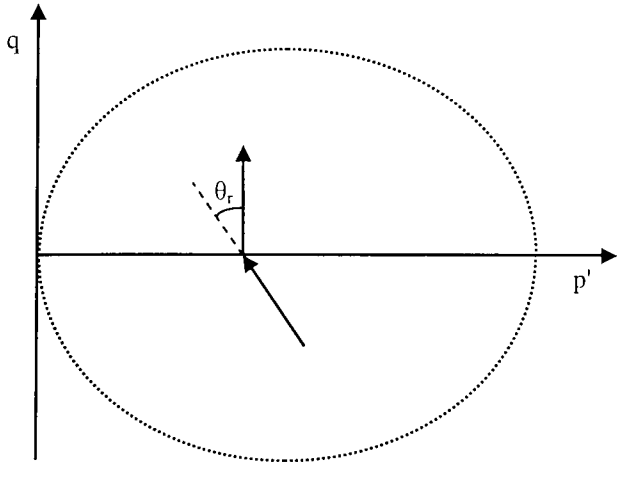


Figure 5.9: Definition of the angle θ_r

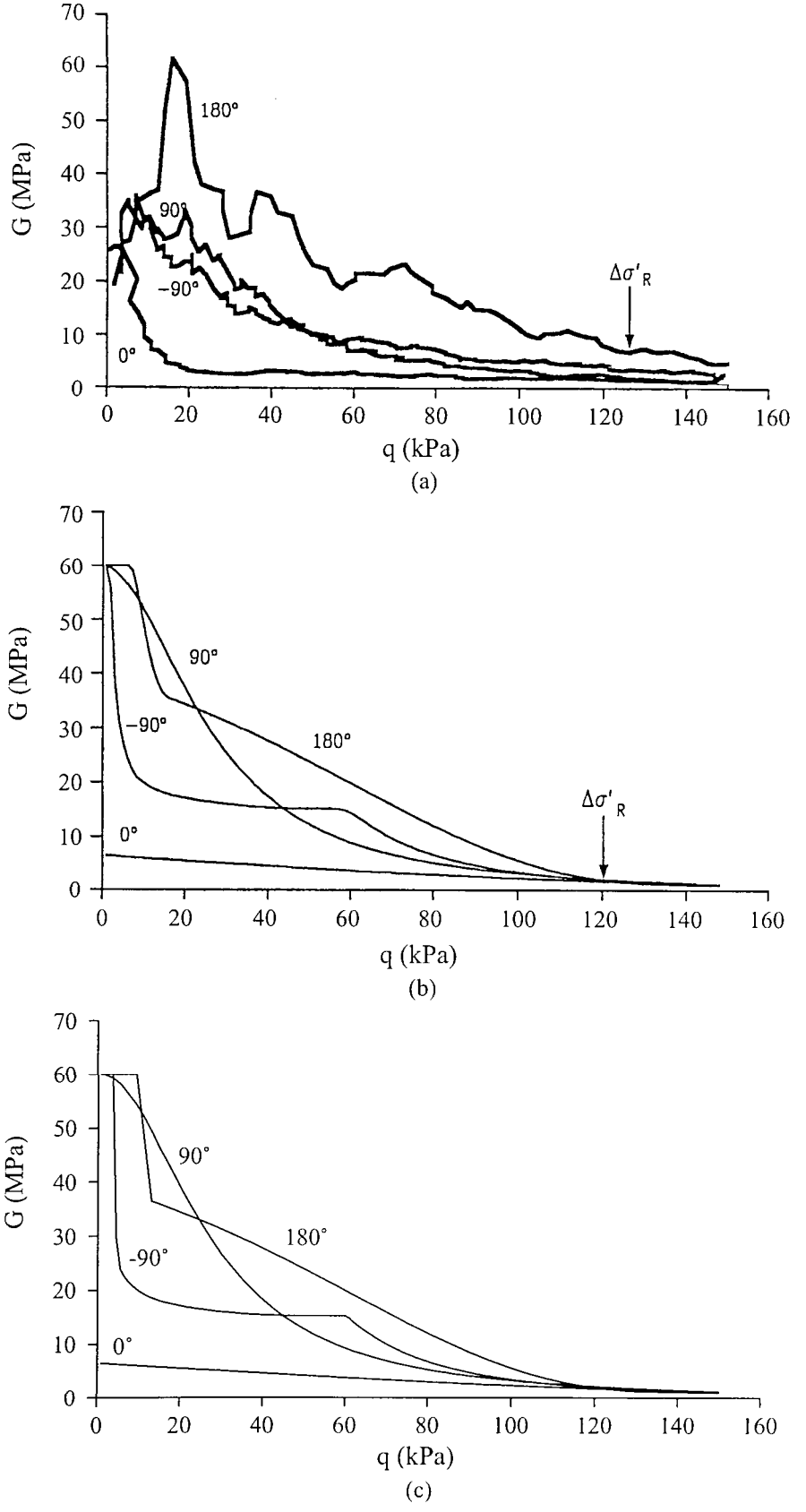
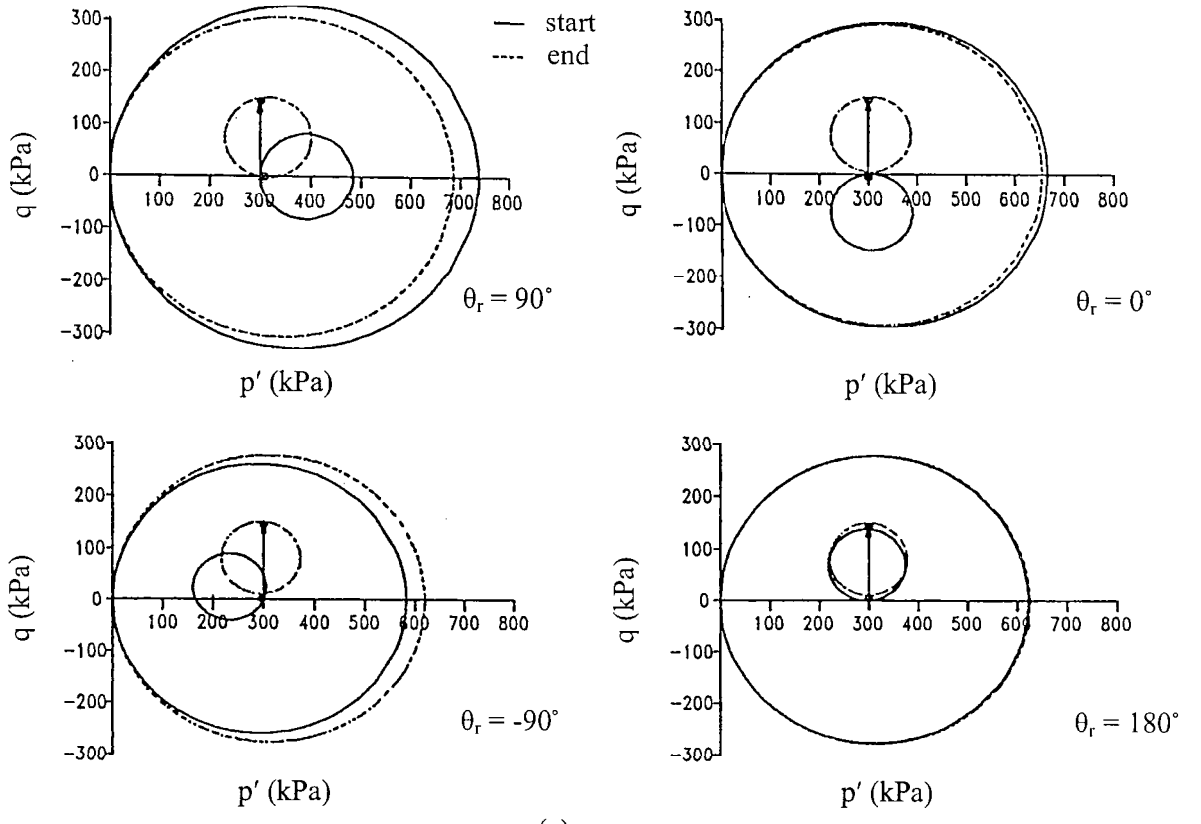


Figure 5.10: Constant p' loading after four stress path rotations: G against q
a) experimental data (after Stallebrass (1990)) b) model predictions (after Stallebrass (1990)) c) predictions of three-surface model as implemented into ICFEP



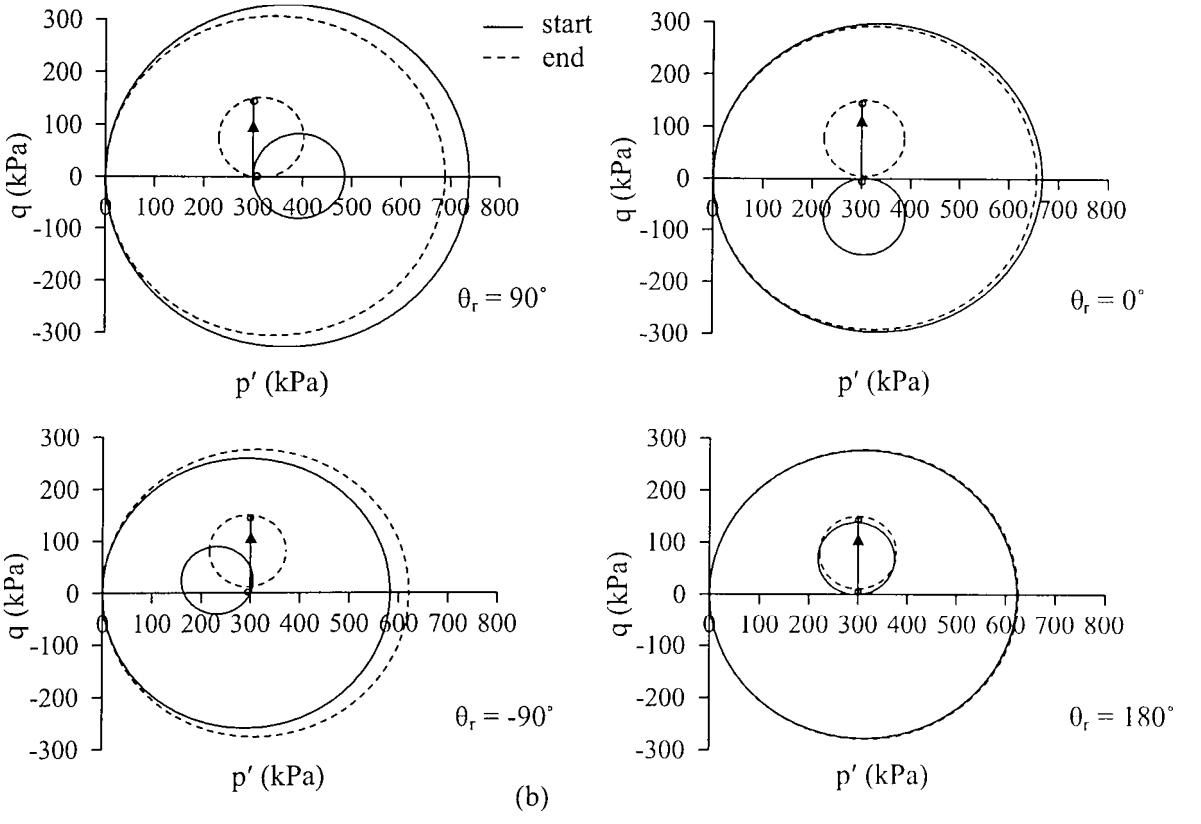


Figure 5.11: Configuration of the three surfaces at the start and end of each cycle a) after Stallebrass (1990)) b) current version of the three-surface model

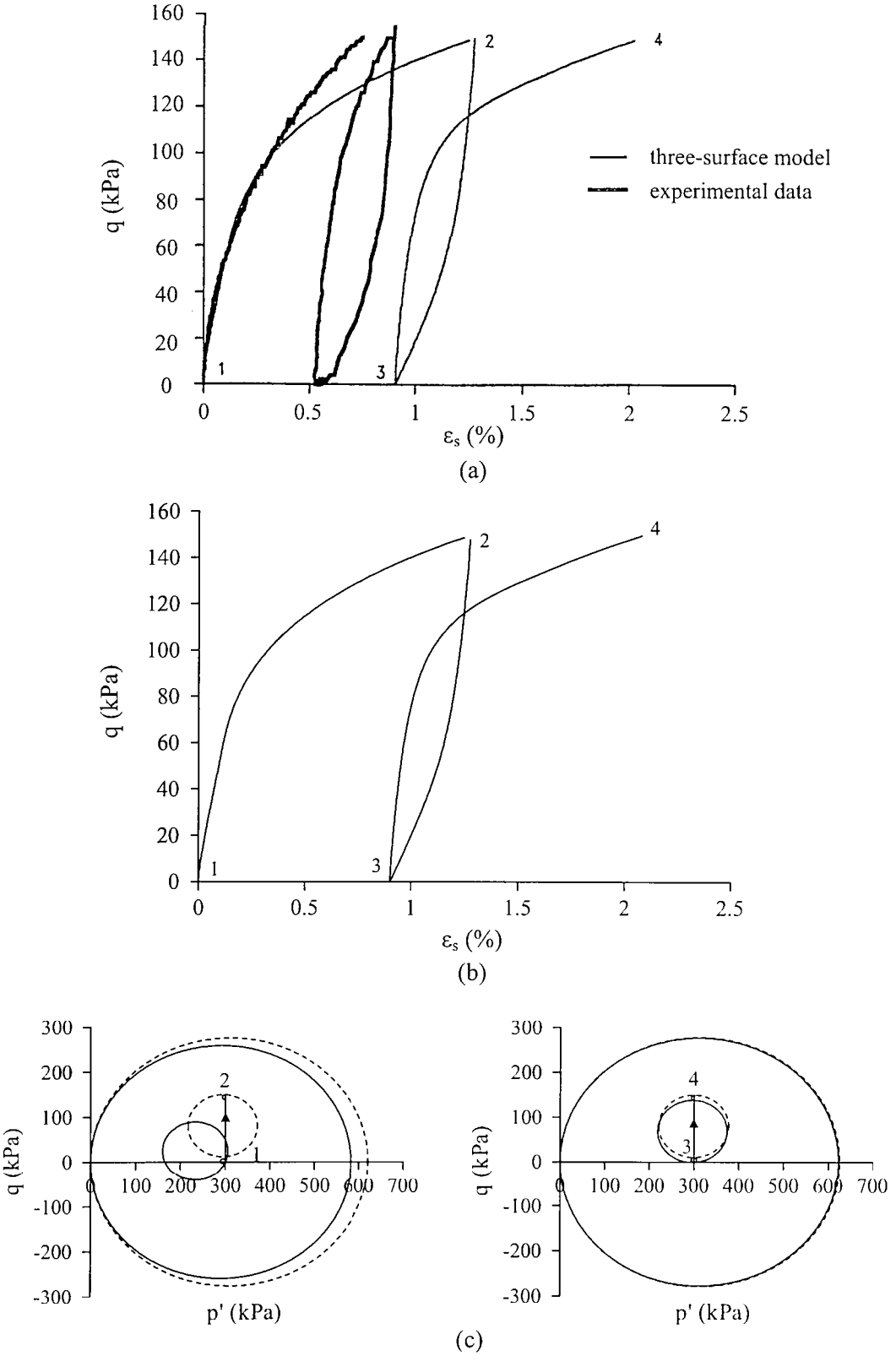


Figure 5.12: Cycles of constant p' loading (θ_r = -90° and θ_r = 180°): q versus ε_s a) experimental data and model predictions (after Stallebrass (1990)) b) predictions of three-surface model as implemented into ICFEP c) sketch showing the location of the surfaces at the start and finish of each cycle

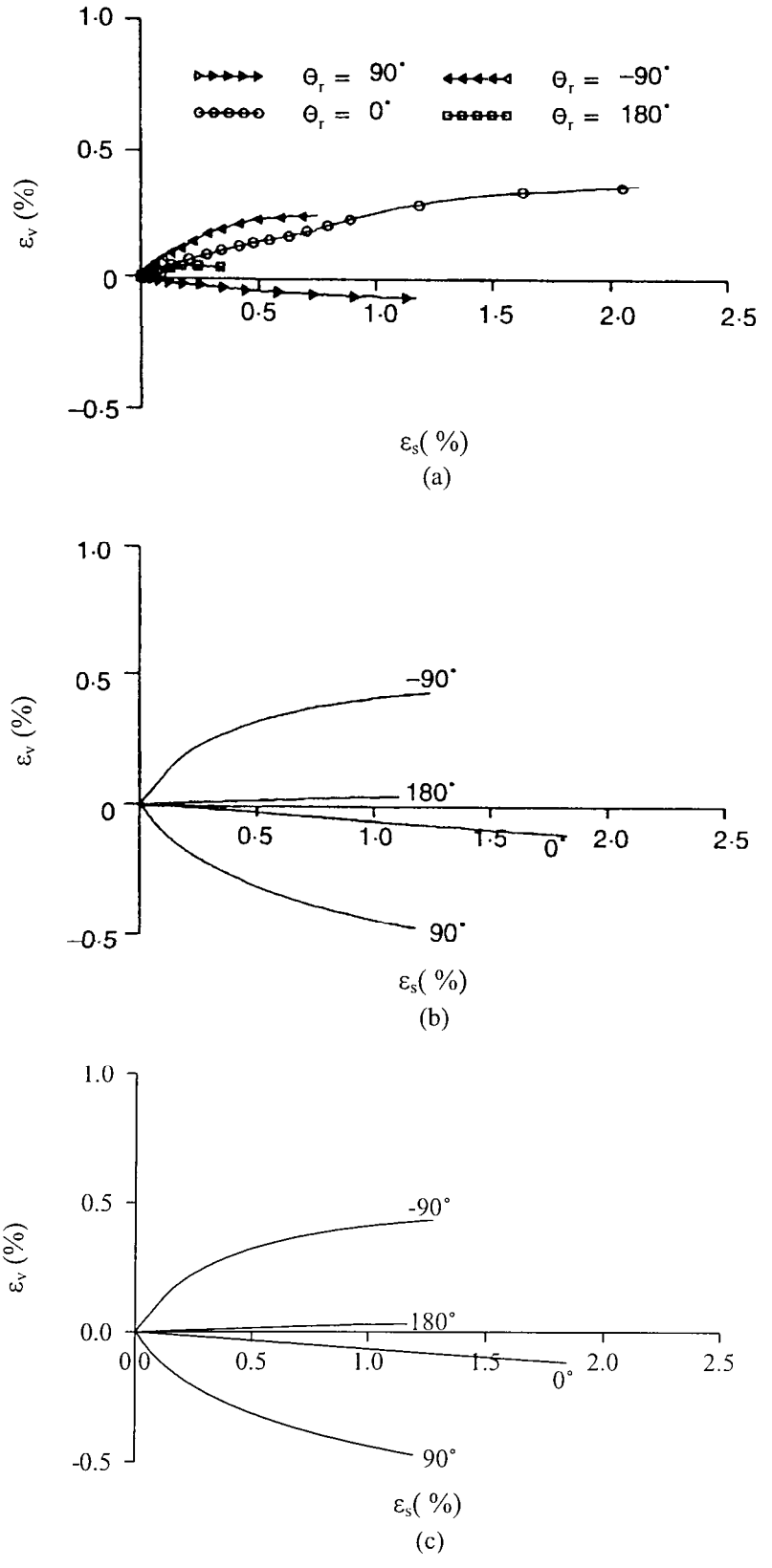


Figure 5.13: Constant p' loading after four stress path rotations: ε_v against ε_s
a) experimental data (after Stallebrass (1990)) b) model predictions (after Stallebrass (1990)) c) predictions of three-surface model as implemented into ICFEP

Figures 5.10c and 5.11b show the predictions of the version of the three-surface model implemented into ICFEP (the model parameters are given in Table 5.2). Comparison of Figures 5.10b and 5.11a with Figures 5.10c and 5.11b respectively, indicates that the predictions of the current version of the three-surface model are in agreement with the predictions presented by Stallebrass (1990).

Figure 5.12a presents the measured and predicted stress-strain data for the constant p' cycle between θ_r = -90° and θ_r = 180° (after Stallebrass (1990)). The location of the surfaces at the start and end of each cycle can be seen in Figure 5.12c. The model seems to overpredict the reduction in stiffness at the end of loading, resulting in higher shear strains. Figure 5.12b shows the predictions of the current version of the three-surface model which agree with those of Figure 5.12a.

The strain paths obtained for the common stress path can be seen in Figure 5.13a. Whether the initial response is dilatant or compressive seems to be influenced by recent stress history. Figure 5.13b shows the model predictions obtained by Stallebrass (1990). Comparison with the experimental results shows that the general pattern of the strain paths is similar to the observed ones (apart from θ_r = 0°), but in general the volumetric strains predicted are higher than the ones observed. Figure 5.13c shows the predictions obtained from the current version of the three-surface model. These are the same as the predictions presented by Stallebrass (1990) in Figure 5.13b. Further discussion of this multi-stage test will follow in Chapter 7 where this is used for the evaluation of all models.

5.5.3 Different yield and plastic potential surfaces in the deviatoric plane

In order to show that the different deviatoric shapes have been implemented correctly in this version of the three-surface model, the same undrained tests of section 4.6.3 were repeated (section 4.6.3 investigated the implementation of the different deviatoric shapes for the two-surface model). These involved the simulation of a number of undrained triaxial compression, triaxial extension and plane strain compression tests, starting from isotropic normally and overconsolidated stress states. Four different cases were considered for the deviatoric shapes of the yield and plastic potential surfaces. In case A the yield and plastic potential surfaces were assumed to have a circular shape. Case B assumed a Mohr-Coulomb hexagon for the shape of the yield surface and a circular shape for the plastic potential. In Case C both the yield and plastic potential surfaces had a Lade shape. Finally, in Case D a Lade shape for the yield surface and a circular shape

for the plastic potential were assumed. These combinations are the same as in section 4.6.3 and the reason for choosing them has already been discussed there.

For the above simulations the set of model parameters for speswhite kaolin (Table 5.2) was used, with the only difference that the parameters defining the shape of the yield and plastic potential surfaces in the deviatoric plane are those given in Table 5.3 for each of the four cases. These parameters were chosen such that all four cases predict the same strength in triaxial compression. The values in Table 5.3 are slightly different than the equivalent ones in Table 4.5 (section 4.6.3) since Stallebrass (1990) assumed a slightly smaller value of M for speswhite kaolin than Al-Tabbaa (1987). Table 5.4 presents the values of θ_f and $g(\theta_f)$ calculated analytically for each case as well as the equivalent values of φ' at failure (the values of $g(\theta_f)$ have been obtained from Equations 4.27 and 4.28 and the values of θ_f for plane strain failure have been calculated from Equation

Case	X	Y	Z	Y_p	Z_p
A	0.51	0.0	1.0	0.0	1.0
C	0.46	0.35	0.25	0.35	0.25
D	0.46	0.35	0.25	0.0	1.0
	φ'	-	-	Y_p	Z_p
B	22.8°	-	-	0.0	1.0

Table 5.3: Model parameters defining the shape of the yield and plastic potential surfaces in the deviatoric plane

Case	Triaxial Compression			Triaxial Extension			Plane strain Compression		
	θ_f	$g(\theta_f)$	φ'_f	θ_f	$g(\theta_f)$	φ'_f	θ_f	$g(\theta_f)$	φ'_f
A	-30°	0.51	22.8°	30°	0.51	31.5°	0°	0.51	30.9°
B	-30°	0.51	22.8°	30°	0.4	22.8°	0°	0.39	22.8°
C	-30°	0.51	22.8°	30°	0.43	24.9°	-14.4°	0.5	26.5°
D	-30°	0.51	22.8°	30°	0.43	24.9°	0°	0.46	27.4°

Table 5.4: Values of θ_f, $g(\theta_f)$ and equivalent values of φ'_f for the four cases analysed

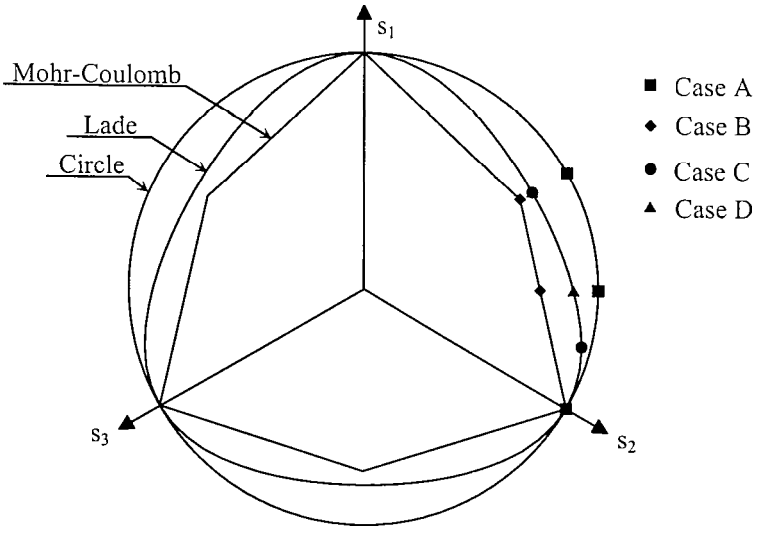


Figure 5.14: Failure surfaces in the deviatoric plane and the values of $g(\theta_f)$ obtained for each case

4.74). Figure 5.14 shows the shape of the failure surfaces for each case and the $g(\theta_f)$ values tabulated in Table 5.4.

Figures 5.15, 5.16, 5.17 and 5.18 present the predicted undrained stress paths in J-p' space for cases A, B, C and D respectively. The failure lines plotted on each graph are those corresponding to the values of $g(\theta_f)$ calculated analytically and quoted in Table 5.4. Figures 5.15 to 5.18 show that the failure conditions predicted by the current version of the three-surface model are in agreement with the analytical calculations. Moreover, it can be shown that the undrained strength for each case can be calculated analytically from the equations of Appendix III and that this agrees with the one predicted from the finite element analyses.

5.5.4 Elasto-plastic transition

As already discussed in section 5.5.2 the model does not predict a smooth elasto-plastic transition when the stress state reaches the kinematic yield surface and this is due to the hardening function assumed in the model. Similar to the two-surface model, this proves to be a drawback of the model when trying to simulate the small strain pre-failure behaviour of overconsolidated clays. Figure 5.19 shows the experimental and predicted results for an undrained triaxial compression test on reconstituted London Clay. Before the start of the shearing stage the sample was one-dimensionally compressed and then

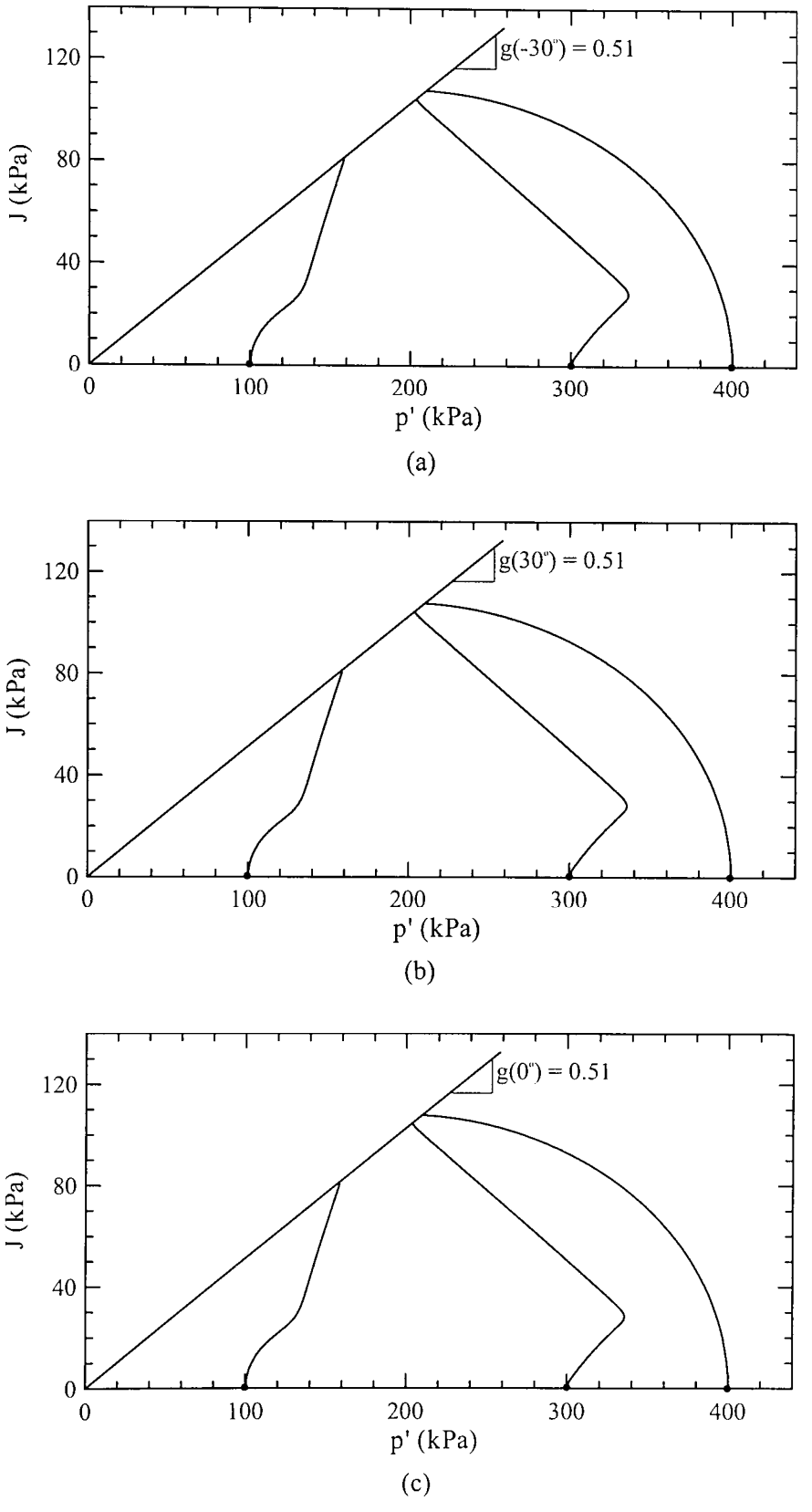
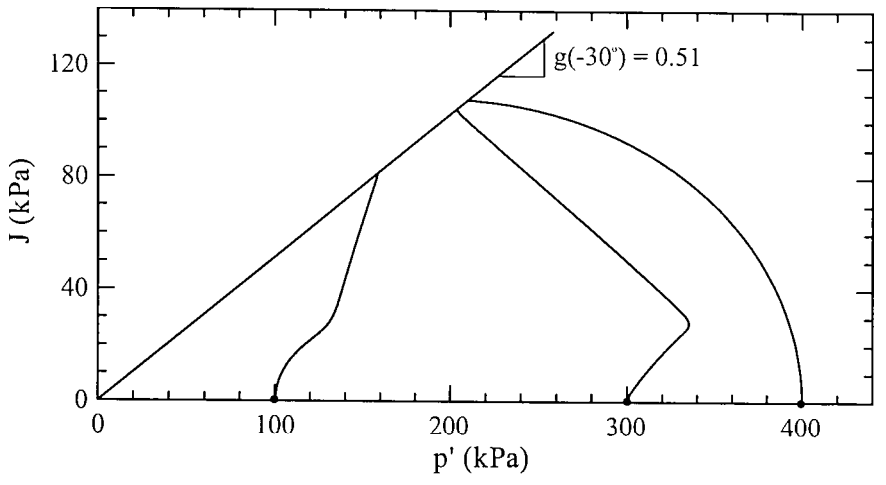
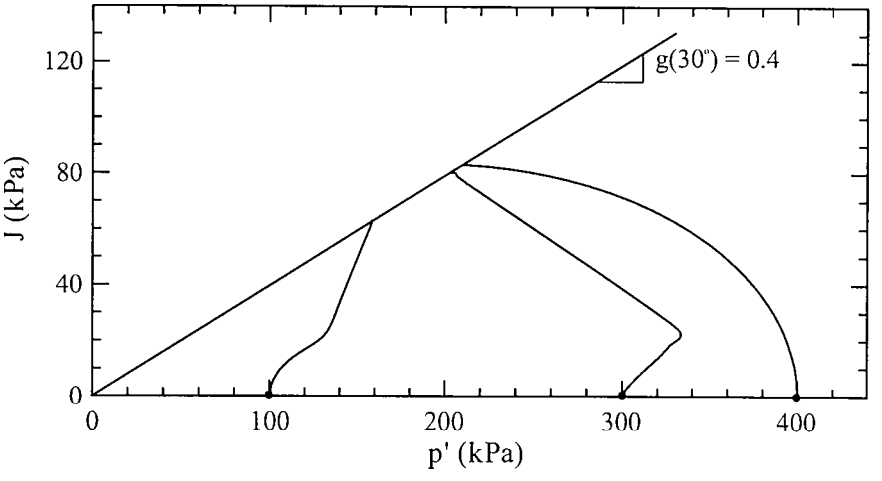


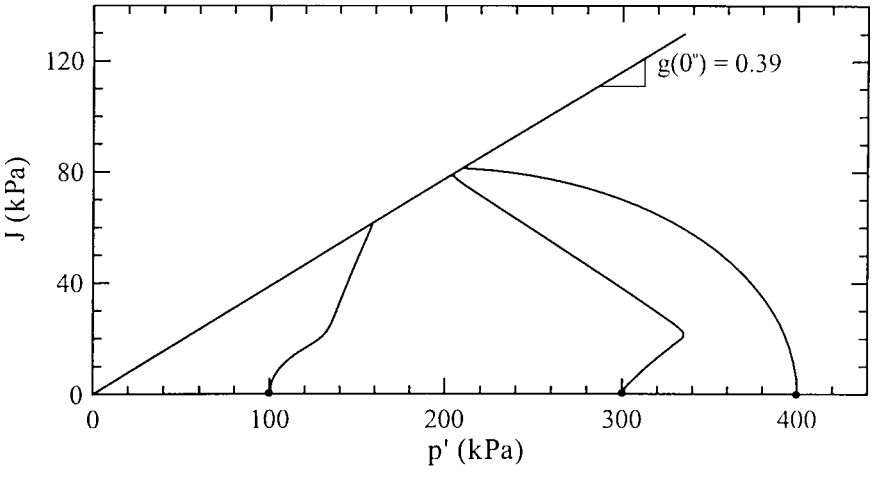
Figure 5.15: Predicted undrained stress paths after an isotropic stress history for case A - circular shape for the yield surface and the plastic potential in the deviatoric plane a) triaxial compression b) triaxial extension c) plane strain compression



(a)



(b)



(c)

Figure 5.16: Predicted undrained stress paths after an isotropic stress history for case B – Mohr-Coulomb shape for the yield surface and circular shape for the plastic potential in the deviatoric plane a) triaxial compression b) triaxial extension c) plane strain compression

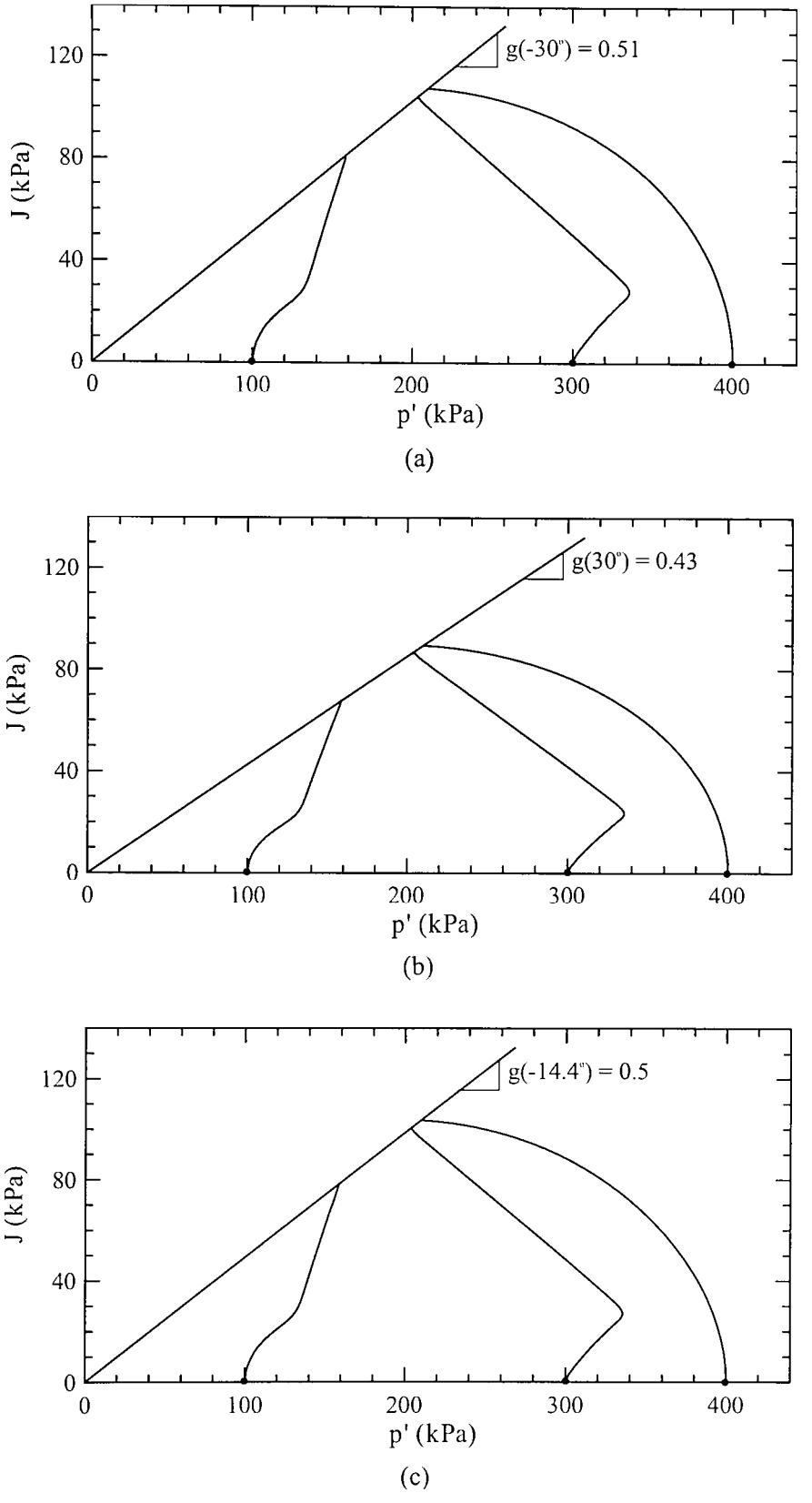


Figure 5.17: Predicted undrained stress paths after an isotropic stress history for case C – Lade shape for the yield surface and the plastic potential in the deviatoric plane a) triaxial compression b) triaxial extension c) plane strain compression

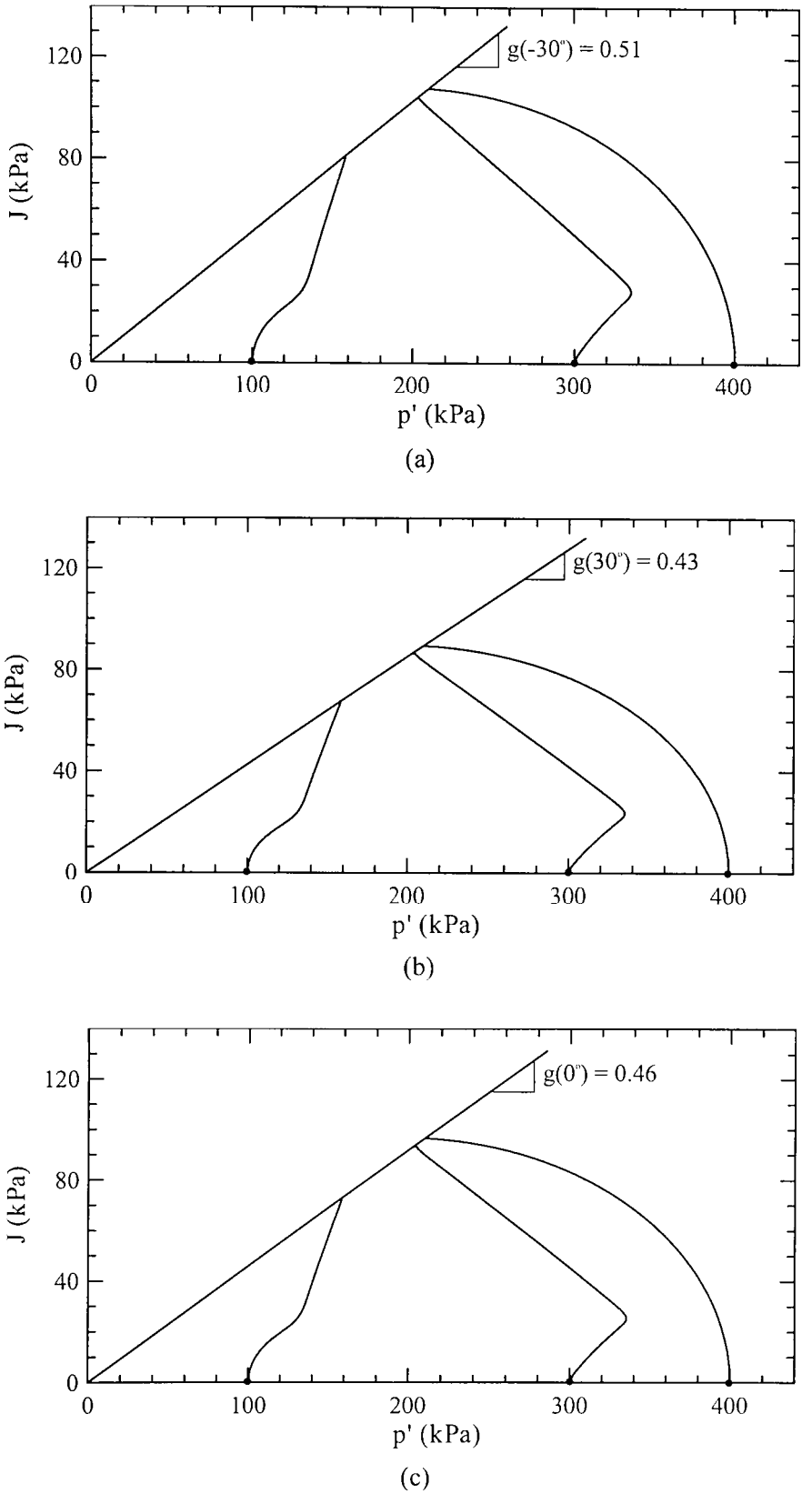


Figure 5.18: Predicted undrained stress paths after an isotropic stress history for case D – Lade shape for the yield surface and circular shape for the plastic potential in the deviatoric plane a) triaxial compression b) triaxial extension c) plane strain compression

swelled to an overconsolidation ratio, *OCR*, of 7. The parameters used in the model simulation are given in Table 5.5 and will be discussed in more detail in Chapter 7. Figure 5.19 shows that the model predicts a drop in stiffness when the stress state becomes elasto-plastic. Similar to the two-surface model, this feature of behaviour results in unrealistic stiffness-strain curves in the small strain range.

N	λ^*	κ^*	A	n	m	φ'	Y_p	Z_p	T	S
3.43	0.097	0.003	590.0	0.87	0.28	22.5°	0.0	1.0	0.2	0.08

Table 5.5: Material parameters used in the current version of the three-surface model for the simulation of the triaxial test in Figure 5.19

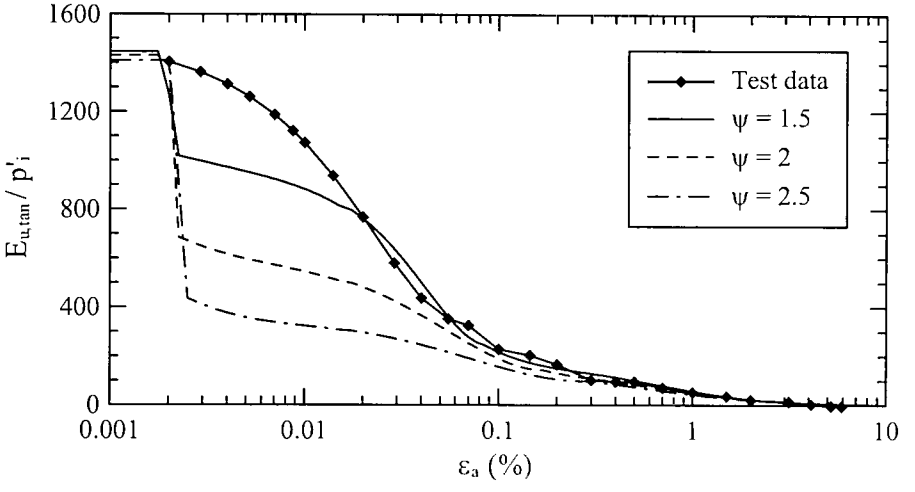


Figure 5.19: Normalised stiffness-strain curve (p'_i is the mean effective stress at the start of shearing) for an undrained triaxial compression test on overconsolidated reconstituted London Clay (experimental results after Jardine (1985))

5.6 Summary

This chapter was divided into four parts. The first part described the original formulation of the three-surface model, developed by Stallebrass (1990). This model is an extension of the two-surface model (Al-Tabbaa (1987)) and incorporates an additional kinematic surface within the bounding surface so as to simulate non-linearity and plasticity from the early stages of loading, as well as the effect of recent stress history, on the behaviour of overconsolidated clays. In the three-surface model the first kinematic surface defines the onset of yielding and is termed the yield surface and the second surface defines the extent of the influence of the recent stress history and hence is named the history

surface. The model requires one additional parameter to the seven of the two-surface model. In terms of the formulation of the model, consideration of the consistency condition of the kinematic yield surface when all three surfaces are in contact shows that the expression of the hardening function used in the model is not consistent with the translation rule of the surfaces when they are in contact.

The second part of the chapter described the extension of the three-surface model from triaxial to general stress space, as well as the improvements that were made in the model during this work. The model is formulated in terms of the volumetric and deviatoric components of the stress and strain tensors, in a similar way to the general formulation of the two-surface model. The improvement made in this general formulation is that the yield and plastic potential surfaces (and hence the failure surface) are not only circular in the deviatoric plane, as assumed in the original formulation, but can take a number of different shapes; hence the model can predict more realistic failure conditions. This general formulation of the model also dealt with the aforementioned inconsistency of the hardening modulus with the translation rule of the surfaces when they are in contact. This problem was solved by changing the active yield surface each time one or more surfaces were in contact and the way this was done was discussed in this second part.

The third part of the chapter discussed the implementation of the general formulation of the model into ICFEP and presented the calculation of the terms required in the implementation.

The validation of the version of the three-surface model implemented into ICFEP was presented in the last part of the chapter. This was done by, firstly, repeating a number of stress paths presented by Stallebrass (1990) and comparing the obtained predictions with the published ones and, secondly, comparing the failure conditions obtained for a number of different combinations of the yield and plastic potential surfaces in the deviatoric plane with analytical calculations. Finally, the elasto-plastic transition predicted by the model was discussed. Similar to the two-surface model, the three-surface model does not predict a smooth elasto-plastic transition and this can be a problem in simulating the highly non-linear pre-failure behaviour of overconsolidated clays in the small strain range. This non-smooth transition can be attributed to the form of the hardening function assumed in the model. In the next chapter, a new hardening function will be adopted for the three-surface model. Further evaluation of the model is given in Chapter 7.

Chapter 6

Modified two- and three-surface models

6.1 Introduction

As already discussed in Chapters 4 and 5, the two-surface and three-surface models predict a non smooth elasto-plastic transition when the stress state engages the first kinematic surface and the behaviour changes from elastic to elasto-plastic. This proves to be an important drawback when trying to simulate the non-linear pre-failure behaviour of overconsolidated clays in the small strain range. This feature of behaviour is related to the form of the hardening modulus adopted in the models. In this chapter a new hardening modulus is proposed for the two- and three-surface models and in this way two new models are formulated, the modified two-surface and modified three-surface models. As it will be shown, the new hardening modulus ensures a smooth elasto-plastic transition and consequently the two new models are capable of simulating realistically pre-failure non-linearity.

6.2 Modified two-surface model

6.2.1 Introduction

This section begins by examining the reason why the hardening modulus of the two-surface model cannot predict a smooth elasto-plastic transition. Before the new hardening modulus for the modified two-surface model is presented, the ideas which led to its formulation are initially described. In particular, two formulations were tested before the third and final formulation was adopted, and these are presented briefly, in

order to help the understanding of the problem. The proposed hardening modulus for the modified two-surface model is then described, followed by the implementation into ICFEP. Finally, in the last part of the section the general characteristics of the modified two-surface model are discussed and the capability of the model to simulate non-linear pre-failure behaviour is evaluated. Further evaluation of the new model is presented in Chapter 7.

6.2.2 Original hardening modulus of the two-surface model

The hardening function adopted in the two-surface model has been described in detail in section 4.3.5 as part of the original triaxial formulation and in section 4.4.6 as part of the general formulation of the version of the two-surface model implemented into ICFEP. Here only the information relevant to the discussion that follows will be presented.

When the kinematic surface moves within the bounding surface, the hardening modulus assumed in the model is:

$$A=\frac{4}{\lambda^{*}-\kappa^{*}}\left[\left(p'-p'_{a}\right)\left[p'_{a}\left(p'-p'_{a}\right)+\frac{1}{2}\left(\frac{\partial F_{y}}{\partial \boldsymbol{s}}:\boldsymbol{s}_{a}\right)+\frac{R^{2}p_{o}'^{2}}{4}\right]+\left(\frac{b}{b_{\max}}\right)^{\psi}\left(\frac{p'_{o}}{2}\right)^{3}\right] \tag{6.1}$$

Equation 6.1 is made up of two components. The first component, A_o, reduces to the modified Cam Clay hardening modulus when the two surfaces are in contact and is given by the following equation:

$$A_{o}=\frac{4}{\lambda^{*}-\kappa^{*}}\left[\left(p'-p'_{a}\right)\left[p'_{a}\left(p'-p'_{a}\right)+\frac{1}{2}\left(\frac{\partial F_{y}}{\partial \boldsymbol{s}}:\boldsymbol{s}_{a}\right)+\frac{R^{2}p_{o}'^{2}}{4}\right]\right] \tag{6.2}$$

The second component, A_1, depends on the degree of approach of the yield surface to the bounding surface and becomes equal to zero when the two surfaces are in contact:

$$A_{1}=\frac{4}{\lambda^{*}-\kappa^{*}}\left(\frac{b}{b_{\max}}\right)^{\psi}\left(\frac{p'_{o}}{2}\right)^{3} \tag{6.3}$$

where b is a measure of the degree of approach of the kinematic surface to the bounding

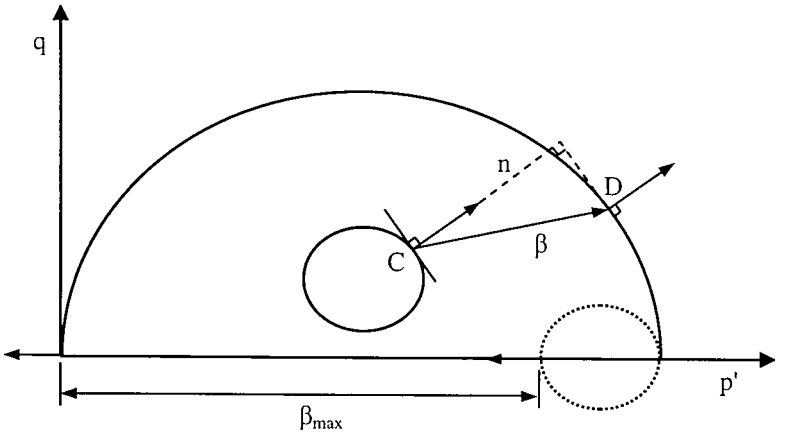


Figure 6.1: Representation in triaxial stress space: diagram defining the main components of the parameter b and the position of the kinematic surface for the maximum value of b, b_{max}

surface. In general stress space the measure b is the product of the tensorial contraction of the direction tensor $\boldsymbol{\beta}$ (which joins the current stress state at the kinematic surface with its conjugate point on the bounding surface) and a direction tensor normal to the kinematic surface at the current stress state, $\boldsymbol{n}$, (Figure 6.1) divided by a measure of the size of the kinematic surface:

$$b = \frac{1}{R\dfrac{p'_o}{2}}\left[\left(p'-p'_a\right)\left[\frac{p'-p'_a}{R}-\left(p'-\frac{p'_o}{2}\right)\right]+\frac{1}{2}\left[\frac{\partial F_y}{\partial \boldsymbol{s}}:\left(\frac{\boldsymbol{s}-\boldsymbol{s}_a}{R}-\boldsymbol{s}\right)\right]\right] \tag{6.4}$$

The maximum value of the function b, b_{max}, is equal to:

$$b_{max} = p'_o\left(1-R\right) \tag{6.5}$$

In order to predict a smooth elasto-plastic transition, the value of the hardening modulus should be infinite when the stress state engages the kinematic surface. This is because when the stress state is within the kinematic surface the strains predicted are elastic and the plastic strains are equal to zero. When the stress state touches the kinematic surface both elastic and plastic strains are predicted, so in order to have a smooth transition the plastic strains should be initially equal to zero and hence the hardening modulus equal to infinity.

Inspection of Equation 6.1 shows that, when the stress state engages the kinematic surface, a finite value of the hardening modulus is calculated. This explains why the model predicts a non-smooth elasto-plastic transition.

6.2.3 Investigating a new hardening function

As aforementioned, two formulations of the hardening modulus were tried before the final hardening modulus was adopted. In this section the ideas behind these two initial formulations are briefly described and the shortcomings of each one of them are discussed. Moreover, the basic idea on which the chosen hardening modulus is based on is briefly presented (a detailed presentation of the hardening modulus of the modified two-surface model is given in the next section).

Following the comments made in the previous section, the hardening modulus required in order to have a smooth variation in stiffness should vary from infinity when the stress state touches the kinematic surface to the value of the hardening modulus on the bounding surface when the two surfaces are in contact. This can be achieved by choosing a function A_1 which varies from infinity, when the stress state first becomes elasto-plastic, to zero, when the two surfaces are in contact.

First formulation

The hardening function, A_1, adopted in the first formulation is of the following form:

$$A_1 \sim \left(\frac{b}{b_{max} - b} \right) \tag{6.6}$$

where b is a measure of the proximity of the kinematic surface to the bounding surface, and is associated with the direction tensor $\boldsymbol{\beta}$, and b_{max} is its maximum value. The value of b_{max} is reset equal to the value of b each time yielding is initiated. Hence, upon initiation of yielding $b = b_{max}$ and $A_1 \sim \infty$ and when the two surfaces are in contact $b = 0$ and $A_1 = 0$. Equation 6.6 is essentially an interpolation rule between these two values of A_1. Therefore, it seems that a function A_1 of the form of Equation 6.6 is capable of predicting a smooth variation in stiffness. (The idea of resetting $b = b_{max}$ upon re-initiation of yielding has been used by Kavvadas and Amorosi (2000) in a different formulation of the hardening modulus).

However, when such a function was implemented into ICFEP, the predicted stiffness variation with strain was not as satisfactory as expected. Figure 6.2b shows a schematic representation of a typical stiffness-strain curve predicted for an undrained triaxial compression test. It can be seen that, although there is not a sudden drop in stiffness when the stress path touches the kinematic yield surface, a relatively fast decay

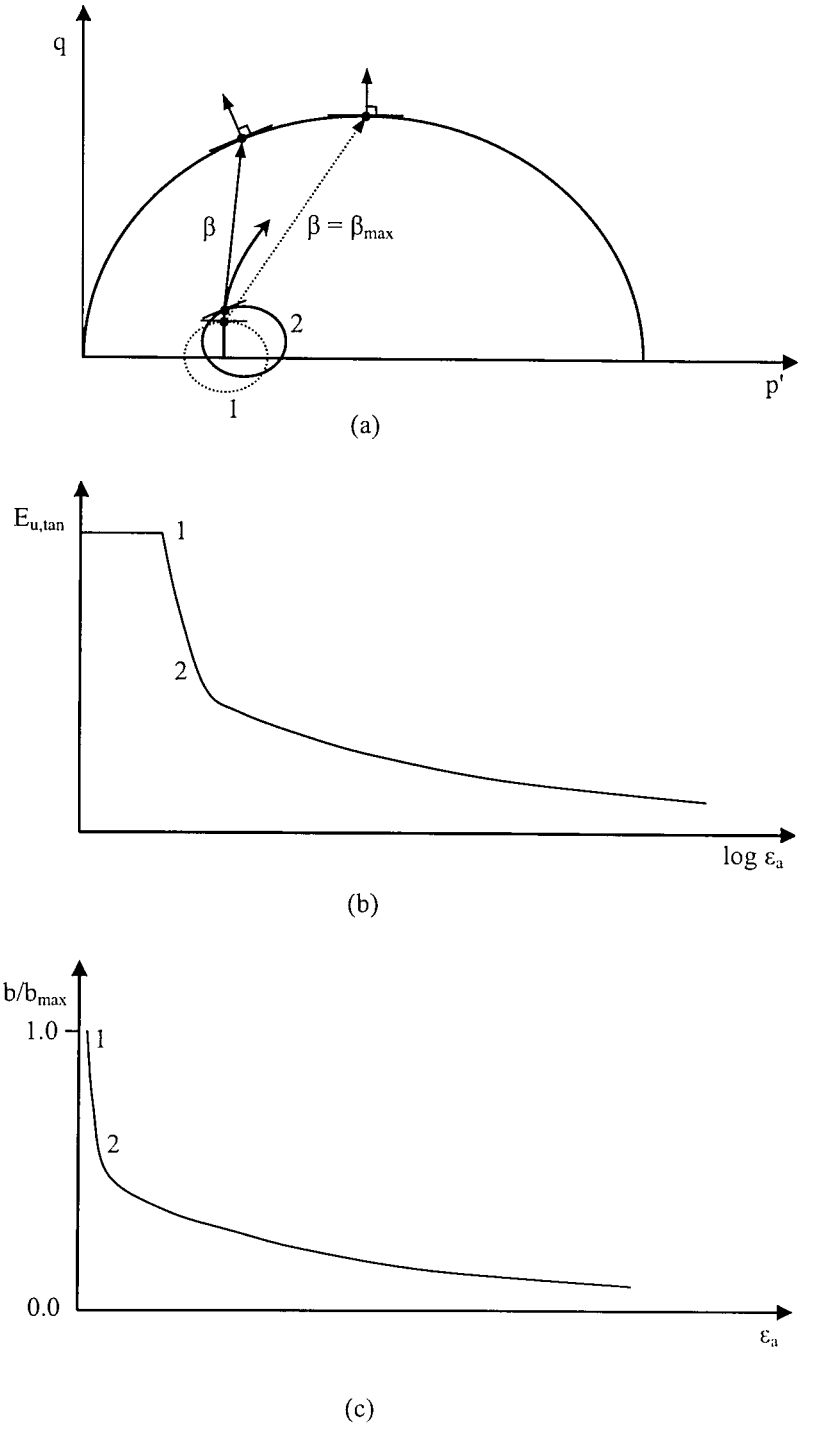


Figure 6.2: Schematic representation of typical results of the first formulation for an undrained triaxial compression test a) stress path b) stiffness-strain curve c) ratio b/b_{max} versus strain

of stiffness with strain can be observed, soon after the stress state becomes elasto-plastic. This feature of behaviour was attributed to the variation of the tensor $\boldsymbol{\beta}$ (or vector β since triaxial conditions apply), and therefore the distance b, at the initial stages of elasto-plastic behaviour. Figure 6.2a shows the variation of the vector β in the initial loading

stages and Figure 6.2c shows a schematic representation of the variation of the ratio b/b_{max} with strain. It seems that for small changes of stress the vector β reduces significantly. This is due to the initial translation of the kinematic surface, which results in the position of the conjugate point moving on the bounding surface. Hence, small movements of the kinematic surface result in significant reductions of the distance b in Equation 6.6 and a fast decay in the values of the hardening function A_1. This results in a fast decay in stiffness in Figure 6.2b. This problem was found to be more pronounced the smaller the kinematic surface is. This is because smaller kinematic surfaces reorientate faster than larger ones, resulting in greater initial variations of the vector β and the distance b.

Second formulation

The hardening function, A_1, adopted in the second formulation is also of the form of Equation 6.6. Similar to the first formulation, b_{max} is set equal to the value of b, when the stress state first becomes elasto-plastic. However, for any subsequent stage, b_{max} is updated with reference to the initial configuration of the kinematic surface upon initiation of yielding. For example, if the change in the size of the bounding surface (p'_o) is ignored, then the value of b_{max} can be calculated as shown in Figure 6.3. Let the current stress state be denoted by C, and the conjugate point on the bounding surface by D. The point E represents the stress state with the same outward normal as D on the position of the kinematic surface upon initiation of yielding. The distance b_{max} is calculated from the direction tensor $\boldsymbol{\beta}_{max}$, which connects the conjugate point D with the point E. In this way the calculation of b_{max} can account for variations of the position of

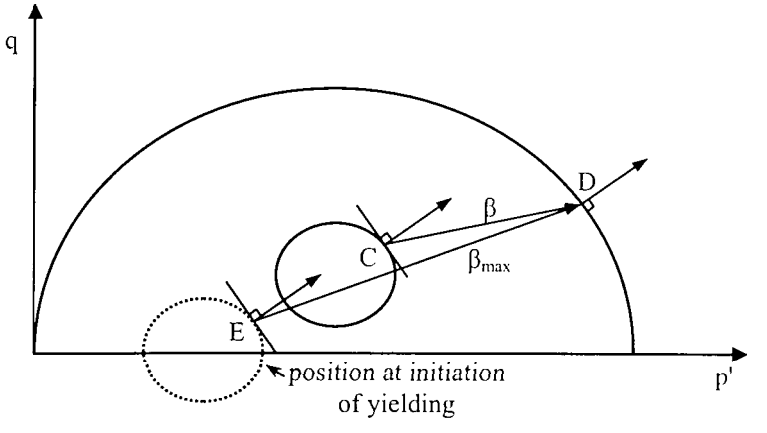


Figure 6.3: Representation in triaxial stress space: calculation of b_{max} for the second formulation (ignoring changes in p'_o)

the conjugate point on the bounding surface. Each time yielding is re-initiated the new configuration of the kinematic surface, upon initiation of yielding, is stored and the calculation of b_{max} for any subsequent stage refers to the new stored position. Figure 6.3 can be modified to account for the change of p'_o between the initial stage and the current

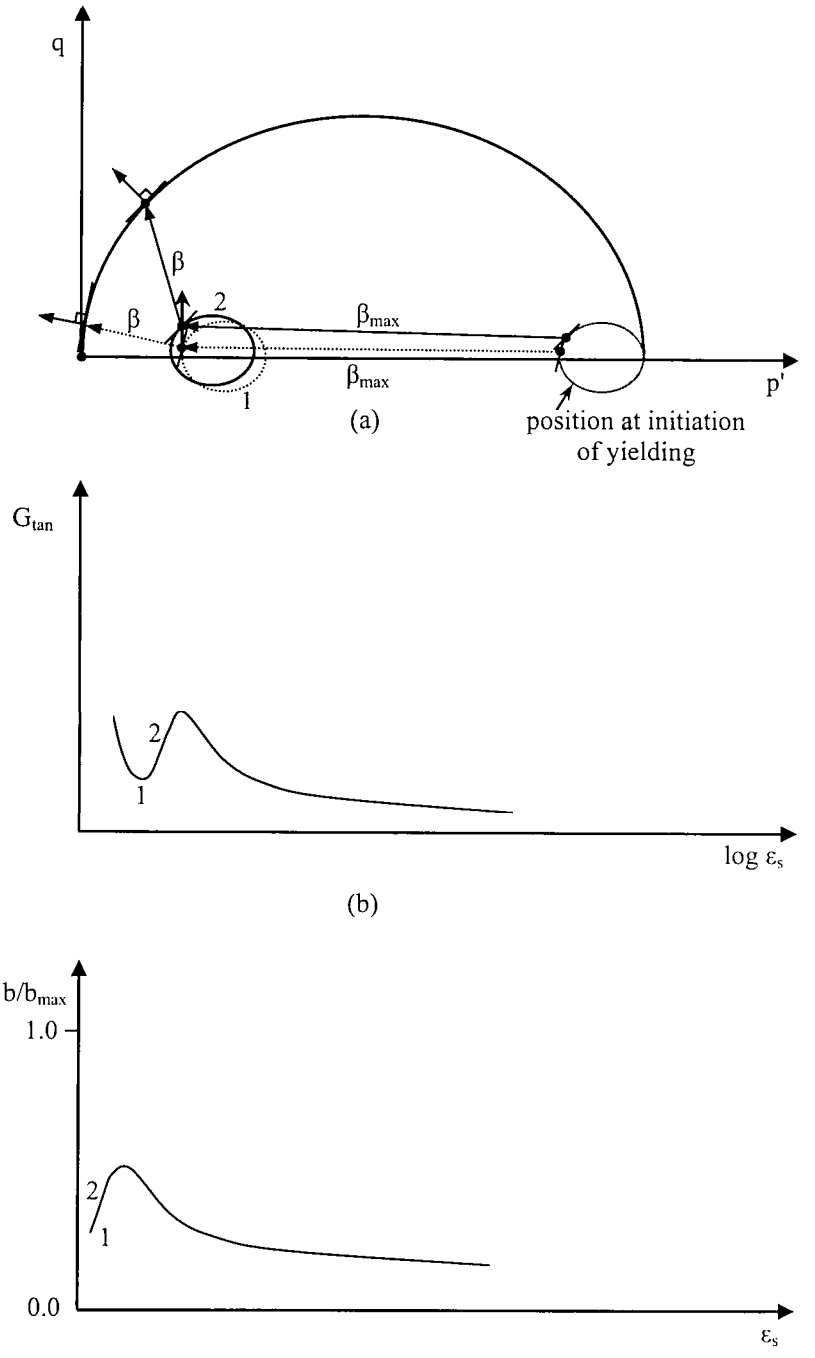


Figure 6.4: Schematic representation of typical results of the second formulation for a constant p' test following isotropic swelling a) stress path b) stiffness-strain curve c) ratio b/b_{max} versus strain

stage, however, for the sake of simplicity this will not be presented here. In this formulation, Equation 6.6 again varies from $A_1 \sim \infty$ when $b = b_{max}$, to $A_1 = 0$ when $b = 0$.

Implementation of the above formulation into ICFEP revealed that this second formulation does predict smooth stiffness-strain curves for stress paths of the type shown in Figure 6.2 and, therefore, the formulation was considered satisfactory at the time. However, new problems began to arise for stress paths in which the direction was abruptly changing without a re-initiation of yielding. Figure 6.4a presents such a stress path. This is a simulation of a triaxial test, involving a path of isotropic swelling followed by a constant p' loading path (for simplicity changes of p'_o have been ignored when plotting the figure). A schematic representation of typical stiffness-strain curves predicted along the constant p' path, by the second formulation, can be seen in Figure 6.4b. Figure 6.4c shows the variation of the ratio b/b_{max} with strain for the same path. The unrealistic increase in stiffness initially in Figure 6.4b can be attributed to the increase in the ratio b/b_{max} in Figure 6.4c. Clearly when there are abrupt changes in the direction of the stress path, without a re-initiation of yielding, it is not reasonable to calculate b_{max} with reference to the initial configuration of the kinematic surface upon initiation of yielding.

Third formulation

This third formulation forms the basis of the chosen hardening modulus for the modified two-surface model. A hardening function, A_1, of the form of Equation 6.6 is also adopted here. Similar to the first and second formulations, the value of b_{max} is set equal to the value of b, when the stress state first becomes elasto-plastic. However, the results of the

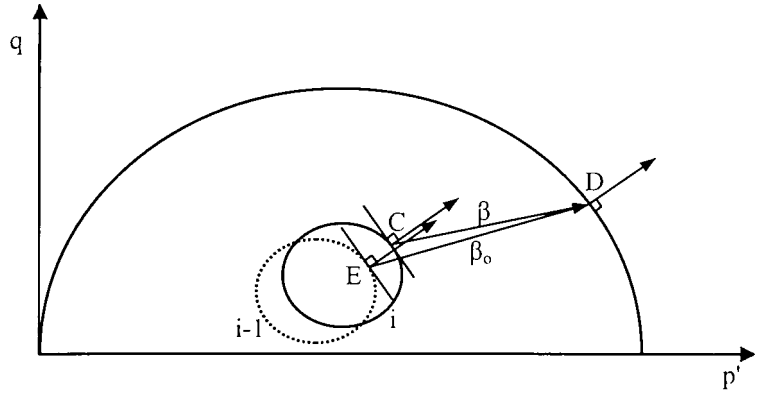


Figure 6.5: Representation in triaxial stress space: calculation of b_o for the third formulation (ignoring changes in p'_o)

second formulation led to the idea of an incremental calculation of b_{max} for any subsequent stage. This can be explained as follows. If i is used in order to denote the current loading stage and i-1 is used to denote the previous loading stage, then the value of ${b_{max}}^{i}$ at the current loading stage i is calculated from the following equation:

$$ {b_{max}}^{i} = \frac{b_o}{b^{i-1}/{b_{max}}^{i-1}} \tag{6.7} $$

where $b^{i-1}/{b_{max}}^{i-1}$ is the ratio of b/b_{max} at the previous loading stage i-1 and the distance b_o is calculated as shown in Figure 6.5. For simplicity, the change in the size of the bounding surface (p'_o) is ignored in Figure 6.5. Let the current stress state at the current loading stage i be denoted by C and the conjugate point on the bounding surface by D. The point E is the stress state with the same outward normal as D on the position of the kinematic surface at the previous loading stage i-1. The distance b_o is calculated from the direction tensor $\boldsymbol{\beta}_o$, which connects the point D with the point E. This incremental calculation of b_{max} accounts for both changes in the position of the conjugate point on the bounding surface, as well as changes in the stress path direction. This idea can then be modified to account for the changes of p'_o. As it will be shown subsequently, the calculation of b_{max} in this way does not depend on the increment size.

The proposed hardening modulus for the modified two-surface model, which is based on this idea, is presented in greater detail in the next section.

6.2.4 Proposed hardening modulus for the modified two-surface model

The hardening function, A_1, chosen for the modified two-surface model, is:

$$ A_1 = \frac{4}{\lambda^* - \kappa^*} \alpha \left(\frac{b^*}{b^*_{max} - b^*} \right) \left(\frac{p'_o}{2} \right)^3 R^2 \tag{6.8} $$

In the above equation, b^* is a measure of the proximity of the kinematic surface to the bounding surface, ${b^*}_{max}$ is its maximum value and α is a parameter which controls the rate of decay of stiffness with strain. The measure of the proximity of the kinematic surface to the bounding surface is denoted by b^*, as compared to b, which is used in the two-surface model, because a slightly different expression is used here. The measure b^* is the product of the tensorial contraction of the direction tensor, $\boldsymbol{\beta}$, and the direction tensor normal to the kinematic surface, $\boldsymbol{n}$, (Figure 6.1):

$$b^* = (p' - p'_a)\left[\frac{p' - p'_a}{R} - \left(p' - \frac{p'_o}{2}\right)\right] + \frac{1}{2}\left[\frac{\partial F_y}{\partial \boldsymbol{s}} : \left(\frac{\boldsymbol{s} - \boldsymbol{s}_a}{R} - \boldsymbol{s}\right)\right] \tag{6.9}$$

As mentioned in the previous section, the maximum value of b^*, $b^*_{\max}$ is calculated as follows. When the stress state first becomes elasto-plastic $b^*_{\max} = b^*$. For any other stage i the value of $b^*_{\max}{}^i$ can be obtained from the following equation:

$$b^{*\,i}_{\max} = \frac{b^*_o}{b^{*i-1} / b^{*\,i-1}_{\max}} \tag{6.10}$$

where b^{*i-1} and $b^*_{\max}{}^{i-1}$ are the values of b^* and $b^*_{\max}$ at the previous loading stage i-1 respectively and b^*_o is calculated as shown in Figure 6.6. Figure 6.6 shows the modifications necessary in order to account for the change in p'_o between the previous and the current loading stages. Figure 6.6a plots the previous loading stage i-1 and Figure 6.6b plots the current loading stage i. As before, the current stress state at the current loading stage i is denoted by C and the conjugate point on the bounding surface by D. Figure 6.6c shows the position of the kinematic and bounding surfaces from which the value of b^*_o can be calculated. This is essentially a homothetic transformation of Figure 6.6a, in which the kinematic and bounding surfaces have the same relative position as in Figure 6.6a, but are scaled by the factor $(p'_o{}^i - p'_o{}^{i-1})/p'_o{}^{i-1}$ so as to account for the change in size of the bounding surface from stage i-1 to stage i. The stress state E in Figure 6.6c has the same outward normal with the conjugate point D. The distance b^*_o is the value of b^* corresponding to the direction tensor $\boldsymbol{\beta}_o$ which connects the conjugate point on the bounding surface, D, to the stress state E. Hence, b^*_o is the product of the tensorial contraction of the tensor $\boldsymbol{\beta}_o$ and a tensor normal to the kinematic surface at the stress state E, $\boldsymbol{n}_o$. Since the stress states C, D and E have the same outward normal $\boldsymbol{n}_o = \boldsymbol{n}$. The direction tensor $\boldsymbol{\beta}_o$ is:

$$\boldsymbol{\beta}_o = \boldsymbol{\sigma}'_D - \boldsymbol{\sigma}'_E = \boldsymbol{\beta} + \boldsymbol{\sigma}'^{\,i}_a - \boldsymbol{\sigma}'^{\,i-1}_a \left(1 + \frac{p'^{\,i}_o - p'^{\,i-1}_o}{p'^{\,i-1}_o}\right) \tag{6.11}$$

where:

$$\boldsymbol{\beta} = \frac{\boldsymbol{\sigma}'^{\,i} - \boldsymbol{\sigma}'^{\,i}_a}{R} - \left(\boldsymbol{\sigma}'^{\,i} - \frac{\boldsymbol{\sigma}'^{\,i}_o}{2}\right) \tag{6.12}$$

and $\boldsymbol{\sigma}'^{\,i}$ and $\boldsymbol{\sigma}'_a{}^{\,i}$ refer to the current stress state C and the centre of the kinematic surface

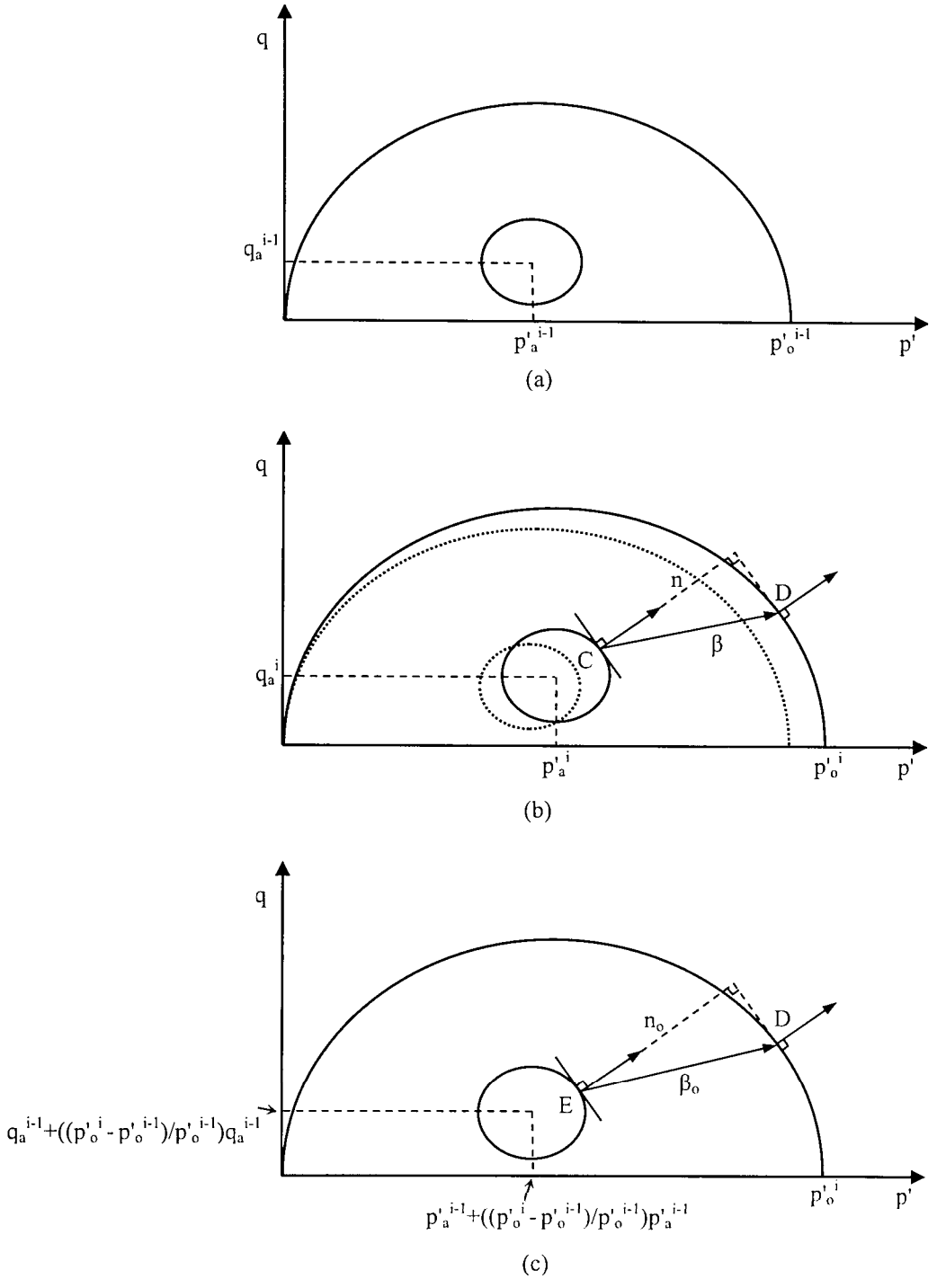


Figure 6.6: Representation in triaxial stress space of a) previous loading stage *i*-1 b) current loading stage *i* c) configuration of the surfaces for the calculation of the value of b^*_o

at the current loading stage *i* respectively.

The resulting b^*_o is:

$$b_o^* = \left(p'^i - p_a'^i\right)\left(p'_D - p'_E\right) + \frac{1}{2}\frac{\partial F_y}{\partial \boldsymbol{s}} : \left(\boldsymbol{s}_D - \boldsymbol{s}_E\right) \tag{6.13}$$

where the terms p'_D - p'_E and $\boldsymbol{s}_D$ - $\boldsymbol{s}_E$ can be calculated from Equation 6.11.

To summarise, Equation 6.8 is an interpolation rule between $A_1 \sim \infty$, upon initiation of yielding ($b^* = b^*_{\max}$), and $A_1 = 0$, when the two surfaces are in contact ($b^* = 0$). Moreover, the term $(p'_o / 2)^3$ is an average value of the hardening modulus on the bounding surface, which is scaled by the factor R^2 for the kinematic yield surface.

The complete proposed hardening function for the case that the kinematic surface moves within the bounding surface is:

$$A = \frac{4}{\lambda^* - \kappa^*}\left[\left(p' - p'_a\right)\left[p'_a\left(p' - p'_a\right) + \frac{1}{2}\left(\frac{\partial F_y}{\partial \boldsymbol{s}} : \boldsymbol{s}_a\right) + \frac{R^2 p_o'^2}{4}\right] + \alpha\left(\frac{b^*}{b^*_{\max} - b^*}\right)\left(\frac{p'_o}{2}\right)^3 R^2\right] \tag{6.14}$$

Incorporation of the above equation into the framework of the two-surface model results in the modified two-surface model. This new model retains the same yield and plastic potential functions, hardening rules and elastic part as the generalised version of the two-surface model described in section 4.4 of Chapter 4. The only ingredient that is different in this new model is the hardening modulus for the case when the kinematic surface moves within the bounding surface and Equation 6.14 is used instead of Equation 4.42 (or 6.1).

6.2.5 Model parameters

The new model has the same number of parameters as the generalised version of the two-surface model. The parameter α in the current hardening modulus replaces the parameter ψ in the previous hardening modulus, whereas the rest of the parameters remain the same. The new model parameters are:

λ^*: the slope of the isotropic normal compression line in ln$v$-lnp' space

κ^*: the slope of the swelling line in ln$v$-lnp' space for a stress path that lies entirely within the kinematic yield surface

μ or G_e, or G_e/p': the Poisson's ratio or the elastic shear stiffness. If Equation 4.51 is used then the material parameters A, n and m must be provided

φ' or X, Y and Z: the angle of shearing resistance or the constants $X = \sin(\varphi'_{\theta=0^\circ})$, Y and Z in Equation 4.28 at the critical state

Y_p and Z_p: the constants Y_p and Z_p in Equation 4.31

R: the ratio of the size of the kinematic yield surface to that of the bounding surface

α: parameter in the hardening modulus A

N: one additional parameter is required to fix the model in $\ln v$-$\ln p'$ space and this is usually taken as the specific volume of the isotropic compression line at $p' = 1$ kPa

The new parameter α (which controls the rate of decay of stiffness) cannot be obtained directly from experimental data (similar to the parameter ψ in the two-surface model) and its value has to be determined by trial and error.

6.2.6 Implementation

The implementation of the modified two-surface model into ICFEP follows the implementation of the generalised formulation of the two-surface model described in section 4.5 of Chapter 4. The only difference arises in the implementation of the new hardening modulus, for the case when the kinematic surface moves within the bounding surface, which actually requires the calculation of some extra terms.

The hardening modulus A for this case can be expressed in vector notation as follows:

$$A = \frac{4}{\lambda^* - \kappa^*}\left[\left(p' - p'_a\right)\left[p'_a\left(p' - p'_a\right) + \frac{1}{2}\left\{\frac{\partial F_y}{\partial s}\right\}^T \{s_a\} + \frac{R^2 p_o'^2}{4}\right] + \alpha\left(\frac{b^*}{b^*_{\max} - b^*}\right)\left(\frac{p'_o}{2}\right)^3 R^2\right] \tag{6.15}$$

where

$$b^* = (p' - p'_a)\left[\frac{p' - p'_a}{R} - \left(p' - \frac{p'_o}{2}\right)\right] + \frac{1}{2}\left\{\frac{\partial F_y}{\partial s}\right\}^T \left\{\frac{s - s_a}{R} - s\right\} \tag{6.16}$$

The value of b^*_{max} is set equal to b^* upon initiation of yielding and for any subsequent stage can be calculated from Equation 6.10. The term b^*_o can be written in vector notation form as:

$$b^*_o = (p' - p'_a)(p'_D - p'_E) + \frac{1}{2}\left\{\frac{\partial F_y}{\partial s}\right\}^T \{s_D - s_E\} \tag{6.17}$$

where p' and p'_a refer to the current stage and the terms p'_D - p'_E and $\{s_D$ - $s_E\}$ can be calculated from Equation 6.11.

The flowchart of the subroutine which is used by the stress point algorithm for the modified two-surface model is given in Appendix V.

6.2.7 General characteristics

The modified two-surface model retains the following general characteristics of the general formulation of the two-surface model. The undrained strength predicted by the model can be calculated from the equations of Appendix III. It can be shown that, similar to the two-surface model, the modified two-surface model can predict lower peak drained stresses for highly overconsolidated states than the modified Cam Clay model. Moreover, the model is capable of predicting anisotropic yielding, depending on the position of the kinematic surface, but isotropic strength. The model also adopts the same range of deviatoric shapes of the yield and plastic potential surfaces, and hence the failure surface, as the general formulation of the two-surface model.

The major improvement of the modified two-surface model over the original two-surface model is the capability to predict a smooth elasto-plastic transition and hence realistic non-linear pre-failure behaviour.

6.2.7.1 Elasto-plastic transition and non-linearity

Figure 6.7 presents the predictions of the model for an undrained triaxial compression test on overconsolidated reconstituted London Clay (OCR = 7). Values of α = 3, 6 and 9 have been used with all other model parameters being summarised in Table 6.1. The

N	λ^*	κ^*	A	n	m	φ'	Y_p	Z_p	R
3.43	0.097	0.003	590.0	0.87	0.28	22.5°	0.0	1.0	0.016

Table 6.1: Material parameters used in the modified two-surface model for the simulation of the triaxial test in Figure 6.7

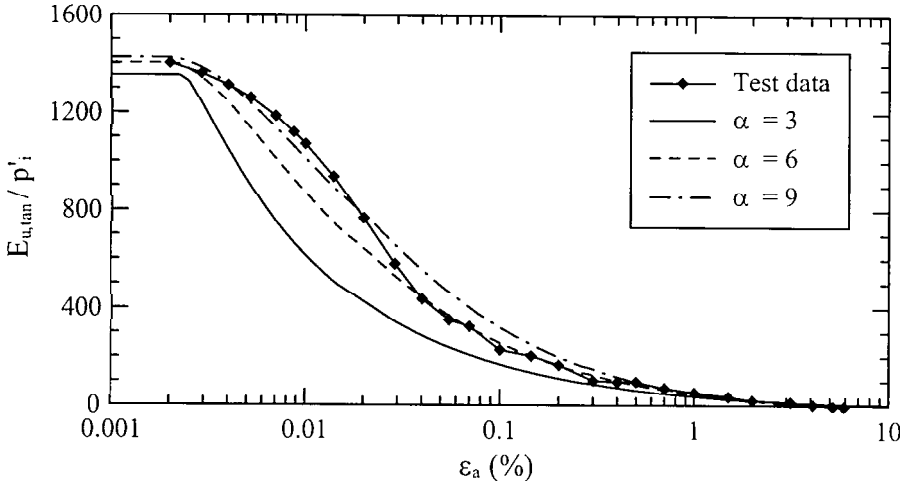


Figure 6.7: Predictions of the modified two-surface model for an undrained triaxial compression test on overconsolidated reconstituted London Clay (test data after Jardine (1985)): Normalised stiffness-strain curve (p'_i is the value of p' at the start of shearing)

predictions of the two-surface model for the same test were discussed in section 4.6.5 and can be seen in Figure 4.27. Figure 6.7 shows that the modified two-surface model predicts a smooth stiffness variation with strain, with no abrupt drop in stiffness once yielding begins. This is true for all values of the material parameter α. In this way, the new model can simulate much more satisfactorily than the two-surface model the non-linear pre-failure behaviour in the small strain range. (Satisfactory predictions are also obtained for stress paths of the type shown in Figure 6.4, see Chapter 7).

In order to show that the calculation of the new hardening modulus for the modified two-surface model is not increment size dependent, the undrained triaxial test presented in Figure 6.7 was repeated for α = 6 and for different increment sizes. Figure 6.8 presents the variation of the ratio b^*/b^*_{max} with strain and the resulting stress-strain curves. As it can be seen the ratio b^*/b^*_{max} does not depend on the increment size (Figure 6.8a). Hence, the new hardening modulus (Equation 6.14) is not increment size dependent. Figure 6.8b confirms that the resulting stress-strain curves do not depend on the increment size.

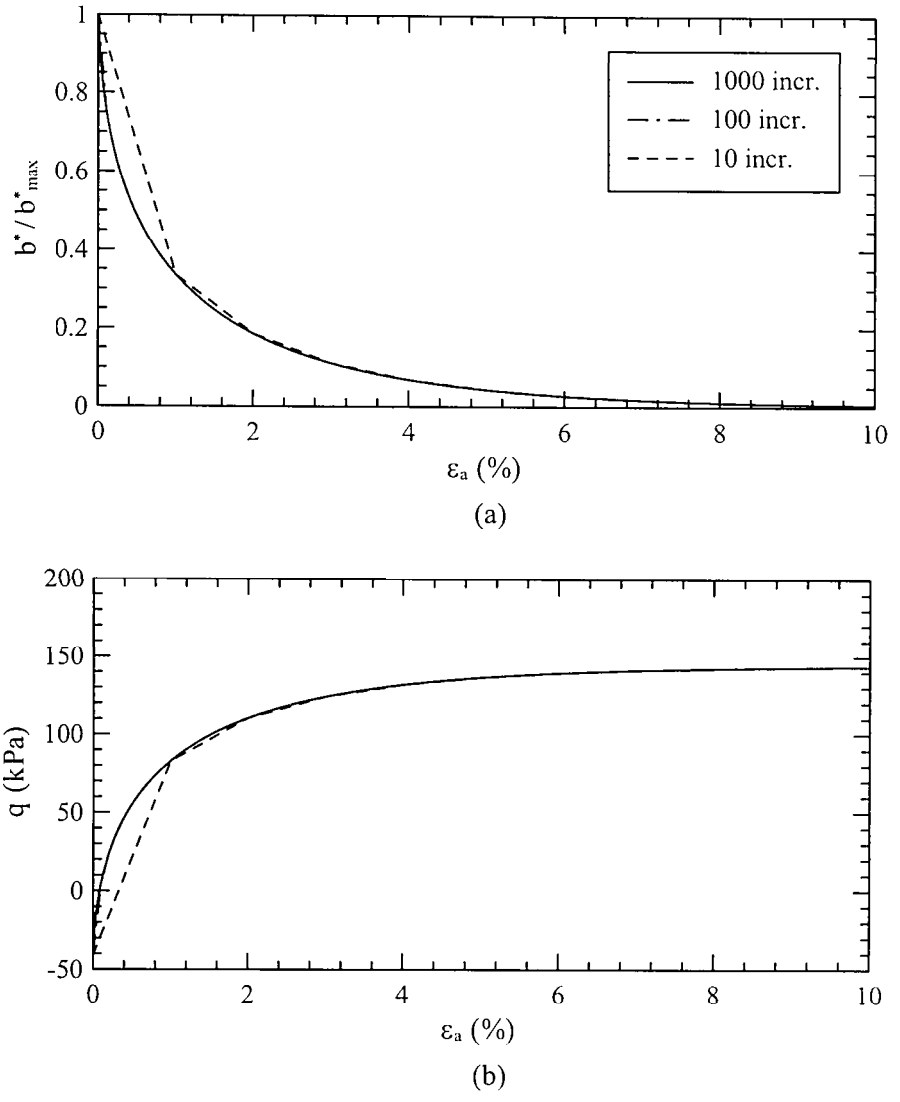


Figure 6.8: Predictions of the modified two-surface model for an undrained triaxial compression test and for different increment sizes a) ratio b^*/b^*_{max} versus strain b) stress-strain curve

6.3 Modified three-surface model

6.3.1 Introduction

This section introduces the new proposed hardening modulus for the modified three-surface model. The implementation of the new hardening modulus and the general characteristics of the model, with particular reference to the elasto-plastic transition predicted by the new model are also discussed. Further evaluation of the model follows in Chapter 7.

6.3.2 Proposed hardening modulus

As already discussed in section 6.2.2, the requirement for a smooth elasto-plastic transition is that the hardening modulus should tend to infinity when the stress state engages the first kinematic surface. The original hardening modulus of the three-surface model (discussed in detail in section 5.2.5 as part of the original triaxial formulation and in section 5.3.5 as part of the general formulation of the version of the model implemented into ICFEP) does not fulfil this requirement and this explains the drop in stiffness observed when the stress state becomes elasto-plastic.

In this section a new hardening modulus is presented for the two following cases; when the kinematic yield surface moves within the history and bounding surfaces and when the yield and history surfaces are in contact and move within the bounding surface. The new hardening modulus is based on the same idea as the proposed hardening modulus for the modified two-surface model.

i) Hardening modulus for the case when the yield surface is moving within the history and bounding surfaces

In this case the kinematic yield surface is the active yield surface and the hardening modulus proposed is the following:

$$A=\frac{4}{\lambda^*-\kappa^*}\left[\left(p'-p'_b\right)\left[p'_b\left(p'-p'_b\right)+\frac{1}{2}\left(\frac{\partial F_y}{\partial \boldsymbol{s}}:\boldsymbol{s}_b\right)+\frac{T^2S^2p'^2_o}{4}\right]+\alpha_1\left(\frac{b_1^*}{b_{1\max}^*-b_1^*}\right)\left(\frac{p'_o}{2}\right)^3T^2S^2+\alpha_2\left(\frac{b_2^*}{b_{2\max}^*-b_2^*}\right)\left(\frac{p'_o}{2}\right)^3T^2S^2\right] \tag{6.18}$$

Equation 6.18 is made up of three components. The first component, A_o, reduces to the modified Cam Clay hardening modulus when all three surfaces are in contact and is given by the following equation:

$$A_o=\frac{4}{\lambda^*-\kappa^*}\left[\left(p'-p'_b\right)\left[p'_b\left(p'-p'_b\right)+\frac{1}{2}\left(\frac{\partial F_y}{\partial \boldsymbol{s}}:\boldsymbol{s}_b\right)+\frac{T^2S^2p'^2_o}{4}\right]\right] \tag{6.19}$$

The second component A_1 is a function of the degree of approach of the yield surface to the bounding surface, b^*_1:

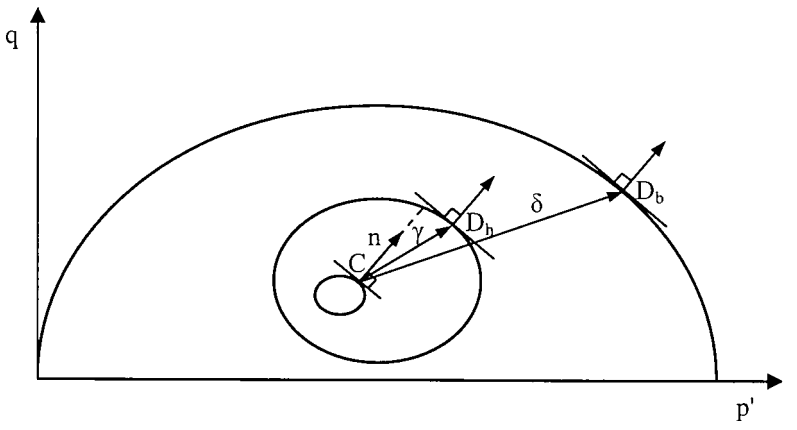


Figure 6.9: Representation in triaxial stress space: diagram defining the main components of the parameters b^*_1 and b^*_2

$$A_1 = \frac{4}{\lambda^* - \kappa^*}\alpha_1 \left(\frac{b_1^*}{b_{1\max}^* - b_1^*}\right)\left(\frac{p_o'}{2}\right)^3 T^2 S^2 \tag{6.20}$$

where α_1 is a material parameter, b^*_1 is the product of the direction tensor $\boldsymbol{\delta}$ (which connects the current stress state C to the conjugate point on the bounding surface D_b) and a direction tensor normal to the yield surface at the current stress state, $\boldsymbol{n}$, see Figure 6.9, and $b^*_{1\max}$ is the maximum value of b^*_1 which will be discussed later.

$$b_1^* = \left(p' - p_b'\right)\left[\frac{p' - p_b'}{TS} - \left(p' - \frac{p_o'}{2}\right)\right] + \frac{1}{2}\left[\frac{\partial F_y}{\partial \boldsymbol{s}} : \left[\frac{\boldsymbol{s} - \boldsymbol{s}_b}{TS} - \boldsymbol{s}\right]\right] \tag{6.21}$$

The third component A_2 is a function of the degree of approach of the yield surface to the history surface, b^*_2:

$$A_2 = \frac{4}{\lambda^* - \kappa^*}\alpha_2 \left(\frac{b_2^*}{b_{2\max}^* - b_2^*}\right)\left(\frac{p_o'}{2}\right)^3 T^2 S^2 \tag{6.22}$$

where α_2 is a material parameter, b^*_2 is the product of the direction tensor $\boldsymbol{\gamma}$ (which connects the current stress state C to the conjugate point on the history surface D_h) and the direction tensor normal to the yield surface at the current stress state, $\boldsymbol{n}$, see Figure 6.9, and $b^*_{2\max}$ is the maximum value of b^*_2.

$$b_2^* = \left(p' - p_b'\right)\left[\frac{p' - p_b'}{S} - \left(p' - p_a'\right)\right] + \frac{1}{2}\left[\frac{\partial F_y}{\partial \boldsymbol{s}} : \left[\frac{\boldsymbol{s} - \boldsymbol{s}_b}{S} - \left(\boldsymbol{s} - \boldsymbol{s}_a\right)\right]\right] \tag{6.23}$$

The maximum values b^*_{1max} and b^*_{2max} are calculated as follows. Upon initiation of yielding $b^*_{1max} = b^*_1$ and $b^*_{2max} = b^*_2$. For any subsequent stage i the maximum values $b^*_{1max}{}^i$ and $b^*_{2max}{}^i$ can be obtained from the following Equations 6.24 and 6.25 respectively.

$$b^*_{1max}{}^i = \frac{b^*_{1,o}}{b_1^{*i-1} / b^*_{1max}{}^{i-1}} \tag{6.24}$$

$$b^*_{2max} = \frac{b^*_{2,o}}{b_2^{*i-1} / b^*_{2max}{}^{i-1}} \tag{6.25}$$

where $b^*_1{}^{i-1}$, $b^*_{1max}{}^{i-1}$, $b^*_2{}^{i-1}$ and $b^*_{2max}{}^{i-1}$ are the values of b^*_1, b^*_{1max}, b^*_2 and b^*_{2max} respectively at the previous stage i-1 and $b^*_{1,o}$ and $b^*_{2,o}$ can be calculated as shown in Figure 6.10. Figure 6.10a plots the previous loading stage i-1 and Figure 6.10b plots the current loading stage i. The current stress state, at the stage i, is denoted by C and the conjugate points on the history and bounding surfaces are denoted by D_h and D_b respectively. Figure 6.10c, which is actually a homothetic transformation of Figure 6.10a, shows the position of the three surfaces from which the functions $b^*_{1,o}$ and $b^*_{2,o}$ can be determined. The relative positions of the three surfaces in Figure 6.10c are the same as in Figure 6.10a but these are scaled by the factor $(p'_o{}^i - p'_o{}^{i-1}) / p'_o{}^{i-1}$ so as to account for the change in size of the bounding surface from stage i-1 to stage i. In Figure 6.10c, the stress state E_h on the history surface and E_y on the yield surface, have the same outward normal as the conjugate point D_b on the bounding surface. The function $b^*_{1,o}$ is the value of b^*_1 corresponding to the direction tensor $\boldsymbol{\delta}_o$ which connects the conjugate point D_b to the stress state E_y on the yield surface. The function $b^*_{2,o}$ is the value of b^*_2 corresponding to the direction tensor $\boldsymbol{\gamma}_o$ which connects the stress state E_h on the history surface to the stress state E_y on the yield surface. Therefore $b^*_{1,o}$ is the product of the tensor $\boldsymbol{\delta}_o$ and a tensor normal to the yield surface at the stress state E_y, $\boldsymbol{n}_o$, and $b^*_{2,o}$ is the product of the tensors $\boldsymbol{\gamma}_o$ and $\boldsymbol{n}_o$. Since the stress states C, D_b and E_y have the same outward normal, $\boldsymbol{n}_o = \boldsymbol{n}$. The direction tensor $\boldsymbol{\delta}_o$ is:

$$\boldsymbol{\delta}_o = \boldsymbol{\sigma}'_{D_b} - \boldsymbol{\sigma}'_{E_y} = \boldsymbol{\delta} + \boldsymbol{\sigma}'^{\,i}_b - \boldsymbol{\sigma}'^{\,i-1}_b \left(1 + \frac{p'^{\,i}_o - p'^{\,i-1}_o}{p'^{\,i-1}_o} \right) \tag{6.26}$$

where:

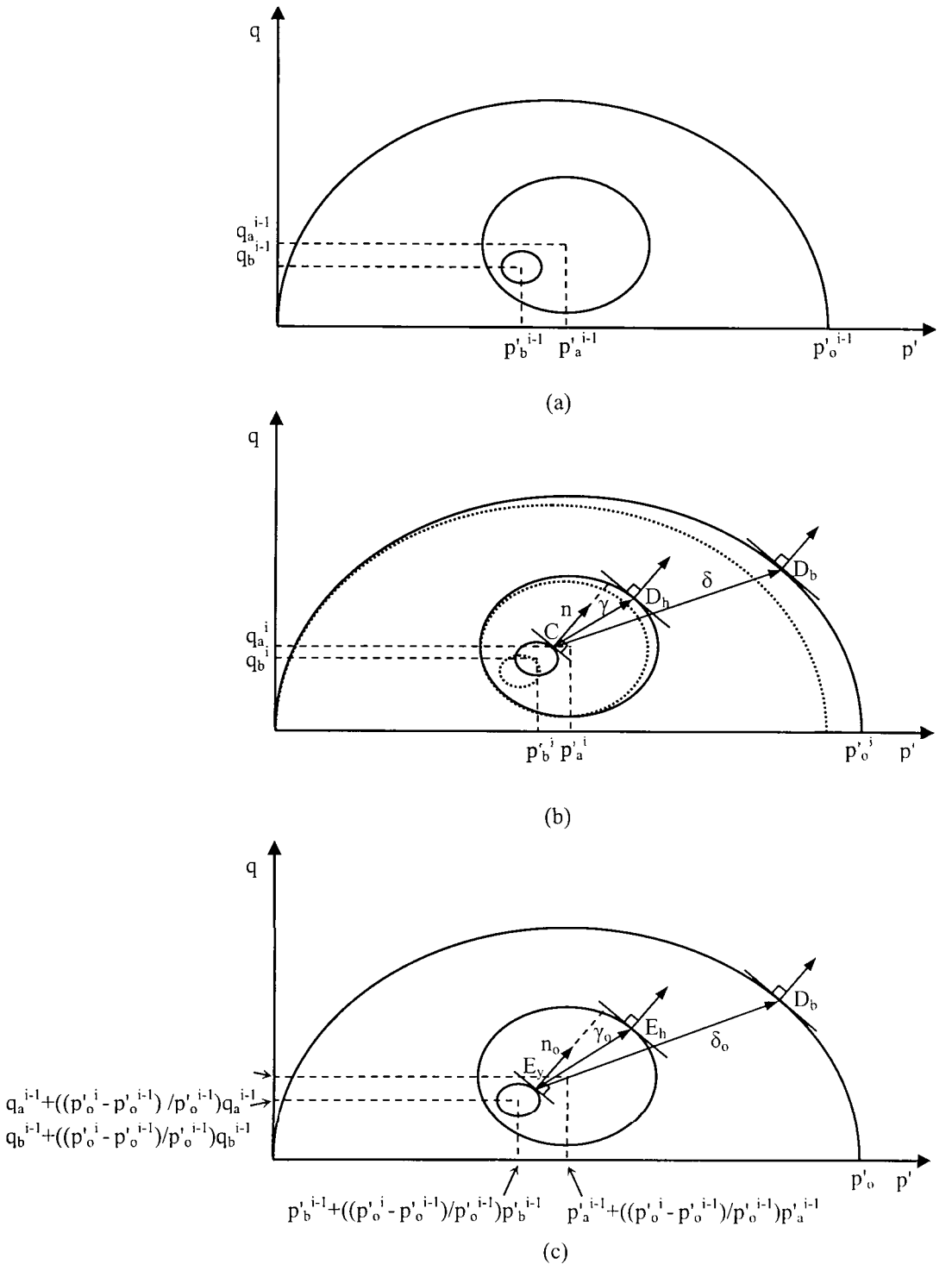


Figure 6.10: Representation in triaxial stress space of a) Previous loading stage *i*-1 b) Current loading stage *i* c) Configuration of surfaces for the calculation of the values of $b^*_{1,o}$ and $b^*_{2,o}$

$$\boldsymbol{\delta} = \frac{\boldsymbol{\sigma}'^{i} - \boldsymbol{\sigma}'^{i}_{b}}{TS} - \left(\boldsymbol{\sigma}'^{i} - \frac{\boldsymbol{\sigma}'^{i}_{o}}{2} \right) \tag{6.27}$$

and σ'^{i} and $\sigma'_{b}{}^{i}$ refer to the current stress state C and the centre of the kinematic surface at the current loading stage i respectively.

The resulting $b^{*}_{1,o}$ is:

$$b^{*}_{1,o} = \left(p'^{i} - p'^{i}_{b}\right)\left(p'_{D_b} - p'_{E_y}\right) + \frac{1}{2}\frac{\partial F_y}{\partial \boldsymbol{s}} : \left(\boldsymbol{s}_{D_b} - \boldsymbol{s}_{E_y}\right) \tag{6.28}$$

where the terms $p'_{Db} - p'_{Ey}$ and $\boldsymbol{s}_{Db} - \boldsymbol{s}_{Ey}$ can be calculated from Equation 6.26.

The direction tensor γ_o is:

$$\gamma_o = \boldsymbol{\sigma}'_{E_h} - \boldsymbol{\sigma}'_{E_y} = \gamma + \boldsymbol{\sigma}'^{i}_{b} + \boldsymbol{\sigma}'^{i}_{b} - \left(\boldsymbol{\sigma}'^{i-1}_{b} + \boldsymbol{\sigma}'^{i-1}_{a}\right)\left(1 + \frac{p'^{i}_{o} - p'^{i-1}_{o}}{p'^{i-1}_{o}}\right) \tag{6.29}$$

where:

$$\gamma = \frac{\boldsymbol{\sigma}'^{i} - \boldsymbol{\sigma}'^{i}_{b}}{S} - \left(\boldsymbol{\sigma}'^{i} - \boldsymbol{\sigma}'^{i}_{a}\right) \tag{6.30}$$

and $\boldsymbol{\sigma}'^{i}$, $\boldsymbol{\sigma}'_{b}{}^{i}$ and $\boldsymbol{\sigma}'_{a}{}^{i}$ refer to the current stress state C, the centre of the kinematic yield surface and the centre of the history surface, at the current loading stage i, respectively.

The resulting $b^{*}_{2,o}$ is:

$$b^{*}_{2,o} = \left(p' - p'_{b}\right)\left(p'_{E_h} - p'_{E_y}\right) + \frac{1}{2}\frac{\partial F_y}{\partial \boldsymbol{s}} : \left(\boldsymbol{s}_{E_h} - \boldsymbol{s}_{E_y}\right) \tag{6.31}$$

where the terms $p'_{Eh} - p'_{Ey}$ and $\boldsymbol{s}_{Eh} - \boldsymbol{s}_{Ey}$ can be calculated from Equation 6.29.

In Equation 6.18, upon initiation of yielding $b^{*}_{1} = b^{*}_{1\max}$, $b^{*}_{2} = b^{*}_{2\max}$ and $A \sim \infty$. Hence Equation 6.18 fulfils the requirement for a smooth elasto-plastic transition.

ii) Hardening modulus for the case when the yield and history surfaces are in contact and they are both moving within the bounding surface

In this case the history surface is the active yield surface, $b^{*}_{2} = 0$, and the hardening modulus is:

$$A=\frac{4}{\lambda^*-\kappa^*}\left[\left(p'-p'_a\right)\left[p'_a\left(p'-p'_a\right)+\frac{1}{2}\left(\frac{\partial F_h}{\partial \boldsymbol{s}}:\boldsymbol{s}_a\right)+\frac{T^2p'^2_o}{4}\right]+\alpha_1\left(\frac{b_1^*}{b_{1\max}^*-b_1^*}\right)\left(\frac{p'_o}{2}\right)^3T^2\right] \tag{6.32}$$

The first component of the hardening modulus, A_o, becomes:

$$A_o=\frac{4}{\lambda^*-\kappa^*}\left[\left(p'-p'_a\right)\left[p'_a\left(p'-p'_a\right)+\frac{1}{2}\left(\frac{\partial F_h}{\partial \boldsymbol{s}}:\boldsymbol{s}_a\right)+\frac{T^2p'^2_o}{4}\right]\right] \tag{6.33}$$

The second component of the hardening modulus, A_1, is:

$$A_1=\frac{4}{\lambda^*-\kappa^*}\alpha_1\left(\frac{b_1^*}{b_{1\max}^*-b_1^*}\right)\left(\frac{p'_o}{2}\right)^3T^2 \tag{6.34}$$

where the measure of the approach of the history surface to the bounding surface, b^*_1, now becomes:

$$b_1^*=S\left[\left(p'-p'_a\right)\left[\frac{p'-p'_a}{T}-\left(p'-\frac{p'_o}{2}\right)\right]+\frac{1}{2}\left[\frac{\partial F_h}{\partial \boldsymbol{s}}:\left(\frac{\boldsymbol{s}-\boldsymbol{s}_a}{T}-\boldsymbol{s}\right)\right]\right] \tag{6.35}$$

The maximum value b^*_{1max} can still be calculated from Equation 6.24. In this case the direction tensor $\boldsymbol{\delta}_o$ is:

$$\boldsymbol{\delta}_o=\boldsymbol{\sigma}'_{D_h}-\boldsymbol{\sigma}'_{E_h}=\boldsymbol{\delta}+\boldsymbol{\sigma}'^{\,i}_a-\boldsymbol{\sigma}'^{\,i-1}_a\left(1+\frac{p'^{\,i}_o-p'^{\,i-1}_o}{p'^{\,i-1}_o}\right) \tag{6.36}$$

where

$$\boldsymbol{\delta}=\frac{\boldsymbol{\sigma}'^{\,i}-\boldsymbol{\sigma}'^{\,i}_a}{T}-\left(\boldsymbol{\sigma}'^{\,i}-\frac{\boldsymbol{\sigma}'^{\,i}_o}{2}\right) \tag{6.37}$$

and $\boldsymbol{\sigma}'^{\,i}$ and $\boldsymbol{\sigma}'_a{}^{\,i}$ refer to the current stress state C and the centre of the history surface, at the current loading stage i, respectively.

The resulting $b^*_{1,o}$ is:

$$b^*_{1,o} = S\left[\left(p'^i - p'^i_a\right)\left(p'_{D_h} - p'_{E_h}\right) + \frac{1}{2}\frac{\partial F_h}{\partial \boldsymbol{s}} : \left(\boldsymbol{s}_{D_h} - \boldsymbol{s}_{E_h}\right)\right] \tag{6.38}$$

where the terms $p'_{Db} - p'_{Eh}$ and $\boldsymbol{s}_{Db} - \boldsymbol{s}_{Eh}$ can be calculated from Equation 6.36.

Inspection of 6.32 shows that this is of the same form as the hardening modulus of the modified two-surface model, but with R replaced by T, F_y replaced by F_h and b^* replaced by b^*_1.

The new modified three-surface model adopts the above proposed hardening modulus but retains the same yield and plastic potential functions, hardening rules and elastic part as the generalised version of the three-surface model implemented into ICFEP. These have been described in Chapter 5 and the reader is referred to section 5.3 for further details. In this model, Equation 6.18 replaces Equation 5.48 and Equation 6.32 replaces Equation 5.56.

6.3.3 Model parameters

In the modified three-surface model the parameters α_1 and α_2 replace the parameter ψ in the generalised version of the three-surface model while the rest of the parameters remain the same. Hence, the new model has one extra parameter. The model requires either eleven parameters, when a Mohr-Coulomb hexagon is used for the shape of the yield surface in the deviatoric plane, or thirteen parameters when a general shape is used. If Equation 4.51 is used for the calculation of the elastic shear modulus, G_e, then two additional parameters are required. The model parameters are:

λ^*: the slope of the isotropic normal compression line in $\ln v$-$\ln p'$ space

κ^*: the slope of the swelling line in $\ln v$-$\ln p'$ space for a stress path that lies entirely within the kinematic yield surface

μ or G_e, or G_e/p': the Poisson's ratio or the elastic shear stiffness. If Equation 4.51 is used then the material parameters A, n and m must be provided

φ' or X, Y and Z: the angle of shearing resistance or the constants $X = \sin(\varphi'_{0-0^\circ})$, Y and Z in Equation 4.28 at the critical state

Y_p and Z_p: the constants Y_p and Z_p in Equation 4.31

T: the ratio of the size of the history surface to that of the bounding surface

S: the ratio of the size of the yield surface to that of the history surface

α_1: parameter in the hardening function A_1

α_2: parameter in the hardening function A_2

N: one additional parameter is required to fix the model in $\ln v$-$\ln p'$ space and this is usually taken as the specific volume of the isotropic compression line at $p' = 1$KPa

The new parameters α_1 and α_2, (which control the decay of stiffness), cannot be measured directly and have to be obtained from parametric studies similar to the parameter ψ in the original model. The parameter α_2 controls the decay of stiffness only for the part of the stress path that remains within the history surface, whereas the parameter α_1 controls the stiffness degradation for stress paths both within and outside the history surface. From the equations of the new hardening modulus it can be seen that for a constant value of the parameter α_1, the higher the value of α_2 is, the higher the stiffness within the history surface and hence the influence of this surface is. In any case the parameter α_2 should always be greater than the parameter α_1.

6.3.4 Implementation

The implementation of the modified three-surface model follows the implementation of the general formulation of the three-surface model described in section 5.4 of Chapter 5, with the only difference being the implementation of the new hardening modulus. The flowchart of the subroutine used by the stress point algorithm is presented in Appendix VI.

i) Hardening modulus for the case when the yield surface is moving within the history and bounding surfaces

Equation 6.18 can be written in a vector-notation form as follows:

$$A=\frac{4}{\lambda^{*}-\kappa^{*}}\left[\left(p'-p'_b\right)\left[p'_b\left(p'-p'_b\right)+\frac{1}{2}\left\{\frac{\partial F_y}{\partial s}\right\}^{T}\left\{s_b\right\}+\frac{T^2S^2p_o'^2}{4}\right]+\right.$$
$$\left.\alpha_1\left(\frac{b_1^{*}}{b_{1\max}^{*}-b_1^{*}}\right)\left(\frac{p'_o}{2}\right)^3T^2S^2+\alpha_2\left(\frac{b_2^{*}}{b_{2\max}^{*}-b_2^{*}}\right)\left(\frac{p'_o}{2}\right)^3T^2S^2\right] \tag{6.39}$$

where

$$b_1^{*}=\left(p'-p'_b\right)\left[\frac{p'-p'_b}{TS}-\left(p'-\frac{p'_o}{2}\right)\right]+\frac{1}{2}\left\{\frac{\partial F_y}{\partial s}\right\}^{T}\left\{\frac{s-s_b}{TS}-s\right\} \tag{6.40}$$

$$b_2^{*}=\left(p'-p'_b\right)\left[\frac{p'-p'_b}{S}-\left(p'-p'_a\right)\right]+\frac{1}{2}\left\{\frac{\partial F_y}{\partial s}\right\}^{T}\left\{\frac{s-s_b}{S}-\left(s-s_a\right)\right\} \tag{6.41}$$

The values of $b^{*}_{1\max}$ and $b^{*}_{2\max}$ are set equal to b^{*}_{1} and b^{*}_{2} upon initiation of yielding and for any subsequent stage can be calculated from Equations 6.24 and 6.25 respectively, in which:

$$b_{1,o}^{*}=\left(p'-p'_b\right)\left(p'_{D_h}-p'_{E_y}\right)+\frac{1}{2}\left\{\frac{\partial F_y}{\partial s}\right\}^{T}\left\{s_{D_h}-s_{E_y}\right\} \tag{6.42}$$

$$b_{2,o}^{*}=\left(p'-p'_b\right)\left(p'_{E_h}-p'_{E_y}\right)+\frac{1}{2}\left\{\frac{\partial F_y}{\partial s}\right\}^{T}\left\{s_{E_h}-s_{E_y}\right\} \tag{6.43}$$

where p' and p'_b refer to the current stage. In Equation 6.42 the terms p'_{Db} - p'_{Ey} and s_{Db} - s_{Ey} can be calculated from Equation 6.26 and in Equation 6.43 the terms p'_{Eh} - p'_{Ey} and s_{Eh} - s_{Ey} can be calculated from Equation 6.29.

ii) Hardening modulus for the case when the yield and history surfaces are in contact and they are both moving within the bounding surface

Equation 6.32 can be re-written in vector notation form:

$$A=\frac{4}{\lambda^*-\kappa^*}\left[\left(p'-p'_a\right)\left[p'_a\left(p'-p'_a\right)+\left\{\frac{\partial F_h}{\partial s}\right\}^T\{s_a\}+\frac{T^2p'^2_o}{4}\right]+\alpha_1\left(\frac{b_1^*}{b_{1\max}^*-b_1^*}\right)\left(\frac{p'_o}{2}\right)^3T^2\right] \tag{6.44}$$

where:

$$b_1^*=S\left[\left(p'-p'_a\right)\left[\frac{p'-p'_a}{T}-\left(p'-\frac{p'_o}{2}\right)\right]+\frac{1}{2}\left\{\frac{\partial F_h}{\partial s}\right\}^T\left\{\frac{s-s_a}{T}-s\right\}\right] \tag{6.45}$$

and $b^*_{1,o}$ becomes:

$$b^*_{1,o}=S\left[\left(p'-p'_a\right)\left(p'_{D_h}-p'_{E_h}\right)+\frac{1}{2}\left\{\frac{\partial F_h}{\partial s}\right\}^T\left\{s_{D_h}-s_{E_h}\right\}\right] \tag{6.46}$$

where p' and p'_a refer to the current stage and the terms p'_{Dh} - p'_{Eh} and s_{Db} - s_{Eh} can be calculated from Equation 6.36.

6.3.5 General characteristics of the model

The model has the same following general characteristics as the general formulation of the three-surface model. The undrained strength predicted by the model can be calculated from the equations of Appendix III. The peak drained stress states obtained for highly overconsolidated states can be shown to be lower than the ones predicted by the modified Cam Clay model. The model can also exhibit anisotropic yielding characteristics in stress paths involving rotation of the principal stresses, but it always predicts isotropic strength. Moreover, it adopts the same shapes of the yield and plastic potential surfaces (and hence the failure surface) in the deviatoric plane as the general formulation of the three-surface model. The model is also capable of predicting the effect of recent stress history and this will be demonstrated in Chapter 7.

The major advantage of the new model over the three-surface model is that it can predict a smooth elasto-plastic transition, simulating in this way more realistically the non-linear small strain pre-failure behaviour of overconsolidated clays.

6.3.5.1 Elasto-plastic transition and non-linearity

Figure 6.11 presents the predictions of the modified three-surface model for an undrained triaxial compression test on reconstituted overconsolidated London Clay (OCR = 7). The model parameters used in the simulation of the test are summarised in Table 6.2. The predictions of the three-surface model for the same test can be seen in Figure 5.19 and were discussed in section 5.5.4. Figure 6.11 shows that the hardening modulus adopted in the modified three-surface model can predict a smooth elasto-plastic transition and stiffness variation with strain, independently of the value of the parameter α_1. In the following chapter it will be shown that this is also true independently of the values of the parameter α_2.

N	λ^*	κ^*	A	n	m	φ'	Y_p	Z_p	T	S	α_2
3.43	0.097	0.003	590.0	0.87	0.28	22.5°	0.0	1.0	0.1	0.16	35.0

Table 6.2: Material parameters used in the modified three-surface model for the simulation of the triaxial test in Figure 6.11

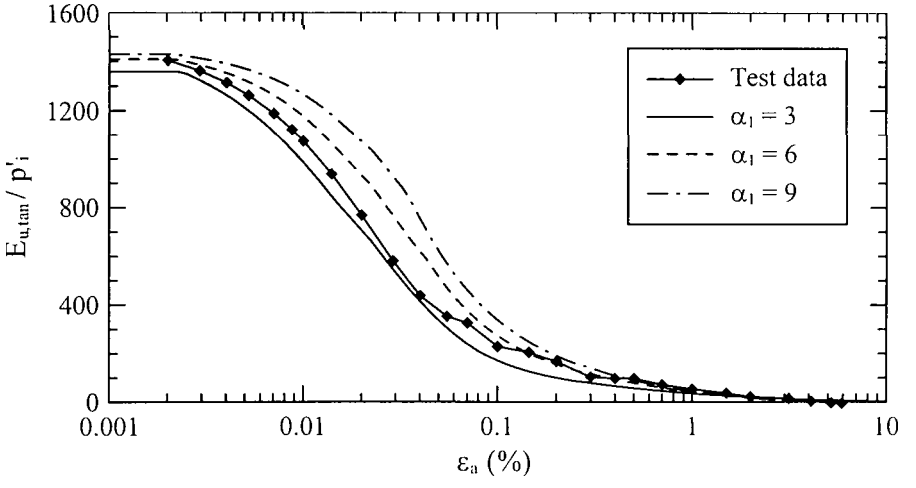


Figure 6.11: Predictions of the modified three-surface model for an undrained triaxial compression test on overconsolidated reconstituted London Clay (test data after Jardine (1985)): Normalised stiffness-strain curve (p'_i is the value of p' at the start of shearing)

6.4 Summary

This chapter presented two new models, the modified two-and three-surface models. The modified two- and three-surface models have the same yield and plastic potential functions, and elastic part as the generalised versions of the two- and three-surface

models respectively (described in Chapters 4 and 5), but different hardening modulus. Unlike the previous hardening modulus of the two- and three-surface models, which results in abrupt drops in stiffness once the stress state becomes elasto-plastic, the new hardening modulus adopted in the modified two- and three-surface models ensures a smooth elasto-plastic transition. The new models were shown to predict smooth stiffness degradation curves and in this way simulate much more realistically pre-failure non-linearity in the small strain range. Further evaluation of the new models follows in Chapter 7.

Chapter 7

Evaluation

7.1 Introduction

This chapter presents an evaluation of the four kinematic hardening models described in Chapters 4, 5 and 6. It is divided into three parts. The first part presents the simulation of a set of triaxial tests on reconstituted London Clay. In this part particular emphasis is given to the ability of the models to simulate pre-failure non-linearity. The second part investigates the capability of the models to reproduce the effect of recent stress history in a multi-stage triaxial test. Finally, the last part looks into the way the models can simulate the effect of stress path direction.

7.2 Modelling triaxial tests on reconstituted London Clay

7.2.1 Introduction

This part involves the simulation of a series of triaxial tests on reconstituted London Clay from the Canons Park site, London (Jardine (1985) and Fourie (1984)). This set of tests has been discussed in Chapter 2 as part of the literature review of the factors that influence soil stiffness (Figure 2.31). The samples were one-dimensionally compressed and then swelled to three overconsolidation ratios (1.5, 3 and 7), and from then on subjected to undrained triaxial compression and extension.

7.2.2 Model parameters

The derivation of the parameters that are common to all four models is presented first. These are the following seven parameters: N, λ^*, κ^*, G_e, φ', Y_p and Z_p. The derivation of the rest of the parameters then follows. These remaining parameters define the behaviour of the kinematic surfaces and are R and ψ, in the case of the two-surface model, R and α, in the case of the modified two-surface model, T, S and ψ, in the case of the three-surface model and T, S, α_1 and α_2 in the case of the modified three-surface model.

i) N and λ^*

The compression parameter λ^* is the slope of the isotropic normal compression line in $\ln v$-$\ln p'$ space. In the critical state framework the compression lines resulting from normal compression at any constant stress ratio have the same gradients. Therefore, in theory, the parameter λ^* can also be determined from constant stress ratio compression tests. Figure 7.1 shows a one-dimensional compression curve, from an oedometer test on reconstituted London Clay, plotted in $\ln v$-$\ln p'$ space. The values of p' have been calculated from the oedoemeter data using an assumed $K_o = 1 - \sin\varphi'$, where $\varphi' = 22.5°$ (this value of φ' will be discussed later). The best line of the form $\ln v = \ln N_{Ko} - \lambda^* \ln p'$ fitted through the data gave values of $\lambda^* = 0.097$ and $N_{Ko} = 3.34$, where N_{Ko} is the specific volume of the K_o compression line at $p' = 1$ KPa. This corresponds to a value of $N = 3.43$, where N is the specific volume of the isotropic compression line at $p' = 1$ KPa.

ii) κ^*

The swelling parameter κ^* is the gradient of the initial (elastic) part of an isotropic swelling line, in $\ln v$-$\ln p'$ space, and actually determines the elastic bulk modulus, K_e, within the kinematic yield surface. An estimate of κ^* can be obtained by plotting the normalised value of the bulk modulus K/p' against the change in stress or strain for an isotropic swelling path, or for any isotropic path following a complete stress path reversal. The value of κ^* is equal to the inverse of K/p' at the start of the curve. In reality, reliable measurements of the bulk modulus are difficult to obtain. Here no such data was available. Figure 7.2 shows the bulk modulus decay curves selected for analysis for the London Clay strata at the proposed new terminal at London's Heathrow Airport (T5), on the basis of back-analysis of oedometer swelling tests. The value of $\kappa^* = 0.003$ that was chosen for the work presented in this chapter corresponds to $K/p' = 333.3$, which plots between the two curves in Figure 7.2.

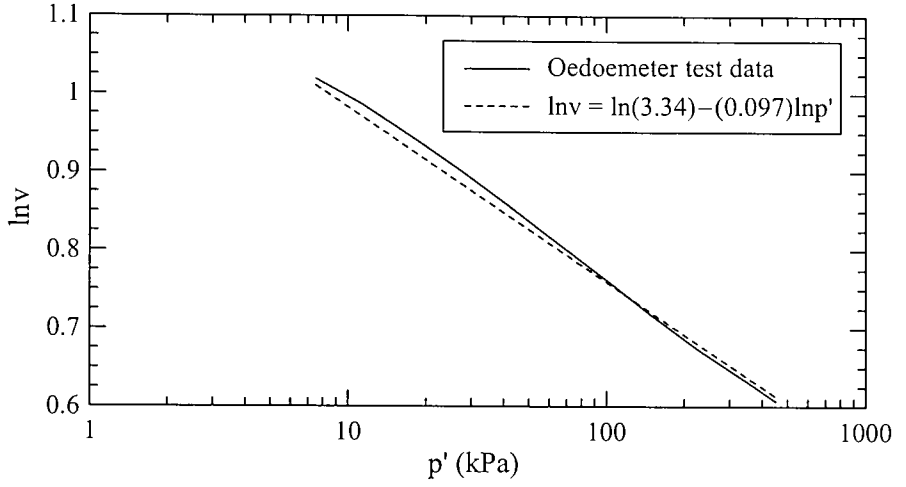


Figure 7.1: Determination of compression parameters (N and λ^*) for reconstituted London Clay (test data from Jardine (1985))

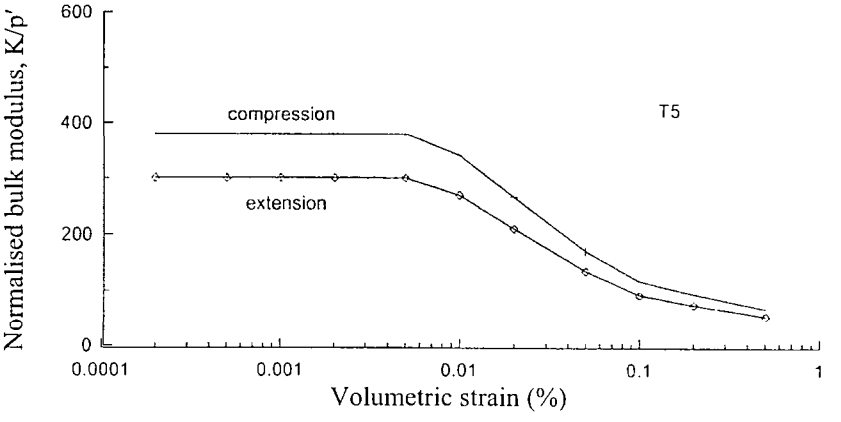


Figure 7.2: Normalised bulk modulus decay curves selected for analysis at T5 (after Hight et al. (2003))

iii) G_e

The elastic shear stiffness, G_e, can be determined from dynamic measurements. However, no such data was available and G_e was assumed to be described by the equation proposed by Viggiani (1992) (Equation 2.10 or 4.51). The constants A, n and m used, were based on the trend lines of Figure 2.14 for a plasticity index of 50, which is an average value of the plasticity index of London Clay at the Canons Park site. The values chosen are slightly higher than the exact values of the trend lines in Figure 2.14, since in some cases the latter predicted values of elastic stiffness lower than the values measured experimentally in the small strain range. The adopted values are A = 590, n = 0.87 and m = 0.28.

iv) φ'

According to Jardine (1985) the ultimate states for all stress paths fall close to a Mohr Coulomb line with $\varphi' = 22.5°$. Hence a Mohr-Coulomb hexagon was assumed for the shape of the yield function in the deviatoric plane, with $\varphi' = 22.5°$ at the critical state.

v) Y_p and Z_p

The shape of the plastic potential was assumed to be a circle in the deviatoric plane. Therefore the adopted values are $Y_p = 0.0$ and $Z_p = 1.0$.

vi) Parameters that define the behaviour of the kinematic surfaces

The rest of the parameters that need to be determined are the parameters R and ψ, for the two-surface model, R and α, for the modified two-surface model, T, S and ψ, for the three-surface model and T, S, α_1 and α_2 for the modified three-surface model. The parameter R and the product TS define the extent of the elastic behaviour. This could be determined from an isotropic loading path following a complete reversal in the stress path direction (Al-Tabbaa (1987) suggested that R could be defined from the initial part of the isotropic swelling line (Chapter 4)). Stallebrass (1990) suggested that since this region is not easily measurable in triaxial tests, the values chosen should be checked against shear stiffness curves. Unfortunately, in the current stiffness data of reconstituted London Clay no elastic region could be identified. Hence, in this work, the parameter R and the product TS were derived from a parametric study. The parameter T, which defines the extent of the influence of recent stress history, could be determined from two isotropic stress paths following two different stress histories, as proposed by Stallebrass (1990) (Chapter 5). However, the tests on reconstituted London Clay did not include such stress paths, and again a parametric study was employed in order to determine the value of T. Finally, the parameters ψ, α, α_1 and α_2, which are the parameters in the hardening modulus A and control the decay of stiffness, cannot be measured directly from the experimental data and can only be determined by trial and error. Hence, a small parametric study was employed for each model in order to determine the values of the parameters that define the behaviour of the kinematic surfaces.

Although the primary objective of this study is the choice of the remaining parameters, a secondary aim is the investigation of the sensitivity of each model to each of these parameters. For this study the predictions of the models for the undrained triaxial compression path initiating from an OCR of 7 are examined (LR7 in Figure 2.31) and

compared with the experimental data. In these analyses the parameters N, λ^*, κ^*, G_e, φ', Y_p and Z_p were set equal to the values chosen above.

Two-surface model

a) R

For these predictions the value of the parameter ψ was set to 5 and the value of the parameter R varied between 0.01 and 0.03. Figure 7.3 shows the effect of varying R on the stress-strain and stiffness-strain response predicted by the two-surface model (the stiffness curve in Figure 7.3 is normalised by p'_i, which is the value of p' at the start of the shearing stage). It can be seen that variations in the value of R influence significantly the predicted behaviour. Increasing R results in a wider elastic plateau, but also in a greater drop in stiffness immediately after the elastic region and hence, in a softer overall behaviour.

b) ψ

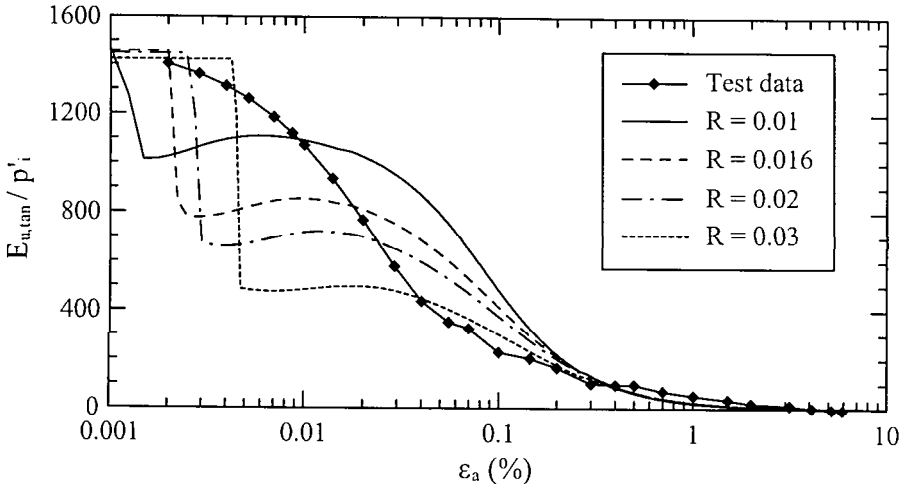
Figure 7.4 illustrates the sensitivity of the model to the parameter ψ. In these analyses the parameter R was equal to $R = 0.016$ and the parameter ψ varied between 4 and 6. The parameter ψ has a similar effect to the parameter R. For higher values of ψ there is a more dramatic reduction in stiffness when plastic straining first occurs and a softer behaviour at both small and large strains. Comparison with the experimental data shows that it is difficult to reproduce a realistic stiffness degradation curve, as already discussed in Chapter 4.

Based on the comparison between model predictions and experimental results (Figures 7.3 and 7.4) the values chosen for the two-surface model are $R = 0.016$ and $\psi = 6$.

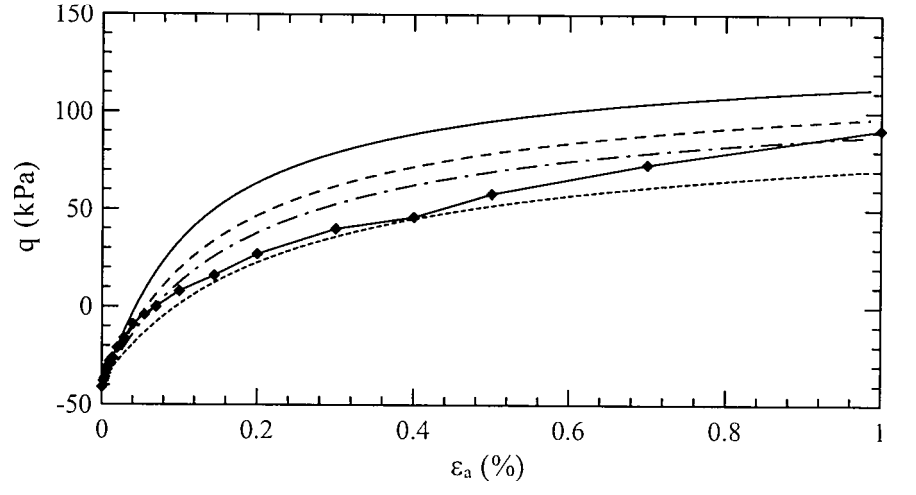
Modified two-surface model

a) R

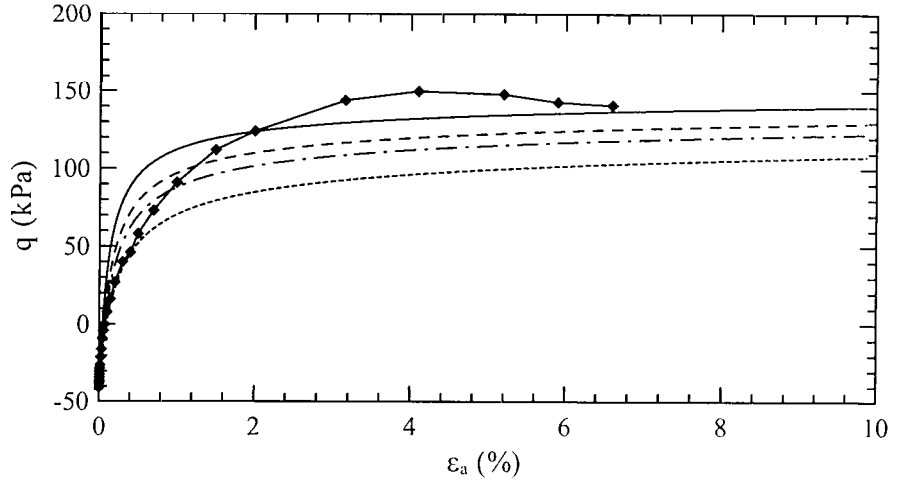
The influence of the parameter R on the stress-strain and stiffness-strain response predicted by the modified two-surface model can be seen in Figure 7.5. In these analyses the parameter α was kept constant at $\alpha = 8$ and the parameter R varied between 0.01 and 0.03. Similar to the two-surface model, increasing R results in a wider elastic plateau. However, unlike the two-surface model, the modified two-surface model does not seem



(a)

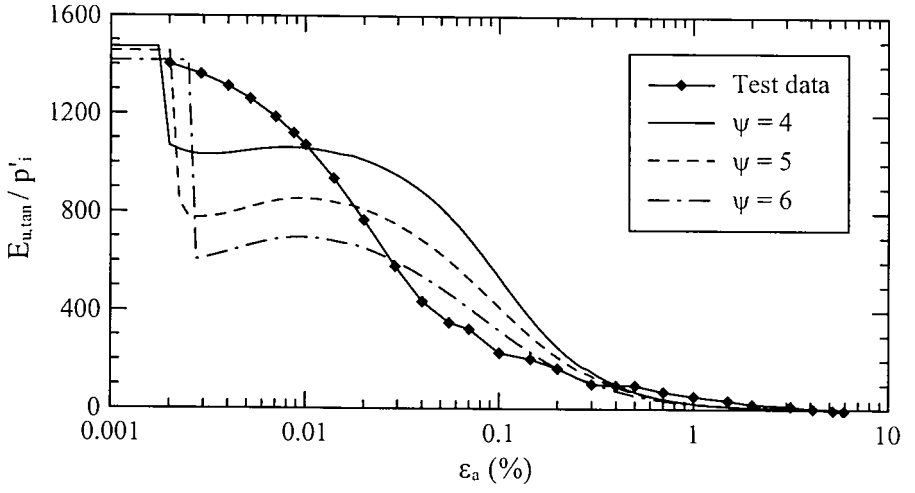


(b)

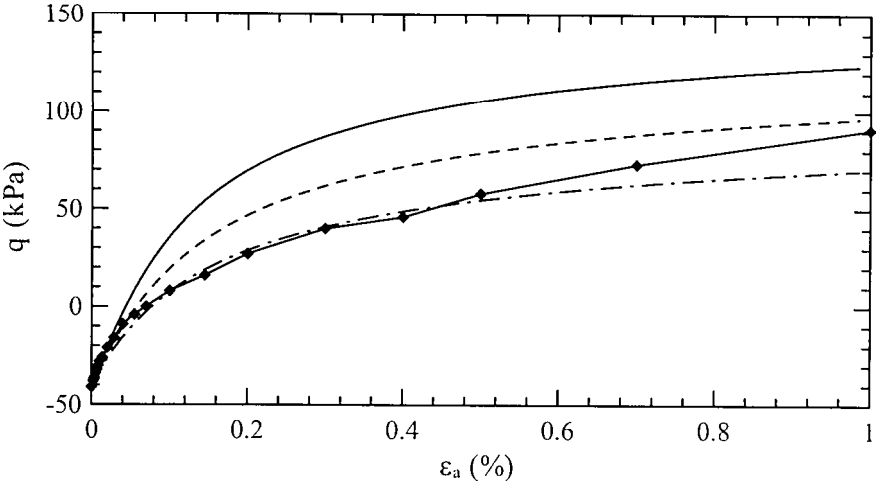


(c)

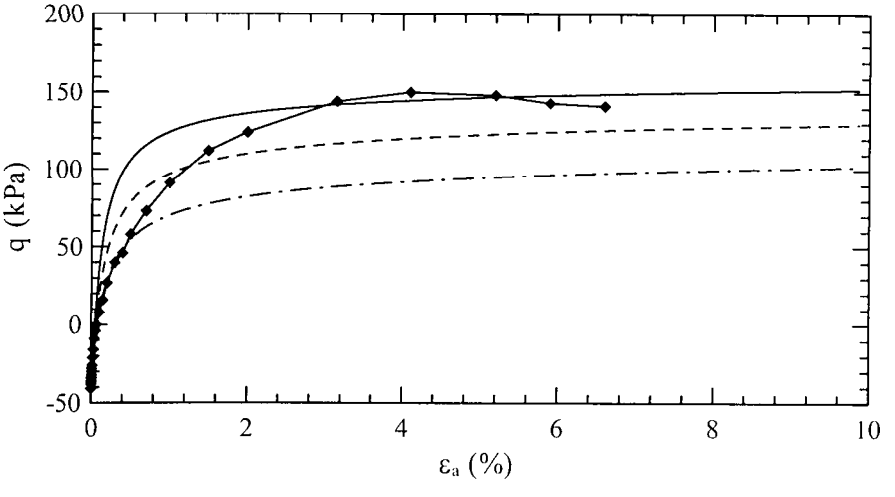
Figure 7.3: Effect of varying *R* for the two-surface model – Test LR7 a) normalised stiffness-strain curve b) stress-strain curve c) stress-strain curve – larger strains (test data from Jardine (1985))



(a)

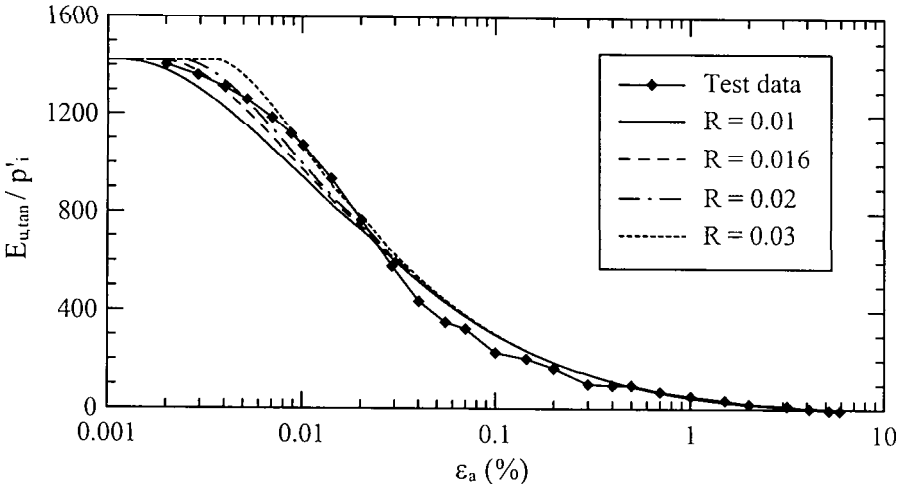


(b)

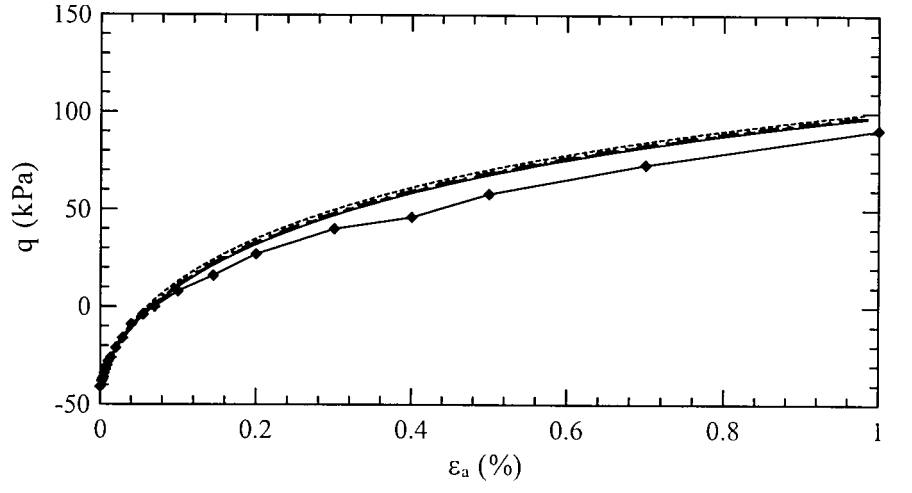


(c)

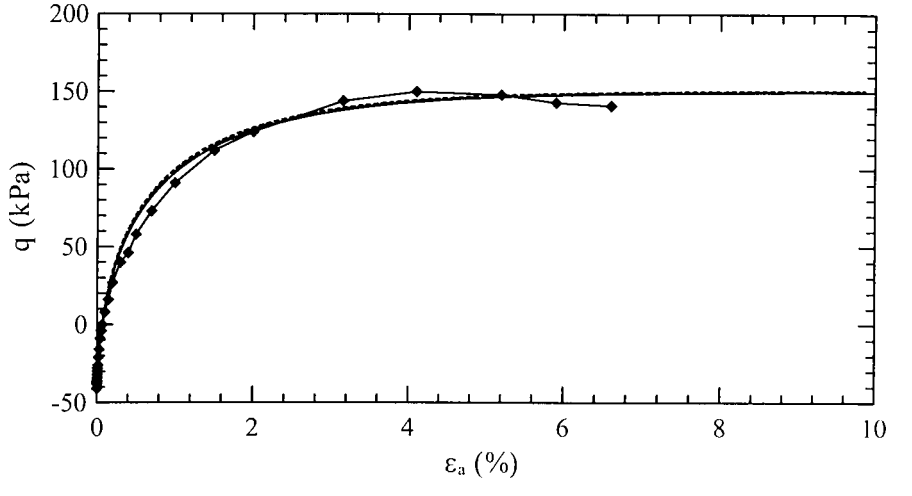
Figure 7.4: Effect of varying ψ for the two-surface model – Test LR7 a) normalised stiffness-strain curve b) stress-strain curve c) stress-strain curve – larger strains (test data from Jardine (1985))



(a)

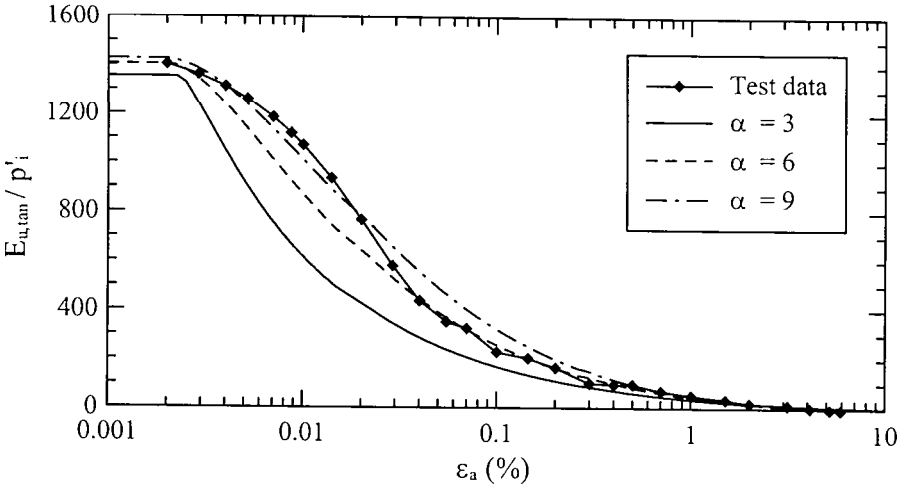


(b)

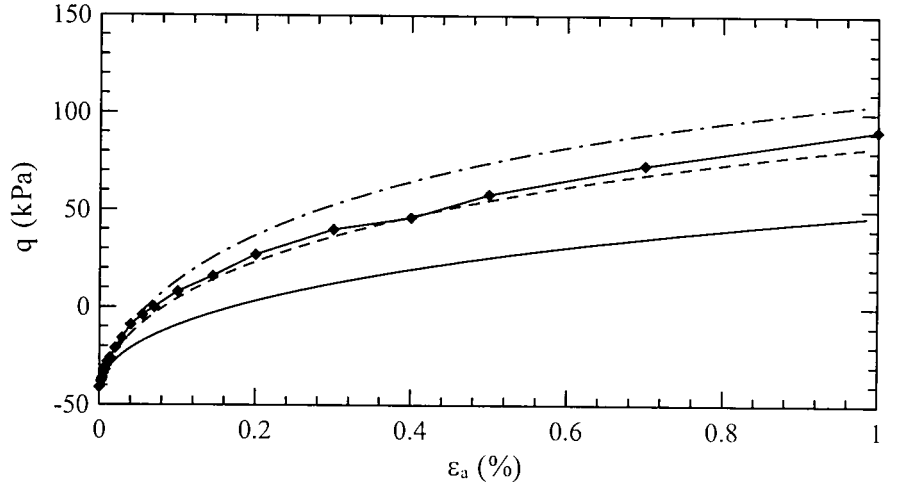


(c)

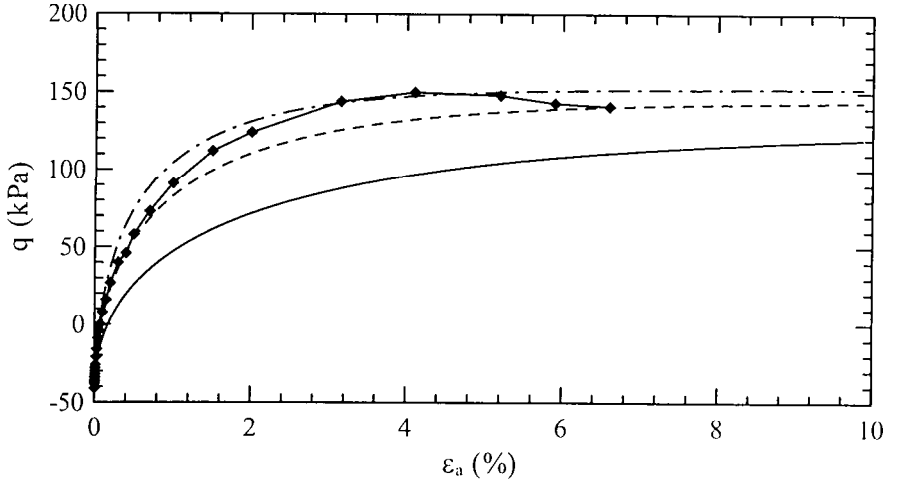
Figure 7.5: Effect of varying *R* for the modified two-surface model – Test LR7
a) normalised stiffness-strain curve b) stress-strain curve c) stress-strain curve – larger strains (test data from Jardine (1985))



(a)



(b)



(c)

Figure 7.6: Effect of varying α for the modified two-surface model – Test LR7
a) normalised stiffness-strain curve b) stress-strain curve c) stress-strain curve – larger strains (test data from Jardine (1985))

to be very sensitive to the variations in the values of R. Figure 7.5 shows that increasing R results in a small increase of stiffness once the stress state becomes elasto-plastic.

b) α

The effect of the parameter α is illustrated in Figure 7.6. Here R was set equal to $R = 0.016$ and α varied between 3 and 9. Unlike R, varying α has an effect on the overall behaviour. Lower values of α result in a faster rate of decay of stiffness once yielding occurs, and therefore in a softer behaviour. Figure 7.6 shows that for all values of α the obtained stiffness degradation curves are smooth.

Based on the results shown in Figures 7.5 and 7.6, the values chosen for the modified two-surface model are $R = 0.016$ and $\alpha = 6$.

Three-surface model

a) S

For these analyses the values of T and ψ were kept constant at $T = 0.2$ and $\psi = 1.5$ and the value of S varied between 0.05 and 0.15 so that the product TS, representing the size of the elastic region, varied between 0.01 and 0.03 (the same as in the two-surface models). The effect of varying the parameter S on the behaviour predicted by the three-surface model can be seen in Figure 7.7. Increasing the parameter S results in a greater drop in stiffness when the stress state becomes elasto-plastic, and also in a wider elastic plateau. This is similar to the effect that R has in the two-surface model, however, unlike R, the effect seems to influence the behaviour only for stress states within the history surface.

b) T

In order to investigate the effect of the size of the history surface, the values of T and S varied so that the product TS (defining the size of the kinematic yield surface) was kept equal to 0.016 for all the analyses. The value of ψ was set equal to 1.5. The effect of the parameter T is illustrated in Figure 7.8. It seems that within the history surface increasing T has the opposite effect of increasing S, it results in a smaller decrease in stiffness once the elastic region is reached. However, once the stress state reaches the history surface (the stress and strain required to reach the history surface increases with the value of T), the higher value of T results in a lower stiffness. This can be seen very

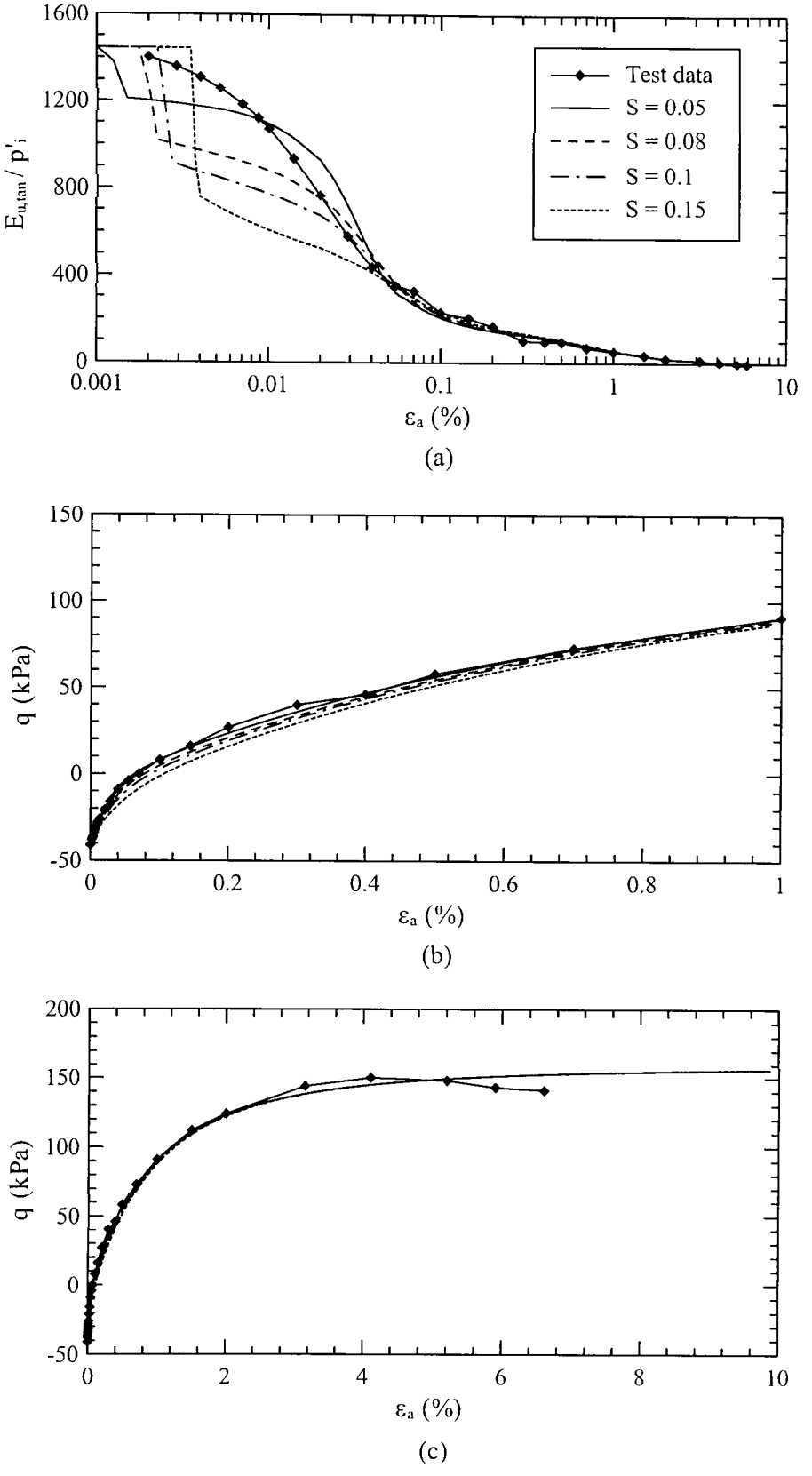


Figure 7.7: Effect of varying *S* for the three-surface model – Test LR7 a) normalised stiffness-strain curve b) stress-strain curve c) stress-strain curve – larger strains (test data from Jardine (1985))

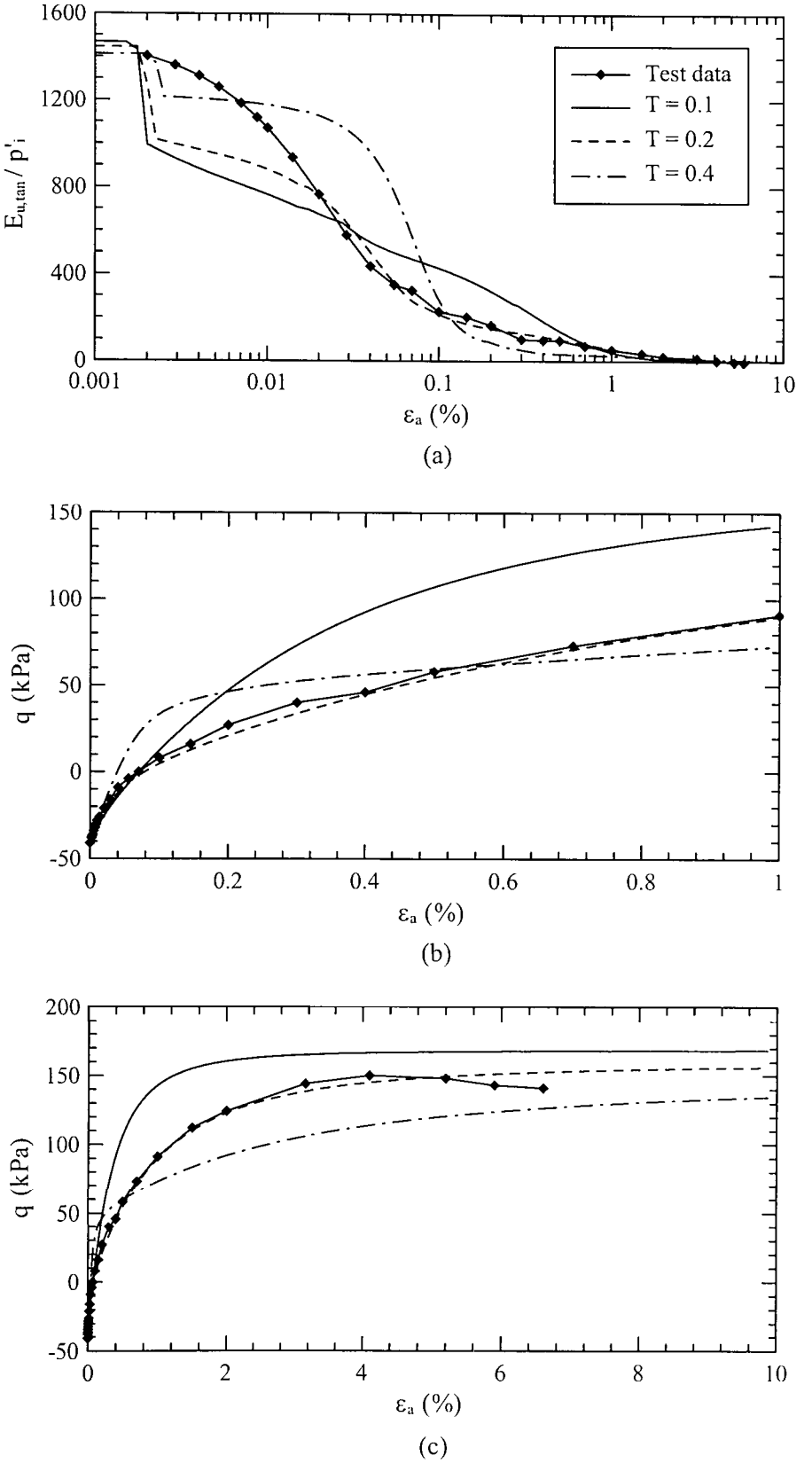


Figure 7.8: Effect of varying T for the three-surface model – Test LR7 a) normalised stiffness-strain curve b) stress-strain curve c) stress-strain curve – larger strains (test data from Jardine (1985))

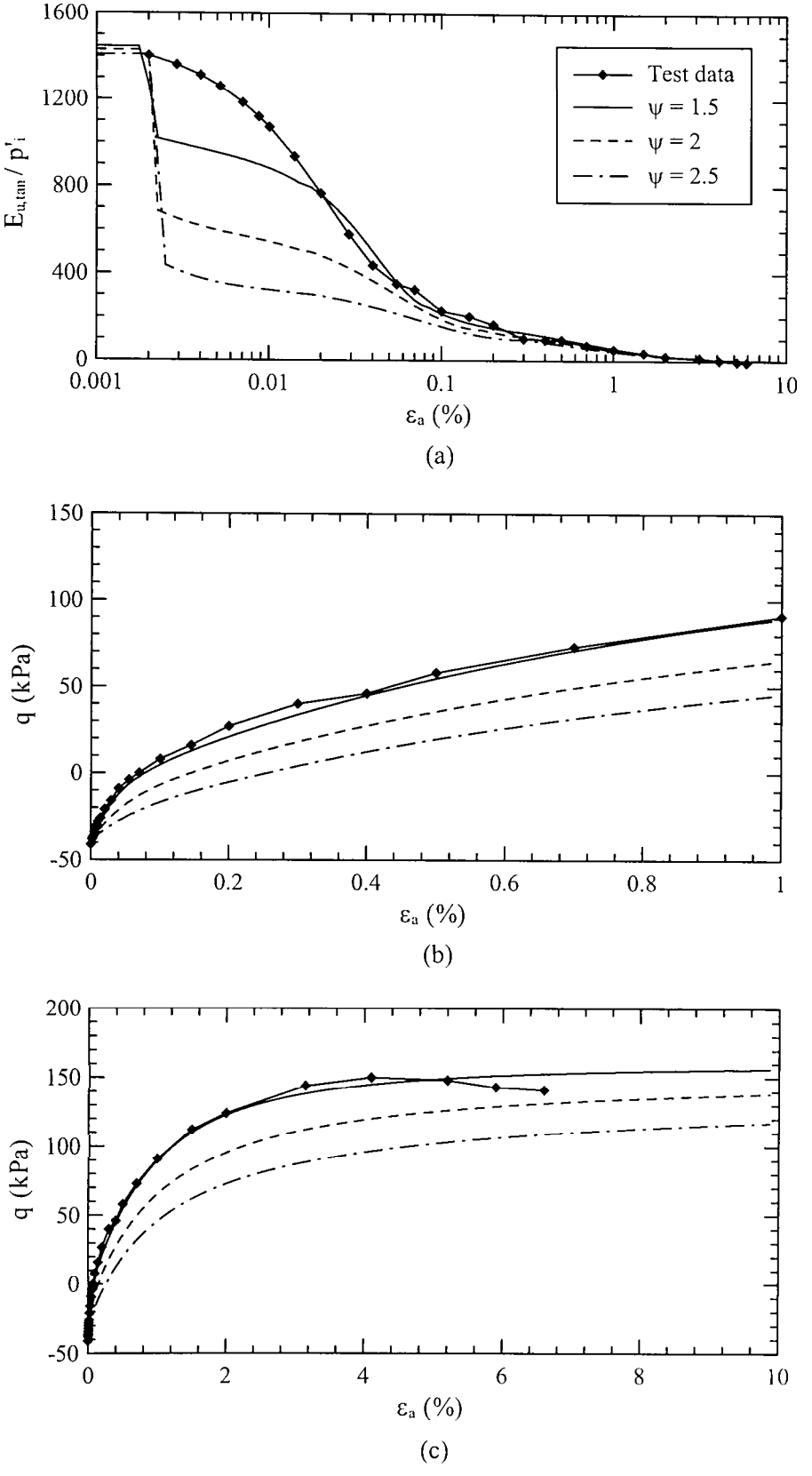


Figure 7.9: Effect of varying ψ for the three-surface model – Test LR7 a) normalised stiffness-strain curve b) stress-strain curve c) stress-strain curve – larger strains (test data from Jardine (1985))

clearly in the stress-strain curves of Figure 7.8b. For $T = 0.4$ the behaviour is initially stiffer and then softer as the strain increases.

c) ψ

Figure 7.9 shows the effect of varying the parameter ψ. Here the values of T and S were kept constant at $T = 0.2$ and $S = 0.08$. Increasing the value of ψ results in a more dramatic decrease in stiffness when plastic straining first occurs and hence in a softer overall response.

The optimum values chosen for the above parameters of the three-surface model are $T = 0.2$, $S = 0.08$ and $\psi = 1.5$.

Modified three-surface model

a) S

In these analyses the values of the parameters T, α_1 and α_2 were kept constant at $T = 0.2$, $\alpha_1 = 6$ and $\alpha_2 = 35$ and the values of the parameter S varied between 0.05 and 0.15 so that the product TS varied between 0.01 and 0.03. Figure 7.10 illustrates the effect of varying the size of the elastic region in the predictions of the modified three-surface model. Increasing S results in a wider elastic plateau and in a small increase in stiffness for stress states inside the history surface. The stiffness response within the history does not seem to be as sensitive to the variations of S as the one predicted by the three-surface model is.

b) T

The effect of changing the size of the history surface can be seen in Figure 7.11. For these predictions the values of α_1 and α_2 were set at $\alpha_1 = 6$ and $\alpha_2 = 35$ and the values of the parameters T and S varied so that the product TS was kept constant at $TS = 0.016$. It seems that for higher values of T a stiffer behaviour is observed within the history surface. Although not shown very clearly in Figure 7.11a, when the history surface is engaged, increasing T results in a slightly lower value of stiffness, which is not as significant as in the case of the three-surface model and does not result in the stress-strain curve for $T = 0.4$ becoming the softest one. Although the modified three surface model seems to be sensitive to the values of the parameter T this effect is not as pronounced as in the three-surface model.

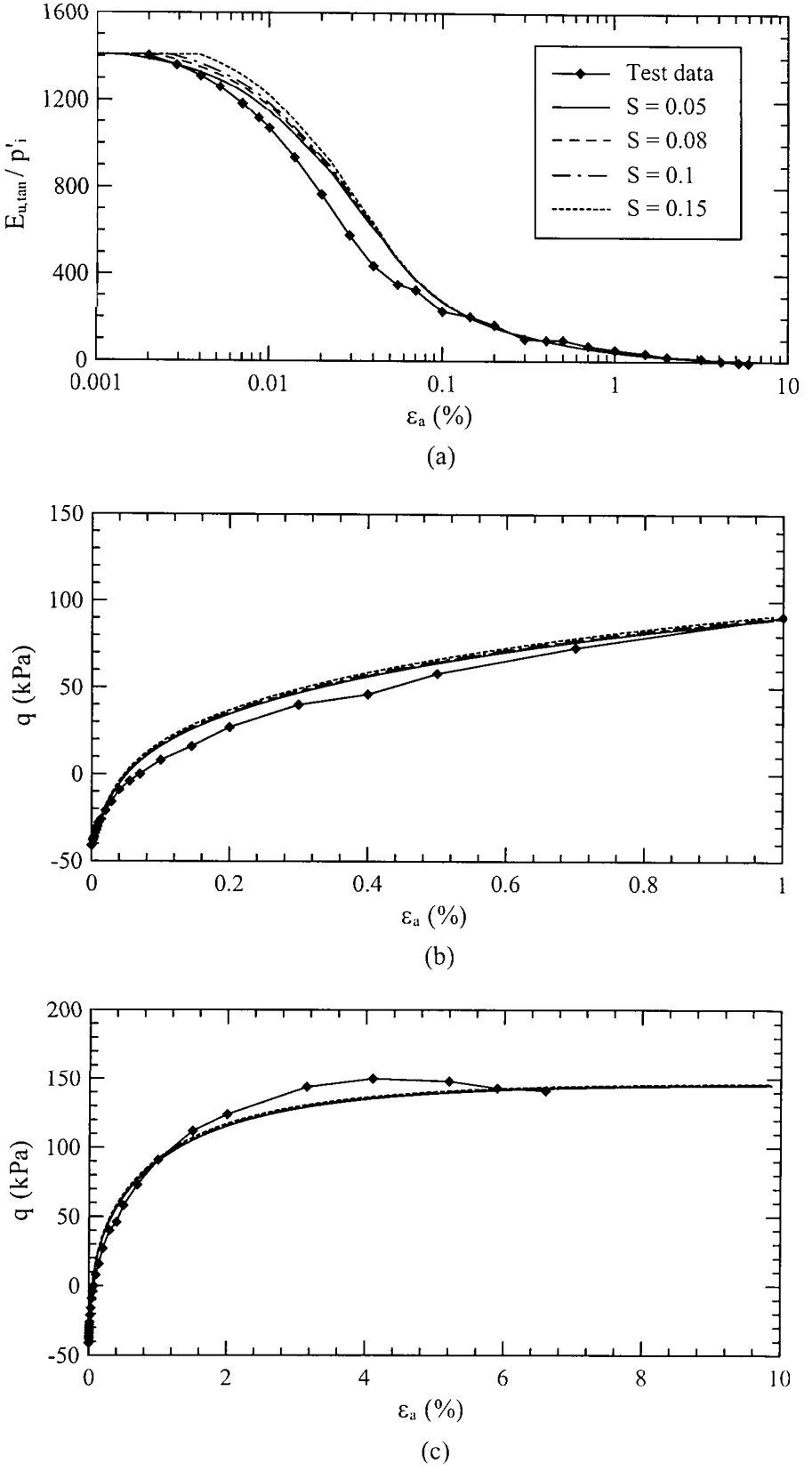


Figure 7.10: Effect of varying *S* for the modified three-surface model – Test LR7 a) normalised stiffness-strain curve b) stress-strain curve c) stress-strain curve – larger strains (test data from Jardine (1985))

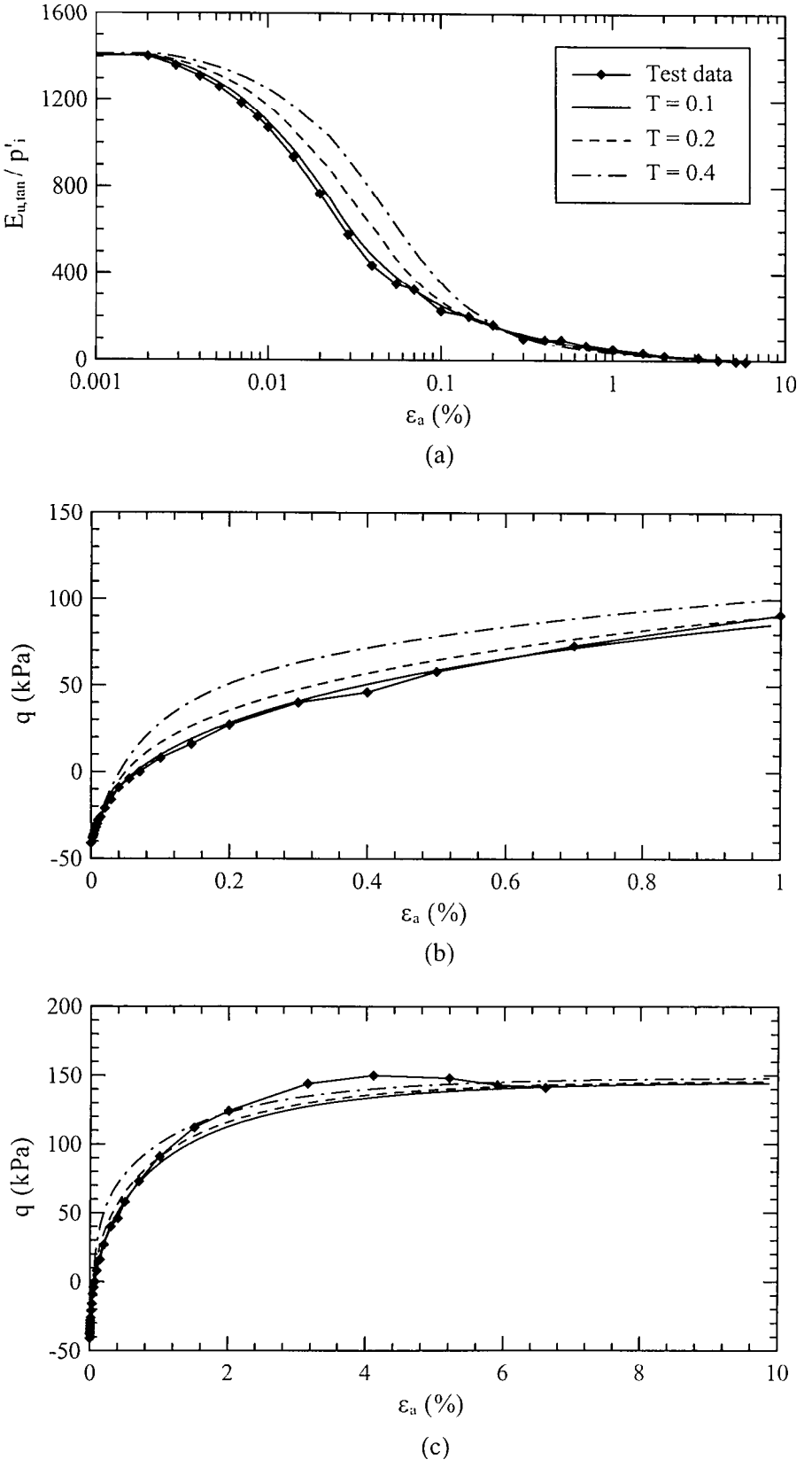


Figure 7.11: Effect of varying T for the modified three-surface model – Test LR7 a) normalised stiffness-strain curve b) stress-strain curve c) stress-strain curve – larger strains (test data from Jardine (1985))

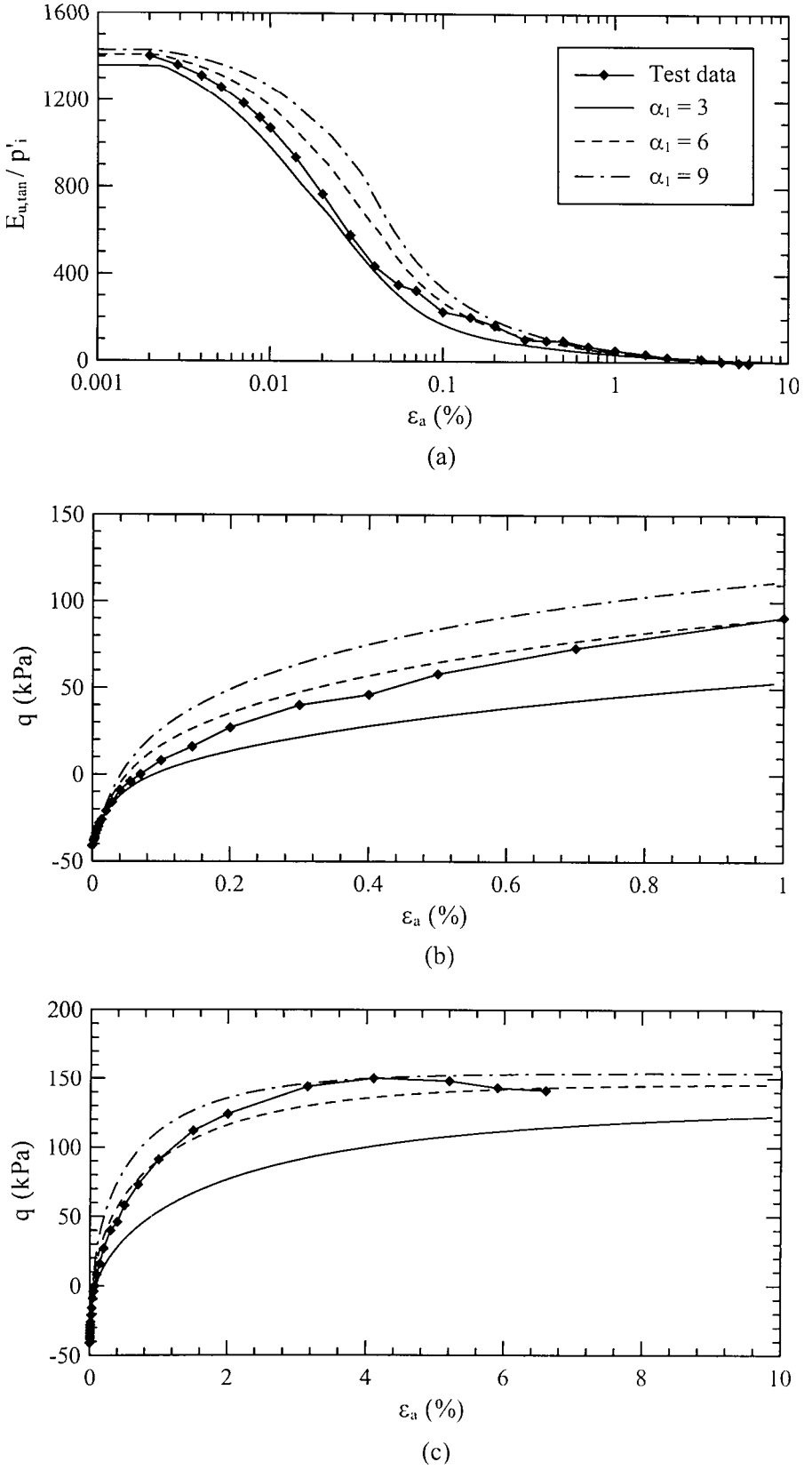


Figure 7.12: Effect of varying α_1 for the modified three-surface model – Test LR7 a) normalised stiffness-strain curve b) stress-strain curve c) stress-strain curve – larger strains (test data from Jardine (1985))

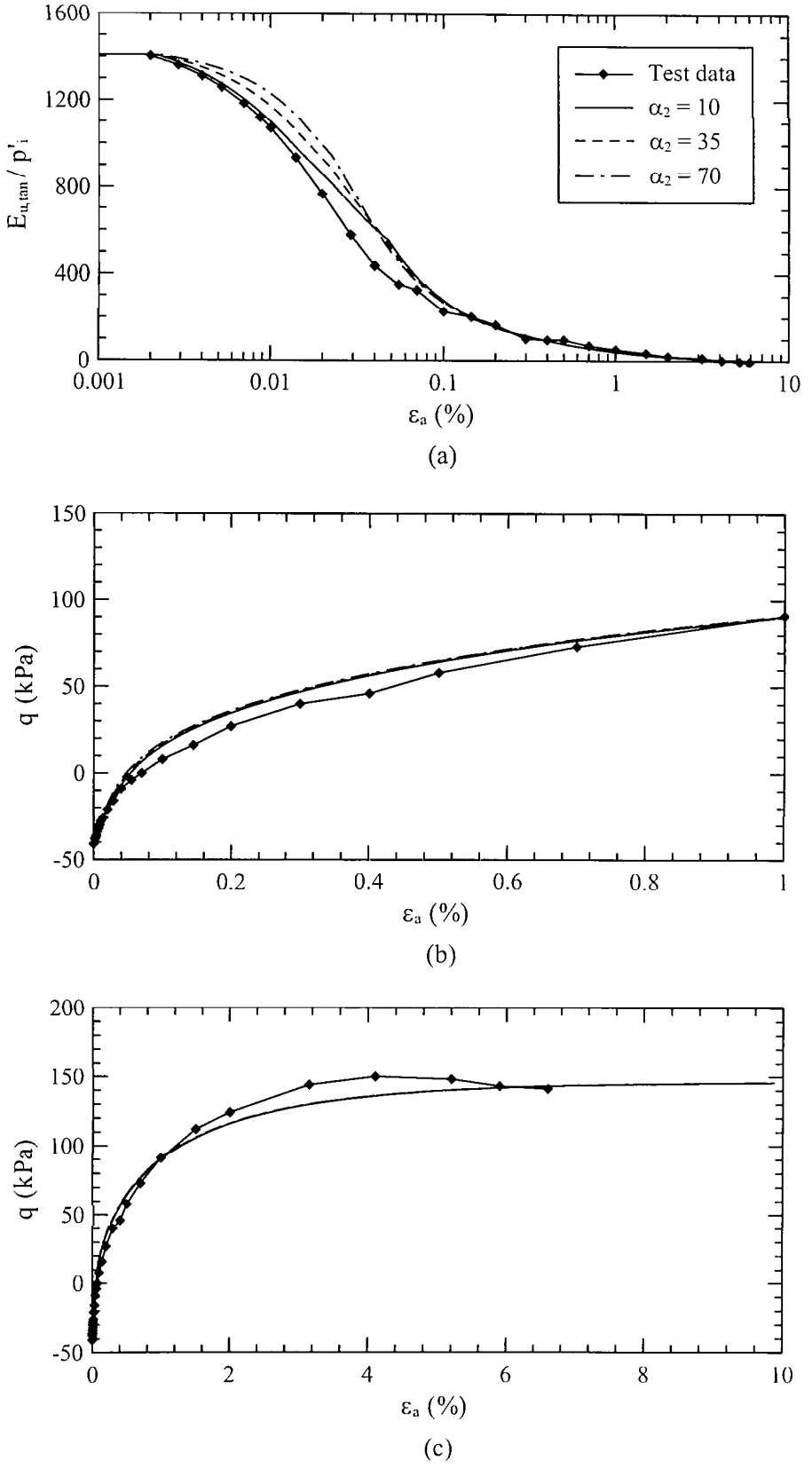


Figure 7.13: Effect of varying α_2 for the modified three-surface model – Test LR7 a) normalised stiffness-strain curve b) stress-strain curve c) stress-strain curve – larger strains (test data from Jardine (1985))

c) α_1

The influence of the parameter α_1 is shown in Figure 7.12. Here the parameters T, S and α_2 were equal to $T = 0.2$, $S = 0.08$ and $\alpha_2 = 35$ and α_1 varied between 3 and 9. Figure 7.12 indicates that lower values of α_1 result in a faster rate of decay of stiffness and hence in a softer overall response. The stiffness degradation curves obtained in any case are smooth with no abrupt change in stiffness when the stress state engages the kinematic yield surface.

d) α_2

For these predictions the parameters T, S and α_1 were kept constant at $T = 0.2$, $S = 0.08$ and $\alpha_1 = 6$ and α_2 varied between 10 and 70. Figure 7.13 indicates that the parameter α_2 influences the response for stress states within the history surface. The higher the value of α_2 the stiffer the behaviour is. The stiffness-strain curves obtained in any case are smooth irrespective of the value of the parameter α_2.

Based on the comparison between model predictions and experimental data (Figures 7.10-7.13), the following parameters were chosen for the modified three-surface model, $T = 0.1$, $S = 0.16$, $\alpha_1 = 6$ and $\alpha_2 = 35$.

It has to be noted that in Figures 7.3c to 7.13c, depending on the values of the parameters that define the behaviour of the kinematic surfaces, the models may not have reached the critical state at an axial strain of 10%. This has the consequence that, depending on the choice of the input parameters, the undrained strength predicted by the equations of Appendix III may be mobilised at very high strains or may never be practically fully mobilised.

Summary of parametric study

a) Sensitivity of each model to the remaining parameters

The two-surface model seems to be sensitive to variations of both the parameters R and ψ. This is because the values of both R and ψ control the amount by which the stiffness drops once yielding is initiated. The modified two-surface model seems to be sensitive to the variations of α but not as sensitive to the variations of the size of the kinematic yield surface as the two-surface model is, since in any case no abrupt reduction in stiffness is observed. The three-surface model is mostly sensitive to the variations of T and ψ, whereas the parameter S influences in a lesser extent the behaviour within the

history surface. All three parameters seem to affect the reduction in stiffness observed when the limit of the elastic region is reached. The modified three-surface model does not show any such effect and is less sensitive to the variations of the parameters T and S than the three-surface model is. The modified three-surface model is sensitive to the value of the parameter α_1 whereas the parameter α_2 influences the behaviour within the history surface.

b) Choice of the remaining parameters

As aforementioned, based on the comparison between model predictions and experimental data the following optimum parameters were chosen: for the two-surface model $R = 0.016$ and $\psi = 6$, for the modified two-surface model $R = 0.016$ and $\alpha = 6$, for the three-surface model $T = 0.2$, $S = 0.08$ and $\psi = 1.5$ and for the modified three-surface model $T = 0.1$, $S = 0.16$, $\alpha_1 = 6$ and $\alpha_2 = 35$. It has to be noted that the size of the history surface that gives the best fit to the experimental data is not the same for the three-surface and the modified three-surface model, and this is a result of deriving this parameter through a parametric study. However, if one wanted to assume the same size of the history surface for both models then the values of $T = 0.2$ and $S = 0.08$ could be assumed for the modified three-surface model, since for this model variations in the values of the parameter T do not have as drastic effect as for the three-surface model. In this case a slightly stiffer behaviour would be predicted for the modified three-surface model as can be seen in Figure 7.11. The set of optimum parameters for each model will be used subsequently in the evaluation of the models, which follows in the next section.

N	λ^*	κ^*	A	n	m	φ'	Y_p	Z_p	R	ψ
3.43	0.097	0.003	590.0	0.87	0.28	22.5°	0.0	1.0	0.016	6.0

Table 7.1: Material parameters for the two-surface model for the simulation of tests on reconstituted London Clay

N	λ^*	κ^*	A	n	m	φ'	Y_p	Z_p	R	α
3.43	0.097	0.003	590.0	0.87	0.28	22.5°	0.0	1.0	0.016	6.0

Table 7.2: Material parameters for the modified two-surface model for the simulation of tests on reconstituted London Clay

N	λ^*	κ^*	A	n	m	φ'	Y_p	Z_p	T	S	ψ
3.43	0.097	0.003	590.0	0.87	0.28	22.5°	0.0	1.0	0.2	0.08	1.5

Table 7.3: Material parameters for the three-surface model for the simulation of tests on reconstituted London Clay

N	λ^*	κ^*	A	n	m	φ'	Y_p	Z_p	T	S	α_1	α_2
3.43	0.097	0.003	590.0	0.87	0.28	22.5°	0.0	1.0	0.1	0.16	6.0	35.0

Table 7.4: Material parameters for the modified three-surface model for the simulation of tests on reconstituted London Clay

7.2.3 Evaluation of the models' predictions

In this section each of the four models is evaluated by comparing the model predictions with the experimental data for the stress paths LR1.5, LR3, LR7, LRE1.5, LRE3 and LRE7 (as mentioned in Chapter 2, LR denotes compression tests, LRE denotes extension tests and the following number denotes the *OCR*).

The values assigned to the model parameters used in the following analyses are the soil properties derived in section 7.2.2 and summarised in Table 7.1, for the two-surface model, Table 7.2 for the modified two-surface model, Table 7.3 for the three-surface model and Table 7.4 for the modified three-surface model. The simulation of the tests involved the modelling of the complete stress history (compression and swelling stages starting from the initial condition of the sample in the stress path cell) before the modelling of the shearing stage.

For each model the stress-strain curves in the small strain range (strains up to 1%) and in the relatively large strain range (strains up to 10%) are compared with the experimental predictions. Moreover, the corresponding stiffness-strain curves are plotted against the experimental results. Particular emphasis is given on the capability of the models to predict behaviour in the small strain range. At the start of loading, a plot of tangent stiffness against strain is a better indicator of small strain response than a simple stress-strain curve. However, at later loading stages the latter provides a better comparison.

It has to be noted that in order to evaluate the tangent stiffness for the initial part of the

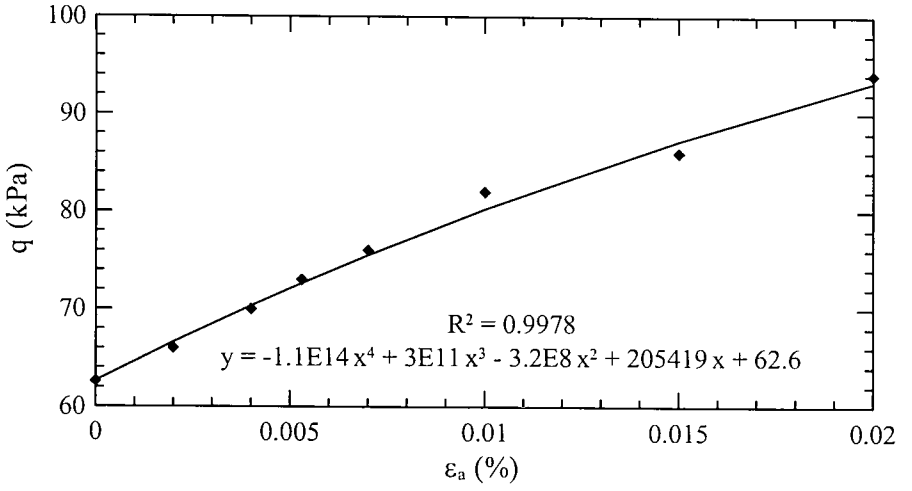


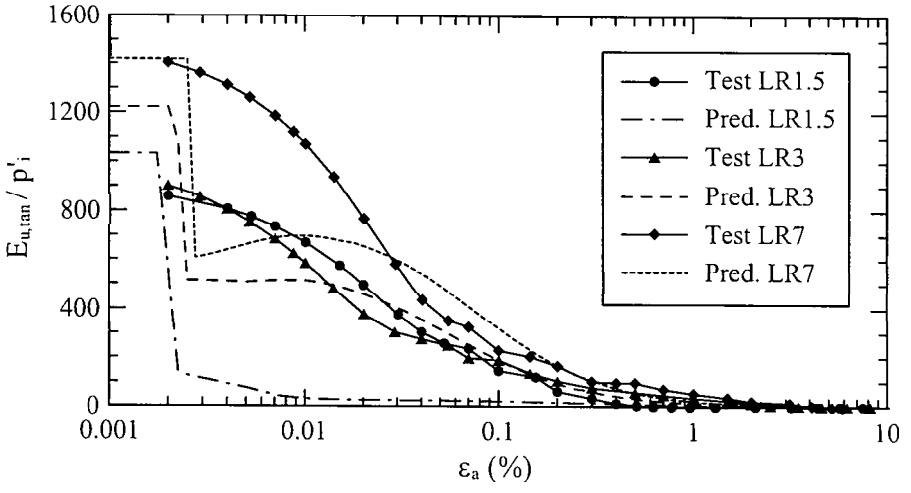
Figure 7.14: Example of curve fitting of the initial part of the stress-strain curve for test LR1.5

experimental stress-strain curves, polynomial curves were fitted to the raw stress-strain data and the tangent modulus was then obtained from differentiation of the polynomial. An example of such a curve is given in Figure 7.14.

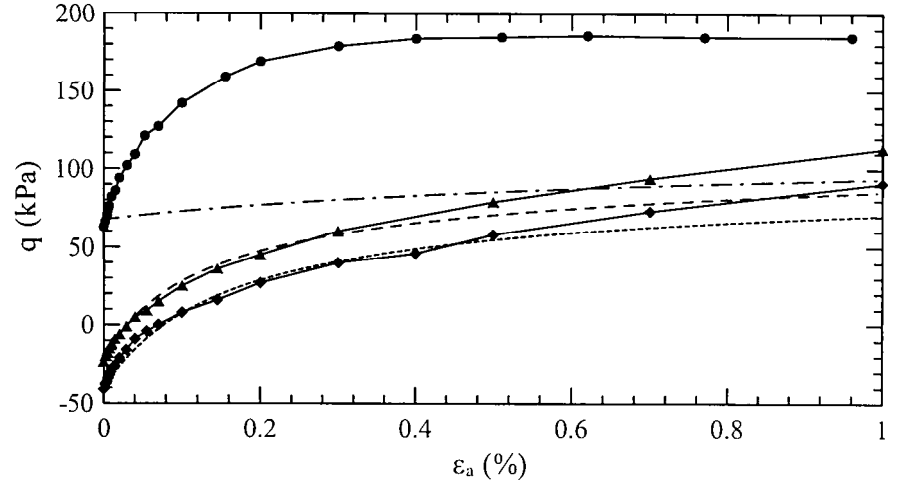
7.2.3.1 Two-surface model

Figure 7.15 presents the predictions of the two-surface model, plotted against the test data, for the compression paths. Figures 7.15b and 7.15c illustrate the stress-strain curves in the small and large strain range. The predicted curves for LR3 and LR7 seem to compare reasonably well with the experimental curves in the small strain range, however, for large strains the curves are significantly underpredicted. For the test LR1.5 the model significantly underpredicts the experimental stress-strain response. Figure 7.15a shows the corresponding plots of the tangent undrained Young's modulus, E_u, normalised by the mean effective stress at the start of the shearing stage p'_i, against axial strain. The model predicts a drop in stiffness once yielding is initiated for all three tests. Moreover, the form of the predicted stiffness curves does not compare favourably with the test data. For the tests LR3 and LR7 the model underpredicts the initial part of the stiffness degradation curve whereas for LR1.5 the model predicts a very low stiffness throughout the small strain range.

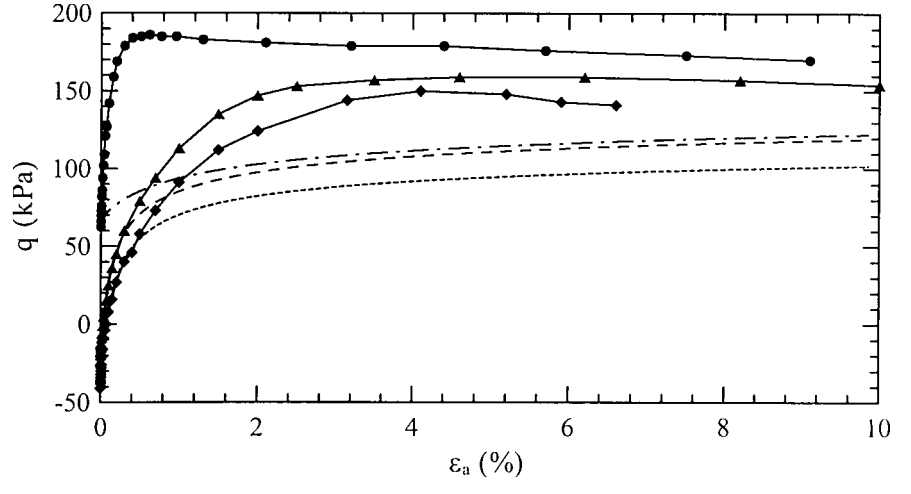
The prediction of the two-surface model for the extension paths can be seen in Figure 7.16. The stress-strain response for strains up to 1% and 10% is shown in Figures 7.16b and 7.16c respectively. For LRE1.5 the model significantly overpredicts the stress



(a)



(b)



(c)

Figure 7.15: Predictions of the two-surface model for the triaxial compression paths a) normalised stiffness-strain curve b) stress-strain curve c) stress-strain curve – larger strains (test data from Jardine (1985))

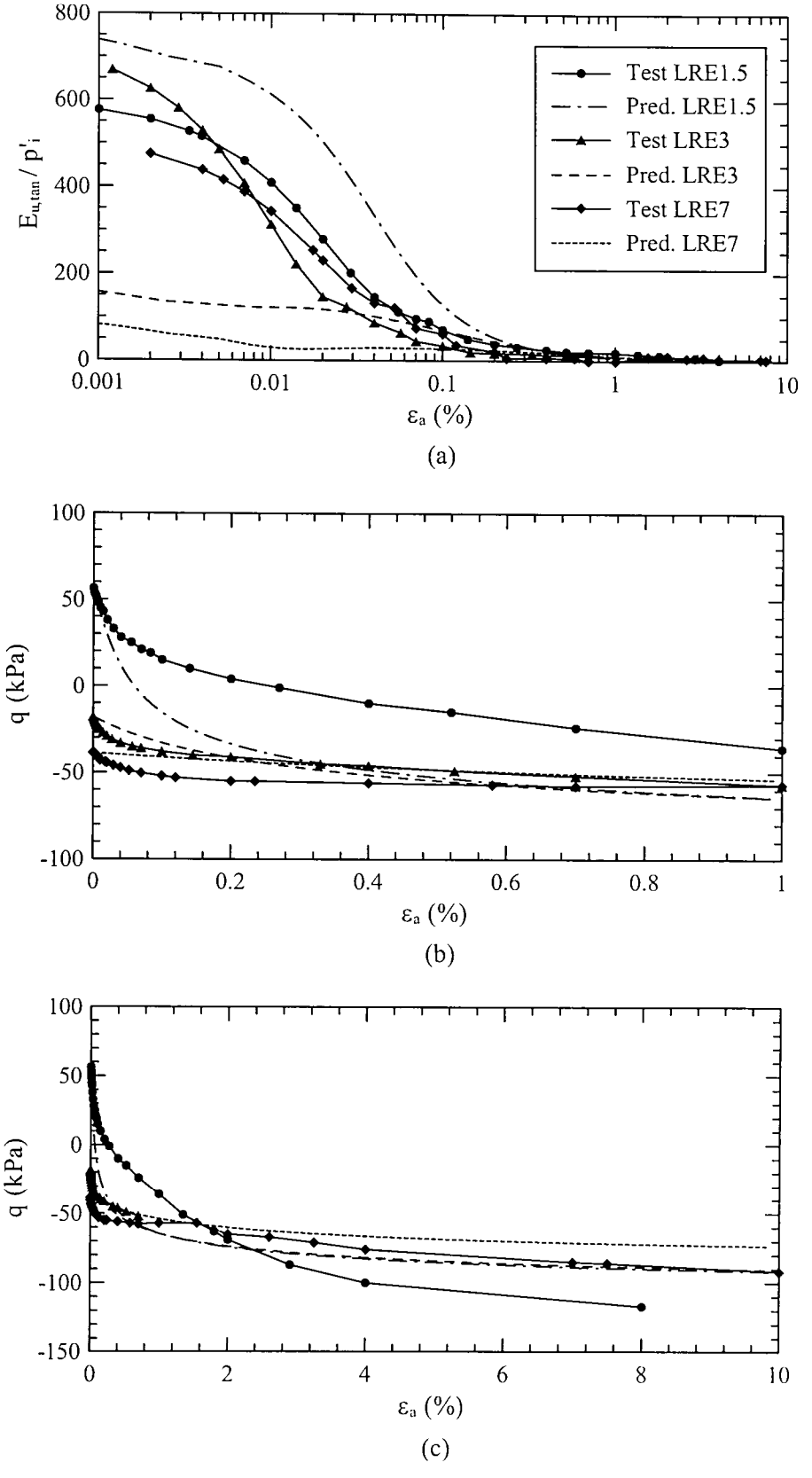


Figure 7.16: Predictions of the two-surface model for the triaxial extension paths a) normalised stiffness-strain curve b) stress-strain curve c) stress-strain curve – larger strains (test data from Jardine (1985))

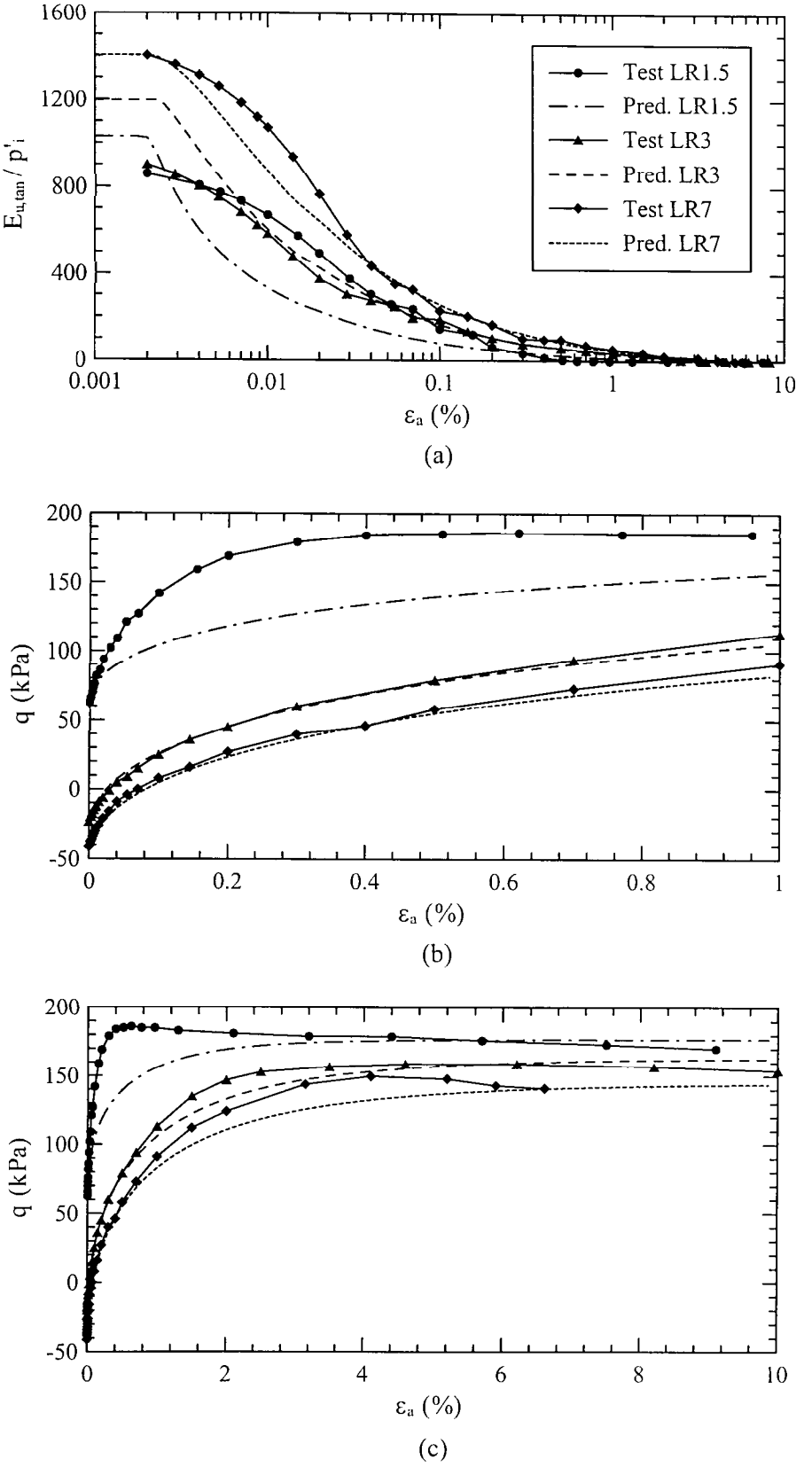
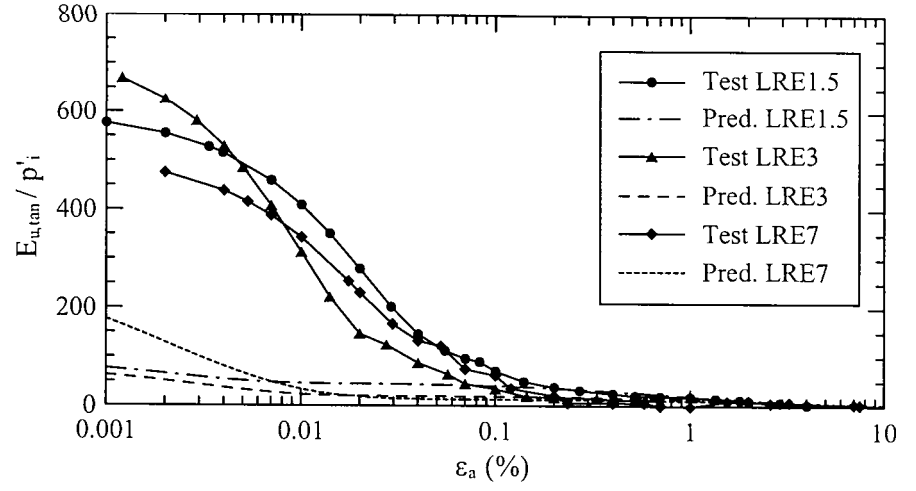
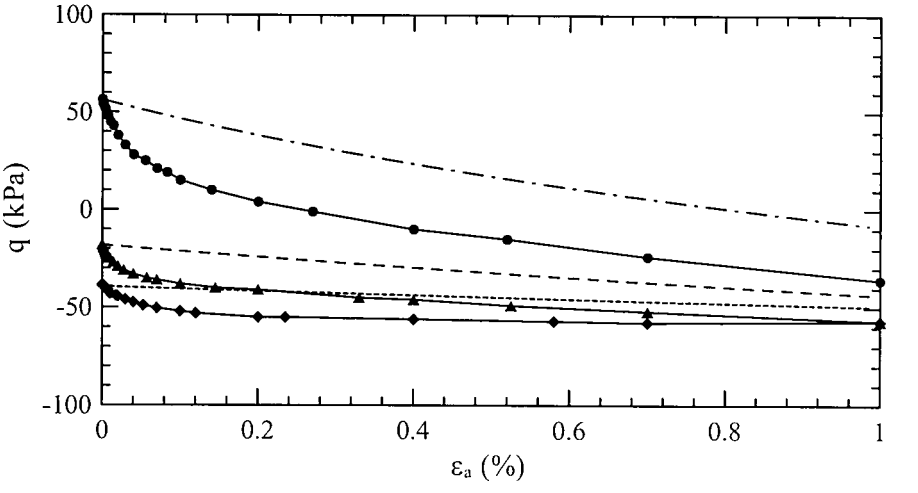


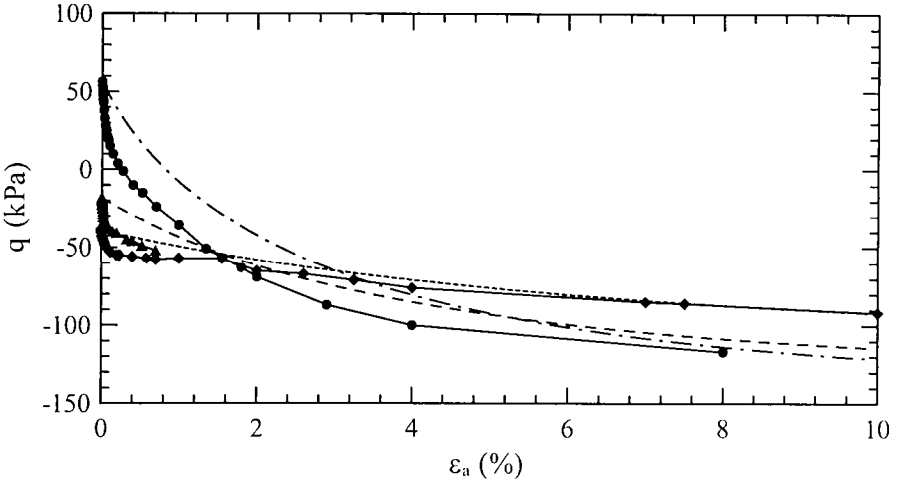
Figure 7.17: Predictions of the modified two-surface model for the triaxial compression paths a) normalised stiffness-strain curve b) stress-strain curve c) stress-strain curve – larger strains (test data from Jardine (1985))



(a)



(b)



(c)

Figure 7.18: Predictions of the modified two-surface model for the triaxial extension paths a) normalised stiffness-strain curve b) stress-strain curve c) stress-strain curve – larger strains (test data from Jardine (1985))

changes up to strains of approximately 2.4% and then underpredicts the stress-strain response. For the paths LRE3 and LRE7 better agreement with the experimental results seems to exist. The corresponding stiffness-strain curves are illustrated in Figure 7.16a. The stiffness for LRE1.5 is overpredicted up to strains of 0.3%. For LRE3 and LRE7 the stiffness is significantly underpredicted for strains up to 0.03% and 0.2% respectively.

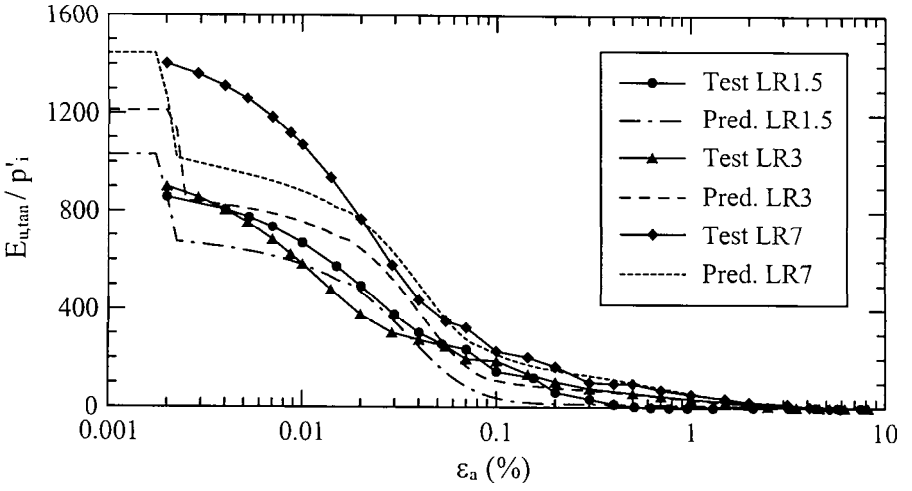
7.2.3.2 Modified two-surface model

Figure 7.17 presents the predictions of the modified two-surface model for the compression paths. For the test LR1.5 the stress-strain response is initially underpredicted but agrees well with the experimental data for strains higher than 3%. The stress-strain curves for LR3 and LR7 are reasonably well reproduced throughout the whole strain range. The corresponding stiffness-strain plots in Figure 7.17a indicate that for LR1.5 the stiffness is underpredicted up to strains of approximately 0.2% (although to a lesser extent than for the two-surface model). On the contrary, for LR3 and LR7 there is a good agreement with the experimental stiffness curves.

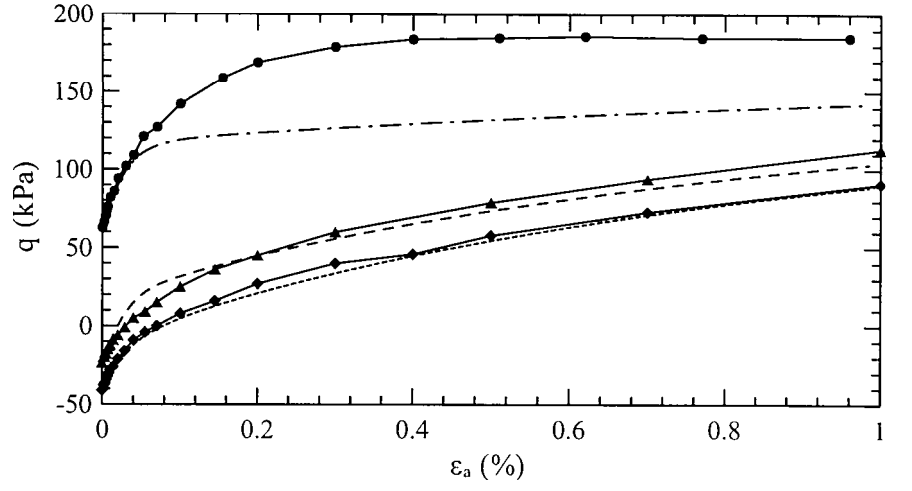
Comparison of the experimental and predicted stress-strain curves for the extension paths (Figures 7.18b and 7.18c) indicates that the model generally underpredicts the measured stress-strain response for all three paths, and particularly for LRE1.5, although the difference seems to decrease at higher strains for LRE1.5 and LRE7 (for LRE7 there is a reasonably good agreement for strains higher than 2%). The test LRE3 stopped earlier so there is no data at large strains. Figure 7.18a shows the corresponding stiffness curves. It can be seen that the model significantly underpredicts the stiffness response for strains up to 0.2%.

7.2.3.3 Three-surface model

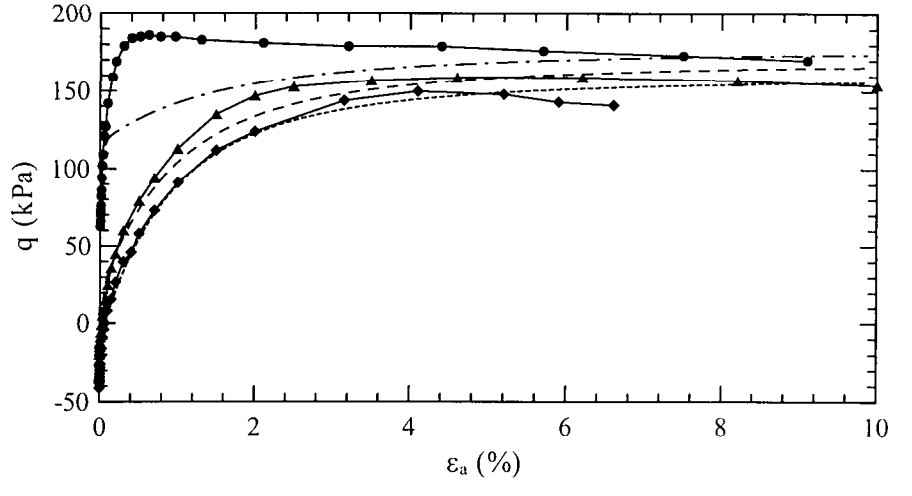
Figure 7.19 illustrates the predictions of the three-surface model for the compression paths. The model seems to underpredict the stress-strain response for the test LR1.5, although the predicted and experimental curves converge at large strains. The predictions for LR3 and LR7 agree well with the experimental results throughout the whole strain range. The corresponding stiffness-strain curves, shown in Figure 7.19a, indicate that the shape of the curves is such that it is difficult to get complete agreement with the experimental data. For LR1.5 the model generally underpredicts the stiffness curve but plots much closer to the experimental results than the two-surface model. For LR3 the opposite is true for strains up to 0.06%. For the test LR7 the model



(a)

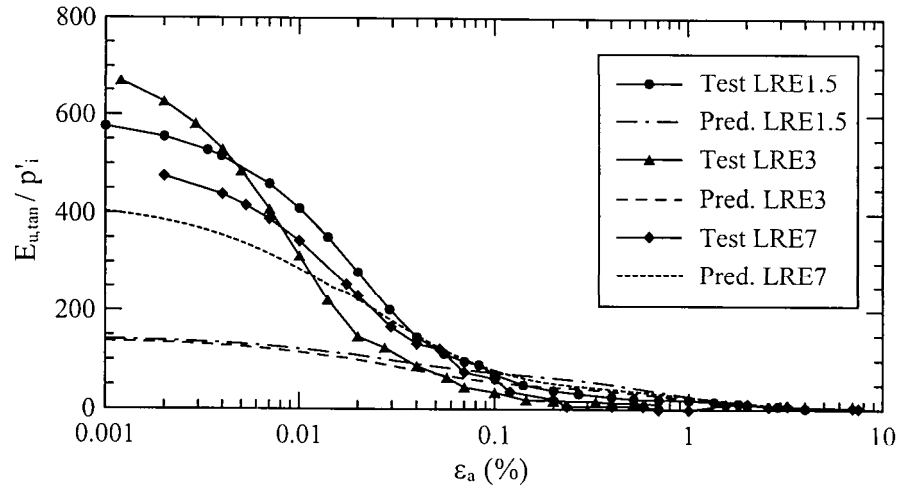


(b)

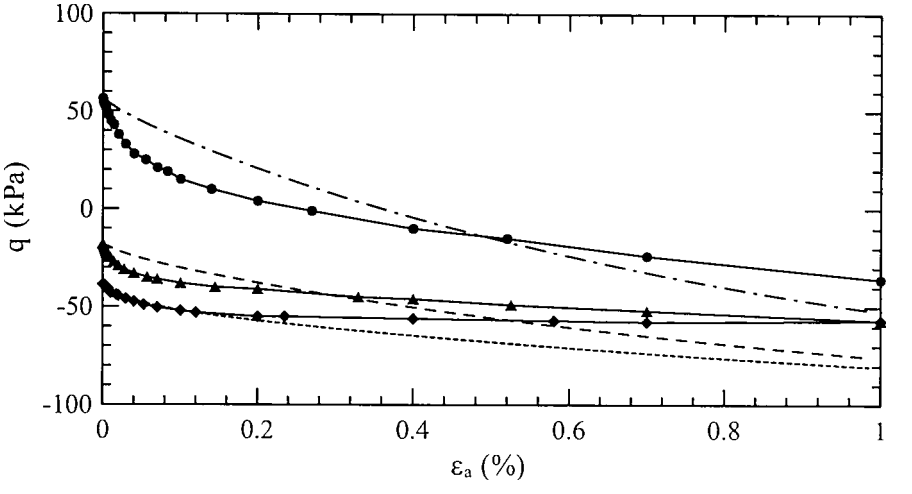


(c)

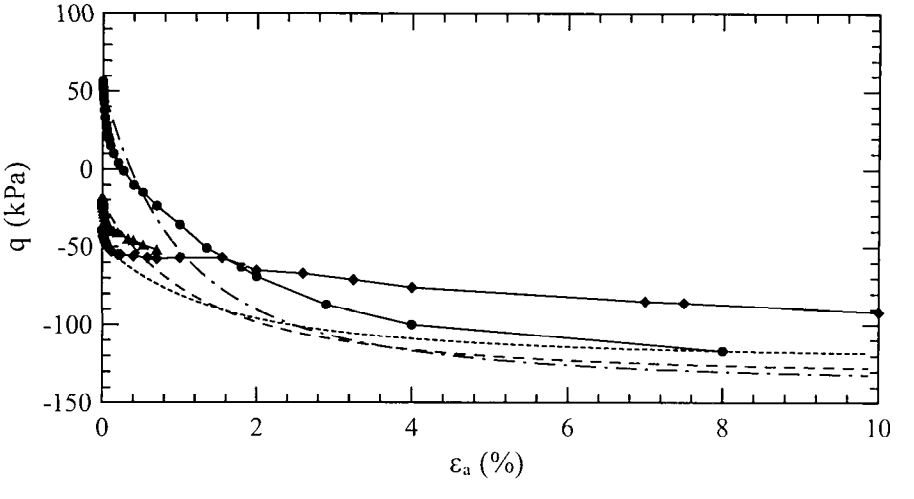
Figure 7.19: Predictions of the three-surface model for the triaxial compression paths a) normalised stiffness-strain curve b) stress-strain curve c) stress-strain curve – larger strains (test data from Jardine (1985))



(a)



(b)



(c)

Figure 7.20: Predictions of the three-surface model for the triaxial extension paths a) normalised stiffness-strain curve b) stress-strain curve c) stress-strain curve – larger strains (test data from Jardine (1985))

underpredicts the stiffness for strains up to 0.02% but then follows quite closely the experimental curve. It should be noted that the drops in stiffness predicted by this model, once yielding is initiated, are smaller than the ones predicted by the two-surface model. This can be attributed to the presence of the history surface in this model, as well as the values chosen for the model parameters.

The predictions of the three-surface model for the extension paths can be seen in Figure 7.20. The stress-strain response for LRE1.5 is initially underpredicted for strains up to ~0.5% but then overpredicted. The same is true for LRE3 but for strains up to ~0.3%. For the test LRE7 the model agrees with the experimental curve for strains up to 0.2% but then significantly overpredicts the response for higher strains. The corresponding stiffness-strain curves in Figure 7.20a show that the model predicts significantly lower values of stiffness than the experimental data shows for strains up to 0.1% and 0.04% for the tests LRE1.5 and LRE7 respectively, and from then on seems to overpredict the stiffness response. Better agreement is shown for the test LRE7 for strains up to approximately 0.02% but for higher strains the stiffness is again overpredicted.

7.2.3.4 Modified three-surface model

Figure 7.21 shows the predictions of the modified three-surface model for the compression paths. For LR1.5 the model underpredicts the stress-strain response in the small strain range (Figure 7.21b) although for strains higher than 3% the model predicts well the experimental curve (Figure 7.21c). For the tests LR3 and LR7 the predicted stress-strain curves agree well with the test data. Figure 7.21a shows the corresponding stiffness-strain curves. For LR1.5 the model generally predicts lower stiffness values than the experimental data but to a much lesser extent than in the case of the two-surface model. For LR3 the stiffness is overpredicted for strains up to 0.04% but the predicted curve has the correct shape and agrees well with the experimental results for higher strains. Finally, for LR7 there is a very good agreement between the predicted and measured response.

The predictions of the modified three-surface model for the extension paths can be seen in Figure 7.22. Figures 7.22b and 7.22c illustrate the predicted stress-strain curves. The model underpredicts the stresses for the LRE1.5 test, although the curves seem to converge at large strains. For LRE3 the stresses are also underpredicted but there is no data at large strains. However, for LRE7 there is a better agreement with the experimental response. Inspection of Figure 7.22a, which presents the corresponding

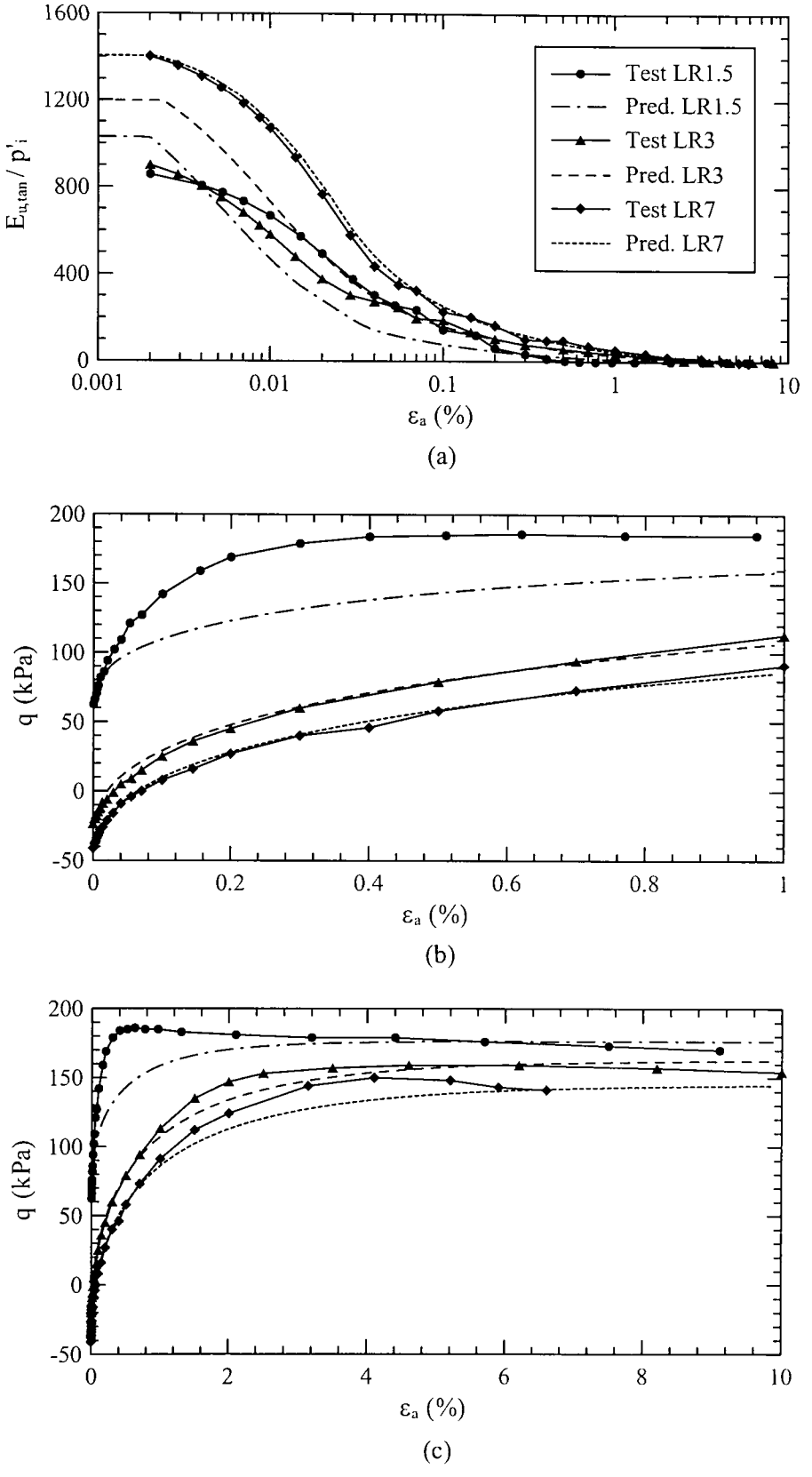
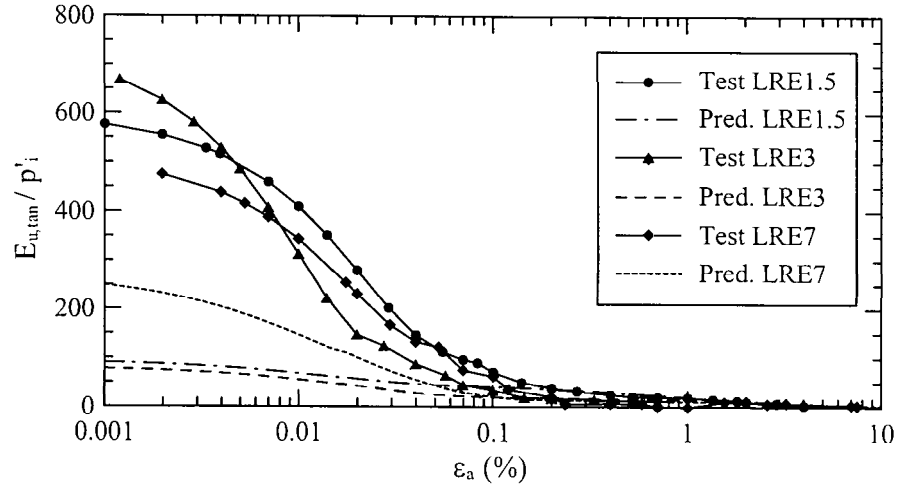
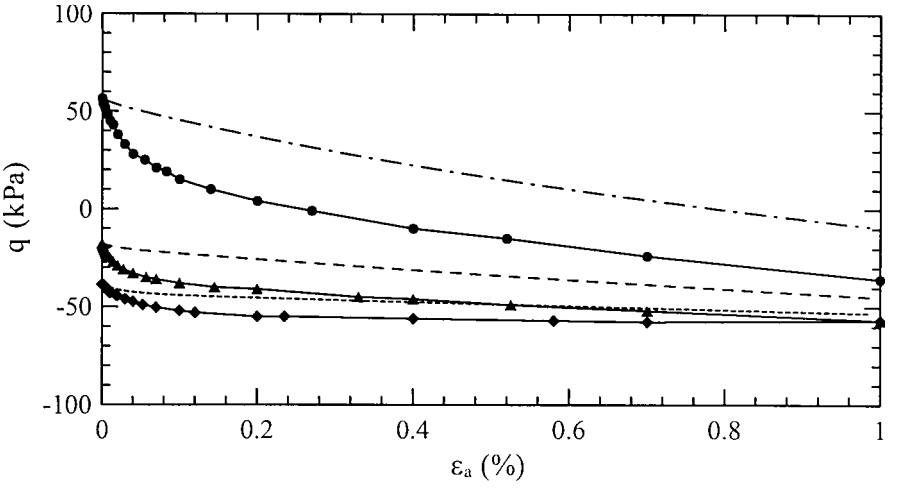


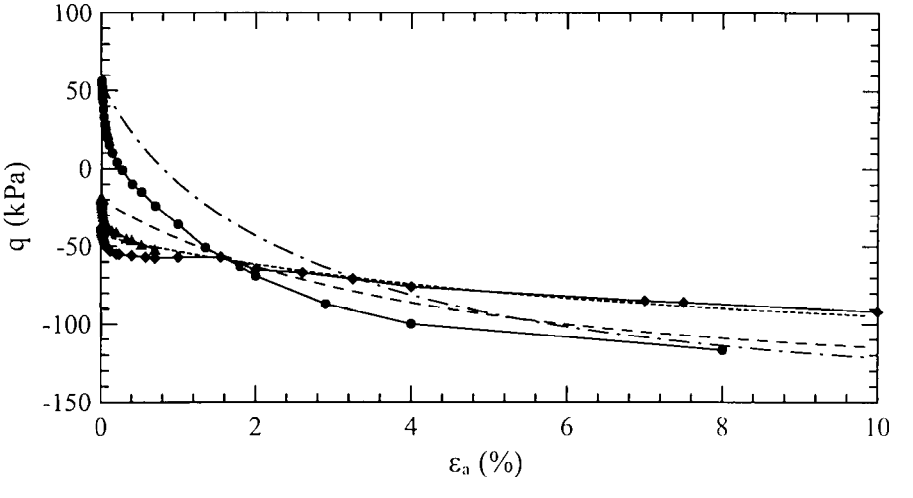
Figure 7.21: Predictions of the modified three-surface model for the triaxial compression paths a) normalised stiffness-strain curve b) stress-strain curve c) stress-strain curve – larger strains (test data from Jardine (1985))



(a)



(b)



(c)

Figure 7.22: Predictions of the modified three-surface model for the triaxial extension paths a) normalised stiffness-strain curve b) stress-strain curve c) stress-strain curve – larger strains (test data from Jardine (1985))

stiffness-strain curves, shows that the model significantly underpredicts the stiffness in the small strain range.

7.2.4 Summary

This section evaluated the capability of the four kinematic hardening models to reproduce the behaviour of overconsolidated reconstituted London Clay. A set of model parameters was derived for each model and the sensitivity of each model to the parameters that control the behaviour of the kinematic surfaces was examined. The ability of the four models to predict, in particular, the highly non-linear behaviour of overconsolidated London Clay in the small strain range can be summarised as follows:

i) Compression paths

All four models seem to underpredict the small strain behaviour of the test LR1.5; this can be seen in both the stress-strain curves for strains up to 1% and the stiffness-strains curves for all four models, and is particularly pronounced in the case of the two-surface model. For the tests LR3 and LR7 all four models predict reasonably well the stress-strain curves for strains up to 1% (the modified two-surface model, the three-surface model and the modified three-surface model also show good agreement for larger strains). In terms of the stiffness-strain curves, the modified two-surface and modified three-surface model predict better shapes and agree better than the two-surface and the three-surface model with the experimental data (the three-surface model gives much better predictions and smaller drops in stiffness, once yielding is initiated, than the two-surface model).

ii) Extension paths

All four models seem to significantly underpredict the initial part of the stiffness-strain curves for the extension paths (with the exception the test LRE1.5 for the two-surface model and the test LRE7 for the three-surface model). This feature of behaviour could be attributed to two reasons. First, for the kinematic hardening models the extension paths constitute a continuation in the direction of the previous swelling path, in the sense, that the configuration of the kinematic surfaces at the end of the swelling path is such that for the extension paths the models carry on behaving plastically, and hence predict low values of stiffness at the start of shearing. (On the contrary the compression paths constitute a reversal in the swelling path direction, the stress state re-enters the kinematic surface and the high elastic stiffness is re-invoked). Second, as mentioned in

Chapter 2, the experimental stress paths were carried out after an ageing period was allowed before the start of each shearing stage. In the case of the extension paths, this may have resulted in higher stiffness in the small strain range than if immediate shearing had taken place.

7.3 Modelling the effect of recent stress history

7.3.1 Introduction

The effect of recent stress history has been introduced in Chapter 2. According to Atkinson et al. (1990) and Stallebrass (1990) the stiffness along a certain loading path depends on the direction of the previous approaching path. The highest stiffness is observed for a stress path rotation of $\theta_r = 180°$, which constitutes a complete reversal in the stress path direction, and the lowest for $\theta_r = 0°$, which is a continuation of the previous stress path direction.

In the kinematic hardening models the configuration of the kinematic surfaces relative to the current stress state provides some information of the previous loading history and dictates the stiffness obtained along a subsequent loading path. Stallebrass (1990) suggested that in order to simulate satisfactorily the effect of recent stress history a second surface had to be introduced within the two-surface model.

This section investigates the capability of all four kinematic hardening models, used in this thesis, to simulate the effect of recent stress history on the pre-failure deformation of overconsolidated clays. For the three-surface model a short discussion has already been presented in Chapter 5 as part of the validation of the model. Here this discussion will be extended and the same multi-stage test will be repeated for the other three models.

As described in Chapter 5, this multi-stage test on speswhite kaolin investigates the behaviour along a common constant p' loading path after four different stress path rotations, $\theta_r = 90°$, 0°, -90° and 180° (the angle θ_r has been defined in Figure 5.9).

7.3.2 Model parameters

The parameters used in the three-surface model for the simulation of the test have been derived by Stallebrass (1990)) for speswhite kaolin and can be seen in Table 5.1. Table

5.2 gives the parameters used in the version of the three-surface model implemented into ICFEP. The parameters adopted for the remaining three models were chosen as follows. The parameters common to all four models, N, λ^*, κ^*, G_e, Y, Z, Y_p and Z_p were kept the same as those of the three-surface model. The size of the kinematic surfaces in the modified three-surface model were kept the same as for the three-surface model. The size of the kinematic yield surface in the two-surface and modified two-surface model was set equal to the product TS, which defines the size of the elastic region, so $R = 0.02$. Since it was outside the scope of this thesis to derive a complete set of parameters for speswhite kaolin for each model, a reasonable value of the remaining parameters, which control the decay of stiffness, ψ, α, α_1 and α_2 was chosen. Hence, it has to be noted that what is of interest here are the general trends predicted by the models, rather than the exact reproduction of the experimental results. The model parameters used in the analyses are given in Table 7.5 for the two-surface model, Table 7.6 for the modified two-surface model and Table 7.7 for the modified three-surface model.

N	λ^*	κ^*	G_e (kPa)	X	Y	Z	Y_p	Z_p	R	ψ
3.139	0.073	0.005	60000.0	0.51	0.0	1.0	0.0	1.0	0.02	6.0

Table 7.5: Material parameters used in the two-surface model for the simulation of the multi-stage test on speswhite kaolin

N	λ^*	κ^*	G_e (kPa)	X	Y	Z	Y_p	Z_p	R	α
3.139	0.073	0.005	60000.0	0.51	0.0	1.0	0.0	1.0	0.02	3.0

Table 7.6: Material parameters used in the modified two-surface model for the simulation of the multi-stage test on speswhite kaolin

N	λ^*	κ^*	G_e (kPa)	X	Y	Z	Y_p	Z_p	T	S	α_1	α_2
3.139	0.073	0.005	60000.0	0.51	0.0	1.0	0.0	1.0	0.25	0.08	1.5	25.0

Table 7.7: Material parameters used in the modified three-surface model for the simulation of the multi-stage test on speswhite kaolin

7.3.3 Evaluation of the models' predictions

7.3.3.1 Two-surface model

Figure 7.23 presents the stiffness against stress change curves, for the constant p' loading path after the four different stress path rotations, predicted by the two-surface model. The configurations of the surfaces at the start and end of each shearing stage can be seen in Figure 7.24. Figure 7.23 indicates that initially a different stiffness curve is predicted for the four different approaching paths, with the highest stiffness predicted for $\theta_r = 180°$. However, as soon as yielding initiates for $\theta_r = 180°$, the stiffness drops to the value predicted for $\theta_r = 0°$ and from then on the model predicts approximately the same

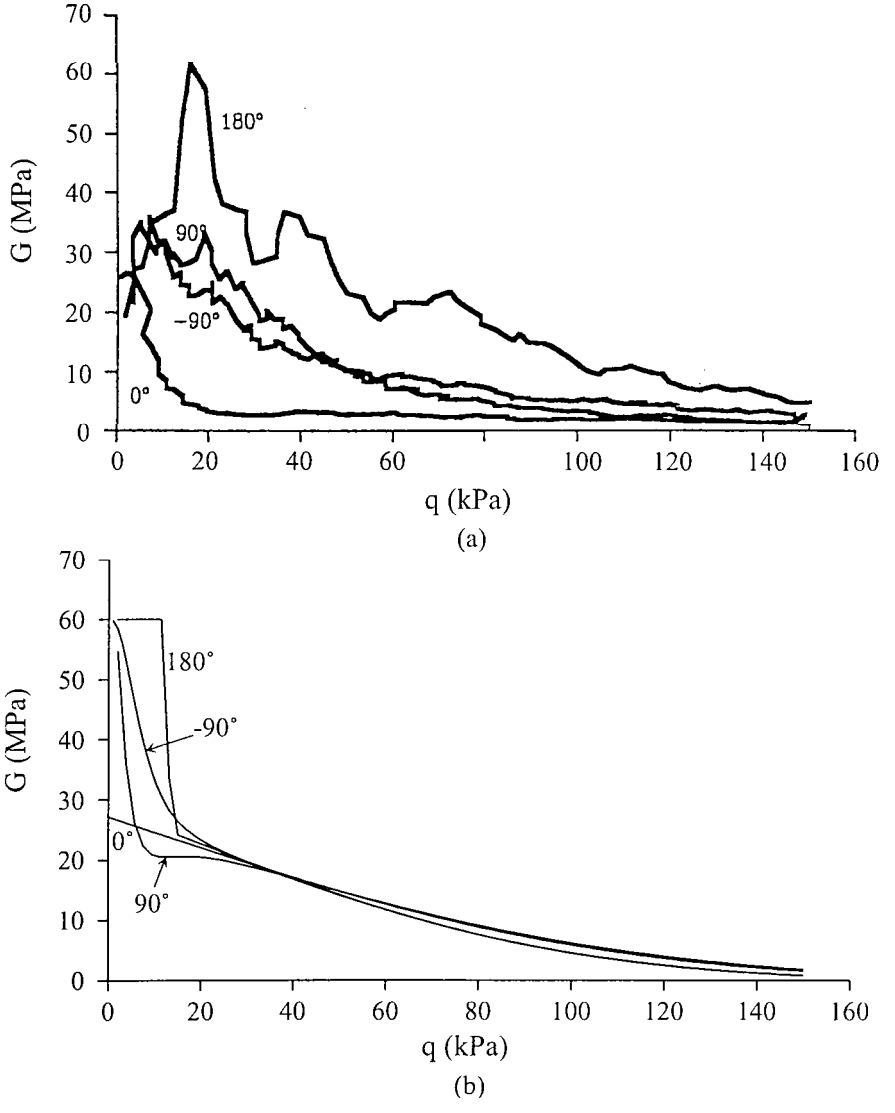


Figure 7.23: Constant p' loading after four stress path rotations: G against q
a) experimental data (after Stallebrass (1990)) b) predictions of two-surface model

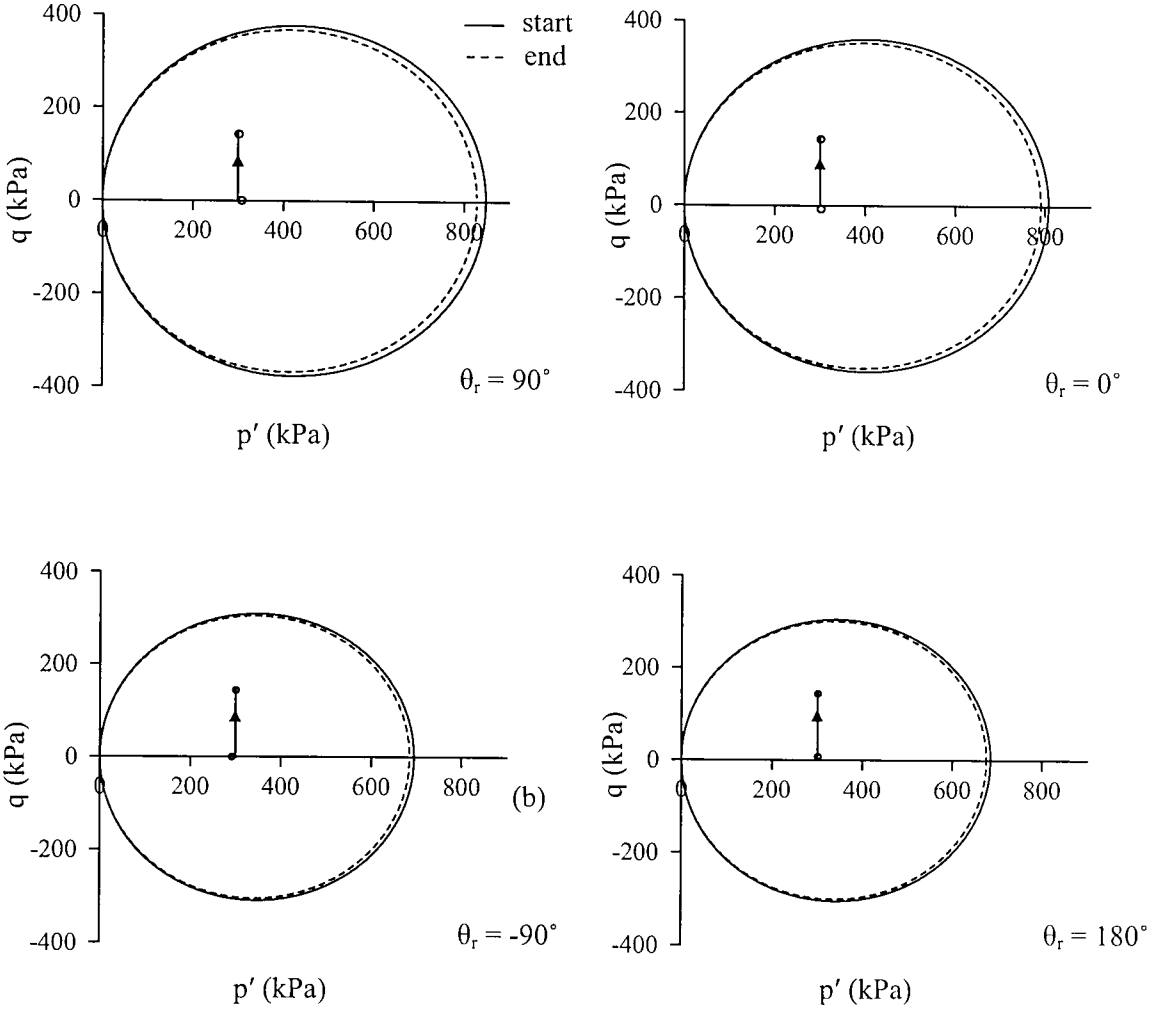


Figure 7.24: Configuration of the surfaces at the start and end of each cycle for the two-surface model

stiffness curves for all four stress path rotations. This is not in agreement with the trend revealed by the experimental data which shows that the stiffness curves do not seem to converge until a much higher stress change. Similar predictions to Figure 7.23 are also obtained for different ψ values.

Figure 7.25 illustrates the strain paths for the common constant p' path predicted by the two-surface model. The model predicts that all strains paths are dilative apart from the strain path for θ_r = -90° which shows a slightly compressive initial response. This is in contrast to the experimental data which shows that only the stress path for θ_r = 90° is dilative, but can be explained by considering the flow rule of the model. Because of the normality rule assumed in the model, whether the behaviour is dilative or compressive, along a constant p' test, depends on the position of the stress state relative to the kinematic surface. If this is to the right of p'_a the behaviour will be compressive, which

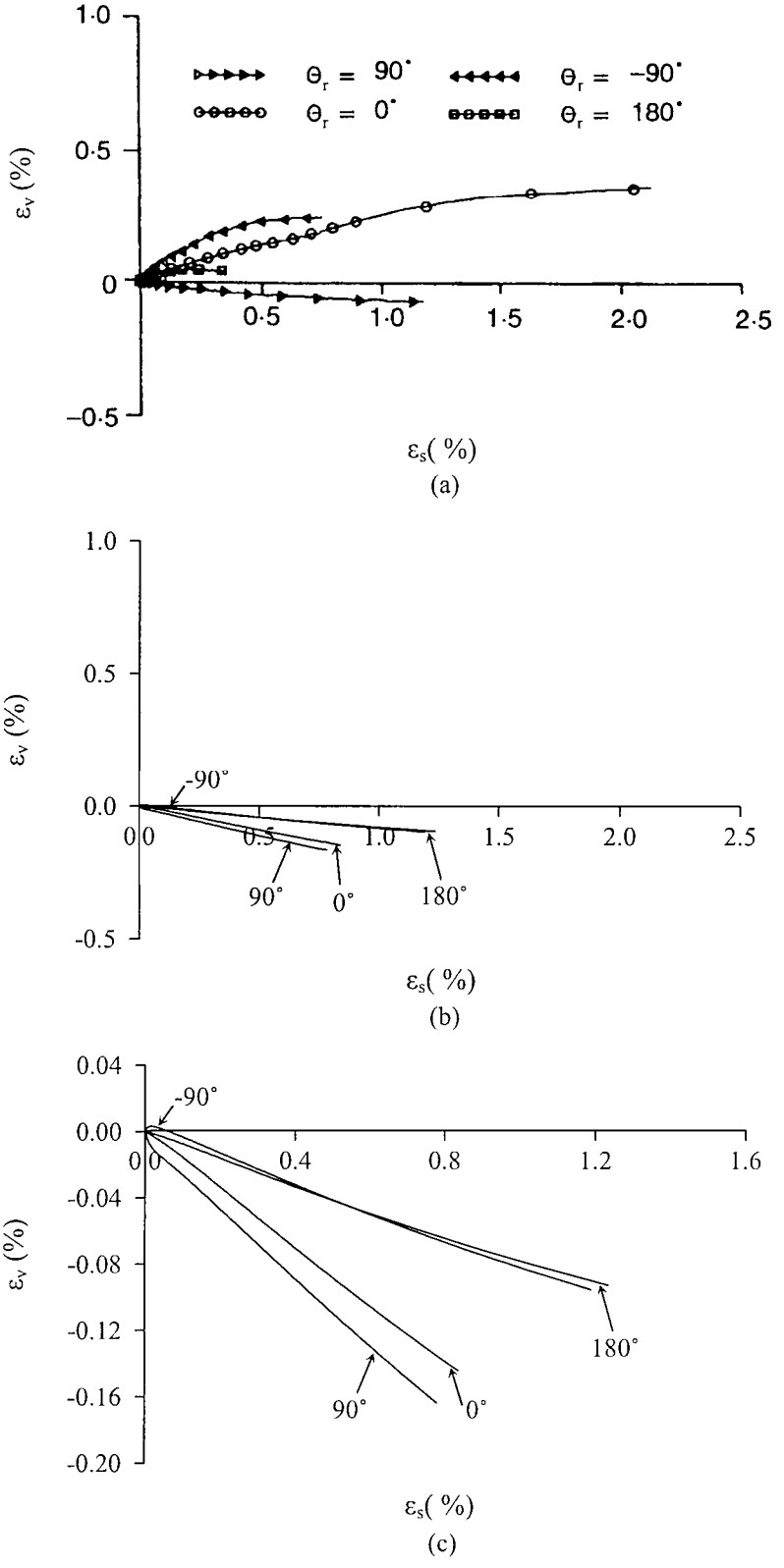


Figure 7.25: Constant p' loading after four stress path rotations: ε_v against ε_s
a) experimental data (after Stallebrass (1990)) b) predictions of two-surface model
c) predictions of two-surface model – bigger scale

is the case initially for θ_r = -90°. However, since the kinematic yield surface is not stationery and translates, the position of the stress state relative to the kinematic yield surface changes and the behaviour can change from compressive to dilative. If the stress state is dry of critical, as is the case here for θ_r = -90°, then the translation of the surface is such that the centre of the kinematic surface moves to the right of the stress state and the behaviour becomes dilative. How quickly this happens depends on the size of the kinematic yield surface, smaller kinematic yield surfaces, like in this case, orientate quicker than larger ones.

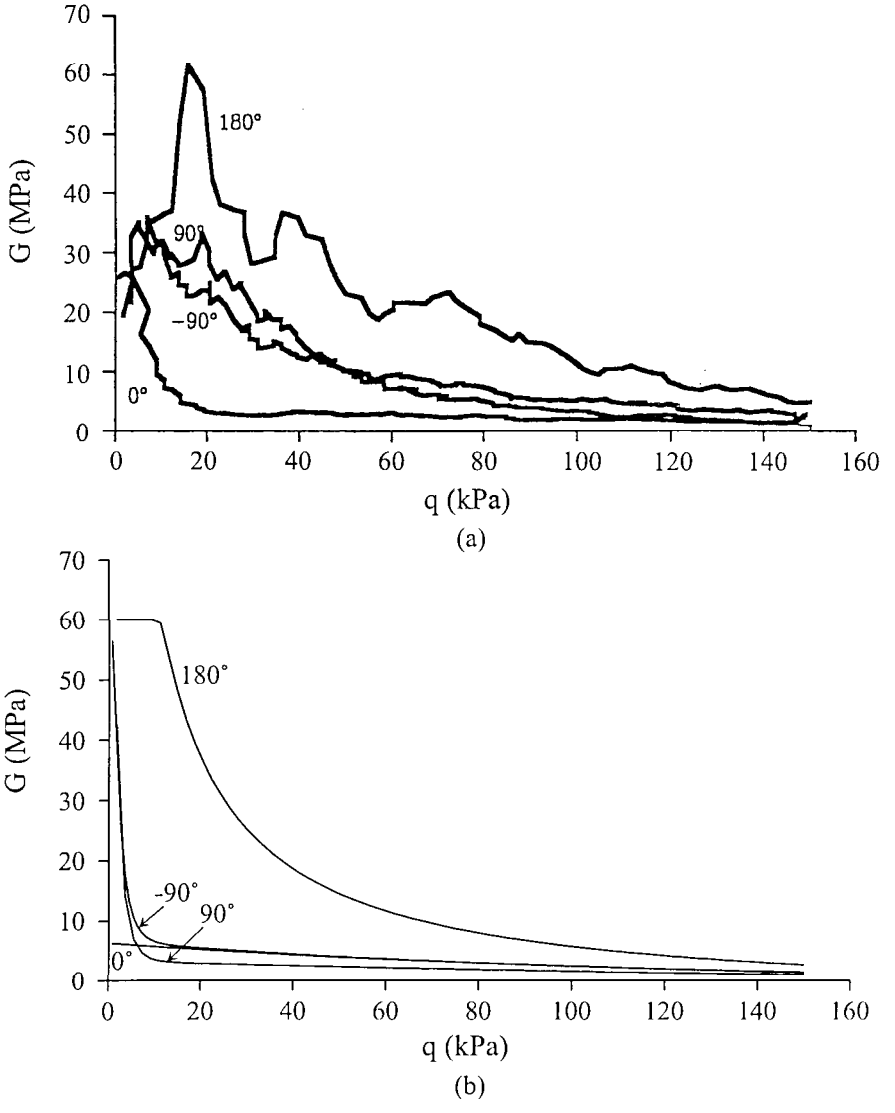


Figure 7.26: Constant p' loading after four stress path rotations: G against q
a) experimental data (after Stallebrass (1990)) b) predictions of modified two-surface model

7.3.3.2 Modified two-surface model

The predictions of the modified two-surface model for the stiffness against stress change curves are illustrated in Figure 7.26. The configurations of the surfaces at the start and end of each cycle can be seen in Figure 7.27.

Figure 7.26 shows that the model is capable of predicting higher stiffness for θ_r = 180° than for θ_r = 0°, which is consistent with the experimental results. Unfortunately for θ_r = 90° and θ_r = -90° the model predicts initially high stiffness which quickly reduces to very low values close to the predictions for θ_r = 0°. This can be explained by considering again the normality rule assumed in the model and will be explained subsequently in the discussion for the modified three-surface model.

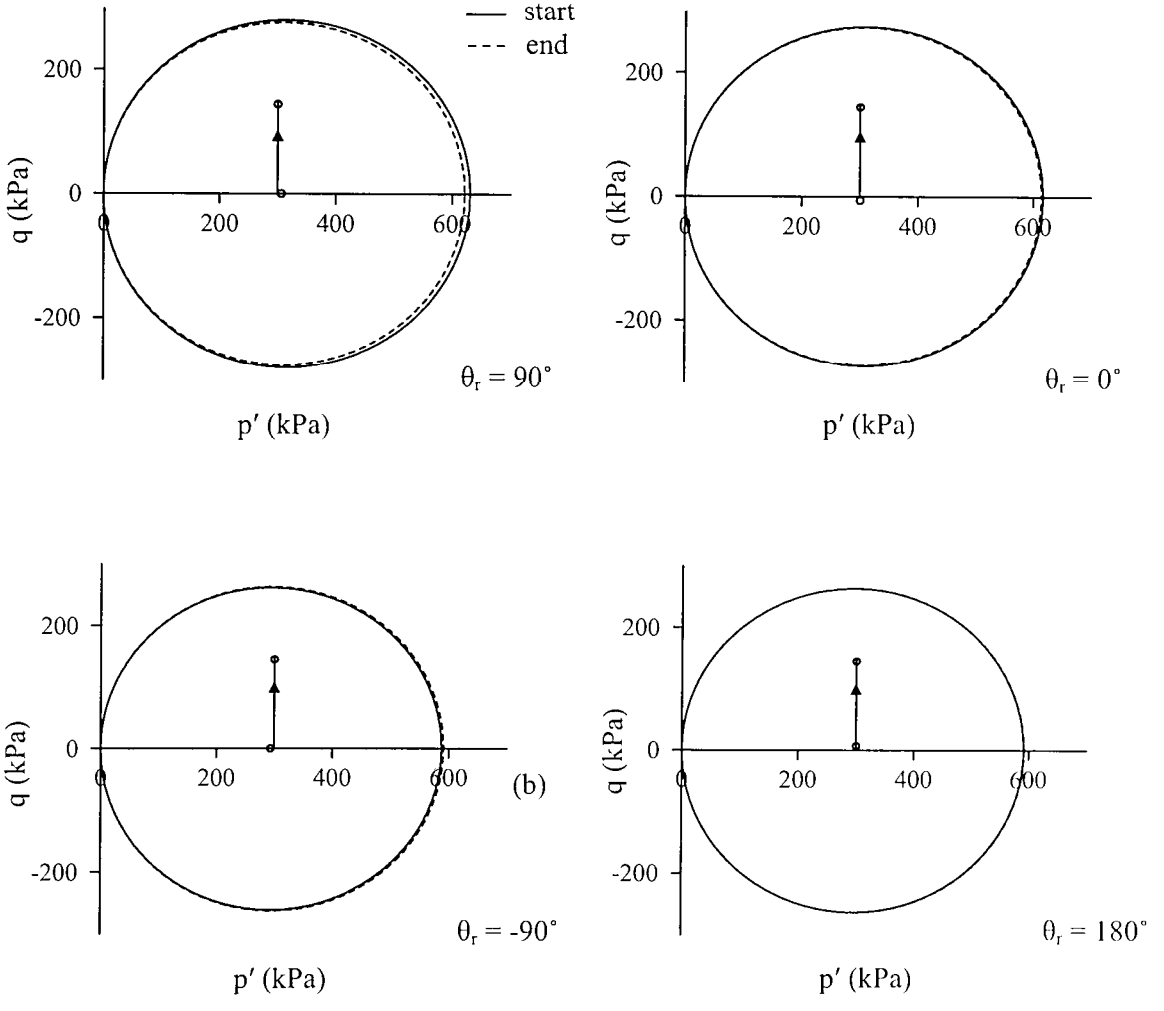


Figure 7.27: Configuration of the surfaces at the start and end of each cycle for the modified two-surface model

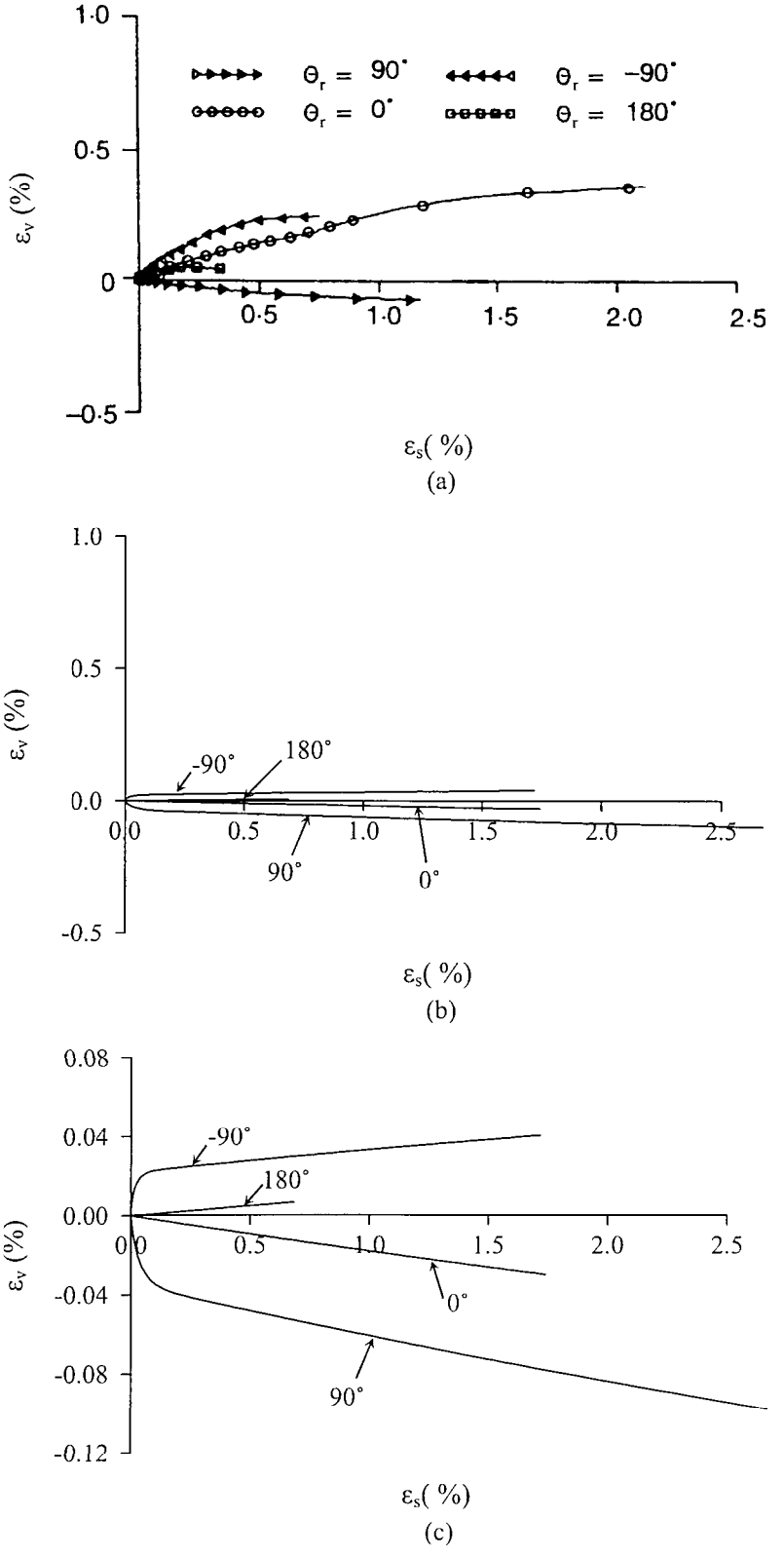


Figure 7.28: Constant p' loading after four stress path rotations: ε_v against ε_s
a) experimental data (after Stallebrass (1990)) b) predictions of modified two-surface model c) predictions of modified two-surface model – bigger scale

The predictions of the modified two-surface model for the strain paths along the constant p' path can be seen in Figure 7.28. The model predicts that the strain paths for θ_r = 0° and θ_r = 90° are dilative and the strain paths for θ_r = -90° and θ_r = 180° are compressive. Similar to the two-surface model, whether the behaviour is compressive or dilative, along a constant p' test, depends initially on the position of the stress state relative to p'_a and subsequently on whether the stress state is dry or wet of critical. (For θ_r = 90° and θ_r = 0°, the stress state is dry of critical, whereas for θ_r = -90° and θ_r = 180° the stress state is wet of critical).

7.3.3.3 Three-surface model

The predictions of the three-surface model have already been presented in Chapter 5. Figure 5.10 presents the stiffness versus stress change curves predicted by the three-surface model for the four stress path rotations together with the experimental results. The configuration of the surfaces at the start and end of each cycle can be seen in Figure 5.11. Figure 5.10b shows that the model is capable of predicting different stiffness curves for the four different approaching paths and that the general pattern of behaviour is reasonably well reproduced. However, as mentioned in Chapter 5, for θ_r = -90° and θ_r = 180° there is a drop in the stiffness curves at the point which the stress state engages the kinematic yield surface. This drop results in the stiffness predicted for θ_r = -90° being lower than the stiffness for θ_r = 90° up to a stress change of 45 kPa. However, inspection of the configuration of the surfaces at the start of the cycle reveals that the opposite would seem more reasonable. Figure 5.11 shows that for θ_r = -90° the kinematic surfaces have not completely re-aligned along the approaching path and hence the constant p' path enters the kinematic yield and history surfaces. For θ_r = 90° the stress state is already on the history surface at the beginning of the cycle. Clearly it is more reasonable to expect a higher stiffness for θ_r = -90° than for θ_r = 90° unlike what the three-surface model predicts in Figure 5.10b.

The pattern of strain paths predicted by the three-surface model together with the corresponding experimental data can be seen in Figure 5.13. As mentioned in Chapter 5, the general pattern of the strain paths is similar to the experimental results, with the only difference that the model predicts that for θ_r = 0° the soil will dilate, whereas the experimental data shows that it compresses. In the three-surface model whether the behaviour is compressive or dilative, along a constant p' test, depends on the position of the stress state relative to the active yield surface. Similar to the two-surface model, if

this is to the right of the centre of the kinematic surface then the predicted behaviour is compressive, whereas if this is to the left then the behaviour is dilative. However, in this model the kinematic yield surface translates relative to the history surface, and hence when the kinematic yield surface is the active yield surface the position of the stress state relative to the history surface is more important than its position relative to the bounding surface. For example, although not shown very clearly in Figure 5.11, for θ_r = 180° the stress state reaches the kinematic yield surface slightly to the right of p'_h and initially the behaviour is compressive. The behaviour remains compressive within the history surface although the stress state is dry of critical, because the translation of the kinematic yield surface relative to the history surface is such that the stress state

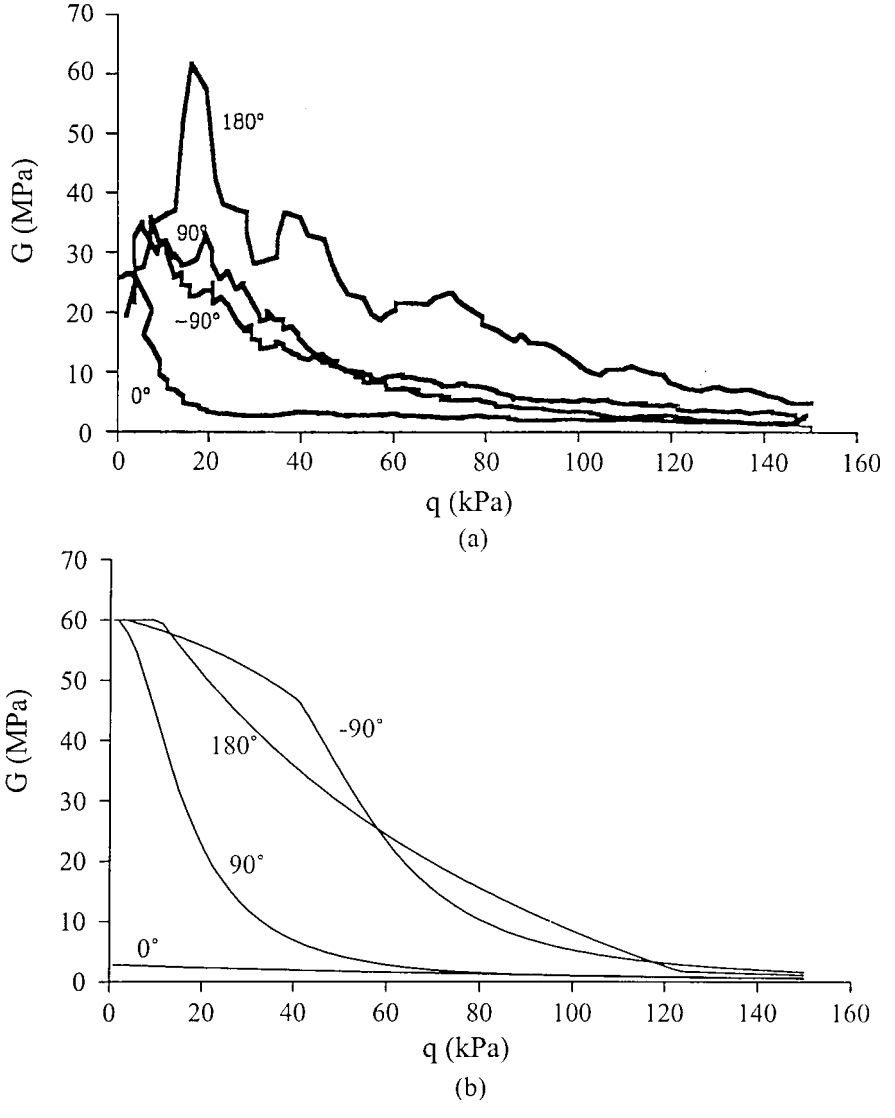


Figure 7.29: Constant p' loading after four stress path rotations: G against q
a) experimental data (after Stallebrass (1990)) b) predictions of modified three-surface model

remains to the right of p'_b. However, once the stress state is on the history surface, the model behaves in the same way as the two-surface models do. The translation of the history surface is relative to the bounding surface and the response eventually depends on whether the stress state is dry or wet of critical. Again how quickly the possible reorientation of the history surface happens depends on the size of the surface. Since history surfaces are larger than the kinematic yield surfaces these would re-orientate slower.

7.3.3.4 Modified three-surface model

The predictions of the modified three-surface model for the stiffness versus stress change curves are illustrated in Figure 7.29. Figure 7.30 presents the configurations of the surfaces at the start and end of each cycle.

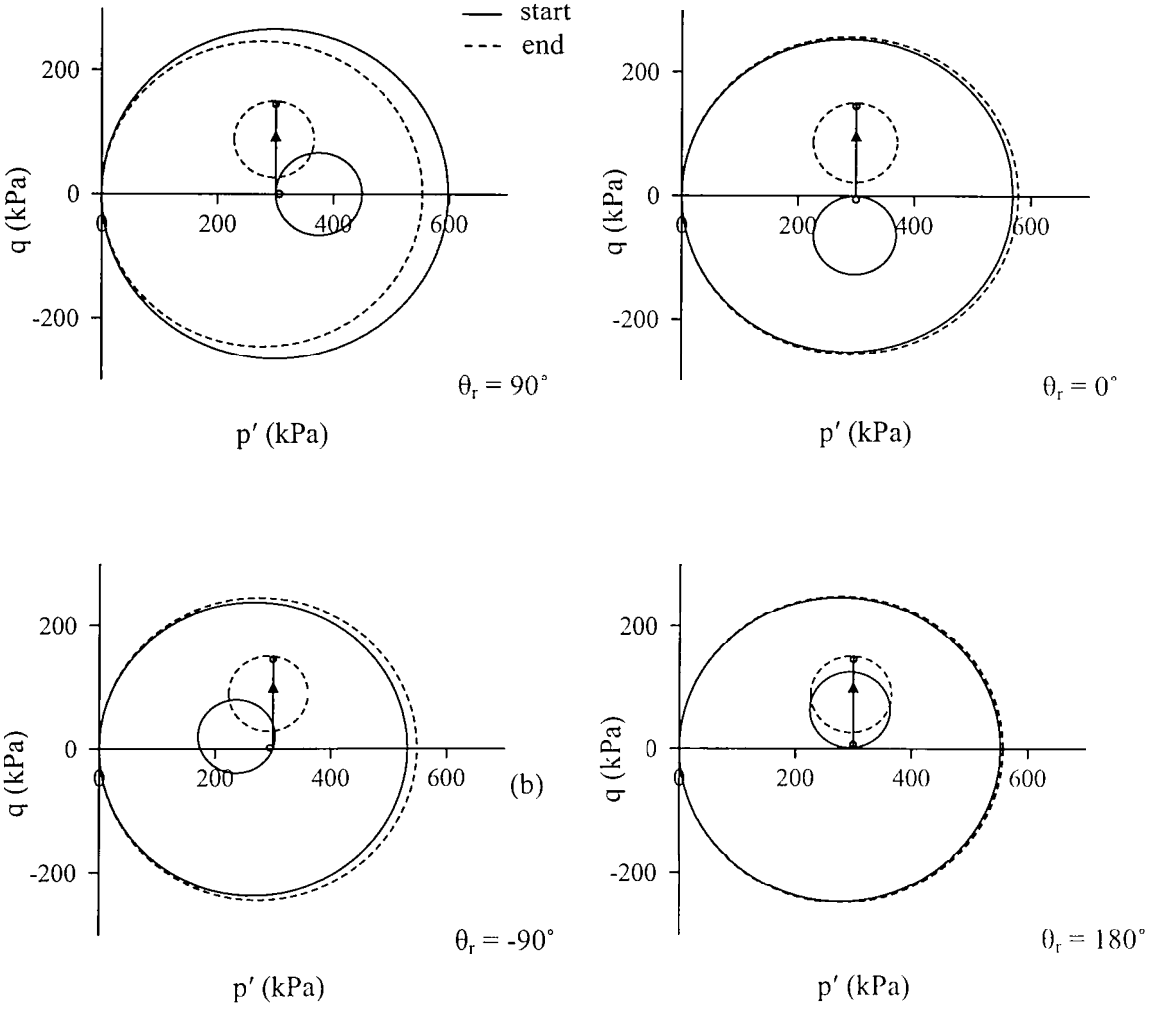


Figure 7.30: Configuration of the surfaces at the start and end of each cycle for the modified three-surface model

Figure 7.29 shows that the model is capable of reproducing well the stiffness curves for θ_r = 90°, 0° and 180° and that no drops in the stiffness curves can be observed. The only difference from the experimental trend is the stiffness curve for θ_r = -90°, which predicts higher stiffness than the curves for θ_r = 90° and 180° for a stress change up to approximately 60 kPa. However, it can be shown that, although this does not agree with the experimental results, it is consistent with the model formulation. For a start it can be shown that the hardening modulus along the stress path for θ_r = 180° is higher than the hardening modulus for θ_r = -90°, although in Figure 7.29 the shear stiffness for θ_r = 180° is lower than the shear stiffness for θ_r = -90° up to q ~ 60 kPa. The explanation for this is again the normality condition assumed in the model. Figure 7.31 shows the direction of the plastic strain increment vector at a deviatoric stress q = 30 kPa for θ_r = -90° and θ_r = 180°. It can be seen that if the plastic strain increment vectors had the same

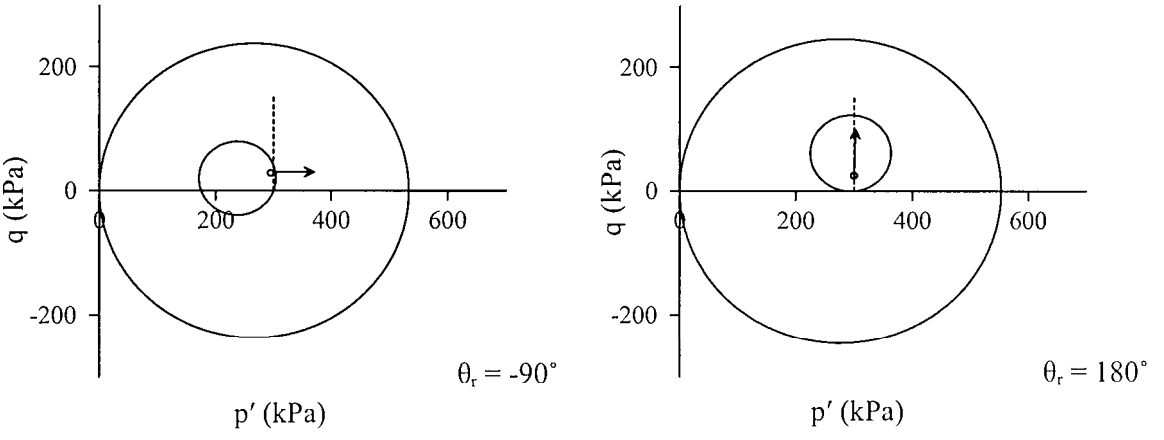


Figure 7.31: Configuration of the surfaces and plastic strain increment vector at q = 30 kPa for the modified three-surface model

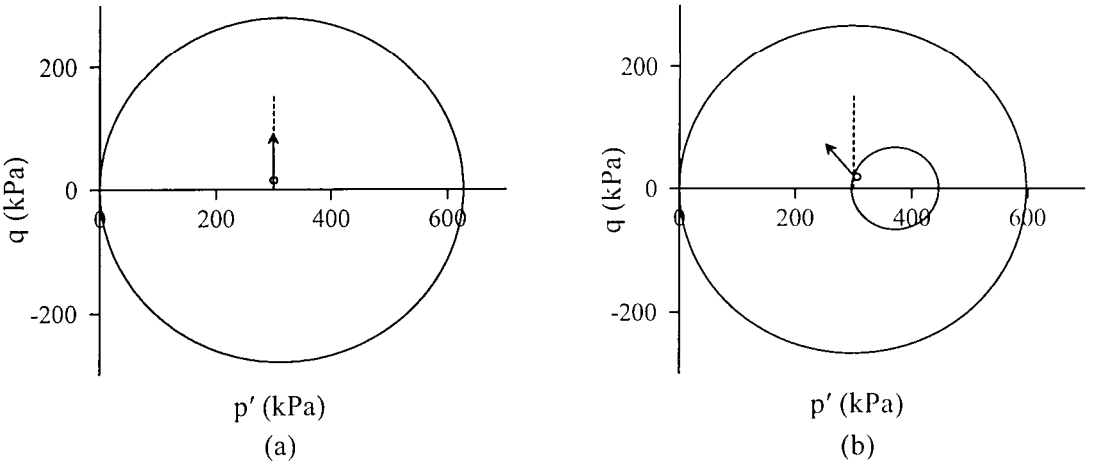


Figure 7.32: Configuration of the surfaces and plastic strain increment vector at q = 20 kPa for θ_r = 90° a) modified two-surface model b) modified three-surface model

magnitude, the plastic shear strain predicted for θ_r = 180° would have been much higher than the one predicted for θ_r = -90°. Therefore, although the value of the hardening modulus for θ_r = 180° is higher than for θ_r = -90°, the resulting plastic shear strain calculated for θ_r = 180° is higher than for θ_r = -90°, and the shear stiffness predicted for θ_r = 180° is lower than for θ_r = -90°. At the later stages of the loading path the translation of the kinematic surfaces results in similar directions of the plastic strain increment vector and then the shear stiffness predicted for θ_r = 180° becomes higher than the one for θ_r = -90°.

The associated flow rule assumed in the models can also explain the fact that for the modified two-surface model the shear stiffness for θ_r = 90° and θ_r = -90° quickly reduces

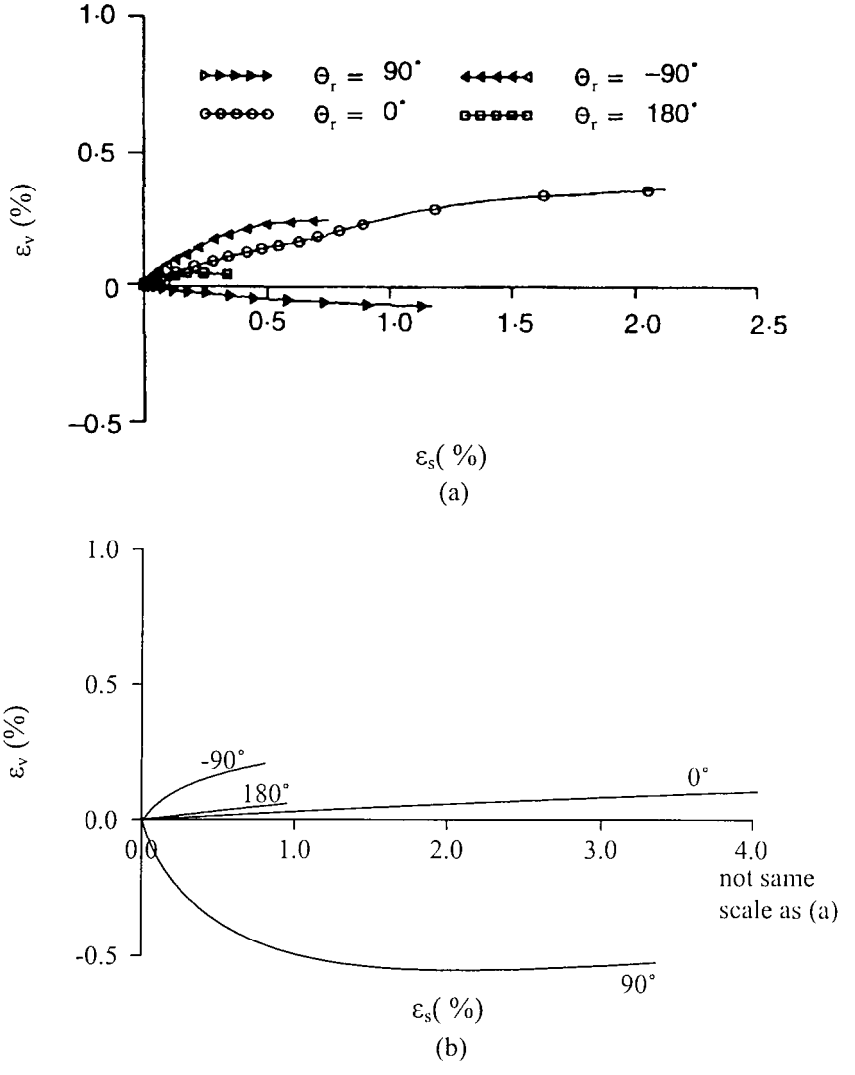


Figure 7.33: Constant p' loading after four stress path rotations: ε_v against ε_s
a) experimental data (after Stallebrass (1990)) b) predictions of modified three-surface model

to very low values, unlike the predictions of the modified three-surface model. Figure 7.32 illustrates the plastic strain increment vector for the loading path after $\theta_r = 90°$ at a stress change of $q = 20$ kPa, for the two models. The hardening modulus at this stage can be shown to be similar for the two models. However, Figure 7.32 shows that for the same magnitude of the plastic strain increment vectors, the direction of the vectors is such that the plastic shear strain for the modified two-surface model would have been much higher than for the modified three-surface model. Hence, although the hardening modulus is similar for both models, the resulting shear stiffness is much lower for the modified two-surface model. The different direction of the plastic strain increment vectors can be attributed to the fact that the history surface (which is the active yield surface) in the modified three-surface model is larger than the kinematic surface in the modified two-surface and the latter re-orientates quicker than the former one.

The predicted strain paths for the modified three-surface model can be seen in Figure 7.33. The model predicts correctly that the strain paths for $\theta_r = 0°$, -90° and 180° are compressive and that the strain path for $\theta_r = 90°$ is the only one which is dilative. Whether the behaviour is compressive or dilative, along a constant p' test, depends on the same factors discussed for the three-surface model. For $\theta_r = 0°$ the behaviour predicted is compressive, due to the fact that the stress state remains on the history surface and it is wet of critical.

7.3.4 Summary

This section investigated the capability of the four kinematic hardening models to predict the effect of recent stress history on the pre-failure behaviour of overconsolidated clays. A multi-stage test, in which the behaviour along a constant p' test was examined after four stress path rotations, was repeated for each model.

The two-surface model was shown not to be able to predict satisfactorily the stiffness-strain curves after the four stress path rotations, since the model predicts approximately the same stiffness curves soon after the stress state engages the kinematic yield surface for $\theta_r = 180°$. This is a consequence of the drop in stiffness predicted by the model and results in the model being unable to retain a memory of the previous stress history, once the stress state becomes elasto-plastic (at least for kinematic yield surfaces of this size). The modified two-surface model was shown to predict well the stiffness curves for $\theta_r = 180°$ and $\theta_r = 0°$. However, the predictions for $\theta_r = 90°$ and $\theta_r = -90°$ were not so satisfactory; the model predicts that for these stress paths the stiffness values quickly

reduce to low values close to $\theta_r = 0°$. The three-surface model was shown to predict well the different stiffness curves after each of the four stress path rotations, however, there is still the problem of the drop in stiffness once the stress state becomes elasto-plastic. Finally, the modified three-surface model was shown to be capable of predicting satisfactorily the stiffness curves for θ_r = 90°, 0° and 180°, whereas the high stiffness predicted for θ_r = -90° can be explained by considering the normality rule assumed in the model.

The strain paths predicted by the models can be explained by considering the flow rule adopted in the models. Whereas for the two-surface and modified two-surface models whether behaviour is dilative or compressive, along a constant p' test, depends on the position of the current stress state relative to the centres of the kinematic yield and bounding surfaces, for the three-surface and modified three-surface models it depends on the position of the stress state relative to all three surfaces. This results in a better qualitative prediction of the strain paths for the three-surface and modified three-surface models.

Overall the presence of the history surface provides a better memory of the previous stress history, as already shown in the work of Stallebrass (1990), who compared the two-surface and three-surface models. Still, the modified two-surface model results in some memory of the previous loading path as it can predict well the stiffness curves for $\theta_r = 180°$ and $\theta_r = 0°$, unlike the two-surface model which does not retain any memory of the previous stress history, once the stress state becomes elasto-plastic.

7.4 Modelling the effect of stress path direction

7.4.1 Introduction

As already discussed in section 2.2.5 of Chapter 2, Clayton and Heymann (2001) suggested that once creep is accounted for, recent stress history has no effect on soil stiffness. Moreover, it was suggested that, after a rest period, the stiffness at very small strains reverts back to the maximum value and the stiffness in the small strain range depends on the direction of the stress path relative to the gross yield surface. For example, according to Clayton and Heymann (2001), compression and extension loading initiating from the stress state C in Figure 7.34a would show initially similar high very small strain stiffness, but the rate of decay of stiffness in the small strain range would be

higher for the stress path that takes the loading closer to the gross yield surface i.e. in this case the extension path.

For the kinematic hardening models the configuration of the kinematic surfaces relative to the current stress state determines the stiffness obtained along a subsequent loading path, as previously mentioned. If the stress state C in Figure 7.34a was reached by the stress history in Figure 7.34b, then loading in compression would re-invoke the high elastic stiffness within the kinematic yield surface, whereas loading in extension would result in lower initial stiffness since the model would continue to behave plastically. If the soil element was brought to the stress state C along a different stress history e.g. the one shown in Figure 7.34c, then the relationship between further compression and extension paths would be different.

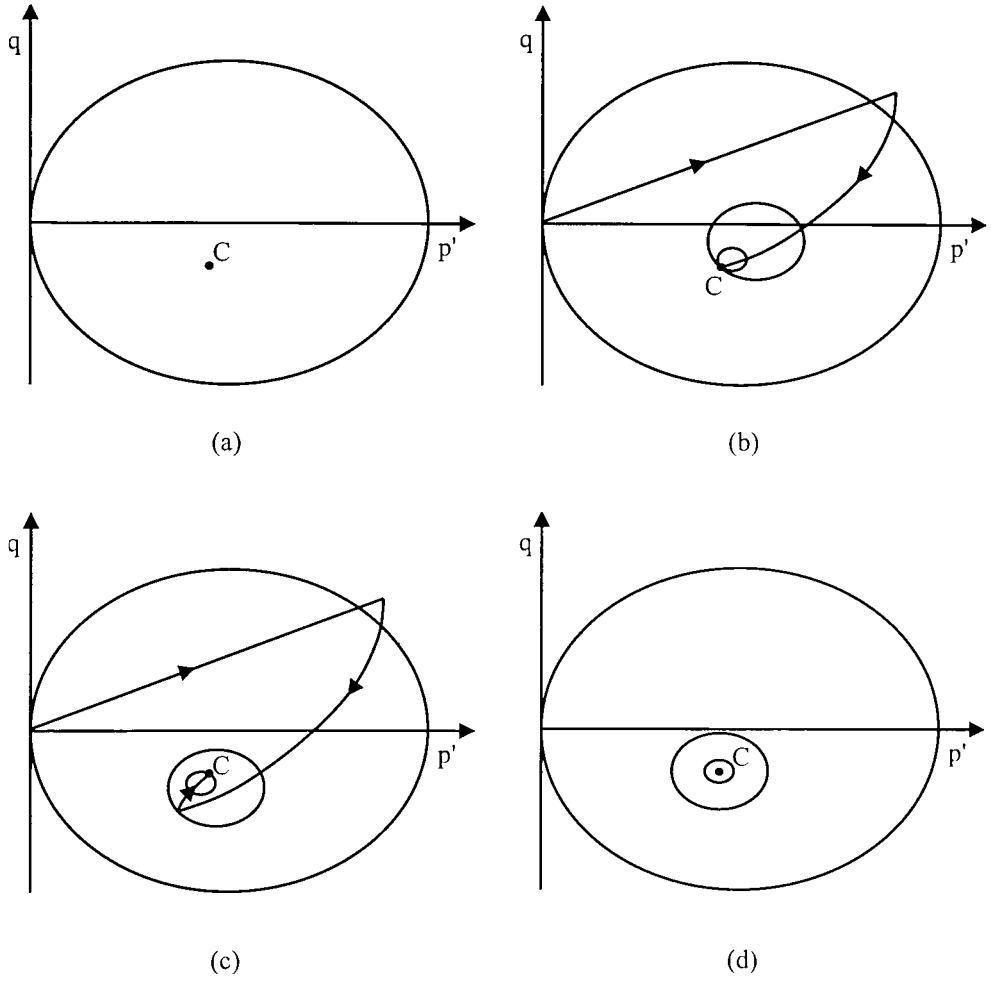


Figure 7.34: Schematic diagram showing a) current stress state C b), c) configuration of kinematic surfaces at the end of two possible previous stress histories d) centring of the kinematic surfaces around the current stress state

One way of simulating the effect of the stress path direction in the kinematic hardening models is to centre the kinematic surfaces around the current stress state C at the end of the previous stress history, see Figure 7.34d. In this way further loading either in compression or extension would start from inside the elastic region and the models would predict the high elastic stiffness initially. On further loading the stress state would reach the kinematic yield surface and since in these models the hardening modulus depends on the relative distance of the kinematic yield and - history and - bounding surfaces, the stress path that takes the loading closer to the bounding surface would show a faster rate of decay of stiffness than the one that takes it away.

In this section this way of modelling the effect of stress path direction is evaluated for all four models. A stress history of an overconsolidated clay deposit (involving one-dimensional compression, swelling, due to erosion, and re-compression, due to subsequent deposition, see Figure 7.34c) is followed and the kinematic surfaces are centred at the end of the stress history around the current stress state, before further undrained triaxial compression (TXC) and extension tests (TXE) are simulated. The behaviour predicted by the compression and extension tests are compared for each model. These predictions are further compared with similar compression and extension analyses in which no centring of the kinematic surfaces at the end of the stress history took place, simulating in this way the effect of the previous stress history (how satisfactorily each of the four models can simulate the effect of recent stress history was investigated in the previous section).

7.4.2 Model parameters

The parameters used in the simulations are the parameters derived from the reconstituted London Clay tests in section 7.3 and can be seen in Tables 7.1, 7.2 and 7.3 for the two-surface, modified two-surface and three-surface model respectively. For the modified three-surface model the same size of the history surface as for the three-surface model is assumed, hence $T = 0.2$, $S = 0.08$ and the rest of the parameters are kept the same as in Table 7.4.

7.4.3 Evaluation of the models' predictions

The first set of analyses, in which the surfaces were centred at the end of the stress history before further shearing took place, is denoted by the letters 'sh-c', whereas the second set, in which there was no centring and the shearing was simulated directly after

the stress history, is denoted by the letters 'sh'.

Figures 7.35, 7.36, 7.37 and 7.38 show the normalised stiffness-strain curves in undrained triaxial compression and extension, predicted by the first set of analyses ('sh-c'), for the two-surface, modified two-surface, three-surface and modified three-surface models respectively.

It can be seen that for all four models the stiffness predicted initially in both compression and extension is equal to the high elastic stiffness. Moreover, when yielding is initiated the stiffness predicted in extension is lower than the stiffness predicted in compression, which is in agreement with the fact that the extension path

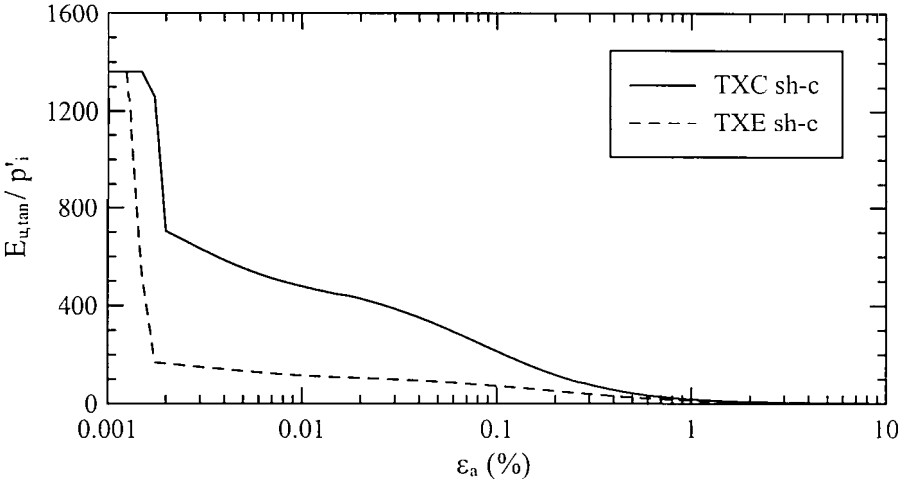


Figure 7.35: Predictions of the two-surface model for analyses 'sh-c': normalised stiffness-strain curves

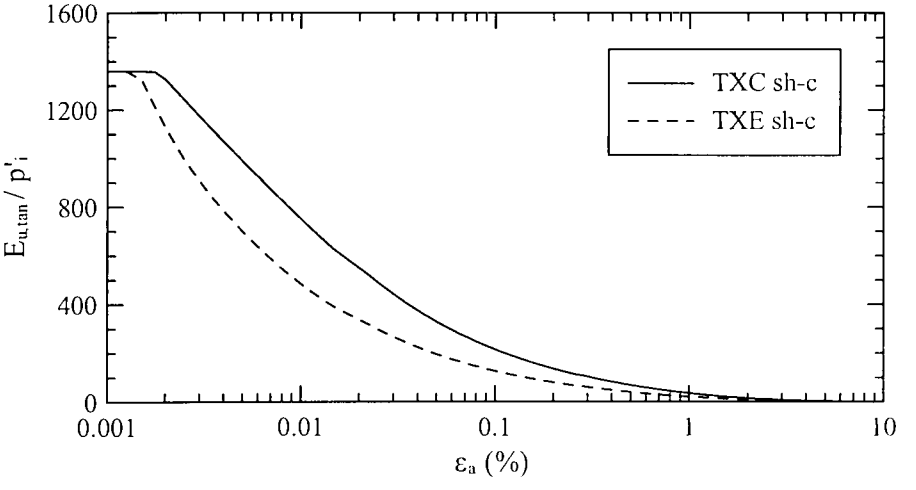


Figure 7.36: Predictions of the modified two-surface model for analyses 'sh-c': normalised stiffness-strain curves

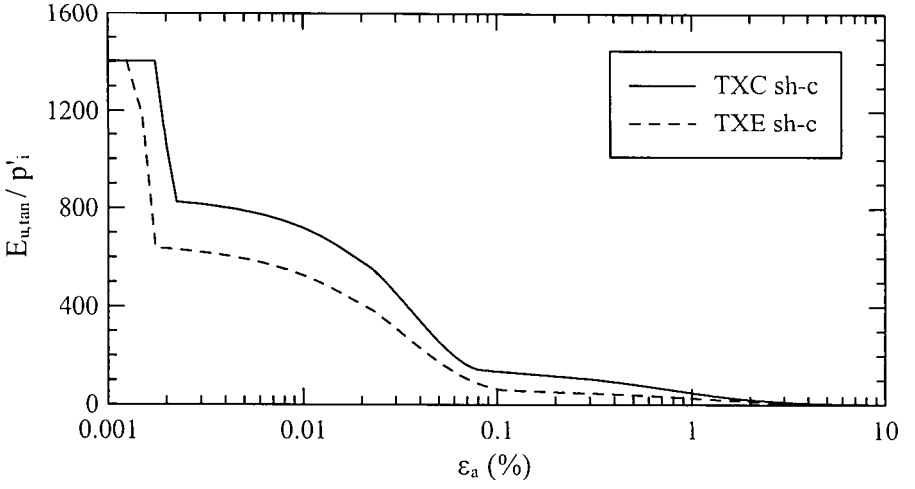


Figure 7.37: Predictions of the three-surface model for analyses 'sh-c': normalised stiffness-strain curves

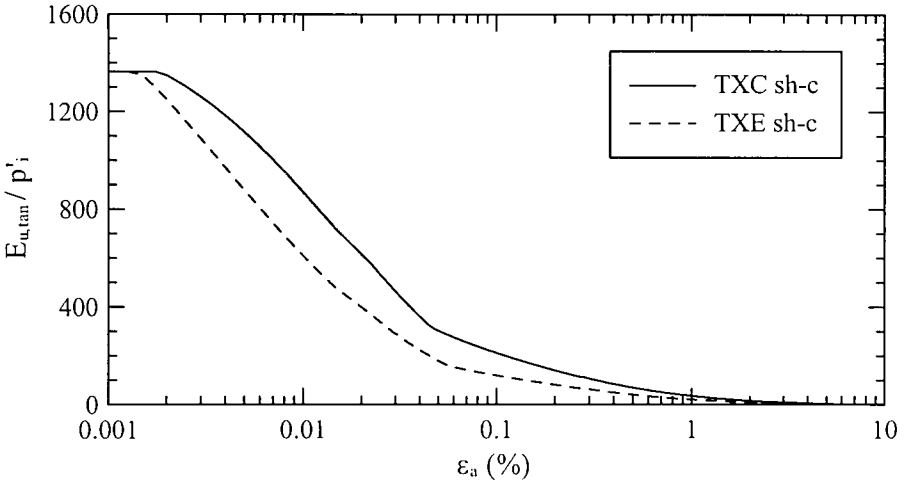


Figure 7.38: Predictions of the modified three-surface model for analyses 'sh-c': normalised stiffness-strain curves

takes the loading closer to the bounding surface. The stiffness curves seem to converge at an axial strain of approximately 1%.

Figures 7.39, 7.40, 7.41 and 7.42 compare the two sets of analyses ('sh' and 'sh-c') for the two-surface, modified two-surface, three-surface and modified three-surface models respectively. A schematic representation of the configuration of the surfaces at the end of the stress history for the set 'sh' is given in Figure 7.34c. As it can be seen, the configuration of the surfaces is such that in the compression mode the model keeps on behaving plastically, whereas the extension mode constitutes a stress path reversal which enters the elastic region. Hence, it is expected that the stiffness in the extension mode would be higher than the stiffness in the compression mode, at least initially.

Figure 7.39, which presents the predictions of the two-surface model, indicates that in the analyses 'sh' the stiffness in extension is higher than the stiffness in compression only when the stress state remains within the kinematic surface. As soon as the stress state engages the surface a drop in stiffness is observed and the stiffness in extension becomes lower than the stiffness in compression and actually equal to the extension stiffness predicted by the analysis 'sh-c'. This is not surprising since in the previous section was shown that the model predicts the same stiffness curves for $\theta_r = 0°$ and 180° after yielding occurs. Similarly, the compression stiffnesses predicted by the two sets of analyses become the same as soon as yielding is initiated in the analysis 'sh-c'. This is a consequence of the hardening function assumed in the model and results in the two sets of analyses predicting the same behaviour after the stress state becomes elasto-plastic.

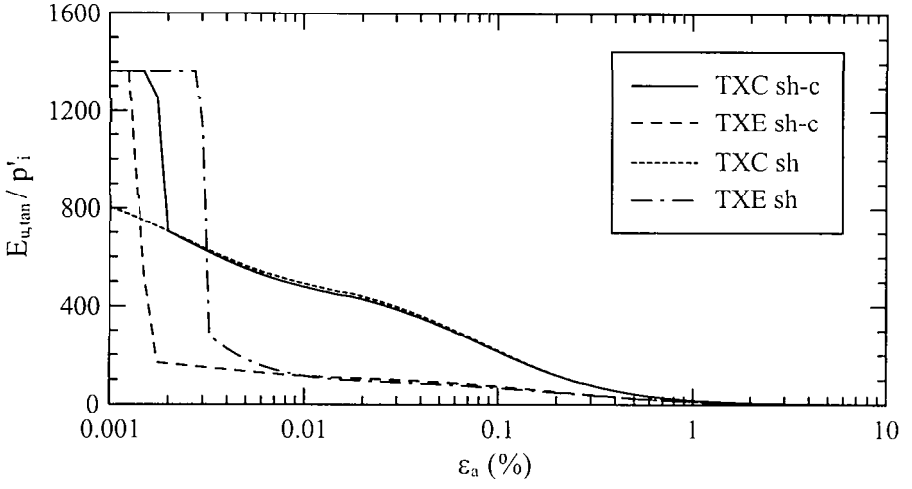


Figure 7.39: Comparison of the predictions of the two-surface model for analyses 'sh-c' and 'sh': normalised stiffness-strain curves

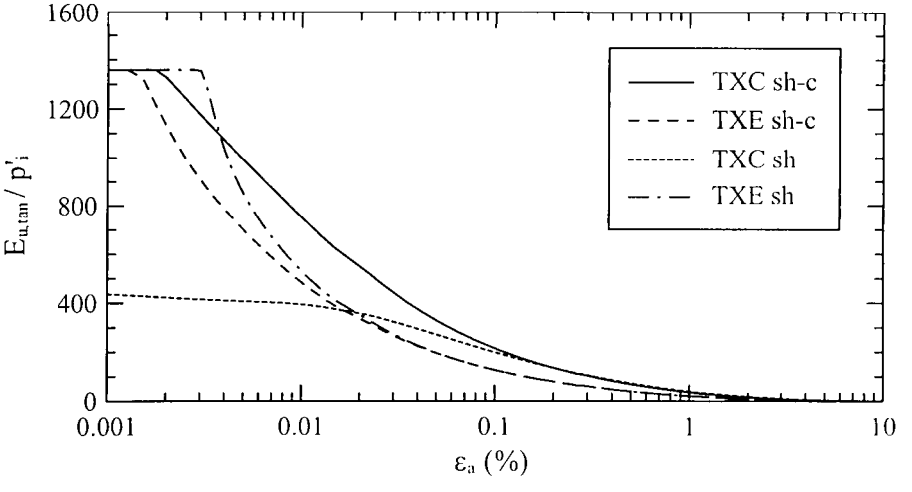


Figure 7.40: Comparison of the predictions of the modified two-surface model for analyses 'sh-c' and 'sh': normalised stiffness-strain curves

The predictions of the modified two-surface model in Figure 7.40 show that this is not the case for this model. In the analyses 'sh' the stiffness predicted in extension remains higher than the stiffness in compression after yielding in extension occurs, and up to an axial strain of 0.02%. Moreover, the extension stiffnesses predicted by the two analyses do not become the same as soon as the stress state engages the kinematic surface but converge at higher strains. The same is true for the stiffness predicted in compression. This results in different stiffness response predicted by the two sets of analyses.

Figure 7.41 indicates that in the analyses 'sh' for the three-surface model there is a drop in the extension stiffness curve when the stress state touches the kinematic yield surface, but the stiffness remains higher than the stiffness in compression. This is due to the

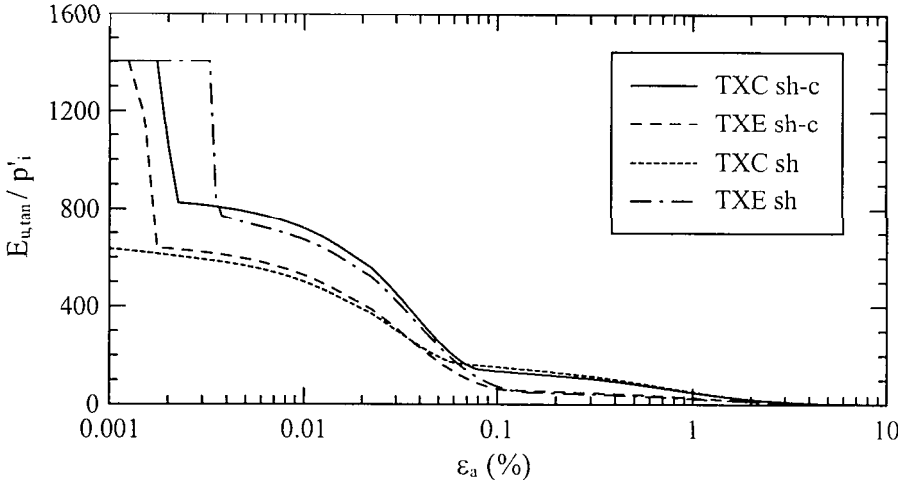


Figure 7.41: Comparison of the predictions of the three-surface model for analyses 'sh-c' and 'sh': normalised stiffness-strain curves

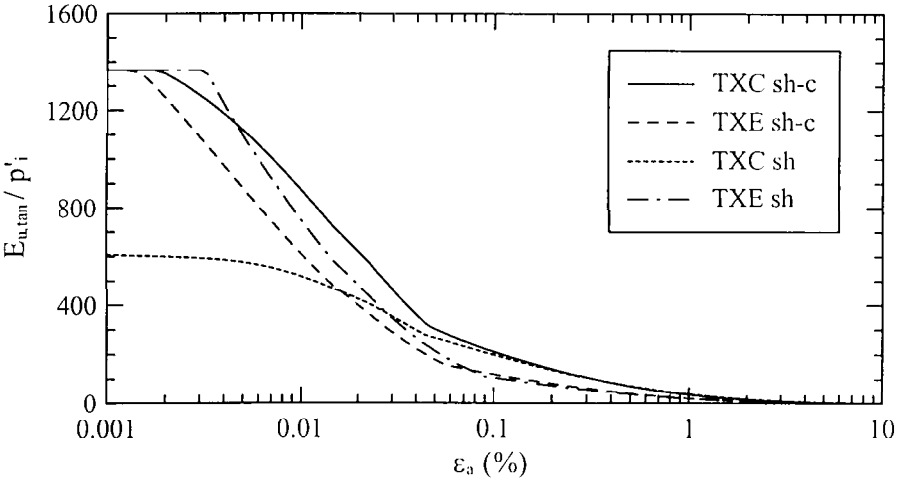


Figure 7.42: Comparison of the predictions of the modified three-surface model for analyses 'sh-c' and 'sh': normalised stiffness-strain curves

presence of the history surface. In this way the extension stiffness curves predicted by the two sets of analyses do not become the same as soon as yielding occurs but converge at much higher strains. The same is true for the compression curves. Unlike the two-surface model, for the three-surface model the two sets of analyses give different predictions.

The predictions of the modified three-surface model for the analysis 'sh', Figure 7.42, show that the stiffness in extension remains higher than the stiffness in compression after yielding for the extension path starts. Again the extension curves predicted by the two analyses converge at much higher strains. The same can be observed for the compression curves. Therefore, the two sets of analyses predict different stiffness response for the modified three-surface model.

7.4.4 Summary

This section showed that the effect of stress path direction can be simulated in the kinematic hardening models by centring the kinematic surfaces around the current stress state. In this way further compression or extension results in the high elastic stiffness predicted initially. For further loading, once yielding is initiated, the models predict lower stiffness for the stress path that takes the loading closer to the bounding surface.

Simulations of undrained triaxial compression and extension tests after the kinematic surfaces were centred at the end of the previous stress history (modelling in this way the effect of stress path direction) were compared with similar analyses in which no centring of the kinematic surfaces at the end of the stress history took place (simulating in this way the effect of recent stress history). The analyses showed that for the two-surface model there is practically no difference between the two sets of analyses once the stress state becomes elasto-plastic. This is a consequence of the model being unable to retain a memory of the previous stress path and predicting the same stiffness response along a certain loading path (once the stress state becomes elasto-plastic), irrespective of the previous configuration of the kinematic surface (at least for kinematic yield surfaces of this size). On the contrary, for the modified two-surface, three-surface and the modified three-surface model a different stiffness-strain response is predicted for each set of analyses. This predicted stiffness response depends on the previous configuration of the kinematic surfaces.

7.5 Summary

This chapter evaluated the capability of the four kinematic hardening models to predict the pre-failure behaviour of overconsolidated clays. In the first part of the chapter a set of triaxial tests on reconstituted London Clay was simulated and the ability of the models to reproduce the observed behaviour, with particular reference to the high pre-failure non-linearity, was examined. The second part of the chapter investigated the capability of the models to reproduce the effect of recent stress history. A multi-stage triaxial test was simulated, in which the behaviour along a constant p' path was examined after four different stress path rotations. Finally, the last part of the chapter examined the way in which the kinematic hardening models can model the effect of stress path direction. A summary on the evaluation of the models' predictions was given at the end of each of the three parts.

Chapter 8

Analysis of an embankment on soft clay using the kinematic hardening models

8.1 Introduction

This chapter investigates the predicted behaviour of an embankment, when its soft clay foundation is modelled with kinematic hardening models. It is divided into two parts. The first part is concerned with the pre-failure behaviour of the embankment. It presents a comparison of the deformational behaviour predicted by the two-surface model, the modified two-surface model and the modified Cam Clay model, when the same undrained strength is assigned to all models. The second part of the chapter studies the failure of the embankment. Different shapes of the yield and plastic potential surfaces in the deviatoric plane are assumed and the effect that these have on the predicted failure height of the embankment is examined.

8.2 Boundary value problem analysed

The embankment analysed in this work was part of a research programme undertaken by Laval University, Canada, in order to study the behaviour of embankments on soft clay deposits. The programme involved the construction of four test embankments on a soft Champlain clay deposit at Saint-Alban, Quebec. The embankment studied here, test embankment A, was built to failure (La Rochelle et al. (1974)).

8.2.1 Ground conditions at Saint-Alban

The typical soil profile at Saint-Alban consists of approximately 2 m of weathered clay crust, overlying a soft silty marine clay deposit, which extends to a depth of approximately 9.7 m, see Figure 8.1. Below the clay there is a layer of clayey silt with sand, which extends to a depth of 13.7 m. This is underlain by a deep layer of dense sand, extending to depths of more than 24 m. The clay deposit beneath the crust is lightly overconsolidated with an *OCR* of approximately 2. The water table is located at a depth of 0.7 m below the ground surface. The bulk unit weight of the soil is 19 kN/m^3 above the water table and 16 kN/m^3 below it. The permeability of the clay deposit is of the order of 10^{-10} to 10^{-9} m/s (Tavenas et al. (1983)).

The undrained strength profile at the site was measured from field vane tests and isotropically consolidated undrained triaxial (CIU) tests, see Figure 8.2 (La Rochelle et al. (1974)). Lefebvre and Pfendler (1996) subsequently carried out a number of direct simple shear tests (DSS), which agreed well with the average field vane strength. (Lefebvre et al. (1988) found that for eastern Canadian clays field vane tests and DSS tests give similar values of undrained shear strength.) As it can be seen in Figure 8.2, the field vane tests show an increased undrained strength at the crust.

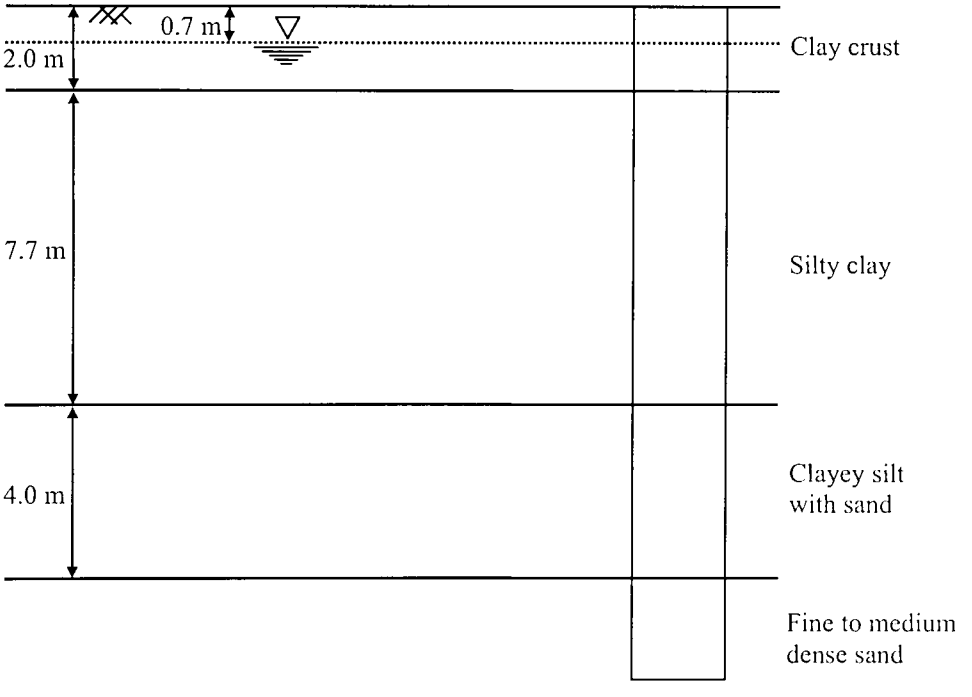


Figure 8.1: Soil profile at the site of Saint-Alban

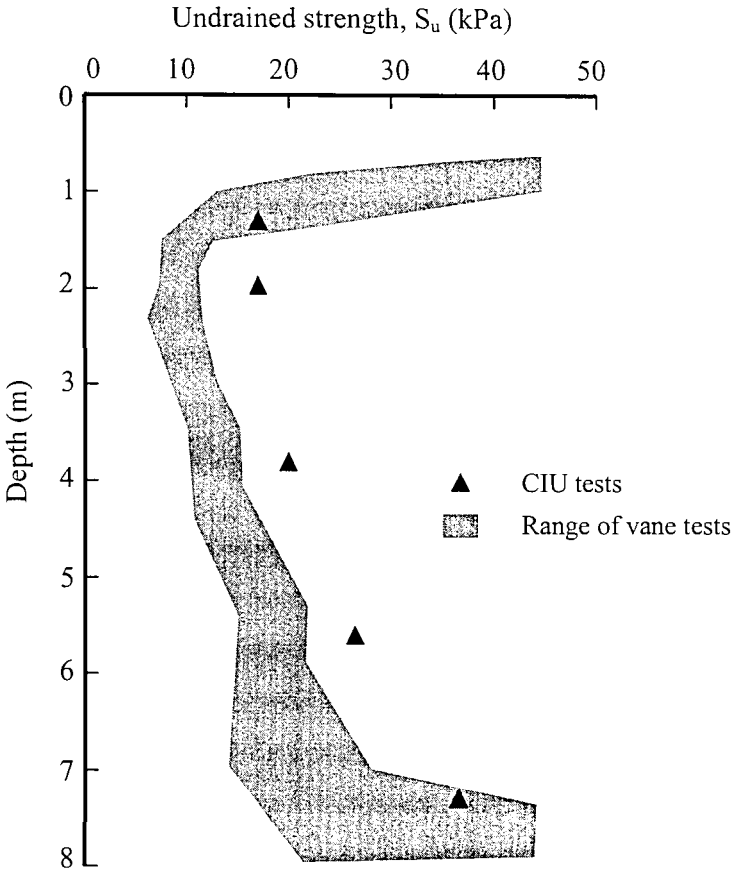


Figure 8.2: Undrained strength profiles for the clay at Saint-Alban (data after La Rochelle et al. (1974))

8.2.2 Geometry and construction of test embankment A

A plan view and typical cross section of test embankment A can be seen in Figure 8.3. Conventional stability analysis, performed before the embankment construction, indicated that the failure height of the embankment would be 4.6 m. The crest length would then have been 30.5 m and the width 7.6 m. The three sides of the embankment, with a slope of 2:1 and a 1.5 m high berm, ensured that the failure would be confined to the fourth side which had a slope of 1.5:1. The fill material of the embankment was a uniform medium to coarse sand.

In the event, failure of the embankment occurred at a height of 3.9 m, less than what was predicted by the conventional analysis. The total period from the start of the construction to failure was 10 days. Due to the low permeability of the clay, negligible consolidation would be expected to have taken place during the construction period in this deposit.

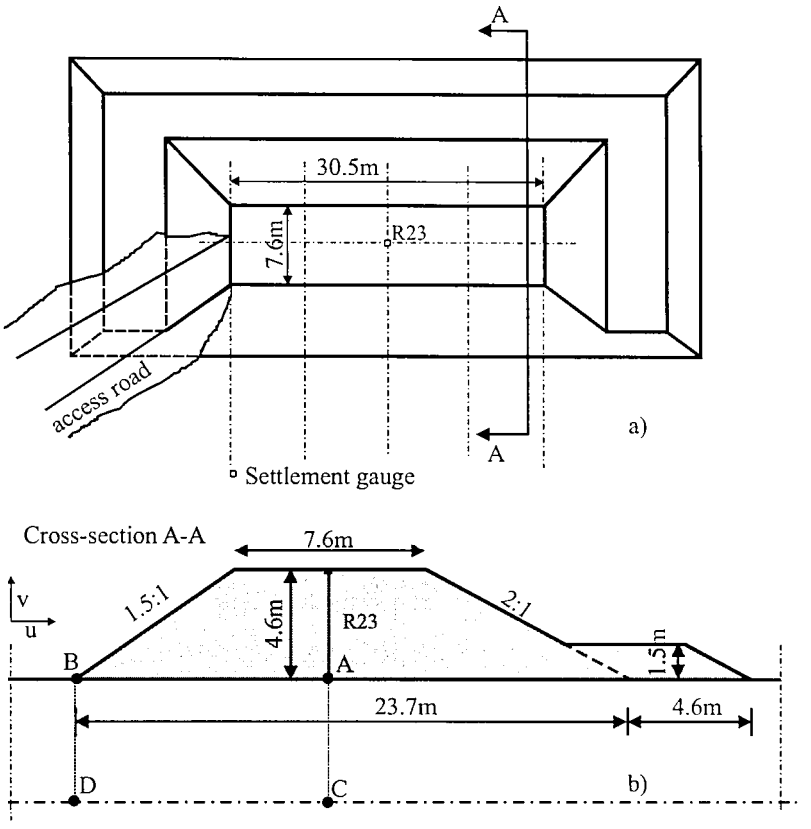


Figure 8.3: Test embankment A a) plan view b) cross section A-A

8.3 Previous finite element analyses of test embankment A

Zdravkovic et al. (2002) performed a number of plane strain finite element analyses of the test embankment A, investigating the effect of strength anisotropy on the behaviour of the embankment. The constitutive models used in the analyses, in order to model the soft clay deposit, included the anisotropic MIT-E3 model (see section 2.3.3.2 of Chapter 2) and the isotropic Modified Cam Clay (MCC) model. The MIT-E3 model has been shown to successfully reproduce soil strength anisotropy (Whittle (1993)), whereas in the isotropic MCC model the strength is independent of the orientation of the principal stresses.

The parameters chosen for the MIT-E3 model predicted the undrained strength profiles shown in Figure 8.4. It can be seen that the undrained strength predicted by the MIT-E3 model for the CIU tests is in good agreement with the experimental CIU profile. Moreover, the predicted direct simple shear (DSS) profile compares well with the average vane strength. Also shown in the figure are the undrained strength profiles in triaxial compression (TXC), plane strain compression (PSC) and plane strain extension (PSE) predicted by the MIT-E3 model for samples at their in-situ states. The finite

element analyses of the embankment using these parameters showed that the anisotropic MIT-E3 model predicted the correct failure height of 3.9 m.

In the MCC model, the prescribed *OCR* profile was varied so that the model predicted a number of different undrained strength profiles in triaxial compression. Zdravkovic et al. (2002) showed that an analysis with the MCC model, in which the predicted isotropic undrained strength profile in triaxial compression corresponded to the TXC profile in Figure 8.4, overpredicted the embankment failure height by 1.0 m. A further analysis with the predicted isotropic undrained strength profile in triaxial compression matching the DSS profile in Figure 8.4 underpredicted the embankment failure height, by 0.6 m. Back-analysis using the MCC model showed that in order to predict the correct failure height of 3.9 m, the model had to match, in triaxial compression, a profile which was 1.25 times the DSS profile.

It should be noted that in the form of the MCC model used in the analyses of Zdravkovic et al. (2002) the shapes of the yield and plastic potential surfaces in the deviatoric plane

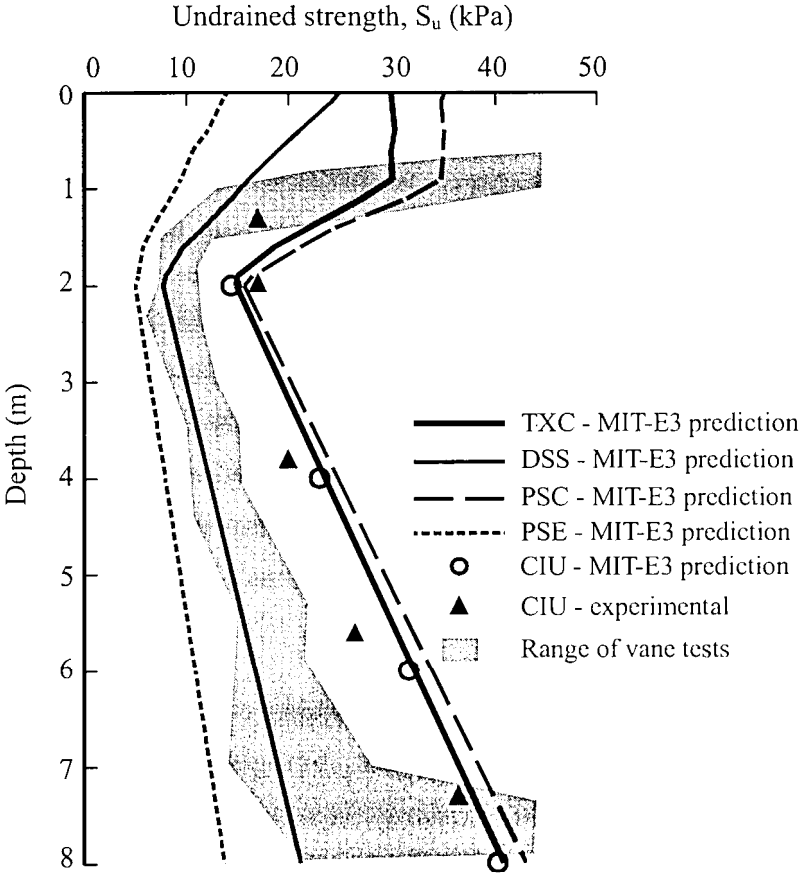


Figure 8.4: Undrained strength profiles for the clay at Saint-Alban – comparison of MIT-E3 predictions with field and experimental data (after Zdravkovic et al. (2002))

were given by a Mohr-Coulomb hexagon and a circle respectively (Potts and Zdravkovic (1999)). This resulted in the undrained strength predicted by the MCC model varying with the Lode's angle, θ, and therefore with the parameter b. Hence, although the model is isotropic, the undrained strength profile predicted under plane strain conditions was different than the one predicted in triaxial compression.

8.4 Constitutive models used in the analyses

8.4.1 Clay deposit

In the analyses presented in this thesis, the soft clay, on which the embankment was built, was modelled using the version of the two-surface model implemented into ICFEP (Chapter 4), the modified two-surface model (Chapter 6) and the modified Cam Clay model. The modified Cam Clay analyses were performed using the two-surface model and setting the size of the kinematic yield surface equal to the size of the bounding surface. The version of the modified Cam Clay model obtained in this way differs from the one used by Zdravkovic et al. (2002) in that the isotropic normal compression and swelling lines are assumed to be straight in $\ln v$-$\ln p'$ space, rather than v-$\ln p'$ space. For abbreviation, the models will be referred to as 2-SKH for the two-surface kinematic hardening model, M2-SKH for the modified two-surface kinematic hardening model and MCC for the version of the modified Cam Clay model used in the analyses of this chapter.

As already discussed in Chapter 4, the 2-SKH and M2-SKH models predict isotropic strength, which is governed by the isotropic bounding surface. Moreover, the yielding and stiffness, for stress paths initiating within the bounding surface, can be anisotropic depending on the position of the kinematic yield surface relative to the stress state at the beginning of the stress path.

In the analyses presented in this chapter no modelling of the previous stress history of the deposits was simulated. Instead, it was assumed that at the start of the analyses the kinematic surface was centred around the initial stress state. This is equivalent to assuming that there is no effect of the previous stress history and that stiffness depends on the stress path direction, once the stress state becomes elasto-plastic (section 7.4 of Chapter 7).

8.4.2 Fill material

The fill material was modelled as linear elastic with a Mohr-Coulomb yield surface and a non-associated flow rule (after Zdravkovic et al. (2002)). A brief summary of the plastic part of the model is presented in section 9.4 of Chapter 9.

8.5 Pre-failure behaviour of the embankment

8.5.1 Introduction

This study compares the pre-failure deformational behaviour of the test embankment A, when its soft clay foundation is modelled using the 2-SKH, M2-SKH and MCC models. As already discussed in the previous chapters, the kinematic hardening models differ from the MCC model in that they predict plasticity and high non-linearity from early stages of loading. Moreover, as discussed in Chapter 7, for the case that the kinematic surface is centred around the initial stress state, the stiffness along a subsequent loading path depends on the direction of the stress path relative to the bounding surface, once yielding is initiated. In most cases (i.e. $K_o \neq 1.0$), this results in a different stiffness response between compression and extension paths. On the contrary, the stiffness within the yield surface of the MCC model is independent of whether the path is of a compression or an extension nature.

Figure 8.5 shows typical stress paths followed by soil elements along the potential failure surface beneath an embankment (Bjerrum (1973)). It can be seen that the stress path, imposed by the construction of the embankment, changes from a compression path

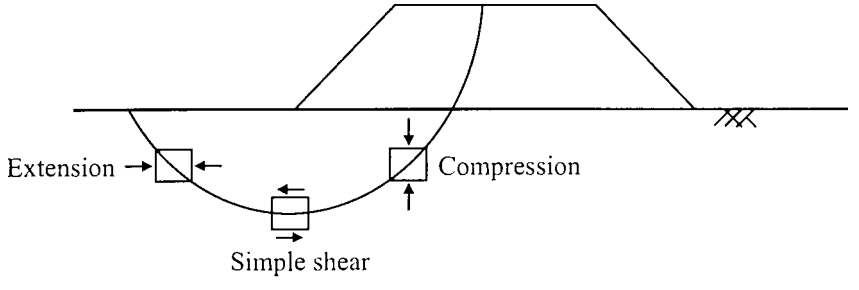


Figure 8.5: Relevance of laboratory tests to the stress paths followed by soil elements along the failure surface beneath an embankment (after Bjerrum (1973))

to an extension path. Hence, the stiffness predicted by the constitutive model in both compression and extension is expected to influence the pre-failure deformational behaviour.

It should be noted that, as shown in the previous chapters, the 2-SKH model differs from the M2-SKH model in that it predicts a non-smooth elasto-plastic transition, which results in an unrealistic drop in stiffness, once the stress state touches the kinematic surface, and in the model being unable to simulate realistically pre-failure non-linearity. This feature of the model is also expected to influence the predicted deformational behaviour of the embankment.

The study presented in this section is divided into two parts. The first part examines the pre-failure behaviour of the test embankment A, when the same undrained strength profile is assigned to the 2-SKH, M2-SKH and MCC models. The second part examines the effect of the drop in stiffness, predicted by the 2-SKH model, on the pre-failure behaviour of the embankment. In this case, the same undrained strength is assigned to the 2-SKH and M2-SKH models but K_o = 1.0 is assumed. This, combined with the fact that the kinematic surface is centred around the initial stress state, results in the same compression and extension stiffness for each model (see section 4.6.4). In this way the effect of the non-smooth elasto-plastic transition can be assessed separately from the effect of different compression and extension stiffness.

8.5.2 Analyses with kinematic hardening models and modified Cam Clay model

8.5.2.1 Introduction

As the 2-SKH, M2-SKH and MCC models predict isotropic strength, the analyses presented in this part do not intend to form a back-analysis of the test embankment A, but rather to investigate the effect that each model has on the deformational behaviour of the embankment when the same undrained strength profile is prescribed to all three models.

8.5.2.2 Analyses details

Four analyses were performed, two analyses in which the clay layer was modelled with the 2-SKH and M2-SKH models and two analyses in which the clay layer was modelled

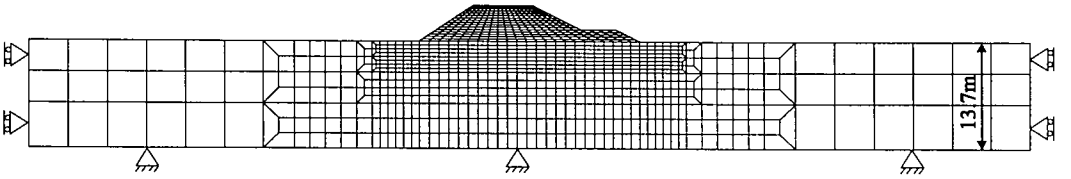


Figure 8.6: Finite element mesh

with the MCC model. These last two analyses differed only in the prescribed elastic shear stiffness profile. In each of the two MCC analyses the elastic shear stiffness was chosen so that the MCC model predicted the same secant undrained Young's modulus, E_u, as either the 2-SKH or the M2-SKH model at a stress level of 50% of the failure stress in triaxial compression (this becomes mores clear in the derivation of the model parameters, which is presented in the next section).

All four analyses were carried out undrained, in the manner described in section 3.3.1.1. The building of the embankment involved the construction of successive layers until failure occurred.

The finite element mesh used in the analyses can be seen in Figure 8.6. All the analyses performed were plane strain. Eight nodded isoparemetric quadrilateral elements with 2x2 integration were used.

8.5.2.3 Model parameters

Clay deposit

The derivation of the parameters for the 2-SKH and M2-SKH models is given first, followed by the derivation of the parameters for the MCC model. For all three models, the shapes of the yield and plastic potential surfaces in the deviatoric plane were assumed to be a Mohr-Coulomb hexagon and a circle respectively.

a) 2-SKH and M2-SKH models

i) N and λ^*

As already explained in Chapter 7, the compression parameters N and λ^* can be derived from any constant stress ratio compression test. These were derived here from an oedometer test from a depth of 6.5 m (data from Leroueil (1977)). Figure 8.7 plots the oedometer data in $\ln v$-$\ln p'$ space. The values of p' were calculated from the oedometer

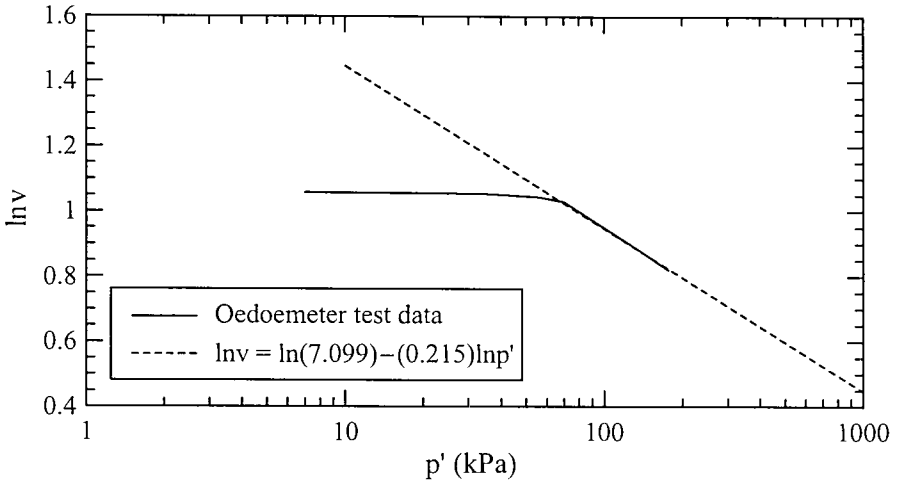


Figure 8.7: Determination of compression parameters (N and λ^*) for the clay at Saint-Alban (test data from Leroueil (1977))

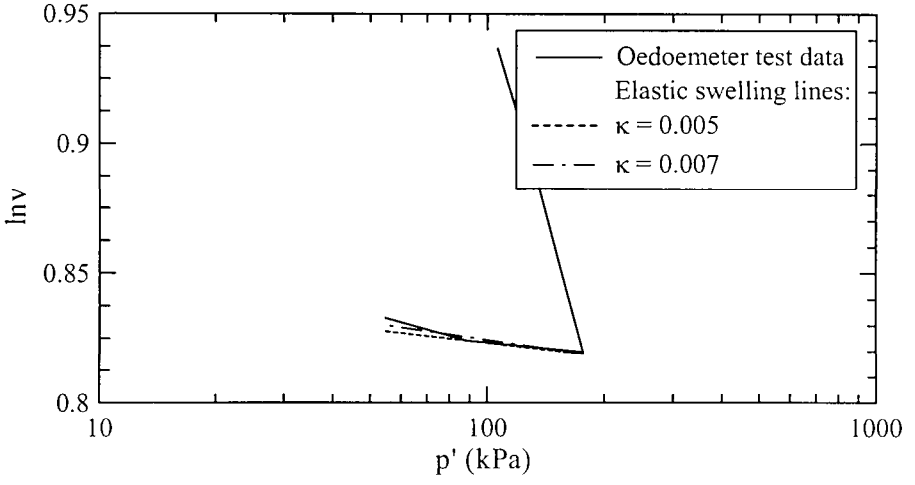


Figure 8.8: Determination of parameter κ^* for the clay at Saint-Alban (test data from Leroueil (1977))

test with an assumed K_o = 1 - sinφ', where φ' = 27°. The best line of the form $\ln v = \ln N_{Ko} - \lambda^* \ln p'$ fitted through the data gave values of λ^* = 0.215 and N_{Ko} = 7.099, where N_{Ko} is the specific volume of the K_o compression line at p' = 1 KPa. This corresponds to a value of N = 7.58, where N is the specific volume of the isotropic compression line at p' = 1 KPa.

ii) κ^*

The swelling parameter κ^* can be determined from the initial (elastic) part of the isotropic swelling line in $\ln v$-$\ln p'$ space. In the absence of such data, the parameter κ^* was estimated by plotting the swelling line of the previous oedometer test, in $\ln v$-$\ln p'$ space, see Figure 8.8. The values of p' were calculated in this case with the value of K_o

given by the Mayne and Kulhawy (1982) equation, $K_o = (1 - \sin\varphi')OCR^{\sin\varphi'}$, where $\varphi' = 27°$. Also shown in Figure 8.8 are elastic swelling lines corresponding to κ^* values of 0.005 and 0.007. A value of κ^* equal to 0.005, which corresponds to the initial part of the swelling line, was assumed. It is very important to note though, that this is not equivalent to determining the parameter of κ^* from an isotropic swelling line. However, it still provides an indication of the value of the parameter.

iii) G_e

The elastic shear stiffness, G_e, assumed in the analyses was based on dynamic field measurements of the elastic shear modulus of the clay deposit (Lefebvre et al. (1994)). Figure 8.9 shows the profile determined by Lefebvre et al. (1994) and the profile assumed in the finite element analyses. It can be seen that the elastic shear modulus profile shows an increased stiffness in the crust and seems to vary with depth in a similar way to the undrained strength profile.

iv) φ'

The value of φ' at the critical state was taken equal to 27°, after Zdravkovic et al. (2002) (based on the work of Leroueil (1977)).

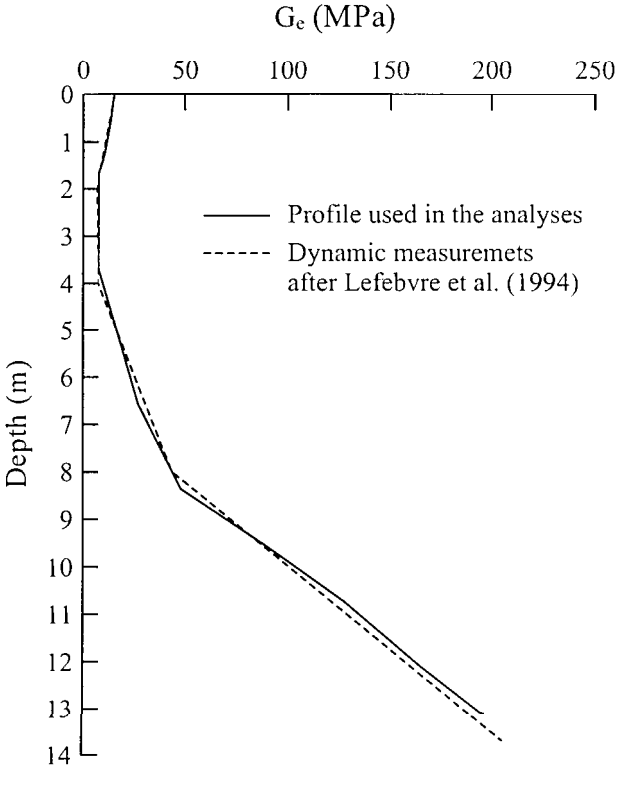


Figure 8.9: G_e profile for the kinematic hardening models

v) Y_p and Z_p

As aforementioned the shape of the plastic potential was assumed to be a circle in the deviatoric plane. Hence, the adopted values were $Y_p = 0.0$ and $Z_p = 1.0$.

vi) R and ψ or α

The remaining parameters are R and ψ for the 2-SKH model and R and α for the M2-SKH model. Since no test data was available with measurements of strains in the very small and small strain region, a value of R equal to 0.06 was adopted for both models, a value of ψ equal to 1.5 was assumed for the 2-SKH model and a value of α equal to 20.0 was adopted for the M2-SKH model. The parameters ψ and α were chosen

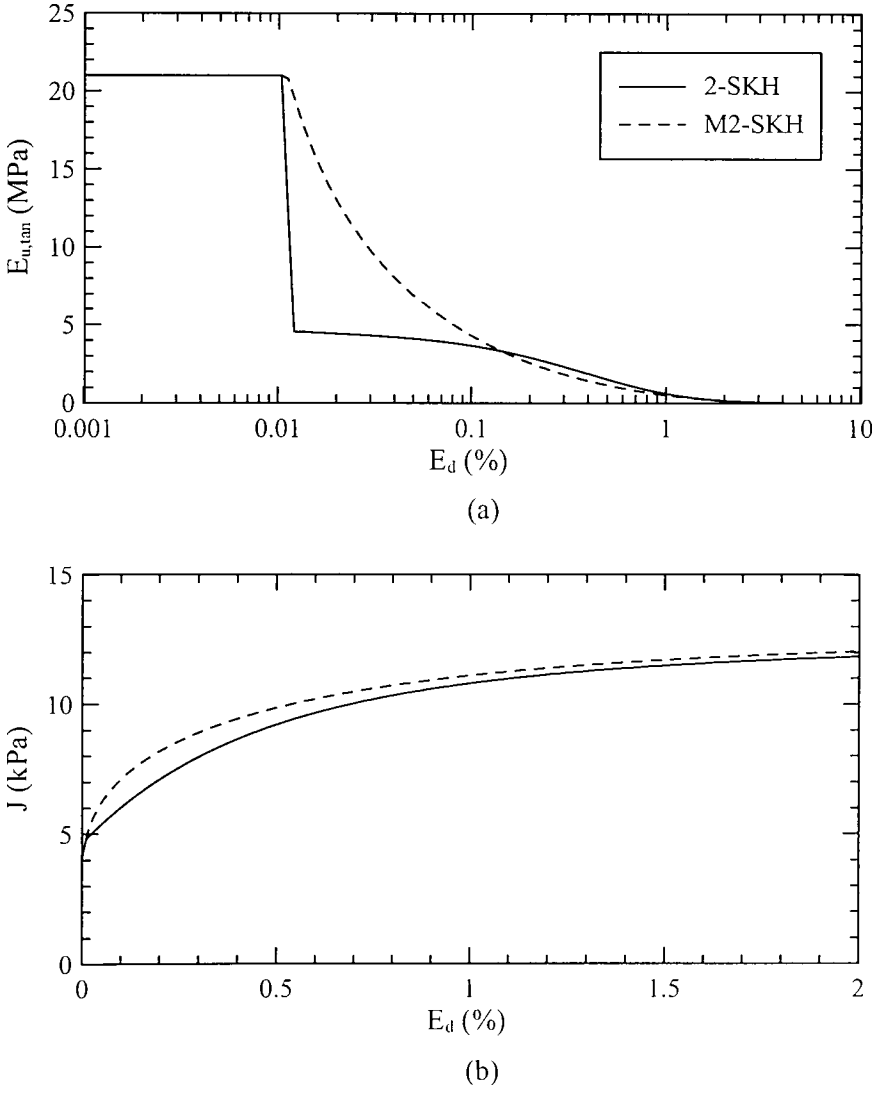


Figure 8.10: Predictions of the 2-SKH and M2-SKH models for an undrained triaxial compression test at a depth of 2.0 m a) stiffness-strain curve b) stress-strain curve

so as to give similar stress-strain curves in triaxial compression. Figure 8.10 plots the stress-strain and stiffness-strain curves obtained from single finite element analyses, modelling an undrained triaxial compression test at a depth of 2.0 m. Figure 8.10a shows that it is difficult to predict exactly the same response for both models, since the 2-SKH model will always predict a drop in stiffness once the stress state touches the kinematic yield surface, and hence lower values of stiffness than the M2-SKH model in the initial part of the small strain range. It should be noted that significant differences in stiffness in the initial part of the small strain range in Figure 8.10a plot as relatively small differences in the stress-strain curves of Figure 8.10b.

The parameters used in the 2-SKH and M2-SKH models are summarised in Tables 8.1 and 8.2 respectively.

N	λ^*	κ^*	G_e	φ'	Y_p	Z_p	R	ψ
7.58	0.215	0.005	see Fig. 8.9	27°	0.0	1.0	0.06	1.5

Table 8.1: Material parameters for the two-surface model for the clay at Saint-Alban

N	λ^*	κ^*	G_e	φ'	Y_p	Z_p	R	α
7.58	0.215	0.005	see Fig. 8.9	27°	0.0	1.0	0.06	20.0

Table 8.2: Material parameters for the modified two-surface model for the clay at Saint-Alban

b) MCC model

i) N and λ^*

The compression parameters N and λ^* for the version of the modified Cam Clay model used here are derived in the same way as for the kinematic hardening models. Therefore, the values of $N = 7.58$ and $\lambda^* = 0.215$ were also assumed for the MCC model.

ii) κ^*

In this version of the modified Cam Clay model, the parameter κ^* is the gradient of the isotropic swelling line in $\ln v$-$\ln p'$ space. Similar to the derivation of the parameter κ^* for the kinematic hardening models, a value of the parameter κ^* for the MCC model can be estimated from the oedometer swelling line plotted in $\ln v$-$\ln p'$ space in Figure 8.8.

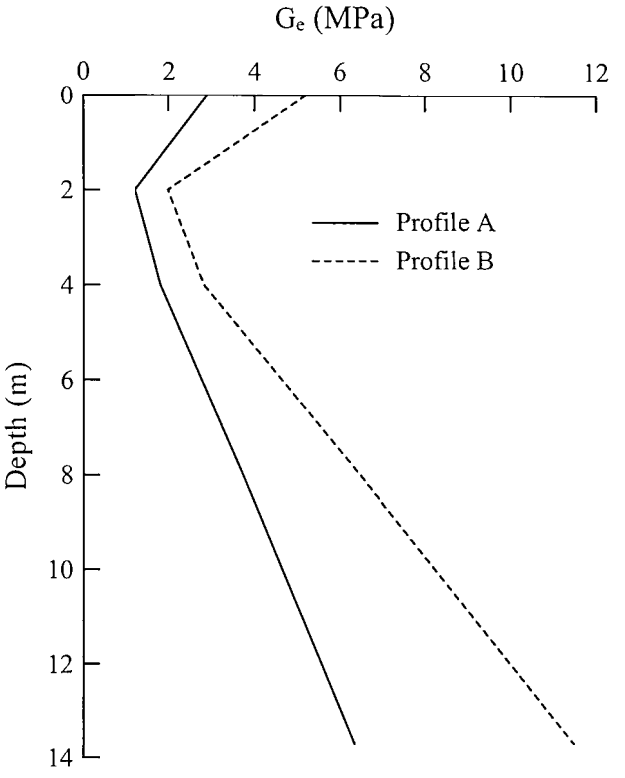


Figure 8.11: G_e profile for the modified Cam Clay model

However, in the MCC model the parameter κ^* represents the gradient of the whole swelling line, rather than the gradient of just the initial part of this line, which is the case for the kinematic hardening models. Hence, for the MCC model an average value of the gradient was estimated and κ^* was taken equal to 0.007.

iii) G_e

Two profiles of the elastic shear modulus, G_e, were assumed for the MCC model. The first profile, profile A, was chosen so that the MCC model predicted the same secant undrained Young's modulus, E_u, as the 2-SKH model at a stress level of 50% in triaxial compression, Figure 8.11. The profile B in Figure 8.11 was chosen so that the MCC model predicted the same E_u as the M2-SKH model at a stress level of 50% in triaxial compression. Figure 8.12 shows an example of the response predicted by the 2-SKH and M2-SKH models and the two G_e profiles for the MCC model, for single finite element analyses modelling an undrained triaxial compression test at a depth of 2.0 m. MCC-A and MCC-B, in the figure, correspond to the analyses with the MCC model for the stiffness profiles A and B respectively.

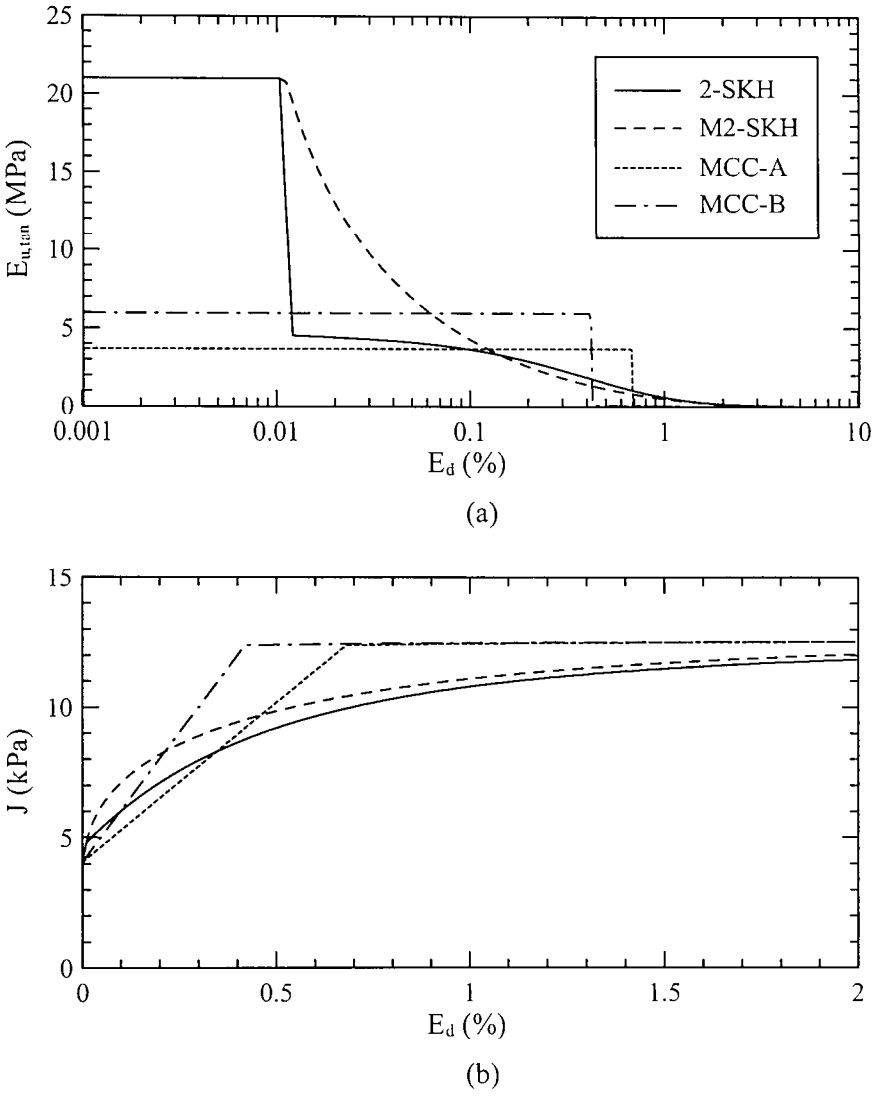


Figure 8.12: Predictions of the 2-SKH, M2-SKH and MCC models for an undrained triaxial compression test at a depth of 2.0 m a) stiffness-strain curve b) stress-strain curve

iv) φ'

Similar to the kinematic hardening models, the value of φ' at the critical state was taken equal to 27°.

v) Y_p and Z_p

The assumed values of Y_p and Z_p were 0.0 and 1.0 respectively, defining a circle in the deviatoric plane.

The parameters used in the MCC model are summarised in Table 8.3.

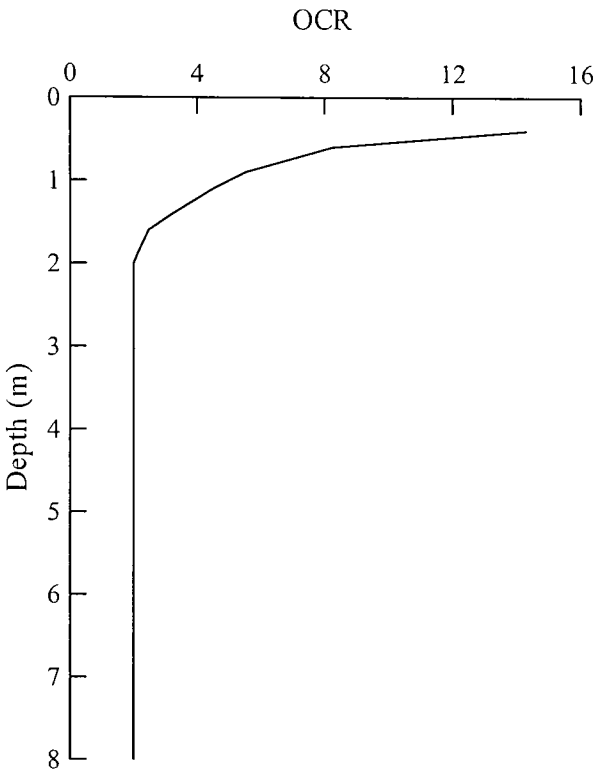


Figure 8.13: *OCR* profile assumed in the analyses

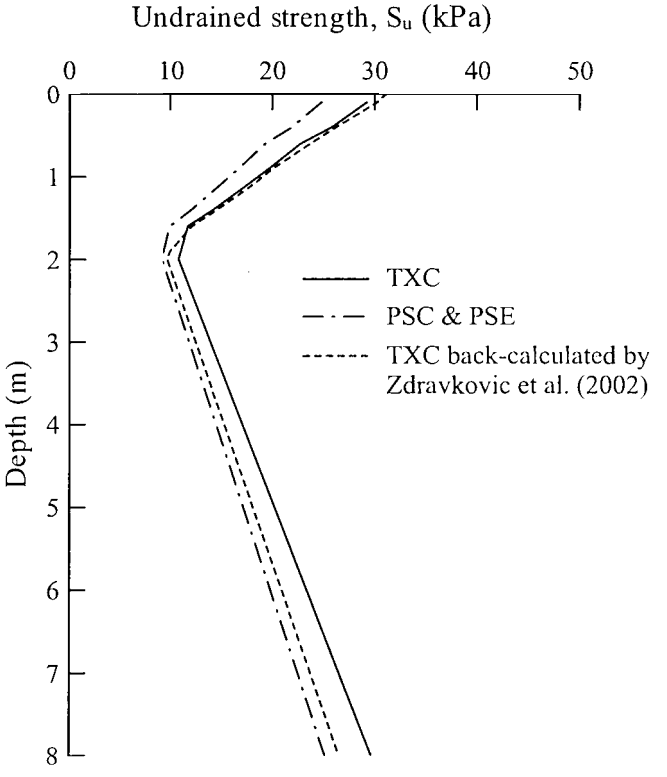


Figure 8.14: Undrained strength profiles predicted by the 2-SKH, M2-SKH and MCC models

N	λ^*	κ^*	G_e	φ'	Y_p	Z_p
7.58	0.215	0.007	see Fig. 8.11	27°	0.0	1.0

Table 8.3: Material parameters for the modified Cam Clay model for the clay at Saint-Alban

The initial prescribed conditions involved an effective stress ratio, K_o, of 0.67. The *OCR* profile with depth, shown in Figure 8.13, was chosen so that all three models predicted the same undrained strength profile in triaxial compression, see Figure 8.14. This undrained strength profile can be calculated from the equations of Appendix III (there is practically no difference in the undrained strength profile due to the different values of κ^* assumed in the kinematic hardening models and the MCC model). The kinematic hardening models and the MCC model predict the same undrained strength profile in plane strain compression and extension and this can also be seen in Figure 8.14. Also shown in Figure 8.14 is the undrained strength profile in triaxial compression back-calculated by Zdravkovic et al. (2002), in order to predict the correct embankment failure height of 3.9 m using the isotropic MCC model. As aforementioned, this corresponds to a profile which is 1.25 times the DSS profile in Figure 8.4.

Fill material

A Young's modulus, E, of 10000 kPa and a Poisson's ratio, μ, of 0.3 were assumed for the fill material. The angle of shearing resistance, φ', was determined by triaxial tests on samples of the fill, compacted at densities comparable to field densities, and equalled 44° (La Rochelle et al. (1974)). The angle of dilation was assumed equal to 22°.

8.5.2.4 Analyses results

A comparison of the predictions of the kinematic hardening models is given first, followed by a comparison of the predictions of the kinematic hardening models with the MCC model.

All four analyses predicted the same embankment failure height of 3.9 m. Figure 8.15 shows the vectors of incremental displacement at failure for the MCC-B analysis. This plot gives an indication of the mechanism forming at failure. Similar failure mechanisms were obtained for the other three analyses.

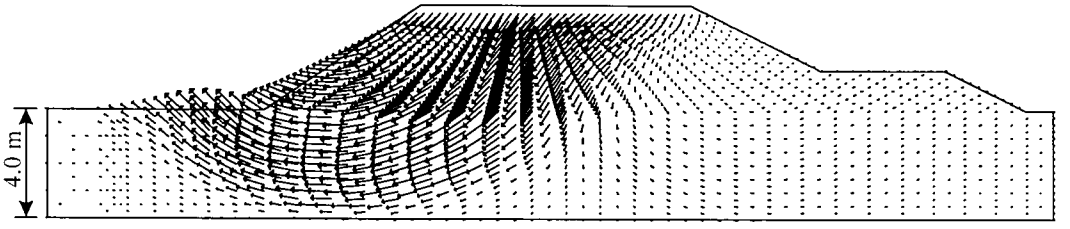


Figure 8.15: Vectors of incremental displacement at failure for analysis MCC-B

In the following figures the sign convention followed is that upwards vertical movements and right horizontal movements are plotted as positive, see Figure 8.3.

Comparison of the kinematic hardening models

Figure 8.16 presents the vertical settlement at the centreline of the embankment (point A in Figure 8.3) plotted against the embankment height for the 2-SKH and M2-SKH models. The M2-SKH model predicts smaller settlement than the 2-SKH model up to an embankment height of approximately 2.7 m. Thereafter the M2-SKH model predicts larger settlement.

Figure 8.17 compares the vertical settlement of the embankment, measured at the bottom of the settlement gauge R23 (point A on Figure 8.3), with the vertical settlement predicted by the two finite element analyses. It should be noted that the settlement gauge was installed after the first 0.6 m of the fill was constructed. The predictions of both models compare reasonably well with the measured data. The 2-SKH model predicts a generally stiffer behaviour, whereas the M2-SKH model predicts a stiffer behaviour up

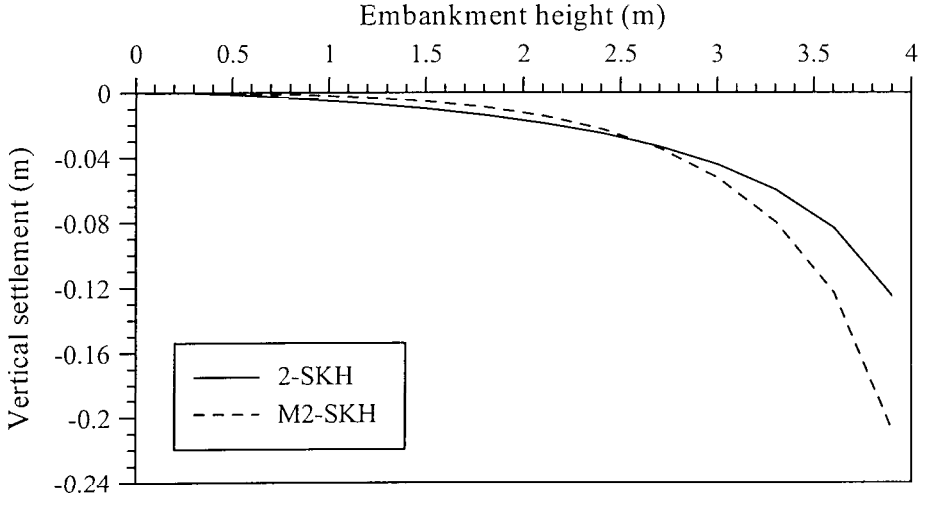


Figure 8.16: Vertical settlement at the centreline of the embankment versus embankment height predicted by the 2-SKH and M2-SKH models

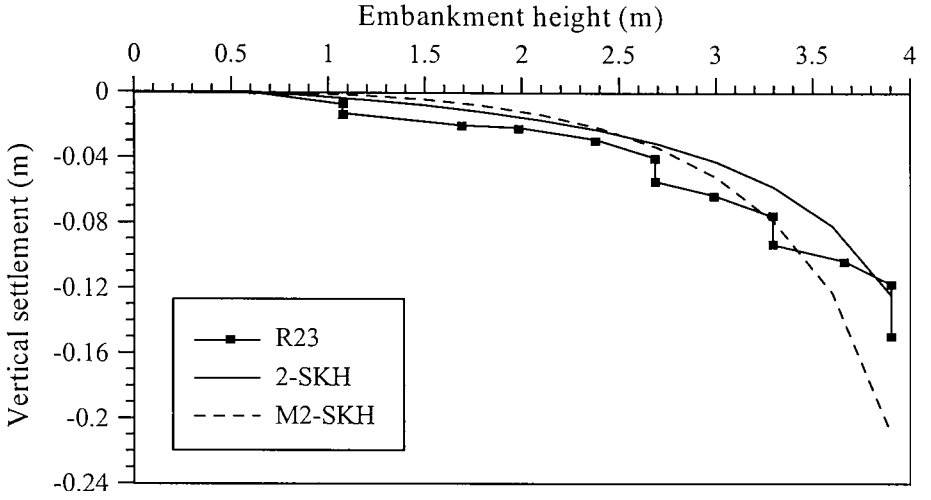


Figure 8.17: Comparison between observed and predicted vertical settlement at the centreline of the embankment

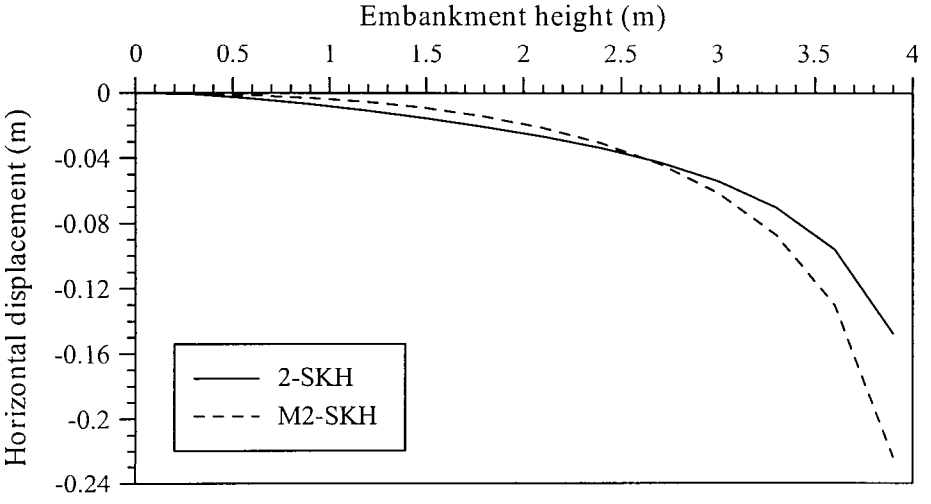


Figure 8.18: Horizontal displacement at the toe of the embankment versus embankment height predicted by the 2-SKH and M2-SKH models

to an embankment height of 3.5 m and thereafter a softer behaviour.

Figure 8.18 plots the horizontal displacement at the toe of the embankment (point B in Figure 8.3) against the embankment height. The response shown in this figure is similar to the response presented in Figure 8.16. The M2-SKH model predicts smaller displacement than the 2-SKH model up to a height of approximately 2.7 m. For higher embankment heights the M2-SKH model predicts larger displacement than that predicted by the 2-SKH model.

This behaviour can be explained by examining the stiffness response of soil elements when subjected to a compression and an extension path. Figure 8.10 illustrates the

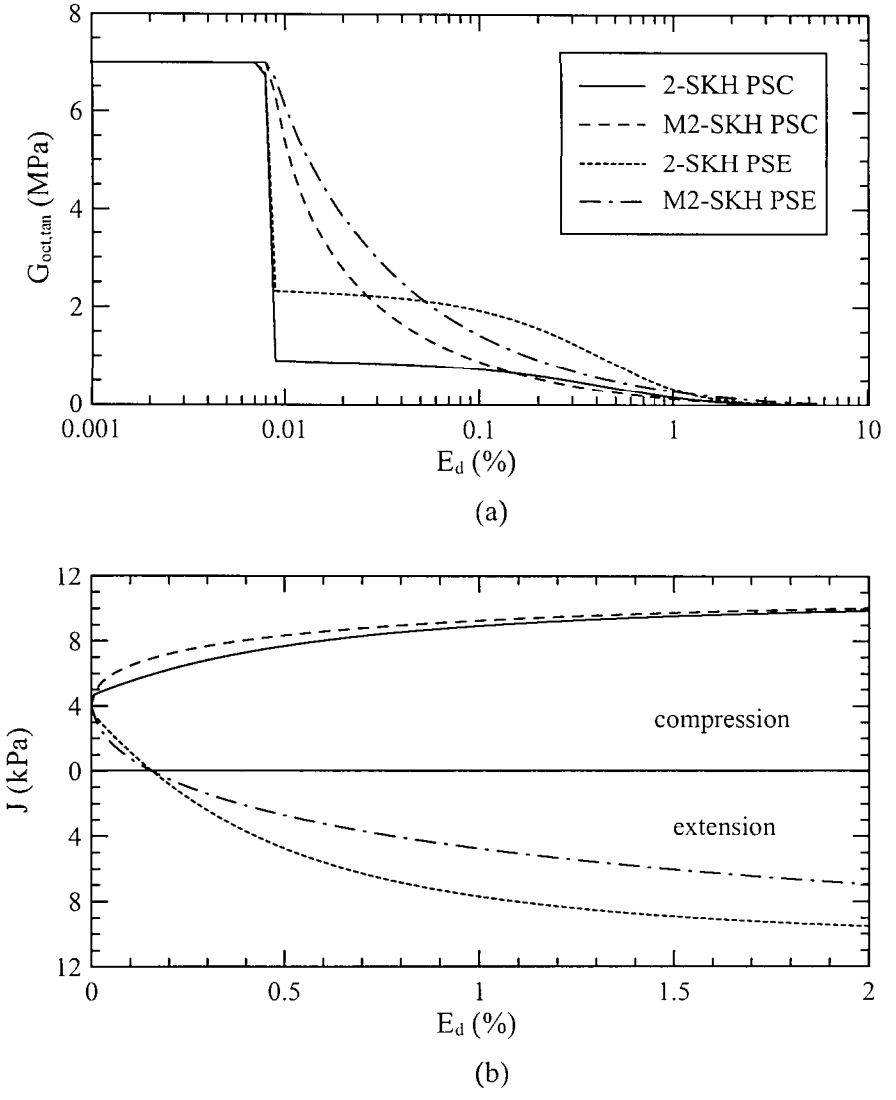


Figure 8.19: Predictions of the 2-SKH and M2-SKH models for a plane strain compression and extension test at a depth of 2.0 m a) stiffness-strain curve b) stress-strain curve

behaviour predicted for an undrained triaxial compression test. However, since the finite element analyses performed are plane strain, what is of relevance here is the stiffness response in plane strain compression and extension. Figure 8.19 presents the stress-strain and stiffness-strain response predicted by the two models for single finite element analyses modelling an undrained plane strain compression and extension test at a depth of 2.0 m. (It is reminded that the tangent stiffness G_{oct} is defined as $G_{oct} = \mathrm{d}J/\mathrm{d}E_d$.) Due to the value of K_o being lower than 1.0 and the fact that the kinematic surface is centred around the stress state at the start of shearing, the stiffness in compression is softer than the stiffness in extension, for each model, once the stress state becomes elasto-plastic. Figure 8.19b shows that the predicted response in plane strain compression is similar to

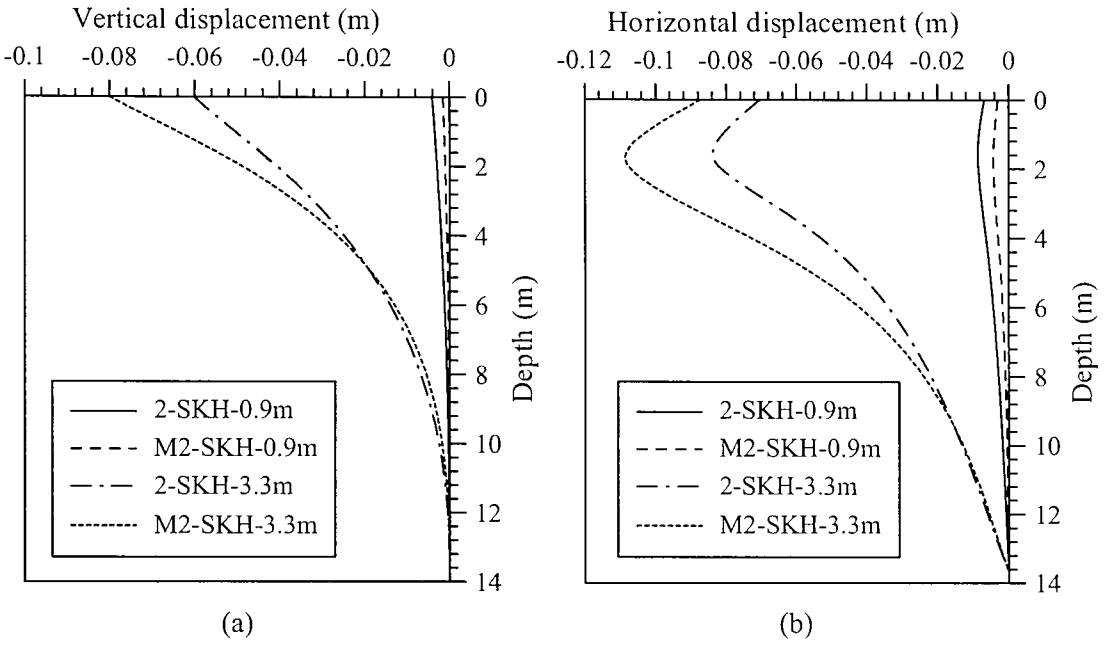


Figure 8.20: Movements predicted by the 2-SKH and M2-SKH models for embankment heights of 0.9 m and 3.3 m a) vertical displacement at the centreline of the embankment b) horizontal displacement under the toe of the embankment

the response predicted for the triaxial compression path (Figure 8.10b). However, the predicted response in plane strain extension is different and although the response of the M2-SKH model in the extension path is initially stiffer, it soon changes to become softer than the response predicted by the 2-SKH model. This observation explains why in the embankment analysis the M2-SKH model predicts an initially stiffer behaviour than the 2-SKH model, which as the embankment height increases, becomes softer than the response predicted by the 2-SKH model (Figures 8.16 and 8.18).

Figure 8.20a shows the vertical movements below the centreline of the embankment (line AC in Figure 8.3) against depth for two embankment heights, 0.9 m and 3.3 m. Figure 8.20b presents the distribution of horizontal movements under the toe of the embankment (line BD in Figure 8.3) with depth for the same embankment heights. Comparison of the movements predicted by the models, for an embankment height of 0.9 m, shows that the M2-SKH model predicted significantly smaller movements than the 2-SKH model. For an embankment height of 3.3 m the M2-SKH model predicted larger vertical movements than the 2-SKH model up to a depth of 5.0 m and larger horizontal movements up to a depth of 10.0 m. Table 8.4 summarises the percentage differences between the maximum vertical movement, beneath the centreline, and the maximum horizontal movement, beneath the toe of the embankment, predicted by the two kinematic hardening models, for four embankment heights.

Embankment height (m)	0.9	1.8	2.4	3.3
$\frac{\lvert v^{max}_{2-SKH}\rvert - \lvert v^{max}_{M2-SKH}\rvert}{\lvert v^{max}_{2-SKH}\rvert}\cdot 100$	62.7	35.9	10.4	-33.09
$\frac{\lvert u^{max}_{2-SKH}\rvert - \lvert u^{max}_{M2-SKH}\rvert}{\lvert u^{max}_{2-SKH}\rvert}\cdot 100$	49.9	20.4	-1.0	-30.2

v : vertical movement below the centreline of the embankment
u : horizontal movement below the toe of the embankment

Table 8.4: Percentage difference between the maximum movements predicted by the 2-SKH and M2-SKH models

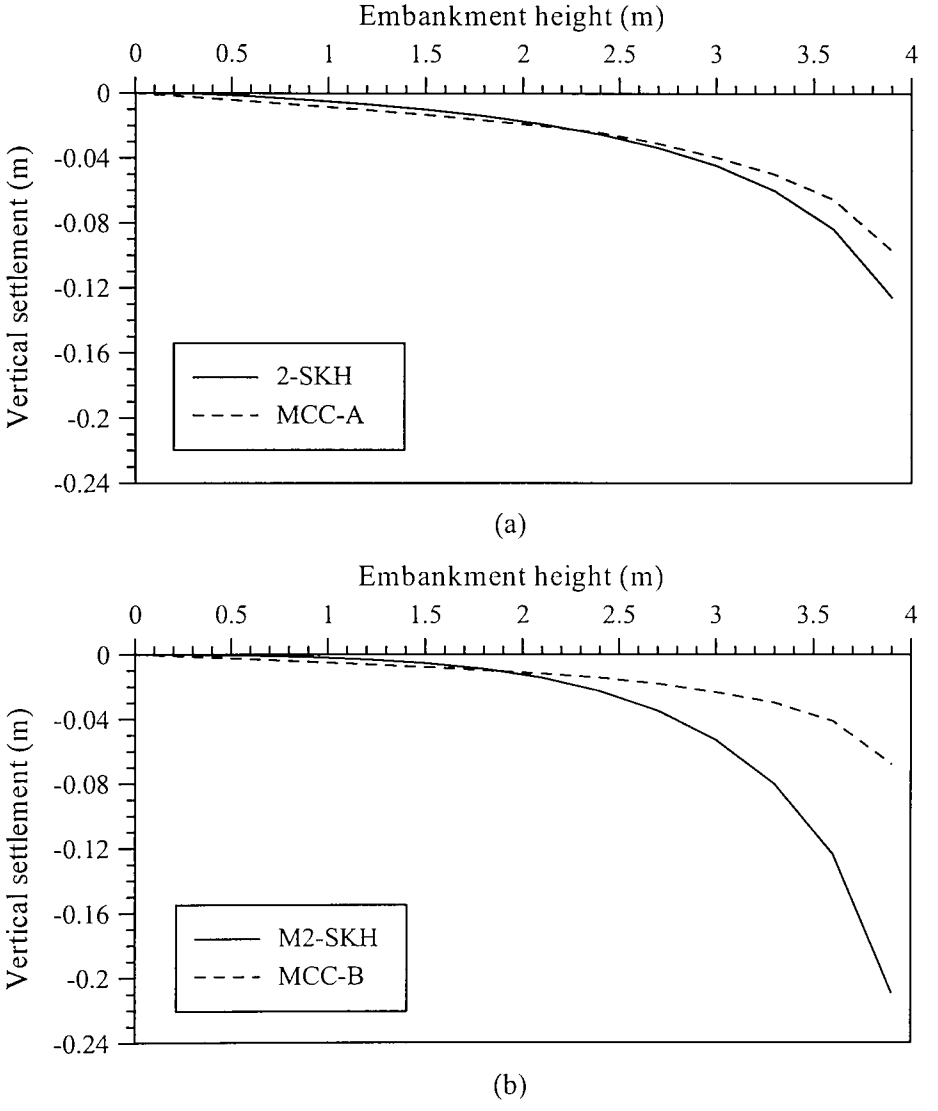


Figure 8.21: Vertical settlement at the centreline of the embankment versus embankment height predicted by a) the 2-SKH and MCC models (analysis MCC-A) b) the M2-SKH and MCC models (analysis MCC-B)

In this section, the predictions of the 2-SKH model are compared with the predictions of the MCC model for the stiffness profile A (analysis MCC-A) and the predictions of the M2-SKH model are compared with the predictions of the MCC model for the stiffness profile B (analysis MCC-B).

Figure 8.21 plots the vertical settlement at the centreline of the embankment against the embankment height. Both analyses with the MCC model predict higher vertical settlement than the kinematic hardening models at the early stages of the embankment construction and smaller settlement at the later stages of the construction. Comparison of

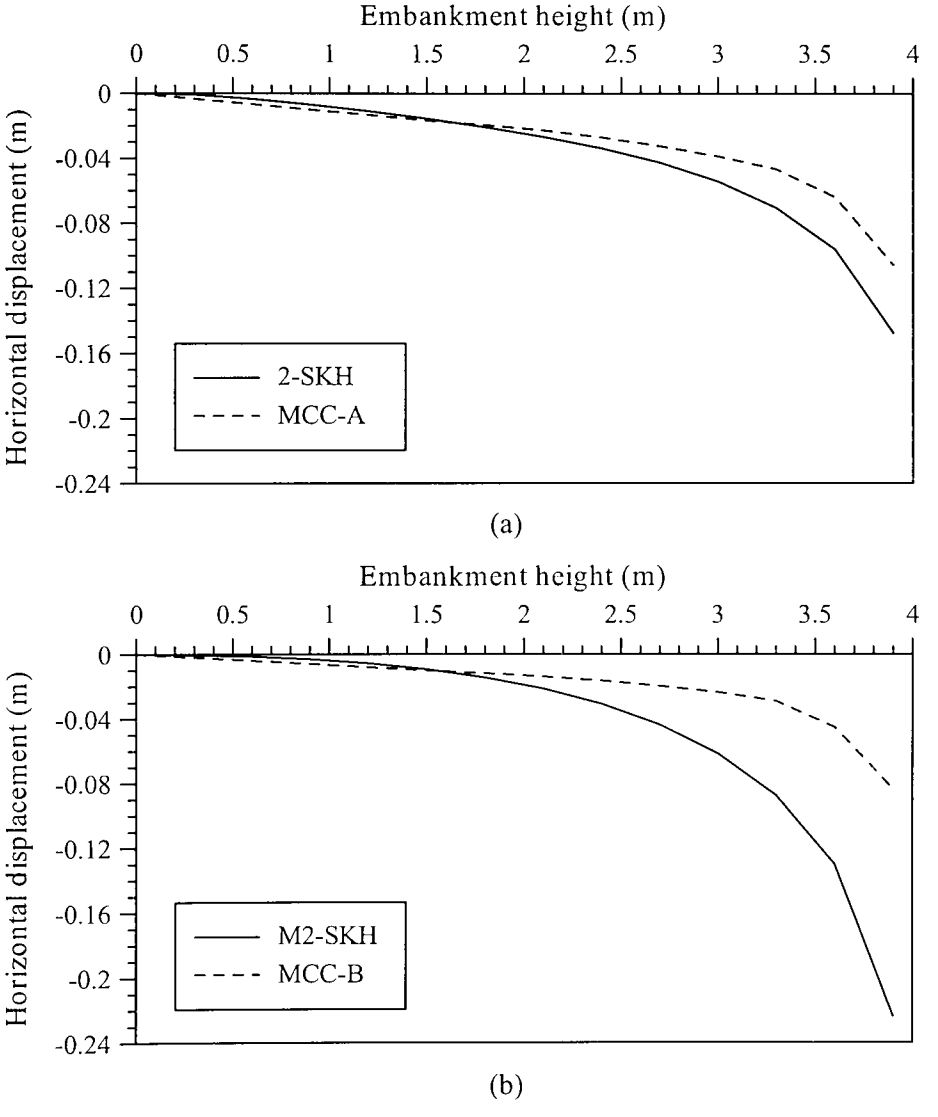


Figure 8.22: Horizontal displacement at the toe of the embankment versus embankment height predicted by a) the 2-SKH and MCC models (analysis MCC-A) b) the M2-SKH and MCC models (analysis MCC-B)

Figures 8.21a and b shows that, at the later stages of the embankment construction, there is a smaller difference in the predicted movements in Figure 8.21a than in Figure 8.21b.

Figure 8.22, which plots the horizontal movement at the toe of the embankment against the embankment height, reveals a similar behaviour. The MCC analyses predict displacements larger than the ones predicted by the kinematic hardening models initially, but smaller after a certain embankment height. Moreover, at the later stages of the construction the difference in horizontal movements in Figure 8.22a is again smaller than the one in Figure 8.22b.

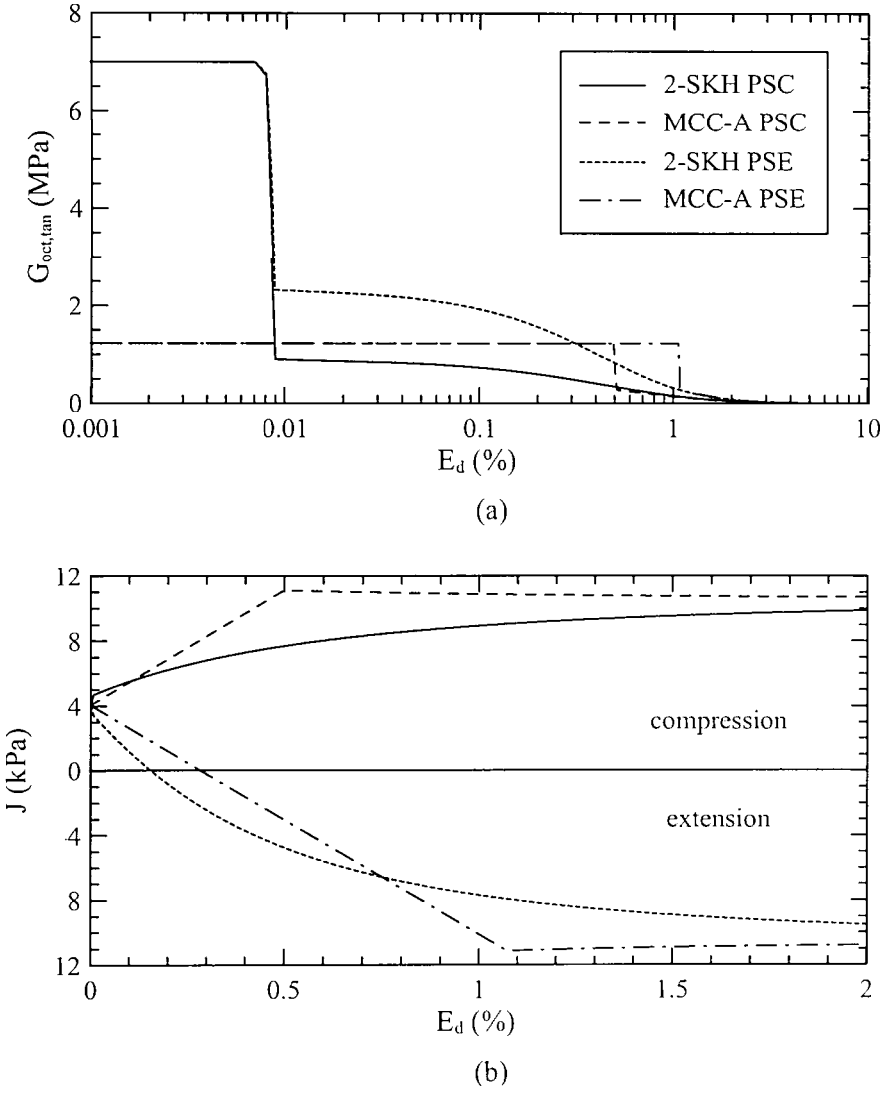


Figure 8.23: Predictions of the 2-SKH and MCC models (analysis MCC-A) for a plane strain compression and extension test at a depth of 2.0 m a) stiffness-strain curve b) stress-strain curve

The observation that the MCC model shows a softer response than the kinematic hardening models initially, but stiffer as the embankment height increases, can be attributed to the linear behaviour of the MCC model, within the yield surface, as compared to the highly non-linear behaviour of the kinematic hardening models, within the bounding surface. As shown in Figure 8.12, if an average stiffness is chosen for the MCC model then this is initially softer and then stiffer than in the kinematic hardening models.

The fact that the difference in the movements predicted by the M2-SKH and MCC-B analyses is higher than the one predicted by the 2-SKH and MCC-A analyses, at the later stages of the analyses, can be explained by examining the response experienced by the

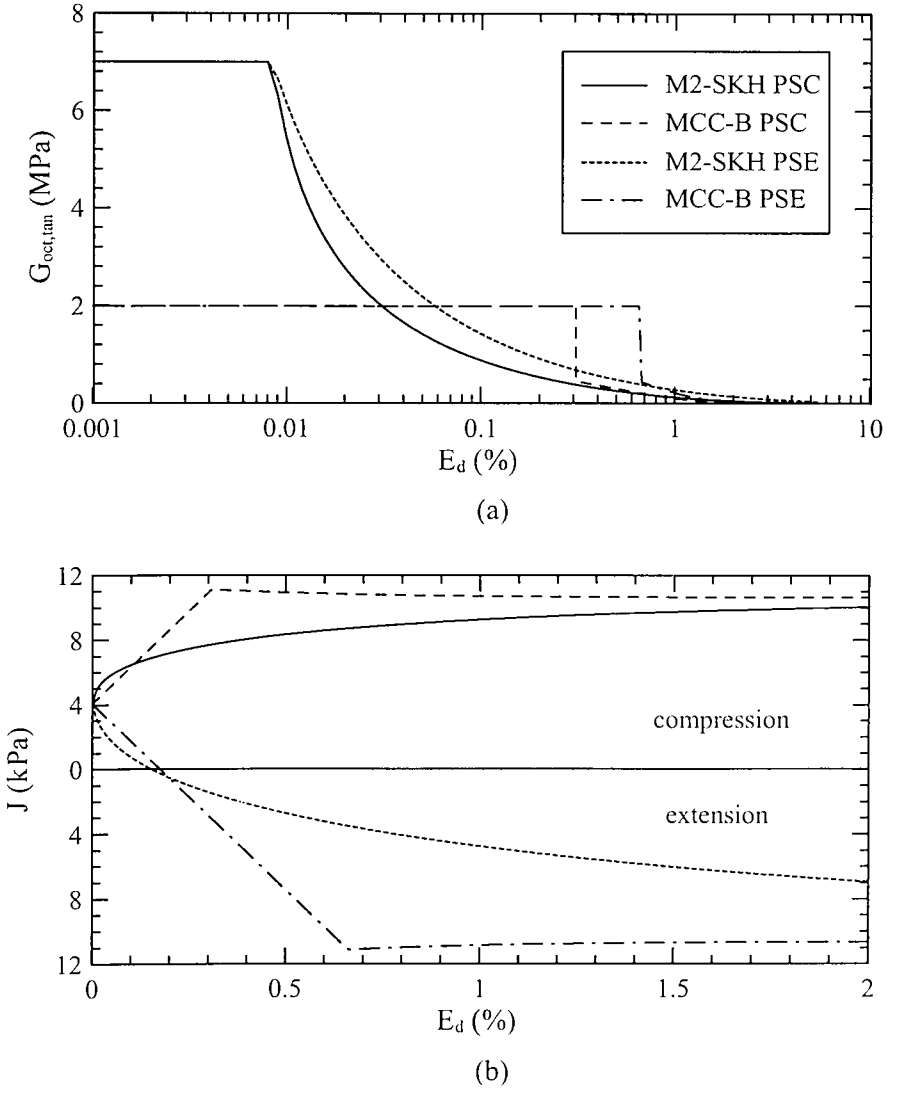


Figure 8.24: Predictions of the M2-SKH and MCC models (analysis MCC-B) for a plane strain compression and extension test at a depth of 2.0 m a) stiffness-strain curve b) stress-strain curve

soil elements during undrained plane strain compression and extension. Figures 8.23 and 8.24 plot the stress-strain and stiffness-strain response predicted by the models for single finite element analyses modelling two such stress paths at a depth of 2.0 m. The MCC model predicts the same stiffness in triaxial compression, plane strain compression and plane strain extension. However, as already shown, the kinematic hardening models predict different stiffness in plane strain compression and plane strain extension. Hence, although the behaviour in compression is relatively similar between Figures 8.23 and 8.24, the behaviour in extension is different, with the MCC model in Figure 8.24 being generally much stiffer than the kinematic hardening model after a deviatoric strain of 0.2%, as compared to Figure 8.23. This explains the higher difference in movements between the MCC-B and M2-SKH analyses than between the MCC-A and 2-SKH analyses.

Figures 8.25a and 8.26a present the distribution of vertical movements with depth below the centreline of the embankment for two embankment heights (0.9 m and 3.3 m) and for the 2-SKH and MCC-A analyses and the M2-SKH and MCC-B analyses respectively. Figures 8.25b and 8.26b illustrate the distribution of horizontal displacements with depth beneath the toe of the embankment for the same embankment heights and for the 2-SKH and MCC-A analyses and the M2-SKH and MCC-B analyses respectively. For the embankment height of 0.9 m the MCC analyses predicted higher movements than the

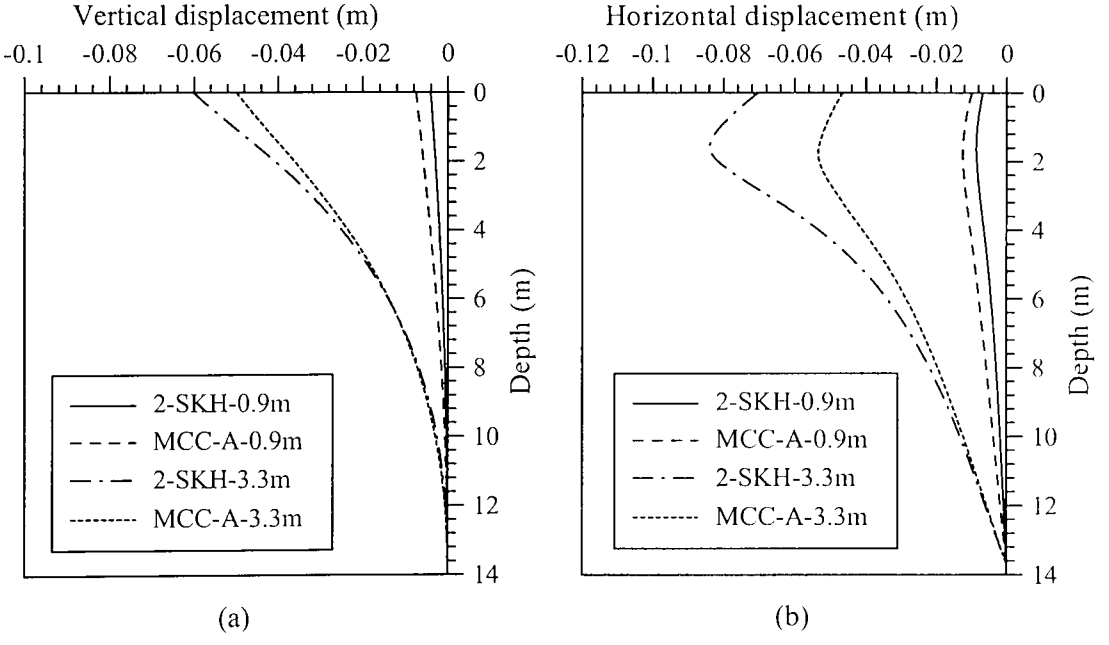


Figure 8.25: Movements predicted by the 2-SKH and MCC models (analysis MCC-A) for embankment heights of 0.9 m and 3.3 m a) vertical displacement at the centreline of the embankment b) horizontal displacement under the toe of the embankment

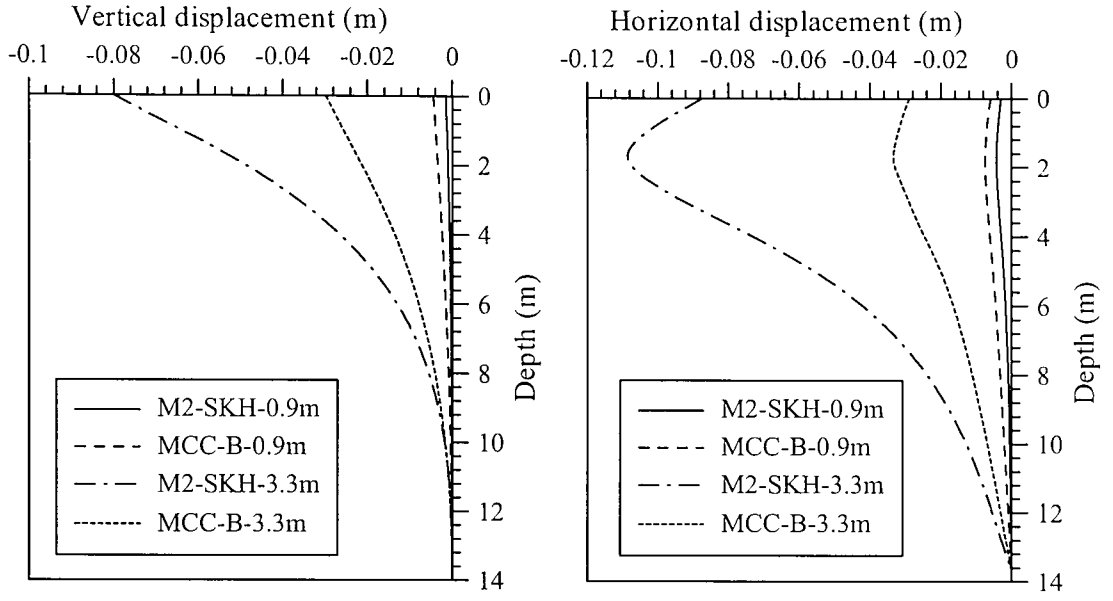


Figure 8.26: Movements predicted by the M2-SKH and MCC models (analysis MCC-B) for embankment heights of 0.9 m and 3.3 m a) vertical displacement at the centreline of the embankment b) horizontal displacement under the toe of the embankment

Embankment height (m)	0.9	1.8	2.4	3.3
$\frac{\lvert v_{2-SKH}^{max}\rvert - \lvert v_{MCC-A}^{max}\rvert}{\lvert v_{2-SKH}^{max}\rvert}\cdot 100$	-85.0	-19.2	4.0	17.0
$\frac{\lvert u_{2-SKH}^{max}\rvert - \lvert u_{MCC-A}^{max}\rvert}{\lvert u_{2-SKH}^{max}\rvert}\cdot 100$	-43.7	4.8	20.1	35.9

v : vertical movement below the centreline of the embankment
u : horizontal movement below the toe of the embankment

Table 8.5: Percentage difference between the maximum movements predicted by the 2-SKH and MCC models (analysis MCC-A)

Embankment height (m)	0.9	1.8	2.4	3.3
$\frac{\lvert v_{M2-SKH}^{max}\rvert - \lvert v_{MCC-B}^{max}\rvert}{\lvert v_{M2-SKH}^{max}\rvert}\cdot 100$	-192.8	-10.2	36.6	62.8
$\frac{\lvert u_{M2-SKH}^{max}\rvert - \lvert u_{MCC-B}^{max}\rvert}{\lvert u_{M2-SKH}^{max}\rvert}\cdot 100$	-73.1	27.6	52.0	69.2

v : vertical movement below the centreline of the embankment
u : horizontal movement below the toe of the embankment

Table 8.6: Percentage difference between the maximum movements predicted by the M2-SKH and MCC models (analysis MCC-B)

equivalent kinematic hardening models, whereas for the embankment height of 3.3 m the opposite is true. Tables 8.5 and 8.6 summarise the percentage difference between the maximum vertical movement, beneath the centreline, and the maximum horizontal movement, beneath the toe of the embankment, predicted by the MCC and 2-SKH models and the MCC and M2-SKH models respectively.

8.5.3 Analyses with kinematic hardening models and $K_o = 1.0$

8.5.3.1 Introduction

In the previous section it was shown that the stiffness in both compression and extension influence the deformational behaviour of the embankment. It was also shown that when the parameters for the two kinematic hardening models were chosen so that the models predicted similar response in compression, the predicted response in extension differed significantly. In order to have a more direct comparison between the two kinematic hardening models the analysis of the embankment was repeated for a K_o value of 1.0. In this case, and with the condition that the kinematic surface is centred around the initial stress state at the start of the analysis, the stiffness in plane strain compression is the same as the stiffness in plane strain extension for each model. In this way it is possible to assess separately the effect of the drop in stiffness, predicted by the two-surface kinematic hardening model, on the deformational pre-failure behaviour of the embankment.

8.5.3.2 Analyses details

Two analyses were performed, one where the clay layer was modelled with the 2-SKH model and one where the clay layer was modelled with the M2-SKH model. Both analyses were carried out undrained.

In order to have approximately the same stress-strain response for both models, it was necessary to prescribe two different values of the parameter α, one for the soil within the clay crust and one for the soil beneath the crust. In order to achieve this, the original mesh was slightly modified such that the surface crust could be represented as a separate layer. The new mesh can be seen in Figure 8.27. Again both analyses were plane strain and used eight nodded isoparametric elements with 2x2 integration.

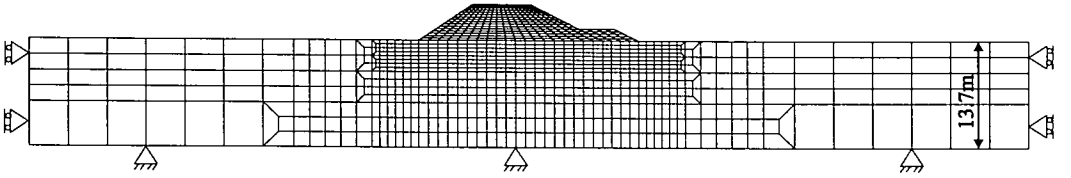


Figure 8.27: Finite element mesh

N	λ^*	κ^*	G_e / p'	X	Y	Z	Y_p	Z_p	R	ψ
7.58	0.215	0.005	500.0	0.454	0.0	1.0	0.0	1.0	0.06	1.5

Table 8.7: Material parameters for the two-surface model for the analyses with $K_o = 1.0$

N	λ^*	κ^*	G_e / p'	X	Y	Z	Y_p	Z_p	R	α
7.58	0.215	0.005	500.0	0.454	0.0	1.0	0.0	1.0	0.06	20.0

Table 8.8: Material parameters for the modified two-surface model for the analyses with $K_o = 1.0$ – soil within the crust

N	λ^*	κ^*	G_e / p'	X	Y	Z	Y_p	Z_p	R	α
7.58	0.215	0.005	500.0	0.454	0.0	1.0	0.0	1.0	0.06	30.0

Table 8.9: Material parameters for the modified two-surface model for the analyses with $K_o = 1.0$ – soil below the crust

8.5.3.3 Model parameters

Clay deposit

The parameters of the kinematic hardening models used in these two analyses are the following:

The parameters N, λ^* and κ^* were kept at the same values as in the previous analyses. The elastic shear modulus, G_e, was assumed to vary with the mean effective stress, p', as $G_e / p' = 500.0$. A circle was assumed for the shape of both yield and plastic potential surfaces in the deviatoric plane. Hence, $Y = Y_p = 0.0$ and $Z = Z_p = 1.0$. The value of X was taken such that these two analyses predicted the same value of $g(\theta)$ in plane strain conditions as the analyses of the previous section. The parameter R was kept equal to 0.06. The parameter ψ in the 2-SKH model was kept at 1.5. In order to match

approximately the same stress-strain response for both models two values of the parameter α in the M2-SKH model were assumed. A value of α equal to 20.0 was assumed for the soil within the crust and a value of α equal to 30.0 was assumed for the soil below the crust. The parameters adopted in these analyses for the 2-SKH model are summarised in Table 8.7. Tables 8.8 and 8.9 summarise the parameters adopted for the M2-SKH model for the soil within and below the crust respectively.

As already mentioned the prescribed initial conditions involved a K_o value of 1.0 constant with depth. In order to make easier the prediction of similar stress-strain behaviour for the two models within the crust a constant average value of *OCR* equal to 6.0 was assumed. The *OCR* value below the crust was kept equal to 2.0.

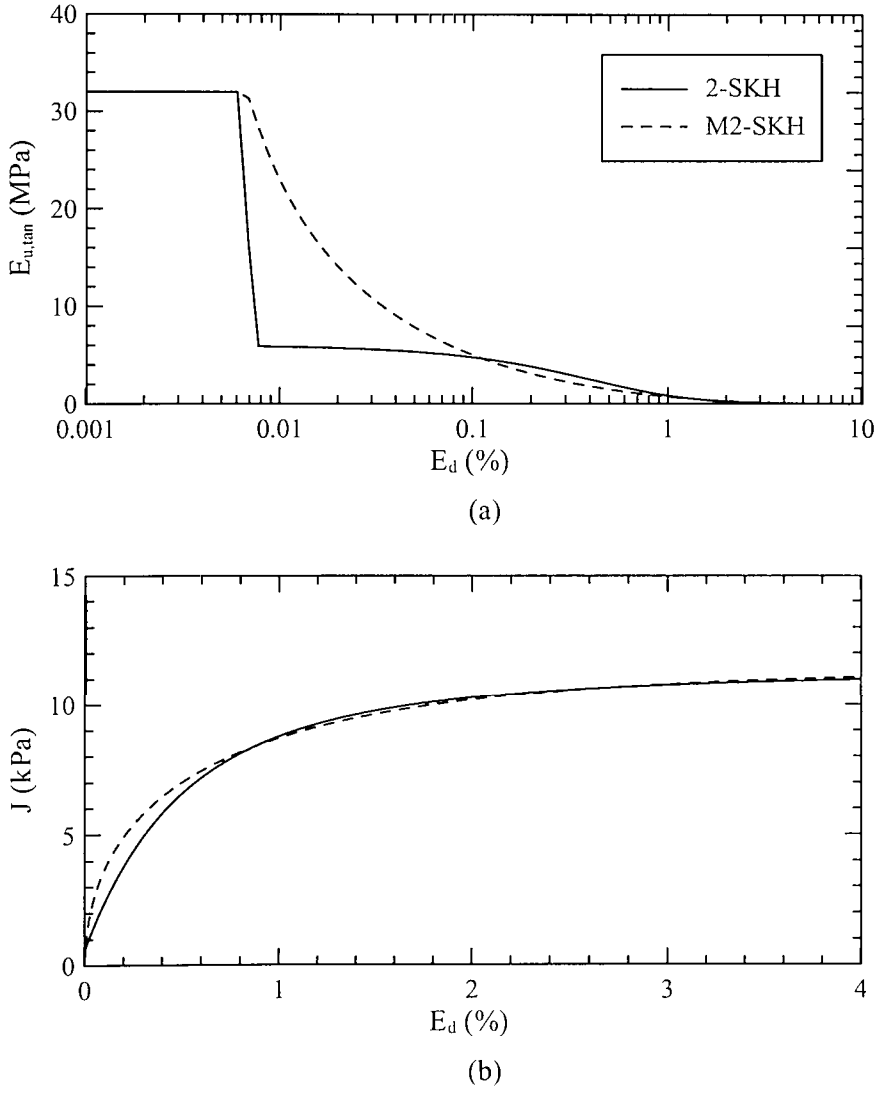


Figure 8.28: Predictions of the 2-SKH and M2-SKH models for an undrained triaxial compression test at a depth of 2.0 m for K_o = 1.0 a) stiffness-strain curve b) stress-strain curve

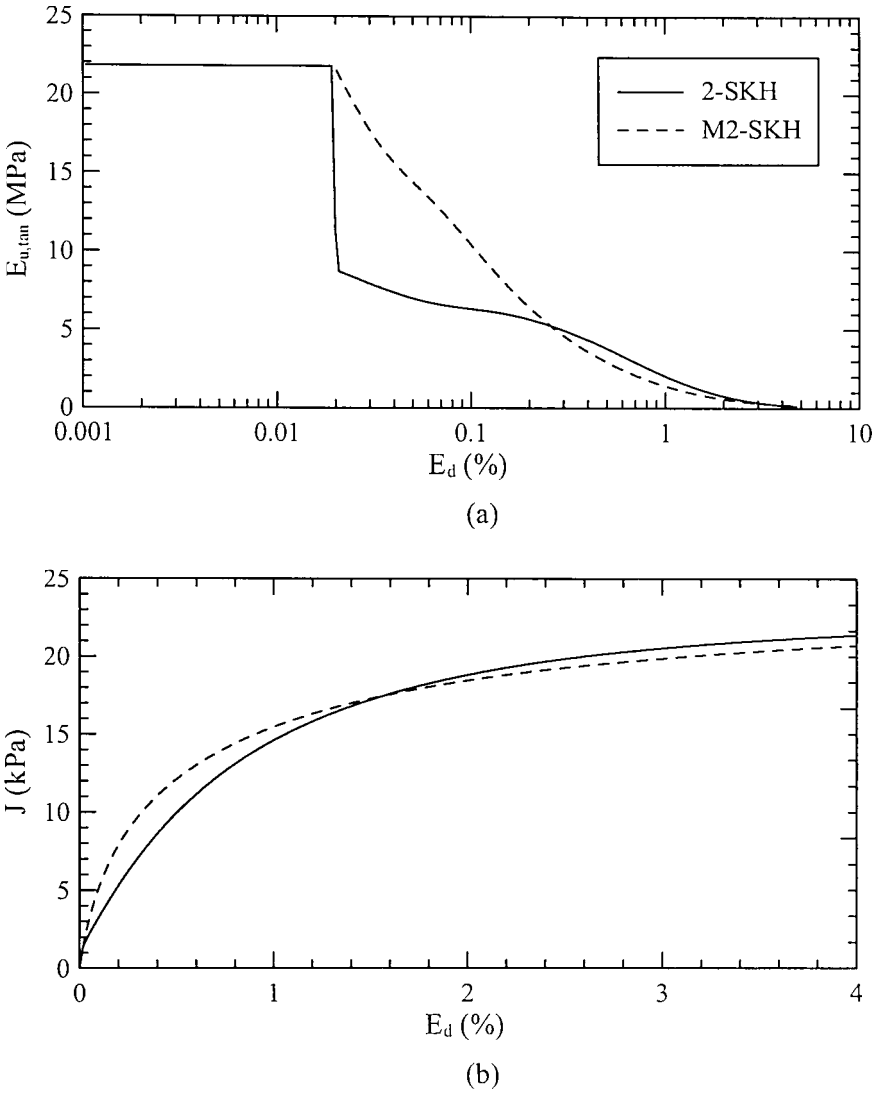


Figure 8.29: Predictions of the 2-SKH and M2-SKH models for an undrained triaxial compression test at a depth of 0.9 m for K_o = 1.0 a) stiffness-strain curve b) stress-strain curve

Figures 8.28 and 8.29 present the stress-strain and stiffness-strain response predicted by the two models at a depth of 2.0 m and 0.9 m respectively, during an undrained triaxial compression test. Since K_o = 1.0 and a circle was assumed for the shapes of the yield and plastic potential surfaces in the deviatoric plane, the same stress-strain and stiffness-strain response can be shown to be predicted also in plane strain compression and plane strain extension. Figures 8.28 and 8.29 show that, due to the drop in stiffness, a softer initial response is predicted for the 2-SKH model, than for the M2-SKH model.

Fill material

The fill material was modelled in the same way as in the previous analyses. The

parameters used are given in section 8.5.2.3.

8.5.3.4 Analyses results

Both analyses predicted a failure height of 2.7 m. Figure 8.30 presents the vectors of incremental displacement at failure for the analysis with the 2-SKH model. It can be seen that the failure mechanism is quite different to the one shown in Figure 8.15. The failure surface in Figure 8.30 is shallow and does not involve a great depth of the clay crust and the layer beneath. This is due to the constant value of *OCR* prescribed in the clay crust, which results in the soil becoming gradually weaker close to the surface. Although this failure mechanism may be unrealistic, the early stages of the analyses, before the failure mechanism starts to form, still provide important information on the deformational behaviour predicted by the two models. A similar failure mechanism was also observed for the analysis with the M2-SKH model.

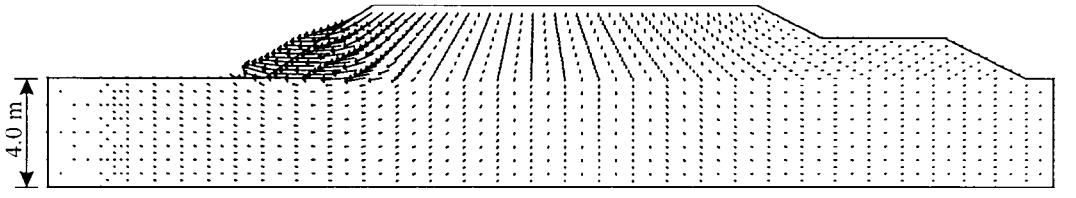


Figure 8.30: Vectors of incremental displacement at failure for the 2-SKH model and $K_o = 1.0$

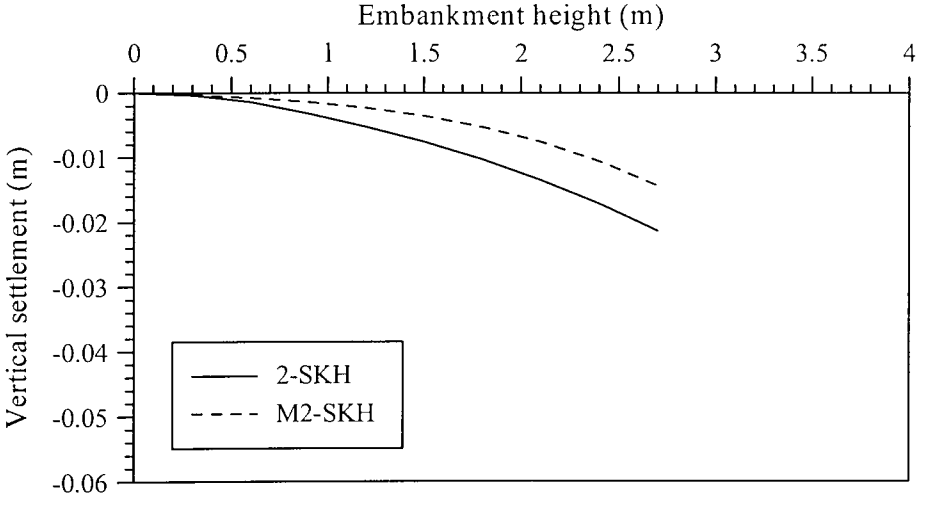


Figure 8.31: Vertical settlement at the centreline of the embankment versus embankment height predicted by the 2-SKH and M2-SKH models for $K_o = 1.0$

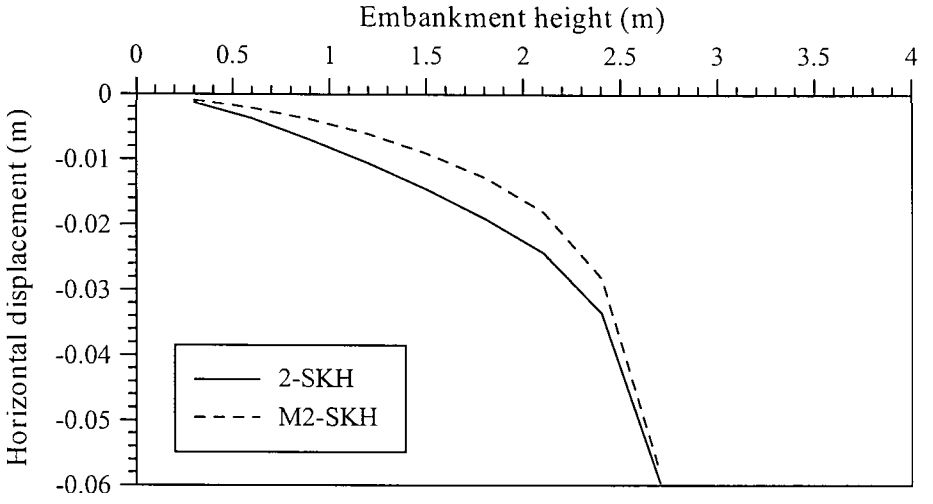


Figure 8.32: Horizontal displacement at the toe of the embankment versus embankment height predicted by the 2-SKH and M2-SKH models for K_o = 1.0

Figure 8.31 illustrates the vertical settlement at the centreline of the embankment plotted against the embankment height. The horizontal displacement at the toe of the embankment is plotted against the embankment height in Figure 8.32. Figure 8.32 shows that there is a sudden increase of the horizontal displacement at the toe, at an embankment height of 2.4 m, which is a sign of the subsequent failure. No such sign can be seen in the vertical settlement in Figure 8.31. This is because the failure mechanism does not involve this area. However, inspection of the movements in Figures 8.31 and 8.32, for embankment heights lower than 2.4 m, shows that both plots reveal similar behaviour. The movements predicted by the M2-SKH model are significantly lower than those predicted by the 2-SKH model. This means that the stiffness-strain behaviour at the small strain range influences significantly the predicted movements, with the drop in stiffness for the 2-SKH model resulting in a considerably softer behaviour for this model.

Although no analyses with the three-surface and modified three-surface models are presented here, a similar behaviour can be expected for the three-surface model, which also exhibits a non-smooth elasto-plastic transition and a drop in stiffness. As shown in Chapter 7, the three-surface model can predict smaller drops in stiffness than the two-surface model, due to the presence of the history surface, and depending on the chosen model parameters. The amount by which the pre-failure movements are under-predicted is expected to depend on the magnitude of the predicted drop in stiffness.

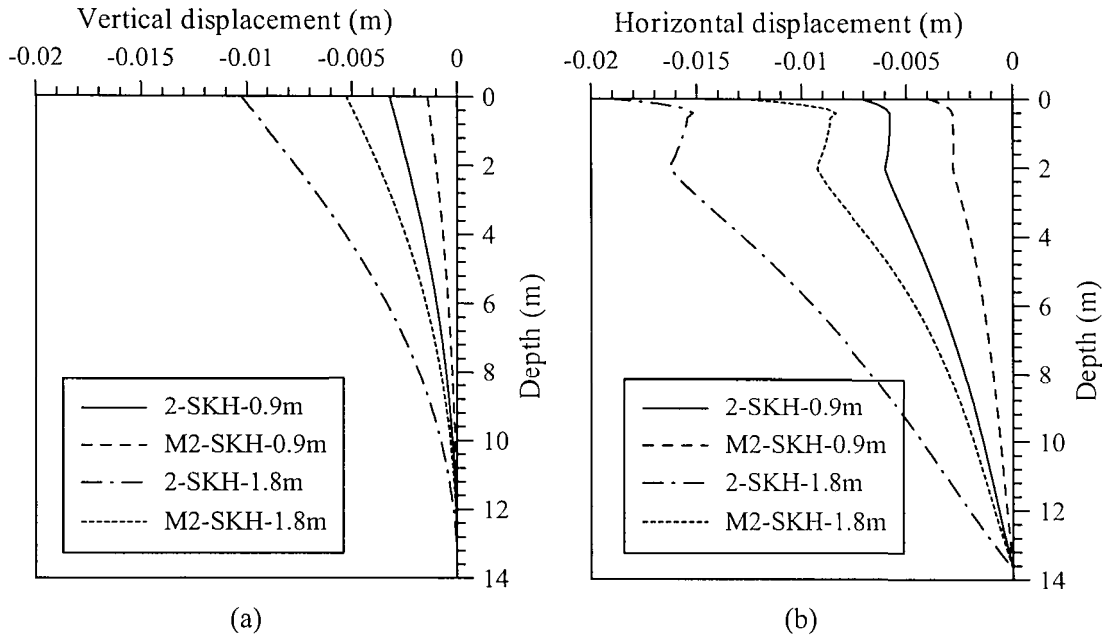


Figure 8.33: Movements predicted by the 2-SKH and M2-SKH models for K_o = 1.0 and embankment heights of 0.9 m and 1.8 m a) vertical displacement at the centreline of the embankment b) horizontal displacement under the toe of the embankment

Embankment height (m)	0.9	1.8	2.4
$\frac{\lvert v^{max}_{2-SKH}\rvert - \lvert v^{max}_{M2-SKH}\rvert}{\lvert v^{max}_{2-SKH}\rvert}\cdot 100$	56.3	48.8	38.3
$\frac{\lvert u^{max}_{2-SKH}\rvert - \lvert u^{max}_{M2-SKH}\rvert}{\lvert u^{max}_{2-SKH}\rvert}\cdot 100$	44.9	33.0	16.0

v : vertical movement below the centreline of the embankment
u : horizontal movement below the toe of the embankment

Table 8.10: Percentage difference between the maximum movements predicted by the 2-SKH and M2-SKH models: K_o = 1.0

Figure 8.33a presents the distribution of vertical movements with depth below the centreline of the embankment for two stages of the analyses (embankment heights of 0.9 m and 1.8 m). Figure 8.33b plots the horizontal movements with depth beneath the toe of the embankment for the same embankment heights. For both stages the movements predicted by the M2-SKH model are lower than those predicted by the 2-SKH model. Table 8.10 summarises the percentage difference between the maximum vertical movement, beneath the centreline, and the maximum horizontal movement, beneath the toe, predicted by the two analyses. It can be seen that for an embankment height of 1.8 m there is still a high percentage difference in the predicted movements as compared to Table 8.4. Moreover, the predicted movements remain always lower for the

M2-SKH model. This is because in this case the predicted stiffness in plane strain extension is the same as the one in plane strain and triaxial compression and this does not become significantly softer for the M2-SKH model as it happens in the analyses presented in the previous section.

8.6 The effect of the deviatoric shapes on the failure height of the embankment

8.6.1 Introduction

This section investigates the effect of the shape of the yield and plastic potential surfaces in the deviatoric plane on the failure height of the embankment. Four different combinations of the yield and plastic potential deviatoric shapes are considered. The same undrained strength profile in triaxial compression is prescribed to all four cases and the failure height of the embankment obtained for each case, under plane strain conditions, is examined.

8.6.2 Analyses details

In the analyses presented in this section only the 2-SKH model was used. It can be shown, though, that similar results can be obtained for the M2-SKH model, since the failure conditions in both models are governed by the same bounding surface.

The four cases considered are described as follows. In case A the yield and plastic potential surfaces were assumed to have a circular shape in the deviatoric plane. In case B the yield surface had the shape of a Mohr-Coulomb hexagon and the plastic potential surface had a circular shape. In case C both the yield and plastic potential surfaces were assumed to have a Lade shape in the deviatoric plane. Finally, in case D, the yield surface had a Lade shape and the plastic potential had a circular shape in the deviatoric plane. These four combinations are the same as those examined in the single element analyses of sections 4.6.3, of Chapter 4 and 5.5.3, of Chapter 5. Moreover, case B is the analysis of the 2-SKH model presented in section 8.5.2.

All the analyses were carried out undrained (see section 3.3.1.1). The finite element mesh used in the analyses is that shown in Figure 8.6. This mesh was generated for a failure height of 4.6 m. In the analyses in which the embankment failure height exceeded

this value, the additional layers were modelled by applying stress increments on the crest, in order to represent the weight of the layers.

8.6.3 Model parameters

Clay layer

For the 2-SKH model the parameters N, λ^*, κ^*, G_e, R and ψ were kept at the same values as in Table 8.1. A K_o = 0.67 and the *OCR* profile of Figure 8.13 were prescribed as initial conditions, similar to section 8.5.2.

The parameters defining the shape of the yield and plastic potential surfaces in the deviatoric plane are summarised in Table 8.11. These parameters were chosen so that all four cases predicted the same values of φ' and $g(\theta)$ in triaxial compression (Table 8.12).

Case	X	Y	Z	Y_p	Z_p
A	0.618	0.0	1.0	0.0	1.0
C	0.54	0.416	0.25	0.416	0.25
D	0.54	0.416	0.25	0.0	1.0
	φ'	-	-	X_p	Z_p
B	27°	-	-	0.0	1.0

Table 8.11: Model parameters defining the shape of the yield and plastic potential surfaces in the deviatoric plane

Case	Triaxial Compression			Plane strain Conditions		
	θ	$g(\theta)$	φ'	θ	$g(\theta)$	φ'
A	-30°	0.618	27°	0°	0.618	38.2°
B	-30°	0.618	27°	0°	0.454	27°
C	-30°	0.618	27°	-16.5°	0.594	31.3°
D	-30°	0.618	27°	0°	0.54	32.7°

Table 8.12: Values of θ, $g(\theta)$ and equivalent values of φ' for the four cases analysed

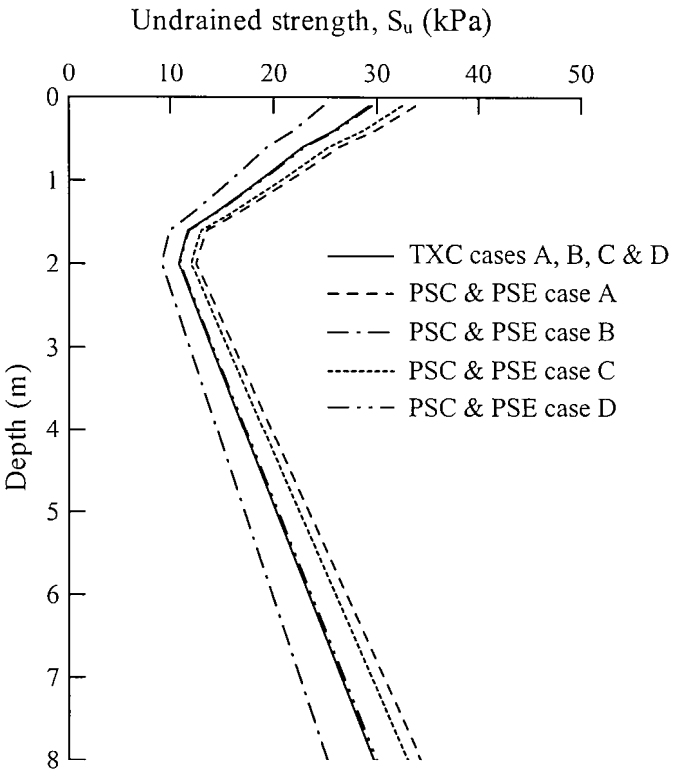


Figure 8.34: Undrained strength profiles predicted by cases A, B, C and D

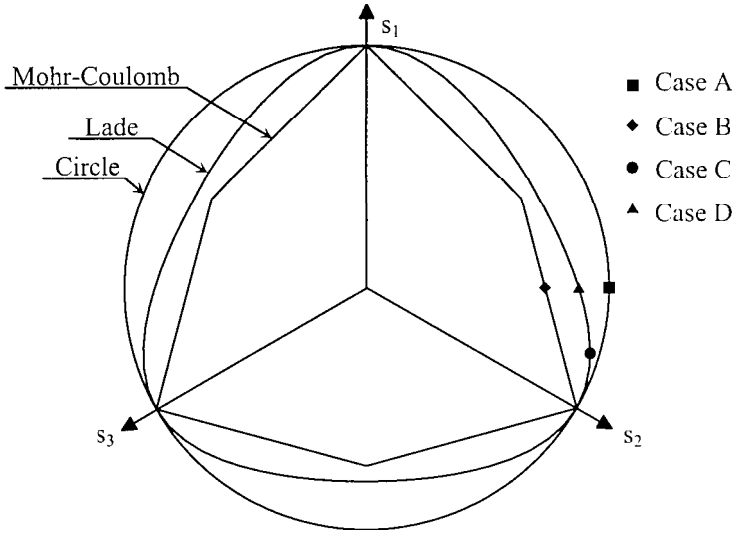


Figure 8.35: Failure surfaces in the deviatoric plane and the values of $g(\theta)$ obtained at plane strain conditions

This resulted in all four cases predicting the same undrained strength profile with depth in triaxial compression, see Figure 8.34. The values of θ, $g(\theta)$ and the equivalent values of φ' obtained under plane strain conditions for each case can be seen in Table 8.12. These values resulted in four different undrained strength profiles under plane strain

conditions which can be seen in Figure 8.34. Figure 8.35 shows the shape of the yield/failure surfaces in the deviatoric plane and the values of $g(\theta)$, which are tabulated in Table 8.12. It is interesting to note that, under plane strain conditions, although the value of φ' for case D is higher than the value of φ' for case C, the value of $g(\theta)$ for case D is lower than the value of $g(\theta)$ for case C and so is the plane strain undrained strength profile in Figure 8.34.

Fill material

The fill material was modelled in the same way as in the previous analyses. The parameters used are given in section 8.5.2.3.

8.6.4 Analyses results

The four analyses predicted different failure heights for the embankment. This was expected as all four cases predicted different undrained strength profiles under plane strain conditions.

Figure 8.36 presents the vertical settlement at the centreline of the embankment against the embankment height for the four analyses. The horizontal displacement at the toe of the embankment against the embankment height can be seen in Figure 8.37.

Table 8.13 quotes the failure height predicted for each case. It can be seen that case B, which is the analysis with the 2-SKH model presented in section 8.5.2, predicted the

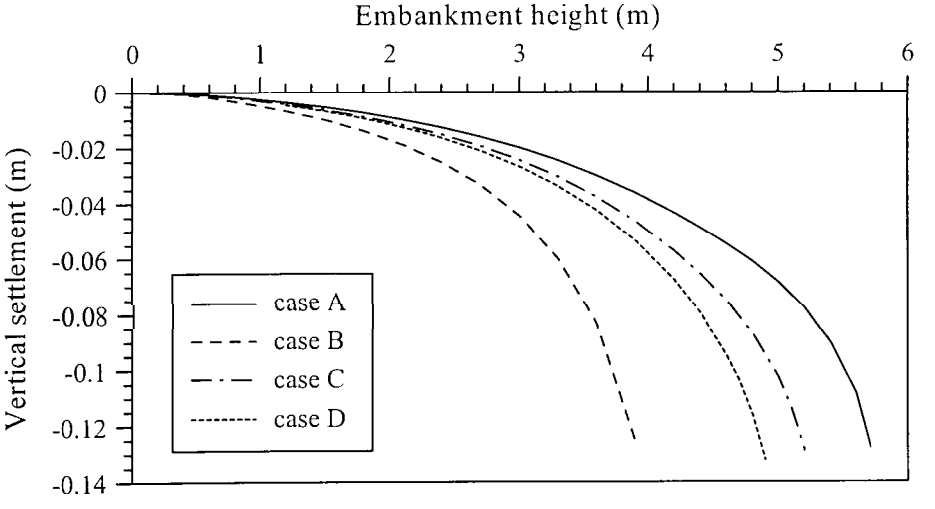


Figure 8.36: Vertical settlement at the centreline of the embankment versus embankment height predicted by cases A, B, C and D

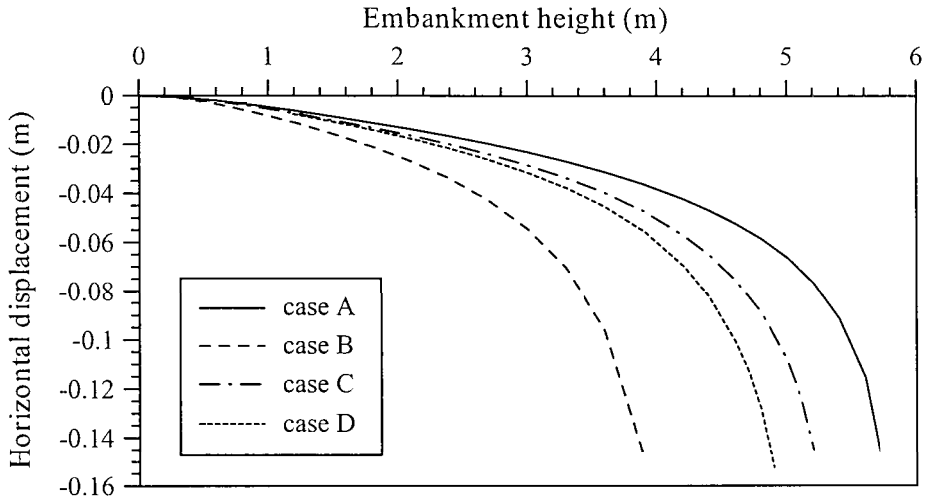


Figure 8.37: Horizontal displacement at the toe of the embankment versus embankment height predicted by cases A, B, C and D

Case	A	B	C	D
Failure height (m)	5.7	3.9	5.2	4.9

Table 8.13: Predicted embankment failure heights

failure height of 3.9 m. Case A, which assumed a circular shape for both yield and plastic potential surfaces, predicted a failure height of 5.7 m. This is approximately 46% higher than the embankment height predicted by case B. Case C, in which both yield and plastic potential surfaces had the Lade shape, predicted a failure height of 5.2 m, which is 33% higher than what case B predicted. Finally, case D (Lade shape for the yield surface and circular shape for the plastic potential) predicted a failure height of 4.9 m. This is almost 26% higher than the height predicted by analysis B. Comparison of analyses C and D, which differed only in the shape of the plastic potential surface, shows that case C predicted a failure height which is 6% higher than case D. It is interesting to note again that case C predicted a higher failure height than case D although the φ' under plane strain conditions for case C is lower than the φ' for case D. Clearly what controls failure in plane strain analyses is the Lode's angle θ and the corresponding $g(\theta)$ value obtained under plane strain conditions.

It is also interesting that in the analyses of Zdravkovic et al. (2002), with the MCC model, the analysis which matched the TXC profile in Figure 8.4 predicted an embankment failure height which was 48% higher than the failure height predicted by the analysis which matched the DSS profile in Figure 8.4. This implies that, for a model

which predicts isotropic strength, the shape of the yield and plastic potential surfaces in the deviatoric plane is equally important as the undrained strength profile chosen for design (i.e. TXC profile or DSS profile). Clearly these should be chosen to be consistent.

8.7 Summary and conclusions

This chapter examined the behaviour of an embankment when the soft clay deposit on which it is founded was modelled with kinematic hardening models. Two studies were presented. The first one investigated the pre-failure deformational behaviour of the embankment, predicted by the two-surface and modified two-surface models, when the same undrained strength was assigned to both models. The behaviour predicted by the two kinematic hardening models was also compared with predictions of the modified Cam Clay model. The second study explored the effect of the shape of the yield and plastic potential surfaces in the deviatoric plane on the predicted failure height of the embankment.

a) First study: Pre-failure behaviour of the embankment

The main differences between the kinematic hardening models and the modified Cam Clay model can be briefly summarised as follows. The kinematic hardening models predict high non-linearity and plasticity from the early stages of loading, while the modified Cam Clay model predicts an elastic almost linear behaviour within the yield surface. Moreover, the kinematic hardening models are capable of predicting different stiffness between compression and extension paths, which is not the case for the modified Cam Clay model. An important difference between the two kinematic hardening models is that the two-surface model shows a non-smooth elasto-plastic transition, which results in an unrealistic drop in stiffness once the stress state becomes elasto-plastic. On the contrary, the modified two-surface model is capable of predicting a smooth elasto-transition, which results in a realistic representation of pre-failure non-linearity.

This study was divided into two parts. The first part examined the deformational behaviour of the embankment, when the same undrained strength profile was assigned to the two-surface, modified two-surface and modified Cam Clay models. The second part assessed the effect of the drop in stiffness predicted by the two-surface model, by comparing the behaviour predicted by the two kinematic hardening models for a

$K_o = 1.0$.

i) Analyses with kinematic hardening models and the modified Cam Clay model

The conclusions that can be drawn from this part of the study are the following:

- When the same undrained strength profile is prescribed to all models, then these predict the same failure height of the embankment. However, a different deformational behaviour is predicted by each model.

- The pre-failure deformations are influenced by non-linearity, as well as the stiffness response in both compression and extension paths.

Comparison of the two kinematic hardening models

- For similar stress-strain curves in compression the models predict a different response in extension. This combined with the drop in stiffness predicted by the two-surface model resulted in the modified two-surface model predicting smaller movements than the two-surface model, up to an embankment height of approximately 2.7 m, and larger movements than the two-surface model, for higher embankment heights.

- For an embankment height of 0.9 m the maximum vertical movement, below the centreline, and the maximum horizontal movement, beneath the toe of the embankment, predicted by the modified two-surface model, were 63% and 50% lower respectively, than those predicted by the two-surface model. For an embankment height of 3.3 m these were 33% and 30% higher respectively.

Comparison of the kinematic hardening models with the modified Cam Clay model

- When an average stiffness, applicable to a stress level of 50% in triaxial compression, is chosen for the modified Cam Clay model, then this study shows that the modified Cam Clay model overpredicts in the initial stages, and underpredicts, in the later stages of the embankment construction, the pre-failure movements, as compared to the kinematic hardening models.

- The difference in the movements predicted at the later stages of construction is even more pronounced when the modified Cam Clay model is compared with the modified two-surface model. This is due to the predicted response depending

not only on linearity but also on the stiffness response in both compression and extension paths.

- For an embankment height of 0.9 m the maximum vertical movement, below the centreline, and the maximum horizontal movement beneath the toe of the embankment, predicted by the modified Cam Clay model, were 85% and 44% higher respectively, than those predicted by the two-surface model. For an embankment height of 3.3 m these were 17% and 36% lower respectively.

- For an embankment height of 0.9 m the maximum vertical movement, below the centreline, and the maximum horizontal movement, beneath the toe of the embankment, predicted by the modified Cam Clay model, were 193% and 73% higher respectively, than those predicted by the modified two-surface model. For an embankment height of 3.3 m these were 63% and 69% lower respectively.

ii) Analyses with kinematic hardening models and $K_o = 1.0$

In these analyses, each kinematic hardening model predicted the same stiffness in compression and extension. In this way, this part of the study isolated the effect of the non-smooth elasto-plastic transition, predicted by the two-surface model, on the pre-failure deformation of the embankment.

The conclusions that can be drawn from this study are the following:

- The drop in stiffness predicted by the two-surface model results in the model significantly overpredicting the pre-failure movements, as compared to the modified two-surface, which predicts a smooth stiffness degradation curve.

- For an embankment height of 0.9 m the maximum vertical movement, below the centreline, and the maximum horizontal movement, beneath the toe of the embankment, predicted by the modified two-surface model, were 56% and 45% smaller respectively, than those predicted by the two-surface model. For an embankment height of 1.8 m these were 49% and 33% lower respectively.

b) Second study: The effect of the deviatoric shapes on the failure height of the embankment

In this study four different combinations of the shape of the yield and plastic potential

surfaces in the deviatoric plane were examined. In all four cases the same undrained strength profile in triaxial compression was prescribed. This resulted in a different undrained strength profile under plane strain conditions. The shapes examined included a Mohr Coulomb shape, a circular shape and a Lade shape for the yield surface and a circular shape and a Lade shape for the plastic potential.

The following conclusions can be drawn from this study:

- All four cases predicted a different failure height for the embankment.
- The highest failure height was predicted for the case in which both yield and plastic potential surfaces had a circular shape. This was 46% higher than the case where the yield surface had the shape of a Mohr Coulomb hexagon and the plastic potential had a circular shape. This latter case also predicted the lowest failure height. The case in which both yield and plastic potential surfaces had a Lade shape and the case in which the yield surface had a Lade shape and the plastic potential had a circular shape predicted a failure height which was 33% and 26% higher respectively than the lowest predicted failure height.
- Hence, it can be concluded that the shape of the yield and plastic potential surfaces in the deviatoric plane can have a significant effect on the predicted failure height of the embankment.
- For a model which predicts isotropic strength the choice of the shape of the yield and plastic potential surfaces in the deviatoric plane is as important as the undrained strength profile chosen for design (i.e. triaxial compression profile or direct simple shear profile).

Chapter 9

The behaviour of kinematic hardening models in tunnelling problems

9.1 Introduction

This chapter investigates the behaviour of the four kinematic hardening models, presented in this thesis, in problems involving tunnel construction. Two studies are presented. The first study explores the behaviour of a tunnel in London Clay. The influence of the configurations of the kinematic surfaces at the end of an assumed geological history and of different initial stress conditions is examined for each model. The second study models the twin tunnels of the Jubilee Line Extension (JLE) of the London Underground network beneath St James's Park (London, UK). In both studies the predictions of the kinematic hardening models are compared with analyses using a non-linear elastic pre-yield model.

Before the two studies are presented, a short literature review of the use of constitutive models in the finite element analysis of tunnels will first be given.

9.2 Constitutive models in tunnelling problems

This review will be mostly concentrated on tunnels excavated in overconsolidated clays. Finite element analyses of tunnel excavation in such soils generally predict shallower and wider surface settlement profiles than observed in practice.

Gunn (1993) demonstrated the importance of modelling the non-linear small strain

behaviour of the soil in the prediction of the surface settlement trough. The use of a non-linear elastic perfectly plastic model improved the predicted settlement profile as compared with linear elastic pre-yield models.

Addenbrooke et al. (1997) reached similar conclusions when investigating the influence of different elastic pre-yield models combined with the same plastic behaviour (Mohr-Coulomb yield surface with a non-associated flow rule). The elastic pre-yield models, used in their analyses, included a linear elastic model, the non-linear model presented by

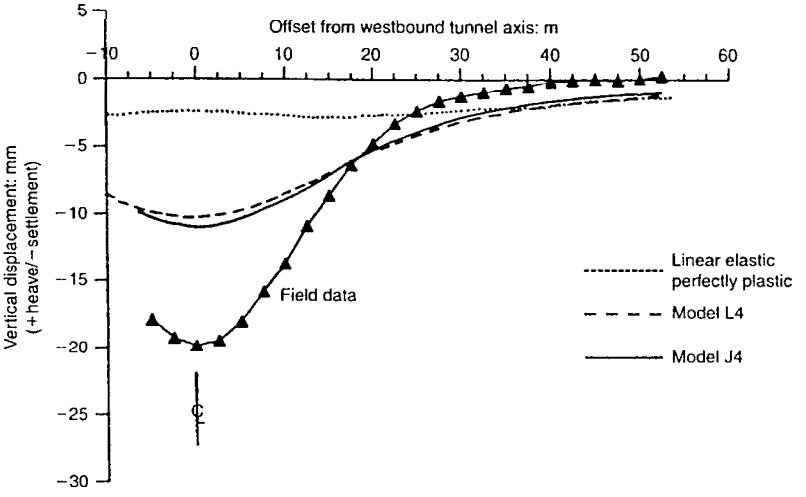


Figure 9.1: The effect of non-linearity on the predicted surface settlement trough: St. James's Park (after Addenbrooke et al. (1997))

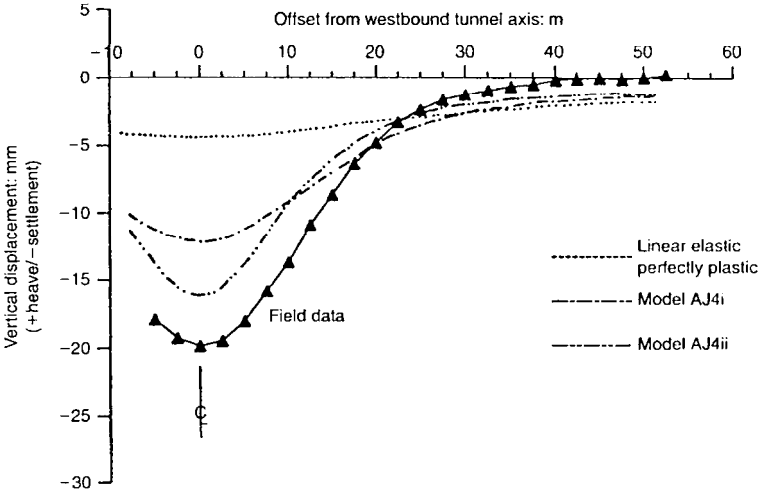


Figure 9.2: The effect of anisotropy on the predicted surface settlement trough: St. James's Park (after Addenbrooke et al. (1997))

Jardine et al. (1986) and Jardine et al. (1991) and the non-linear model developed by Puzrin and Burland (1998) (these last two models have been reviewed in section 2.3.3.1 and in the work of Addenbrooke et al. were referred to as models J4 and L4 respectively). The models were used to analyse the twin tunnels of the Jubilee Line Extension beneath St. James's Park, which were constructed within the overconsolidated London Clay stratum. Figure 9.1 shows the predicted surface settlement troughs above the westbound tunnel plotted against the field data. Both non-linear models (J4 and L4) predicted similar profiles which were deeper and narrower in comparison with the linear elastic model. However, the predictions of the non-linear models were still too shallow and wide when compared with the field measurements.

Simpson et al. (1996), on the basis of finite element analyses of the Heathrow Express trial tunnel, suggested that introducing anisotropy improved the predicted surface settlement profile. However, Addenbrooke et al. (1997) found that the use of an anisotropic pre-yield model improved substantially the predicted settlement trough, above the westbound tunnel at St. James's Park, only if a very soft anisotropic shear modulus was used, which cannot be justified from test data on London Clay. Figure 9.2 presents the predictions of two analyses using an anisotropic version of model J4 (referred to as model AJ4). Analysis AJ4i adopted anisotropic ratios based on the work of Burland and Kalra (1986) ($m' = G_{vh}/E_v' = 0.444$) whereas in analysis AJ4ii an unrealistically small ratio $m' = 0.2$ was assumed. Figure 9.2 shows that the analysis AJ4i improved slightly the predicted settlement trough whereas analysis AJ4ii predicted a much deeper settlement trough closer to the field observations.

The first use of kinematic hardening models in tunnelling problems was carried out by Stallebrass et al. (1994), who used the three-surface kinematic hardening model to perform an investigation into the effect of recent stress history on ground movements around tunnels. A deep and a shallow tunnel were considered. A number of different stress histories relevant to overconsolidated clays were simulated before the excavation of the tunnels. The K_o values resulting at the end of the stress histories were similar in all the analyses. Figures 9.3a and 9.3b present the surface settlement profiles for the shallow and the deep tunnel respectively (it should be noted that the volume loss varied between 1.06% and 1.29% for the shallow tunnel and between 2.78% and 3.27% for the deep tunnel). The key in the figure gives a sketch of the recent stress paths followed by the soil in the vicinity of the tunnel, together with the approximate positions of the two

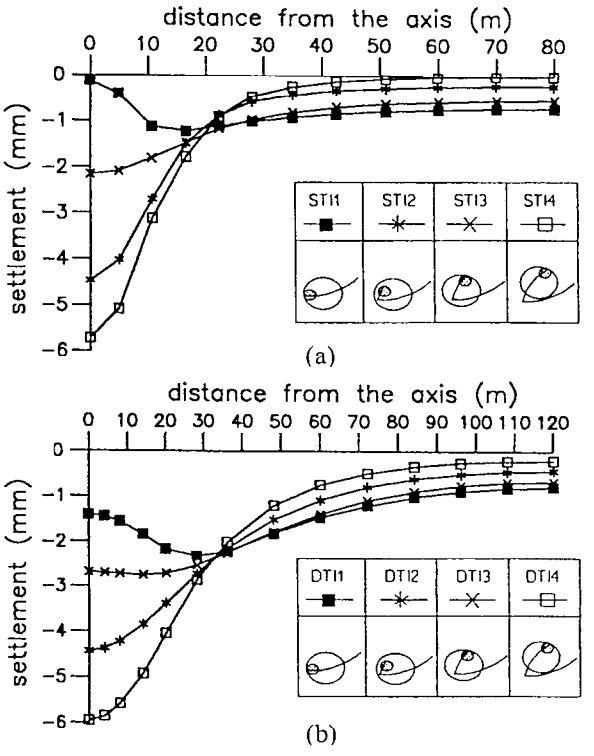


Figure 9.3: The effect of recent stress history on the predicted surface settlement trough a) shallow tunnel b) deep tunnel (after Stallebrass et al. (1994))

kinematic surfaces, the yield and history surfaces, before excavation. Figure 9.3 indicates that the recent stress history has a strong effect on the predicted surface settlement trough.

All the analyses reported above are plane strain analyses. In reality tunnel construction is a three dimensional process. The inability to predict the surface settlement troughs above tunnels excavated in overconsolidated clays, in plane strain analyses, has often be attributed to the two dimensional nature of the analyses. However, recent three dimensional finite element analyses (Dolezalova (2002), Franzius (2004)) have shown that 3D modelling does not improve substantially the transverse surface settlement profile predicted by the 2D analyses in a high K_o regime. Moreover, both 2D and 3D analyses indicate that the predicted surface settlement trough is highly dependent on the value of K_o. It has been shown that a deep and narrow settlement trough close to the field observations can be achieved if K_o = 0.5 is assumed (Dolezalova (2002)), or introduced locally around the tunnel (Addenbrooke (1996)). However, this value of K_o is clearly relatively low when considering highly overconsolidated clays.

9.3 Geometry of the problem

For both studies the geometry of the twin tunnels at St. James's Park was used. The soil profile at St. James's Park can be seen in Figure 9.4. It consists of a layer of Made Ground underlain by Alluvium. This is in turn underlain by a layer of Terrace Gravel. Below the Terrace Gravel there is a deep layer of London Clay. Nyren et al. (2001) reported that the London Clay at St. James's Park extends to depths in excess of 40 m below the ground level. The water table is located at the top of the Terrace Gravel.

The finite element mesh used in the analyses is presented in Figure 9.5. All the analyses performed were plane strain with 2x2 integration and used eight nodded isoparametric quadrilateral elements.

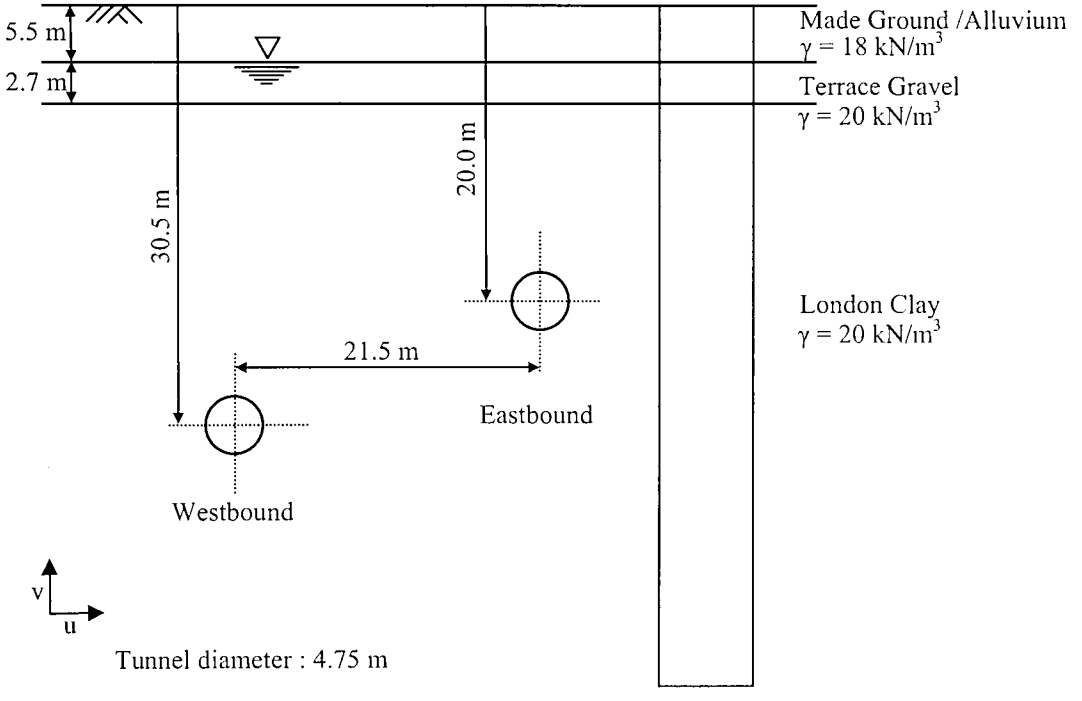


Figure 9.4: Soil profile and tunnel geometry at St. James's Park

9.4 Constitutive models used in the analyses

9.4.1 London Clay

All four kinematic hardening models, described in Chapters 4, 5 and 6, were used in order to model the London Clay deposit. In abbreviation, the models will often be

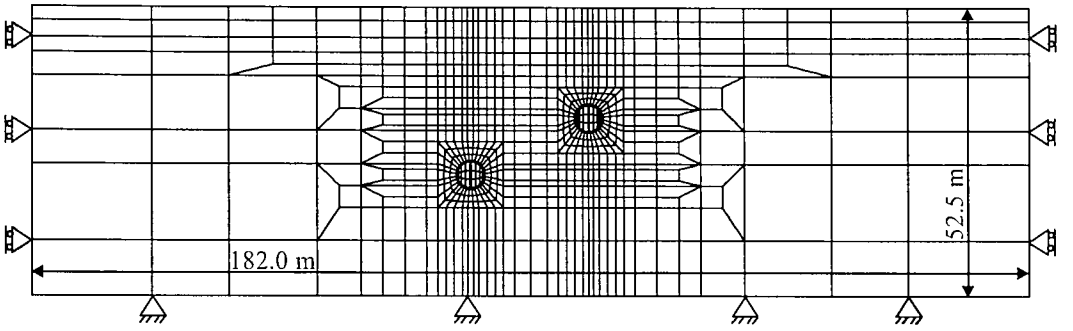


Figure 9.5: Finite element mesh

referred to as 2-SKH for the two-surface kinematic hardening model, M2-SKH for the modified two-surface kinematic hardening model, 3-SKH for the three-surface kinematic hardening model and M3-SKH for the modified three-surface kinematic hardening model. Moreover, the model J4 used by Addenbrooke et al. (1997) for the analyses of the twin tunnels at St. James's park was also used in these analyses. As already mentioned, this model combines the non-linear elastic model presented by Jardine et al. (1986) and Jardine et al. (1991) (see section 2.3.3.1), with a Mohr-Coulomb yield surface and a non-associated flow rule.

Model J4

The expressions that describe the variation of the tangent shear modulus, G, and bulk modulus, K, with mean effective stress, p', and strain level in the non-linear elastic region, as implemented into ICFEP, are given as follows:

$$\frac{3G}{p'} = A + B\cos\left(\alpha X^{\gamma}\right) - \frac{B\alpha\gamma X^{\gamma-1}}{2.303}\sin\left(\alpha X^{\gamma}\right) \tag{9.1}$$

$$\frac{K}{p'} = R + S\cos\left(\delta Y^{\eta}\right) - \frac{S\delta\eta Y^{\eta-1}}{2.303}\sin\left(\delta Y^{\eta}\right) \tag{9.2}$$

where:

$$X = \log_{10}\left(\frac{E_d}{\sqrt{3}C}\right) \tag{9.3}$$

$$Y = \log_{10}\left(\frac{\varepsilon_v}{\sqrt{3}T}\right) \tag{9.4}$$

In the above equations the deviatoric strain, E_d, and the volumetric strain, ε_v, are described by Equations 1.21 and 1.20 respectively, and A, B, C, R, S, T, α, γ, δ and η are material constants.

Due to the trigonometric nature of Equations 9.1 and 9.2, minimum ($E_{d\ min}$, $\varepsilon_{v\ min}$) and maximum ($E_{d\ max}$, $\varepsilon_{v\ max}$) strain limits are set, below and above which the tangent shear and bulk moduli vary only with mean effective stress. Furthermore, the magnitude of the stiffness is prevented from falling below specified minimum values, G_{min} and K_{min}.

The Mohr-Coulomb yield surface can be expressed in terms of the invariants, p', J and θ, described by Equations 1.8, 1.9 and 1.11 respectively, as follows:

$$F = J - (\alpha + p')\, g(\theta) = 0 \tag{9.5}$$

where α is the tensile limit of p' and is related to the cohesion, c', as $\alpha = c'/g(\theta = 0°)$, θ is the Lode's angle and $g(\theta)$ is given by Equation 4.27:

$$g(\theta) = \frac{\sin\varphi'}{\cos\theta + \dfrac{\sin\theta \sin\varphi'}{\sqrt{3}}} \tag{9.6}$$

where φ' is the angle of shearing resistance.

The representation of the yield surface in J-p' space and the deviatoric plane can be seen in Figure 9.6.

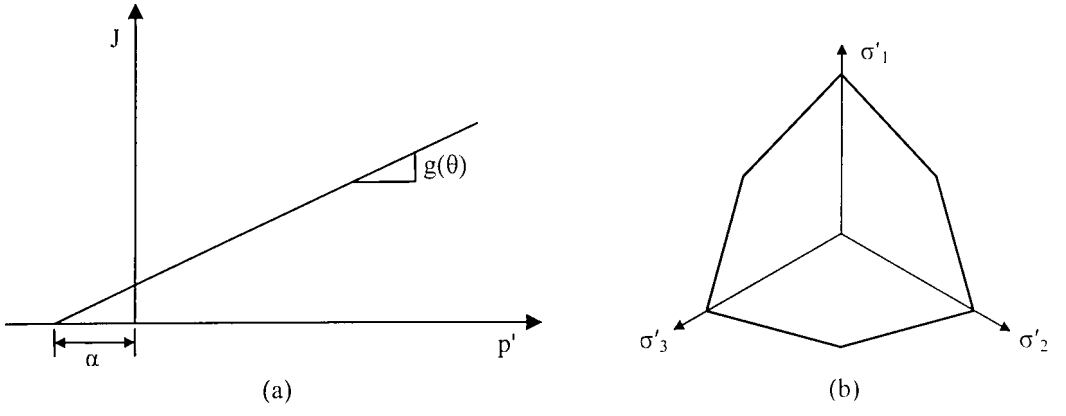


Figure 9.6: Mohr-Coulomb yield surface a) J-p' space b) Deviatoric plane

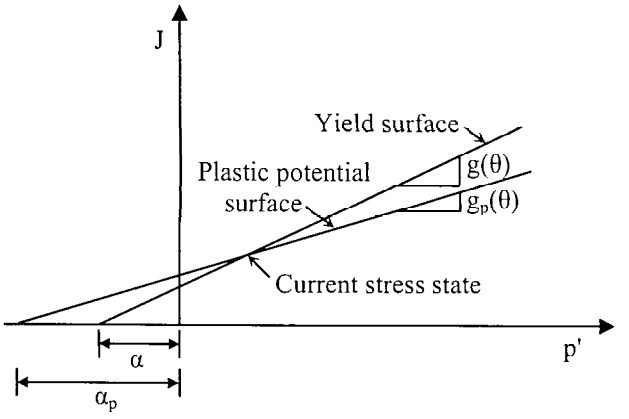


Figure 9.7: Mohr-Coulomb yield surface and plastic potential surface

The plastic potential adopted in the model has a similar form to Equation 9.5 but with φ' replaced by the angle of dilation, v:

$$F = J - \left(\alpha_p + p'\right) g_p\left(\theta\right) = 0 \tag{9.7}$$

where α_p is akin to α in the yield function, see Figure 9.7, and $g_p(\theta)$ is given by the following equation:

$$g_p\left(\theta\right) = \frac{\sin v}{\cos\theta + \frac{\sin\theta \sin v}{\sqrt{3}}} \tag{9.8}$$

No hardening law is adopted in the model and hence the yield surface stays fixed in J-p'-θ space.

9.4.2 Terrace Gravel

The Terrace Gravel was modelled with model J4 in all the analyses.

9.4.3 Made Ground/Alluvium

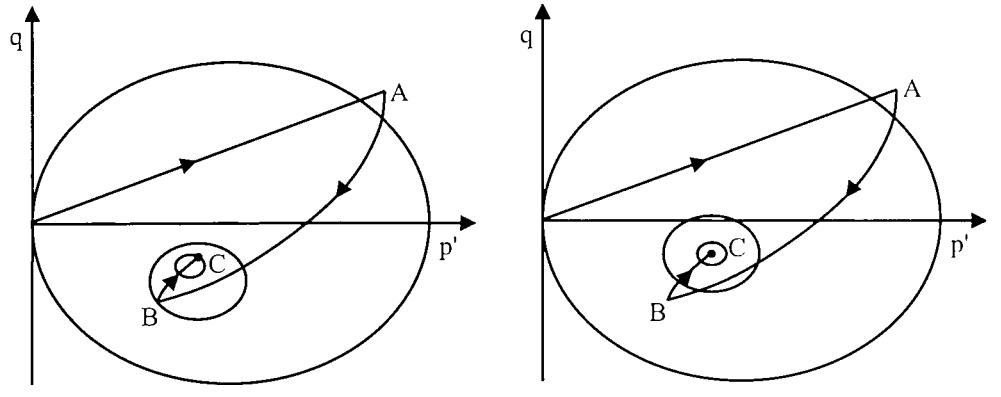
The layers of Made Ground and Alluvium were modelled as a single layer using an isotropic linear elastic model.

9.5 Analyses of a tunnel in London Clay

9.5.1 Introduction

This study investigates the effect of initial conditions on the behaviour of a 30.5 m deep and a 20 m deep tunnel in London Clay, for each of the four kinematic hardening models. The initial conditions examined involve the configuration of the kinematic surfaces, and the K_o profile before the excavation of the tunnel. The above analyses are compared with analyses using the model J4. Moreover, in this study, the effect of the rate of decay of stiffness assumed in the constitutive models is also investigated.

The effect of the configuration of the kinematic surfaces is examined by considering a typical geological history of the London Clay deposit, involving erosion of the overlying deposits and the upper part of the London Clay, followed by deposition of the gravel layers. Figure 9.8a shows a typical stress path followed by a London Clay element in the vicinity of the tunnels, during the above geological history, and the configuration of the kinematic surfaces at the end of it. This is the first configuration of the surfaces considered in the analyses (configuration A). Since in the kinematic hardening models the configuration of the kinematic surfaces provides a memory of the previous stress history, configuration A simulates the effect of the recent stress history on the subsequent excavation of the tunnel (how satisfactorily each of the four models can



(a) Configuration A

(b) Configuration B

Figure 9.8: a) Configuration of the kinematic surfaces at the end of the assumed geological history for an element of London Clay in the vicinity of the tunnels
b) centring of the kinematic surfaces at the end of the geological history

simulate the effect of the recent stress history has been investigated in section 7.3). The second configuration of the surfaces considered in the analyses is shown in Figure 9.8b (configuration B). In this configuration the kinematic surfaces are centred around the current stress state at the end of the geological history. This configuration simulates the effect of stress path direction on the subsequent excavation of the tunnel (see section 7.4). As mentioned in section 2.2.5 of Chapter 2, Clayton and Heymann (2001) suggested that once ageing is taken into account, then there is no effect of the recent stress history and in this case the stiffness depends on the stress path direction.

The effect of the initial K_o profile and the rate of decay of stiffness assumed in the model is investigated for the configuration of the kinematic surfaces shown in Figure 9.8b (configuration B).

In this study, the geometry of St. James's Park, shown in Figure 9.4, was used. However, since only one tunnel was considered at a time, the two tunnels are not referred here as westbound or eastbound, but rather as 30.5 m and 20 m deep tunnels.

9.5.2 Model parameters

London Clay

As aforementioned the London Clay stratum was modelled with all four kinematic hardening models and model J4. The parameters used in the kinematic hardening models were those derived from the set of tests on reconstituted London Clay presented in Chapter 7 and are summarised in Tables 7.1, 7.2 and 7.3 for the two-surface, modified two-surface and three-surface model respectively. For the modified three-surface model the same size of the history surface as for the three-surface model is assumed, hence $T = 0.2$, $S = 0.08$ and the rest of the parameters are kept the same as in Table 7.4.

For the model J4 the use of the parameters adopted by Addenbrooke et al. (1997) for the non-linear elastic part of the model was initially considered. Figure 9.9 compares the stiffness-strain curve resulting from these parameters (curve J4-1) with the experimental data from tests LR1.5, LR3 and LR7 (see Chapter 7). It can be seen that the overall predicted response is softer (up to axial strains of approximately 0.2%) than all three experimental curves. For this reason a new set of parameters was adopted for the non-

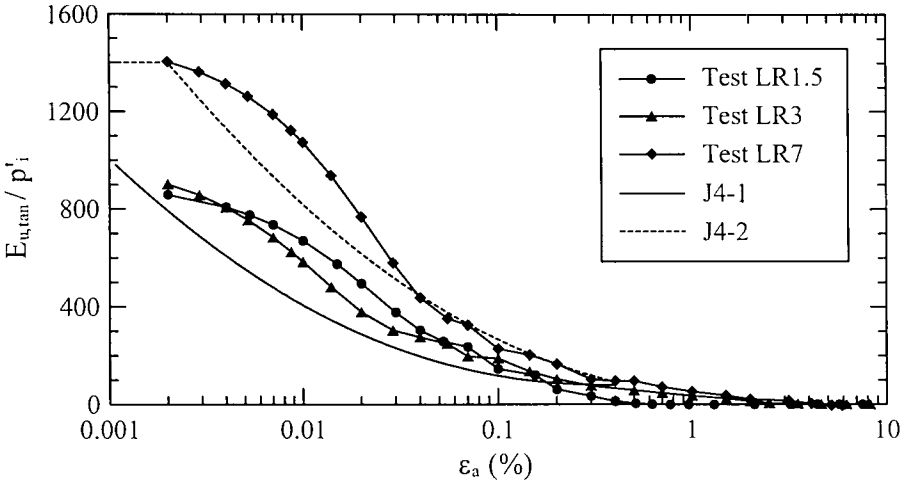


Figure 9.9: Choice of parameters for the non-linear elastic part of model J4

linear elastic part of the model, with the view of matching the stiffness curve for LR7 (OCR = 7) which is more relevant for these analyses. The new parameters are summarised in Table 9.1. The resulting stiffness-strain curve plots as curve J4-2 in Figure 9.9. Table 9.3 summarises the adopted yield and plastic potential parameters.

Terrace Gravel

The parameters for the Terrace Gravel, which was modelled with model J4, were taken from Addenbrooke et al. (1997). Table 9.2 summarises the parameters required in the non-linear elastic part of the model and Table 9.3 gives the Mohr-Coulomb yield and plastic potential parameters.

Made Ground/Alluvium

A Young's modulus E = 5000 kPa and a Poisson's ratio μ = 0.3 were assumed for the layer of Made Ground and Alluvium.

A	B	C (%)	α	γ	$E_{d\,min}$ (%)	$E_{d\,max}$	G_{min}
1600.0	1550.0	$1.0\text{x}10^{-4}$	1.2	0.617	$3.464\text{x}10^{-3}$	0.69282	2333.3
R	S	T (%)	δ	η	$\varepsilon_{v\,min}$ (%)	$\varepsilon_{v\,max}$	K_{min}
600.0	580.0	$1.0\text{x}10^{-3}$	1.9	0.420	$5.0\text{x}10^{-3}$	0.15	3000.0

Table 9.1: Material parameters for the non-linear elastic part of model J4 for London Clay

A	B	C (%)	α	γ	$E_{d\,min}$ (%)	$E_{d\,max}$	G_{min}
1380.0	1248.0	$5.0\text{x}10^{-4}$	0.974	0.940	$8.833\text{x}10^{-4}$	0.34641	2000.0
R	S	T (%)	δ	η	$\varepsilon_{v\,min}$ (%)	$\varepsilon_{v\,max}$	K_{min}
275.0	225.0	$2.0\text{x}10^{-3}$	0.998	1.044	$2.1\text{x}10^{-3}$	0.20	5000.0

Table 9.2: Material parameters for the non-linear elastic part of model J4 for Terrace Gravel

Parameters	Terrace Gravel	London Clay
c'	0	0
φ'	35.0°	22.5°
v	17.5°	11.25°

Table 9.3: Mohr-Coulomb yield and plastic potential parameters for model J4

9.5.3 Analyses details

i) Analyses with the kinematic hardening models modelling the London Clay stratum

The following sets of analyses were performed with the kinematic hardening models modelling the London Clay deposit. Sets 1 and 2 investigate the effect of the configuration of the kinematic surfaces; set 3 investigates the effect of the initial K_o profile for the kinematic surface configuration B (Figure 9.8b). Finally set 4 investigates the effect of the degradation of stiffness also for the kinematic surface configuration B.

Set 1:

Consists of 8 analyses. This set of analyses modelled the geological history of the London Clay deposit and the subsequent excavation of the tunnel. The configuration of the surfaces at the end of the geological history, in the vicinity of the tunnels, and before the tunnel excavation, can be seen in Figure 9.8a (configuration A). The initial conditions at the start of the geological history represented the London Clay strata before erosion during the last ice age took place (point A in Figure 9.8a). The elements representing the Made Ground/Alluvium and the Terrace Gravel in the finite element mesh (Figure 9.5) were absent and an overburden stress of 1835 kPa existed at the

surface of the mesh, representing approximately 180 m of overburden material. An indication of the possible overburden depth is provided by Chandler (1999), who noted that for Ashford Common geological evidence suggests that approximately 200 m of the upper part of the London Clay and the overlying deposits have been eroded. The assumed overburden stress results in an overconsolidation ratio *OCR* of approximately 6 and 8 at the tunnel axis of the 30.5 m and 20 m deep tunnels respectively. The water table was assumed to be located 2.7 m below the current water level (i.e. on the top of today's London Clay) and the pore water pressure distribution was hydrostatic with depth. An initial effective stress ratio K_o = 0.617 (K_o = 1 - sinφ' where φ' = 22.5°) was prescribed. The modelling of the geological history involved the gradual removal of the overburden stress, representing erosion (point A to point B in Figure 9.8a), followed by the construction of the Terrace Gravel and Made Ground/Alluvium layers, modelling the reloading of the London Clay due to subsequent deposition (point B to point C in Figure 9.8a). At the same time the water level was raised by 2.7 m to the top of the Terrace Gravel, maintaining the pore water pressure distribution hydrostatic with depth. An effective stress ratio K_o = 0.5 was prescribed for the Made Ground/Alluvium and Terrace Gravel. This first stage of the analysis was carried out drained. The K_o and p'_o / p' profiles obtained at the end of the modelling of the geological history can be seen in Figures 9.10 and 9.11 respectively. The subsequent excavation of the tunnel was carried out undrained (in the manner described in section 3.3.1.1). This analysis was

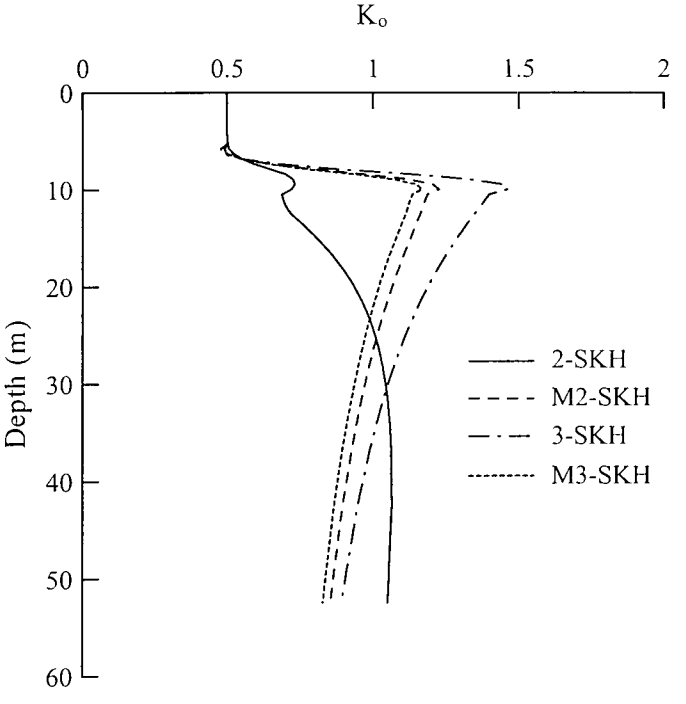


Figure 9.10: K_o profiles predicted at the end of the geological history

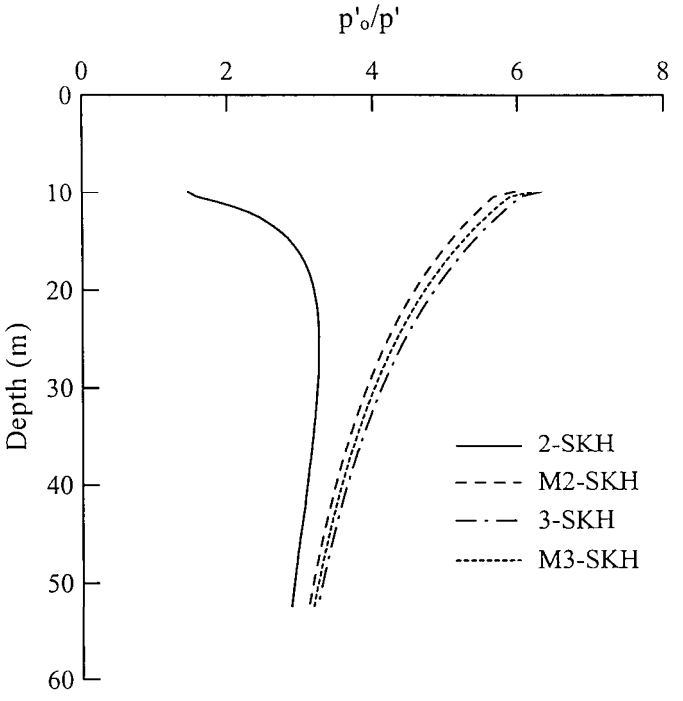


Figure 9.11: p'_o / p' profiles predicted at the end of the geological history

carried out for each of the kinematic hardening models and for each of the 30.5 m deep and 20 m deep tunnels.

Set 2:

Consists of 8 analyses. In this set of analyses the geological stress history was simulated as described in set 1. However, at the end of the geological history and before the excavation of the tunnels the kinematic surfaces were centred around the current stress state. The configuration of the surfaces before the excavation of the tunnel can be seen in Figure 9.8b (configuration B). The excavation of the tunnel was carried out undrained. This process is equivalent to analyses in which no geological history is modelled before the excavation of the tunnel, but instead the K_o and p'_o / p' profiles of Figures 9.10 and 9.11 are prescribed as initial conditions and at the start of the analyses the kinematic surfaces are centred around the current stress states. This analysis was repeated for each of the kinematic hardening models and for each of the 30.5 m deep and 20 m deep tunnels.

In the following sets of analyses, only the kinematic surface configuration B was considered. For these analyses no geological history was modelled. Instead the initial conditions involved a prescribed K_o and p'_o / p' profile and the kinematic surfaces were centred around the current stress state at the start of the analysis. The water table was

located at the top of the Terrace Gravel and the pore pressure profile was hydrostatic with depth. The excavation of the tunnels was carried out undrained (see section 3.3.1.1).

Set 3:

Consists of 24 analyses. Three K_o profiles were considered in the analyses, see Figure 9.12. Profile A, which is a K_o profile of 0.5 constant with depth, profile B, which is the K_o profile predicted by the three-surface model in Figure 9.10 and profile C, which is a K_o profile of 0.5 in the Made Ground/Alluvium and Terrace Gravel and 1.5 constant with depth in the London Clay. The same initial p'_o / p' profile was prescribed for all four models, and this was the profile predicted by the three-surface model in Figure 9.11. These three profiles were examined for all four models and two tunnel depths.

Set 4:

Consists of 3 analyses. In this set of analyses only the two-surface model was employed. The initial prescribed conditions involved the K_o and p'_o / p' profiles predicted by the two-surface model in Figures 9.10 and 9.11 respectively. In these analyses the value of the parameter ψ was varied between 4 and 6. The analyses were carried out only for the 30.5 m deep tunnel.

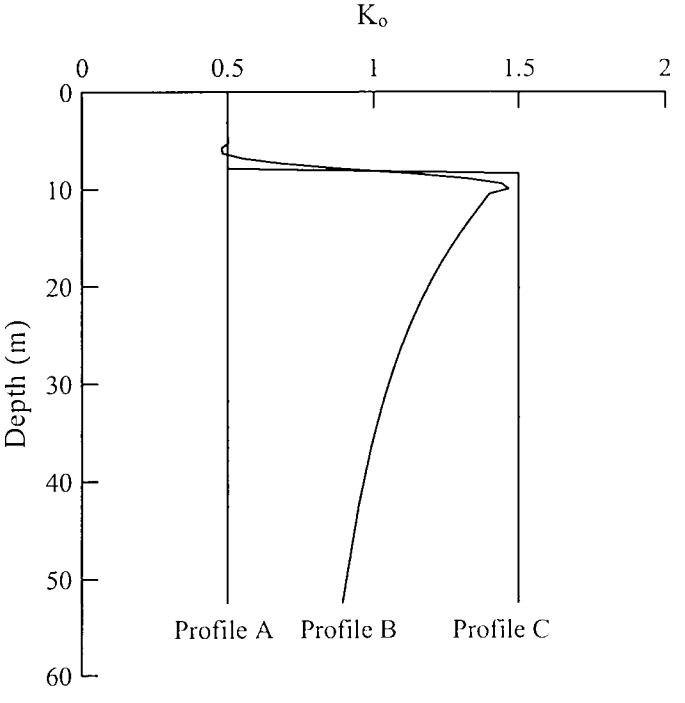


Figure 9.12: Assumed K_o profiles for the analyses of set 3

i) Analyses with model J4 modelling the London Clay stratum

The following set of analyses was performed with model J4 modelling the London Clay deposit:

Set 5:

Consists of 8 analyses. In this set of analyses the prescribed initial conditions were the following. The water level was located at the top of the Terrace Gravel, with pore pressure distribution hydrostatic with depth. Four K_o profiles were considered in the analyses, profiles A, B and C shown in Figure 9.12 and the profile predicted by the modified two-surface model in Figure 9.10, which was named profile D, see Figure 9.13. The excavation of the tunnel was carried out undrained. The analyses were carried out for both the 30.5 m deep and the 20 m deep tunnels.

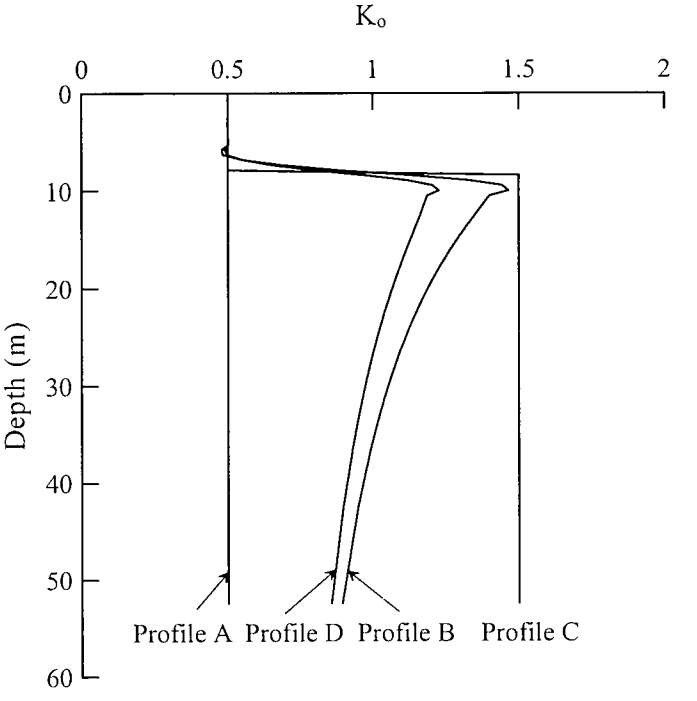


Figure 9.13: Assumed K_o profiles for the analyses of model J4 – set 5

As already mentioned, all the above analyses were plane strain. In order to model the three-dimensional tunnel excavation using plane strain analyses the 'volume loss control' method was adopted (Addenbrooke (1996), Schroeder (2003)). According to this method the tunnel excavation is simulated by reducing incrementally the nodal forces around the tunnel perimeter. Throughout the excavation process the volume of the developing surface settlement trough is monitored. The 'ground loss' or 'volume loss' is defined as the volume of soil excavated in excess of the final tunnel volume and is

expressed as a percentage of the theoretical volume of the tunnel. If the tunnel excavation takes place in a low permeability clay, like London Clay, then the excavation conditions can be considered undrained. This means no volume change, in which case the volume loss is equal to the volume of the surface settlement profile. In the 'volume loss control' method once the desired volume loss is achieved, the tunnel lining can be constructed. The excavation of the tunnel is then completed, allowing the forces in the tunnel lining to build up.

In the following analyses the volume loss during the tunnel excavation was monitored and the results are presented at the same volume loss of 1% (unless otherwise stated). In these analyses no tunnel lining was constructed.

9.5.4 Analyses results

9.5.4.1 Sets 1 and 2 - Effect of the configuration of the kinematic surfaces

Figure 9.14 illustrates the K_o profiles obtained at the end of the geological history together with the K_o profile estimated by the equation proposed by Mayne and Kulhawy (1982). It can be seen that the M2-SKH, 3-SKH and M3-SKH models predict similar

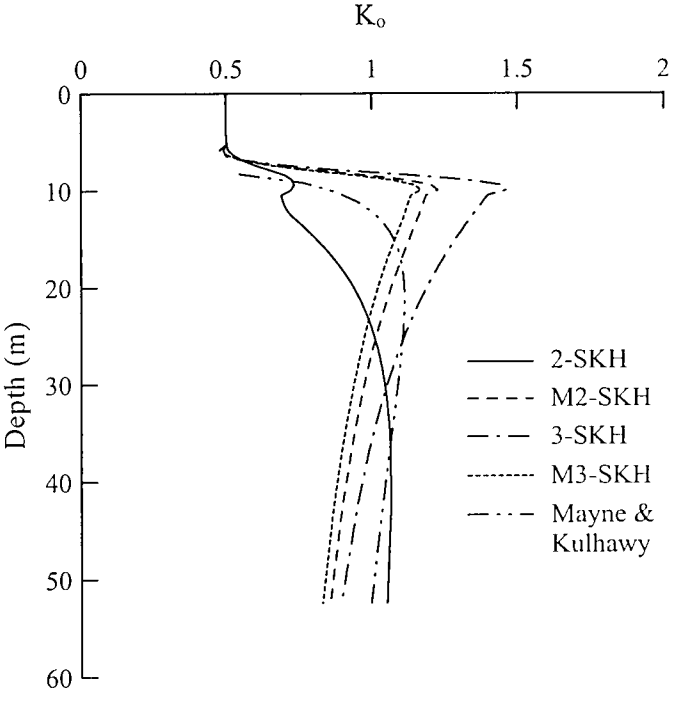


Figure 9.14: K_o profiles predicted at the end of the geological history and the K_o profile calculated from the equation of Mayne and Kulhawy (1982)

shapes of the K_o profile in the London Clay stratum. This is a profile gradually reducing with depth. On the contrary, the profile predicted by the 2-SKH model is of a different shape and seems to gradually increase with depth, up to a depth of 45 m from where on it stays approximately constant. The shape of the profile predicted by the Mayne and Kulhawy (1982) equation seems to have a shape between the two and within, or close to, the range of values predicted by the kinematic hardening models. The p'_o / p' profiles predicted by the kinematic hardening models at the end of the geological history have already been presented in Figure 9.11 and reveal a similar trend; the M2-SKH, 3-SKH and M3-SKH models predict very similar profiles whereas the 2-SKH model predicts a profile of different shape and of lower values.

The effect of the configuration of the kinematic surfaces will be initially presented for the 30.5 m deep tunnel and then for the 20 m deep tunnel. The notation used in the following figures is the following: the name of the constitutive model used for the modelling of the London Clay deposit is given first, followed by a number which denotes the set of analyses. For example 3-SKH-1 denotes the analysis of set 1 carried out with the three-surface model. The sign convention followed in the figures of this chapter is that upwards vertical movements and right horizontal movements are plotted as positive, see Figure 9.4.

i) 30.5 m deep tunnel

Figure 9.15 presents the surface settlement profiles for the analyses of set 1 (configuration A in Figure 9.8a). It can be seen that all four models give quite similar

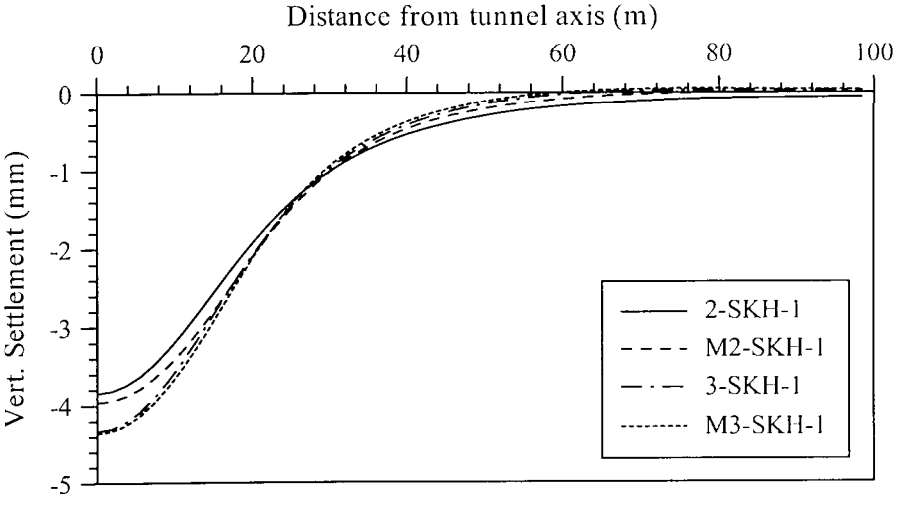


Figure 9.15: Surface settlement profiles predicted by set 1: 30.5 m deep tunnel

predictions, with the M3-SKH model predicting the deepest and the 2-SKH model predicting the shallowest trough. Table 9.4 gives the volume loss and the percentage of unloading at which the volume loss was obtained for each analysis. It is evident that different degrees of unloading were required to achieve the same volume loss, with the two-surface model (2SKH-1) obtaining it at a much lower percentage of unloading than the other analyses. If a tunnel lining had been constructed at the same volume loss of 1%, then constructing this earlier in the case of the analysis 2-SKH-1 would have resulted in higher forces in the tunnel lining, in the short term, as compared to the other analyses.

Figure 9.16 illustrates the surface settlement troughs predicted by the analyses of set 2 (configuration B in Figure 9.8b). Here the M2-SKH, 3-SKH and M3-SKH models give similar predictions, whereas the 2-SKH model predicts a deeper settlement trough than the other three models. Table 9.5 summarises the volume loss and the percentage unloading for the analyses set 2. Similar to set 1, the analyses of set 2 obtained the same volume loss at different percentages of unloading, indicating different forces in the tunnel lining. Inspection of both Tables 9.4 and 9.5 shows that the highest percentage of unloading is achieved by the M3-SKH model, followed by the M2-SKH model, then the 3-SKH model and finally the 2-SKH model which achieves much lower percentages of unloading. As it will be discussed subsequently, the percentage of unloading at which a certain volume loss is obtained can be related to the decay of stiffness employed in each model.

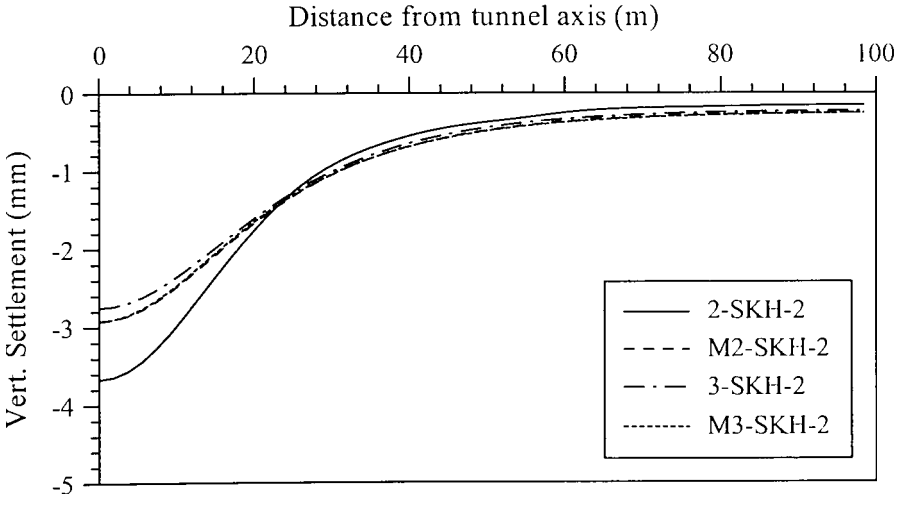


Figure 9.16: Surface settlement profiles predicted by set 2: 30.5 m deep tunnel

Analysis	2-SKH-1	M2-SKH-1	3-SKH-1	M3-SKH-1
Volume loss (%)	1.04	1.03	1.04	1.03
Percentage of unloading (%)	28	50	44	56

Table 9.4: Volume loss and percentage of unloading for set 1: 30.5 m deep tunnel

Analysis	2-SKH-2	M2-SKH-2	3-SKH-2	M3-SKH-2
Volume loss (%)	1.03	1.02	0.96	1.02
Percentage of unloading (%)	28	58	46	60

Table 9.5: Volume loss and percentage of unloading for set 2: 30.5 m deep tunnel

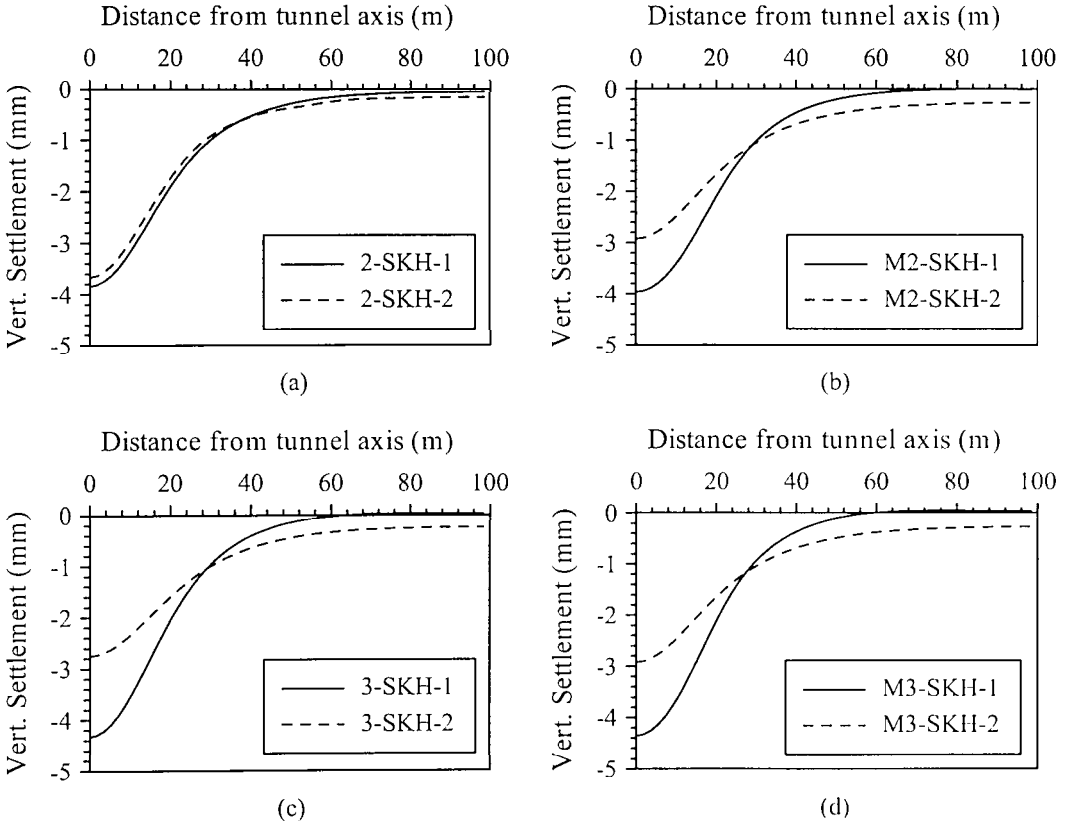


Figure 9.17: Comparison of surface settlement profiles predicted by sets 1 and 2: 30.5 m deep tunnel a) two-surface model b) modified two-surface model c) three-surface model d) modified three-surface model

Figure 9.17 compares the settlement profiles for configurations A and B (sets 1 and 2) and for each kinematic hardening model. Figure 9.17a shows that for the two-surface model there is a very small difference between the two sets of analyses. On the contrary, for the other three kinematic hardening models, set 1 (configuration A) predicts deeper and narrower settlement profiles than set 2 (configuration B).

The reason behind the above observations can be attributed to the stiffness response experienced by the soil elements during each analysis. The tunnel excavation subjects some elements to compression paths and other elements to extension paths. As it will be shown, the relative stiffness response between the elements subjected to compression and the elements subjected to extension seems to influence the predicted surface settlement profile.

In the analyses of sets 1 and 2, due to the different configuration of the kinematic surfaces at the start of the tunnel excavation, a different relative stiffness response in compression and extension would be expected for each set of analyses (see section 7.4). An example of an element subjected to a compression path, during the tunnel excavation, is the element at the springline of the tunnel, whereas an example of an element subjected to an extension path is the element at the crown of the tunnel (see Figure 9.18). Figure 9.19 plots the shear stiffness-strain curves experienced by the soil elements at the crown and springline of the tunnel for both sets 1 and 2 and for each kinematic hardening model (it is reminded that the tangent stiffness G_{oct} is defined as $G_{oct} = \mathrm{d}J/\mathrm{d}E_d$). Figure 9.19a shows that for the 2-SKH model there is practically no difference between the stiffness responses predicted by sets 1 and 2 after a deviatoric strain of approximately 0.02%. This behaviour of the two-surface model is not surprising and has been encountered before in Chapter 7 (Figure 7.39 of section 7.4). As already discussed in Chapter 7, this is a consequence of the drop in stiffness observed in

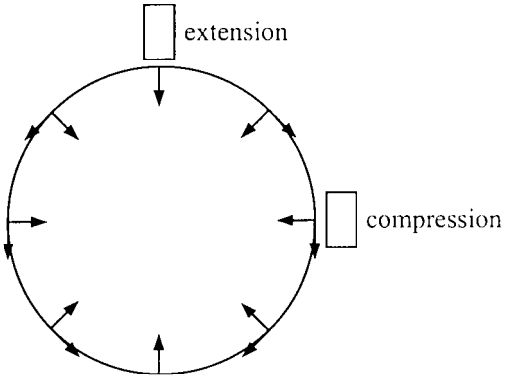


Figure 9.18: Forces imposed on the tunnel boundary due to excavation

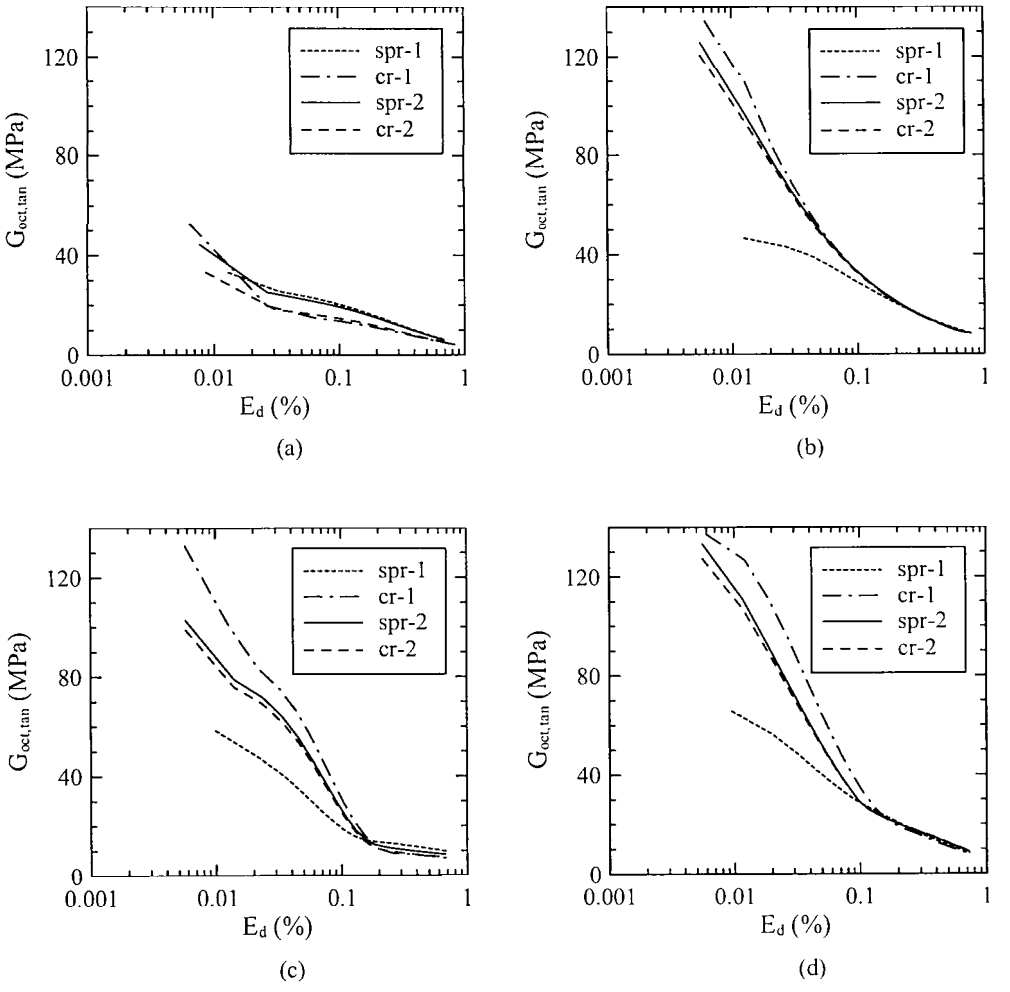


Figure 9.19: Comparison of stiffness-strain curves at the springline and crown of the tunnel for sets 1 and 2: 30.5 m deep tunnel a) two-surface model b) modified two-surface model c) three-surface model d) modified three-surface model

the two-surface model, which results in the model being unable to retain a memory of the previous stress history, and hence predicting approximately the same stiffness response once the stress state becomes elasto-plastic, irrespective of the previous configuration of the kinematic surface (at least for the size of the kinematic surface assumed in the analyses). The practically same stiffness response predicted by the two-surface model in Figure 9.19a for configurations A and B could explain the very small difference in the settlement profiles predicted by sets 1 and 2 in Figure 9.17a. Figures 9.19b, c and d show that this is not the case for the other three models and that a different stiffness response is obtained for each set of analyses. For set 1 the element at the springline of the tunnel (subjected to compression) shows initially much lower stiffness than the element at the crown of the tunnel (subjected to extension), which is consistent with the kinematic surface configuration A. For set 2 (configuration B) the stiffness response at the springline is similar to the one at the crown. In the latter case

this happens due to the K_o value being close to unity. The different stiffness response predicted for the two configurations A and B seems to be the reason why a different surface settlement trough is predicted by sets 1 and 2 for the three remaining models, since this is the only difference in the analyses. It seems that the deeper settlement trough is obtained for set 1 rather than set 2. As already discussed, the configuration of set 1 can be considered to simulate the effect of recent stress history on the tunnel excavation, whereas the configuration of set 2 simulates the effect of stress path direction. It should be noted that inspection of Figures 9.19a-d shows that the 2-SKH model predicts a softer response than the other three models for deviatoric strains up to 0.1%.

Comparison with the Gaussian distribution

The empirical approach to the prediction of the transverse settlement profile caused by tunnel construction is to assume that it follows a Gaussian error curve (Peck (1969)):

$$S = S_{\max} e^{\frac{-x^2}{2i^2}} \tag{9.9}$$

where S is the vertical settlement at a distance x from the centreline of the tunnel, S_{max} is the maximum vertical settlement at the centreline of the tunnel and i is the distance of the point of inflexion of the curve from the centreline of the tunnel. On the basis of field observations (O'Reilly and New (1982), Rankin (1988)) a value of i equal to half the depth of the tunnel axis is usually adopted for clays and is used here.

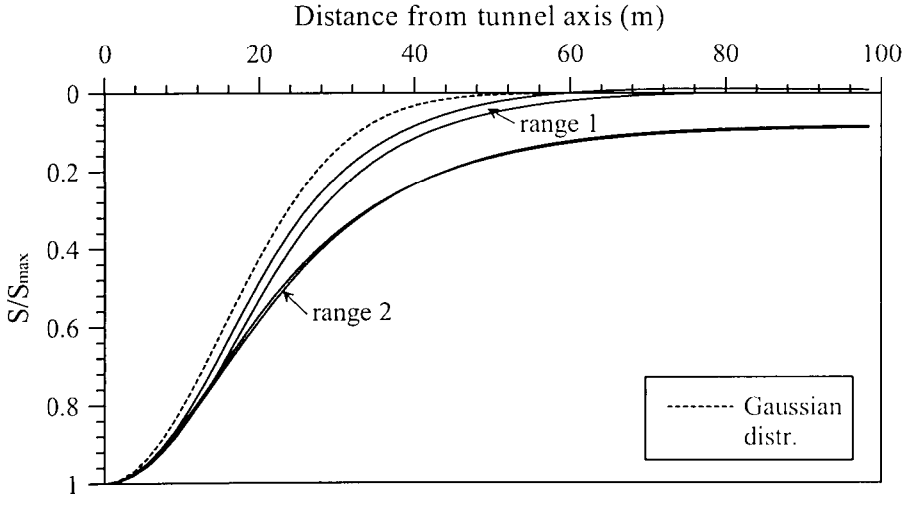


Figure 9.20: Comparison of normalised surface settlement profiles with the Gaussian distribution: 30.5 m deep tunnel

Figure 9.20 compares the Gaussian distribution with the ranges of normalised surface settlement troughs predicted by the M2-SKH, 3-SKH and M3-SKH models for sets 1 and 2 (range 1 and 2 respectively in the figure). The predictions of range 1 can be seen to plot closer to the Gaussian distribution than the predictions of range 2.

ii) 20 m deep tunnel

The surface settlement profiles predicted by the analyses of set 1 for the 20 m deep tunnel are presented in Figure 9.21. The deepest settlement trough is predicted by the 2-SKH model, followed by the 3-SKH model, then the M3-SKH model and finally the M2-SKH model.

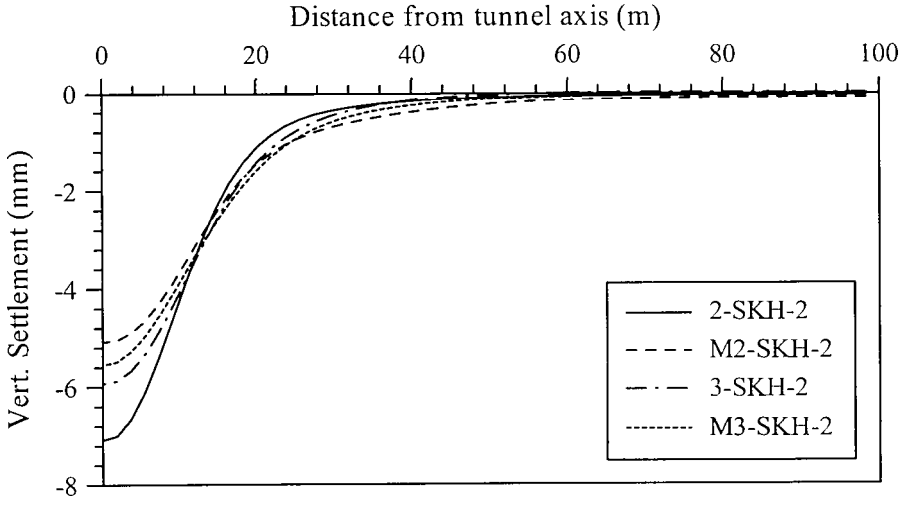


Figure 9.21: Surface settlement profiles predicted by set 1: 20 m deep tunnel

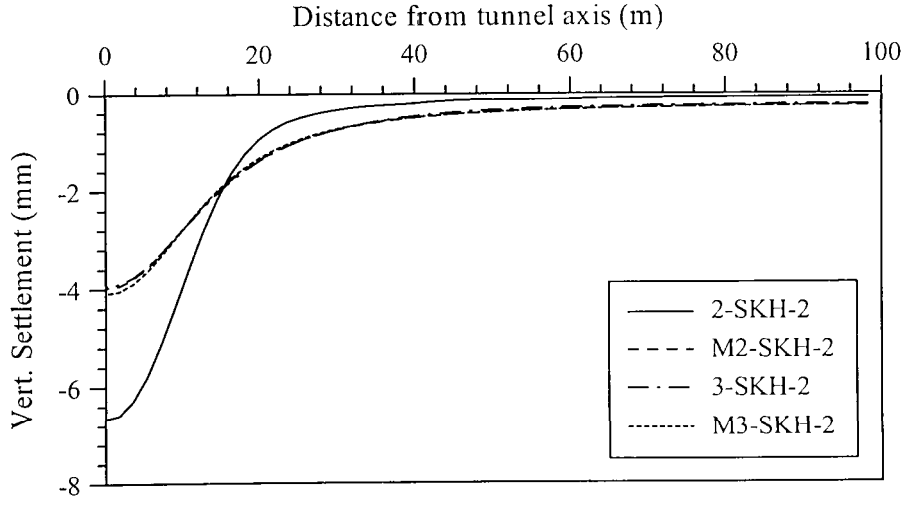


Figure 9.22: Surface settlement profiles predicted by set 2: 20 m deep tunnel

Analysis	2-SKH-1	M2-SKH-1	3-SKH-1	M3-SKH-1
Volume loss (%)	1.05	1.02	0.98	1.02
Percentage of unloading (%)	30	62	54	68

Table 9.6: Volume loss and percentage of unloading for set 1: 20 m deep tunnel

Analysis	2-SKH-2	M2-SKH-2	3-SKH-2	M3-SKH-2
Volume loss (%)	1.02	1.01	0.98	1.00
Percentage of unloading (%)	28	72	58	74

Table 9.7: Volume loss and percentage of unloading for set 2: 20 m deep tunnel

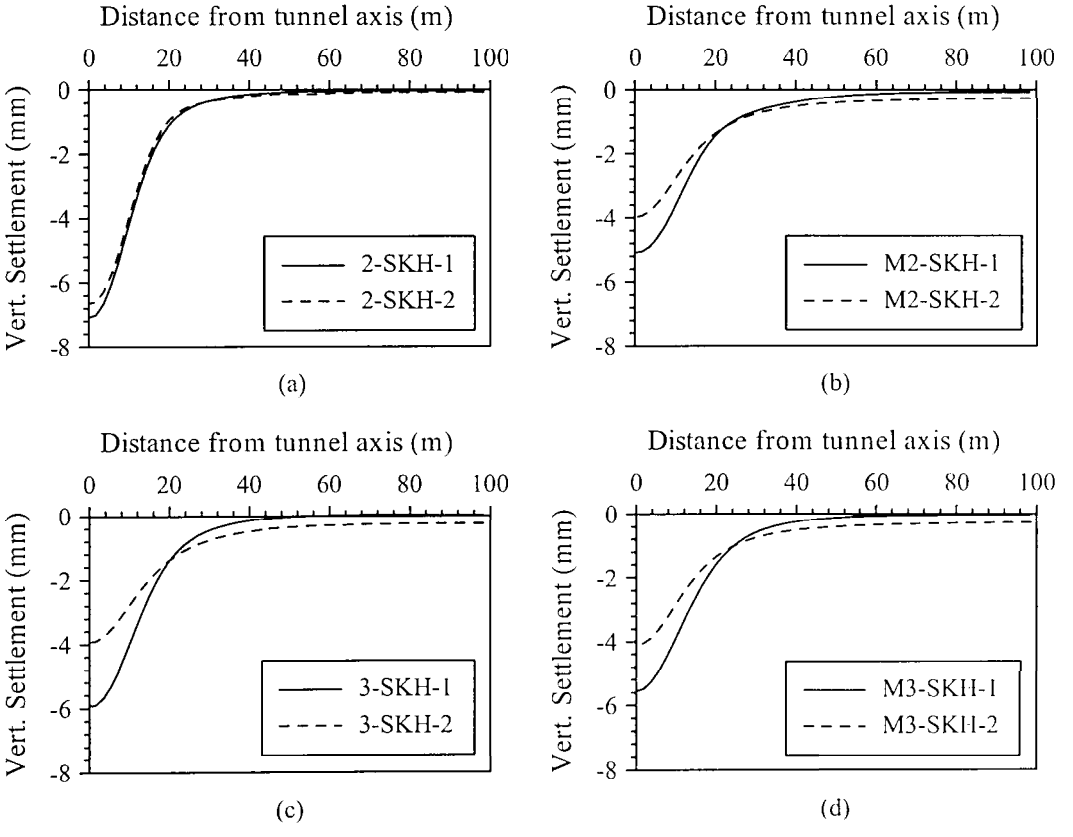


Figure 9.23: Comparison of surface settlement profiles predicted by sets 1 and 2: 20 m deep tunnel a) two-surface model b) modified two-surface model c) three-surface model d) modified three-surface model

Figure 9.22 illustrates the predictions of the analyses set 2. Here the predictions of the M2-SKH, 3-SKH and M3-SKH models are very close, whereas the 2-SKH model predicts a much deeper settlement profile. As it will be shown later, the much deeper trough predicted by the 2-SKH model can be attributed partly to the K_o value at the axis of the tunnel (and the effect that this has on the behaviour of the model) and partly to a softer response predicted by the 2-SKH model when compared with the other three models.

Tables 9.6 and 9.7 summarise the volume loss and the corresponding percentage of unloading for each analysis. Similar to the 30.5 m deep tunnel, inspection of Tables 9.6 and 9.7 indicates that for the same volume loss the highest percentage of unloading is obtained by the M3-SKH model, followed by the M2-SKH model, which is in turn

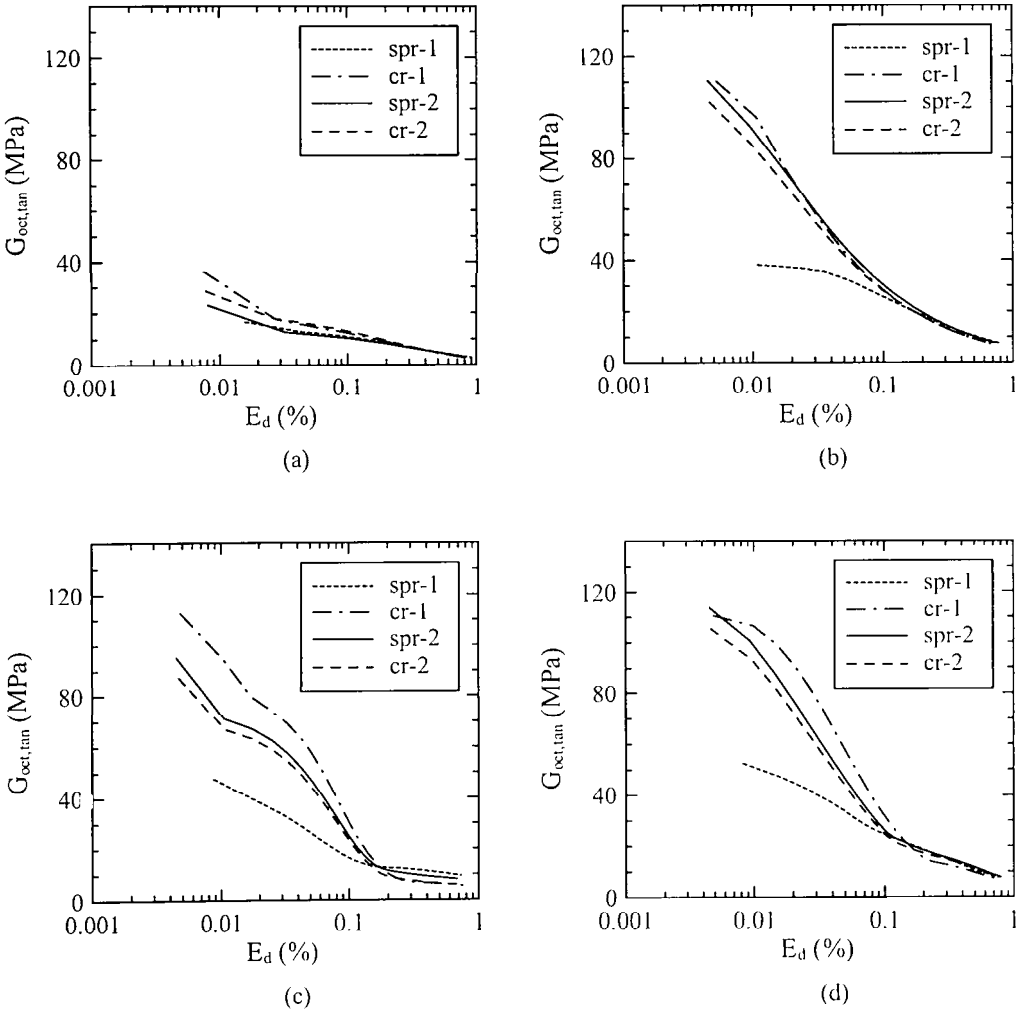


Figure 9.24: Comparison of stiffness-strain curves at the springline and crown of the tunnel for sets 1 and 2: 20 m deep tunnel a) two-surface model b) modified two-surface model c) three-surface model d) modified three-surface model

followed by the 3-SKH model. Again the 2-SKH model predicts much lower unloading percentages than any of the other three models.

Figure 9.23 compares the surface settlements troughs for the kinematic surface configurations A and B (sets 1 and 2) and for each model. It can be seen that, similar to the 30.5 m deep tunnel, the predictions of the 2-SKH model are very similar for both configurations. This is not the case for any of the other three models which predict a deeper and narrower settlement profile for the configuration A than the configuration B. Inspection of the stiffness-strain curves experienced by the soil elements at the springline and crown of the tunnel (Figure 9.24) shows that the 2-SKH model predicts approximately the same stiffness response for the two sets of analyses. This explains the similar profiles in Figure 9.23a. On the contrary, the other three models predict different stiffness response for each configuration. Similar to the 30.5 m deep tunnel, for the configuration A, the models predict a much lower initial stiffness for the element at the springline (which is subjected to compression) than the element at the crown (which is subjected to extension). For the configuration B, which also gives the shallowest profile, similar stiffness is predicted for both elements.

Comparison with the Gaussian distribution

Figure 9.25 compares the ranges of predictions of the M2-SKH, 3-SKH and M3-SKH models for sets 1 and 2 (ranges 1 and 2 respectively) with the Gaussian distribution. Similar to the 30.5 m deep tunnel the predictions of range 1 plot much closer to the Gaussian distribution than the predictions of range 2.

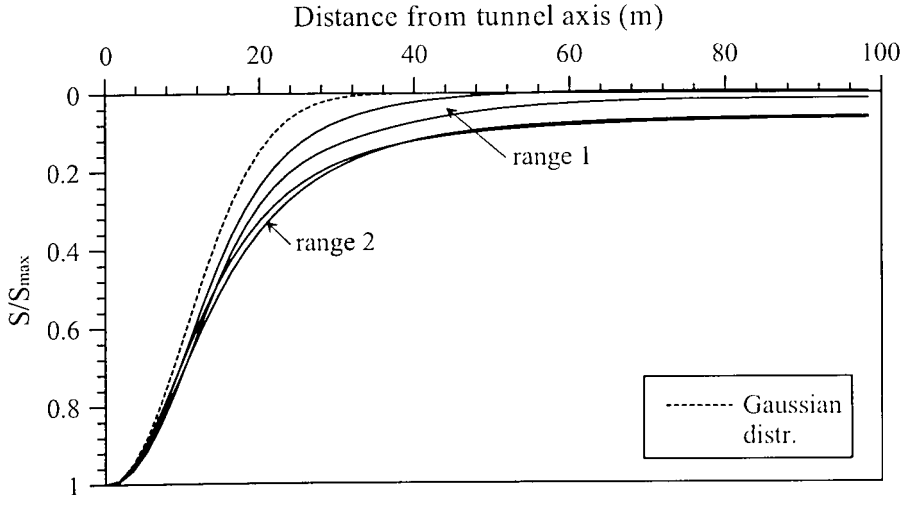


Figure 9.25: Comparison of normalised surface settlement profiles with the Gaussian distribution: 20 m deep tunnel

9.5.4.2 Sets 1, 2 and 5 – Comparison with the non-linear model J4

i) 30.5 m deep tunnel

Figure 9.26 presents the settlement troughs predicted by analyses J4-5B and J4-5D (J4 denotes the constitutive model used for modelling the London Clay, 5 denotes the sets of analyses and the last letter denotes the K_o profile assumed in the analysis, see Figure 9.13). In the same figure the ranges of predictions of the models M2-SKH, 3-SKH and M3-SKH for the analyses sets 1 and 2 (range 1 and 2 respectively in the figure) are plotted for comparison. It can be seen that the predictions of model J4 fall within or close to range 2 (kinematic surface configuration B). This is because the J4 model

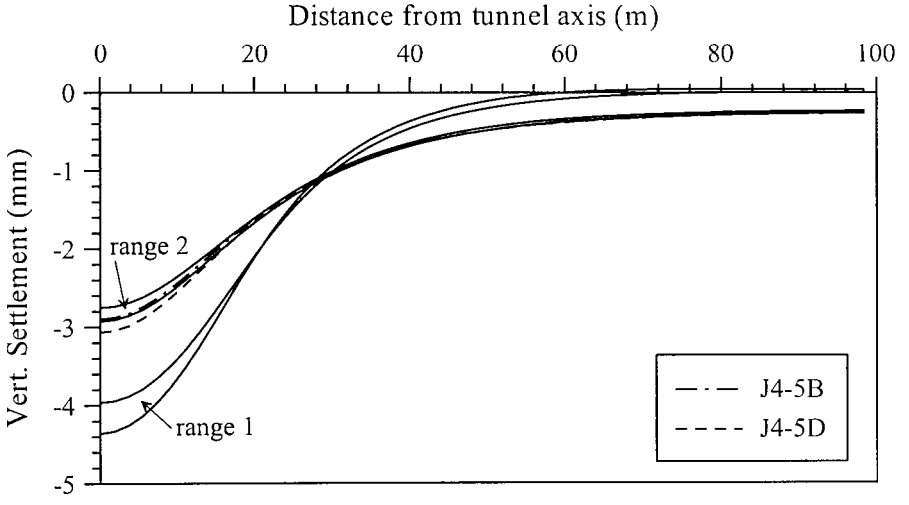


Figure 9.26: Surface settlement profiles predicted by model J4 (K_o profiles B and D): 30.5 m deep tunnel

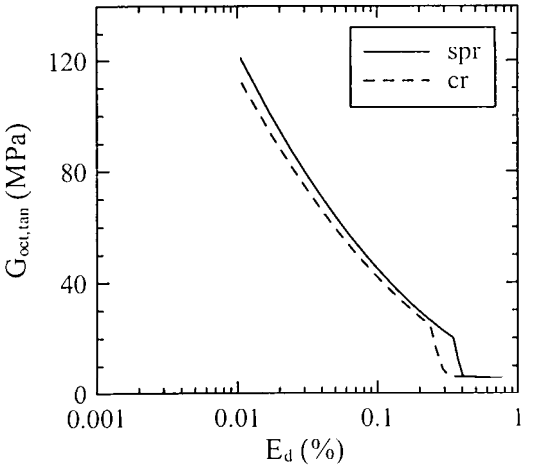


Figure 9.27: Comparison of stiffness-strain curves at the springline and crown of the tunnel for analysis J4-5B: 30.5 m deep tunnel

predicts similar stiffness in compression and extension, which is similar to the stiffness that models M2-SKH, 3-SKH and M3-SKH predict for the configuration B. This is demonstrated by comparison of Figure 9.27, which plots the stiffness-strain curves at the springline and crown of the tunnel for the analysis J4-5B, with the equivalent stiffness-strain curves for the analyses M2-SKH-2, 3-SKH-2 and M3-SKH-2 in Figure 9.19. The volume loss and the corresponding percentage unloading for the analyses J4-5B and J4-5D are given in Table 9.8. Figure 9.28, which presents a comparison with the Gaussian distribution, shows that the predictions of model J4 plot close to range 2.

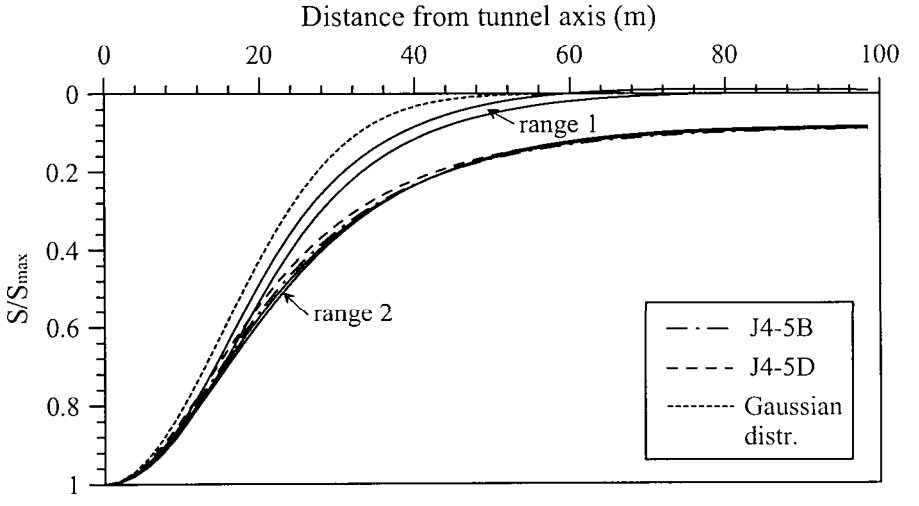


Figure 9.28: Comparison of normalised surface settlement profiles predicted by model J4 (K_o profiles B and D) with the Gaussian distribution: 30.5 m deep tunnel

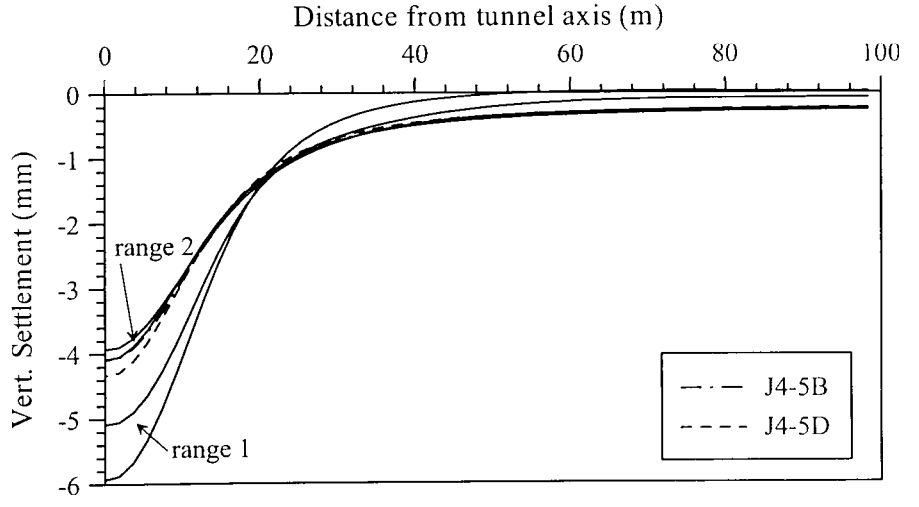


Figure 9.29: Surface settlement profiles predicted by model J4 (K_o profiles B and D): 20 m deep tunnel

ii) 20 m deep tunnel

Figure 9.29 illustrates the predictions of the analyses J4-5B and J4-5D, together with the ranges of predictions of the models M2-SKH, 3-SKH and M3-SKH for sets 1 and 2 (range 1 and 2 respectively in the figure) for the 20 m deep tunnel. Figure 9.29 indicates that, similar to the previous findings, the settlement troughs of the J4 model plot close to range 2. Figure 9.30 plots the stiffness-strain curves of the soil elements at the crown and the springline of the tunnel for the analyses J4-5B. It can be seen again that the model J4 predicts similar stiffness in compression and extension, which is similar to what the M2-SKH, 3-SKH and M3-SKH models predict for the kinematic surface configuration B in Figure 9.24. Figure 9.31 compares the predictions of model J4 with

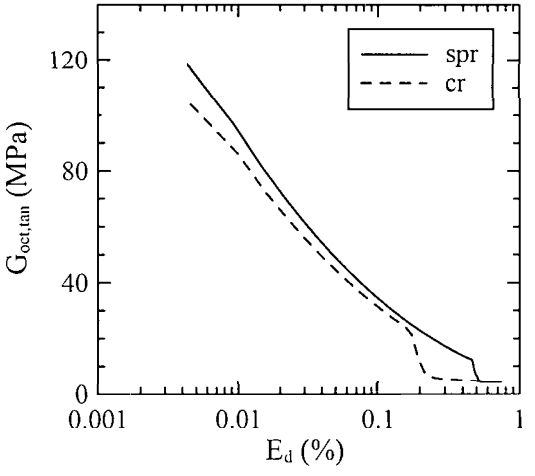


Figure 9.30: Comparison of stiffness-strain curves at the springline and crown of the tunnel for analysis J4-5B: 20 m deep tunnel

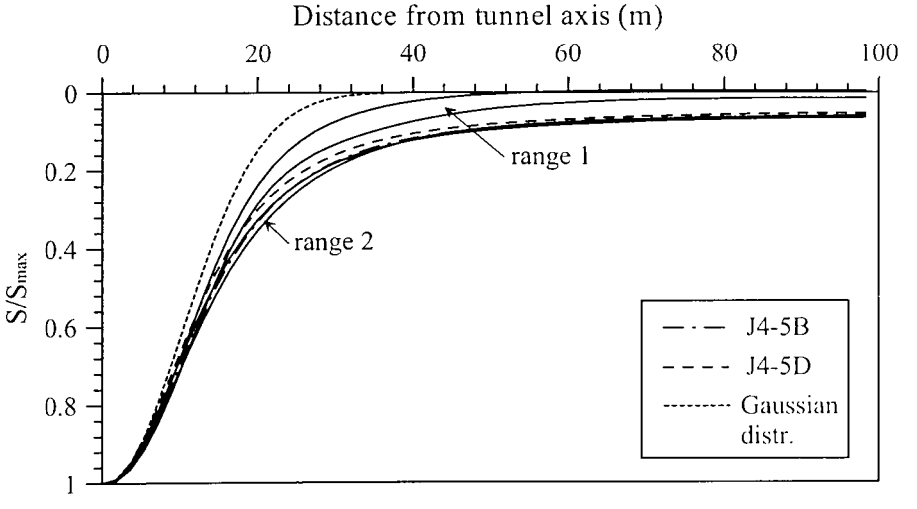


Figure 9.31: Comparison of normalised surface settlement profiles predicted by model J4 (K_o profiles B and D) with the Gaussian distribution: 20 m deep tunnel

the Gaussian distribution and the normalised ranges 1 and 2. Similar to Figure 9.28 the predictions of model J4 plot close to range 2. The volume loss and the corresponding percentage unloading for the analyses J4-5B and J4-5D can be seen in Table 9.8.

Tunnel	30.5 m deep tunnel		20 m deep tunnel	
Analysis	J4-5B	J4-5D	J4-5B	J4-5D
Volume loss (%)	1.01	1.04	1.00	0.99
Percentage of unloading (%)	66	65	70	68

Table 9.8: Volume loss and percentage of unloading for analyses J4-5B and J4-5D

9.5.4.3 Sets 3 and 5 - Effect of K_o profile

i) 30.5 m deep tunnel

As already mentioned in section 9.2, the K_o profile assumed in the finite element analyses of tunnel excavations is known to influence significantly the predicted surface settlement profile (Addenbrooke (1996), Gens (1995)). Figure 9.32 shows the predictions of two analyses, in which the London Clay stratum was modelled as linear elastic with stiffness constant with depth (E = 180000 kPa and μ = 0.2), for the K_o profiles A and C, in Figure 9.12. The results are presented at a volume loss of 0.7% (since the analysis for the profile A did not reach the volume loss of 1%). It can be seen that the K_o profile of 0.5 in the London Clay predicts a deeper and narrower settlement trough than the K_o profile of 1.5. The shear stiffness of the springline and crown is the same for both K_o values and can be seen in Figure 9.33.

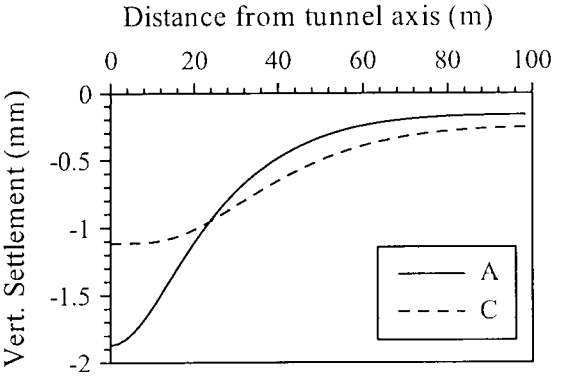


Figure 9.32: Surface settlement profiles predicted by linear elastic model with constant stiffness (K_o profiles A and C): 30.5 m deep tunnel

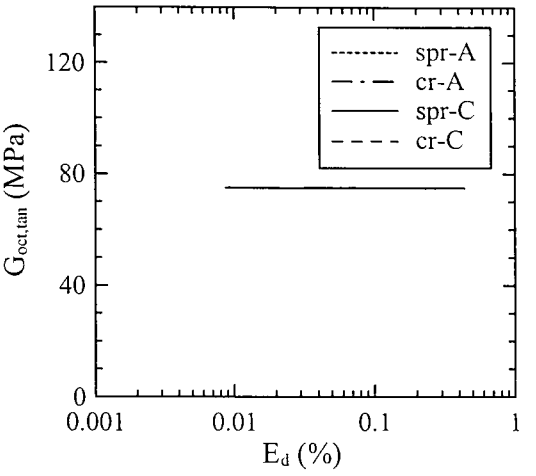


Figure 9.33: Comparison of stiffness-strain curves at the springline and crown of the tunnel for linear elastic model with constant stiffness (K_o profiles A and C): 30.5 m deep tunnel

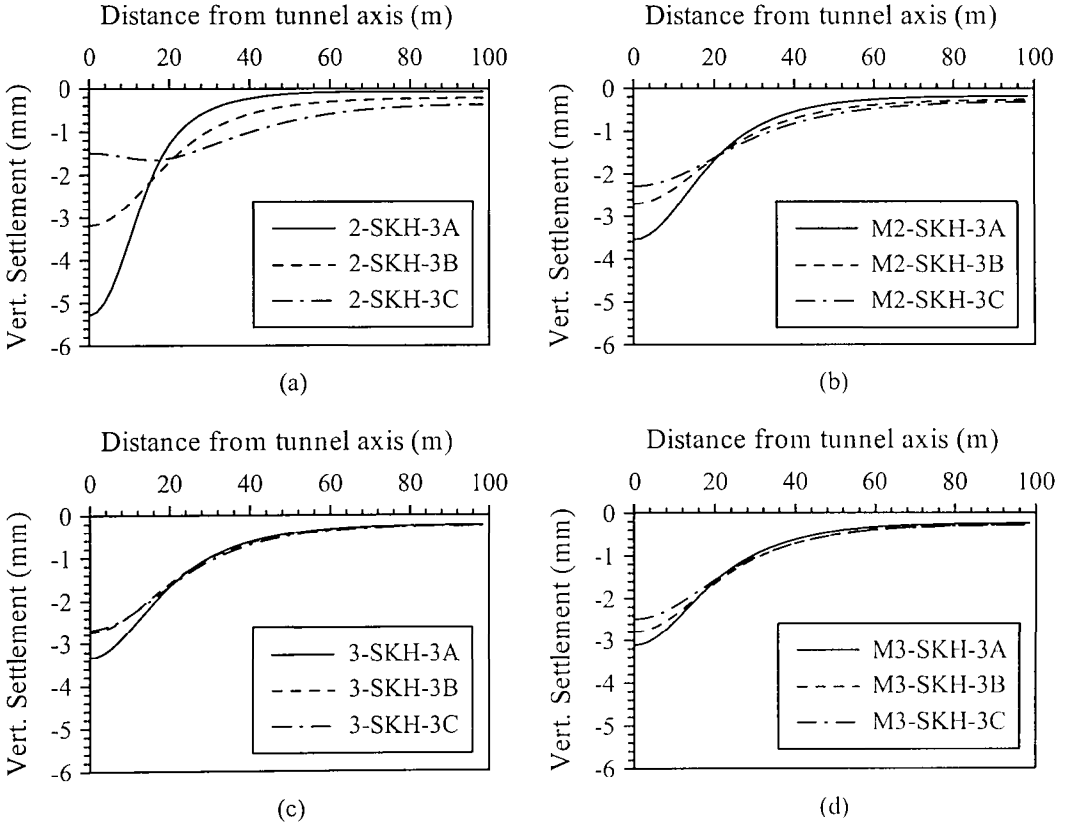


Figure 9.34: Surface settlement profiles predicted by set 3 (K_o profiles A, B and C): 30.5 m deep tunnel a) two-surface model b) modified two-surface model c) three-surface model d) modified three-surface model

In the kinematic hardening models and for the kinematic surface configuration B the assumed K_o value also dictates the relative stiffness between the elements subjected to compression paths and the elements subjected to extension paths. This in turn has been

shown to influence the predicted settlement trough (section 9.5.4.1). Figure 9.34 presents the settlement profiles predicted by the analyses of set 3 for the K_o profiles A, B and C (Figure 9.12). It can be seen that the 2-SKH model seems to be influenced significantly by the assumed K_o profile. As expected, the lower the value of K_o is, the deeper and narrower the settlement trough is (the prediction for the profile C, in particular, is also of the wrong shape). The same trend seems to be valid for the M2-SKH model, but the assumed K_o profile seems to influence the predictions to a much lesser extent. For the 3-SKH and M3-SKH models the effect of the K_o profile seems to be even smaller, although the same trend of the lower K_o profile giving the deeper settlement trough still applies. Figure 9.35 plots the stiffness-strains curves experienced

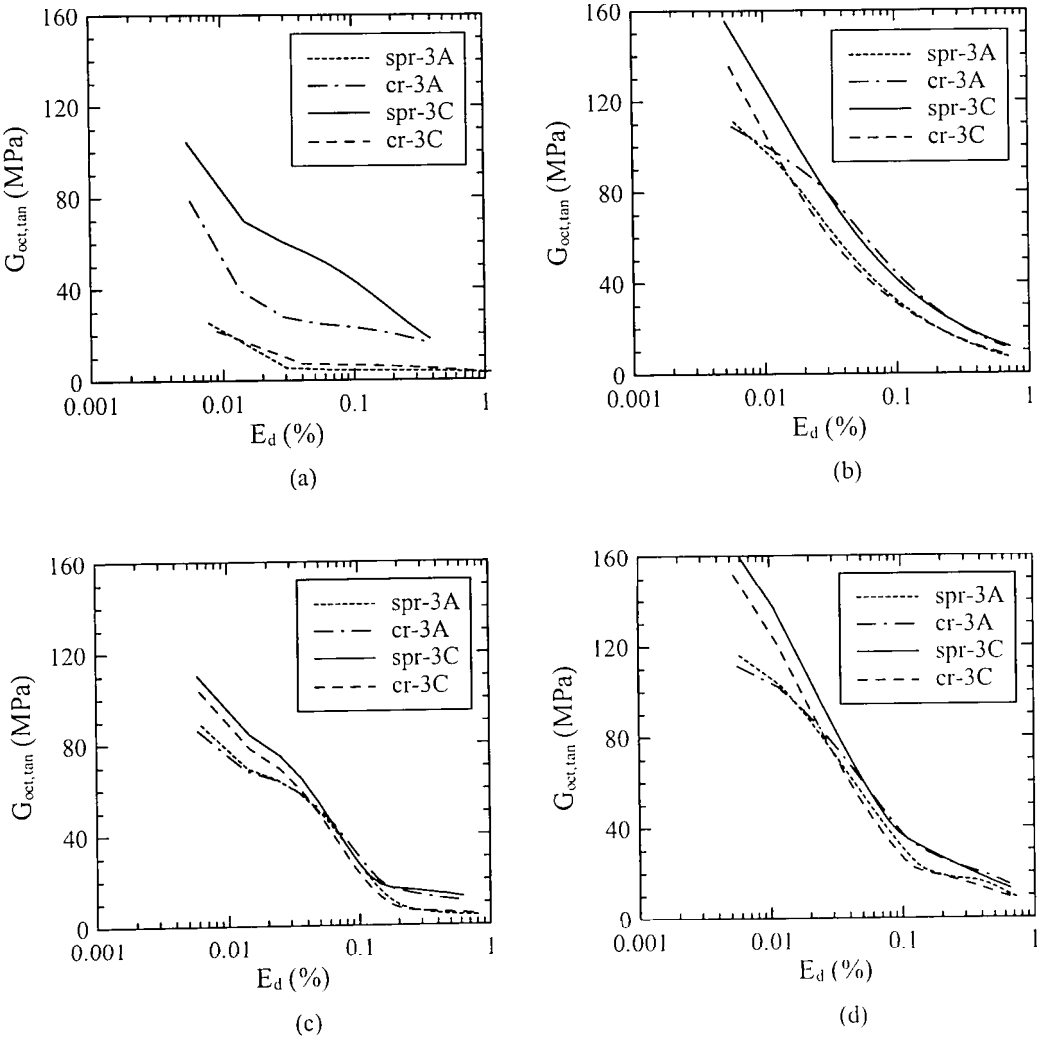


Figure 9.35: Comparison of stiffness-strain curves at the springline and crown of the tunnel for set 3 (K_o profiles A and C): 30.5 m deep tunnel a) two-surface model b) modified two-surface model c) three-surface model d) modified three-surface model

by the soil elements at the springline and crown of the tunnel (which are subjected to compression and extension respectively) for the K_o profiles A and C and for each model. Figure 9.35 indicates that for the K_o profile of 0.5 (K_o profile A) all models predict a generally softer behaviour for the element at the spingline than the element at the crown of the tunnel. The opposite holds for the K_o profile of 1.5 in the London Clay (K_o profile C). In this case the element at the spingline of the tunnel shows a stiffer behaviour than the element at the crown. According to what was shown in section 9.5.4.1, this relative shear stiffness between compression and extension would result in a deeper settlement trough for the K_o profile of 0.5 than for the K_o profile of 1.5. This is probably added to the effect that K_o on its own has on the predicted settlement trough for the same springline and crown stiffness (e.g. Figure 9.32). The reason that K_o influences much more the 2-SKH model than any other kinematic hardening model is that, as shown in Figure 9.35, there is a big difference in the relative shear stiffness between compression and extension predicted for each K_o profile by this model. The remaining kinematic hardening models predict a much smaller difference in relative stiffness, hence showing a smaller influence of the value of K_o.

Figure 9.36 presents the effect of K_o on the non-linear model J4. A deeper settlement profile is predicted by the lower value of K_o. Figure 9.37 shows the stiffness-strain curves for the elements at the springline and crown of the tunnel and for the K_o profiles A and C. It can be seen that, although the pre-yield model predicts similar non-linear degradation of stiffness with strain for both elements (Figure 9.27), for the K_o profile of 0.5 (profile A) the element at the springline becomes plastic earlier, hence resulting in a softer response than the element at the crown. For the K_o profile of 1.5 in the London Clay (profile C) it is the element at the crown which becomes plastic and thus softer

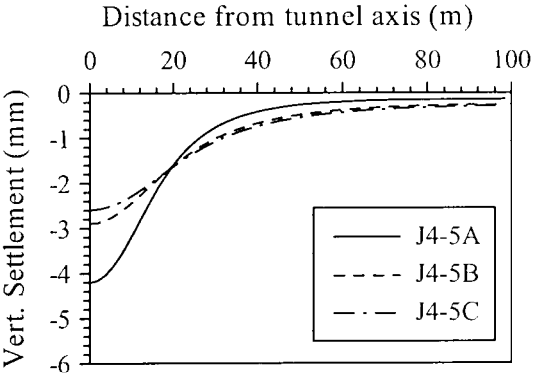


Figure 9.36: Surface settlement profiles predicted by model J4 (K_o profiles A, B and C): 30.5 m deep tunnel

earlier. Similar to what was shown above for the kinematic hardening models, this relative difference in stiffness between compression and extension is additive to the effect that K_o would have on its own.

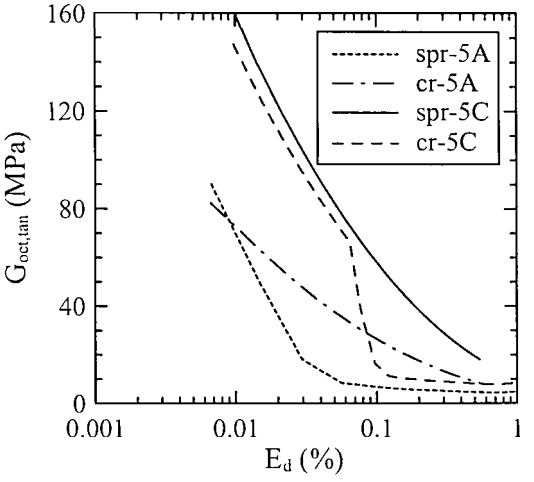


Figure 9.37: Comparison of stiffness-strain curves at the springline and crown of the tunnel for model J4 (K_o profiles A and C): 30.5 m deep tunnel

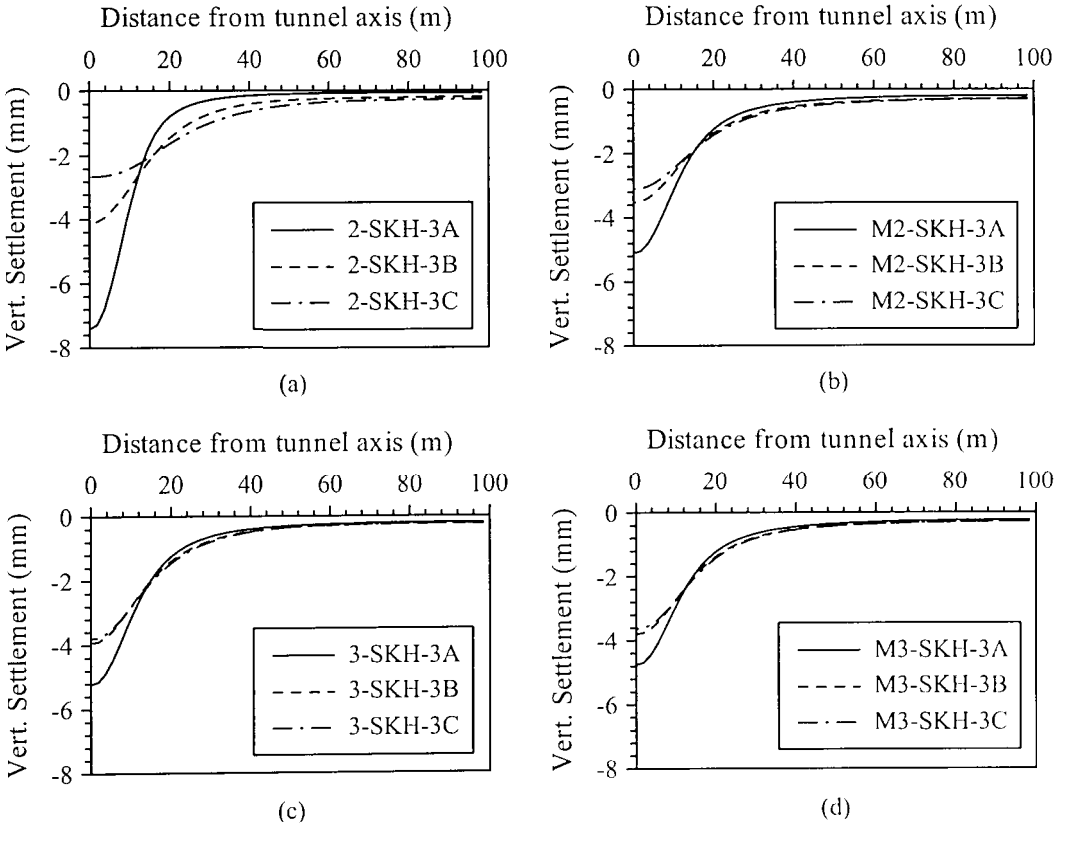


Figure 9.38: Surface settlement profiles predicted by set 3 (K_o profiles A, B and C): 20 m deep tunnel a) two-surface model b) modified two-surface model c) three-surface model d) modified three-surface model

i) 20 m deep tunnel

Figure 9.38 illustrates the surface settlement troughs predicted by each kinematic hardening model for the 20 m deep tunnel and for the three K_o profiles, A, B and C. A similar effect of K_o on the predictions of each model, as for the 30.5 m deep tunnel, can be observed. All models are influenced by K_o and predict a deeper and narrower profile for the K_o profile A. K_o seems to affect more significantly the predictions of the 2-SKH model and to a lesser extent the predictions of the other three kinematic hardening models. Figure 9.39 presents the stiffness-strain curves at the springline and crown of the tunnel for each model. Similar to the previous findings for the 30.5 m deep tunnel, the K_o profile A results in the springline element showing a generally softer response than the crown element, whereas the opposite is true for the K_o profile C. Again this

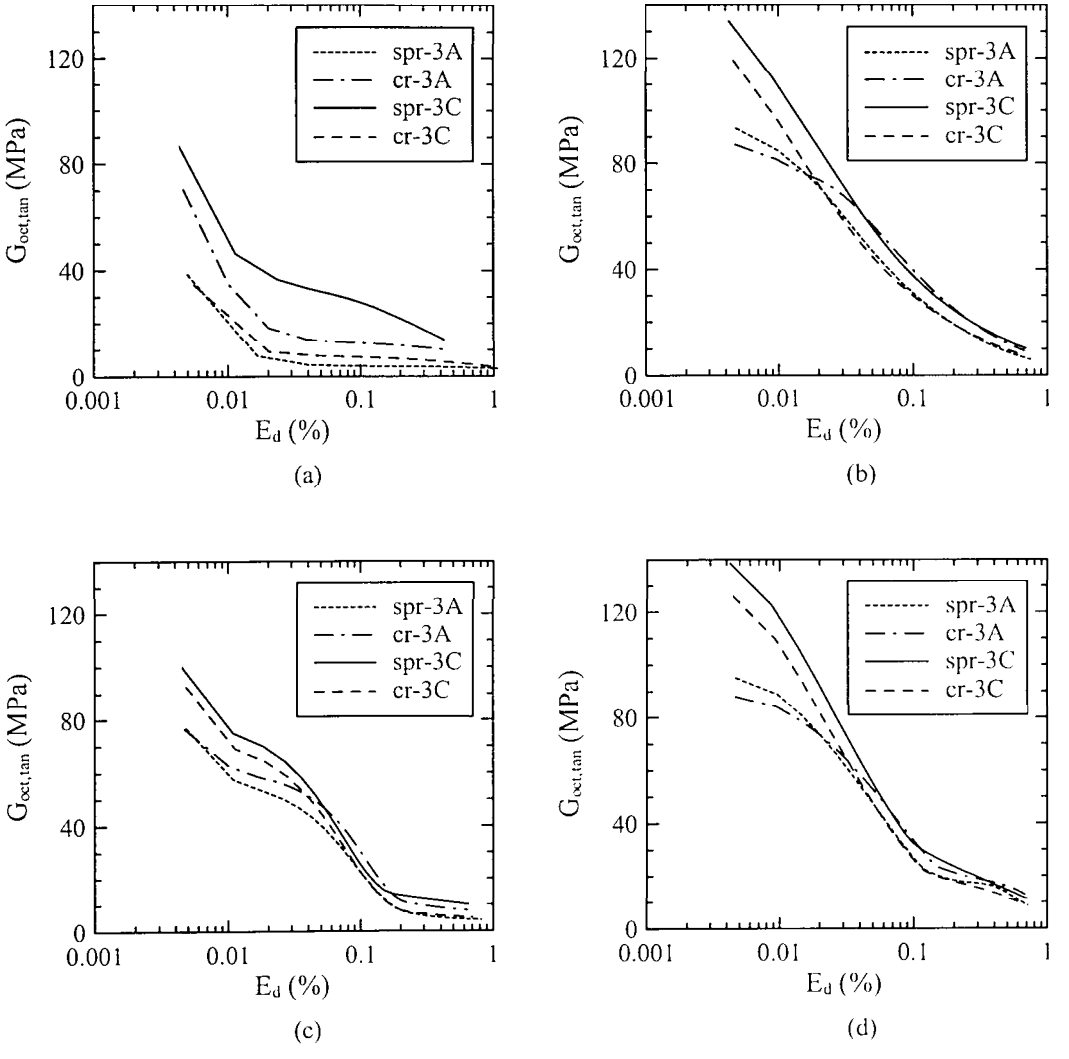


Figure 9.39: Comparison of stiffness-strain curves at the springline and crown of the tunnel for set 3 (K_o profiles A and C): 20 m deep tunnel a) two-surface model b) modified two-surface model c) three-surface model d) modified three-surface model

relative difference in stiffness is more pronounced for the 2-SKH model than the other three models.

The effect of K_o on the predictions of the 2-SKH model can also partly explain the deeper settlement trough predicted by the analysis 2-SKH-2, as compared to the analyses M2-SKH-2, 3-SKH-2 and M3-SKH-2 in Figure 9.22. The lower value of K_o for the two-surface model, at the 20 m deep tunnel axis, resulted in the element at the springline of the tunnel being softer than the element at the crown for the analysis 2-SKH-2 (Figure 9.24), whereas the opposite is true for the other three analyses of set 2.

Figure 9.40 presents the surface settlement troughs predicted by the model J4 for the K_o profiles A, B and C. Inspection of Figures 9.40 and 9.38 shows that K_o seems to influence the predictions of model J4 significantly, but in a lesser extent than the 2-SKH model.

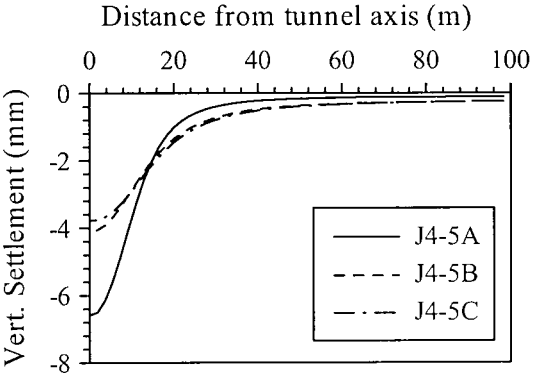


Figure 9.40: Surface settlement profiles predicted by model J4 (K_o profiles A, B and C): 20 m deep tunnel

9.5.4.4 Set 4 – Effect of rate of decay of stiffness

Figure 9.41 shows the surface settlement profiles predicted by the two-surface model for three values of the parameter ψ. Table 9.9 summarises the volume loss and the unloading percentage achieved in each analysis. The effect of varying the parameter ψ in the 2-SKH model has been investigated in Chapter 7. As it was shown (Figure 7.4) the higher value of ψ results in a softer response once the stress state becomes elasto-plastic. Figure 9.41 illustrates that for a higher value of ψ and, hence a softer response, a deeper settlement trough is predicted. Moreover, Table 9.9 indicates that the softer response accelerates the development of volume loss with percentage unloading and hence the same volume loss is obtained quicker or otherwise at a smaller percentage of unloading. The same conclusions are reached if different rates of decay of stiffness are adopted in

the remaining three models.

These conclusions can explain why in the analyses of sets 1 and 2 the predictions of the 2-SKH model achieved the same volume loss at a much smaller percentage of unloading, as compared to the predictions of the other three models. This is because the value of ψ adopted in the analyses resulted in a big drop of stiffness once the stress state became elasto-plastic and hence in a softer response as compared to the other three models and as shown in Figures 9.19 and 9.24.

For the 3-SKH model, the drop in stiffness predicted, once the stress state becomes elasto-plastic, is smaller than for the 2-SKH model and does not result in such a softer initial response as for the 2-SKH model. However, inspection of Tables 9.4-9.7 shows that the 3-SKH model always reaches the volume loss of 1% in a lower percentage of unloading than the M2-SKH and M3-SKH models.

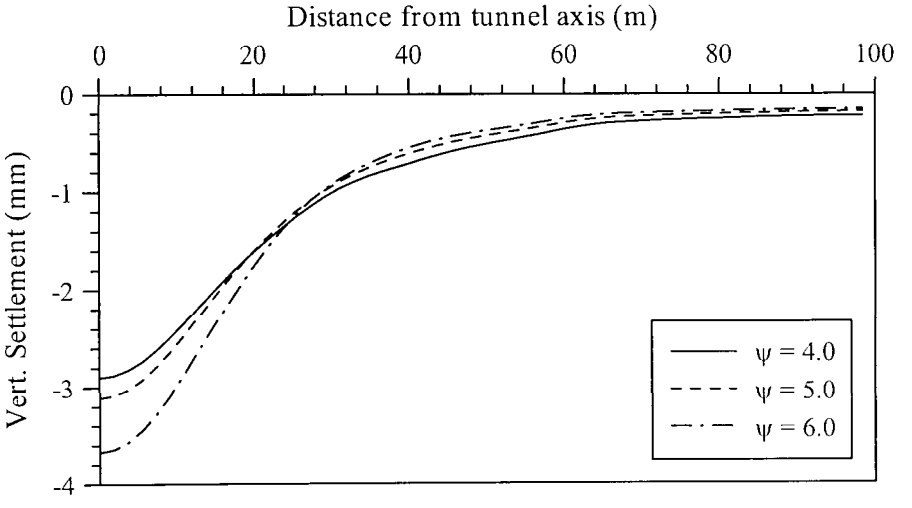


Figure 9.41: Surface settlement profiles predicted by the two-surface model – set 4: 30.5 m deep tunnel

Analysis	$\psi = 4.0$	$\psi = 5.0$	$\psi = 6.0$
Volume loss (%)	1.00	0.97	1.03
Percentage of unloading (%)	54	38	28

Table 9.9: Volume loss and percentage of unloading for set 4 (2-SKH model): 30.5 m deep tunnel

9.6 Analyses of the twin tunnels at St. James's Park

9.6.1 Introduction

The analyses in this study model the twin tunnels which were constructed as part of the Jubilee Line Extension (JLE) beneath St. James's Park. The soil profile and the geometry of the tunnels have been presented in Figure 9.4. The westbound tunnel was driven first, followed by the excavation of the eastbound tunnel 8.5 months later. Ground movements due to tunnelling were measured extensively as part of the JLE project and are presented in Standing et al. (1996) and Nyren (1998). A volume loss of 3.3% was measured for the westbound tunnel. This volume loss was unexpectedly high compared with the previously measured values for tunnels driven in the London Clay, which usually varied between 1.0 and 2.0%. This is believed to be a result of a number of reasons, including lower than usual undrained strengths, varying permeabilities and excavation methods associated with a rapid rate of advance (Nyren et al. (2001)). The measured volume loss for the eastbound tunnel was 2.9% (Standing et al. (1996)).

As mentioned in section 9.2, the geometry of the twin tunnels at St. James's Park has been analysed before by Addenbrooke et al. (1997) using a variety of pre-yield elastic linear and non-linear constitutive models, including model J4. As already discussed, their work showed that non-linear elastic pre-yield models predict deeper settlement troughs than linear elastic pre-yield models.

In this chapter the twin tunnels are analysed using the four kinematic hardening models. Moreover, an analysis with the non-linear model J4 is repeated (with slightly different pore pressure and K_o profiles than those used by Addenbrooke et al. (1997)). All analyses are compared with the measured field data.

9.6.2 Model parameters

London Clay

The London Clay was modelled with all four kinematic hardening models and model J4. When trying to use the parameters adopted in section 9.5 it was found that the analysis with model J4 did not reach the required volume loss of 3.3% for the westbound tunnel. Moreover, the analyses with the kinematic hardening models achieved the volume loss of 3.3% at high percentages of unloading, 88% for the M2-SKH model, 78% for the

3-SKH, 95% for the M3-SKH model, with the exception of the two-surface model which reached it at 50%. The high percentages of unloading for all models (apart from the two-surface model) can be attributed to two reasons. First, as aforementioned, the volume loss of 3.3% is unusually high for tunnels in London Clay (a typical volume loss of e.g. 1.5-2% was achieved in the finite element analyses at much smaller unloading percentages). Second, as shown in the previous section, the percentage unloading at which the volume loss is reached is a consequence of the stiffness-strain response assumed in the model. This implies that, apart from the two-surface model, the rest of the parameters used in section 9.5 could be too stiff for modelling the London Clay at St. James's Park (the parameters for the two-surface model have been shown to result in softer response than the other models). This could be a result of attempting to use parameters derived from tests on reconstituted London Clay from another site (Canons Park site). In the absence of test data from the St. James's Park site, the parameters used in the constitutive models for the London Clay stratum were chosen as follows. For the model J4, the parameters used by Addenbrooke et al. (1997) for the non-linear elastic part of the model were adopted, see Table 9.10. As shown in section 9.5.2 (Figure 9.9) these parameters result in softer response for the model J4 than the parameters adopted in the previous section 9.5.2. For the two-surface model the parameters were kept the same as in section 9.5.2 (Table 7.1), since these resulted in softer overall response than the other models. For the rest of the kinematic hardening models new values of the parameters that control the decay of stiffness were adopted and the rest of the parameters were kept the same as in section 9.5. The parameters that control the decay of stiffness are α, for the modified two-surface model, ψ, for the three-surface model and α_1 and α_2 for the modified three-surface model. These parameters were chosen on the basis of single finite element analyses simulating an undrained triaxial compression test and an undrained triaxial extension test at the westbound tunnel axis. The initial stress conditions were taken from Figures 9.10 and 9.11 and the configuration of the kinematic surfaces at the start of shearing was the configuration A in Figure 9.8a. The new parameters are summarised in Tables 9.11-9.13 and the predictions for the undrained triaxial compression and extension tests, based on these parameters, can be seen in Figures 9.42 and 9.43 respectively.

Terrace Gravel

The Terrace Gravel was modelled with the same parameters as in section 9.5.2.

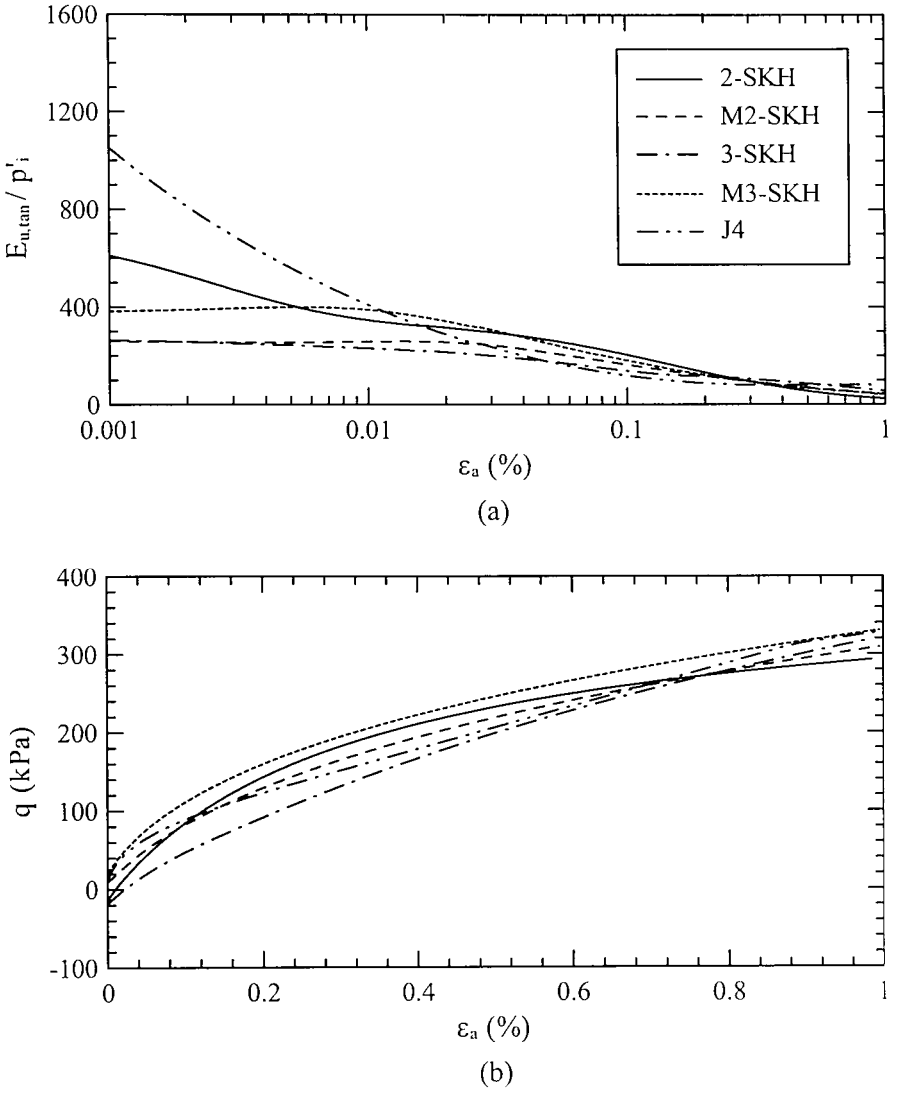


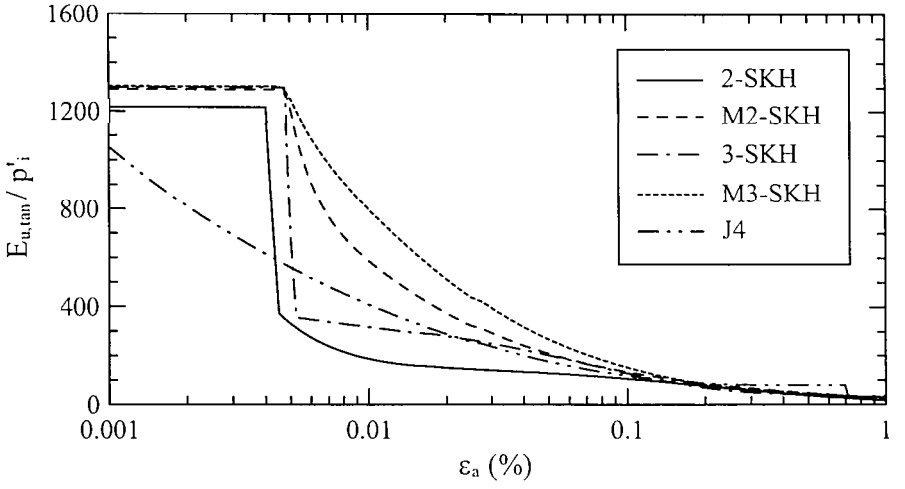
Figure 9.42: Predictions of the models' parameters for an undrained triaxial compression test at the westbound tunnel axis a) normalised stiffness-strain curve b) stress-strain curve

Made Ground/Alluvium

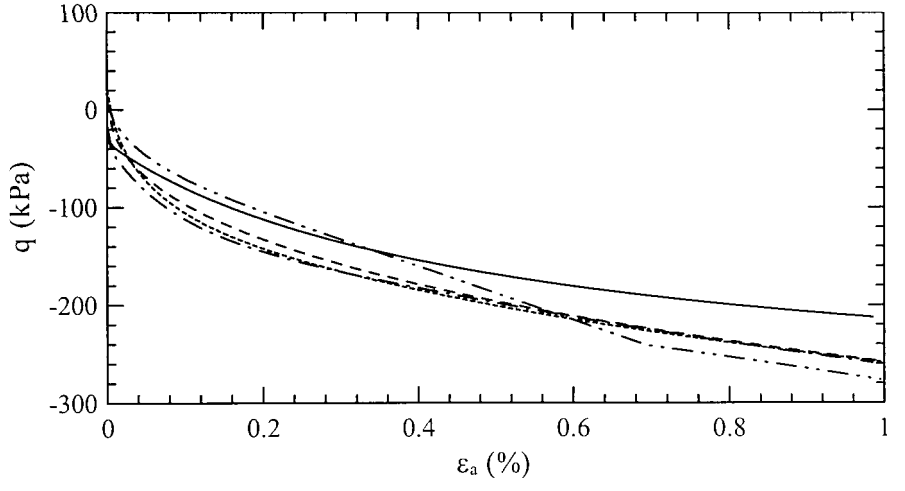
The Made Ground/Alluvium was also modelled with the same parameters as in section 9.5.2.

Tunnel Lining

In these analyses a tunnel lining was constructed once the desired volume loss was reached. This was modelled with beam elements, as a continuous elastic ring of concrete. The parameters used are listed in Table 9.14, defining a linear elastic material model. The unit weight of the tunnel lining was taken equal to 24 KN/m^3.



(a)



(b)

Figure 9.43: Predictions of the models' parameters for an undrained triaxial extension test at the westbound tunnel axis a) normalised stiffness-strain curve b) stress-strain curve

A	B	C (%)	α	γ	$E_{d\,min}$ (%)	$E_{d\,max}$	G_{min}
1120.0	1016.0	$1.0\text{x}10^{-4}$	1.335	0.617	$8.660\text{x}10^{-4}$	0.69282	2333.3
R	S	T (%)	δ	η	$\varepsilon_{v\,min}$ (%)	$\varepsilon_{v\,max}$	K_{min}
549.0	506.0	$1.0\text{x}10^{-3}$	2.069	0.420	$5.0\text{x}10^{-3}$	0.15	3000.0

Table 9.10: Material parameters for the non-linear elastic part of model J4 for London Clay used in the analysis of the twin tunnels at St. James's Park

N	λ^*	κ^*	A	n	m	φ'	Y_p	Z_p	R	α
3.34	0.097	0.003	590.0	0.87	0.28	22.5°	0.0	1.0	0.016	2.0

Table 9.11: Material parameters for the modified two-surface model for London Clay used in the analysis of the twin tunnels at St. James's Park

N	λ^*	κ^*	A	n	m	φ'	Y_p	Z_p	T	S	ψ
3.34	0.097	0.003	590.0	0.87	0.28	22.5°	0.0	1.0	0.2	0.08	2.2

Table 9.12: Material parameters for the three-surface model for London Clay used in the analysis of the twin tunnels at St. James's Park

N	λ^*	κ^*	A	n	m	φ'	Y_p	Z_p	T	S	α_1	α_2
3.34	0.097	0.003	590.0	0.87	0.28	22.5°	0.0	1.0	0.1	0.16	2.0	10.0

Table 9.13: Material parameters for the modified three-surface for London Clay used in the analysis of the twin tunnels at St. James's Park

Young's modulus, E (kPa)	28×10^6
Poisson's ratio, μ	0.15
Cross-sectional area (m^2/m)	0.2
Second moment of area (m^4/m)	6.6667×10^{-4}
Unit weight (kN/m^3)	24.0

Table 9.14: Tunnel lining parameters

9.6.3 Analyses details

In the following analyses the 'volume loss control' method (described in section 9.5.3) was adopted in order to model the three-dimensional tunnelling problem with plane strain finite element analyses.

i) Analyses with the kinematic hardening models modelling the London Clay stratum

The analyses with the kinematic hardening models modelling the London Clay stratum were carried out as follows:

At the start of the excavation of the westbound tunnel the K_o and p'_o / p' profiles of Figures 9.10 and 9.11 were prescribed for each model, with the configuration of the kinematic surfaces A (Figure 9.8a). The water table was at the top of the Terrace Gravel and the pore pressure distribution was hydrostatic with depth. The westbound tunnel was excavated undrained. Once the volume loss of 3.3% was reached the tunnel lining was constructed. The undrained excavation of the eastbound tunnel then followed (no rest period between the excavation of the two tunnels was modelled). Once the volume loss of 2.9% was achieved the tunnel lining in the eastbound tunnel was constructed.

ii) Analyses with model J4 modelling the London Clay stratum

The analyses with model J4 modelling the London Clay deposit were carried out as follows:

At the start of the excavation of the westbound tunnel the initial conditions involved the K_o profile D in Figure 9.13. The pore pressure conditions were the same as in the analyses with the kinematic hardening models. Similar to these analyses, the westbound tunnel was excavated first, undrained, and the tunnel lining was constructed once the volume loss of 3.3% was obtained. The undrained excavation of the eastbound tunnel followed, with the tunnel lining being constructed at a volume loss of 2.9%.

An additional analysis was carried out with model J4, which followed the same procedure as above, but before the excavation of the eastbound tunnel high initial stiffness was re-invoked across the entire mesh. This was done by zeroing the strains throughout the whole mesh, before starting the eastbound tunnel excavation, and hence forcing the model J4 to start again from the high initial stiffness. This is an approach suggested by Jardine et al. (1991) in order to simulate the high stiffness observed on stress path reversals. Unlike the kinematic hardening models, which automatically detect stress path reversals wherever these are happening, model J4 can only re-invoke high stiffness at the beginning of a user-defined increment in the elements of the mesh defined again by the user, regardless of the actual location of the reversals. This analysis will be referred to as analysis J40.

9.6.4 Analyses results

9.6.4.1 Westbound tunnel

Figure 9.44 presents the surface settlement profiles above the westbound tunnel for all models. Field data (after Standing et al. (1996)) are also plotted for comparison. The M2-SKH, 3-SKH and M3-SKH models predict similar settlement troughs which are deeper and narrower than the ones predicted by the 2-SKH and J4 models (these last two models predict also similar profiles). However, comparison with the field observations shows that the finite element predictions are still wider and shallower than measured. It should be noted, though, that the measured settlement profile does not follow exactly a Gaussian distribution (Standing et al. (1996) and Nyren et al. (2001)).

Table 9.15 summarises the volume loss and percentage unloading before the tunnel lining was constructed. It can be seen that the measured volume loss was achieved at

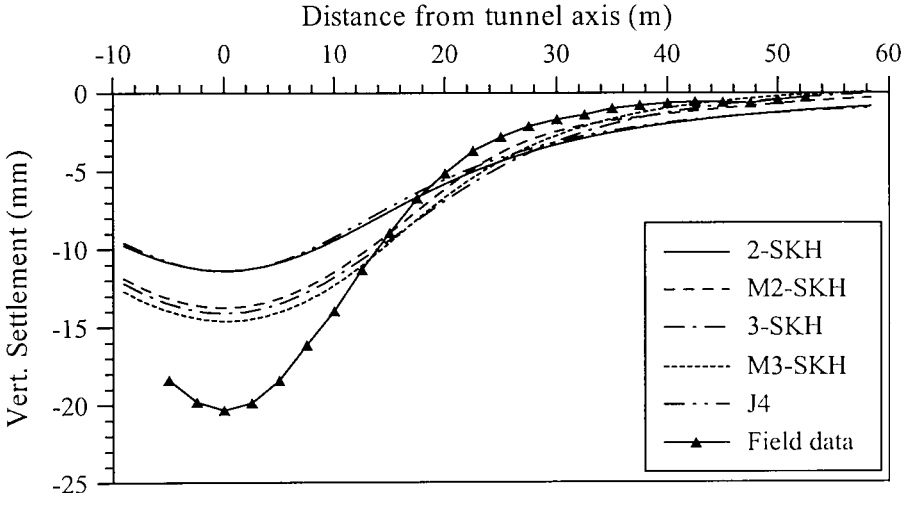


Figure 9.44: Surface settlement profiles: westbound tunnel

Analysis	2-SKH	M2-SKH	3-SKH	M3-SKH	J4
Volume loss (%)	3.31	3.31	3.36	3.28	3.32
Percentage of unloading (%)	50	57	51.4	60	68

Table 9.15: Volume loss and percentage of unloading before the lining was constructed to achieve the volume loss of 3.3% for the westbound tunnel excavation

different degrees of unloading, which, however, varied only between 50% and 60% for the kinematic hardening models. The model J4 obtained this at 68%.

Figure 9.45 presents the subsurface vertical movements with depth predicted by all models directly above the centreline and at a distance of 4 m from the centreline of the tunnel at both sides. The displacements measured at the extensometers at the same locations are also plotted on the same figure (after Standing et al. (1996)). All models predict an increase in vertical movement with depth, which agrees with the trend revealed by the field measurements. At the locations Ax and Cx the predicted movements always remain smaller than the measured values. At the location Bx the predicted movements are generally lower than the measured ones, but they increase close to the tunnel crown and compare reasonably well with the maximum measured value. Moreover, Figure 9.45 shows that, although the M2-SKH, 3-SKH and M3-SKH models predict similar surface settlement troughs and hence values of the vertical movement at the surface, the M3-SKH model predicts a different distribution of vertical movements with depth than the other two models. The M2-SKH and 3-SKH models give similar distributions. The 2-SKH and J4 models, which predicted similar surface settlement profiles, also predict different vertical movement distributions. For locations Ax and Cx and location Bx, from the surface up to approximately a tunnel diameter above the crown of the tunnel, the highest vertical displacements are predicted by the M3-SKH model and the lowest by the 2-SKH model. It should be noted that the distribution of vertical movements predicted by the finite element analyses at locations Ax and Cx is symmetrical whereas the field measurements in Figure 9.45 show a slight asymmetry.

Figure 9.46 plots the distribution of subsurface horizontal movements with depth predicted at a distance of 4 m from the centreline of the tunnel at both sides. Figure 9.46 shows that the field data (after Nyren (1998)) show a pronounced asymmetry. Moreover, at the location Ai the horizontal movements are always directed towards the tunnel whereas at the location Ci the displacements up to a depth of 20 m below ground level are in the opposite direction. This is surprising since the excavation of the westbound tunnel is not influenced by any existing structure and hence, one would expect similar horizontal movements on either side of the tunnel. As expected, the movements predicted by the finite element analyses are symmetrical at the two locations. All models predict horizontal movements towards the excavated tunnel. If the measured values at location Ai are taken as correct, then all models seem to overpredict the maximum

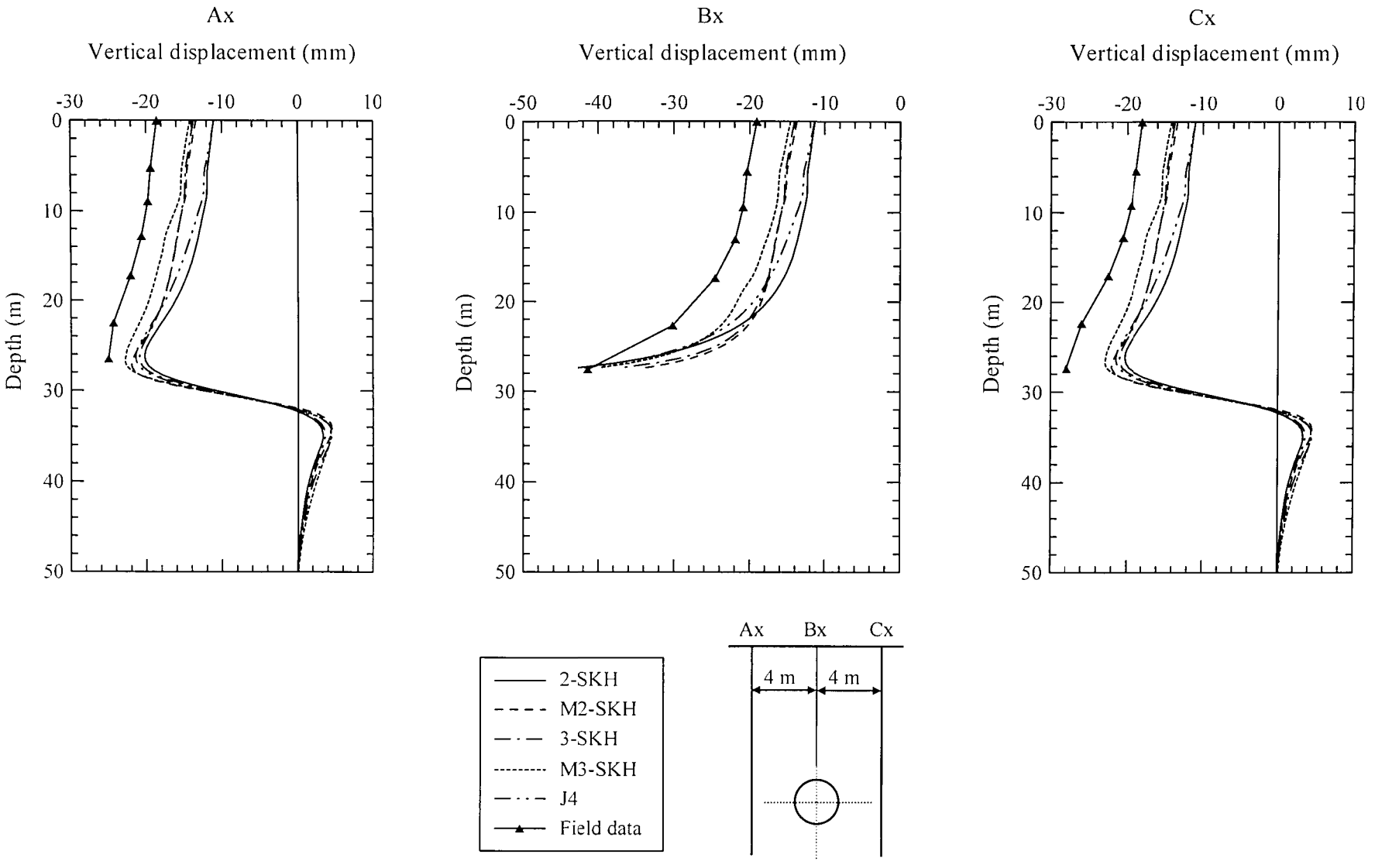


Figure 9.45: Distribution of vertical movements with depth: westbound tunnel

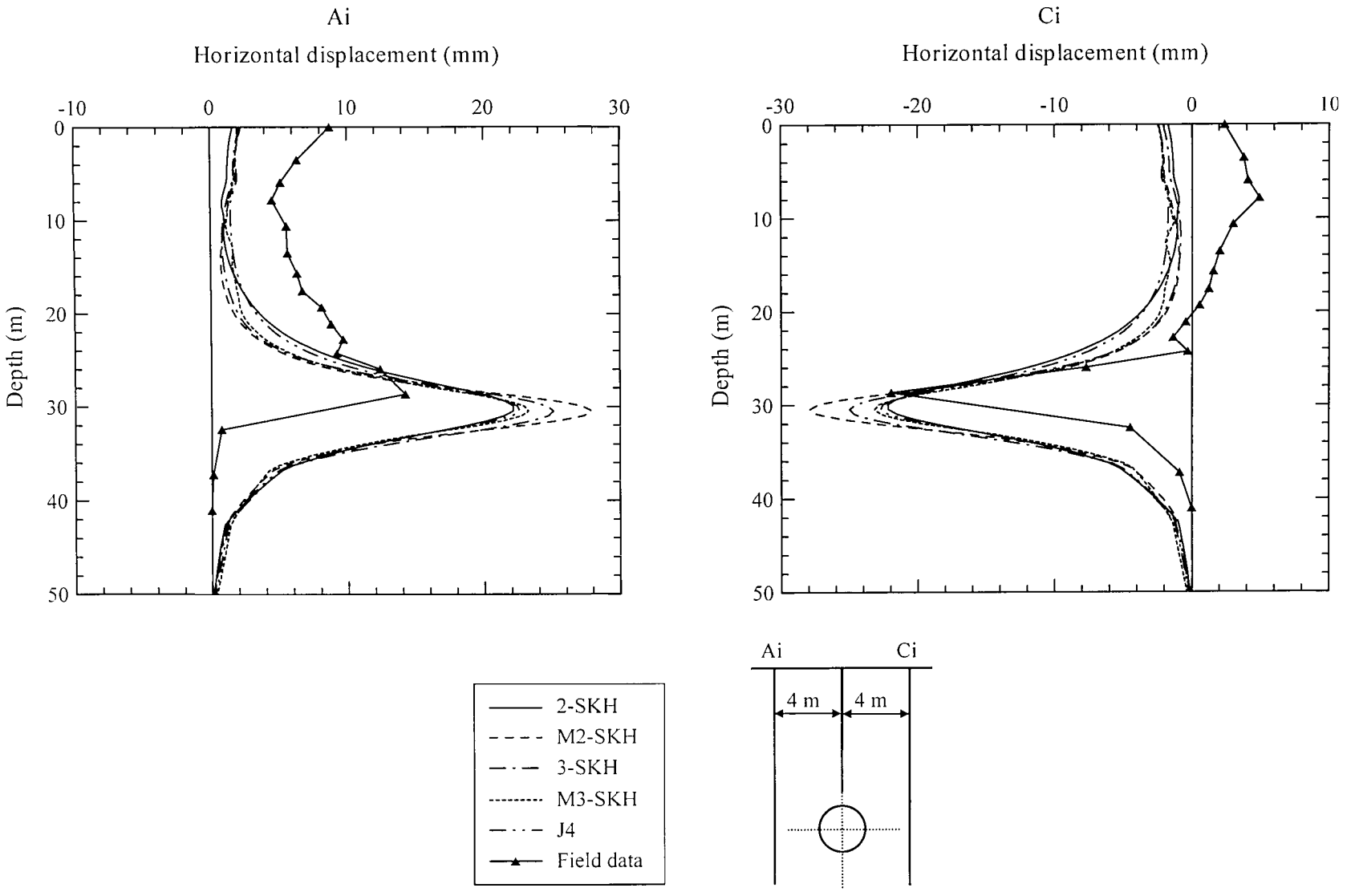


Figure 9.46: Distribution of horizontal movements with depth: westbound tunnel

horizontal movement. However, because of the marked asymmetry revealed by the measurements, no definite conclusion can be drawn from the comparison of the finite element predictions with the field data.

9.6.4.2 Eastbound tunnel

Figure 9.47 presents the surface settlement profiles predicted by all models above the eastbound tunnel, plotted against the field data, as a result solely of the excavation of the eastbound tunnel. Figure 9.47 indicates that the shallowest settlement trough is predicted by the model J4 whereas the deepest one is predicted by the 2-SKH model. The deep settlement trough predicted by the latter model can be explained by the value of K_o at the eastbound tunnel axis and the effect that this has on the particular model (see section 9.5.4.3). The field measurements in Figure 9.47 show an asymmetry about the tunnel axis, with the profile being wider on the side of the previously constructed westbound tunnel than on the opposite side. From the profiles predicted by the kinematic hardening models, the M3-SKH model shows an asymmetry about the centreline of the tunnel, whereas the other models do no predict any marked asymmetry. Similar to the results presented by Addenbrooke et al. (1997), the analysis J40 predicts deeper settlement trough than the analysis J4, but the asymmetry of the surface settlement profile predicted by the analysis J4 is lost.

Table 9.16, which summarises the volume loss and corresponding percentage of unloading before the construction of the lining, indicates that the measured volume loss was obtained at different degrees of unloading, varying between 46 to 76%.

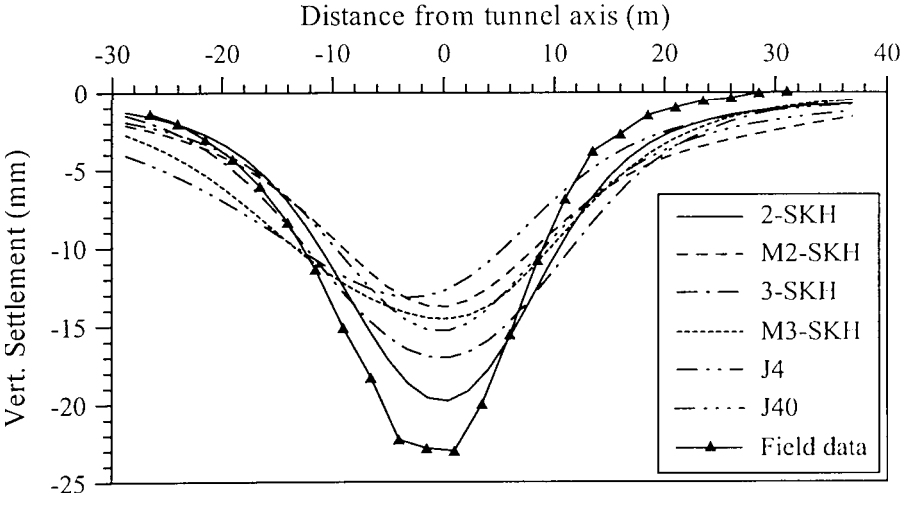


Figure 9.47: Surface settlement profiles: eastbound tunnel

Analysis	2-SKH	M2-SKH	3-SKH	M3-SKH	J4	J40
Volume loss	2.98	2.98	3.0	2.89	2.97	2.96
Percentage of unloading (%)	46	76	62	72	62	68

Table 9.16: Volume loss and percentage of unloading before the lining was constructed to achieve the volume loss of 2.9% for the eastbound tunnel excavation

It is interesting to examine the stress path followed by an element close to the eastbound tunnel axis due to the construction of the westbound tunnel. Figure 9.48 presents such a stress path. The element is subjected to compression, with J increasing up to point A. This point represents the increment of the analysis at which the required volume loss is achieved and the tunnel lining is constructed. The excavation of the tunnel is then completed allowing the forces on the tunnel lining to build up. Point B in Figure 9.48 represents the end of the tunnel construction. It can be seen that from A to B the value of J is decreasing. The excavation of the eastbound tunnel then follows with J increasing again. It is obvious that from A to B a small stress reversal takes place. In the kinematic hardening models this causes the stress state to move within the kinematic yield surface. On the subsequent excavation of the eastbound tunnel, after point B, the high elastic stiffness is therefore re-invoked. In the case of the 2-SKH and 3-SKH models, due to the drop in stiffness that takes place once the stress state becomes elasto-plastic, this small stress reversal is not expected to influence significantly the results. However, in the case of the M2-SKH and M3-SKH models which predict smooth elasto-plastic transition, the

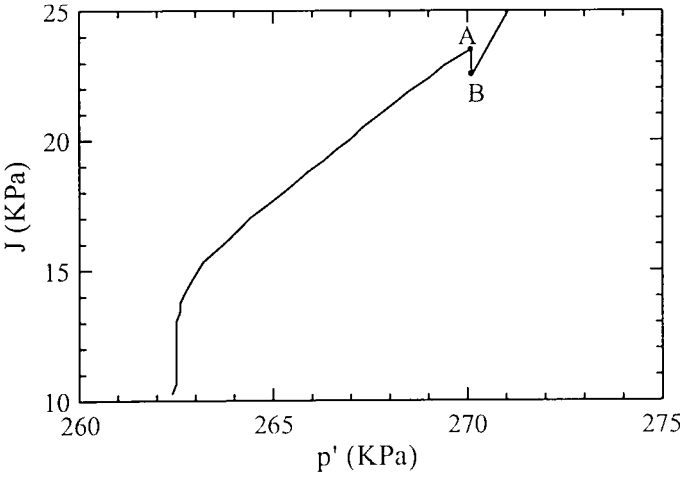


Figure 9.48: Stress path experienced by an element close to the eastbound tunnel axis due to construction of the westbound tunnel

stiffness predicted after the point B, is much higher than what would have been predicted if no stress reversal had taken place. Hence, in this case, the stress reversal, after the construction of the tunnel lining, is expected to influence the predicted settlement trough above the eastbound tunnel. It should be noted, though, that in reality tunnel excavation is a three-dimensional process. In these analyses the 3-D nature of the problem was represented with plane strain analyses using the 'volume loss control' method. Hence, it is not known whether this kind of stress reversal is a result of the plane strain modelling of the problem or would also happen in a 3-D finite element analysis or even in reality.

9.7 Summary and conclusions

This chapter explored the behaviour of the kinematic hardening models, presented in this thesis, in tunnelling problems. Two studies were carried out; a study of the behaviour of a tunnel excavated in London Clay (for two tunnel depths) and a case study of the twin tunnels of the Jubilee Line Extension beneath St. James's Park. The analyses of the kinematic hardening models were compared with analyses using a non-linear elastic pre-yield model (model J4).

a) First study: Analyses of a tunnel in London Clay

This study investigated the influence of the initial conditions before the excavation of the tunnel for each kinematic hardening model. The initial conditions considered were i) the configuration of the kinematic surfaces at the end of the geological history and ii) the assumed initial K_o profile. Moreover, a set of analyses looking into the effect of the stiffness degradation with strain assumed in the models was also carried out. The geological history followed in the analyses was one of unloading due to erosion followed by reloading due to deposition of the overlying layers. Two configurations of the kinematic surfaces were considered in the analyses. The first one resulted from the assumed geological history and simulated the effect of recent stress history. In the second one the surfaces were centred around the stress state at the end of the geological history simulating in this way the effect of stress path direction. The effect of K_o and the stiffness degradation assumed in the models were examined for the second configuration of the kinematic surfaces.

The conclusions that can be drawn from this study are the following:

- For the same K_o profile the predicted surface settlement trough is controlled by the relative stiffness response between the soil elements subjected to compression paths and the soil elements subjected to extension paths.

- The modified two-surface model, the three-surface model and the modified three-surface model predict a deeper and narrower surface settlement trough for the first kinematic surface configuration, resulting from the geological history and simulating the effect of recent stress history, than the second configuration, which simulates the effect of stress path direction. The surface settlement troughs, predicted by these models, for the first kinematic surface configuration plot also much closer to the Gaussian distribution, than the predicted profiles for the second kinematic surface configuration. In the first configuration the stiffness in compression is softer than the stiffness in extension, whereas in the latter case the stiffness in compression and extension is similar. It should be noted that Clayton and Heymann (2001) have recently suggested that if ageing is taken into account then there is no effect of recent stress history and in this case the effect of stress path direction is the one that becomes important.

- The two-surface model gives very similar predictions of the surface settlement trough for the two configurations of the kinematic surface. This can be explained by the inability of the model to retain a memory of the previous stress history and hence predicting approximately the same stiffness response once the stress state becomes elasto-plastic, irrespective of the previous configuration of the kinematic surface (at least for the size of the kinematic surface considered in the analyses).

- The surface settlement profiles predicted by the non-linear model J4 fall within or close to the range of profiles predicted by the modified two-surface model, the three-surface model and the modified three-surface model for the second configuration of the kinematic surfaces. Hence, the profiles predicted by the non-linear J4 model are also shallower and wider than the ones predicted by the same kinematic hardening models for the first kinematic surface configuration. This is because the model J4 predicts similar stiffness in compression and extension and similar to the stiffness that the modified two-surface model, the three-surface model and the modified three-surface model predict for the second

configuration of the kinematic surfaces.

- For the second kinematic surface configuration, which was investigated in this study, the initial K_o profile assumed in the analyses influences the surface settlement troughs predicted by all four kinematic hardening models. For all models the lower value of K_o results in the deepest and narrowest settlement trough. For the second kinematic surface configuration, the value of K_o dictates the relative stiffness between the elements subjected to compression paths and the elements subjected to extension paths (once the stress state is elasto-plastic). This effect is additive to the effect that K_o already has for the same compression and extension stiffness. The two-surface model is influenced significantly by the assumed K_o profile. The modified two-surface model is influenced to a lesser extent, whereas for the three-surface model and the modified three-surface model there is an even smaller effect.

- The non-linear model J4 seems also to be influenced significantly by the assumed K_o profile but to a lesser extent than the two-surface model.

- A softer behaviour assumed in the kinematic hardening models, once the stress state becomes elasto-plastic, results in a relatively deeper settlement trough and in achieving the same volume loss at a smaller percentage of unloading.

- In the case of the two-surface model the drop in stiffness predicted, once yielding is initiated, results in a much softer behaviour than the other models. Hence, the two-surface model reaches the same volume loss at much lower percentages of unloading. In the case of the three-surface model the predicted drop in stiffness results also in the model reaching the same volume loss in lower unloading percentages than the modified two- and three-surface models. However, since the drop in stiffness is smaller than what the two-surface model predicts, there is also a smaller difference in the obtained unloading percentages. If a tunnel lining were to be constructed, then constructing this earlier would have resulted in higher loading forces in the lining.

b) Second study: Analyses of the twin tunnels at St. James's Park

In this study the predictions of the kinematic hardening models and the non-linear model J4 were compared with field data from the instrumented case study of the construction of the two tunnels beneath St. James's Park. The following conclusions can be drawn

from this study:

i) Westbound tunnel

- The modified two-surface, three-surface and modified three-surface models gave similar predictions of the surface settlement profile above the westbound tunnel. The two-surface model and model J4 also predicted similar settlement troughs, which, however, were shallower than those predicted by the other models.

- The models achieved the measured volume loss at different degrees of unloading (50-68%), therefore predicting different forces in the tunnel lining.

- All predicted surface settlement troughs were too wide and shallow when compared to the field observations.

- Although the modified two-surface, the three-surface and modified three-surface models predicted similar settlement troughs, the modified three-surface model predicted higher values of vertical movements with depth than the modified two-surface and the three-surface models. The two-surface model, which predicted similar settlement troughs to the model J4, predicted lower vertical movements with depth than the model J4. From the surface to one diameter above the tunnel crown, the highest vertical movements were predicted by the modified three-surface model and the lowest by the two-surface model.

- All predicted subsurface vertical movements with depth, at a distance of 4 m from the centreline of the tunnel, on either side of the tunnel, were smaller than the observed ones, for all models used in the analyses. The same was true for the predicted distribution of vertical movements with depth directly above the tunnel. However, the predicted vertical movement close to the crown of the tunnel compared reasonably well with the measured value.

- The field observations of the distribution of horizontal movements with depth at a distance of 4 m from the centreline of the tunnel, show a marked asymmetry, although the excavation of the tunnel is not influenced by any existing structure. Therefore no definite conclusion can be drawn from the comparison of the finite element predictions with the field observations.

ii) Eastbound tunnel

- The deepest settlement trough, closer to the field observations, was predicted by the two-surface model and the shallowest by the J4 model. The deep settlement trough predicted by the two-surface model can be explained by the value of K_o at the eastbound tunnel axis and the effect that this has on the particular model.

- The models achieved the volume loss at different unloading percentages varying from 46% to 76%.

- The 2-D modelling of the westbound tunnel construction can cause stress reversals prior to the eastbound tunnel excavation. This is not expected to influence the predictions of the two-surface and three-surface models, but causes hardening of the relevant soil elements in the case of the modified two-surface and modified three-surface models, hence influencing the predicted response.

- The predicted settlement troughs are still shallower and wider than the field observations.

Chapter 10

Summary and conclusions

10.1 Introduction

The main aim of this research was to improve the predictions of the behaviour of overconsolidated clays, and in particular the predictions of the pre-failure behaviour, through the study of constitutive models based on the kinematic hardening concept. The methodology followed was to choose two existing constitutive models that are capable of capturing important features of the behaviour of overconsolidated clays, the two-surface (Al-Tabbaa (1987)) and the three-surface (Stallebrass (1990)) kinematic hardening models. As part of this work the two models were improved and formulated in general stress space. The models were then implemented into the Imperial College Finite Element Program (ICFEP). Although these models offer a substantial improvement in modelling the behaviour of overconsolidated clays, it soon became apparent that both models predict a non-smooth transition from elastic to elasto-plastic behaviour. This proves to be a significant drawback when simulating the non-linear pre-failure behaviour of overconsolidated clays. As part of this work this feature of behaviour was improved by proposing a new hardening modulus for both models and in this way two new models were formulated and implemented into ICFEP, the modified two-surface and modified three-surface kinematic hardening models. The four kinematic hardening models were evaluated and compared to experimental results where possible. The models were then used in the finite element analysis of two boundary value problems. The two-surface and modified two-surface models were used in the analyses of an embankment founded on a lightly overconsolidated clay deposit, while all four models were used in the analyses of tunnels excavated within the heavily overconsolidated London Clay.

10.2 Typical characteristics of overconsolidated clays

The pre-failure deformation of overconsolidated clays is highly non-linear and inelastic, except at very small strains, where a region of almost constant stiffness is usually identified and within which the behaviour is often assumed to be elastic.

The pre-failure behaviour of overconsolidated clays is well known to depend on many factors. The ones explored in this work are the effect of recent stress history and the effect of stress path direction. According to the effect of recent stress history, as reported by Atkinson et al. (1990), the stiffness along a certain loading path depends on the direction of the previous stress path. The highest stiffness is observed when the new stress path constitutes a complete reversal in the previous stress path direction (θ_r = 180°), and the lowest stiffness is observed when the new stress path is a continuation of the previous stress path direction (θ_r = 0°). However, Clayton and Heymann (2001) have recently suggested that once creep is accounted for, then there is no effect of the previous stress history. According to Clayton and Heymann (2001), a rest period results in the stiffness at the very small strains reverting back to the maximum value and the rate of decay of stiffness in the small strain range depending on the stress path direction; the softer response exhibited by the stress path that takes the loading closer to the gross yield surface.

10.3 Kinematic hardening models

The kinematic hardening models introduce a number of kinematic yield surfaces within the conventionally defined yield surface, termed the bounding surface. The behaviour within the first kinematic surface is assumed to be elastic. When the stress state touches the first kinematic surface the behaviour becomes elasto-plastic and the kinematic surface is then dragged along the stress path. In this way, the kinematic hardening models are capable of simulating plasticity and non-linearity from the early stages of loading. Moreover, in these models, the configuration of the kinematic surfaces in stress space provides some memory of the previous loading history.

The two existing kinematic hardening models chosen to be implemented into ICFEP were the two-surface model, developed by Al-Tabbaa (1987) and the three-surface model, developed by Stallebrass (1990). Both models were originally developed in triaxial stress space.

The two-surface model is an extension of the modified Cam Clay model. It introduces a single kinematic yield surface within the modified Cam Clay bounding surface. The model requires seven parameters, five of which have their origin in the modified Cam Clay model.

The three-surface model is an extension of the two-surface model. It introduces an additional kinematic surface, the history surface, so as to simulate satisfactorily the effect of recent stress history. The model requires one additional parameter to the seven required by the two-surface model.

As aforementioned, both models were formulated in general stress space, as part of this work. The models were further improved by introducing different shapes of the yield and plastic potential surfaces in the deviatoric plane. Moreover, in the case of the two-surface model a new translation rule was adopted for the case that the two surfaces are in contact. The new translation rule guarantees that the surfaces remain in contact for further loading.

Both models were shown to predict an abrupt elasto-plastic transition, which results in a drop in stiffness once yielding is initiated. This feature of behaviour is attributed to the hardening modulus assumed in both models. In order to improve this deficiency, two new models were formulated, the modified two-surface and modified three-surface models. The new models differ from the generalised versions of the two- and three-surface models only in the adopted hardening modulus. The new hardening modulus for the modified two- and three-surface models ensures a smooth elasto-plastic transition and stiffness degradation curves. The two new models were formulated directly in general stress space.

Common features of the generalised versions of the two- and three-surface models and the modified two- and three-surface models are the following:

- The models are formulated in terms of the volumetric and deviatoric components of the stress and strain tensors and therefore have an anisotropic formulation.

- The models can predict anisotropic yielding and stiffness characteristics, for stress paths that initiate within the bounding surface, depending on the configuration of the kinematic surfaces relative to the initial stress state. However, the strength predicted by the models is isotropic, since this is

governed by the isotropic bounding surface.

- The shape of the yield and plastic potential surfaces in the deviatoric plane is not necessarily circular but can take a number of different shapes, simulating in this way more realistic failure conditions. The yield surface can take either the shape of a Mohr-Coulomb hexagon or the general shape proposed by van Eekelen (1980), while the plastic potential takes the latter shape. Depending on the choice of the input parameters, the general shape proposed by van Eekelen (1980) can simulate different shapes including the one proposed by Lade (Lade and Duncan (1975)) and a circular shape.

- When all surfaces are in contact and for continuous yielding all four models degenerate to the modified Cam Clay model.

- The concept of changing the active yield surface each time one or more surfaces are in contact was adopted in all models, overcoming, in this way, the problem of the inconsistent hardening modulus and the translation rule of the surfaces when these are in contact.

- The elastic shear strains can be calculated by assuming a constant Poisson's ratio, μ, a constant elastic shear modulus, G_e, a constant ratio G_e/p', or an elastic shear modulus G_e calculated by an equation of the form proposed by Viggiani (1992) (Equation 4.51).

The introduction of different shapes of the yield and plastic potential surfaces in the deviatoric plane and the use of Equation 4.51 introduce additional model parameters. The generalised version of the two-surface model and the modified two-surface model require either nine parameters when the shape of the yield surface in the deviatoric plane is a Mohr-Coulomb hexagon or eleven if a general shape is adopted instead. The generalised version of the three-surface model requires ten or twelve parameters depending on the shape of the yield surface in the deviatoric plane, while the modified three-surface model requires eleven or thirteen parameters.

For all four models, five of the parameters have their origin in the modified Cam Clay model. In the two-surface and the modified two-surface models two additional parameters are required in order to define the behaviour of the kinematic surface. In the three-surface model three parameters are required in order to define the behaviour of the two kinematic surfaces, whereas in the modified three-surface model four parameters are

required. The adopted hardening modulus in the latter model introduces an additional parameter as compared to the hardening modulus of the three-surface model. These parameters can be derived from standard isotropic and triaxial tests as described in Chapters 4, 5 and 6 (the elastic shear modulus G_e can also be deduced from dynamic measurements). The rest of the parameters required in the generalised formulations of the models control the shape of the yield and plastic potential surfaces in the deviatoric plane. For all four models, if the elastic shear modulus, G_e, is defined by Equation 4.51, then two extra parameters are required.

The four models were implemented into ICFEP. The calculation of the terms required for the implementation of the models and the flowcharts of the subroutines of the models have been presented in detail.

10.4 Evaluation of the kinematic hardening models

The evaluation of the four kinematic hardening models was subdivided into three parts. In the first part a set of undrained triaxial tests on reconstituted London Clay was simulated and the capability of the models to simulate pre-failure non-linearity, in particular, was investigated. In the second part the ability of the models to simulate the effect of recent stress history was studied. Finally, the last part examined the way the models can simulate the effect of stress path direction.

The conclusions drawn from these studies can be summarised as follows:

a) Pre-failure non-linearity

Compression tests:

- The modified two-surface, the three-surface and the modified three-surface models predicted reasonably well the stress-strain curves at *OCR* values of 3 and 7 up to large strains. The two-surface model predicted reasonably well the same stress-strain curves up to strains of 1%.

- The modified two- and three-surface models predicted smooth stiffness degradation curves which agreed better with the experimental data than the ones predicted by the two- and three-surface models. Hence, the modified models are an improvement over the original models.

- Both the two- and three-surface models predicted drops in stiffness once yielding was initiated. However, the three-surface model predicted smaller drops of stiffness and compared better with the experimental data than the two-surface model. This is due to the presence of the history surface in this model, as well as the chosen model parameters.

Extension tests:

- The simulation of the extension tests was less satisfactory. All models generally underpredicted the initial part of the stiffness-strain curves. This was attributed to the rest period allowed before shearing the samples in the laboratory, which possibly resulted in increased stiffness in the small strain range. However, no such time effects were modelled in the numerical simulation of the tests and, for the extension tests, the models kept on behaving plastically, hence, predicting low values of stiffness initially.

b) Effect of recent stress history

- The two-surface model is unable to retain a memory of the previous stress history, once the stress state touches the kinematic yield surface (at least for the size of the kinematic yield surface examined in this work).

- The modified two-surface is capable of retaining some memory of the previous loading path, since it can predict qualitatively the stiffness curves for $\theta_r = 0^\circ$ and $\theta_r = 180^\circ$, but not the ones for $\theta_r = 90^\circ$ and $\theta_r = -90^\circ$. Hence, this is another improvement over the two-surface model.

- The three-surface model predicted reasonably well the stiffness curves after each of the four stress path rotations. However, not all curves are smooth and a drop in stiffness is still predicted once yielding is initiated.

- The modified three-surface model predicted satisfactorily the stiffness curves for $\theta_r = 0^\circ$, $\theta_r = 90^\circ$ and $\theta_r = 180^\circ$, but predicted high stiffness for $\theta_r = -90^\circ$. However, the high stiffness predicted for this path can be explained by considering the normality rule assumed in the model.

- Overall, the presence of the history surface in the three-surface and modified three-surface models provides a better memory of the previous stress history over the two-surface and modified two-surface models. It also results in a better

qualitative prediction of the observed strain paths.

c) Effect of stress path direction

- The effect of stress path direction, as reported by Clayton and Heymann (2001), can be simulated in the four kinematic hardening models by centring the kinematic surfaces around the current stress state at the end of the previous stress history.

Comparison of undrained triaxial compression and extension tests in which the kinematic surfaces were centred around the current stress state at the end of a previous assumed stress history (simulating in this way the effect of stress path direction), with similar analyses in which there was no centring of the kinematic surfaces at the end of the previous stress history, showed the following:

- For the two-surface model there was practically no difference between the two sets of analyses, once the stress state touched the kinematic surface. This was attributed to the inability of the model to retain a memory of the previous stress history and resulted in the stiffness response predicted by the model being independent of the previous configuration of the kinematic surface, once yielding is initiated.

- For the other three models each set of analyses resulted in a different stiffness response, which depended on the configuration of the kinematic surfaces at the start of shearing.

- In general, the kinematic hardening models predict a different stiffness response between compression and extension paths (at least for $K_o \neq 1.0$).

10.5 The use of kinematic hardening models in the analyses of an embankment

The predicted short term behaviour of an embankment, when its soft clay foundation is modelled with the kinematic hardening models, was investigated through two studies. The first study compared the pre-failure deformational behaviour of the embankment predicted by the two-surface and modified two-surface models. The predictions of the two kinematic hardening models were also compared with the predictions of the

modified Cam Clay model. The second study examined the effect of the shape of the yield and plastic potential surfaces in the deviatoric plane on the predicted failure height of the embankment.

The conclusions reached from these studies can be summarised as follows:

a) Pre-failure deformational behaviour of the embankment

- When the same undrained strength profile was assigned to all three models (two-surface, modified two-surface and modified Cam Clay), then these predicted the same failure height, but different deformational behaviour of the embankment.

- The pre-failure deformations were found to be influenced by both non-linearity and the difference in the stiffness response between compression and extension paths.

Concerning the comparison of the two kinematic hardening models:

- When the model parameters were chosen so that both models predicted similar response in compression, the modified two-surface model predicted smaller movements in the initial stages and larger movements in the later stages of the embankment construction than the two-surface model. This was attributed to the different response predicted by the two models in extension, as well as the non-smooth elasto-plastic transition predicted by the two-surface model.

- When K_o = 1.0 was assumed in the analyses, in which case the stiffness in compression was the same as the stiffness in extension, for each model, the two kinematic hardening models still predicted a different deformational behaviour. The modified two-surface model predicted considerably smaller movements than the two-surface model. This was attributed to the non-smooth elasto-plastic transition predicted by the two-surface model, which resulted in an underprediction of the stiffness, once yielding was initiated, and hence in a softer response as compared to the modified two-surface model. Although no analyses were carried out with the three-surface model, a similar response is expected, since this model also shows an abrupt elasto-plastic transition. The amount by which the pre-failure movements are underpredicted is expected to depend on the magnitude of the drop in stiffness.

Concerning the comparison of the kinematic hardening models with the modified Cam Clay model:

- When an average stiffness applicable to a stress level of 50% in triaxial compression was chosen for the modified Cam Clay model, then this overpredicted in the initial stages and underpredicted in the later stages of the embankment construction the pre-failure movements, as compared to the kinematic hardening models. The difference was attributed to the non-linear behaviour predicted by the kinematic hardening models, as compared to the almost linear behaviour of the modified Cam Clay model within the yield surface, as well as the fact that the kinematic hardening models predict a different stiffness response between compression and extension, as compared to the same stiffness in compression and extension predicted by the modified Cam Clay model, within the yield surface.

b) Failure height of the embankment

- When the same undrained strength is prescribed in triaxial compression, the predicted failure height of the embankment, under plane strain conditions, is strongly influenced by the shape of the yield and plastic potential surfaces in the deviatoric plane.

- For a model which predicts isotropic strength the choice of the shape of the yield and plastic potential surfaces in the deviatoric plane is as important as the undrained strength profile chosen for design (i.e. triaxial compression profile or direct simple shear profile).

10.6 The use of kinematic hardening models in tunnelling problems

The behaviour of the four kinematic hardening models in tunnelling problems was examined through two studies. The first study explored the influence of i) the initial configuration of the kinematic surfaces, ii) the initial K_o profile and iii) the stiffness degradation with strain on the surface settlement profiles induced by the undrained excavation of a tunnel, within the heavily overconsolidated London Clay. The second study modelled the twin tunnels of the Jubilee Line Extension, beneath St. James's Park

and the predictions were compared with available field data. The analyses of the kinematic hardening models were also compared with analyses using a non-linear elastic pre-yield model, combined with a Mohr-Coulomb yield surface and a non-associated flow rule.

The conclusions drawn from these studies can be summarised as follows:

a) Analyses of a tunnel in London Clay

Concerning the effect of the configuration of the kinematic surfaces prior to tunnel excavation:

- For the modified two-surface, three-surface and modified three-surface models the predicted surface settlement trough was shown to depend on the configuration of the kinematic surfaces at the start of the tunnel excavation. This was attributed to the fact that different kinematic surface configurations resulted in different relative stiffness responses between compression and extension paths.

- For the above three models a deeper and narrower settlement trough was predicted for the kinematic surface configuration which resulted from the simulation of the previous geological history (modelling erosion and subsequent deposition) than for the configuration in which the surfaces were centred around the initial stress state and which simulated the effect of stress path direction. In the former configuration the stiffness response in compression was softer than the stiffness response in extension, whereas in the latter configuration the stiffness response in compression and extension was similar. The profiles predicted in the first case also plot much closer to the Gaussian distribution curve than for the second case.

- For the two-surface model the predicted surface settlement trough was shown to be almost independent of the configuration of the kinematic surface prior to tunnel excavation. This was attributed to the inability of the model to retain a memory of the previous stress history, once yielding is initiated, and hence predicting approximately the same relative stiffness response between compression and extension paths independently of the previous kinematic surface configuration (at least for the size of the kinematic surface considered in these analyses).

Concerning the comparison of the predictions of the kinematic hardening models with the predictions of the non-linear elastic pre-yield model:

- The non-linear elastic model predicted settlement troughs which plot close or within the range predicted by the modified two-surface, three-surface and modified three-surface models for the configuration simulating the effect of stress path direction. These were shallower and wider than those predicted by the same three kinematic hardening models for the kinematic surface configuration resulting from the simulation of the geological history. This was attributed to the fact that the non-linear model predicted similar stiffness response in compression and extension, which was comparable to the stiffness response predicted by the three kinematic hardening models for the configuration simulating the effect of stress path direction.

Concerning the effect of the initial K_o profile for the kinematic surface configuration which simulates the effect of stress path direction:

- All four kinematic hardening models are influenced by the K_o profile but to a different extent. The two-surface model is influenced significantly, the modified two-surface model is influenced in a lesser extent, while the three-surface and modified three-surface models show an even smaller effect. This is due to the fact that, apart from the effect that the K_o profile has if the soil has the same compression and extension stiffness, the K_o value also controls the relative stiffness response between compression and extension paths. For the two-surface model the variations in the values of K_o resulted in a bigger relative difference between the stiffness response in compression and extension than for the other three models.

Concerning the effect of the rate of decay of stiffness:

- A quicker rate of stiffness decay with strain resulted in a relatively deeper settlement trough and in achieving the same volume loss at lower percentage of unloading. If a tunnel lining were to be constructed, then constructing this earlier would have resulted in higher loading forces on the lining.

- The two-surface model achieved the same volume loss at much lower unloading percentages than the other models. This is due to the drop in stiffness predicted by the model, once the stress state becomes elasto-plastic, which resulted in a

much softer behaviour for this model as compared to the other models.

- The three-surface model also obtained the same volume loss quicker than the modified two-surface and modified three-surface models. However, due to the smaller drop in stiffness predicted by the model, as compared to the two-surface model, the same volume loss was achieved later than for the two-surface model.

b) Twin tunnels at St. James Park

Westbound tunnel:

- The surface settlement profiles predicted by all models are too shallow and wide when compared to the field measurements.

- For similar surface settlement troughs, the models predicted different profiles of subsurface vertical movements. However, all the predictions are too small when compared with the measured movements at a distance of 4.0 m from the centreline of the tunnel. The predicted vertical subsurface movements directly above the tunnel are generally smaller than the observed ones, apart from the vertical movement close to the crown of the tunnel, which compared reasonably well with the measured value.

- No definite conclusion can be drawn from the comparison of the horizontal movements at a distance of 4.0 m from the centreline of the tunnel with the observed data. This is because the measured profiles show an unexpected marked asymmetry.

Eastbound tunnel:

- The surface settlement profiles predicted by all models are too shallow and wide when compared to the field measurements.

- The deeper settlement trough, closer to the field observations, which is predicted by the two-surface model, can be explained in terms of the K_o value at the eastbound tunnel axis for this model and the effect that this has on the behaviour of the particular model.

- Modelling of the construction of the westbound tunnel lining in plane strain analyses causes stress path reversals prior to the eastbound tunnel excavation. While this is not expected to affect the response predicted by the two- and three-

surface models, it influences the behaviour of the modified two- and three-surface models by causing hardening of the relevant soil elements.

10.7 Recommendations for further research

The following recommendations for further research are presented for four areas of interest: experimental studies, evaluation of kinematic hardening models, numerical studies and constitutive modelling.

10.7.1 Experimental studies

The finite element analyses presented in Chapter 9 investigated two scenarios. In the first scenario it was assumed that stiffness depends on the previous stress history. The second scenario assumed that stiffness is independent of the previous stress history and that it only depends on the stress path direction. Comparison of the results obtained demonstrated that a different predicted response is obtained for each scenario. Therefore, this study suggests that more experimental investigations are needed in order to assess and clarify the effect of recent stress history, the effect of stress path direction and the effect that ageing periods have on them.

10.7.2 Evaluation of kinematic hardening models

In terms of the evaluation of the kinematic hardening models presented in this thesis:

The evaluation of the kinematic hardening models presented in this thesis has mostly concentrated on modelling the undrained behaviour of overconsolidated clays. However, the models could be further evaluated by also simulating a set of drained tests and comparing the predicted behaviour with the experimental results.

In terms of the evaluation of any kinematic hardening model:

The behaviour of the kinematic hardening models has often been evaluated in the past by examining only the predicted behaviour along compression paths, and hence, the behaviour along extension paths has often been overlooked. However, the work presented in this thesis has highlighted the importance of the soil stiffness response in both compression and extension paths. Since any kinematic hardening model predicts a different stiffness response between compression and extension paths, it is important

that in the evaluation of the kinematic hardening models the predicted response against extension paths is equally examined.

10.7.3 Numerical studies

A main advantage of the kinematic hardening models over linear and non-linear elastic models is the fact that the former allow for the development of plastic strains from the early stages of loading and therefore are capable of capturing the hysteretic behaviour observed during cycles of unloading and reloading. Unfortunately, the boundary value problems considered in this thesis did not investigate this feature of behaviour. Hence, it would be interesting to use these models in boundary value problems involving cyclic loading. For example Kovacevic et al. (2004) have recently used the two-surface model in the finite element analysis of a dam subjected to cycles of reservoir drawdown and impounding. The predictions of the two-surface model were compared with the predictions of another two constitutive models, the modified Cam Clay model and Lade's single hardening model, and also compared with available field data. The conclusion reached was that the two-surface model gave better predictions than the other two models and the reason for this was attributed to the capability of the model to predict the hysteretic behaviour observed during cycles of unloading and reloading.

In addition, both boundary value problems, analysed as part of this thesis, were concerned with the undrained behaviour of overconsolidated clays. However, it would be interesting to examine the performance of the models also in drained or coupled finite element analyses.

10.7.4 Constitutive modelling

Obvious improvements of the kinematic hardening models presented in this thesis are extensions of the models to account for i) the effects of structure in natural soils, ii) additional effects of anisotropy and iii) time effects.

Effects of structure and additional effects of anisotropy:

As mentioned in the literature review of this thesis, Baudet (2001) has already extended the three-surface model and Rouainia and Muir Wood (2000) have extended the two-surface model in order to model the effects of structure. Moreover, the kinematic hardening models proposed by Gajo and Muir Wood (2001) and Callisto et al. (2002)

introduce rotated yield and bounding surfaces to account for anisotropy in strength. However, although these models constitute a significant improvement in modelling the behaviour of clays, they still predict a non-smooth elasto-plastic transition, which has been shown to be an important deficiency when simulating pre-failure non-linearity. Similar to the two-surface and three-surface models, the problem of the abrupt elasto-plastic transition in these more advanced models can be solved by modifying the hardening modulus. For example, the new hardening modulus adopted in the modified two-surface and modified three-surface models can be easily incorporated within those existing models.

Time effects:

The models in their present form cannot account for time effects. Stallebrass (1990) proposed a way time effects could be included in the three-surface model. It was suggested that creep can be included by allowing plastic volumetric strains to develop at a constant stress state at a rate controlled by a creep equation. In this way the surfaces would expand while the stress state would remain the same and hence the stress state would end up within the elastic region. For any subsequent loading the high elastic stiffness would be predicted initially. Another way of modelling time effects in the kinematic hardening models would be to allow a time dependent movement of the kinematic surfaces in a way that after sufficiently long enough time the surfaces would end up being centred around the current stress state. However, both approaches have an obvious drawback. This is that as soon as the stress state ends up within the elastic region, high elastic stiffness would be predicted on any subsequent loading. Hence, unfortunately it would not be possible to simulate a gradual increase of stiffness with time.

References

Addenbrooke T.I. (1996). *Numerical analysis of tunnelling in stiff clay.* PhD thesis, Imperial College, University of London, London, UK.

Addenbrooke T.I., Potts D.M. and Puzrin A.M. (1997). The influence of pre-failure soil stiffness on the numerical analysis of tunnel construction. *Geotechnique*, Vol. 47, No. 3, pp. 693-712.

Al-Tabbaa A. (1987). *Permeability and stress-strain response of speswhite kaolin.* PhD thesis, University of Cambridge, Cambridge, UK.

Al-Tabbaa A. and Wood D.M. (1989). An experimental based "bubble" model for clay. *International Conference on Numerical Models in Geomechanics*, A. Pietruszczak and G.N. Pande (eds.), Balkema, pp. 91-99.

Atkinson J.H. and Bransby P.L. (1978). *The mechanics of soils. An introduction to critical state soil mechanics.* London : McGraw-Hill.

Atkinson J.H., Richardson D. and Stallebrass S.E. (1990). Effect of recent stress history on the stiffness of overconsolidated soil. *Geotechnique*, Vol. 40, No. 4, pp. 531-540.

Atkinson J.H. and Sallfors G. (1991). Experimental determination of stress-strain-time characteristics in laboratory and in situ tests. *Proceedings of the 10th European Conference on Soil Mechanics and Foundation Engineering*, Florence, Vol. 3, pp. 915-956.

Baudet B.A. (2001). *Modelling effects of structure in soft natural clays.* PhD thesis, City University, London, UK.

Bishop A.W., Webb D.L. and Lewin P.I. (1965). Undisturbed samples of London Clay from the Ashford Common Shaft: strength-effective stress relationships. *Geotechnique*, Vol. 15, No. 1, pp. 1-31.

Bjerrum L. (1967). 7th Rankine Lecture : Engineering geology of Norwegian normally-consolidated marine clays as related to settlements of buildings. *Geotechnique*, Vol. 17, No. 2, pp. 81-118.

Bjerrum L. (1973). Problems of soil mechanics and construction on soft clays and structurally unstable soils (collapsible, expansive and others). *Proceedings of the 8th International Conference on Soil Mechanics and Foundation Engineering*, Moscow, Vol. 3, pp. 111-159.

Burland J.B. (1989). Ninth Laurits Bjerrum Memorial Lecture: "Small is beautiful"- the stiffness of soils at small strains. *Canadian Geotechnical Journal*, Vol. 26, pp. 499-516.

Burland J.B. (1990). 30th Rankine Lecture : On the compressibility and shear strength of natural clays. *Geotechnique*, Vol. 40, No. 3, pp. 329-378.

Burland J.B. and Symes M. (1982). A simple axial displacement gauge for use in the triaxial apparatus. *Geotechnique*, Vol. 32, No. 1, pp. 62-65.

Burland J.B. and Kalra J.C. (1986). Queen Elizabeth II Conference Centre: geotechnical aspects. *Proceedings of the Institution of Civil Engineers*, Vol. 80, pp. 1479-1503.

Butterfield R. (1979). A natural compression law for soils. *Geotechnique*, Vol. 29, No. 4, pp. 469-480.

Callisto L., Gajo A. and Muir Wood D. (2002). Simulation of triaxial and true triaxial tests on natural and reconstituted Pisa clay. *Geotechnique*, Vol. 52, No. 9, pp. 649-666.

Chandler R.J. (1999). Clay sediments in depositional basins: the geotechnical cycle. *Quarterly Journal of Engineering Geology and Hydrogeology*, Vol. 33, pp. 7-39.

Clayton C.R.I. and Heymann G. (2001). Stiffness of geomaterials at very small strains. *Geotechnique*, Vol. 51, No. 3, pp. 245-255.

Costa-Filho L.M. and Vaughan P.R. (1980). Discussion on "A computer model for the analysis of ground movements in London clay" by Simpson et al. (1979). *Geotechnique*, Vol. 30, pp. 336-339.

Coop M.R., Atkinson J.H. and Taylor R.N. (1995). Strength and stiffness of structured and unstructured soils. *Proceedings of the 11th European Conference on Soil*

Mechanics and Foundation Engineering, Copenhagen, Vol. 1, pp. 55-62.

Cotecchia F. and Chandler R.J. (1997). The influence of structure on the pre-failure behaviour of a natural clay. *Geotechnique*, Vol. 47, No. 3, pp. 523-544.

Cotecchia F. and Chandler R.J. (2000). A general framework for the mechanical behaviour of clays. *Geotechnique*, Vol. 50, No. 4, pp. 431-447.

Dafalias Y.F. and Herrmann (1980). A bounding surface soil plasticity model. *International Symposium on Soils under Cyclic and Transient loading*, Swansea, Vol. 1, pp. 335-345.

Dafalias Y.F. and Herrmann (1982). Bounding surface formulation of soil plasticity. *Soil Mechanics-Transient and Cyclic Loads*, G.N. Pande and O.C. Zienkiewicz (eds.). John Wiley and Sons Ltd.

Dafalias Y.F. and Popov E.P. (1975). A model of nonlinearly hardening materials for complex loadings. *Acta Mechanica*, Vol. 21, pp. 173-192.

Dafalias Y.F. and Popov E.P. (1976). Plastic internal variables formalism of cyclic plasticity. *Journal of Applied Mechanics, ASME*, Vol. 98, pp. 645-650.

Dolezalova M. (2002). Approach to numerical modelling of ground movements due to shallow tunnelling. *Proceedings of the 2nd International Conference on Soil Structure Interaction in Urban Civil Engineering*, pp. 365-374.

Eekelen H.A.M. van (1980). Isotropic yield surfaces in three dimensions for use in soil mechanics. *International Journal for Numerical and Analytical Methods in Geomechanics*, Vol. 4, pp. 89-101.

Fourie A.B. (1984). *The behaviour of retaining walls in stiff clay*. PhD thesis, Imperial College, University of London, London, UK.

Franzius J.N. (2004). *The behaviour of buildings due to tunnel induced ground movements*. PhD thesis, Imperial College, University of London, London, UK.

Gajo A. and Muir Wood D. (2001). A new approach to anisotropic, bounding surface plasticity: general formulation and simulations of natural and reconstituted clay behaviour. *International Journal for Numerical and Analytical Methods in Geomechanics*, Vol. 25, pp. 207-241.

Gens A. (1982). *Stress-strain and strength of a low plasticity clay*. PhD thesis, Imperial College, University of London, London, UK.

Gens A. (1995). General report: Prediction, performance and design. *Pre-Failure Deformation of Geomaterials*, Shibuya, Mitachi and Miura (eds.), Balkema, Vol. 2, pp. 1233-1247.

Georgiannou V.N., Rampello S. and Silvestri F. (1991). Static and dynamic measurements of undrained stiffness on natural overconsolidated clays. *Proceedings of the 10th European Conference on Soil Mechanics and Foundation Engineering*, Florence, Vol. 1, pp. 91-96.

Graham J., Noonan M.L. and Lew K.V. (1983). Yield states and stress-strain relationships in a natural plastic clay. *Canadian Geotechnical Journal*, Vol. 20, pp. 502-516.

Gunn M.J. (1993). The prediction of surface settlement profiles due to tunnelling. *Predictive Soil Mechanics*. Thomas Telford, London, UK, pp. 304-316.

Hardin B.O. and Black W.L. (1968). Vibration modulus of normally consolidated clay. *Journal of the Soil Mechanics and Foundations Division, ASCE*, Vol. 94, No. SM2, pp. 353-369.

Hardin B.O. and Black W.L. (1969). Closure to: Vibration modulus of normally consolidated clay. *Journal of the Soil Mechanics and Foundations Division, ASCE*, Vol. 95, No. SM3, pp. 1531-1537.

Hardin B.O. (1978). The nature of stress-strain behavior for soils. *Proceedings of Specialty Conference on Earthquake Engineering and Soil Dynamics, ASCE*, Pasadena, California, pp. 3-90.

Hashiguchi K. (1980). Constitutive equations of elastoplastic materials with elastic-plastic transition. *Journal of Applied Mechanics, ASME*, Vol. 47, pp. 266-272.

Hashiguchi K. (1985). Two- and three-surface models of plasticity. *Proceedings of the 5th International Conference on Numerical Methods in Geomechanics*, Nagoya, pp. 285-292.

Hashiguchi K. (1989). Subloading surface model in unconventional plasticity. *International Journal of solids and structures*, Vol. 25, pp. 917-945.

Hashiguchi K. and Ueno M. (1977). Elastoplastic constitutive laws of granular materials. *Constitutive equations of soils, Proceedings of the 9th International Conference on Soil Mechanics and Foundation Engineering*, Special session 9, Tokyo, pp. 73-82.

Heymann G. (1998). *The stiffness of soils and weak rocks at very small strains*. PhD thesis, University of Surrey, Guildford, UK.

Hight D.W., Gens A. and Symes M.J. (1983). The development of a new hollow cylinder apparatus for investigating the effects of principal stress rotation in soils. *Geotechnique*, Vol. 33, No. 4, pp. 355-384.

Hight D.W., McMillan F., Powell J.J.M., Jardine R.J. and Allenou C.P. (2003). Some characteristics of London Clay. *Characterisation and engineering properties of natural soils*, Vol. 2, Tan et al. (eds.), Balkema, Lisse, pp. 851-946.

Hird C.C. and Pierpoint N.D. (1997). Stiffness determination and deformation analysis for a trial excavation in Oxford Clay. *Geotechnique*, Vol. 47, No. 3, pp. 665-691.

Hvorslev M.J. (1937). Uber die Festigkeitseigenschaften gestorter bindiger Boden. *Ingerniorvidenshabelige Skriften*, no. 45, Danmarks Naturvidenshabelige Samfund, Kopenhavn, Denmark.

Isenhower W.M. and Stokoe K.H. (1981). Strain-rate dependent shear modulus of San Francisco Bay Mud. *Proceedings of the International Conference on recent advances in earthquake engineering and soil dynamics*, University of Missouri-Rolla, Vol. 2, pp. 597-602.

Iwan W.D. (1967). On a class of models for the yielding behavior of continuous and composite systems. *Journal of Applied Mechanics, ASME*, Vol. 34, pp. 612-617.

Jamiolkowski M., Lancellotta R. and Lo Presti D.C.F. (1995). Remarks on the stiffness at small strains of six Italian clays. *Pre-Failure Deformation of Geomaterials*, Shibuya, Mitachi and Miura (eds.), Balkema, Vol. 2, pp. 817-836.

Janbu N. (1963). Soil compressibility as determined by oedometer and triaxial tests. *Proceedings of the 2nd European Conference on Soil Mechanics*, Wiesbaden, Vol. 1, pp. 19-24.

Jardine R.J. (1985). *Investigations of pile-soil behaviour with special reference to the foundations of offshore structures*. PhD thesis, Imperial College, University of London, London, UK.

Jardine R.J. (1992). Some observations on the kinematic nature of soil stiffness. *Soils and Foundations*, Vol. 32, No. 2, pp. 111-124.

Jardine R.J. (1995). One perspective of the pre-failure deformation characteristics of some geomaterials. *Pre-Failure Deformation of Geomaterials*, Shibuya, Mitachi and Miura (eds.), Balkema, Vol. 2, pp. 855-886.

Jardine R.J., Symes M.J. and Burland J.B. (1984). The measurement of soil stiffness in the triaxial apparatus. *Geotechnique*, Vol. 34, No. 3, pp. 323-340.

Jardine R.J., Fourie A., Maswoswe J. and Burland J.B. (1985). Field and laboratory measurements of soil stiffness. *Proceedings of the 11th International Conference on Soil Mechanics and Foundation Engineering*, San Francisco, Vol. 2, pp. 511-514.

Jardine R.J., Potts D.M., Fourie A.B. and Burland J.B. (1986). Studies of the influence of non-linear stress-strain characteristics in soil-structure interaction. *Geotechnique*, Vol. 36, No. 3, pp. 377-396.

Jardine R.J., Potts D.M., St. John H.D. and Hight D.W. (1991). Some practical applications of a non-linear ground model. *Proceedings of the 10th European Conference on Soil Mechanics and Foundation Engineering*, Florence, Vol. 1, pp. 223-228.

Jovicic V. (1997). *The measurement and interpretation of small strain stiffness of soils*. PhD thesis, City University, London, UK.

Jovicic V. and Coop M.R. (1998). The measurement of stiffness anisotropy in clays with bender element tests in the triaxial apparatus. *Geotechnical Testing Journal*, Vol. 21, No. 1, pp. 3-10.

Kavvadas M. and Amorosi A. (2000). A constitutive model for structured soils. *Geotechnique*, Vol. 50, No. 3, pp. 263-273.

Kovacevic N., Vaughan P.R and Potts D.M. (2004). A comparison between observed and predicted deformations of an old dam during reservoir operation. *International Conference on Numerical Models in Geomechanics*, In print.

Krieg R.D. (1975). A practical two surface plasticity theory. *Journal of Applied Mechanics, ASME*, Vol. 42, pp. 641-646.

Lade P.V. and Duncan J.M. (1975). Elastoplastic stress-strain theory for cohesionless soil. *Journal of the Geotechnical Engineering Division, ASCE*, Vol. 101, pp. 1037-1053.

Lambe T.W. and Whitman R.V. (1969). *Soil Mechanics*. John Wiley and Sons Inc., New York.

La Rochelle P., Trak B., Tavenas F. and Roy M. (1974). Failure of a test embankment on a sensitive Champlain clay deposit. *Canadian Geotechnical Journal*, Vol. 11, pp. 142-164.

Lefebvre G., Ladd C.C. and Pare J.-J. (1988). Comparison of field vane and laboratory undrained shear strength in soft sensitive clays. *Vane shear strength testing in soils: Field and laboratory studies, ASTM STP 1014*, A.F. Richards (eds.), American society for testing and materials, Philadelphia, pp. 233-246.

Lefebvre G., Leboeuf D., Rahhal M.E., Lacroix A. and Warde J. (1994). Laboratory and field determinations of small-strain shear modulus for a structured Champlain clay. *Canadian Geotechnical Journal*, Vol. 31, pp. 61-70.

Lefebvre G. and Pfendler P. (1996). Strain rate and preshear effects in cyclic resistance of soft clay. *Journal of Geotechnical Engineering, ASCE*, Vol. 122, No. 1, pp. 21-26.

Leonards G. A. and Ramiah B.K. (1959). Time effects in the consolidation of clays. *ASTM Special Technical Publication*, No. 254, pp. 116-130.

Leroueil S. (1977). *Quelques considerations sur le comportement des argiles sensibles*. PhD thesis, University of Laval, Quebec, Canada.

Leroueil S. and Vaughan P.R. (1990). The important and congruent effects of structure in natural soils and weak rocks. *Geotechnique*, Vol. 40, No. 3, pp. 467-488.

Lings M.L., Pennington D.S. and Nash D.F.T. (2000). Anisotropic stiffness parameters and their measurement in a stiff natural clay. *Geotechnique*, Vol. 50, No. 2, pp. 109-125.

Marsland A. (1971). Laboratory and in-situ measurements of the deformation moduli of London Clay. *Proceedings of Symposium on the interaction of structure and foundation*. University of Birmingham, pp. 7-17.

Matsuoka H. and Nakai T. (1974). Stress-deformation and strength characteristics of soil under three different principal stresses. *Proceedings Jap. Soc. Civ. Eng.*, Vol. 232, pp. 59-70.

Mayne P.W. and Kulhawy F.H. (1982). K_o-OCR relationships in soil. *Journal of the Geotechnical Engineering Division, ASCE*, Vol. 108 (GT6), pp. 851-872.

Mitchell J.K. (1976). *Fundamentals of soil behaviour*. John Wiley and Sons Inc., New York.

Mroz Z. (1967). On the description of anisotropic workhardening. *Journal of the Mechanics and Physics of Solids*, Vol. 15, pp. 163-175.

Mroz Z. Norris V.A. and Zienkiewicz O.C. (1978). An anisotropic hardening model for soils and its application to cyclic loading. *International Journal for Numerical and Analytical Methods in Geomechanics*, Vol. 2, pp. 203-221.

Mroz Z. Norris V.A. and Zienkiewicz O.C. (1979). Application of an anisotropic hardening model in the analysis of elasto-plastic deformation of soils. *Geotechnique*, Vol. 29, No. 1, pp. 1-34.

Mroz Z. Norris V.A. (1982). Elastoplastic and viscoplastic constitutive models for soils with application to cyclic loading. *Soil Mechanics-Transient and Cyclic Loads*, G.N. Pande and O.C. Zienkiewicz (eds.). John Wiley and Sons Ltd.

Ng C.W.W. and Lings M.L. (1995). Effects of modelling soil nonlinearity and wall installation on back-analysis of deep excavation in stiff clay. *Journal of geotechnical engineering*, Vol. 121, pp. 687-695.

Nyren R.J. (1998). *Field measurements above twin tunnels in London Clay*. PhD thesis, Imperial College, University of London, London, UK.

Nyren R.J., Standing J.R. and Burland J.B. (2001). Surface displacements at St James's Park greenfield reference site above twin tunnels through the London Clay. *Building response to tunnelling; Volume 2: case studies*, J.B. Burland, J.R. Standing and F.M. Jardine (eds.), Thomas Telford, London, UK, pp. 387-400.

O'Reilly M.P. and New B.M. (1982). Settlements above tunnels in the United Kingdom-their magnitude and prediction. *Tunnelling' 82*, Institution of Mining and Metallurgy, London, pp. 173-181.

Parry R.H. and Nadarajah V. (1973). A volumetric yield locus for lightly overconsolidated clay. *Geotechnique*, Technical Note, Vol. 23, No. 3, pp. 450-453.

Peck R.B. (1969). Deep excavations and tunnelling in soft ground. *Proceedings of the 7th International Conference on Soil Mechanics and Foundation Engineering*, Mexico City, State of the art, Vol. 3, pp. 225-290.

Potts D.M. and Gens A. (1984). The effect of the plastic potential in boundary value problems involving plane strain deformation. *International Journal for Numerical and Analytical Methods in Geomechanics*, Vol. 8, pp. 259-286.

Potts D.M. and Zdravkovic L. (1999). *Finite element analysis in geotechnical engineering: theory*. Thomas Telford, London.

Potts D.M. and Zdravkovic L. (2001). *Finite element analysis in geotechnical engineering: application*. Thomas Telford, London.

Prevost J.H. (1977). Mathematical modelling of monotonic and cyclic undrained clay behaviour. *International Journal for Numerical and Analytical Methods in Geomechanics*, Vol. 1, pp. 195-216.

Prevost J.H. (1978a). Anisotropic undrained stress-strain behavior of clays. *Journal of the Geotechnical Engineering Division, ASCE*, GT8, Vol. 104, pp. 1075-1090.

Prevost J.H. (1978b). Plasticity theory for soil stress-strain behavior. *ASCE, EM Division*, Vol. 104, pp. 1177-1196.

Puzrin A.M. and Burland J.B. (1998). Non-linear model of small-strain behaviour of soils. *Geotechnique*, Vol. 48, No. 2, pp. 217-233.

Puzrin A.M. and Burland J.B. (2000). Kinematic hardening plasticity formulation of small strain behaviour of soils. *International Journal for Numerical and Analytical Methods in Geomechanics*, Vol. 24, pp. 753-781.

Rankin W.J. (1988). Ground movements resulting from urban tunnelling: predictions and effects. *Engineering geology of underground movements*, The geological society, London, pp. 79-92.

Rampello S. and Silvestri F. (1993). The stress-strain behaviour of natural and reconstituted samples of two overconsolidated clays. *Geotechnical Engineering of Hard Soils-Soft Rocks*, Anagnostopoulos et al. (eds.), Balkema, Rotterdam, pp. 769-778.

Rendulic L. (1937). Ein Grundgesetz der Tonmechanik und sein experimenteller Beweis. *Der Baunginenieur*, Vol. 18, pp. 459-467.

Richart F.E., Hall J.R. and Woods R.D. (1970). *Vibrations of soils and foundations*. Prentice-Hall, Inc., Englewood Cliffs, New Jersey.

Roscoe K.H. and Schofield A.N. (1963). Mechanical behaviour of an idealised 'wet' clay. *Proceedings of the 2nd European Conference on Soil Mechanics*, Wiesbaden, Vol.1, pp. 47-54

Roscoe K.H. and Burland J.B. (1968). On the generalised stress-strain behaviour of 'wet' clay. *Engineering plasticity*, Cambridge University Press, pp. 535-609

Rouainia M. and Muir Wood D. (2000). A kinematic hardening constitutive model for natural clays with loss of structure. *Geotechnique*, Vol. 50, No. 2, pp. 153-164.

Rowe P.W. (1971). Theoretical meaning and observed values of deformation parameters for soils. *Proceedings of the Roscoe Memorial Symposium on Stress-strain behaviour of Soils*, pp. 143-194.

Schmertmann J.H. (1991). 25th Terzaghi Lecture: The mechanical aging of soils. *Journal of geotechnical engineering*, Vol. 117, No. 9, pp. 1288-1330.

Schroeder F.C. (2003). *The influence of bored piles on existing tunnels*. PhD thesis, Imperial College, University of London, London, UK.

Simpson B., O'Riordan N.J. and Croft D.D. (1979). A computer model for the analysis of ground movements in London Clay. *Geotechnique*, Vol. 29, No. 2, pp. 149-175.

Simpson B. (1992). 32th Rankine Lecture: Retaining structures: displacement and design. *Geotechnique*, Vol. 42, No. 4, pp. 541-576.

Simpson B., Atkinson J.H. and Jovicic V. (1996). The influence of anisotropy on calculations of ground settlements above tunnels. *Geotechnical aspects of underground construction in soft ground*, Mair and Taylor (eds.), Balkema, pp. 591-594.

Sloan S.W. (1987). Substepping schemes for the numerical integration of elastoplastic stress-strain relations. *International Journal for Numerical Methods in Engineering*, Vol. 24, pp. 893-911.

Smith P.R. (1992). *Properties of high compressibility clays with reference to construction on soft ground*. PhD thesis, Imperial College, University of London, London, UK.

Smith P.R, Jardine R.J. and Hight D.W. (1992). The yielding of Bothkennar clay. *Geotechnique*, Vol. 42, No. 2, pp. 257-274.

Som N.N. (1968). *The effect of stress path on the deformation and consolidation of London Clay*. PhD thesis, Imperial College, University of London, London, UK.

St. John H.D. (1975). *Field and theoretical studies of the behaviour of ground around deep excavations in London Clay*. PhD thesis, University of Cambridge, Cambridge, UK.

Stallebrass S.E. (1990). *Modelling the effect of recent stress history on the deformation of overconsolidated soils*. PhD thesis, City University, London, UK.

Stallebrass S.E., Jovicic V. and Taylor R.N. (1994). The influence of recent stress history on ground movements around tunnels. *Pre-Failure Deformation of Geomaterials*, Shibuya, Mitachi and Miura (eds.), Balkema, Vol. 1, pp. 615-620.

Stallebrass S.E. and Taylor R.N. (1997). The development and evaluation of a constitutive model for the prediction of ground movements in overconsolidated clay. *Geotechnique*, Vol. 47, No. 2, pp. 235-253.

Standing J.R., Nyren R.J. and Burland J.B. (1996). The measurement of ground movements due to tunnelling at two control sites along the Jubilee Line Extension. *Geotechnical aspects of underground construction in soft ground*, Mair and Taylor (eds.), Balkema, pp. 751-756.

Tatsuoka F. and Shibuya S. (1992). Deformation characteristics of soils and rocks from field and laboratory tests. *Proceedings of the 9th Asian Regional Conference on Soil Mechanics and Foundation Engineering*, Bangkok, Vol. 2, pp. 101-170.

Tavenas, F.A., Jean P., Leblond P., and Leroueil S. (1983). The permeability of natural soft clays. Part II: Permeability characteristics. *Canadian Geotechnical Journal*, Vol. 20, pp. 654-660.

Viggiani G. (1992). *Small strain stiffness of fine grained soils*. PhD thesis, City University, London, UK.

Viggiani G. and Atkinson J.H. (1995). Stiffness of fine-grained soil at very small strains. *Geotechnique*, Vol. 45, No. 2, pp. 249-265.

Whittle A.J. (1993). Evaluation of a constitutive model for overconsolidated clays. *Geotechnique*, Vol. 43, No. 2, pp. 289-313.

Whittle A.J., Hashash Y.M.A. and Whitman R.V. (1993). Analysis of a deep excavation in Boston. *Journal of the Geotechnical Engineering Division, ASCE*, Vol. 119, No. 1, pp. 69-90.

Wroth C.P. and Houlsby G.T. (1985). Soil mechanics – property characterisation, and analysis procedures. *Proceedings of the 11th International Conference on Soil Mechanics and Foundation Engineering*, San Francisco, Vol. 1, pp. 1-55.

Zdravkovic L., Potts D.M and Jardine R.J. (2001). A parametric study of the pull-out capacity of bucket foundations in soft clay. *Geotechnique*, Vol. 51, No. 1, pp. 55-67.

Zdravkovic L., Potts D.M and Hight D.W. (2002). The effect of strength anisotropy on the behaviour of embankments on soft ground. *Geotechnique*, Vol. 52, No. 6, pp. 447-457.

Zienkiewicz O.C., Chan A.H.C., Pastor M., Schrefler B.A. and Shiomi T. (1999), *Computational geomechanics with special reference to earthquake engineering,* John Wiley & Sons, Chichester, UK.

Zytynski M., Randolph M.F., Nova R. and Wroth C.P. (1978). Short communications on modelling the unloading-reloading behaviour of soils. *International Journal for Numerical and Analytical Methods in Geomechanics*, Vol. 2, pp. 87-94.

Appendix I

Calculation of the derivatives $\{\partial Q/\partial s\}$ and $\{\partial \det(s\text{-}s_a)/\partial s\}$

Calculation of derivatives $\{\partial Q/\partial s\}$:

From Equation 4.60 the term Q is equal to:

$$Q=(\boldsymbol{s}-\boldsymbol{s}_a):(\boldsymbol{s}-\boldsymbol{s}_a)=(\sigma'_x-p'-\sigma'_{xa}+p'_a)^2+(\sigma'_y-p'-\sigma'_{ya}+p'_a)^2+(\sigma'_z-p'-\sigma'_{za}+p'_a)^2+2(\tau_{xy}-\tau_{yxa})^2+2(\tau_{yz}-\tau_{yza})^2+2(\tau_{zx}-\tau_{zxa})^2 \tag{I.1}$$

The derivatives $\{\partial Q/\partial s\}$ can be calculated by differentiating Equation I.1:

$$\frac{\partial Q}{\partial(\sigma'_x-p')}=2(\sigma'_x-p'-\sigma'_{xa}+p'_a) \tag{I.2}$$

$$\frac{\partial Q}{\partial(\sigma'_y-p')}=2(\sigma'_y-p'-\sigma'_{ya}+p'_a) \tag{I.3}$$

$$\frac{\partial Q}{\partial(\sigma'_z-p')}=2(\sigma'_z-p'-\sigma'_{za}+p'_a) \tag{I.4}$$

$$\frac{\partial Q}{\partial \tau_{xy}}=4(\tau_{xy}-\tau_{xya}) \tag{I.5}$$

$$\frac{\partial Q}{\partial \tau_{yz}} = 4\left(\tau_{yz} - \tau_{yza}\right) \tag{I.6}$$

$$\frac{\partial Q}{\partial \tau_{zx}} = 4\left(\tau_{zx} - \tau_{zxa}\right) \tag{I.7}$$

Calculation of derivatives $\{\partial \det(\boldsymbol{s}-\boldsymbol{s}_a)/\partial \mathrm{s}\}$:

The determinant of the tensor $(\boldsymbol{s}-\boldsymbol{s}_a)$ is:

$$\begin{aligned}\det\left(\boldsymbol{s}-\boldsymbol{s}_a\right) = {} & \left(\sigma'_x - p' - \sigma'_{xa} + p'_a\right)\left(\sigma'_y - p' - \sigma'_{ya} + p'_a\right)\left(\sigma'_z - p' - \sigma'_{za} + p'_a\right) - \\ & \left(\sigma'_x - p' - \sigma'_{xa} + p'_a\right)\left(\tau_{yz} - \tau_{yza}\right)^2 - \\ & \left(\sigma'_y - p' - \sigma'_{ya} + p'_a\right)\left(\tau_{zx} - \tau_{zxa}\right)^2 - \\ & \left(\sigma'_z - p' - \sigma'_{za} + p'_a\right)\left(\tau_{xy} - \tau_{yxa}\right)^2 + \\ & 2\left(\tau_{xy} - \tau_{yxa}\right)\left(\tau_{yz} - \tau_{yza}\right)\left(\tau_{zx} - \tau_{zxa}\right)\end{aligned} \tag{I.8}$$

The derivatives $\{\partial \det(\boldsymbol{s}-\boldsymbol{s}_a)/\partial \mathrm{s}\}$ are calculated by differentiating Equation I.8:

$$\frac{\partial \det\left(\boldsymbol{s}-\boldsymbol{s}_a\right)}{\partial\left(\sigma'_x - p'\right)} = \left(\sigma'_y - p' - \sigma'_{ya} + p'_a\right)\left(\sigma'_z - p' - \sigma'_{za} + p'_a\right) - \left(\tau_{yz} - \tau_{yza}\right)^2 \tag{I.9}$$

$$\frac{\partial \det\left(\boldsymbol{s}-\boldsymbol{s}_a\right)}{\partial\left(\sigma'_y - p'\right)} = \left(\sigma'_x - p' - \sigma'_{xa} + p'_a\right)\left(\sigma'_z - p' - \sigma'_{za} + p'_a\right) - \left(\tau_{zx} - \tau_{zxa}\right)^2 \tag{I.10}$$

$$\frac{\partial \det\left(\boldsymbol{s}-\boldsymbol{s}_a\right)}{\partial\left(\sigma'_z - p'\right)} = \left(\sigma'_x - p' - \sigma'_{xa} + p'_a\right)\left(\sigma'_y - p' - \sigma'_{ya} + p'_a\right) - \left(\tau_{xy} - \tau_{yxa}\right)^2 \tag{I.11}$$

$$\begin{aligned}\frac{\partial \det\left(\boldsymbol{s}-\boldsymbol{s}_a\right)}{\partial \tau_{xy}} = {} & -2\left(\sigma'_z - p' - \sigma'_{za} + p'_a\right)\left(\tau_{xy} - \tau_{yxa}\right) + 2\left(\tau_{yz} - \tau_{yza}\right) \\ & \left(\tau_{zx} - \tau_{zxa}\right)\end{aligned} \tag{I.12}$$

$$\begin{aligned}\frac{\partial \det\left(\boldsymbol{s}-\boldsymbol{s}_a\right)}{\partial \tau_{yz}} = {} & -2\left(\sigma'_x - p' - \sigma'_{xa} + p'_a\right)\left(\tau_{yz} - \tau_{yza}\right) + 2\left(\tau_{xy} - \tau_{yxa}\right) \\ & \left(\tau_{zx} - \tau_{zxa}\right)\end{aligned} \tag{I.13}$$

$$\frac{\partial \det\left(\boldsymbol{s}-\boldsymbol{s}_a\right)}{\partial \tau_{zx}} = -2\left(\sigma'_y - p' - \sigma'_{ya} + p'_a\right)\left(\tau_{zx} - \tau_{zxa}\right) + 2\left(\tau_{xy} - \tau_{yxa}\right)\left(\tau_{yz} - \tau_{yza}\right) \tag{I.14}$$

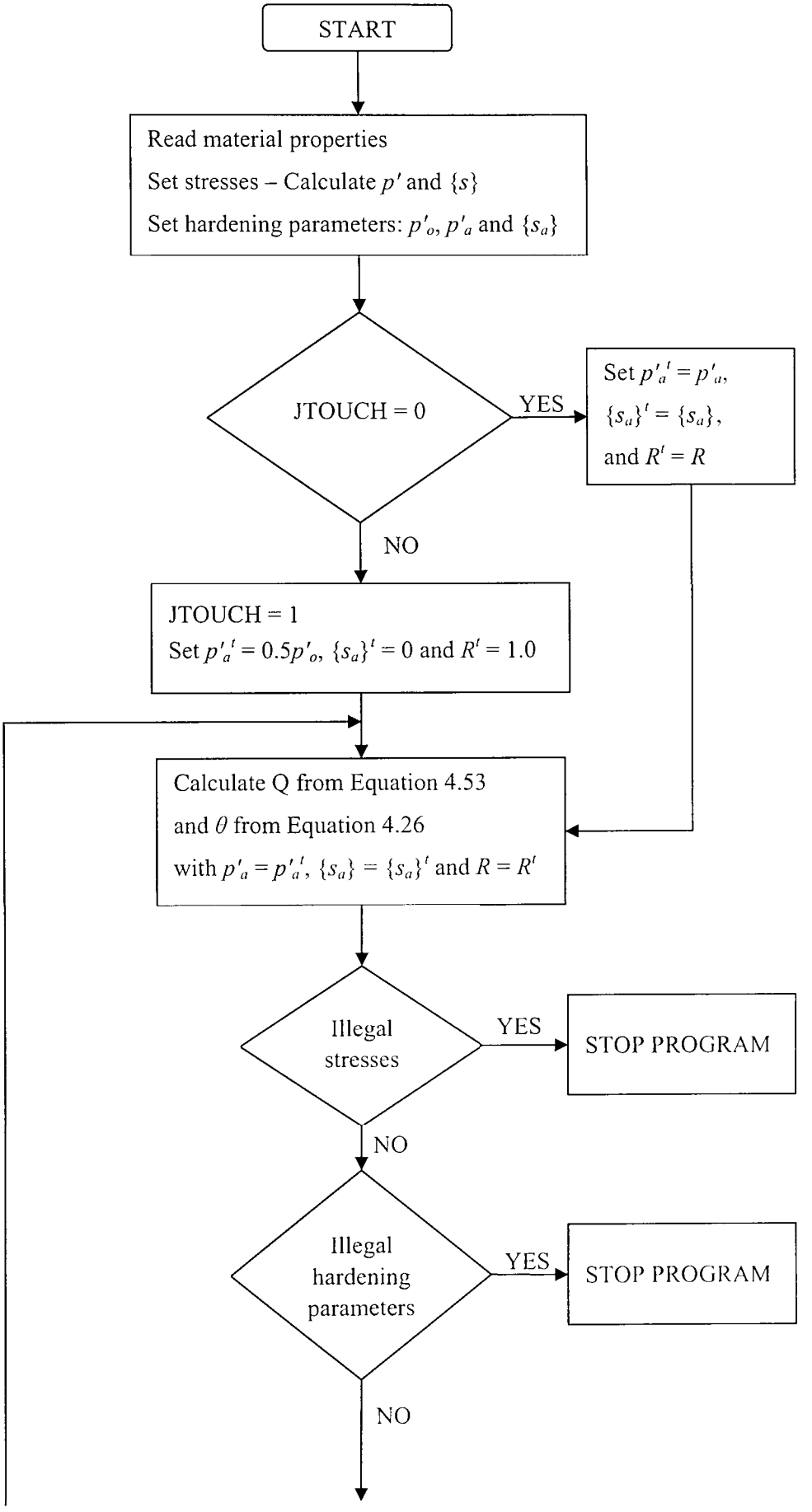
Appendix II

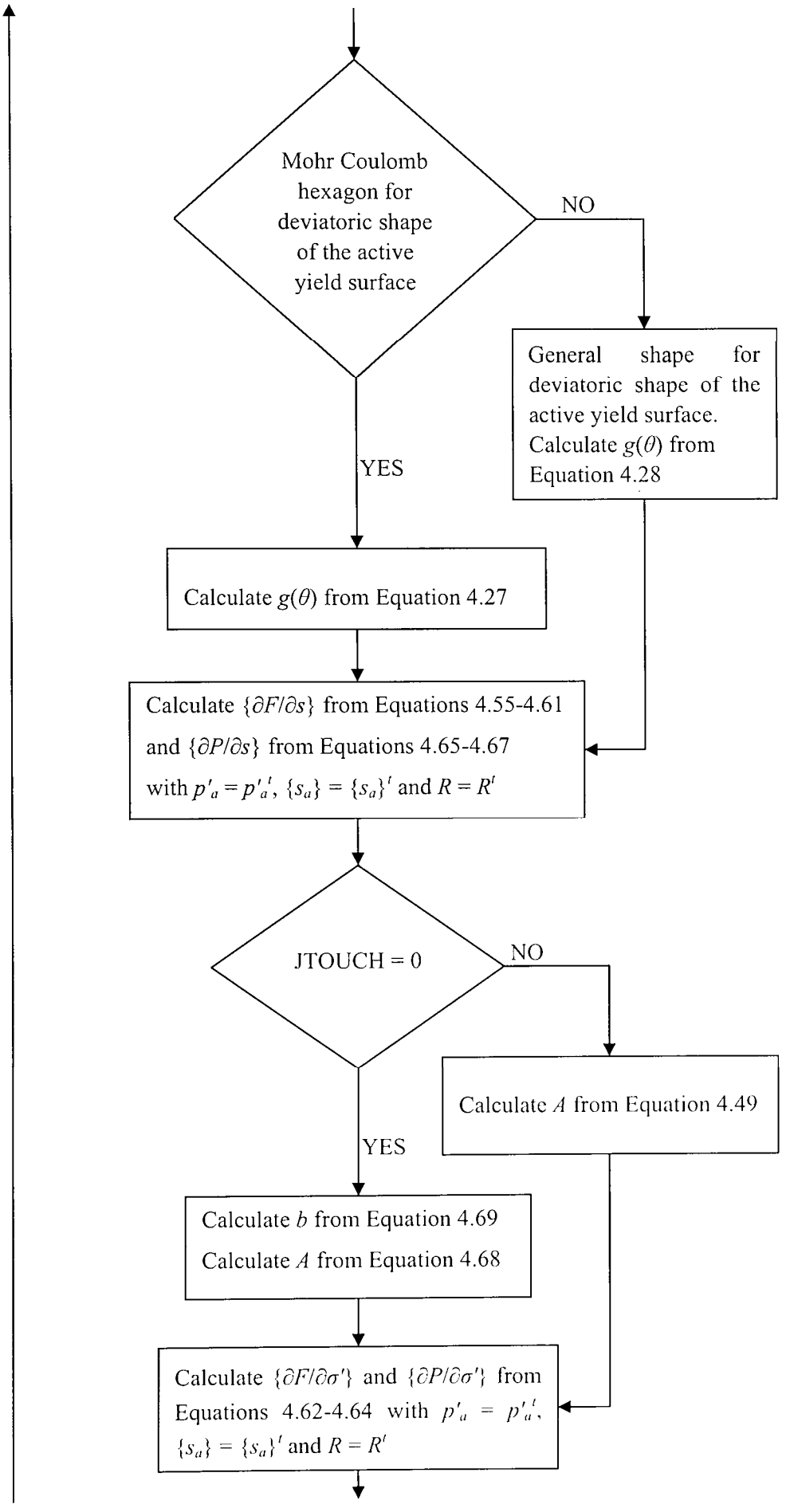
Flowchart for the two-surface model

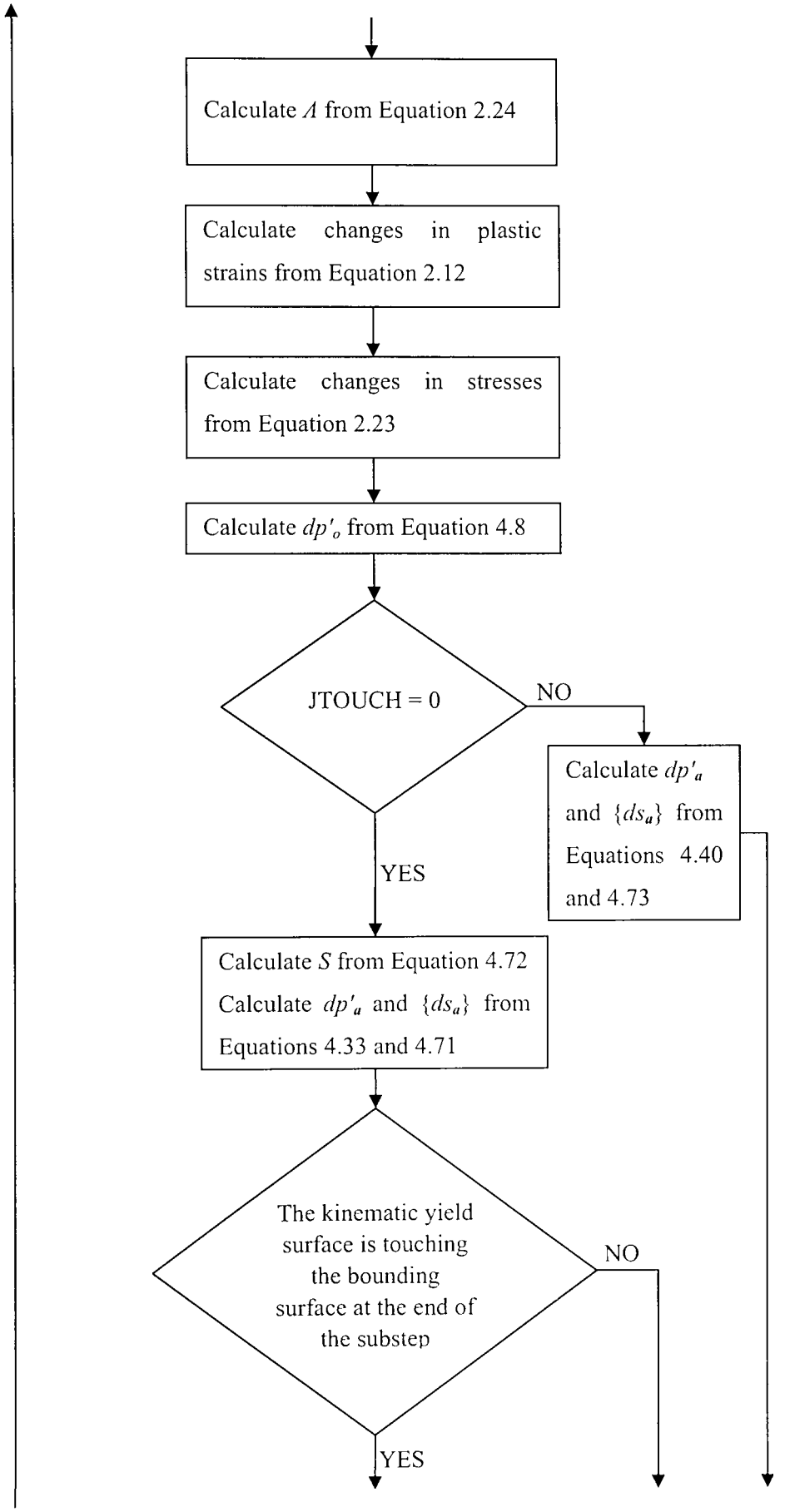
The following flowchart is used by the stress point algorithm to calculate the changes in stresses, plastic strains and hardening parameters during a substep. The yield and plastic potential derivatives are calculated by using appropriate temporary values of p'_a, $\{s_a\}$ and R, depending on which is the active yield surface, as explained in Chapter 4. In any case the equations in which the temporary values p'^t_a, $\{s_a\}^t$ and R^t are used will be indicated. The parameter JTOUCH is used in order to identify the relative positions of the surfaces.

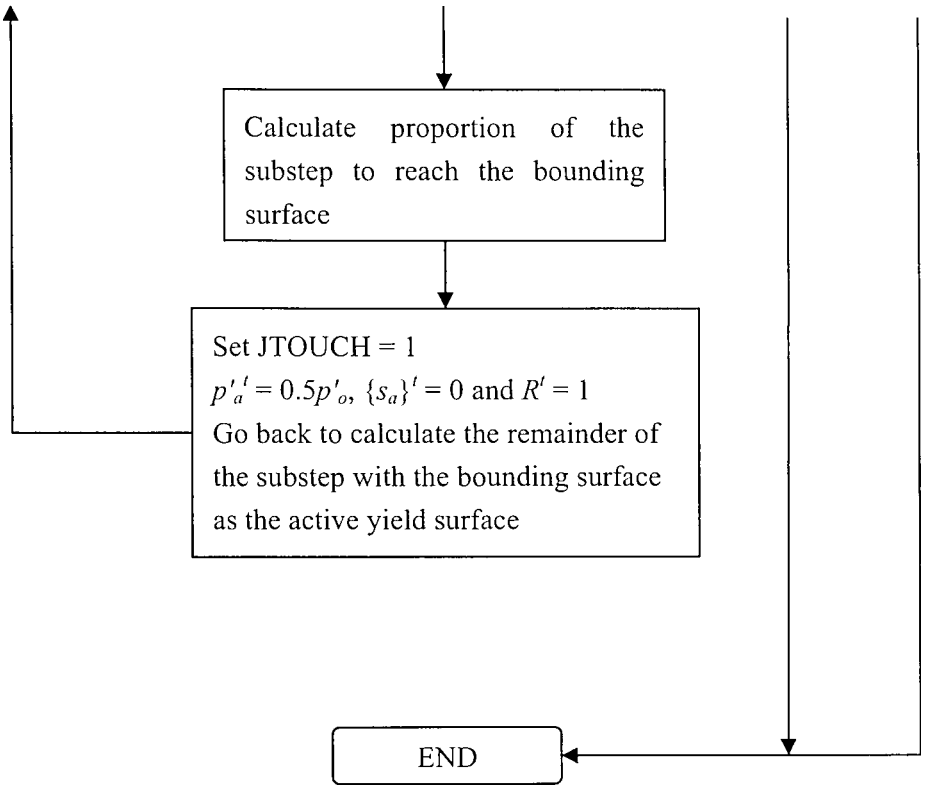
JTOUCH = 0 : If the kinematic yield surface and bounding surface are not in contact. In this case the kinematic yield surface is the active yield surface. The temporary values are $p'^t_a = p'_a$, $\{s_a\}^t = \{s_a\}$ and $R^t = R$.

JTOUCH = 1 : If the two surfaces are in contact. In this case the bounding surface is the active yield surface. The temporary values are $p'^t_a = 0.5p'_o$, $\{s_a\}^t = 0$ and $R^t = 1.0$.


START
Read material properties
Set stresses – Calculate p' and $\{s\}$
Set hardening parameters: p'_o, p'_a and $\{s_a\}$
JTOUCH = 0
YES
Set $p'^t_a = p'_a$,
$\{s_a\}^t = \{s_a\}$,
and $R^t = R$
NO
JTOUCH = 1
Set $p'^t_a = 0.5p'_o$, $\{s_a\}^t = 0$ and $R^t = 1.0$
Calculate Q from Equation 4.53
and θ from Equation 4.26
with $p'_a = p'^t_a$, $\{s_a\} = \{s_a\}^t$ and $R = R^t$
Illegal stresses
YES
STOP PROGRAM
NO
Illegal hardening parameters
YES
STOP PROGRAM
NO


Mohr Coulomb hexagon for deviatoric shape of the active yield surface
NO
YES
General shape for deviatoric shape of the active yield surface. Calculate $g(\theta)$ from Equation 4.28
Calculate $g(\theta)$ from Equation 4.27
Calculate $\{\partial F/\partial s\}$ from Equations 4.55-4.61 and $\{\partial P/\partial s\}$ from Equations 4.65-4.67 with $p'_a = p'^{t}_a$, $\{s_a\} = \{s_a\}^t$ and $R = R^t$
JTOUCH = 0
NO
YES
Calculate A from Equation 4.49
Calculate b from Equation 4.69
Calculate A from Equation 4.68
Calculate $\{\partial F/\partial \sigma'\}$ and $\{\partial P/\partial \sigma'\}$ from Equations 4.62-4.64 with $p'_a = p'^{t}_a$, $\{s_a\} = \{s_a\}^t$ and $R = R^t$


Calculate A from Equation 2.24
Calculate changes in plastic strains from Equation 2.12
Calculate changes in stresses from Equation 2.23
Calculate dp'_o from Equation 4.8
JTOUCH = 0
NO
YES
Calculate dp'_a and $\{ds_a\}$ from Equations 4.40 and 4.73
Calculate S from Equation 4.72
Calculate dp'_a and $\{ds_a\}$ from Equations 4.33 and 4.71
The kinematic yield surface is touching the bounding surface at the end of the substep
NO
YES


Calculate proportion of the substep to reach the bounding surface
Set JTOUCH = 1
$p'_a{}^t = 0.5p'_o$, $\{s_a\}^t = 0$ and $R^t = 1$
Go back to calculate the remainder of the substep with the bounding surface as the active yield surface
END

Appendix III

Undrained strength for the two- and three- surface models

In this appendix the expressions for the calculation of the undrained strength, S_u, predicted by the two- and three-surface models are given. As mentioned in Chapter 4 this can be calculated if the size of the bounding surface (i.e. the parameter p'_o) is known at the beginning of undrained shearing.

The undrained strength at failure can be expressed as a function of the deviatoric stress at failure, J_f, as follows:

$$S_u = J_f \cos\theta \tag{III.1}$$

Each stress state within the bounding surface plots on an elastic wall. This can be explained as follows. When the stress state is within the yield surface the behaviour predicted is elastic and the stress path moves within the current elastic wall; however, when the stress state reaches the yield surface, yielding occurs, the behaviour becomes elasto-plastic and the stress path moves to new elastic walls. A representation of this process is shown in Figure III.1 for an isotropic swelling path. For the path AB the behaviour is elastic and the path moves within the current elastic wall. At B the stress state reaches the yield surface and the path BCD moves to new elastic walls. Therefore although the behaviour along the stress path BCD is elasto-plastic, each stress state, B, C, or D plots on a different elastic wall.

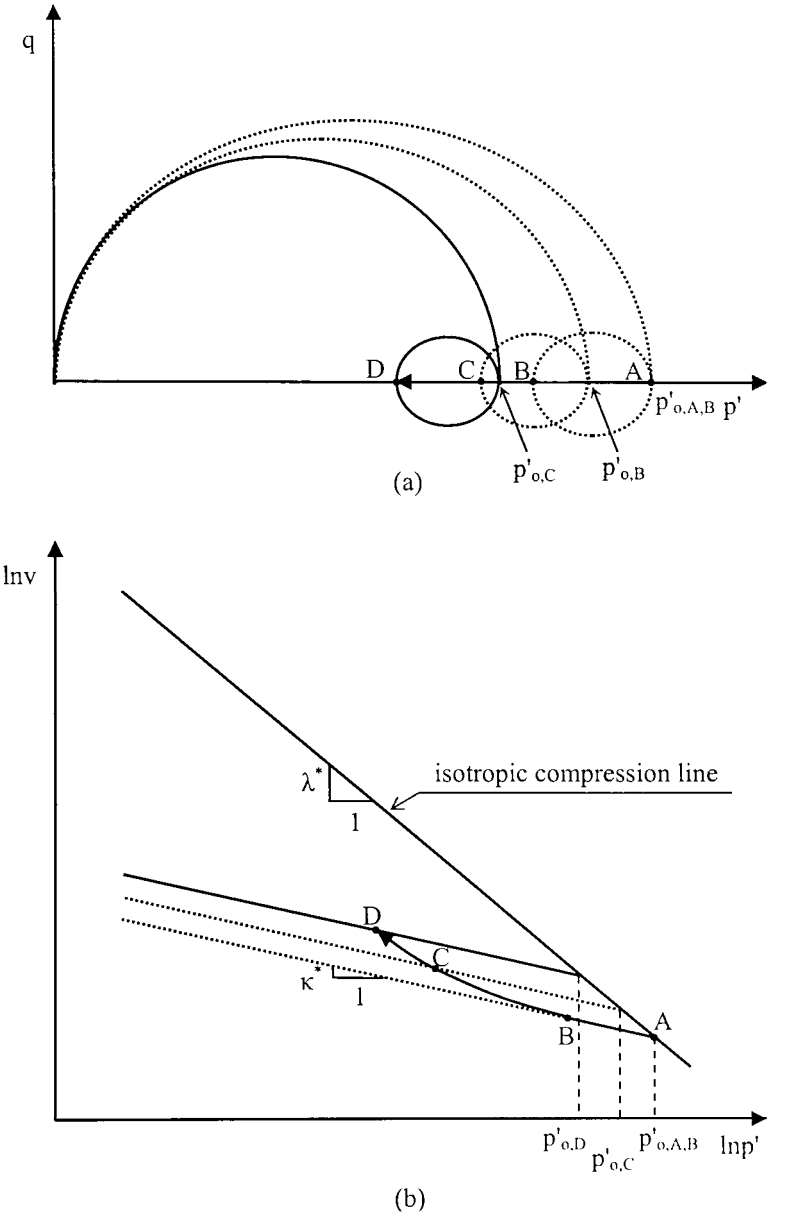


Figure III.1: Diagram showing how the stress state moves to new elastic walls

Therefore the stress state at the beginning of undrained shearing, p'_i, can be related to the size of the current bounding surface, p'_o and the equivalent pressure on the isotropic compression line at the current specific volume, p'_e, see Figure III.2, as follows:

$$\frac{p'_o}{p'_i} = \left(\frac{p'_o}{p'_e}\right)^{\frac{\lambda^*}{\kappa^*}} \tag{III.2}$$

When the soil is at the critical state the stresses J_{cs} and p'_{cs} are related as follows:

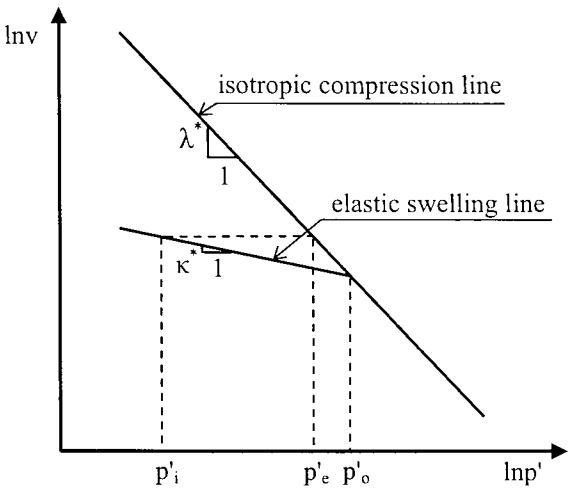


Figure III.2: Diagram showing the equivalent elastic swelling line corresponding to the stress state at the beginning of undrained shearing

$$J_{cs} = p'_{cs} g(\theta) \tag{III.3}$$

Since an undrained test is a stress path at constant specific volume (no volume change) the mean effective stress at the critical state, p'_{cs}, can be related to the equivalent pressure, p'_e, and the size of the bounding surface at the critical state, $p'_{o,cs}$, through an equation similar to Equation III.2:

$$\frac{p'_{o,cs}}{p'_{cs}} = \left(\frac{p'_{o,cs}}{p'_e} \right)^{\frac{\lambda^*}{\kappa^*}} \tag{III.4}$$

Also at critical state:

$$p'_{cs} = \frac{p'_{o,cs}}{2} \tag{III.5}$$

Combining Equations III.4 and III.5 gives:

$$p'_{o,cs} = p'_e (2)^{\frac{\kappa^*}{\lambda^*}} \tag{III.6}$$

Substitution of Equation III.2 in Equation III.6 gives:

$$p'_{cs} = \frac{p'_o}{2}\left(\frac{2p'_i}{p'_o}\right)^{\frac{\kappa^*}{\lambda^*}} \tag{III.7}$$

Substitution of the above in Equation III.3 gives the deviatoric stress at the critical state, J_{cs}:

$$J_{cs} = \frac{p'_o}{2} g(\theta)\left(\frac{2p'_i}{p'_o}\right)^{\frac{\kappa^*}{\lambda^*}} \tag{III.8}$$

If the deviatoric stress at the critical state, J_{cs}, is also considered to be the deviatoric stress at failure, J_f, then substitution of Equation III.8 into Equation III.1 gives the expression for the calculation of the undrained strength:

$$S_u = \frac{p'_o}{2} g(\theta)\left(\frac{2p'_i}{p'_o}\right)^{\frac{\kappa^*}{\lambda^*}} \cos\theta \tag{III.9}$$

It has to be noted that, as it is discussed in Chapter 7, depending on the values of the input parameters that control the behaviour of the kinematic surfaces, the models reach the critical state at different strain levels. This has the result that the undrained strength predicted by Equation III.9 may be mobilised at very high strains or may never be practically fully mobilised.

Appendix IV

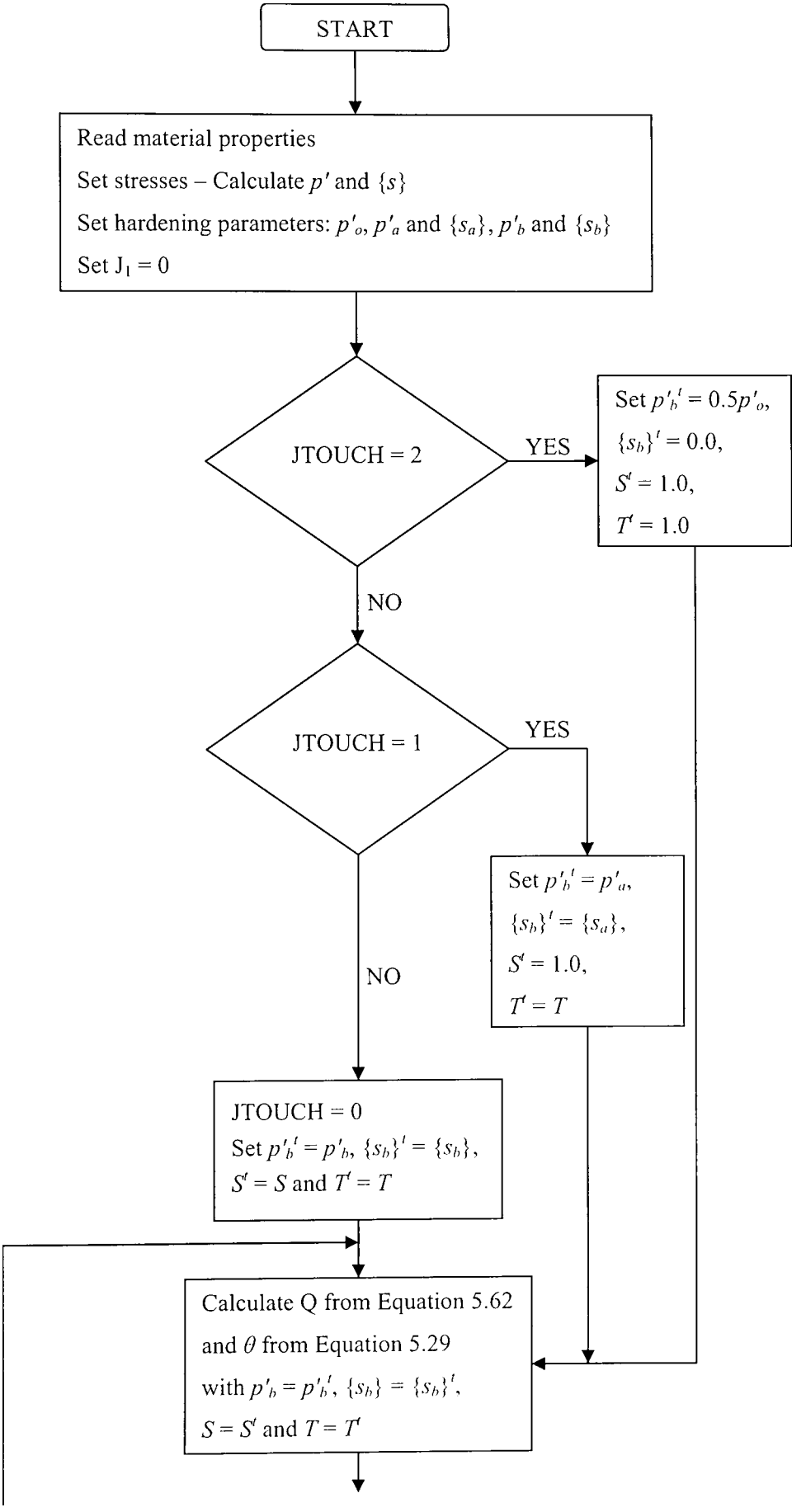
Flowchart for the three-surface model

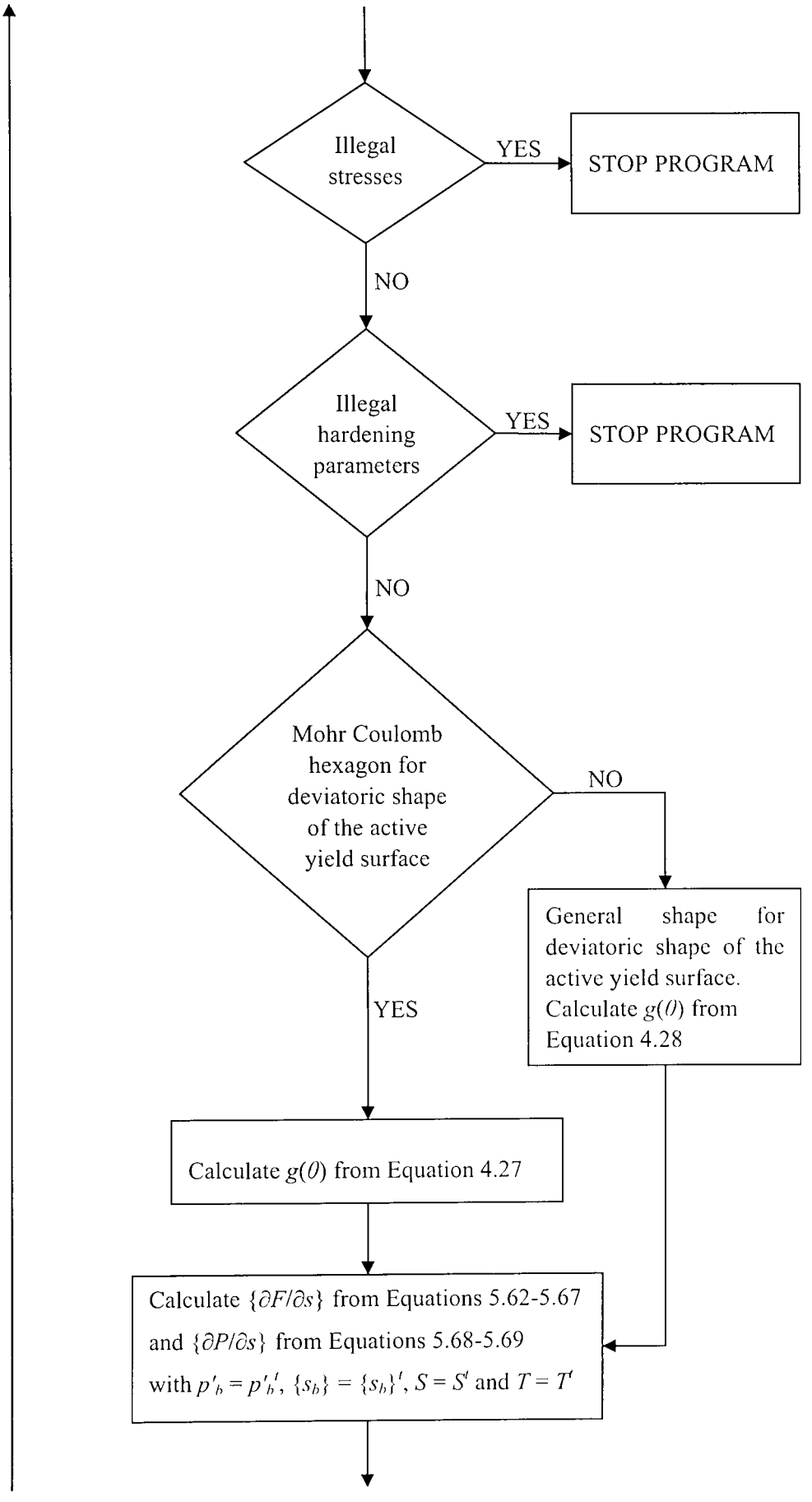
The following flowchart is used by the stress point algorithm to calculate the changes in stresses, plastic strains and hardening parameters during a substep. The yield and plastic potential derivatives are calculated by using appropriate temporary values of p'_b, $\{s_b\}$, S and T, depending on which is the active yield surface, as explained in Chapter 5. Any case in which the temporary values p'^t_b, $\{s_b\}^t$, S^t and T^t are used will be indicated. The parameter JTOUCH is used in order to identify the relative positions of the surfaces.

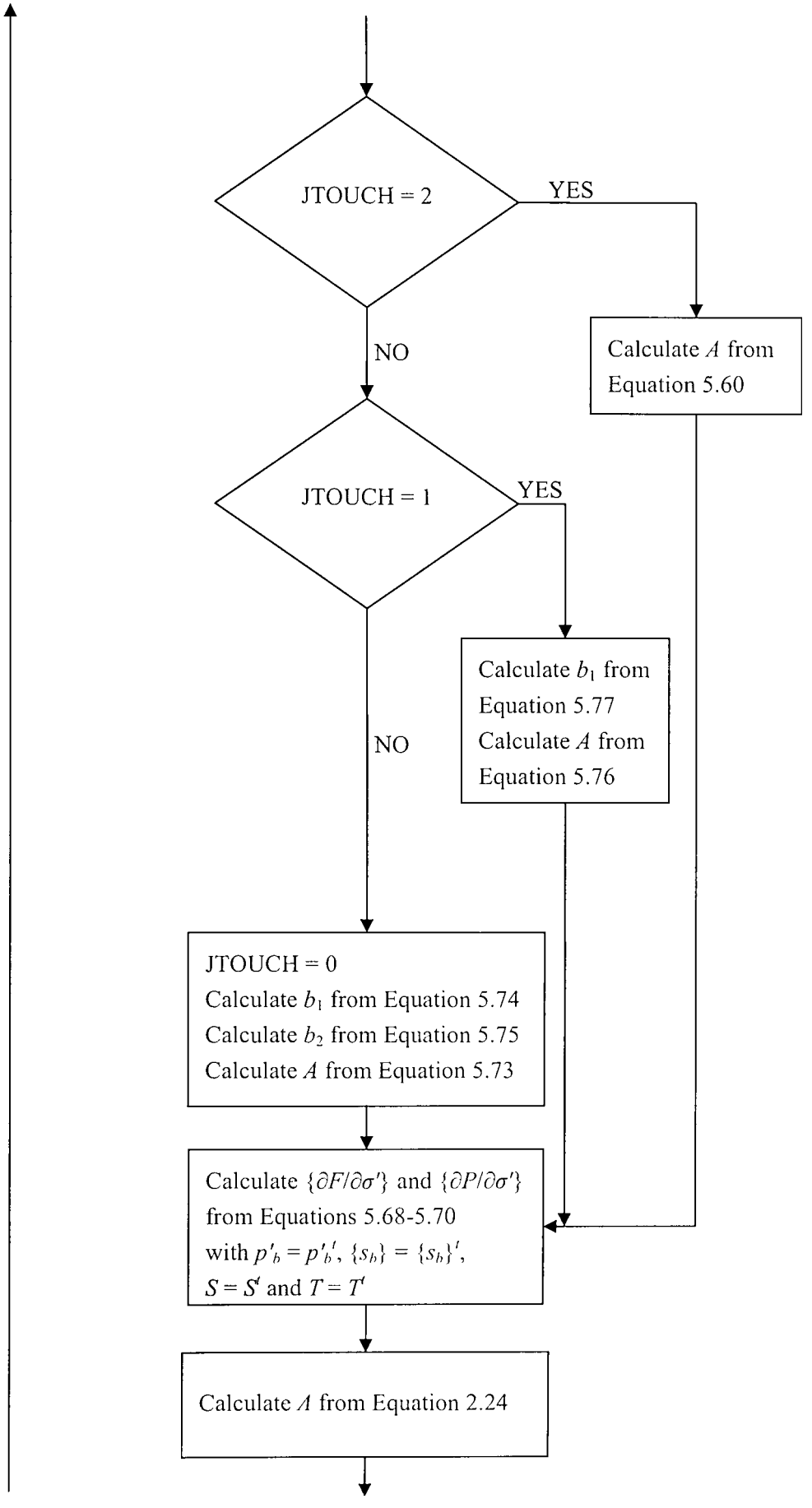
JTOUCH = 0 : If none of the surfaces are in contact. In this case the yield surface is the active yield surface. The temporary values are $p'^t_b = p'_b$, $\{s_b\}^t = \{s_b\}$, $S^t = S$ and $T^t = T$.

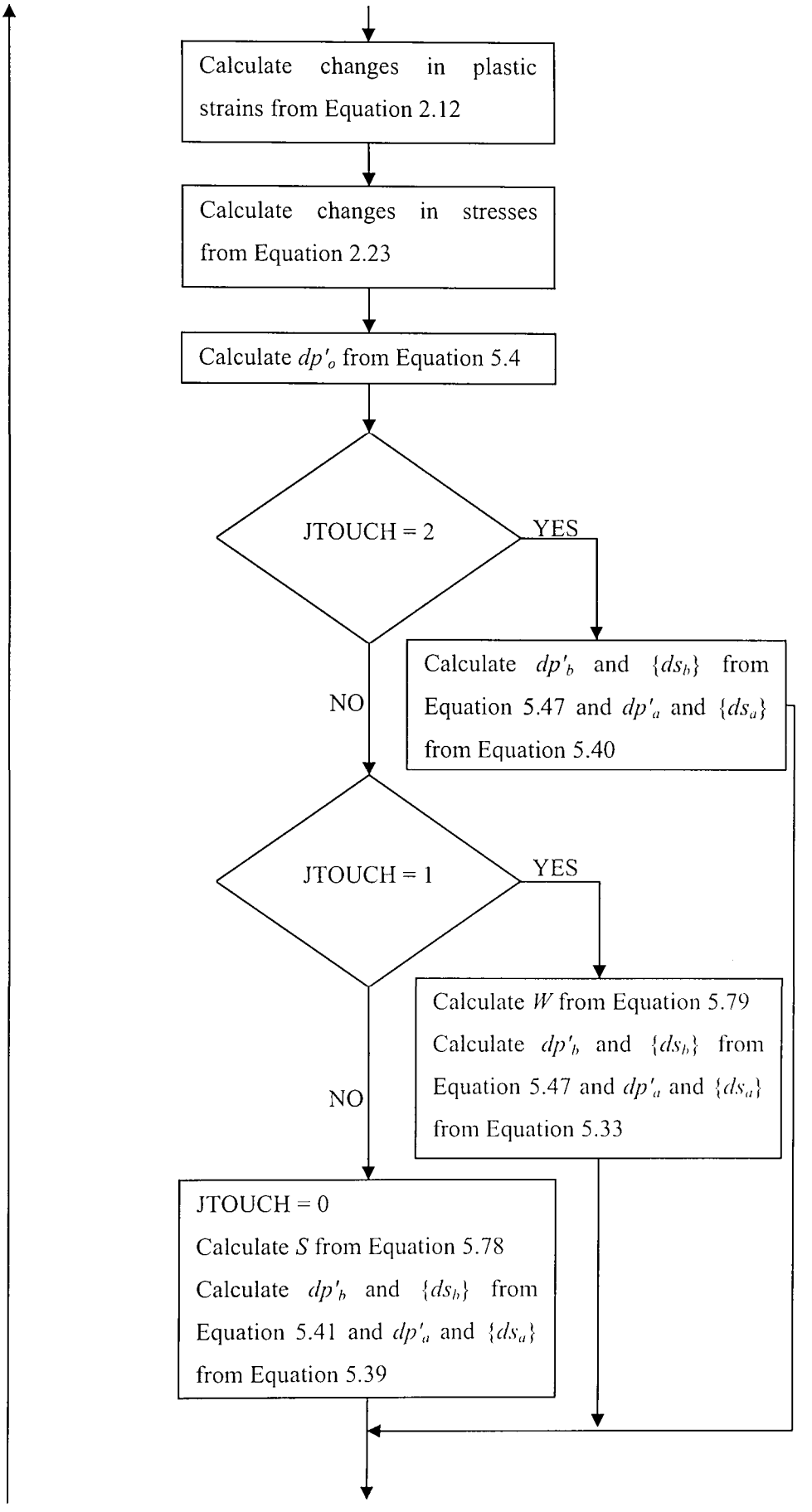
JTOUCH = 1 : If the yield and history surfaces are in contact. In this case the history surface is the active yield surface. The temporary values are $p'^t_b = p'_a$, $\{s_b\}^t = \{s_a\}$, $S^t = 1.0$ and $T^t = T$.

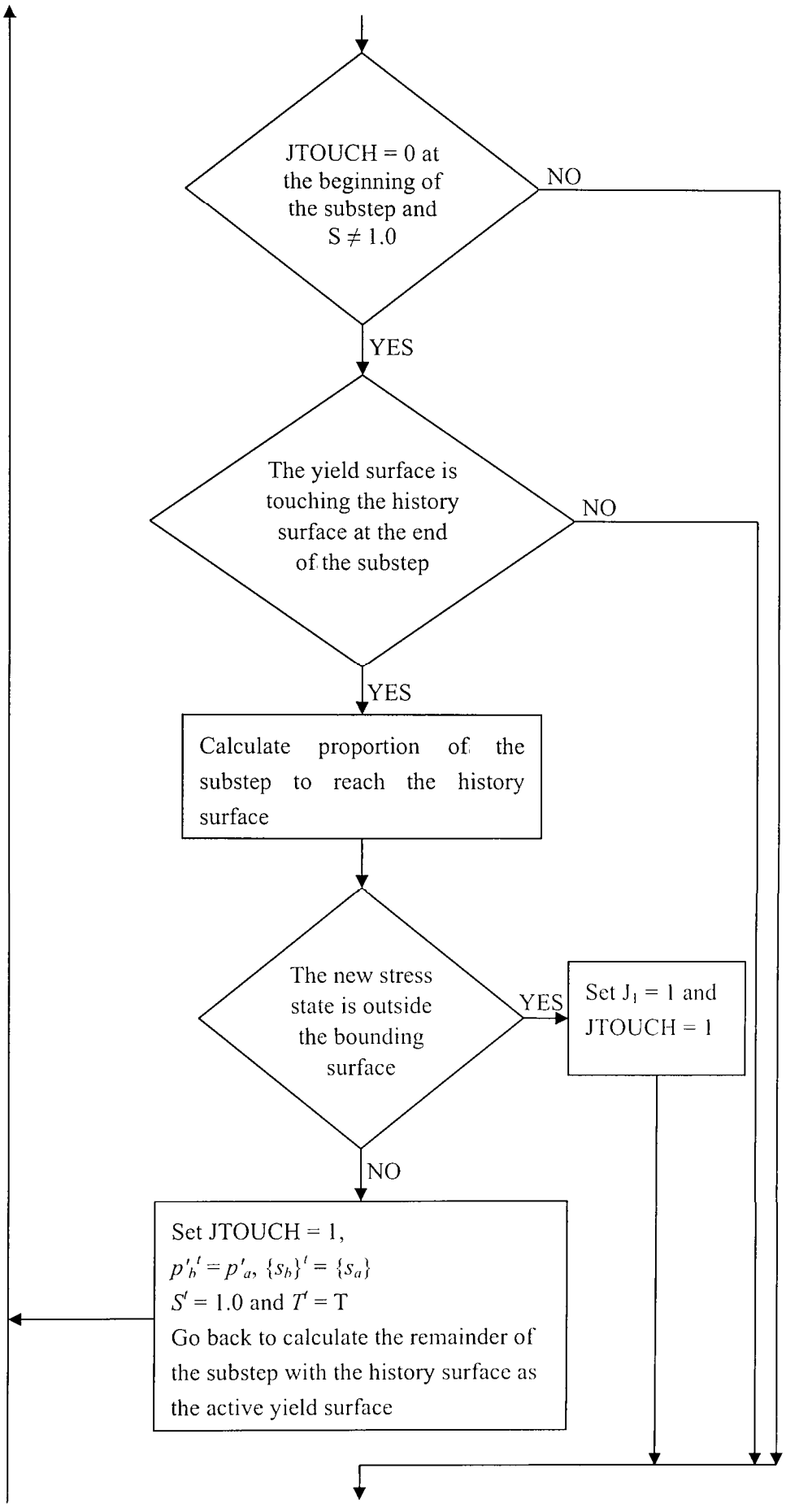
JTOUCH = 2 : If all three surfaces are in contact. In this case the bounding surface is the active yield surface. The temporary values are $p'^t_b = 0.5p'_a$, $\{s_b\}^t = 0.0$, $S^t = 1.0$ and $T^t = 1.0$.

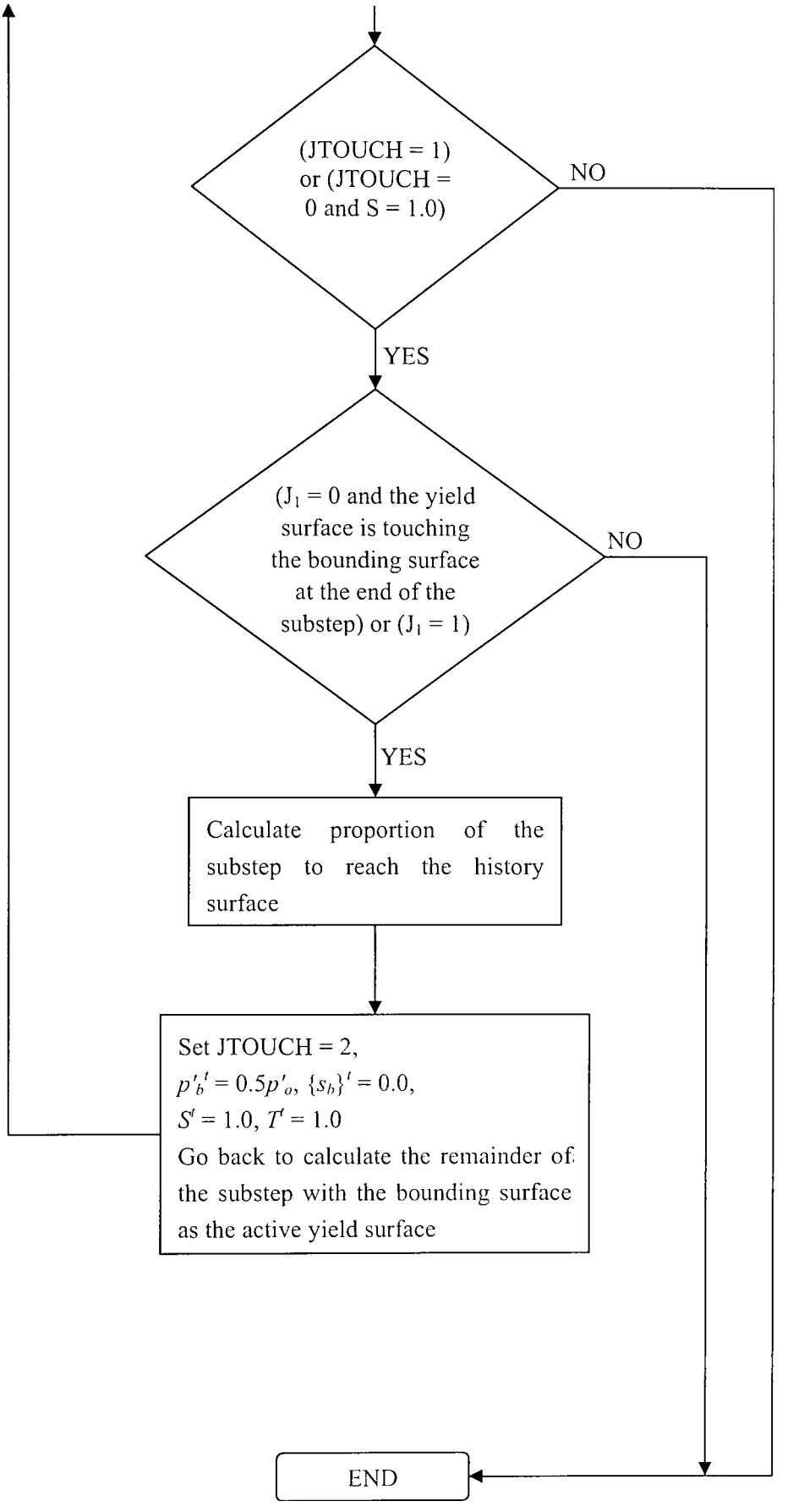

START
Read material properties
Set stresses – Calculate p' and $\{s\}$
Set hardening parameters: p'_o, p'_a and $\{s_a\}$, p'_b and $\{s_b\}$
Set $J_1 = 0$
JTOUCH = 2
YES
Set $p'^t_b = 0.5p'_o$,
$\{s_b\}^t = 0.0$,
$S^t = 1.0$,
$T^t = 1.0$
NO
JTOUCH = 1
YES
Set $p'^t_b = p'_a$,
$\{s_b\}^t = \{s_a\}$,
$S^t = 1.0$,
$T^t = T$
NO
JTOUCH = 0
Set $p'^t_b = p'_b$, $\{s_b\}^t = \{s_b\}$,
$S^t = S$ and $T^t = T$
Calculate Q from Equation 5.62
and θ from Equation 5.29
with $p'_b = p'^t_b$, $\{s_b\} = \{s_b\}^t$,
$S = S^t$ and $T = T^t$


Illegal stresses
YES
STOP PROGRAM
NO
Illegal hardening parameters
YES
STOP PROGRAM
NO
Mohr Coulomb hexagon for deviatoric shape of the active yield surface
NO
General shape for deviatoric shape of the active yield surface. Calculate g(θ) from Equation 4.28
YES
Calculate g(θ) from Equation 4.27
Calculate {∂F/∂s} from Equations 5.62-5.67 and {∂P/∂s} from Equations 5.68-5.69 with p'b = p'b', {sb} = {sb}', S = S' and T = T'


JTOUCH = 2
YES
NO
Calculate A from Equation 5.60
JTOUCH = 1
YES
NO
Calculate b_1 from Equation 5.77
Calculate A from Equation 5.76
JTOUCH = 0
Calculate b_1 from Equation 5.74
Calculate b_2 from Equation 5.75
Calculate A from Equation 5.73
Calculate $\{\partial F/\partial\sigma'\}$ and $\{\partial P/\partial\sigma'\}$ from Equations 5.68-5.70 with $p'_b = p'^{t}_b$, $\{s_b\} = \{s_b\}^t$, $S = S^t$ and $T = T^t$
Calculate A from Equation 2.24


Calculate changes in plastic strains from Equation 2.12
Calculate changes in stresses from Equation 2.23
Calculate dp'_o from Equation 5.4
JTOUCH = 2
YES
NO
Calculate dp'_b and $\{ds_b\}$ from Equation 5.47 and dp'_a and $\{ds_a\}$ from Equation 5.40
JTOUCH = 1
YES
NO
Calculate W from Equation 5.79
Calculate dp'_b and $\{ds_b\}$ from Equation 5.47 and dp'_a and $\{ds_a\}$ from Equation 5.33
JTOUCH = 0
Calculate S from Equation 5.78
Calculate dp'_b and $\{ds_b\}$ from Equation 5.41 and dp'_a and $\{ds_a\}$ from Equation 5.39


JTOUCH = 0 at the beginning of the substep and S ≠ 1.0
NO
YES
The yield surface is touching the history surface at the end of the substep
NO
YES
Calculate proportion of the substep to reach the history surface
The new stress state is outside the bounding surface
YES
Set J_1 = 1 and JTOUCH = 1
NO
Set JTOUCH = 1,
$p'_b{}^t = p'_a$, $\{s_b\}^t = \{s_a\}$
S^t = 1.0 and T^t = T
Go back to calculate the remainder of the substep with the history surface as the active yield surface


(JTOUCH = 1) or (JTOUCH = 0 and S = 1.0)
NO
YES
(J_1 = 0 and the yield surface is touching the bounding surface at the end of the substep) or (J_1 = 1)
NO
YES
Calculate proportion of the substep to reach the history surface
Set JTOUCH = 2,
$p'_b{}^t = 0.5p'_o$, $\{s_b\}^t = 0.0$,
$S^t = 1.0$, $T^t = 1.0$
Go back to calculate the remainder of the substep with the bounding surface as the active yield surface
END

Appendix V

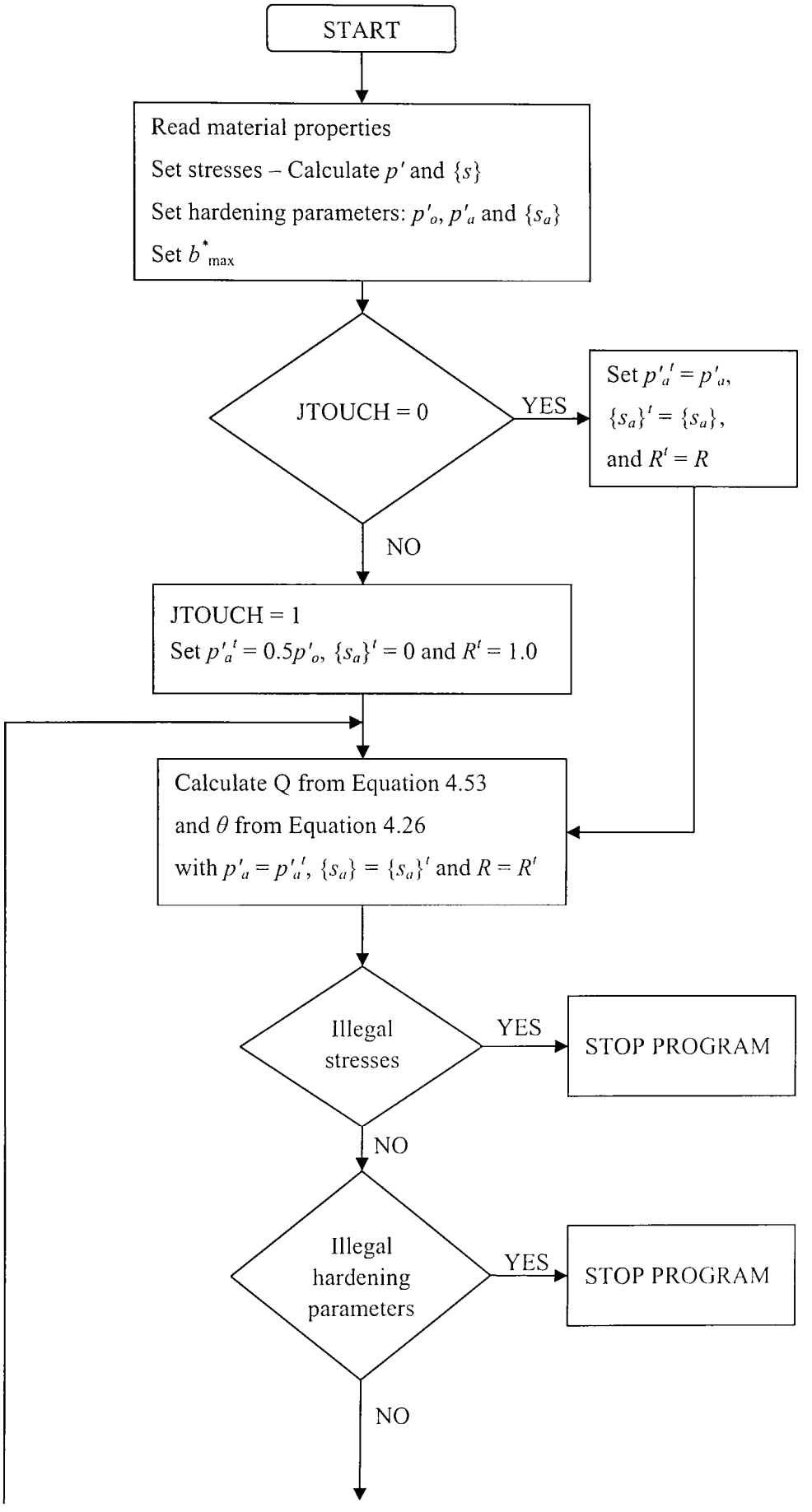
Flowchart for the modified two-surface model

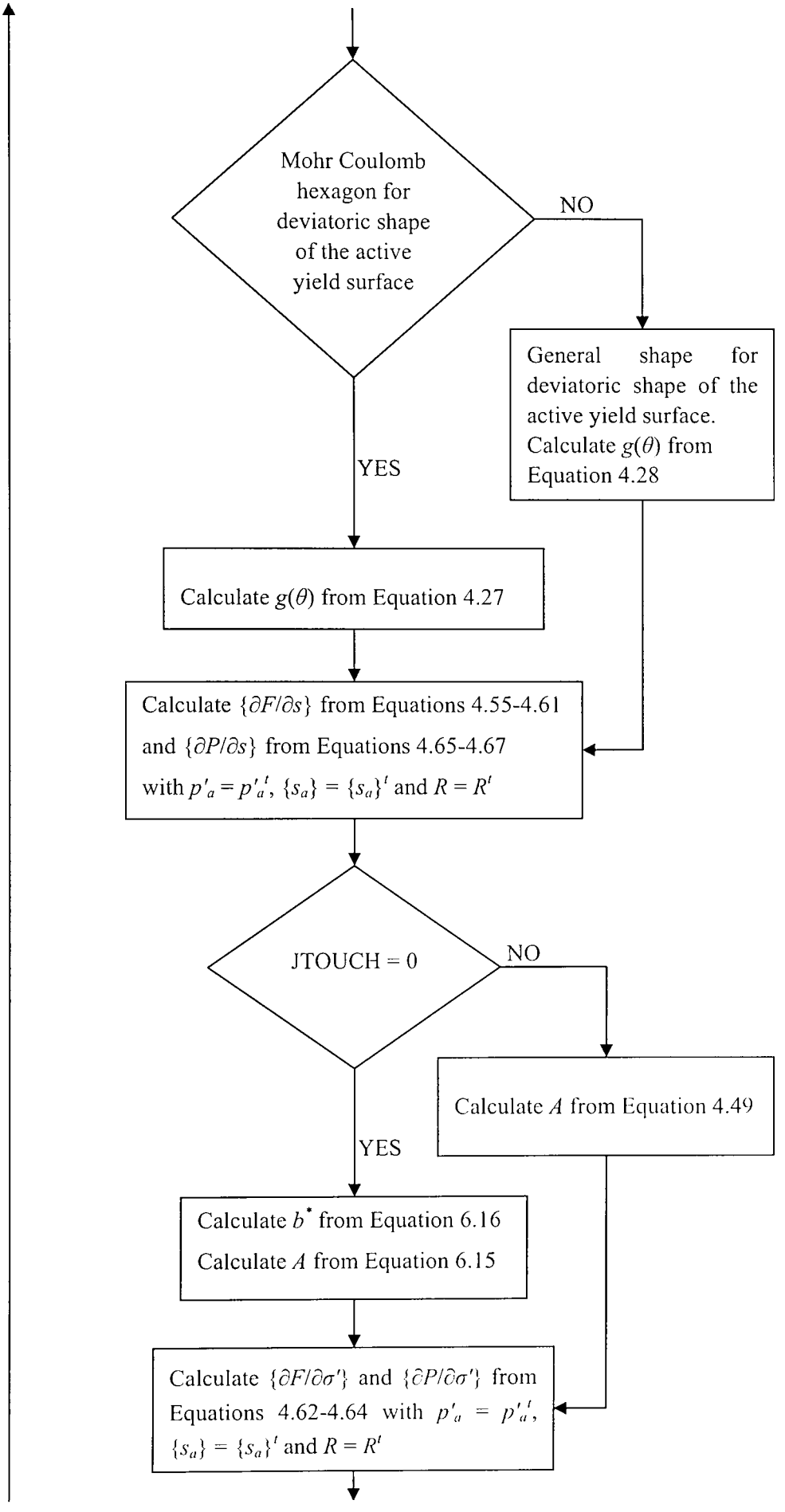
The following flowchart is used by the stress point algorithm to calculate the changes in stresses, plastic strains and hardening parameters during a substep. The yield and plastic potential derivatives are calculated by using appropriate temporary values of p'_a, $\{s_a\}$ and R, depending on which is the active yield surface, similarly to the two-surface model. The parameter JTOUCH is again used in order to identify the relative positions of the surfaces.

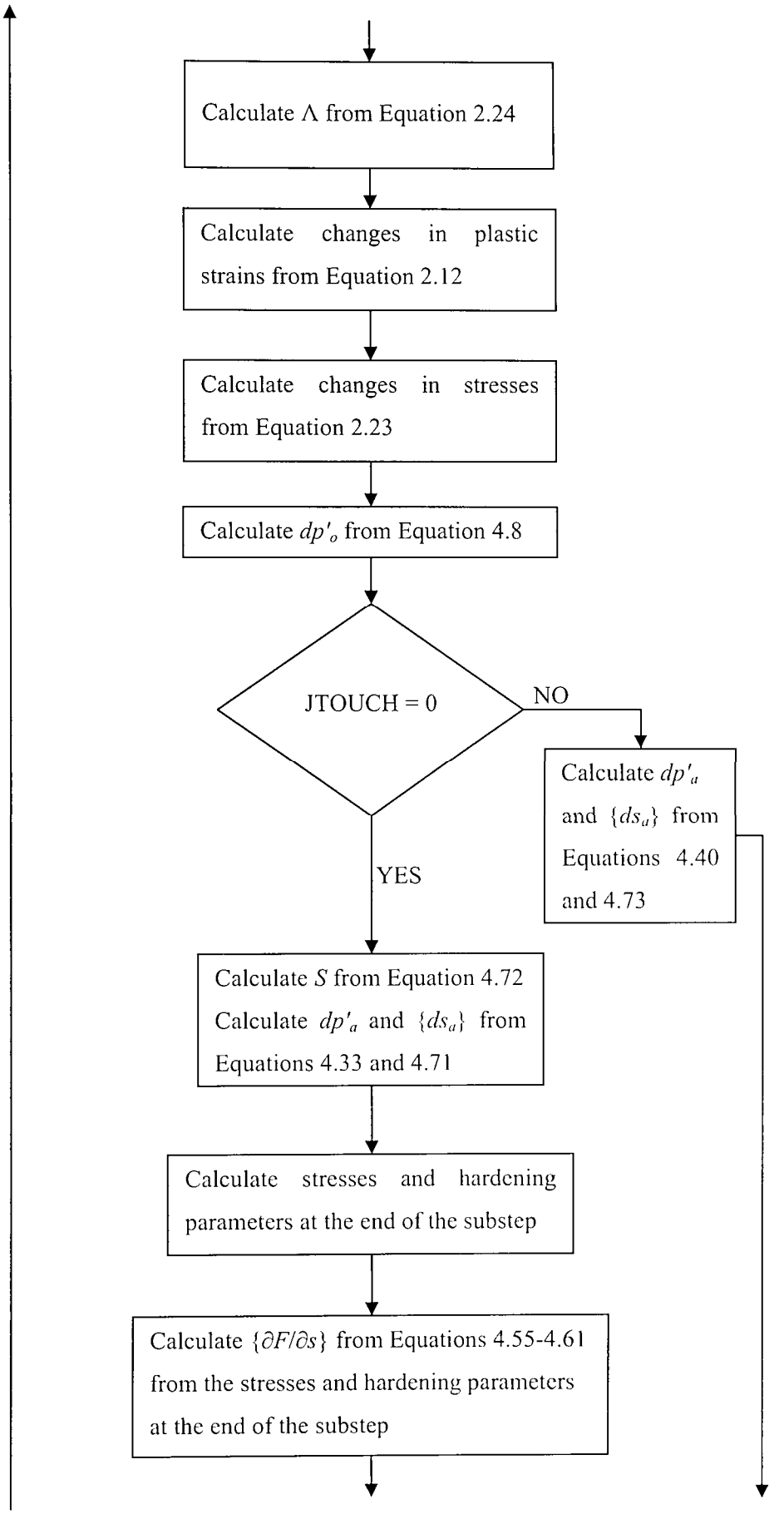
JTOUCH = 0 : If the kinematic yield surface and bounding surface are not in contact. In this case the kinematic yield surface is the active yield surface. The temporary values are $p'^{t}_{a} = p'_a$, $\{s_a\}^t = \{s_a\}$ and $R^t = R$.

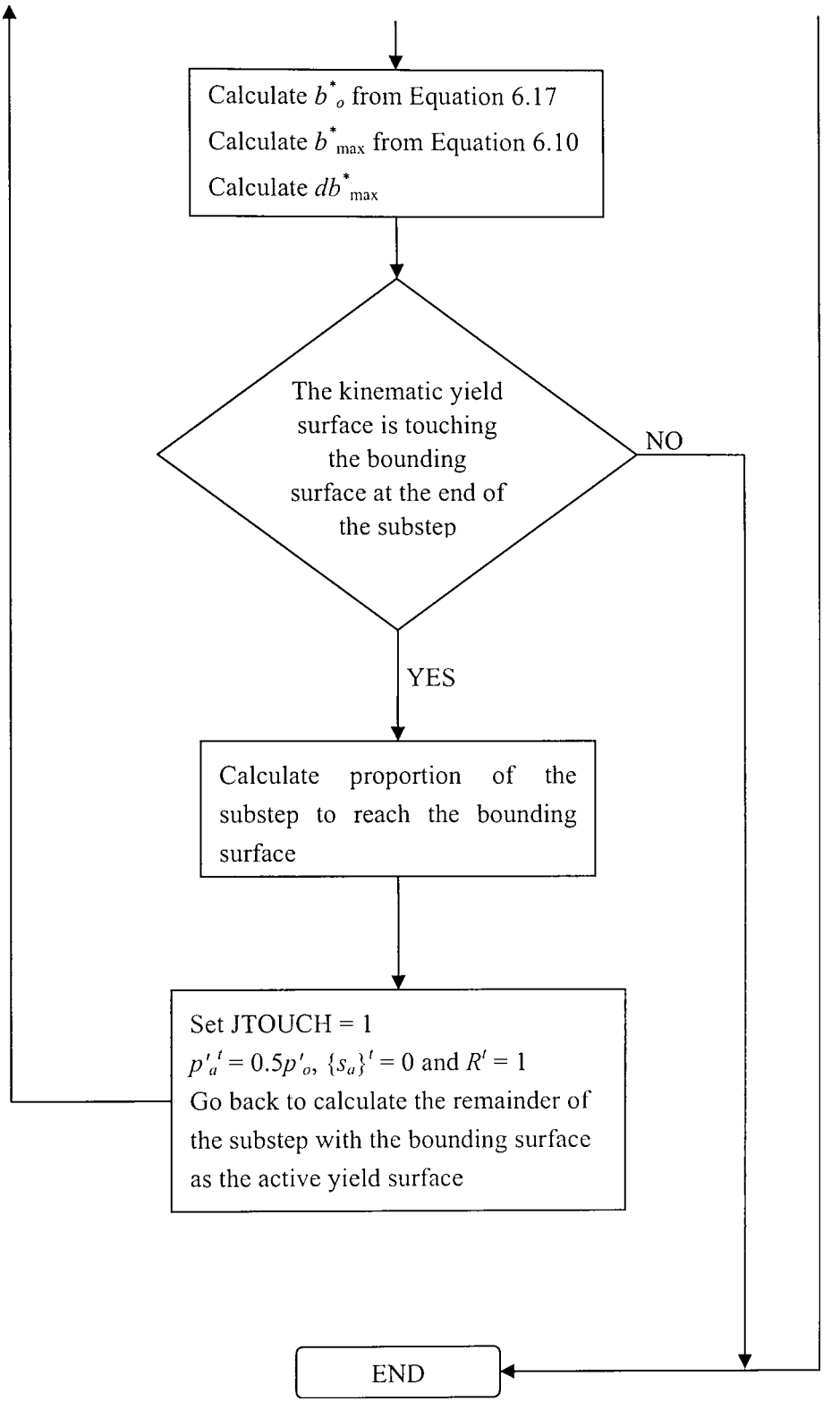
JTOUCH = 1 : If the two surfaces are in contact. In this case the bounding surface is the active yield surface. The temporary values are $p'^{t}_{a} = 0.5p'_o$, $\{s_a\}^t = 0$ and $R^t = 1.0$.

In this model the maximum value of b^*, b^*_{max}, is set equal to b^* upon initiation of yielding. For any subsequent stage the calculation of the value of b^*_{max} (Equation 6.10) requires information from the previous loading stage. Therefore, the value of b^*_{max} that is required at the beginning of a substep can be calculated from the end of the previous substep. This means that in the stress point algorithm the value of b^*_{max} can be treated as a hardening parameter (see section 3.4.1.1). The calculation of b^*_{max} at the end of the substep also requires the additional calculation of the yield function derivatives at the end of the substep.


START
Read material properties
Set stresses – Calculate p' and $\{s\}$
Set hardening parameters: p'_o, p'_a and $\{s_a\}$
Set b^*_{max}
JTOUCH = 0
YES
Set $p'^t_a = p'_a$,
$\{s_a\}^t = \{s_a\}$,
and $R^t = R$
NO
JTOUCH = 1
Set $p'^t_a = 0.5p'_o$, $\{s_a\}^t = 0$ and $R^t = 1.0$
Calculate Q from Equation 4.53
and θ from Equation 4.26
with $p'_a = p'^t_a$, $\{s_a\} = \{s_a\}^t$ and $R = R^t$
Illegal stresses
YES
STOP PROGRAM
NO
Illegal hardening parameters
YES
STOP PROGRAM
NO


Mohr Coulomb hexagon for deviatoric shape of the active yield surface
NO
YES
General shape for deviatoric shape of the active yield surface. Calculate $g(\theta)$ from Equation 4.28
Calculate $g(\theta)$ from Equation 4.27
Calculate $\{\partial F/\partial s\}$ from Equations 4.55-4.61 and $\{\partial P/\partial s\}$ from Equations 4.65-4.67 with $p'_a = p'^{t}_a$, $\{s_a\} = \{s_a\}^t$ and $R = R^t$
JTOUCH = 0
NO
YES
Calculate A from Equation 4.49
Calculate b^* from Equation 6.16
Calculate A from Equation 6.15
Calculate $\{\partial F/\partial \sigma'\}$ and $\{\partial P/\partial \sigma'\}$ from Equations 4.62-4.64 with $p'_a = p'^{t}_a$, $\{s_a\} = \{s_a\}^t$ and $R = R^t$


Calculate Λ from Equation 2.24
Calculate changes in plastic strains from Equation 2.12
Calculate changes in stresses from Equation 2.23
Calculate dp'_o from Equation 4.8
JTOUCH = 0
NO
YES
Calculate dp'_a and $\{ds_a\}$ from Equations 4.40 and 4.73
Calculate S from Equation 4.72
Calculate dp'_a and $\{ds_a\}$ from Equations 4.33 and 4.71
Calculate stresses and hardening parameters at the end of the substep
Calculate $\{\partial F/\partial s\}$ from Equations 4.55-4.61 from the stresses and hardening parameters at the end of the substep


Calculate b^*_o from Equation 6.17
Calculate b^*_{max} from Equation 6.10
Calculate db^*_{max}
The kinematic yield surface is touching the bounding surface at the end of the substep
NO
YES
Calculate proportion of the substep to reach the bounding surface
Set JTOUCH = 1
$p'^t_a = 0.5p'_o$, $\{s_a\}^t = 0$ and $R^t = 1$
Go back to calculate the remainder of the substep with the bounding surface as the active yield surface
END

Appendix VI

Flowchart for the modified three-surface model

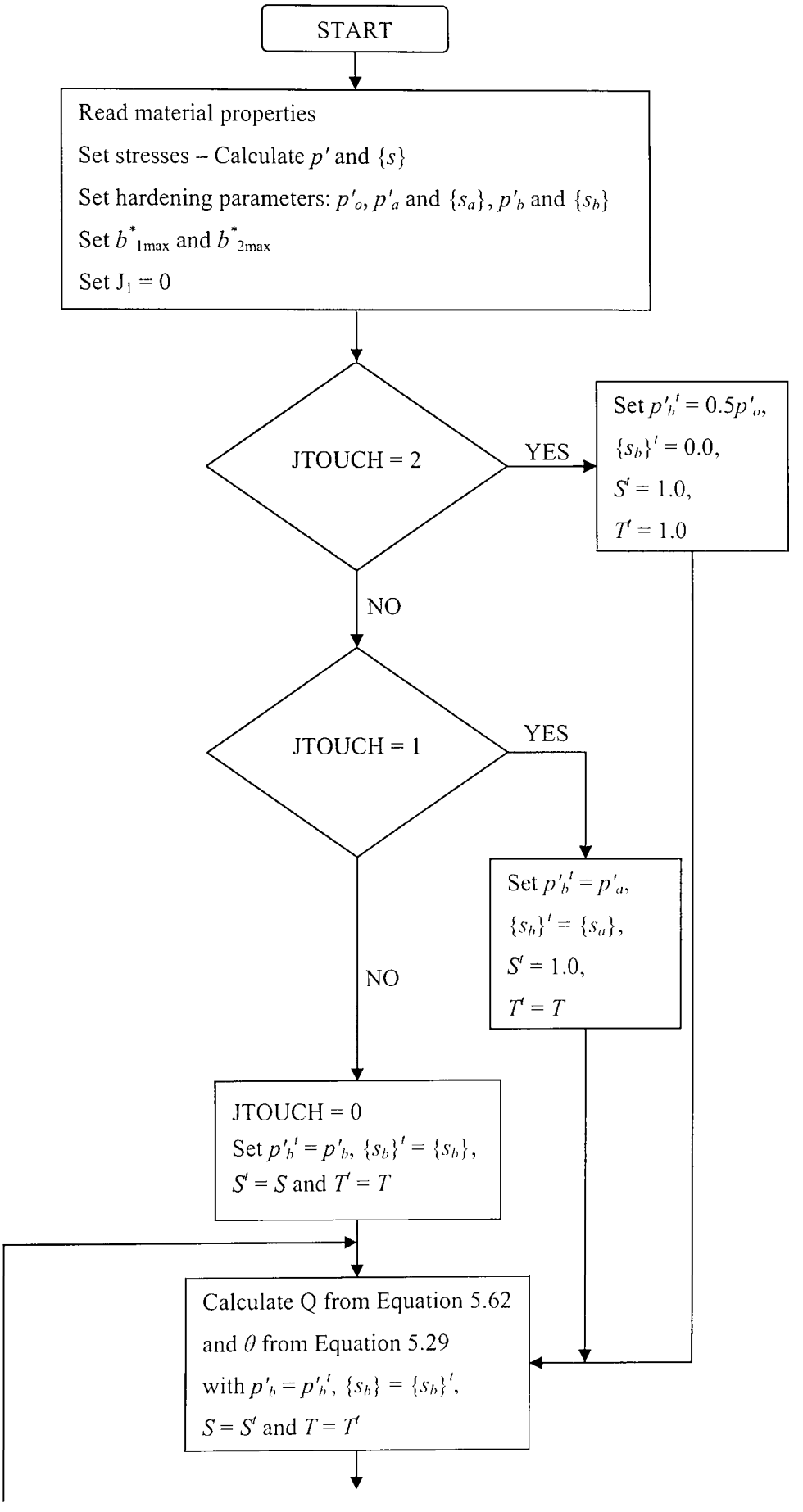
This flowchart is used by the stress point algorithm to calculate the changes in stresses, plastic strains and hardening parameters during a substep. The yield and plastic potential derivatives are calculated by using appropriate temporary values of p'_b, $\{s_b\}$, S and T, depending on which is the active yield surface, similarly to the three-surface model. The parameter JTOUCH is used in order to identify the relative positions of the surfaces.

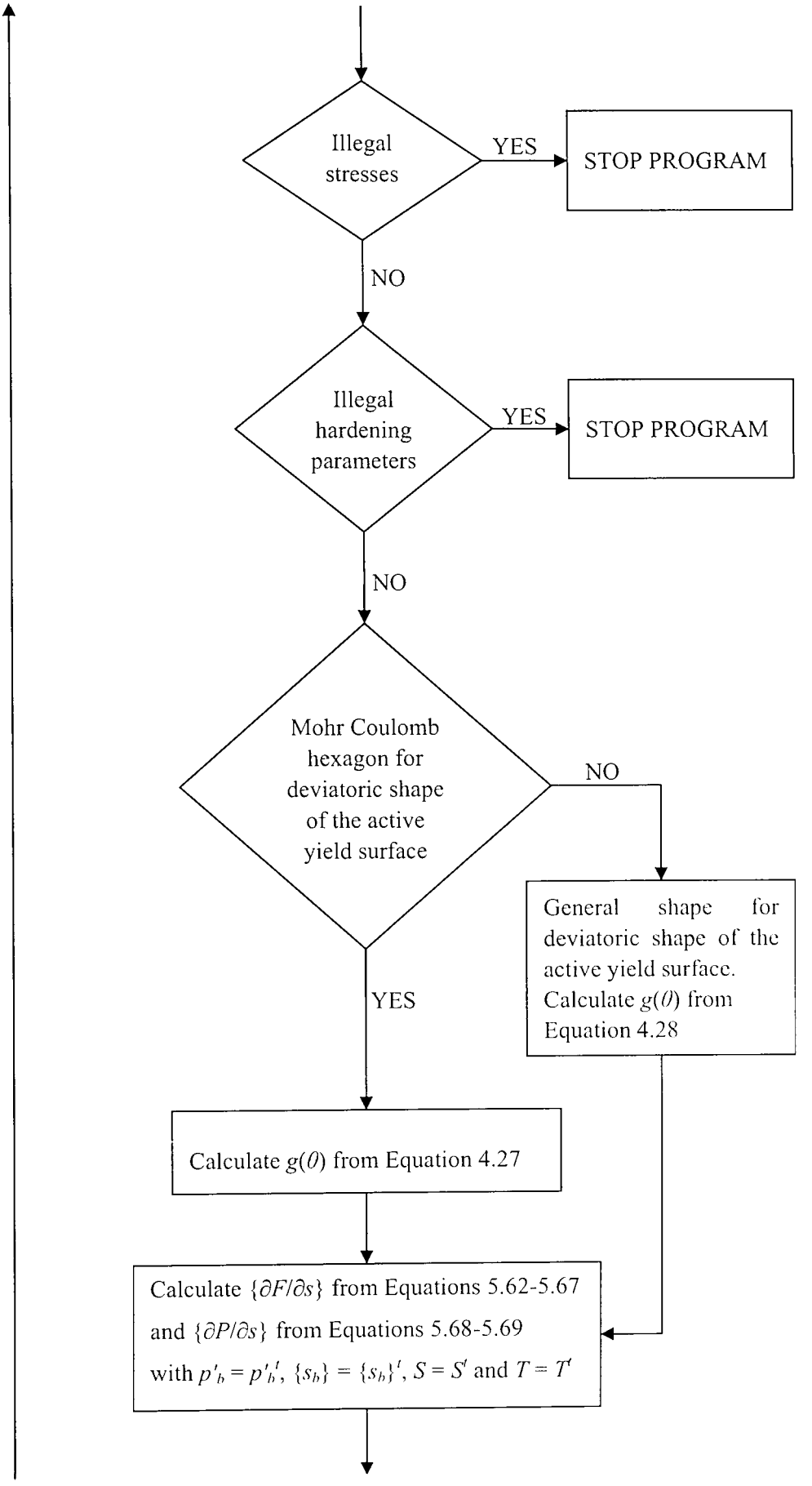
JTOUCH = 0 : If none of the surfaces are in contact. In this case the yield surface is the active yield surface. The temporary values are $p'^{t}_{b} = p'_b$, $\{s_b\}^t = \{s_b\}$, $S^t = S$ and $T^t = T$.

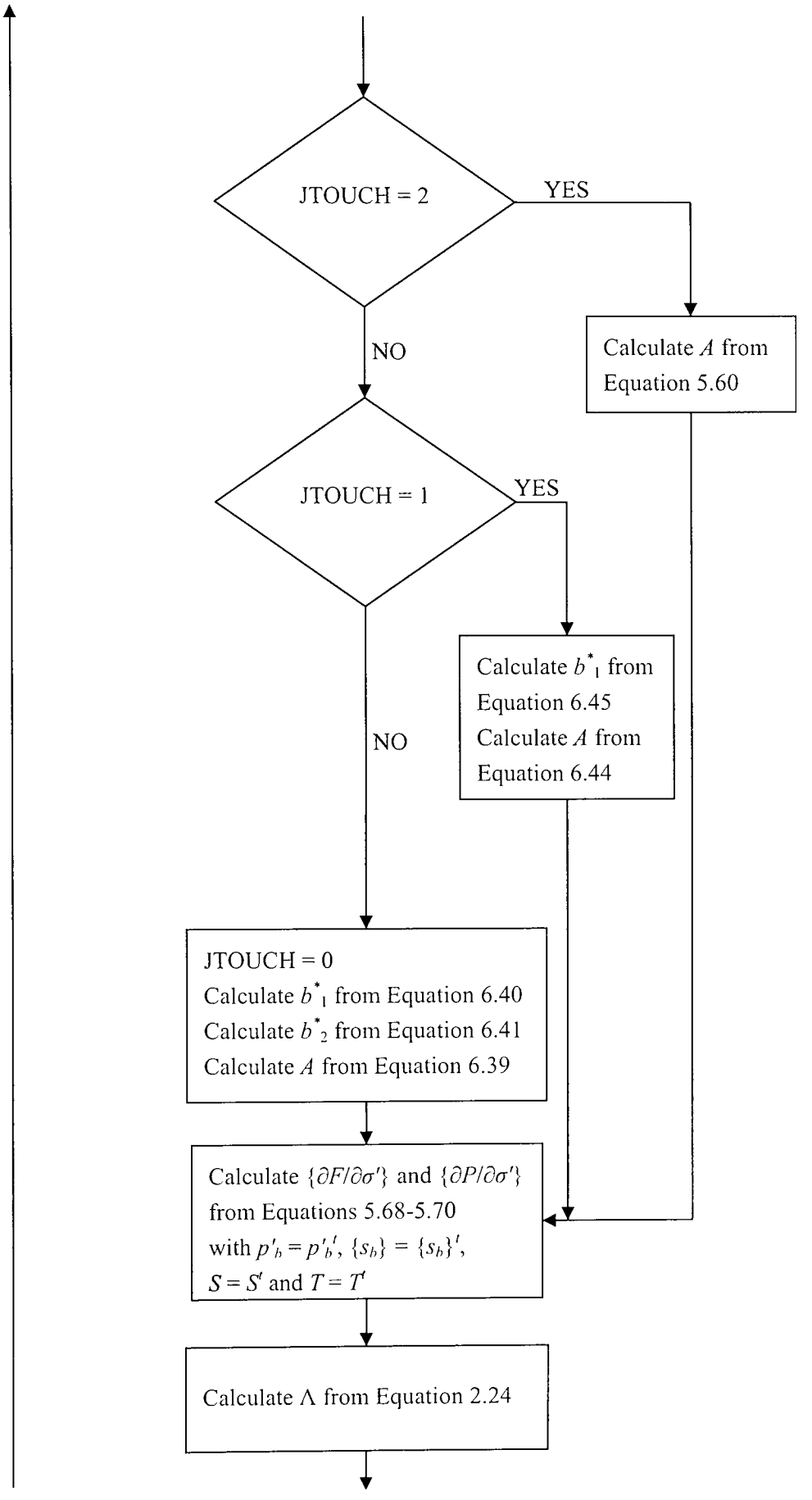
JTOUCH = 1 : If the yield and history surfaces are in contact. In this case the history surface is the active yield surface. The temporary values are $p'^{t}_{b} = p'_a$, $\{s_b\}^t = \{s_a\}$, $S^t = 1.0$ and $T^t = T$.

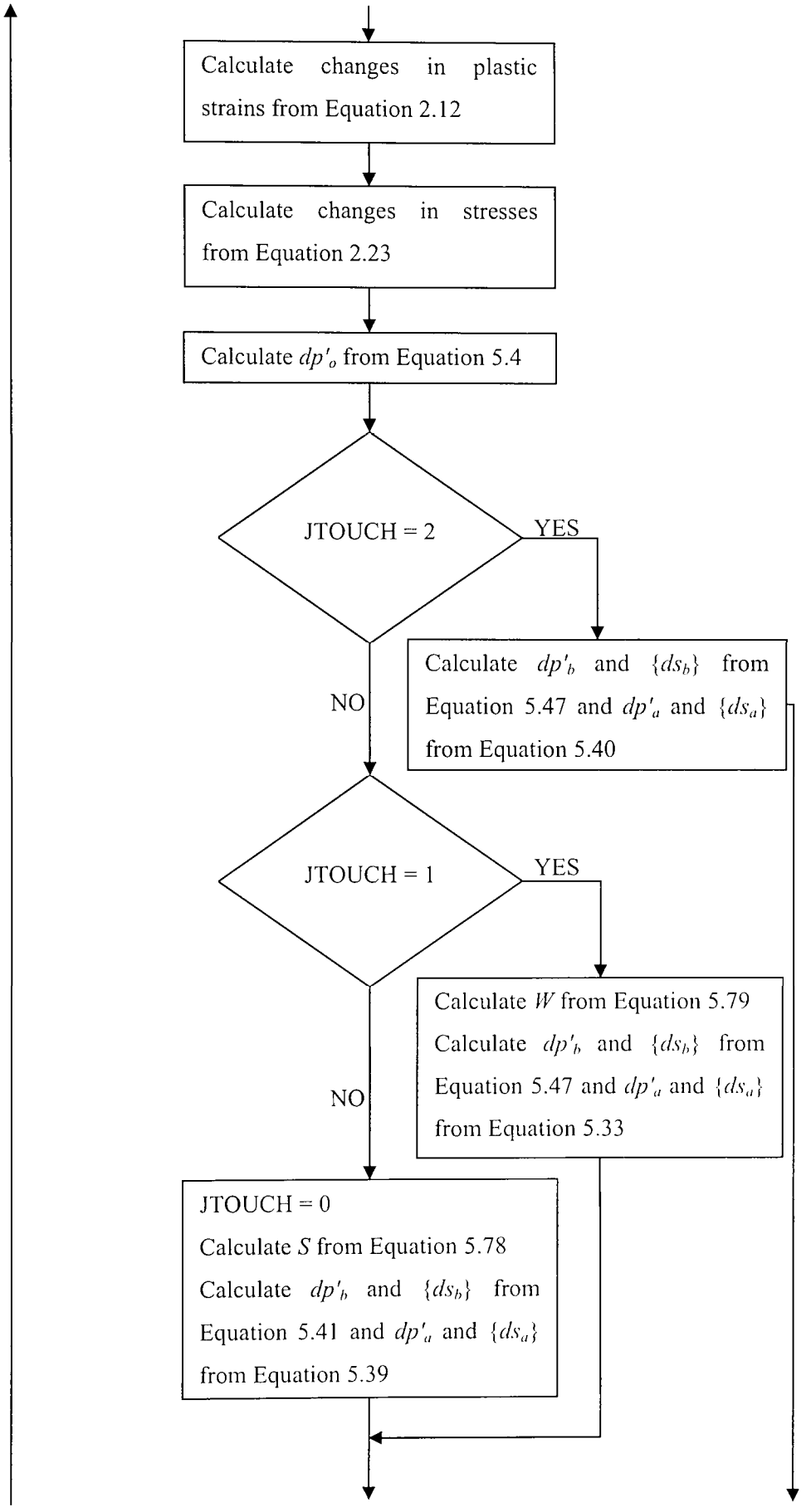
JTOUCH = 2 : If all three surfaces are in contact. In this case the bounding surface is the active yield surface. The temporary values are $p'^{t}_{b} = 0.5p'_o$, $\{s_b\}^t = 0.0$, $S^t = 1.0$ and $T^t = 1.0$.

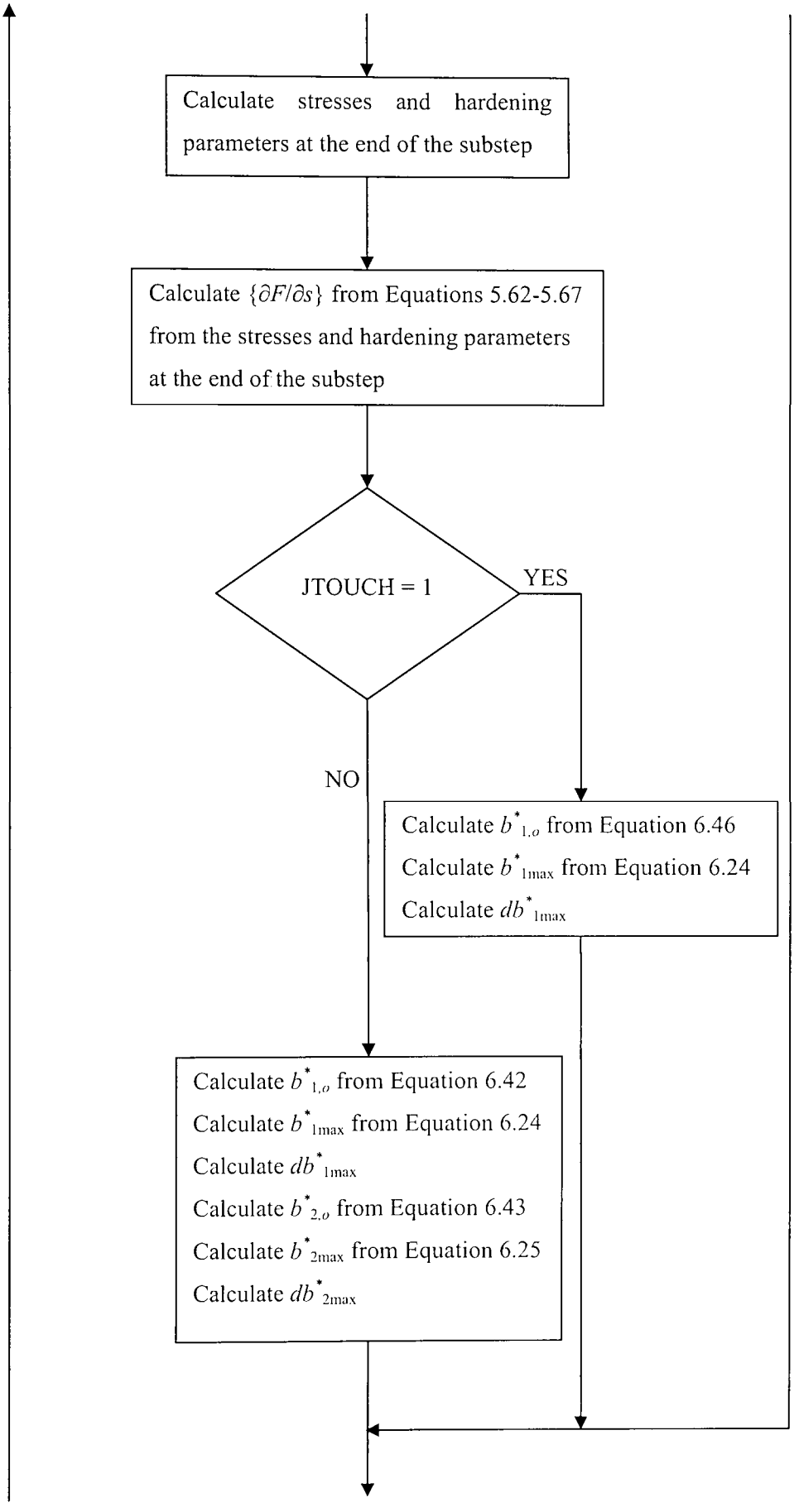
The maximum values b^*_{1max} and b^*_{2max} are set equal to b^*_1 and b^*_2 upon initiation of yielding and for any subsequent stage can be calculated from Equations 6.24 and 6.25 respectively. Similar to the implementation of the modified two-surface model, the values of b^*_{1max} and b^*_{2max} required at the beginning of a substep are calculated from the end of the previous substep and in the stress point algorithm b^*_{1max} and b^*_{2max} are treated as hardening parameters.

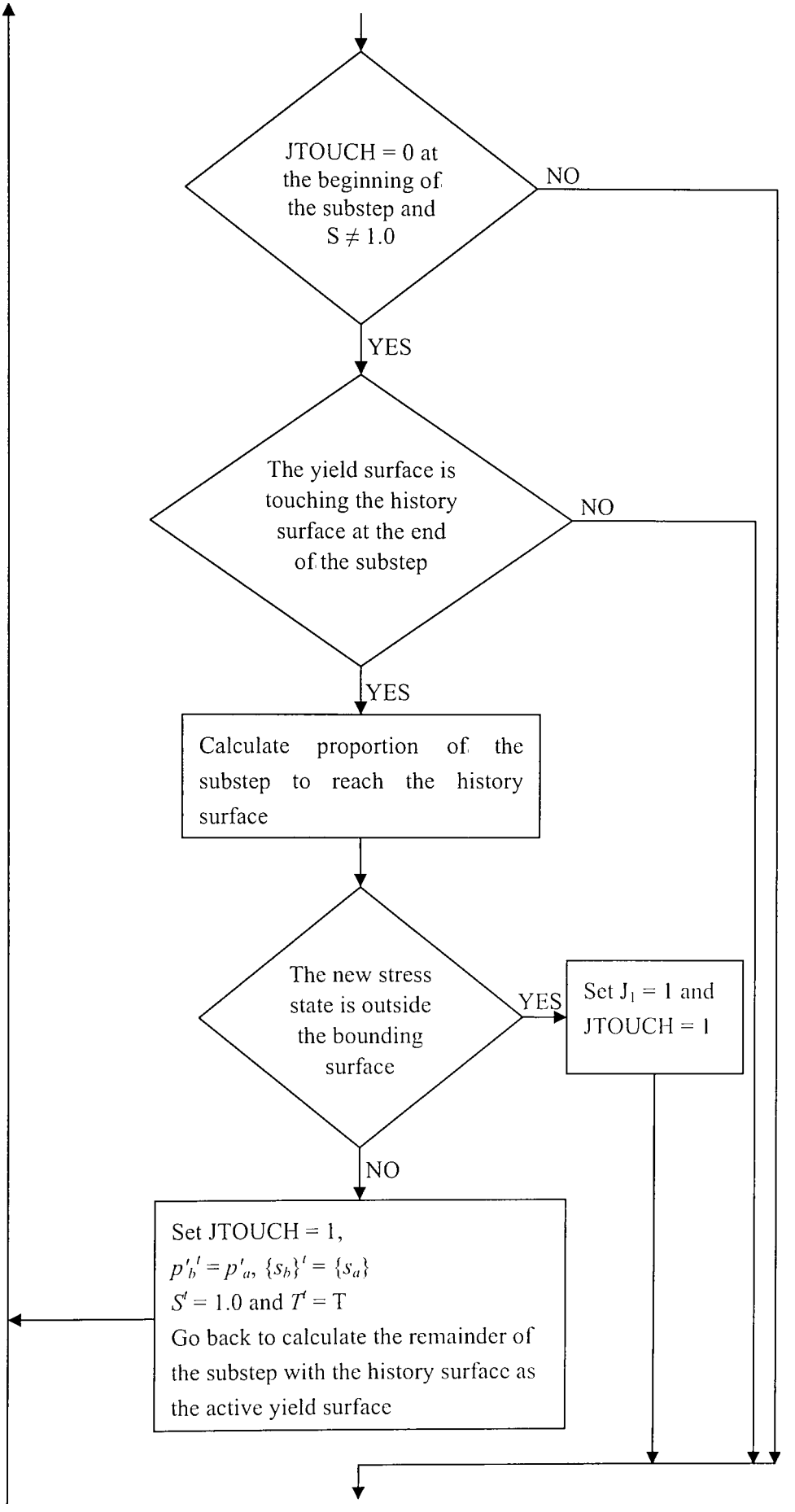

START
Read material properties
Set stresses – Calculate p' and $\{s\}$
Set hardening parameters: p'_o, p'_a and $\{s_a\}$, p'_b and $\{s_b\}$
Set b^*_{1max} and b^*_{2max}
Set $J_1 = 0$
JTOUCH = 2
YES
Set $p'^t_b = 0.5p'_o$,
$\{s_b\}^t = 0.0$,
$S^t = 1.0$,
$T^t = 1.0$
NO
JTOUCH = 1
YES
Set $p'^t_b = p'_a$,
$\{s_b\}^t = \{s_a\}$,
$S^t = 1.0$,
$T^t = T$
NO
JTOUCH = 0
Set $p'^t_b = p'_b$, $\{s_b\}^t = \{s_b\}$,
$S^t = S$ and $T^t = T$
Calculate Q from Equation 5.62
and θ from Equation 5.29
with $p'_b = p'^t_b$, $\{s_b\} = \{s_b\}^t$,
$S = S^t$ and $T = T^t$

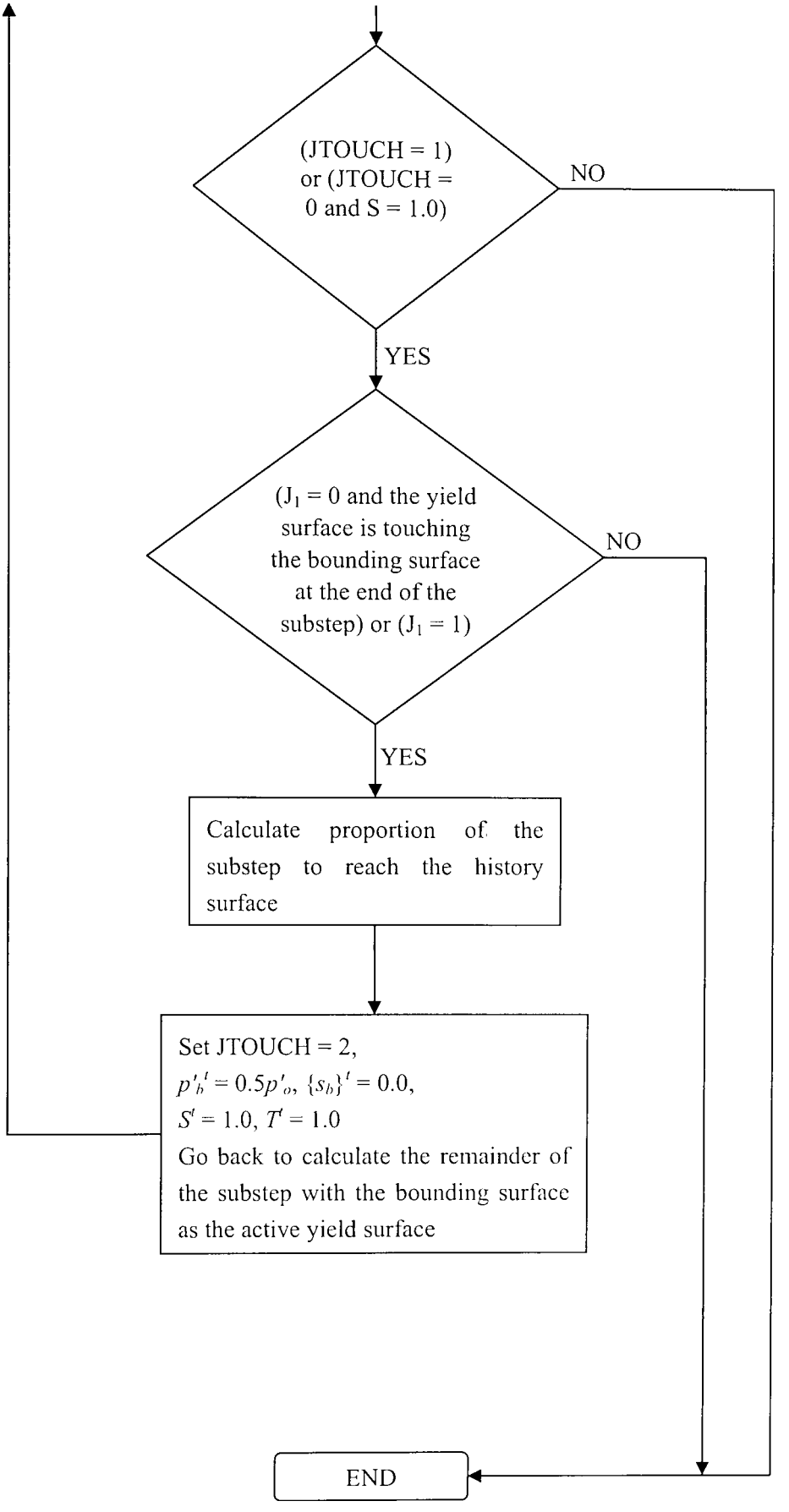

Illegal stresses
YES
STOP PROGRAM
NO
Illegal hardening parameters
YES
STOP PROGRAM
NO
Mohr Coulomb hexagon for deviatoric shape of the active yield surface
NO
General shape for deviatoric shape of the active yield surface. Calculate $g(\theta)$ from Equation 4.28
YES
Calculate $g(\theta)$ from Equation 4.27
Calculate $\{\partial F/\partial s\}$ from Equations 5.62-5.67 and $\{\partial P/\partial s\}$ from Equations 5.68-5.69 with $p'_h = p'^t_h$, $\{s_h\} = \{s_h\}^t$, $S = S^t$ and $T = T^t$


JTOUCH = 2
YES
NO
Calculate A from Equation 5.60
JTOUCH = 1
YES
NO
Calculate b^*_1 from Equation 6.45
Calculate A from Equation 6.44
JTOUCH = 0
Calculate b^*_1 from Equation 6.40
Calculate b^*_2 from Equation 6.41
Calculate A from Equation 6.39
Calculate $\{\partial F/\partial\sigma'\}$ and $\{\partial P/\partial\sigma'\}$ from Equations 5.68-5.70 with $p'_b = p'_b{}'$, $\{s_b\} = \{s_b\}'$, $S = S'$ and $T = T'$
Calculate Λ from Equation 2.24


Calculate changes in plastic strains from Equation 2.12
Calculate changes in stresses from Equation 2.23
Calculate dp'_o from Equation 5.4
JTOUCH = 2
YES
NO
Calculate dp'_b and $\{ds_b\}$ from Equation 5.47 and dp'_a and $\{ds_a\}$ from Equation 5.40
JTOUCH = 1
YES
NO
Calculate W from Equation 5.79
Calculate dp'_b and $\{ds_b\}$ from Equation 5.47 and dp'_a and $\{ds_a\}$ from Equation 5.33
JTOUCH = 0
Calculate S from Equation 5.78
Calculate dp'_b and $\{ds_b\}$ from Equation 5.41 and dp'_a and $\{ds_a\}$ from Equation 5.39


Calculate stresses and hardening parameters at the end of the substep
Calculate {∂F/∂s} from Equations 5.62-5.67 from the stresses and hardening parameters at the end of the substep
JTOUCH = 1
YES
NO
Calculate $b^*_{1,o}$ from Equation 6.46
Calculate b^*_{1max} from Equation 6.24
Calculate db^*_{1max}
Calculate $b^*_{1,o}$ from Equation 6.42
Calculate b^*_{1max} from Equation 6.24
Calculate db^*_{1max}
Calculate $b^*_{2,o}$ from Equation 6.43
Calculate b^*_{2max} from Equation 6.25
Calculate db^*_{2max}


JTOUCH = 0 at the beginning of the substep and S ≠ 1.0
NO
YES
The yield surface is touching the history surface at the end of the substep
NO
YES
Calculate proportion of the substep to reach the history surface
The new stress state is outside the bounding surface
YES
Set J1 = 1 and JTOUCH = 1
NO
Set JTOUCH = 1,
p'b' = p'a, {sb}' = {sa}
S' = 1.0 and T' = T
Go back to calculate the remainder of the substep with the history surface as the active yield surface


(JTOUCH = 1) or (JTOUCH = 0 and S = 1.0)
NO
YES
(J_1 = 0 and the yield surface is touching the bounding surface at the end of the substep) or (J_1 = 1)
NO
YES
Calculate proportion of the substep to reach the history surface
Set JTOUCH = 2,
$p'_b{}^t = 0.5p'_o$, $\{s_b\}^t = 0.0$,
$S^t = 1.0$, $T^t = 1.0$
Go back to calculate the remainder of the substep with the bounding surface as the active yield surface
END